Springer Hydrogeology

Philippe Gourbesville
Jean Cunge
Guy Caignaert *Editors*

Advances in Hydroinformatics

SIMHYDRO 2012 – New Frontiers of Simulation

Springer

Springer Hydrogeology

For further volumes:
http://www.springer.com/series/10174

Philippe Gourbesville · Jean Cunge
Guy Caignaert
Editors

Advances in Hydroinformatics

SIMHYDRO 2012 – New Frontiers of Simulation

Springer

Editors
Philippe Gourbesville
University of Nice-Sophia Antipolis
Sophia Antipolis
France

Guy Caignaert
Society Hydrotechnique of France
Paris
France

Jean Cunge
La Tronche
France

ISBN 978-981-4451-41-3 ISBN 978-981-4451-42-0 (eBook)
DOI 10.1007/978-981-4451-42-0
Springer Singapore Heidelberg New York Dordrecht London

Library of Congress Control Number: 2013946410

Printed on acid-free paper

Springer is part of Springer Science+Business Media (www.springer.com)

Preface

Modeling in fluid mechanics, hydraulics, and hydrology, whether using digital tools or scale models, has reached sufficient maturity to be in daily use by engineers for analysis, design, and for communication. Increasingly complex cases can be handled, thanks to ever more sophisticated tools and increasingly abundant computing power. The emerging environment populated with new generation of sensors, using cloud computing resources, is challenging the current practices of modeling and request innovation in methodology and concepts for a real integration into the decision-makings processes.

With respect to these issues, however, still a number of questions remain open: coupling of models, data acquisition and management, uncertainties, use of 3D CFD, models for complex phenomena, and for large-scale problems. All those points are continuously explored and investigated by researchers, scientist, and engineers. Like in all scientific domains, most recent and advanced developments have to be discussed and shared. The SimHydro 2012 conference contributes to this work by providing a platform exchanges and discussion for the different actors of the water domain.

SimHydro is a permanent cycle of conferences held every 2 years, hosted by Polytech'Nice Sophia Antipolis and organized by the Société Hydrotechnique de France (SHF) and its European partners. It aims, as the subject, recent advances in modeling and hydroinformatics and at the participation and exchanges at European scale (it is open for all other researchers and participants but the purpose is to maintain a specific platform for the region that was a birthplace of both domain). That is why the SimHydro language is English.

The latest SimHydro conference was held in Sophia Antipolis, France, from 12 to 14 September 2012. The conference was jointly organized by the SHF, the Association Française de Mécanique (AFM) and the University of Nice Sophia Antipolis/Polytech Nice Sophia and with the support of IAHR, Eau, and DREAM clusters. The conference has attracted 171 delegates from 38 (although most of them European) countries and who have participated in 14 sessions where 86 papers have been presented. The program was organized around three main themes:

- New trends in modeling for marine, river, and urban hydraulics;
- Stakeholders and practitioners of simulation;
- 3D CFD and applications.

Within (?) these general themes, topics like coupling of models, data assimilation and uncertainties, urban flooding, data and uncertainties in hydraulic modeling, model efficiency and real situations, new methods for numerical models, hydraulic machinery, 3D flows in the near field of structure, and models for complex phenomena have been covered. The conference, by attracting researchers, engineers and decision makers, has promoted and facilitated the dialog between communities with round tables where needs and expectations have been discussed. Exchanges have been very fruitful on crucial questions related to sources of uncertainty in modeling, the state-of-the-art in research and development in domain of numerical fluid mechanics, the stakeholder's capacity to understand results, the means for dialog directly or indirectly between the stakeholders and the model developers, the information's exchange between stakeholders and developers.

In order to contribute to this dialog and to provide useful references, the organizers of SimHydro 2012 have decided to elaborate this book. This volume gathers a selection of the most significant contributions received and presented during the conference. The objective is to provide to the reader a global overview on the on-going developments and the state-of-the-art taking place in three major themes which are:

- The data and uncertainties in hydraulic modeling for engineering and some specific applications of modeling;
- The new numerical methods and approaches for modeling systems;
- 3D computational fluid dynamics and applications.

Obviously, all dimensions of these themes cannot be covered in a single book. However, the editors are convinced that the contents may contribute to provide to the reader essential references for understanding the actual challenges and developments in the hydroinformatics field.

This volume represents the sum of the efforts invested by the authors, members of the scientific committee, and members of the organizing committee. The editors are also grateful for the dedicated assistance of the reviewers who worked tirelessly behind the scene to ensure the quality of the papers. We hope this book will serve as a reference source on hydroinformatics for researchers, scientist, engineers, and managers alike.

Sophia Antipolis, October 2012

Philippe Gourbesville
Jean Cunge
Guy Caignaert

Contents

Part I
Data and Uncertainties in Hydraulic Modeling for Engineering, Specific Applications of Modeling

Introduction to Part I: Data and Uncertainties in Hydraulic Modelling for Engineering, Specific Applications of Modelling

Philippe Gourbesville, Jean Cunge and Guy Caignaert

In this first part, it gathers a global overview of the ongoing developments and applications of hydroinformatics tools and methods in engineering projects. The various chapters provide to the reader a good idea about the various methodologies applied today to investigate some complex phenomena which have to be carefully understood during engineering projects. Most of the applications are based on numerical models which are currently widely used and applied within projects. However, as underlined and demonstrated by Jean Cunge in the first introductive chapter, it is essential to keep in mind the reality of the physical processes that we try to represent with our models and which reflect only a partial dimension of the complex reality under a specific set of conditions. The chapters in Part I show how models could be properly implemented and may provide relevant results.

A major emerging field for hydroinformatics is linked to the assessment in real time of the status of a hydrosystem. Irrigation networks, water distribution systems, and rivers are complex systems which request a constant monitoring and control in order to ensure efficiency and safety in the case of flood warning issue for example. The data mining and control methods, initiated mainly in the industrial domain, have massively invaded the water domain and are today integrated within the systems which are applied for real-time operations. This trend is constantly supported by the growing performances and the availability of the computing resources. The possibilities offered by the parallel computing and the access to high-performance computing resources allow today to run in real time

P. Gourbesville (✉)
University of Nice-Sophia Antipolis, 930 Route Des Colles 06903 Sophia Antipolis, France
e-mail: gourbesv@unice.fr

J. Cunge
31 Rue Doyen Gosse 38700 La Tronche, France
e-mail: jacunge@orange.fr

G. Caignaert
Society Hydrotechnique of France, 25 Rue des Favorites 75015 Paris, France
e-mail: Philippe.Gourbesville@unice.fr

P. Gourbesville et al. (eds.), *Advances in Hydroinformatics*,
Springer Hydrogeology, DOI: 10.1007/978-981-4451-42-0_1,

some of the most sophisticated deterministic models, which can assist the decision-making process. At the same time, the new facilities do not solve all difficulties and the difficult issues of the uncertainty remain a central question for all applications. In the chapter, different approaches are presented in order to quantify uncertainties and to express them to public. This last point still represents a major challenge for the engineering community which has to communicate to the public on sensitive subject like dam break.

If the numerical models are widely used and performed in many engineering project, some specific cases may request the use of physical and scale models. The complexity of processes especially when physical processes like sediment transport are involved represents a limit of the existing deterministic models and is associated with a large uncertainty. The physical experiment associated with the numerical simulations may significantly help to improve the quality of the simulations by reducing the uncertainty. This type of approach represents a sector where progresses and experiments could support the efficiency of the models. In a similar way, the coupling of models—1D and 2D—demonstrates a clear improvement of results. However, if this approach is being now more and more applied, there is a need to work on the definition of the exchange terms between the two types of models.

The urban domain with the associated water services represents clearly a new frontier for the development of a new generation of hydroinformatics systems which have to be able to integrate a wide range of aspects like the data collection—sensor networks—the decision-making process, and the public awareness. The growing complexity of the urban environment characterized with the densification process and the need of secured services requests the development of a global information system where hydroinformatics elements have to be integrated. Several applications presented in different chapters demonstrate this emerging trend. The availability of sensors and the implementation of monitoring networks will bring in a flow of data in quantities of few orders of magnitude greater than they have existed up to now and that has to be managed. Acquisition, analysis, and storage are some of the new challenges which request new developments. These subjects, introduced by the new generation of devices and by the availability of data, will drive to review some of the actual paradigms and will lead to question of the very concept of what is information. Quality and sustainability of data will become essential issues which have to be answered with the global integration in the information system. At the same time, the water–energy nexus is also appearing especially when optimization is requested to perform some pumping and distribution operations. This link between water and energy represents, for sure, one of the directions where new developments will take place.

What Do We Model? What Results Do We Get? An Anatomy of Modelling Systems Foundations

Jean A. Cunge

Abstract The chapter is a reminder, a follow-up of the road-map that leads from observation of natural situation to colourful presentation of results of modelling that are supplied to the user and decision makers. It is unfortunate matter of fact that too many people involved in modelling do not know how the very heart of the software they use was conceived and on what physical and mathematical hypotheses it is based. Most of the users do not realise what are the limitations in the validity of the results that may be traced back to the limitations of the stages of this road-map. Using as the departure point and an example 1D modelling, the chapter describes and, up to a point, lists the chain of intellectual activities that can be summarised as follows: observation of the nature (flow); hypotheses concerning main physical phenomena; formulation of physical laws (e.g. conservation laws) for isolated systems where only these phenomena exist; mathematical formulation of these laws (differential, integral, etc., equations); parameterisation of phenomena not described by equations; impossibility to solve the equations; numerical algorithms solutions of which converge to those of equations; interpretation of parameters and approximate solutions obtained from algorithms; interpretation of results. The purpose is to let the users of commercial software to understand how the very heart of the modelling system they use was conceived and why the validity of the results obtained in the end is limited by the hypotheses of the original concept. In conclusions, the following question is put to the reader: can a modeller who is not sufficiently knowledgeable about all the links of this chain tell his "client" what are possible doubts or deviations between what was just simulated and the reality?

Keywords Numerical simulation · Computational hydraulics · De Saint–Venant hypotheses · Numerical solutions · Results of modelling and hypotheses of equations

J. A. Cunge (✉)
SHF, Erasmus Mundus Project Euro-Aquae, 31 Rue Doyen Gosse
38700 La Tronche, France
e-mail: jacunge@orange.fr

P. Gourbesville et al. (eds.), *Advances in Hydroinformatics*,
Springer Hydrogeology, DOI: 10.1007/978-981-4451-42-0_2,

1 Introduction

When use of numerical simulation in hydraulics or, in much larger area of water industry and management is considered, one may in legitimate way ask oneself the question: what should a modeller, a user of a commercial modelling software, know about the very heart of it, that is, about how the basic knowledge of physics has been represented in the software he uses and resulted in output pictures he sees (or forwards to his client) on the screen? There are the notions that are introduced in the debate that the present author considers as possibly dangerous if not well understood. One of those is the notion introduced into the hydro technical world by Abbott [1, 2] that there are groups of knowledge providers and knowledge consumers. Unless really well understood (and this asks for careful reading and analysing of the description of these terms in the chapters refereed to), the quick and widely spread conclusion is that the knowledge necessary to model is encapsulated in the software and there is no problem anymore: anybody can model anything with the bought software system. Coming back to knowledge providers and knowledge consumers, the distinction which is supposed to characterise our society, it would be better to talk about technology providers and consumers. Consider an analogy between modeller using commercial software and a car driver. 99 % car drivers in the world have no slightest idea of physical phenomena going in their engine under the bonnet. They have been provided an encapsulated technology package and immense majority of them do not know the principles of explosion engine or diesel one. They learned how to drive but know nothing about scientific and industrial developments that led to this technology and, with a country-dependent variable percentage of killed on the roads, most of drivers are still here, in-spite being knowledge ignoramus. The user is a consumer of the technology that was encapsulated and provided to him by Volkswagen or whatever. I do not feel that he is a knowledge consumer—he has no access to knowledge under any shape to be consumed. It is true that if his ignorance leads to wrong use of this technology, generally the damages are limited (if he runs into a tree) although can be dramatic for limited number of others (if he provokes a head-on collision with other car). The situation is very different with modelling software systems because the modelling results are being used to most important decision concerning investments, structures, management of water systems, etc. Except for very simple situations, a user of modelling software must be indeed knowledgeable about basic hypotheses and physical laws lying as foundations of the software as well as of the methods encapsulated in it. And it can happen that a user of such software who is a technology consumer in the above-described sense of the term, employing the technology "encapsulated" by the "provider", supplies the results and conclusions that provoke, in turn, a catastrophe.

In what follows we shall describe holistically some aspects of one specific area of such "encapsulation" and for one limited class of phenomena only. It concerns the chain of knowledge acquisition and application that leads a creator of the software simulation system to achieve its development. The class of problems

taken as example is essentially one-dimensional unsteady free-surface fixed-bed channel flow. In conclusions, we shall repeat the following question to the reader: can a modeller who is not knowledgeable about all the links of this chain tell his "client" what are possible doubts or deviations between what was just simulated and the reality?

2 Chain of Concepts and Steps Leading from Hypotheses to Results

2.1 Observation of the Nature (Flow): Hypotheses Concerning Main Physical Phenomena

Observation of the flow in any natural or even artificial stream, especially during flood, leads to the conclusion of incredible complexity of details next to impossible to understand or to describe. However, if the local detailed small scale is replaced by the scale of several hundred metres or more the main ideas are obvious: the flow has one privileged direction, the water is subject to gravity forces and also to inertia forces and there certainly exists a resistance to the flow causing energy dissipation. Moreover, our interest (should we say engineering or macroscopic?) is mainly in knowing what is the free-surface elevation (stage) and discharge along the observed reach and not in details. Since the area of the wetted cross section A is defined by the water stage y (depth h) then, if the flow has a privileged direction, it is useful to imagine brutal simplification that the water velocity is also directed along this axis. In other words, one assumes that the longitudinal velocity u is so important with respect to the transversal one than the latter can be neglected. Rough observation shows that water velocity at a given point does not vary much with the depth and, if the cross section is compact and the width reasonable, that the elevation of the free surface across the stream does not vary much neither. These observations led De Saint–Venant to the set of basic hypotheses that are very far from reality but which nevertheless concern essence of phenomena of engineering interest and decisive to overall description of the flow. The hypotheses are listed in the sequel and it is obvious that they can be true only for an idealised situation (Fig. 1):

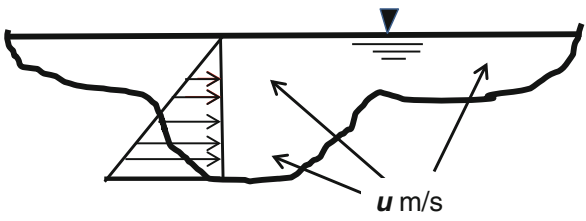

Fig. 1 De Saint–Venant hypotheses

1. Uniform longitudinal velocity u at every point of the cross section.
2. Transversal free surface at any section horizontal.
3. Hydrostatic pressure distribution along each vertical.
4. Head losses can be represented by Chèzy-type formula valid in steady flow.

2.2 Formulation of Physical Laws (e.g., Conservation Laws) for Isolated Systems Where Only These Phenomena Exist: Mathematical Formulation of These Laws (Differential, Integral, etc., Equations)

The simplified, idealised situation is concerned: a flow along inclined channel of constant slope and a cross section $A(y)$. A classic approach is to analyse a control volume contained spatially 'between two verticals distant Δx one from another and temporarily between two instants separated by time Δt. The control volume is supposed to be an isolated system between two cross sections distant Δx and between two instants separated by the time Δt volume of water of which (with balance due to inflow and outflow) as well as the energy must be conserved. These two conservation laws are the foundation from which it is possible to draw mathematical equations. For the volume, it is obvious: if during time interval Δt there is more water discharge Q inflowing into the control module then outflowing, then the elevation y and cross section A will increase. For the energy, because of its dissipation, the sum of potential and kinetic energies decreases over the distance Δx and varies with time. The kinetic energy is expressed in terms of time and space variations of section-constant velocity $u = Q/A$. The decrease in the total energy is equal to its dissipation over the distance Δx. Assuming that ($\Delta x \to 0$; $\Delta t \to 0$) one obtains two equations known as De Saint–Venant equations:

Conservation of the volume within an infinitely short control volume:

$$\frac{\partial A}{\partial t} + \frac{\partial Q}{\partial x} = 0; \quad Q = uA;\ A = A(y) \tag{1}$$

And conservation of the energy within this volume:

$$\frac{1}{g}\left\{\frac{\partial u}{\partial t} + \frac{\partial}{\partial x}\left[\frac{u^2}{2}\right]\right\} + \frac{\partial y}{\partial x} = Ku|u| \tag{2}$$

where $K = K(n, h)$, $h =$ depth, $n =$ empirical parameter of energy dissipation (or resistance to the flow).

2.3 Parameterisation of Phenomena Not Described by Equations

Antoine Chézy was the first one to note that in a long channel of constant slope the "initial flow velocity …diminishes or augments rapidly enough to reduce to a

uniform and constant velocity which is due to the slope of the channel and to gravity, of which effect is restrained by the resistance of *friction* against the channel boundaries". And further on: "…velocity due to gravity…is only uniform when it no longer accelerates, and gravity does not cease to accelerate except when its action upon the water is equal to the resistance occasioned by the boundary of the channel; but the resistance is as the square of the velocity because of the number and the force of the particles colliding at the given time; it is also a part of the perimeter of the section of the flow which touches the boundary of the channel" [3]. Everything is said. Chézy used the *concept* of friction analogy to describe the energy dissipation: there is a resistance (energy dissipation) that until today we do not know how to formalise its exact mechanism (which is the turbulence). Its scale and complexity are not in proportion with our purpose: to describe the flow over "engineering" length. Hence, the need to parameterise these complex mechanisms keeping essential factors in: resistance is proportional to the square of the velocity and to the wetted perimeter or, inversely, the velocity u is proportional to the square root of the slope S and hydraulic radius R. This is the Chézy formula:

$$u = k\sqrt{SR} \tag{3}$$

Note that the coefficient k is the parameter that replaces the description of the process of energy dissipation (something we still cannot pretend to know well and to be able to formulate correctly). Note also that while in De Saint–Venant equations k is the only one empirical and subjective parameter, the Chézy formula (and then its follow-ups such as Manning or Strickler formulas) is valid but for steady-state flow. Thus, De Saint–Venant hypothesis that "the resistance law is the same as for steady-state flow" may in certain situations be questionable.

2.4 Impossibility to Solve the Equations and Conditions of Existence of the Solutions

To solve the problem as stated by De Saint–Venant means to find two *continuous differentiable* functions of independent variables u(x, t) and y(x, t) satisfying Eqs. (1) and (2). It must be kept in mind of a modeller that such *solution would be the description of the situation limited by the hypotheses and not the full description of real-life flow*. Hence, it is not possible to expect from the solution anything more (e.g., nonuniform velocity repartition, information on transversal slope of free-surface or transversal velocity component). Moreover, we cannot solve these two equations. Indeed, the two De Saint–Venant equations are a system of two non-linear partial differential equations of hyperbolic type. The problem is that mathematics do not know how to solve *exactly* such equations. If we consider a simple partial differential equation such as:

$$\frac{\partial f}{\partial t} + a\frac{\partial f}{\partial x} = 0; \quad f(x,0) = f_0(x), \ -\infty < x < +\infty \tag{4}$$

then we know that there exists exact, "analytical" solution for this equation:

$$f(x,t) = f_0(x - at) \tag{5}$$

But for De Saint–Venant equations such solution is not available has not been found by mathematicians. Let us consider a space (*x, t*) and half space of it $t > 0$. Then, it has been proved that *if* there exist initial conditions smooth enough, that is, if at the time $t = 0$, there do exist functions $u(x, 0)$ and $y(x, 0)$ *and* their derivatives, then the *existence* of solutions for some time interval $0 < t < T$ can be proved. This is what we call the *initial well-posed problem*: we know that solution exists but we cannot find it under exact closed form. Hence, there is necessary to seek an approximate (numerical) solution. Situation is even more complicated when finite length of the stream is considered (x segment is $x_0 < x < x_L$). It is still possible to prove that the solution exists for $0 < t < T$ within these space limits but the *mixed problem* (initial and boundary conditions) must be well posed. That means that appropriate boundary conditions and continuous solutions of Eqs. (1) and (2) must be given at the boundaries $x = x_0$ and $x = x_L$ for all $t > 0$. The case of unsteady subcritical flow and upstream boundary condition provides an illustration of the fact that things are not as simple as they may look or be presented. While imposing $u(x_0, t)$ or $y(x_0, t)$ corresponds to well-posed problem, it can be proved that imposing a rating curve $Q(y)$ at the upstream boundary $x = x_0$ makes the bounded solution of the problem impossible while the same type of condition (rating curve) at the downstream boundary $x = x_L$ is correct from mathematical point of view. Note, however, that in hydrology practice rating curve function $Q(y)$ is typically single valued and, hence, it corresponds to a *steady*-state flow. When such rating curve is the downstream-imposed boundary condition, it introduces errors to the solution of the *unsteady* flow Eqs. (1) and (2). In other words, the solution with such downstream boundary condition does exist, but in fact, it is not the solution of the original equations! The conclusion and warning is that the Eqs. (1) and (2) alone do not suffice our purpose even if we assume that reality obeys De Saint–Venant hypotheses: the initial and boundary conditions formulated in terms of the independent variables $u(x, t)$ and/or $y(x, t)$ make integral part of the problem that is known as a *mixed* (initial and boundary values) *Cauchy problem*. And, again, it is not the solution that we can find but only conditions of its existence.

2.5 Numerical Algorithms Solutions of Which Converge to Those of the Equations

In order to deal with the difficulty, we have to *replace* Eqs. (1) and (2) and their boundary conditions by some other systems that we *can* solve. This may be justified only if we can prove that the solutions of such surrogate systems are not

very far from the solutions of original equations—those are what we called approximate numerical solutions.

Since we wish only to point out to the conceptual track of creation of the heart of modelling systems, we shall here limit ourselves to just one of various numerical methods of approximation, namely the finite difference methods (FDM). The FDM of integration of systems of differential, integro-differential or integral equations of mathematical physics consist in transformation of derivatives into difference ratios and of integrals into the summations. In practice that means a transfer from the infinite space of functions of continuous arguments to the finite space of grid-functions and transformation of the equations of continuous functions into algebraic equations for which exist numerical methods to find approximate solution.

Note the original equations are replaced by algebraic equations, and then, the latter are solved approximately. Two questions are to be answered:

- Is the system of algebraic equations well posed, that is, can it be solved even approximately?
- How to be sure that after such double stage the approximate solution of algebraic systems is not too "far" from the analytical solutions (which cannot be found) of the original systems. And is it possible to reduce the difference between the two?

The grid-functions are the networks or grids of enumerable computational points and *the approximate solutions are sought at these discrete points*. Such approach is convenient in practice, but it introduces difficulties to prove mathematically the convergence of the FDM results to those of the original equations because the approximating grid functions (solution of FDM) and continuous approximated functions (solution of differential equations) are defined in different spaces having different norms. Using more descriptive approach to the problem, consider as in Fig. 2 a grid of computational points distant Δx_i one from another and the Δt_n time intervals for which the solution is sought. Suppose that indeed the unknown values of originally sought continuous functions $u(x, t)$ and $y(x, t)$ are approximated at grid points by FDM approximations $\tilde{u}(x_i, t_n)$, $\tilde{y}(x_i, t_n)$. Suppose now that we refine space grid by using new distance $\Delta x_k = 0.5\ \Delta x_i$. Then, new solution at grid points would be obtained: $\{\hat{u}(x_k, t_n), \hat{y}(x_k, t_n)\}$.

Then, the following questions become legitimate:

1. What is the difference between the solutions $\{u(x, t), y(x, t)\}$ and $\{(x_i, t_n)\tilde{y}(x_i, t_n)\}$?
2. What is the difference between the solutions $\{\hat{u}(x_k, t_n)\tilde{y}(x_k, t_n)\}$ and $\{(x_i, t_n)\tilde{y}(x_i, t_n)\}$?
3. Is the solution $\{(x_k, t_n)\tilde{y}(x_k, t_n)\}$ "better" than the solution $\{\tilde{u}(x_i, t_n)\tilde{y}(x_i, t_n)\}$?
4. What means "better"?

Note the reasoning and criteria of being better or not should be with respect to the solutions of the original equations. The results obtained are considered as better or worse not in comparing them with the reality but with the unknown solutions of differential equations.

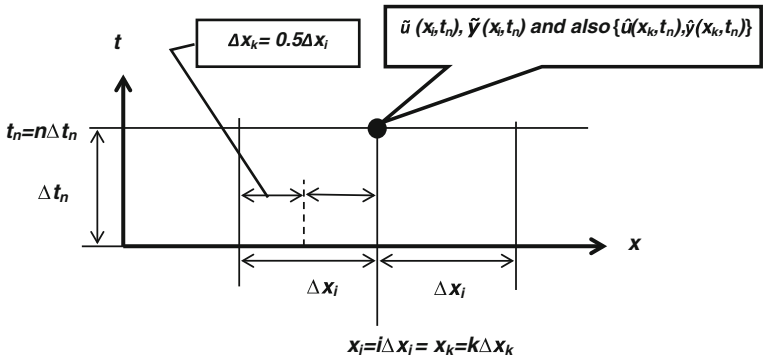

Fig. 2 Grid of computational points

There is no direct way to answer question (1) The question (2) can be answered by running two computations, one with Δx_i and other with $\Delta x_k = 0.5\ \Delta x_i$. But to answer question (3), it is necessary to answer the question (4) first: if one reduces the computational steps dividing them by 2, are approximate solutions converge to the analytical solutions?

The answer is that in general case *it is not true*. To clarify this point, one must take into consideration the way the derivatives in original equations were approximate by finite differences and, hence, how the differential equations themselves were replaced by difference algebraic equations.

Consider simple (as compared with De Saint–Venant Eqs. (1)and (2)) case and the grid (i, n) as in Fig. 2:

$$\frac{\partial f}{\partial t} + \frac{\partial f}{\partial x} = 0; \tag{6}$$

The derivatives can be approximate in various ways for time and space derivatives, for example,

$$\frac{\partial f}{\partial t} \approx \frac{f_i^{n+1} - f_i^n}{\Delta t_n}; \quad \frac{\partial f}{\partial t} \approx \frac{f_i^{n+1} - 0.5(f_{i+1}^n + f_{i-1}^n)}{\Delta t_n}; \tag{7}$$

$$\frac{\partial f}{\partial x} \approx \frac{f_{i+1}^n - f_{i-1}^n}{2\Delta x_i}; \quad \frac{\partial f}{\partial x} \approx \frac{f_{i+1}^n - f_i^n}{\Delta x_i}; \quad \frac{\partial f}{\partial x} \approx \frac{f_i^n - f_{i-1}^n}{\Delta x_i}; \tag{8}$$

Developing grid-functions Eqs. (6), (7) in Taylor series around (i, n) point and substituting in Eq. (6) one finds that differential form Eq. (6) is replaced by a finite difference equation. The unknown values f^{n+1} for each point x_i $i = 1, 2, \ldots, L$ can be then computed with orders of truncation error such as Δx, Δx^2, Δt, Δt^2, or with ratios of these time or space steps. That means that the approximation is each time *consistent* because when $(\Delta x, \Delta t) \to 0$ then the finite difference equation will tend towards differential form of Eq. (6). *But to maintain the degree of consistent*

approximation for each case, both Δx and *Δt must decrease simultaneously and their ratio such as appearing in finite difference equation must be kept constant during this process.* Another important problem is *numerical stability* of the finite difference scheme. For example, the use of the first time approximation of Eq. (7) and of the first space approximation of Eq. (8) leads to absolutely unstable numerically finite difference scheme and no valid results for f^{n+1} at point I can be obtained.

The finite difference solution found at the computational grid points *would converge to the solution of the differential equations they approximate but under certain conditions*: the approximation must be consistent, the finite difference scheme must be stable and both differential and finite difference problems must be well posed (including boundary and initial conditions). And if the convergence is thought numerically by repeating computations while refining computational grid $(\Delta x,\ \Delta t) \rightarrow 0$ then the successive computations must maintain the relationship between Δx and Δt obtained from consistent approximation. Now, we can answer the question of grid refining as shown in Fig. 2, namely: if the time step is divided by 2, will the results better? From the computational point of view, no! Indeed the time step should be reduced at the same time in order to maintain consistency of approximation. However, it is obvious that reduce the space step should improve topography representation in our model if the topography is introduced again in new details and this may well be essential.

As illustration of the fact that consistency of the scheme with equation is not enough to ensure the convergence consider the following example [4]. Let the partial differential Eq. (6) with the forward-space consistent scheme:

$$\frac{f_i^{n+1} - f_i^n}{\Delta t_n} + \frac{f_{i+1}^n - f_i^n}{\Delta x_i} = 0 \quad \rightarrow \quad f_i^{n+1} = \left(1 + \frac{\Delta t_n}{\Delta x_i}\right) f_i^n - \frac{\Delta t_n}{\Delta x_i} f_{i+1}^n; \tag{9}$$

Note that the finite difference scheme is consistent with differential equation but numerically unstable.

As initial conditions for the *differential* equation, we take

$$\text{If } -1 \le x \le 0,\ f_0(x) = 1; \quad \text{elsewhere } f_0(x) = 0;$$

The solution of the partial differential equation is a shift of f_0 to the right by t. In particular, for t greater than 0, there are positive values of x for which $f(t,\ x)$ is nonzero. This is illustrated in Fig. 3. Let us take for difference scheme the initial data as:

$$f_i^0 = 1 \quad for\ -1 \le i\Delta x \le 0; \quad f_i^0 = 0\ elsewhere$$

Equation (9) shows that the values of grid-function f_i^{n+1} for $\Delta t/\Delta x = 1$, for $n > 0$ and $i > 0$ will always be zero. Hence, the computed values of grid-function *will never converge* towards the solution of differential equation although the finite difference scheme is consistent with this equation.

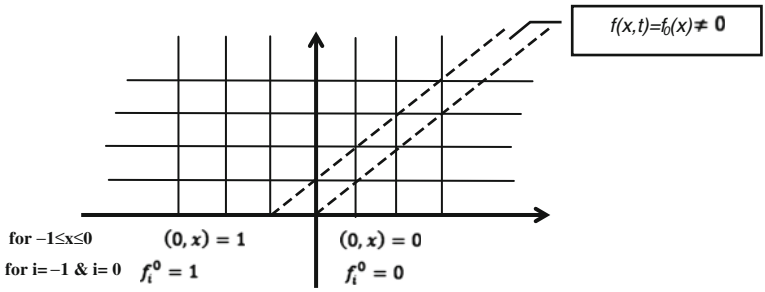

Fig. 3 Consistency alone does not imply convergence

But if instead Eq. (9), the following consistent approximation is considered:

$$\frac{f_i^{n+1} - f_i^n}{\Delta t_n} + \frac{f_i^n - f_{i-1}^n}{\Delta x_i} = 0 \quad \rightarrow \quad f_i^{n+1} = \left(1 - \frac{\Delta t_n}{\Delta x_i}\right) f_i^n + \frac{\Delta t_n}{\Delta x_i} f_{i-1}^n; \tag{10}$$

then with $\Delta t/\Delta x \leq 1$, the result is stable and correct, and hence, the scheme is convergent.

2.6 Interpretation of Parameters and Approximate Solutions Obtained from Algorithms: Interpretation of Results

As shown above, the only parameter in De Saint–Venant equation is the coefficient k in Chézy formula (Eq. 3). The coefficient k is the parameter that replaces essentially the description of the process of energy dissipation (something we still cannot pretend to know well and to be able to formulate correctly without including some other parameters). There may be other phenomena that are not represented in Eqs. (1) and (2), for example, subgrid phenomena, but it must be clear that, precisely, they are not represented. Essential point is to understand that as long as we can relate this parameter to the reality (e.g., as long as we can assume that for a sand bed, the value of k varies within reasonable and known limits) such parameterisation is useful. If, however, by calibration or "tuning" one finds, through the modelling of past floods for a given river reach that may contain all kinds of obstacles and local head losses, some global value of k, then of course such value of the parameter has no physical meaning. In such a case, a modeller is parameterising the situations that are due to unknown factors (not a general situation of the flow in a channel but rather specific situation of resistance encountered in a given reach during a given flood event) and thus jeopardises the

predictivity of the model. This is often a price for reproducing past-observed floods with models that do not contain all topography, structures, etc.

The results obtained by above-described procedures are to be interpreted in respect of what these procedures contain. There is no hope to expect that modelling based on the approximate resolution of partial differential equations can supply anything more that the values of grid-functions $\{\tilde{u}(x_i, t_n)\tilde{y}(x_i, t_n), i = 1,2,\ldots L; n = 0,1, \ldots, N\}$ that are approximation to continuous functions $\{u(x, t), y(x, t)\}$. Obvious consequence is that the four hypotheses used to set up Eqs. (1) and (2) are built-in in the results of all 1D modelling systems based on De Saint–Venant equations. Important point is also the fact that the result of simulation is the approximate solution only at the grid points. Nothing can be said about what happens between two grid points unless a complementary hypothesis assuming the continuity of the grid-functions is ensured between the points. Thus, interpolation between the computational points or a search for improvement of the results using higher-order approximation of derivatives through the extrapolation formulas involving several grid points is hazardous. The interpretation of the results must also take into account how the computations were conducted: to refine space grid of computational points in two consecutive computations is not enough to improve the quality of results from one simulation to another.

In general, the interpretation of the results may lead to inaccurate or even false conclusions and, then, policies and decision. Consider the example of flood insurance problems for dwelling on the inundated plain created by 1D-modelled free-surface elevation. As demonstrated, the free surface across the river is computed as horizontal at any time of the flood and computed velocity is uniform within the whole section. This is notoriously false: even if the flow is of one-dimensional character in unsteady flood of reasonable duration the free surface will be higher along the river axis than on the plain, the duration of inundation will not be the same and velocity very different. Nowadays, we often have available the digital terrain models (DTM). Using GIS techniques, it is enough to superimpose the 1D flow model results and DTM to produce illusion of accuracy. There are numerous cases of similar situations, especially when the studies (compulsory in many EU countries) of inundation risks are conducted. The reasons are of two origins: available budgets that push clients to less-qualified service suppliers using cheaper tools and lack of knowledge of the decision makers. How many of everyday users of market-available 1D software think of De Saint–Venant hypotheses when producing "inundation maps" from the colourful results supplied by GUI? Imagine that topography used in a model of an area was manufactured a couple of years ago and that since local forest service built a dirt service road crest of which is 1 metre above original plain elevation. Somebody unable to analyse the results in function of basic hypotheses and of sound knowledge of hydraulics will not be able to seek and find the differences between the results of 1D model and the free-surface elevation observed during last year flood.

3 A Remarkable Example of Limitation of De Saint–Venant Approach

Consider a case of a trapezoidal concrete derivation channel several kilometres long and conveying a steady flow discharge towards a power station, irrigation area, etc. What happens when the gates (or turbines) downstream close rapidly? In classic hydraulics curricula, the case becomes a 1D unsteady flow as downstream positive-steep front wave (discontinuity, roller, bore) propagates upstream the channel. Question is: is it possible with a commercial De Saint–Venant-based code to simulate the situation and define the heights of the dykes along this channel? Still classic answer is yes, and the computed result is as in Fig. 4a. In many (if not most) cases, the real situation is different. Like shown in Fig. 4b (and in Fig. 5), the upstream propagating wave is under the shape of undular bore height of which may be twice of that of steep front wave [5].

In this particular case, De Saint–Venant hypotheses of uniform velocity and hydrostatic pressure are wrong and no commercial software based on such hypotheses can produce acceptable results. And, once the structure built and water spilling out of channel at every manoeuver of the gates, there may occur serious consequences if the modeller or his client do not know hydraulics in depth: the client may well feel that modelling is a humbug, inapplicable to engineering problems. At the very best, the used software would be disqualified.

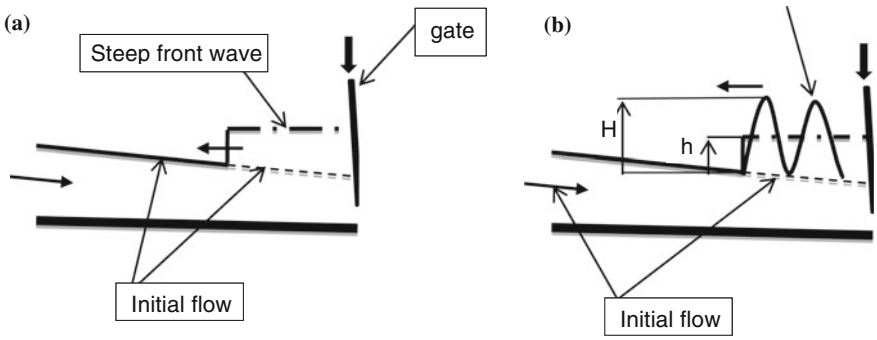

Fig. 4 Closure of downstream gate **a** simulation results from 1D De Saint–Venant-based code (steep front bore of height h), **b** often observed reality—undular bore of height $H = 1.2–2.1$ h

Fig. 6.10. Advancing undular surge in a Durance River (France) power canal (courtesy Electricité de France)

Fig. 5 **a** from [5]. **b** Tests of release in Chaudanne HP station (France), courtesy Electricité de France

4 Conclusions

From mathematical point of view, the results of models are nothing more than, at their best, approximate solution of original differential equations. From the engineering point of view, the interpretation of the results is essential because of the limitative basic hypotheses on which equations are built and because the computer output cannot supply more than these hypotheses allow. If there is a contradiction, an in-depth analysis is necessary. A modeller who is not sufficiently knowledge-

able about links of the chain leading from hypotheses to results may not be able to supply his "client" with appropriate conclusions indicating how the original hypotheses and subsequent approximations may make the results differ from the reality. Given that the "client" is typically a decision maker in wide sense of the word: investor, public body, administration, etc., it is important that he realises the situation and makes sure to find necessary and qualified assistance in order not to be at the mercy of the modelling studies supplier.

References

1. Abbott, M. B., & Vojinovic, Z. (2009). Applications of numerical modelling in hydroinformatics. *Journal of Hydroinformatics, 11*(3–4), 308–319.
2. Abbott, M. B., & Vojinovic, Z. (2012). *Flood risk and social justice*. New York: IWA Publishing.
3. Chézy, A. (1768). Original manuscript of the report prepared for the French Academy of Science contained in the files of the Ecole des Ponts et Chaussée. In G Mouret (Ed), Antoine Chézy: Histoire d'une formule d'hydraulique. Annales des Ponts et Chaussées, (1921–II)
4. Strikwerda, J. C. *Finite difference schemes and partial differential equation* (2nd ed.). Society for Industrial and Applied Mathematics (SIAM), Philadelphia
5. Cunge, J. A., Holly, F. M, Jr, & Verwey, A. (1980). *Practical aspects of computational river hydraulics*. Boston, London, Melbourne: Pitman Advanced Publishing program.

Use of Standard 2D Numerical Modeling Tools to Simulate Surface Runoff Over an Industrial Site: Feasibility and Comparative Performance Survey Over a Test Case

Morgan Abily, Claire-Marie Duluc and Philippe Gourbesville

Abstract Intense pluvial generated surface flow over an industrial facility represents a flood risk requiring an appropriated approach for risk assessment. Runoff over industrial site might have flow regime changes, wild flooding/drying extend, as well as small water deep properties. This makes standard bidimensional (2D) numerical surface flow models use particularly challenging. Indeed, numerical treatment of these properties might not be specifically supported by models. Furthermore, it gets close by their traditional application domain limits. Accordingly, an assessment of this group of numerical tool use for such a purpose needs to be in detailed studied to evaluate feasibility, performance, and relevance of their use in this context. This chapter aims to focus on common 2D numerical modeling tools use for application over an industrial plant test case to simulate surface runoff scenarios. Feasibility of such an approach is hereby studied. Performances and relevance of this attempt are evaluated. Our test case has specificities of real industrial plants in terms of domain extend, topography, and surface drainage structures. Tested scenarios state a uniform net 100 mm 1 h long rainfall event in a context of storm water sewer pipe failure. Selected tested models were a 2D finite differences diffusive wave model and an array of different 2D shallow water equation [2D shallow water equations (SWEs)]–based models. Comparison has been conduced over computed maximal water depth and water deep evolution. Results reveal a feasibility of these tools application for the studied specific purpose. They underline the necessity of a highly fine spatial and temporal

M. Abily (✉) · P. Gourbesville
University of Nice Sophia Antipolis/Polytech'Nice-Sophia/ Innovative City, 930 Route des Colles 06903 Sophia Antipolis Cedex, France
e-mail: abily@polytech.unice.fr

P. Gourbesville
e-mail: Philippe.Gourbesville@unice.fr

C.-M. Duluc
Institut de Radioprotection et de Sûreté Nucléaire (IRSN), PRP-DGE, SCAN, BEHRIG, BP17, 92262 Fontenay-aux-Roses Cedex, France
e-mail: claire-marie.duluc@irsn.fr

P. Gourbesville et al. (eds.), *Advances in Hydroinformatics*, Springer Hydrogeology, DOI: 10.1007/978-981-4451-42-0_3,

discretization. Tested categories of average 2D SWEs–based models show in a large extend similar results in water depth calculation. Used indicator of results reliability estimation did not point out major critical aspects in calculation. Limits inherent of these categories of models use for this domain of application are underlined. Relevance of this approach is raised up.

Keywords Flood risk assessment · Surface runoff modeling · Industrial site · 2D shallow water equations · MIKE · TELEMAC

1 Introduction

Flood risk over industrial sites includes surface runoff generated by intense pluvial events. For sensitive industrial sites, this risk has to be assessed as it might lead to issues for industrial activities, environment, and for human protection. A new guide for nuclear power plant protection against flooding risk has been elaborated by the Institut de Radioprotection et de Sûreté Nucléaire (IRSN) for the French Safety Authority (ASN). The guide [1] defines a set of Standard Flood Risk Situations (SFRS) to be taken in consideration for safety assessment of nuclear power plants. This guide notably includes a SFRS defining a framework for intense pluvial generated runoff risk assessment. This SFRS recommends that a plant has to be able to cope with a 1 h long rainfall event with a hundred year return period; meanwhile, sewer system network is considered as locally non-available. Through this SFRS, aim is to consider two possible aspects in safety failure which might occur during an intense rainfall event scenario: (1) a clogging of sewer network access and (2) a possibility of rainfall events occurrence exceeding the return period for which the sewer system has been designed and implemented.

Different approaches for the runoff SFRS application are possible. (1) A spreading of the cumulated rainfall volume over the industrial site might be an approach to consider for flat sites, to identify pounded areas. It has to be noticed that this quantitative approach do not take hydrodynamic aspects into accompt. (2) Using fine topographical data, main drainage path and pounded areas can be identified. This method is rather qualitative and does not integer quantitative aspects. (3) Numerical modeling of runoff as a free surface flow is a practice often used at larger scale for flood risks assessment and might be applied for runoff over high-resolution topography studies. Indeed, gaining ground of standard numerical modeling tools use for surface runoff component modeling at high resolution is observed [2, 3]. At the same time, nowadays techniques for high-resolution topographical data gathering are becoming commonly used. Modern techniques as light detection and ranging (LIDAR) [4] and unmanned aerial vehicle (UAV) photogrammetry [5] can produce digital elevation models (DEMs) with a resolution consistent enough to finely represent surface drainage influencing structures up (e.g., walls, side walks, curbs). Nevertheless, runoff over an industrial site

environment might have rapid flow regime change and high gradient properties, representing numerical challenges for standards modeling tools. Moreover, if high-resolution topographical data integration within hydraulic models might be interesting to represent small-scale structures that affect surface flow patterns, issues might be encountered for these data use with standard numerical modeling tools.

Taking these aspects in consideration, this study investigates on relevance and feasibility of standard 2D numerical modeling tools use within the recommended runoff SFRS context. Indeed, these tools use for a purpose different from the ones for which they have originally been designed for rises questions up about validity, feasibility, limits, and relevance of such an approach. This chapter aims to point out through a methodology applied on a test case–based study, relevance, and limits of standard 2D numerical modeling tools use for runoff induced flood risk assessment. Moreover, objective is also to point out what should be regarded in methodology for models optimization and for error detection. First, this chapter details main lines of the used method for tests and comparisons of selected modeling tools within runoff SFRS framework. Next, results are presented and discussed, comparing performance and limits of tested numerical modeling tools. Finally, a feedback on validity, limits, and relevance of standard numerical modeling tool performance for high-resolution runoff modeling in runoff SFRS context is raised up.

2 Modeling Framework and Method for Comparison

2.1 Tested Categories of Numerical Modeling Tools

A numerical modeling approach classically requires different aspects to be regarded before its application, mainly including the objectives of the model, the physical processes included through model's mathematical formulation, the dimension of the phenomena, the numerical scheme, and the numerical method used for discretization of the continuous phenomena and to resolve equations. For modeling tool selection process, these aspects are considered, headed by following constraint: modeling tools and modeling approach have to be based on standard tools commonly used by consulting company and not involve any specific development. Objectives of the modeling approach in runoff SFRS context should be to help for (1) at least a relative identification of runoff induced maximal water depth (h_{max}) and for (2) an understanding of runoff hydrodynamics over a specific site configuration.

For the application purpose, the use of 1D model has not been considered as a relevant approach as the runoff phenomena is clearly 2D. The use of pseudo-2D models require a good *a priori* knowledge of flow direction and involve a time-consuming task for model construction. Three-dimensional model use does not

appear to be necessary here as the vertical dimension of the phenomena is negligible compare to horizontal ones and will involve intensive computational effort. Therefore, methodology for runoff modeling was tested with commonly used 2D-free surface flow numerical modeling tools. Firstly, due to the physics of the runoff process (2D); secondly, due to the increasing popular use of this kind of modeling tools for overland flooding risk studies by consulting companies, and eventually due to the assumed ease of use of this category of tools for high-resolution data implementation.

For overland flow, standard 2D-free surface numerical modeling tools are most commonly based on 2D shallow water equations (SWEs) resolution and were therefore chosen for our application, notwithstanding latent uncertainty on validity of friction terms mathematical representation for our purpose, which would require to be more fundamentally studied. Runoff over an industrial site might have properties of rapid flow regime change, small water depth over high topographical gradient, wet/dry transitions as well as steady flow and pounded areas occurrences. These aspects represent numerical challenges for 2D SWEs–based standard numerical modeling tools which might not have proper numerical treatments of these properties included. Consequently, to identify and highlight advantages and limits of different numerical approaches, a wide range of models were compared. The complete resolution of 2D SWEs was tested with tools relying on an array of different numerical methods (Table 1). A modeling tool using 2D SWEs diffusive wave approximation (MIKE SHE) was included in comparison to check whether the underlying assumption of inertial terms neglecting sound acceptable for high-resolution runoff modeling purpose and to see is this category of tool can be used to give a first quick h_{max} estimation.

Non-structured mesh use seems adapted for our purpose, allowing to refine mesh around flow pattern affecting structures. Nevertheless, their construction

Table 1 Selected modeling tools and their numerical methods

Modeling tool		Equation	Mesh	Numerical methods	Tested numerical scheme
MIKE SHE	2011 software release	Diffusive wave approximation of 2D SWEs	Structured	Finite differences	Gauss–Seidel method (SOR)
MIKE 21		Complete 2D SWEs	Structured	Finite differences	ADI, with a treatment for high Froude number flow
MIKE 21 FM		Complete 2D SWEs	Non-structured	Finite volumes	Euler explicite, Roe solver
TELEMAC 2D	Version v6p1	Complete 2D SWEs	Non-structured	Finite volumes	Kinetic second order
TELEMAC 2D		Complete 2D SWEs	Non-structured	Finite elements	SUPG

might get complicated requiring mesh generators key to include properly this system of flow pattern affecting structure which is densely represented in case of an industrial site. Mesh-structured models use might not seem to be the most suited for a complex topography representation as they do not offer mesh refinement possibilities. Nevertheless, a high-resolution grid use might partially compensate for this aspect. Even though high-resolution grid use for calculation involves a high number of computational points and therefore a high computational cost, the direct use of a grid is attractive in terms of time gain in model construction.

Over industrial site, runoff flow specificities require numerical methods which can, at least, stably handle flow regime changes and numerical shocks occurrences. The MIKE 21 Alternate Direction Implicit (ADI) method has been implemented by the Danish Hydraulic Institute (DHI) with a specific treatment to handle supercritical flow occurrences, using numerical diffusion to stabilize model through an upwind treatment of 2D SWEs convective terms [6, 7]. MIKE 21 as well as MIKE 21 FM uses a threshold value system to handle moving boundaries problems (cells wetting/drying) [8, 9]. Two different finite volume methods (FVM) were tested: (1) MIKE 21 FM which is cell-centered and (2) TELEMAC 2D which is vertex based. TELEMAC 2D FVM was used with a "well-balanced" scheme including a rewriting of the SWEs using a hydrostatic reconstruction leading to an oscillation free and permanently positivity of the solution [10]. Tested TELEMAC 2D finite element method (FEM) relies on a stream upwind Petrov–Galerkin (SUPG) numerical scheme, decentering the basis functions in order to account for the flow direction in the discretization of the advection terms.

2.2 Test Case for Runoff SFRS Modeling

Three types of scenarios matching with the SFRS framework were tested (Fig. 1). These scenarios introduce the same total quantity of water in the model and consider infiltration process as negligible. First and second scenarios (S1 and S2) were two one hour long rainfall events of 100 mm. S1 had a constant 100 $mm.h^{-1}$

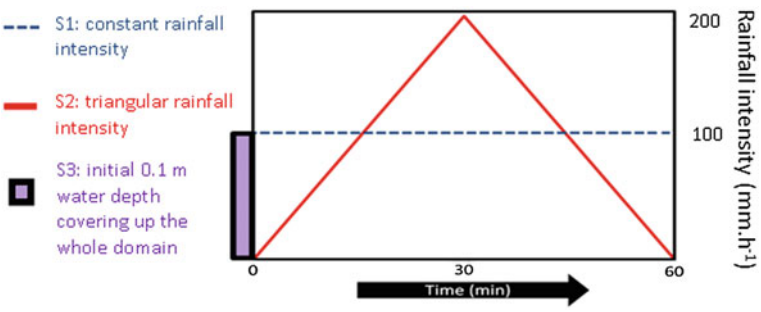

Fig. 1 Diagramatic representation of the three types of scenarios

rainfall intensity. S2 had a triangular rainfall intensity variation, linearly rising up to a maximum of 200 $mm.h^{-1}$ at 30 min, then linearly decreasing back to 0 $mm.h^{-1}$ at 60 min. Third scenario (S3) was a 0.1 m height water surface initially covering the entire domain up. Even though S1/S2 and S3 lead to different hydrodynamic conditions, their complementary inclusion in the tested method can give an insight (1) to help for the hydrodynamic understanding and to point out sensitive configuration on a site, (2) to highlight different categories of difficulties encountered by modeling tools.

Created test case is a 60,000 m^2 industrial site which includes representation of surface drainage influencing structures such as roads with slopes orientating runoff to water-collecting structures, side walks, road curbs, gutters, and door steps (Fig. 2). Access to buried sewer network is considered as non-available. To achieve a horizontal topographical resolution fine enough to represent surface drainage influencing structures in urban type environment, the interval of spot elevation data should be in the range of 0.1–0.4 m for DEM generation [11]. Created DEM was a 0.1 m per 0.1 m horizontal resolution grid. This grid resolution fits with required horizontal precision to represent above-mentioned structures and is compatible with standard geomatic technologies for spatially dense topographical data information gathering [4, 5].

The modeled domain boundaries were closed. A reservoir was located downstream, for water evacuation and storage, far enough not to influence backward flow condition in the area of interest. An important aspect was to use a spatial discretization fine enough to keep on representing runoff influencing structures as included in the high-resolution DEM. Consequently, for most of tested tools, temporal discretization had to be fine as well, mainly due to numerical methods inherent Courant–Friedrichs–Lewy (CFL) number restrictions. For models using structured mesh, the 0.1 m per 0.1 m resolution DEM grid was directly used as a staggered grid when possible. Figure 3 illustrates the resolution of the unstructured mesh used for TELEMAC models.

Buildings were ever included in calculation domain as elevation data or ever excluded from it, using their footprint as break line and adding a normal no slip

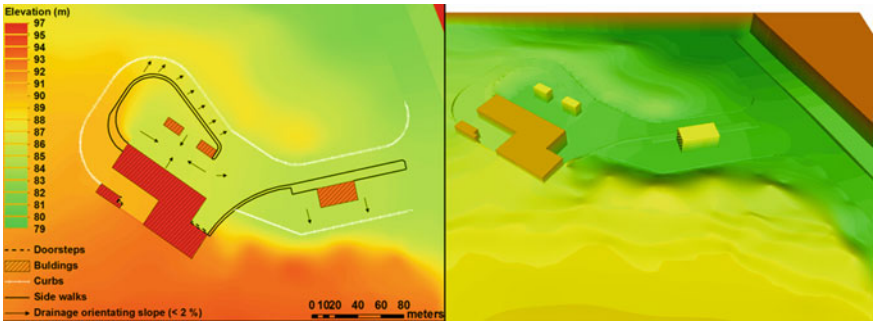

Fig. 2 Represented surface drainage influencing infrastructures on the created test case (*left*) and 3D view of created 0.1 m horizontal resolution DEM (*right*)

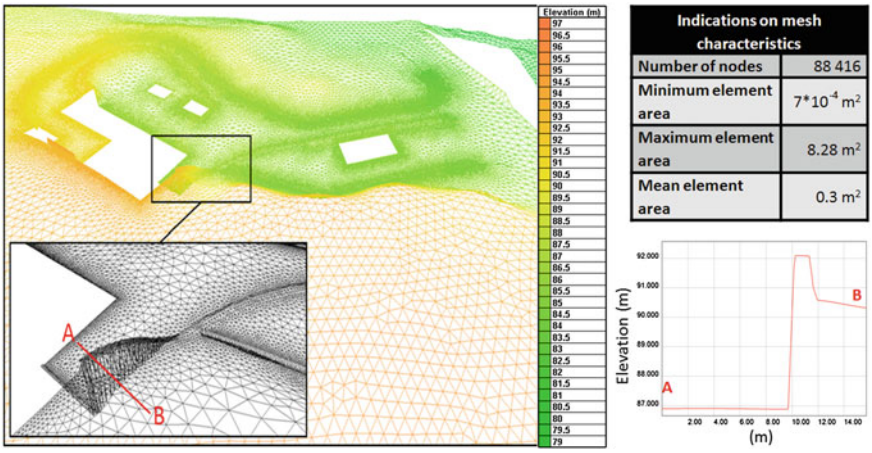

Fig. 3 Illustration of the unstructured mesh created for TELEMAC model with details on refinement around structures

boundary condition. These two approaches are considered as equally performing in building representation for flood extends assessment in high-resolution urban modeling [10]. Water flowing from building roofs was included in models as source points representing gutter discharges. For energy losses due to roughness and to eddy viscosity, chosen approach was to integrated them using standard practice and coefficient values commonly used in urban flooding modeling practice, notwithstanding that it would require a more important effort to assess if such kind of integration is still valid for our purpose. Strickler roughness coefficients of 60 and 27 $m^{1/3}.s^{-1}$ were applied, respectively, to constructed and non-constructed areas. Smagorinsky eddy viscosity approach was used to accompt energy losses due to horizontal turbulence.

2.3 *Methodology for Approach Relevance and Performance Assessment*

Parameter of interest was the runoff reached h_{max}, especially in constructed area. Therefore, h_{max} values and water depth evolution computed by models were relatively compared as no possibility to validate computed results with observation was available.

A sound check on computation reliability indicators has been implemented to identify and to troubleshoot critical aspects in modeling. Aim was (1) to optimize models performance and (2) to identify potential incoherence in calculation. The verified indicators of computation reliability were mass balance, CFL number, velocity, characteristic time check, and oscillations occurrences.

Moreover, flexibility offered by modeling tools for optimal use has been tested and taken into consideration for the modeling approach performance survey. Interest has been keen on possibility of: the three scenarios implementation, adapted spatial and temporal discretization use, treatment/handle of flow induced numerical specificities. Finally, as it was aimed to keep the modeling exercise under realistic elaboration and running time constraints that might be encountered in practical engineering studies, modeling tool ease of use for high-resolution runoff modeling was an aspect to be regarded and to be compared as well.

3 Results and Discussion

Scenarios S1, S2, S3 implementations was constrained by different limitations in selected software. Table 2 sums up scenarios modeling possibilities reached with the different tools. MIKE SHE and MIKE 21 could stably run all tested scenarios. In MIKE 21 FM, the finite volume method is not stable in case of high gradient and, for instance, it has required to exclude wall-type infrastructure from mesh for S1 and S2 runs (the wall highlighted in Fig. 3), whereas for S3, a stable run could not be performed. These stability aspects are both numerical method and mesh quality dependent. These issues were not encountered with TELEMAC 2D models but runs introducing rainfall is not a standard available option and would require additional programming effort. Therefore, it was not possible to run S1 and S2 scenarios with TELEMAC 2D. This option of rainfall introduction as source term will be included in next TELEMAC version (v6p2). An illustration of first seconds of scenario S3 run with MIKE 21 water depth evolution is represented in Fig. 4.

3.1 Results Overview on Parameter of Interest

3.1.1 Water Depth

Chiefly, depending on nature of implemented scenarios, runoff hydrodynamic and reached h_{max} are different, as illustrated by Fig. 5. Indeed, both intense rainfall events (S1, S2) conduce to an overflow of surface drainage structures like road

Table 2 Simulations possibly reached with selected standard modeling tools for runoff scenarios (where X is for a successfully reached stable modeling)

	S1: constant rainfall event	S2: triangular rainfall event	S3: initial 0.1 m high water depth
MIKE SHE	X	X	X
MIKE 21	X	X	X
MIKE 21 FM	X	X	No stable configuration reached
TELEMAC 2D	Option not available		X

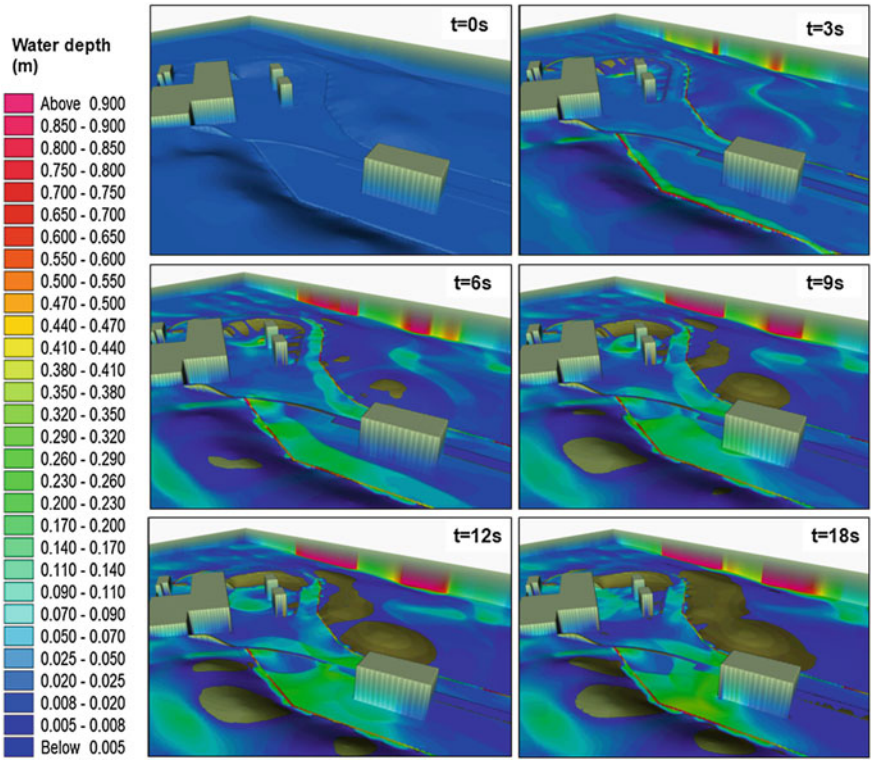

Fig. 4 Illustration of first seconds of S3 (0.1 m initial water depth) simulation run with MIKE 21

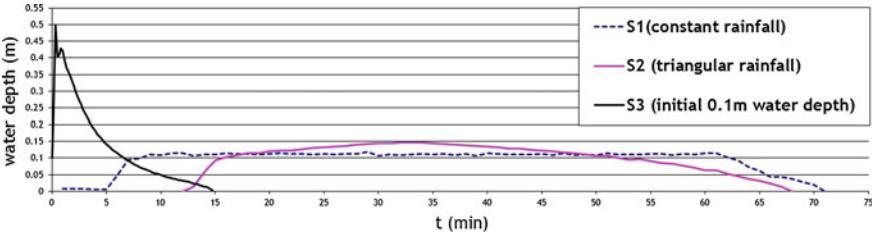

Fig. 5 Water depth reached at point 10 with MIKE 21 for the three scenarios (point location in Fig. 6)

curbs as illustrated in Fig. 6. As the catchment analysis through GIS and empirical formula use shows a quick concentration time (about 3 min), differences in maximal rainfall intensity consequently lead to differences in reached h_{max}. Important initial quantity of water (S3) leads to a different hydrodynamic with a quickest and highest reach h_{max}.

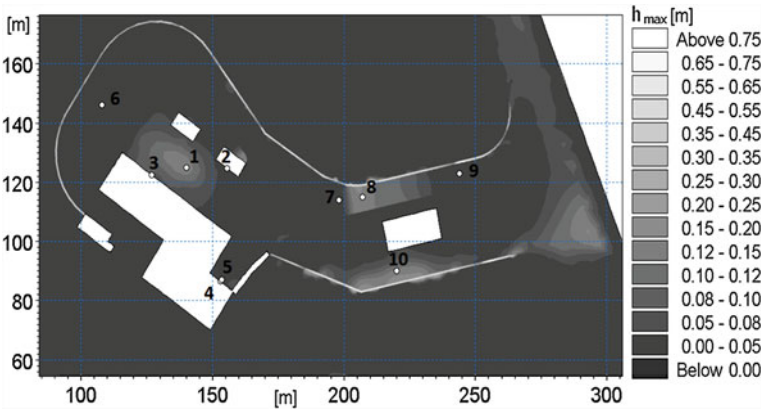

Fig. 6 Average of complete 2D SWEs-based models h_{max} values, reached at 10 points for the three scenarios, with bars indicating maximal h_{max} and minimal h_{max} values reached by models

Regarding tested numerical modeling tools, MIKE SHE was used and configured with the aim to get quick results and to see if a diffusive wave assumption–based model use was acceptable for our approach. Though roughly matching with the results we get with other complete 2D SWEs–based models, some areas around buildings which are founded to be flooded with other models are not with MIKE SHE. Moreover, runoff hydrodynamic over flat areas and pounded areas is inaccurately treated. This is due to the fact that only gravitational forces are considerate for flow motion within MIKE SHE [12]. Therefore, we stopped to considerate this modeling tool use as relevant for our objectives as these aspects are an important issue for our purpose.

Globally speaking, 2D SWEs–based models lead to comparable h_{max} values for a given scenario (Fig. 7). Differences in results firstly depend on differences in

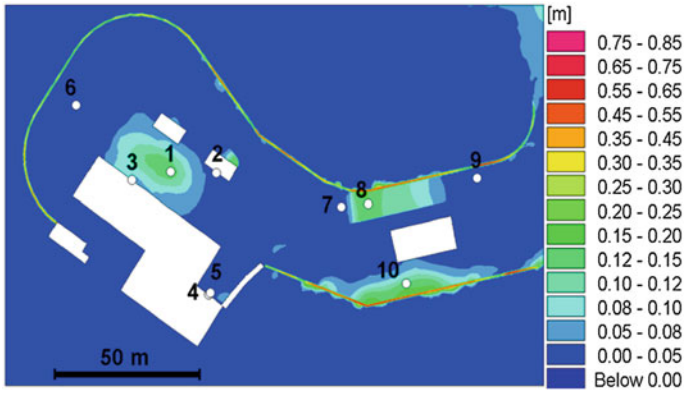

Fig. 7 Ten points location and h_{max} values reach with MIKE 21 FM for S2

spatial discretization which rely on the mesh performance to accurately represent topography. Moreover, h_{max} value is an averaged value for a given mesh cell, and though location of points of interest are the same, mesh cell size are different between models. Secondly, even though optimization in setup was performed, some numerical methods (for instance, with MIKE 21 models) still produce spurious oscillations and therefore lead to slight overestimations of h_{max} values.

Regarding runoff water depth evolutions, results from the different 2D SWEs-based models globally have comparable behavior as well. Nevertheless, differences might appear in first minutes of simulations. Indeed, when using a threshold value system for wetting/drying of cells treatment (in MIKE 21 and MIKE 21 FM models), below these threshold values, 2D SWEs are not fully resolved. Then, in a rainfall scenario case, the hydrodynamic behavior before the time at which the cumulated rainfall intensity exceed the threshold value, rely on a simplified SWEs resolution. The threshold value has to be low enough to limit such kind of effects influence on overall results relevance.

3.1.2 Computation Reliability Indicators

Globally, indicators did not reveal majors inconsistency in computation. To reach this, it has been necessary to optimized models setup, (mainly through discretization adaptations) to keep CFL number under restrictive values. This can induce limitations in modeling tool use. For instance, MIKE 21 can stably run only for a maximal CFL number under 0.2 to cope with a stable treatment of supercritical flow. Mass balance checks did not reveal any important problem in conservation of water quantities. MIKE 21 has nevertheless, up to a 4 % mass creation for S3 scenario after a 30-min-long simulation. This is due to the fact that spurious oscillations are more important with this model and negatives water depths are reset to a small positive value, therefore creating mass in models. Velocity check gives an order of magnitude of values which sound realistic with the physic of the phenomena (maximal velocity is about 3–4 $m.s^{-1}$), and no artificial polarization is detected. A sound check of concentration time and lag time was done as well, and values calculated from models results are comparable with results calculated from empirical formula estimations. Spurious oscillations are in detail regarded through limnigrammes as illustrated in Fig. 8. Indeed, due to relatively small water depth considered in this specific application, oscillation magnitude can significantly increase results uncertainty. Smoothing of solution due to the numerical diffusion, induced by some numerical method to stabilize computation might impact results accuracy as well.

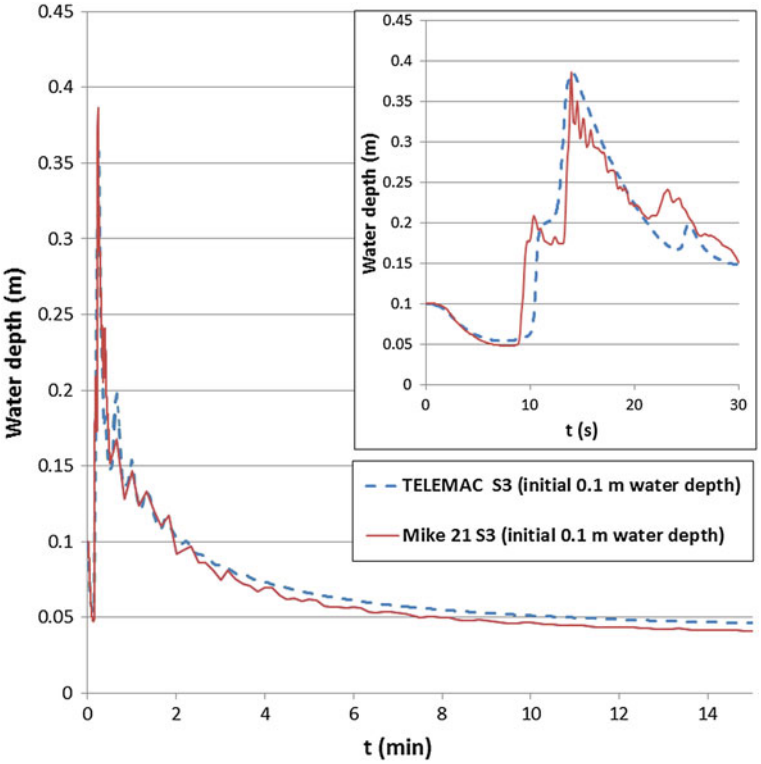

Fig. 8 Limnigramme at point 3 for S3 scenario with MIKE 21 and TELEMAC 2D (using finite volumes numerical method)

3.2 Selected Tools Performance Comparison

For the specific application on high definition areas, added value and limits of each modeling tools regarding factor influencing model possibility and quality are summarized in Table 3. Regarding a structured mesh use possibility, with MIKE 21, the DEM raster can be directly used as a staggered mesh. Nevertheless, the software has a constant time step lower limit of 0.01 s. For computation stability sake (constrained by the CFL number), the 0.1 m resolution grid direct use as a mesh was not stable with such time step limitation. Therefore, the grid resolution had to be decreased to 0.3 m to maintain a CFL number compatible with a switch in numerical method for an upwind treatment of convective terms of 2D SWEs (CITER). Indeed, in case of supercritical flow and high gradient occurrence, stability relies on this numerical treatment. For the test case, this 0.3 m discretization spatial resolution was fine enough for drainage influencing infrastructure representations, but for more complex cases it might lead to restriction for this modeling tool use. Concerning MIKE 21 FM, models encountered difficulty to stably deal with high gradient

Table 3 Modeling tools main possibilities and limits encountered over our test case for high-resolution runoff modeling

	Use with 3 scenarios	High-resolution data use and discretization	Stability and high gradient induced limitations	Wet/dry treatment and oscillation occurrences
MIKE SHE	Possible with S1, S2, S3	2D SWEs simplification lead to differences with other models results, over our test case this category of model use is not considered as properly performing for our specific purpose		
MIKE 21	Possible with S1, S2, S3	Software Δt lower limit induce a CFL dependent limit for fine grid use	Stable through diffusion introduction under important CFL restrictions	Threshold value can be low enough for our purpose, oscillations might be important
MIKE 21 FM	Not stable with S3	Mesh generator not well suited for our application specificities	Stability problem with high gradient. Could require a specific meshing treatment	Threshold system and oscillation can be lowered enough for our purpose
TELEMAC 2D	No option for rainfall scenarios (S1, S2)	Adapted	Stable with FEM (upwinding and diffusion induced method), stable with FVM (kinetic scheme)	"Well-balanced" kinetic scheme allow a performing treatment

occurrences. This can be partially overcome, ever by excluding high gradient infrastructure from modeled domain when possible and acceptable, or ever by a more important workload on mesh refinement. Indeed, unstructured mesh generation was effectuated with both MIKE generator (for MIKE 21 FM) and Blue Kenue (for TELEMAC 2D). For our application purpose, ease of a mesh construction with pertinent refinement is founded to be superior with Blue Kenue mesh generator. Stability in MIKE 21 and TELEMAC 2D (FEM with SUPG) is increased using numerical diffusion (notably by an upwinding treatment of convective terms). It has to be kept in mind that such method is a decrease of solution accuracy.

The numerical treatment of wetting/drying, as well as spurious oscillations limitations in flat/pounded areas and in cases of a reached steady flow state, is treated in a stable manner with TELEMAC 2D kinetic scheme. The treatment of these properties by MIKE 21 and MIKE FM models is compatible with our application as well but has to be carefully regarded as for instance threshold treatment system use induce differences in rainfall scenarios, as the complete resolution of 2D SWEs starts only after that cumulated rainfall exceeded the threshold.

4 Conclusions

To fit with SFRS framework and objectives for runoff induced flood risk assessment over an industrial site, the use of standard 2D-free surface flow numerical modeling tool is founded to be a reliable method which can provide an interesting support. Nevertheless, such type of approach requires cautions in results validity interpretation and raise up practical limits for adapted models creation with standard modeling tools. This study helped to rise up a basic methodology for 2D standard numerical modeling tool use, highlighting influent parameters and critical aspects to address for selected category of tools employment.

Simplified 2D SWEs approach as the diffusive wave approximation relies on assumption that influence of some terms can be neglected. Over our test case, for high-resolution runoff modeling, these terms significantly impacts reached water depth and deserve to be accurately represented. Here, this category of model is not suited for our purpose. Fully resolved 2D SWEs–based modeling tools seemed to be more adapted for high-resolution runoff modeling for objectives of runoff induced maximal water depth estimation and site hydrodynamic understanding. Nevertheless, numerical representation and treatment of parameters like manning coefficient and eddy viscosity deserved to be more fundamentally studied.

Tested and compared numerical modeling tools produce comparable results independently of the used numerical method, even if requiring important optimization in models creation and setup. In most practical runoff modeling application cases, use of numerical modeling approach for the scenarios defined by the SFRS framework will lead to result which can not be validated by measurement. Therefore, it sounds essential to check and to identify potential troubles and limits in calculation through computation reliability indicator use. A complementary use of different models relying on different numerical schemes might help to assets inherent relative limits and performances of created models.

Standard numerical modeling tools use for high-resolution runoff modeling spotlight disparities among tools in terms of practical aspects. High-resolution topographical data integration can be properly done but modeling tools cannot equally fulfill requirement for establishment of an adapted discretization. Here, this is the case in terms of ease to create an adapted mesh and in terms of temporal discretization limitations. Modeling tools cannot equally possibly represent all categories and variations of scenarios (rainfall/initial water depth). Modeling tools stability to handle high gradient occurrences, moving boundary treatment, and spurious oscillations induce different limits related to discretization and used numerical scheme.

In terms of relevance, numerical modeling approach for runoff flood risk assessment can give a valuable insight to evaluate facility exposure to runoff risk. Moreover, the approach might highlight comprehension of dynamical aspects of the phenomena on a specific site and help for site management regarding this kind of risk exposure. For such a purpose, the complementary use of different nature of scenarios is an interesting approach.

References

1. ASN (2010). Protection des installations nucléaires de base contre les inondations externes. Projet de guide de l'ASN n 13, p. 44.
2. Ciliberti, S. A., Gomez, M., Macchione, F., Russo, B., & Villanueva, A. (2008). *2D analysis for local flooding assessment in a new square of Barcelona during storm events* (p. 9). 11th International Conference on Urban Drainage, Edinburg, Scotland, UK.
3. Gomez, M., Macchione, F., & Russo, B. (2011). Methodologies to study the surface hydraulic behaviour of urban catchments during storm events. *Water Sciences and Technologies, 63*(11), 9.
4. Aktaruzzaman, M., Schmidt, T. (2009). *Detailed digital surface model (DSM) generation and automatic object dection to facilitate modelling of urban flooding*. ISPRS Workshop, Hannover.
5. Remondino, F., Barazzetti, L., Nex, F., Scaioni, M., Sarazzi, D. (2011). *UVA photogrammetry for mapping and 3D modelling*: *Current status and future perspectives*. International archives of the photogrammetry, remote sensing and spatial information sciences, conference on unmanned aerial vehicle in Geomatics (Vol. XXXVIII-1/C22, p. 7). Zurich, Switzerland.
6. DHI. (2007). *MIKE 21 flow model, Hydrodynamic module: Scientific documentation* (p. 58). Danish: Danish Hydraulics Institute.
7. McCowan, A. D., Rasmussen, E. B., Berg, P. (2001). Improving the performance of a two-dimensional hydraulic model for floodplain applications. In T. I. O. Engineers (Ed.), *Hydraulics in civil engineering* (p. 11). Hobart, Australia.
8. DHI. (2007). *MIKE 21 and MIKE 3 flow model FM, hydrodynamic and transport module: Scientific documentation* (p. 50). Danish: Danish Hydraulics Institute.
9. Audusse, E., Bouchut, F., Bristeau, M. O., Klein, R., & Perthame, B. (2004). A fast and stable well-balanced scheme with hydrostatic reconstruction for shallow water flows. *Journal of Scientific Computation, 25*(6), 2050–2065.
10. Schubert, J. E., Sanders, B. F., Smith, M. J., & Wright, N. G. (2008). Unstructured mesh generation and land cover-based resistance for hydrodynamic modelling of urban flooding. *Advances in Water Resources, 31*, 1603–1621.
11. Mark, O., Weesakul, S., Apirumankul, C., Boonya-Aroonnet, S., & Djordjevic, S. (2004). Potential and limitations of 1D modelling of urban flooding. *Journal of Hydrology, 299*(3), 284–299.
12. DHI. (2007). *MIKE she user manual: Reference guide* (Vol. 2, p. 386). Danish: Danish Hydraulics Institute.

Hydraulic Modelling for Rhône River Operation

Laëtitia Grimaldi, Guillaume Bontron and Pierre Balayn

Abstract CNR is France's leading producer of exclusively renewable energy—with 18 hydroelectric power plants along the Rhône, providing a capacity of 3,000 MW. In order to operate these plants, the CNR has developed several made-to-measure hydroinformatic tools for various purposes, whether they are studies or operational applications. The studies undertaken are mainly based upon type 1-D looped-network hydraulic model with storage areas, covering the full length of the Rhône. For the use of specific studies, these models can be backed up by more detailed modelling: 2D or 3D. With this in mind, accuracy of results is a major factor and the ongoing trend is for increasingly complex models. However, this trend is incompatible with the need for robust & real-time operational solutions in an industrial context. For this reason, the study models have had to be adapted to varying operational requirements, using a number of different strategies to meet the specific requirements of each individual operational application. This multiplicity of usages means that constant vigilance is required to maintain the consistency of codes and modelling data, notably when updating reference models. As part of the SYSSIH project (hydraulic simulation system), CNR is currently setting up a common platform, to gather all the modelling tools and models needed for a full range of operational uses. This restructuring will facilitate the maintenance of tools and their customisation to future requirements.

Keywords Operational use of hydraulic models · Model maintenance · 1D hydroinformatic modelling

L. Grimaldi (✉) · G. Bontron · P. Balayn
Compagnie Nationale du Rhône, 2 rue André Bonin, 69316 Lyon Cedex 04, France
e-mail: grimaldi@cnr.tm.fr

G. Bontron
e-mail: g.bontron@cnr.tm.fr

P. Balayn
e-mail: p.balayn@cnr.tm.fr

P. Gourbesville et al. (eds.), *Advances in Hydroinformatics*,
Springer Hydrogeology, DOI: 10.1007/978-981-4451-42-0_4,

1 Introduction

CNR, France's leading producer of exclusively renewable energy, controls a variety of production facilities: hydroelectric power plants, wind farms and solar power plants. Among these, the Rhône river concession is the main asset, with a generating capacity of around 3,000 MW, supplied by the 18 hydroelectric plants along the river.

Hydraulic modelling is omnipresent in CNR's Rhône operations. It can be found in both the studies, used to assure the company meets the obligations imposed upon a concession holder, and within the industrial river management optimisation processes, which of course, require strict adherence to a rigorous hydraulic safety framework. CNR has always invested in hydraulic modelling and has developed made-to-measure hydroinformatic tools, specifically designed to meet each of these needs.

These tools are constructed around distinct operational requirements, involving differing modelling requirements: while the 'study' field requires accuracy above all, the 'operational' field (for industrial users or training) stresses robustness.

2 The 'Studies' Field and its Accuracy Requirements

2.1 Modelling Requirements

CNR carries out a large number of hydraulic studies, whether to respect specifications and to validate various existing operational methods as a concession holder for the Rhône, or for future development projects.

CNR's general specifications include individual 'special specifications' (CCS) for each installation. Each of these 'special specifications' includes the concession holder's obligations, notably in terms of hydraulic flow: respect for operational instructions, respect for the natural water levels prior to the development building along undyked sections, discharge capacity of the design flood and respect for freeboard heights on non-submersible banking. CNR must be capable proving that these specifications are respected. To achieve this, CNR produce regularly updated hydraulic models: for each of the reaches modelled, we call 'reference model' the model used to verify that the concession holder is adhering to their contractual requirements.

Beyond these concession holder's requirements, CNR uses its modelling tools to validate exceptional 'special case' operating modes along the Rhône: floods with equipment outages (barrage gates and generator units), fast transient phenomenon (e.g., due to generating unit trips), operating at low water table levels, supporting upstream sediment flushing operations, etc.

The principle requirement for these hydraulic models is that they provide a complete overview of water flow hydrodynamics, sufficiently accurate to meet the

initial requirements behind the study. Faced with these requirements, the CNR has equipped itself with complete hydraulic models, capable of supplying data on water height, flow rates and speeds. These models are regularly updated to assure they are an accurate reflection of the current status of the Rhône.

2.2 Methods and Tools

The full length of the Rhône has been modelled and broken down, for reasons of practicality, into 20 reaches covering the Rhône itself with several additional models covering tributaries. A typical reach would comprise: the natural Rhône river course and the tailrace channel of upstream development, the reservoir and the run-of-the-river barrage and headrace channel of the considered development.

Each reach is represented by a 1-D looped-network hydraulic model, with additional storage areas. This model gathers:

- the network, corresponding to the topology of the reach, topographical information (using geographical data) and calibration settings such as Strickler's roughness coefficients,
- the scenario containing the hydraulic initial conditions and the boundary conditions.

It is based on the computing core used to solve the hydraulic equations needed to calculate the flow results: discharges, speeds and water levels.

The computing core, Crue, is shared by all of the Rhône models. It relies on the shallow water equations plus some structure hydraulic equations. CNR started developing the core, using Fortran, in the 1980s, and it is still used internally. Version 9 is released, while version 10 is currently under development using C++.

Fudaa-Crue, a hydraulic modelling tool using Java, is also used with the Crue computing core. It allows users to create the network of a model by assembling hydraulic modelling entities: branches with various hydraulic laws (shallow water equations, orifice laws, weir laws, regulated barrage, etc.), cross-sectional profiles, junction nodes, storage areas, etc. The software is capable of imposing hydraulic conditions and setting model parameters. This tool is built upon the Fudaa open-source framework, designed for hydraulic modelling and administered by a consortium of public authorities (Cetmef and Irstea) and companies (mainly EDF and CNR) (Fig. 1).

For geographical pre- and post-processing, the modelling software géoGAMA-Crue has been developed by CNR. It stands as a set of tools based on the SIG ArcGIS environment. It is used to process geographical data, from various sources and various levels of accuracy, for use in hydraulic models.

Along certain reaches, classic study models are insufficient to meet the needs of certain specific problems, for example, providing a spatial understanding of the random nature of flooding on specific sites or estimating the capacity for sediment transportation. Therefore, specific models are also required:

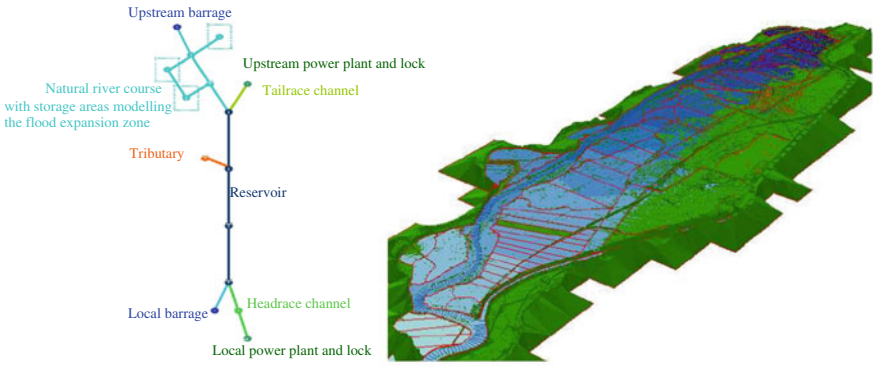

Fig. 1 (*left*) Diagram of a single reach of the Rhône with installations; (*right*) Topological close-up of the Montélimar model of the Rhône with its tailrace channel, natural river course and storage areas; the headrace channel from the upstream reach and the confluence of the Ardèche with the natural Rhône river course are also shown

- Transcritical 1-D modelling, using the following tools: Fudaa-Mascaret (Cetmet-EDF), Hec-Ras (US Army Corps of Engineers) or Flutor (CNR).
- 1-D transient modelling for studies of hydroelectric plant trips, using Crue (selection of suitable digital parameters),
- 2-D modelling using Telemac tools (EDF-Télémac Consortium).
- 3-D modelling using Fluent tools (ANSYS) to size complex installations such as locks, hydraulic power plants or even dams; these models are generally subcontracted to specialised design engineering offices.
- Hydrosedimentary modelling, notably using RubarBE by Irstea, who are supported by the CNR-jointly financing several PhD on the subject.

2.3 The Data

The data used in the hydraulic models of the Rhône come from a number of sources:

- Topological data are produced by the CNR's metrological teams or acquired from third parties, principally IGN. The data are also gleaned from terrestrial surveys, photogrammetry and, increasingly, from the use of LIDAR. These data are then used in the form of digital terrain models and characteristics lines (e.g., the tops of dykes).
- The bathymetric data are, in the main, produced by CNR itself, using its hydrographic survey vessel [1].
- The hydraulic data from the Rhône itself are gleaned from sensor stations, which constantly measure levels and flow rates [2]. These data are backed up by periodic readings from water lines, reading kilometric scales over various flow

ranges. Finally, these data are completed by readings from floods, high water mark readings and flooded zone limits.

All these data are collected and checked for coherence by CNR's metrologic teams. The data are stored in (and accessed from) Bathy (bathymetric database), Hydromet (hydrometeorological database) and SIG (topological and modelling database), developed by CNR.

An internal process, entitled 'Monitoring and Maintenance of the Riverbeds of the Rhône River and its Tributaries', guarantees that the data used to ensure that the CNR upholds its concession holder's obligations and is verified for each reach every 5 years on average, as well as after any large-scale flooding. Thus, the reference model for each reach is regularly updated using up-to-date topographical and bathymetric data. Evolving techniques mean that at each model update, the data available are more consistent and more accurate. In parallel, the requirements for accurate modelling results and the ability to represent a wide range of flow conditions will, over time, become evermore strict. These two dynamic factors are pushing forwards into ever increasingly accurate modelling and leading to the production of evermore complex models. CNR has put particular effort into assuring that any updates to the reference models are passed on to the operational models.

3 The Operational Context and the Need for Robust Systems

3.1 The Requirements of the Operational System: A Balance Between Complex Yet Robust Models

Within the context of the previously detailed studies, the trend is to prioritise accuracy and therefore increasingly complex models. However, is this tendency pertinent for operational use?

Operational use covers all 'real-time' activities, such as power plant control (predictive control using on-board models [3]), short-term simulations providing a 6-hour forecast for remote operators, energy production planning and forecasting of flood propagation for internal use. These are also used to train operators in the manual control of developments under all circumstances.

The principle for the operational use of river models is based upon the necessity of producing results, without which whole industrial processes may be shut down. The two obligatory conditions for these models to be usable within this context are, firstly, a guarantee of functionality under all circumstances, without interventions by modellers and within a pre-established level of accuracy, and, secondly, response times compatible with real-time and iterative loop operations.

This imposes strict limits in terms of the stability and robustness of the model. Depending on the application, these limits, to a greater or lesser extent, may be

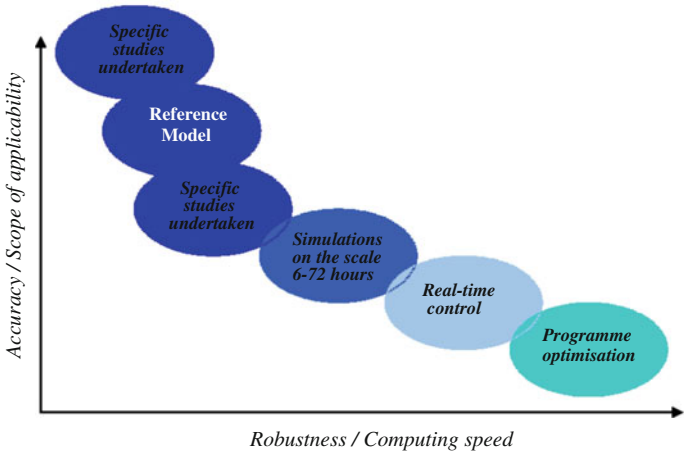

Fig. 2 Schematic representation of the balance between accuracy and stability for hydraulic models used for various different applications. Applications requiring higher levels of accuracy are those used within studies (*top left* of the plan), those needing to be more robust are those used within an operational context (*lower right* of plan)

competing with accuracy (Fig. 2). In actual fact, to improve robustness and/or computing time, after optimising digital parameters, it is generally necessary to simplify the models and thus limit their field of use and/or accuracy.

Thus, starting from as polyvalent a reference model as possible—which in itself may give rise to a number of variants for specific studies—any 'operational' model is specialised to match the final requirements. The filiation with the reference model ensures that the operational model remains coherent with the concession holder's obligations.

3.2 Adapting Model Types to Match Operational Requirements

The various operational uses for the models all have differing requirements in terms of robustness and computational speed. For example, those models computing the propagation of floods along the Rhône river cannot be simplified too much in terms of the exceptional flow rates they are required to simulate. In return, they consider a sufficiently long lead time to permit human intervention, changing the digital parameters to match flow rate conditions and even allowing a local reworking of the structure of the model itself. On the other hand, industrial models being run on-board as part of control mechanisms must be capable of running in loop mode without human intervention. This requirement for a robust system goes hand-in-hand with a simplification of scale. However, the subsequent loss of

Table 1 Production of operational models based upon reference model with respect to use

Model	Aim	Robustness	accuracy	computation	choice of model
Reference model	Verification of respect for concession holder's requirements, including high flow rate modes		++++	+	Fine modelling with inclusion of all available data. Inclusion of accurate hydraulic control depending on set points
Propagation of floods	Simulation of floods propagation along the Rhône river	++	++	++	Local simplification of the geometry of the mathematical model
Simulation on centralised operational a 6–72 h lead time	Centralised operational forecasts showing behaviour of reservoirs, centred around average	+++	++	++	Simplification of the geometry of the mathematical model with simulation every 100s.
SImulateur de training operators to conduite des (barrage control simulator)	Flow rates manually control barrages	++++	++	++	Simplification of the geometry of the mathematical model
On-board control model of local	Automatic real time	++++	++	+++	Simplification of the geometry of the mathematical model
Energy production programming	installation, automation and simulation of the behaviour of impoundments for the optimisation of energy production	++++	+	++++	with simulation every 100s. Q/Q Muskingum-type modelling

accuracy can be countered by frequent recalibration using observed water levels (simulations repeated every 100s in CNR hydraulic controls).

Various modelling strategies have been used, from very fast simplified Q/Q Muskingum-type models to the complete linking of 1-D hydraulic models with storage areas over the full length of the river. The various modelling choices made are all summarised in Table 1.

3.3 Boundary Conditions

This requirement for model stability and robustness leads to a similar requirement being imposed on the availability of the input data used as boundary conditions in operational models. These data are divided into two types: observations of the hydraulic state of the river and forecasts of future Rhône inflow (tributaries, ungauged intermediate inflow, etc.)

In order to guarantee the availability of these data, the CNR has introduced a series of strategies throughout the data acquisition chain to match data use: redundant sensors and power supplies, partnerships with sites useful for forecasting but not required for control, use of separate control and forecast databases, fail-safe modes, etc. For example, within the hydrometric database, we have developed a 'best of' module, used to assure the availability of critical real-time data and control the changeover to fail-safe mode. Thus, if a piece of data is unavailable or its accuracy is doubtful, the module automatically chops to a backup data source or a combination of backup readings to ensure that the forecasting modules are constantly fed with the necessary data.

4 Maintaining Consistency Between Models

4.1 Model Update Procedure

A model is made up of three fundamental components:

- Geographical footprint, corresponding to the hydraulic reach being studied.
- Validity date, linked to the validity of the data used to build and calibrate the model.
- The aim of the model—translating the compromises created by modelling—determining the scope of the validity for extrapolations of the model itself.

For each of the Rhône's reaches, the reference model is regularly updated by the CNR's study teams. This model is used to assure that the concession holder's requirements are being respected and to trigger, as and when required, river bed maintenance operations along both the Rhône and its tributaries.

Starting from the reference model, an operational model can be created to meet specific operational requirements: this may involve specialisation of data and the removal or alteration of certain of the entities included in the reference model, for example, certain storage areas could be removed or grouped, certain weir-feeding flood expansion zones could be simplified in the modelling. The aim, in general, is to avoid having to change digital parameters (e.g., reducing computing time-step) to prevent the propagation of digital instabilities when filling the storage areas. In this situation, a less accurate result is acceptable in order to improve stability and rapidity. The operational model, specialised for a given purpose, conserves the essential data from its reference model, particularly up-to-date bathymetric and topographical data.

All changes required when creating a specialised model are saved to a knowledge base. This can then be used to save time and improve efficiency when updating the specialised model. In reality, a reference model exists for a given validity date. When new calibration data become available, the creation of a new version of the specialised model may be begun, using the updated version of the reference model. In practice, this new version is only rolled out if there are significant changes in bathymetric data, topography, principle characteristics of major installations, between two generations of the reference model. This optimises the update procedure for models by prioritising those tasks returning the highest added value. The models are then saved and distributed via a centralised hydraulic model reference library (Fig. 3).

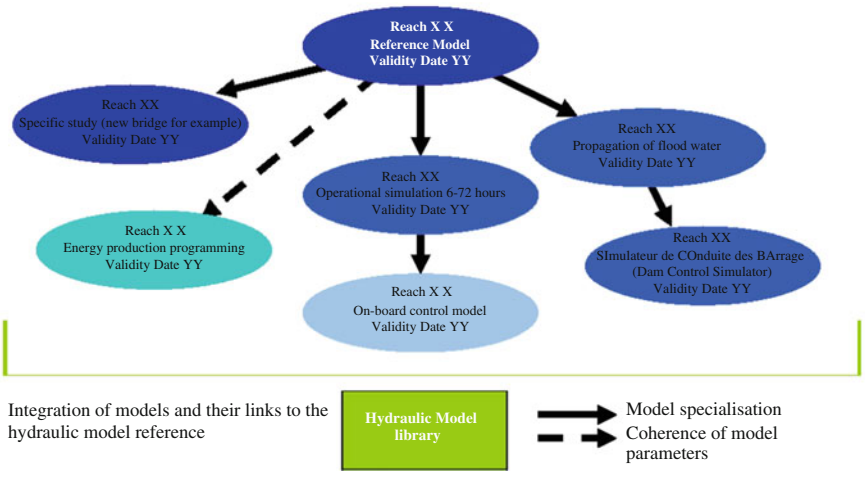

Fig. 3 The process of specialising models, illustration of the relationships between various models for a single reach of river on a given date

4.2 SYSSIH—Operational Support to Improve Coherence

The components parts of the models and software used to meet the various hydraulic simulation requirements must be rationalised, centralised and available from a single point. The aim of this is to limit the risk of diverging models and avoid being confronted with incompatibilities between models and the software being used to run them. It is simple to see that the hydraulic models employed by the simulator used to train operators in manual barrage control (SICOBA: 'SImulation pour la COnduite manuelle des BArrages' in French) must be coherent (i.e., must be based on the reference model with the correct validity date) with those used operationally in-board in the local hydraulic control. Among other advantages, this means that non-regression tests can be rationalised.

With this in mind, all common elements of CNR simulation tools are available via a single platform, SYSSIH—'SYStème de SImulation Hydraulique' (hydraulic simulation system in English). This platform centralises all elements of the various CNR simulation tools (computing core, hydraulic model network, simulation scenarios, hydraulic control models and module linkage sequencer) and provides a single source for all of CNR's operational hydraulic simulation tools: real-time tools for hydraulic control, flood propagation tools, short-term forecasting simulation tools for remote control, SICOBA training tools, etc.

5 Conclusion and Perspectives

Hydraulic modelling is widely used in the operational management of the Rhône river, whether this is directly integrated as part of predictive hydraulic control or within the simulation tools used in plant control. These various industrial applications have requirements, in terms of robustness and operating speeds, which may be incompatible with the reference model used to verify respect for the concession holder's obligations. This reference model must be adapted to the needs and constraints of each operational application (Fig. 4).

This multiplicity of usages means that constant vigilance is required to maintain the coherency of the code and hydraulic models used in the various applications, notably when updating reference models. For this reason, CNR has put together a system to provide consistency and coherence across the various models in use. This organisation is based on the use of a model library, tracing filiation links between the various versions of the models, as well as by developing a single, shared hydraulic simulation platform.

Even though the current system is fully operational, it is by no means locked down: changing requirements and technique evolutions may lead to the introduction of improvements as part of the operational life cycles of the various tools. Thanks to the organisation currently being used, hydraulic modelling is capable of evolving and changing to meet future requirements, while conserving a trace and a

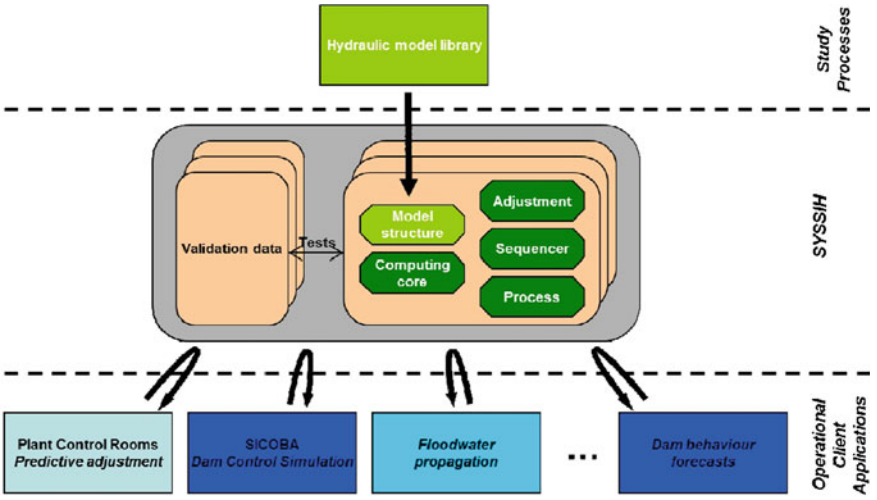

Fig. 4 Schematic diagram of the SYSSIH platform hosting the simulation components and links to the hydraulic modelling tools

coherence across all potential changes. With this dynamic of progress, CNR is currently carrying out studies and developments aimed at integrating, over the medium term, upgrades such as data assimilation [4] or the integration of probability-based approaches so as to be able to express the incertitudes inherent in hydraulic simulations as a function of the input data.

References

1. Blanquart, B. (2008). Estimation of the incertitudes in bathymetric measurements applied to crosssectional profiles taken by DR launches. CETIAT, Study Report No.2660063.
2. Grimaldi, L., & Haond, M. (2008). The CNR's continuous measurement network TSM. 2, 93–108.
3. Pagès, J.-C., (2000). Modelling, analysis and control of Rhône river installations using predictive controls Local and centralised management of flood events PhD Thesis, University Claude Bernard Lyon1.
4. Nelly, J.-B., Malaterre, P.-O., Dorée, C., & Sau, J. (2011). Data assimilation for real-time estimation of hydraulic states and unmeasured perturbations in a 1D hydrodynamic model. *Journal of Mathematics and Computers in Simulation, 81*(10), 2201–2214.

Numerical Modeling: A Tool for the Decision-Making Process

Cédric Bernardi, Claire Auriault, Monique Bourrilhon and Pierre Maruzewski

Abstract The decision-making process regarding the choice of renewable sources for energy supply is multidimensional. A number of aspects at different levels are to be taken into account such as economical, technical, environmental, and social. Reaching clear and unambiguous solutions may be very challenging even if the consideration is limited to a technoeconomical optimum. The need to develop tools for the design of electric power plants based on renewable energy resources arises from this difficulty. At the Hydro Engineering Center (HEC), considering main equipments criteria that are production and safety, useful numerical tools are developed to allow the modeling of hydraulic transients and the prediction of annual energy. Indeed, transients and energy production calculations help to costly optimize not only the sizing of the machines but also the complete hydraulic layout. For these purposes, specific numerical tools are dedicated to specific needs.

Keywords Modeling · Transient · Annual energy · Hydroelectrical activities

C. Bernardi (✉) · C. Auriault · M. Bourrilhon · P. Maruzewski
Electricite de France, Hydro Engineering Center, Savoie Technolac, F-73373, Le Bourget-du-Lac, France
e-mail: cedric.bernardi@edf.fr

C. Auriault
e-mail: claire.auriault@edf.fr

M. Bourrilhon
e-mail: monique.bourrilhon@edf.fr

P. Maruzewski
e-mail: pierre.maruzewski@edf.fr

P. Gourbesville et al. (eds.), *Advances in Hydroinformatics*, Springer Hydrogeology, DOI: 10.1007/978-981-4451-42-0_5,

1 Introduction

A hydroelectric project combines various fields of expertise. Thus, the work involved in seeking a solution requires an adequate assessment technically based on multiple criteria methods due to the range of expertise fields: civil engineering, electromechanic, supervisory control and data acquisition, economy without forgetting the social and environmental aspects. To progress in those studies, each field is awaiting information from others and the results of each study are input data to other fields.

Numerical modeling is a useful tool to support strategic decision during a hydroelectric project. It allows taking into account a large range of criteria. This extending range of criteria is influenced by the authorities who are mainly politicians, investors, and regulatory administrators. It is also the first way to evaluate risks and address unforeseen problems in a more systematical way than either guessing or forecasting. By simulating the future hydropower plant operations, each field of expertise can compare different technical solutions to choose the best one according to its criteria. The finished result should enable the authorities to draw up a series of alternatives and to choose the most acceptable settlement.

That is the reason why the Hydro Engineering Center (hereafter HEC), the hydraulic integrated engineering of "Electricité de France," develops its own modeling tools or models. As HEC is being organized in skills' departments, these tools help finding the best compromise inside a department or help managing interfaces between two departments during a project.

In the field of electromechanic, among the many criteria involved in a hydroelectric project, the safety and performance are those that rely almost exclusively on modeling tools. To ensure the safety of populations and structures or to comply with requirements from the local grid, some decisions oblige to reconsider the project profitability or feasibility due to major impact on equipments or waterways.

2 Modeling Tools

2.1 Generalities

In order to complete modeling, necessary information must be reliable and well formatted. The flow of main information can be described in order to understand the role of the modeling tools in the decision–making process (Fig. 1).

A preliminary feasibility study concludes to an estimated total capacity of the future hydropower plant depending on the topology and site hydrology. Civil works engineering sizes the dam and the hydraulic design of the waterways. Then, electromechanical studies can start.

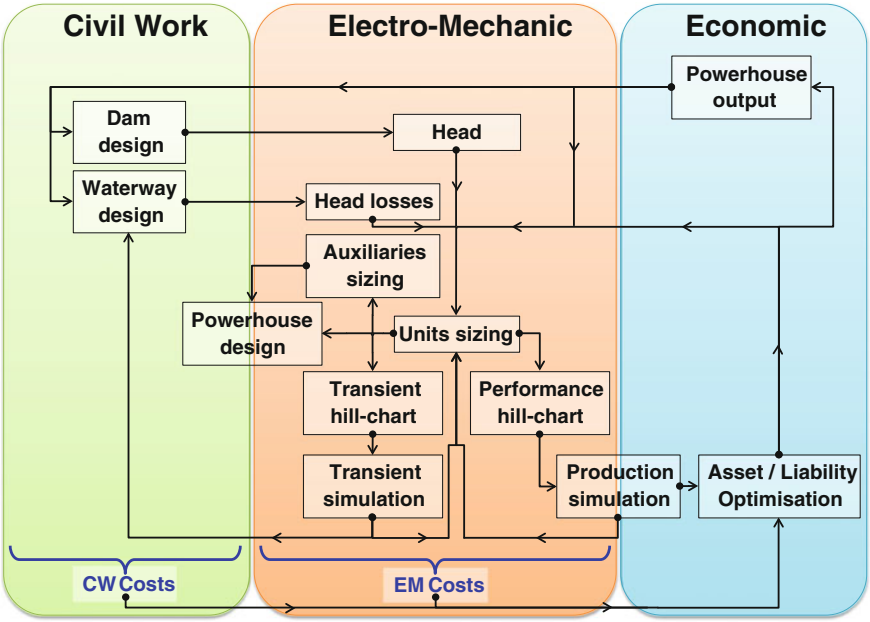

Fig. 1 Hydroelectric project map from an electromechanical point of view

2.2 Head Losses

Head losses and discharge depend on each other. Because they influence the operation range of the turbines and the behavior of surge tank, head losses coefficients are one of the basic data of any hydroelectric project. Thus, they are one of the first data integrated in energy production and transient modeling. If they can be roughly estimated in the preliminary steps of a project, regular and singular head losses need to be precisely calculated for the needs of modeling.

To facilitate usual singular head losses calculation, HEC developed a tool aggregating main results of specialized international publications. The benefit of this tool is that it uses the formulae best adapted to hydroelectric schemes, based on return of experience from measurements on existing power plants.

Thanks to this useful tool, head losses calculation can be quickly performed after any change in the waterway design and the impact of modifications can be readily estimated through modeling.

2.3 Unit Type and Sizing

If the final unit sizing relies entirely on the turbine manufacturer, HEC needs to anticipate the technical tender answer of specialized constructors to evaluate the

project feasibility and profitability. Indeed, after waterways characteristics, the modeling tools need units' characteristics that rely on the turbine type and preliminary sizing.

Depending on the head range, the choice of turbine type can be easy. For heads allowing more than one type of turbine, many different criteria can influence the turbine choice and sizing. The main ones are cost, performances, and behavior during transients. There are also reliability, flexibility, and maintenance.

Turbine presizing main input data are as follows:

- net head (deduced from the dam water levels and the head losses calculation);
- unit maximum discharge or output;
- electric grid frequency at the powerhouse location;
- minimum tailwater level.

The turbine presizing settles the following parameters:

- The rotation speed: With the capacity, it is an input parameter for the alternator design. For a design head, the higher is the speed and the smaller are the turbine dimensions and costs.
- The diameter and geometry: Dimensions of the turbine have an influence on the powerhouse arrangement, and they depend mainly on the runner diameter.
- The unit setting level: Determined in such a way to limit the cavitation phenomena, it is a major parameter for civil works, particularly in the case of pit powerhouse or river dam.

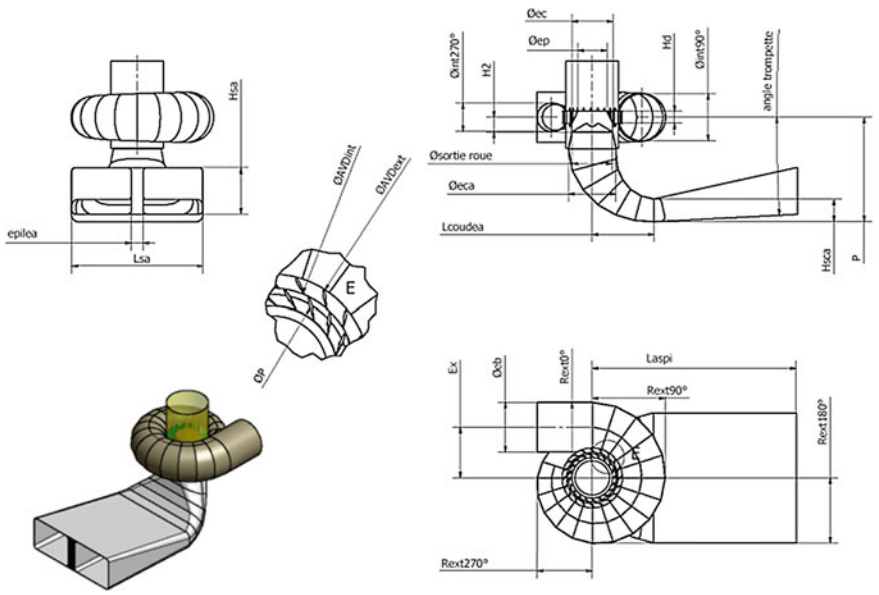

Fig. 2 Result from DEMHY

Through its involvement in numerous international hydroprojects, HEC developed dedicated software DEMHY, see Bellet et al. [1]. It allows to quickly obtaining a pertinent unit presizing compatible with the know-how of turbines' manufacturers. In combination with a parametric 3D CAD model, it facilitates powerhouse design (Fig. 2).

2.4 Definition of Turbine Characteristics

2.4.1 Generalities

Hill charts, resulting from the manufacturer design, define the behavior of the machine in every operational configurations of the future hydraulic scheme arrangement.

Some tools have been developed by HEC to display and transform hill charts in view to use them in modeling. A distinction has been made between "performances" and "transient" hill charts: The first ones are a set of points/curves describing precisely the hydraulic performances of the machine in its steady-state operating zone. The second ones are a set of points/curves describing the behavior of the machine in an enlarged operating zone. If mathematical treatment needs are globally the same between performances and transient hill charts, their different uses lead to develop dedicated treatment tool.

2.4.2 OUTPERF: Performances Hill Chart

The main functions and their principles are the following:

- Integration of an existing hill chart (data from site performance measurements or from model test measurements of EDF projects) to the database: All hill charts are stored with the same references to get a uniform and coherent database. Starting from a list of points (head, discharge, efficiency) or equivalent in reduced coordinate system, the functions build a regular rectangular (head, discharge) mesh between minimum and maximum values. The size of the mesh can be chosen by the user. The program then calculates a 2D surface on this mesh. A smoothing parameter can be defined to stick to the input points or on the contrary, when it is needed, to create a smoother surface. The interpolation error between input and output data is plotted, so that the user can judge of the validity of the result.
- Creation of a new project from a hill chart of the database: From the main results of unit sizing and the choice of a reference hill chart of the database, the function creates a new prototype hill chart adapted to the new project, taking into account efficiency scale effect calculated with IEC 60193.

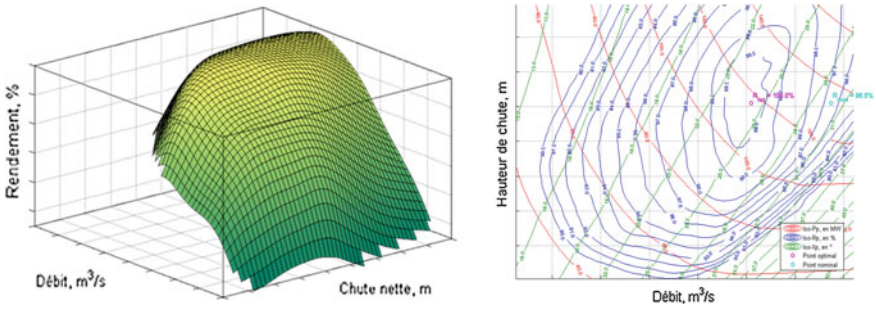

Fig. 3 Typical OUTPERF display

- Translation of a hill chart: The function allows some translations of a reference hill chart in the flow, head, or efficiency direction, in reduced or in prototype coordinates. A target point can also be set for best efficiency point. This function is useful when a reference hill chart of close specific speed does not exist in the database. In that case, it is necessary to adapt manually a reference to the new project. It has to be used with caution by an aware user to ensure the physical validity of the transformation.
- Determination of operating points and weighted efficiency.
- Computation and display of circuit characteristic: With the input data of minimum and maximum discharge, hydraulic circuit global head loss coefficient, and functions of minimal and maximal gross head variation with discharge, the function calculates and plots the characteristic curves of the hydraulic circuit. Plotted together with the machine hill chart, it allows displaying the effective operating zone of the machine placed in its waterways.
- Display of hill charts: The function enables us to plot the hill charts in reference or prototype coordinates (see Fig. 3).

2.4.3 TACTIC: Transient Hill Chart

Depending on the complexity of waterway configuration, the hydraulic machine may operate in extreme conditions such as under negative heads. For such modeling, the efficiency is less critical. Characteristics need to be defined in the entire machine quadrant and even in the four quadrants for some machines.

The transient hill charts tool is named as TACTIC, see Winckler et al. [2]. As OUTPERF for performances hill charts, it is a function toolbox that integrates, treats, displays, and formats transient hill charts used by HEC internal transient software. The user fills the type of machine, the synchronous speed, the runner diameter, and the raw data from model tests or site measurements. If recent data are well defined in numerical format, opening, head, discharge, and torque are known for the same measured point; old ones are often in graphical format: Each opening corresponds to a curve in two separated charts head discharge and head

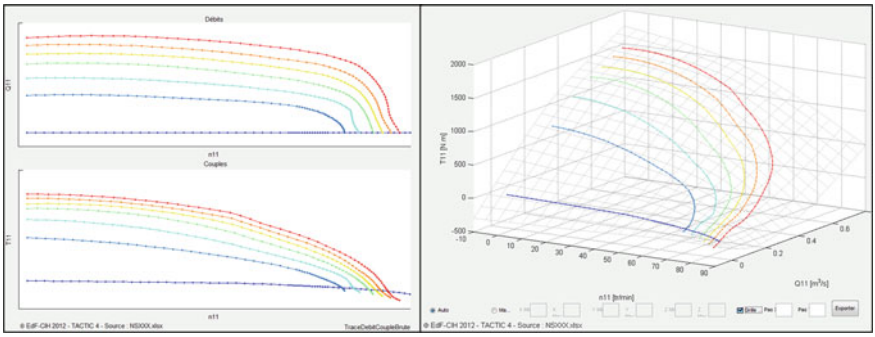

Fig. 4 Typical TACTIC display

torque. TACTIC allows reconstituting fictitious measurement points and calculates all the corresponding dimensionless terms.

After detection of the various operating areas, data are interpolated in order to obtain a regular resolution of the hill chart that facilitates the calculations of the transient modeling software (Fig. 4).

2.5 Transient Analysis with BELIER

The BELIER software developed at HEC evaluates the pressure and discharge in the tunnels and conducts at any time during operation, for example during turbine start-up and shutdown, see Calendray et al. [3]. The Belier software has been used for many projects over the years, see Huvet et al. [4].

The numerical models used in Belier are systematically compared to field tests as part of HEC's continuing pursuit of quality assurance, and a validation handbook keeps track of those comparisons of calculations to measured values.

BELIER is used in different stages of a new project:

- Tender (prefeasibility, feasibility, and engineering report):
  - to compute overpressure in tunnels or pipes during operation (start-up, shutdowns, governing orders, opening/closing of valve);
  - to help choose the type and dimensions of the surge shaft (diameter, elevation of the base, and the summit);
  - to help choose a technique for operation of gates and of the distributors or runner blades in order to ensure the best possible compromise between the overpressure in the collecting works and overspeed of the machinery;
  - to determine the characteristics of the machine: submergence, runner inlet and outlet diameter, moment of inertia of the rotating parts (runner + shaft + generator);

- Contract:
  - to check the project data;
  - to choose the possible combined operations.
- Commissioning: to optimize the parameters of the governing system.

BELIER can also be used:

- for an uprating or renovation project;
- to determine the impact of new operating parameters (increase discharge, faster start-up);
- to expertise accidents or anomalies during operation.

The steady-state or initial-state calculation methodology allows the calculation of meshed networks and takes into account all the components modeled. The transient calculation methodology is essentially based on the characteristics method solving the Allievi's equation in pipes, as shown in system (1), where Q is the discharge through the pipe, g is the acceleration due to gravity, S and L are the cross-section and length of the pipe, H is the piezometric head, k is the head losses coefficient, and a is the wave speed.

$$\begin{cases} \frac{dQ}{dt} = gS\left[\frac{H_{\text{inlet}} - H_{\text{outlet}}}{L} - kQ|Q|\right] \\ \frac{dH}{dt} = -\frac{a^2}{gSL}\Delta Q \end{cases} \tag{1}$$

In tunnels, only water hammer is taken into account (no pressure surge), and these equations are simplified:

$$H_{\text{outlet}} - H_{\text{inlet}} = \frac{L}{gS}\frac{dQ}{dt} + kQ^2 \tag{2}$$

These equations are completed by equations for each component, such as machine, surge shaft, and reservoirs.

Equations for machines:

- Speed change equation:

$$I\frac{dn}{dt} = T_{\text{hydraulic}} \tag{3}$$

$$Q = f(t) \tag{4}$$

- Head balance equation:

$$\text{Net Head} = H = H_{\text{inlet machine}} + \frac{Q_{\text{inlet}}^2}{2gS_{\text{inlet}}^2} - H_{\text{outlet machine}} - \frac{Q_{\text{outlet}}^2}{2gS_{\text{outlet}}^2} \tag{5}$$

where I is the inertia, n the rated speed, and T the hydraulic torque.

Equations for surge shaft:

Assuming that the piezometric head is constant in the surge tank and there is no pressure surge in the surge shaft.

$$\begin{cases} \frac{dZ_{\text{surge shaft}}}{dt} = \frac{1}{S_{ss}}(Q_{\text{Tunnel}} - Q_{\text{Penstock}}) \\ H_{SS} = Z_{SS} + \frac{Q_T^2}{2gS_T^2} + k_{\text{dia}}|Q_T - Q_P|(Q_T - Q_P) \end{cases} \tag{6}$$

Model of surge shaft with lower and upper chambers is also available.

Equations in upstream and downstream reservoirs:

Assuming that the total pressure is constant and equal to the water elevation and the water level is constant.

$$\begin{cases} H_{\text{Upstream reservoir}} = \left[H + \frac{Q^2}{2gS^2}\right]_{\text{in the headrace tunnel}} + k_{\text{reservoir outlet}} Q|Q| \\ H_{\text{Downstream tank}} = \left[H + \frac{Q^2}{2gS^2}\right]_{\text{in the tailrace tunnel}} - k_{\text{reservoir intake}} Q|Q| \end{cases} \tag{7}$$

Model of reservoir with a changing water level is also available.

2.6 Annual Energy Strategy

The ability to predict the annual energy production is crucial to the development of a hydroelectric project as it is the sale of energy that provides the income necessary to recoup the capital investment. This subsection provides guidance on the estimation of the energy output from a hydroelectric power plant.

The energy output is directly proportional to the water flow duration curve of the river Q_r. It will vary from year to year depending on the amount of rain falling and of the spring thaw on the river: During a wet period, more energy would be generated, and for a dry period, the plant may fail to meet the predicted total output.

However, sometimes an ecological flow Q_{eco} is requested for the environmental aspect, then the available flow duration curve Q_r—Q_{eco} represents the flow data for the annual energy prediction. In any case, the area below the curve represents the volume of water available for hydropower generation. It can therefore be combined with the net head and mechanical and electrical efficiencies to calculate the annual energy output. This procedure should be carried out in a stepwise fashion across the curve to take into account the increase in net head and reduction in turbine efficiency as the available flow reduces.

Thus, the annual energy production is defined by

$$AE = \int_0^T \rho g \eta_g \eta_{\text{turbine}}(t) N(t) H_n(t) Q_{\text{turbine}}(t) dt \tag{8}$$

where N is the number of turbines for a current flow, ρ the water density, g the acceleration due to gravity, η_g the generator efficiency, η_{turbine} the hydraulic turbine efficiency, H_n the net head, Q_{turbine} the unitary turbine flow, and T the number of operating hours during one year.

As shown in Eq. (8), the annual energy production depends on the number of turbines used for a current flow data, on the current flow data, on the corresponding net head, and on the turbine efficiency.

Two strategies are developed according to the strategy presented by Maruzewski et al. [5]: one for a powerhouse with one type of turbine U1 and one for a powerhouse with two types of turbines U1 and U2.

2.6.1 One Type of Turbine U1

The ST1 strategy of operating conditions for the best prediction of the annual energy production should be summarized as follows:

find k such as:

$$\begin{cases} Q_{U1,\,\text{turbine}}(t) = \begin{cases} \frac{Q_r(t)-Q_{\text{eco}}}{k} & \text{if } Q_r(t) - Q_{\text{eco}} \le N_{U1,\,\text{total}} Q_{U1,\,\text{turbine},\,\max}(t) \\ \frac{N_{U1,total} Q_{U1,turbine,\max}(t)}{k} & \text{otherwise} \end{cases} \\ \max\left(\eta_{U1,\,\text{turbine}}(t)\right) \\ k \cdot P_{e,U1}(t) \le P_{\text{installed}} \end{cases} \tag{9}$$

where $N_{U1,\ total}$ is the maximum number of turbines, $Q_{U1,\ turbine,\ max}$ the maximum unitary flow of turbine U1, $P_{e,\ U1}$ the U1 output, and $P_{installed}$ the total installed capacity of the powerhouse.

2.6.2 Two Types of Turbines U1 and U2

For a new project of development of the powerhouse, a second type of turbine U2 with a lower output is added to the previous ones. Furthermore, the operating range of turbine U2 is supposed to be within the operating range of turbine U1. Thus, the ST2 strategy of operating conditions for two types of turbines U1 and U2 for the best prediction of the annual energy production should be summarized as follows:

find the couple (l, k) such as:

$$\begin{cases} Q_{U2,\,\text{turbine}}(t) = Q_{U2,\,\text{turbine},\,\max}(t) \\ Q_{U1,\,\text{turbine}}(t) = \begin{cases} \frac{Q_r(t)-Q_{\text{eco}}-l\cdot Q_{U2,\,\text{turbine},\,\max}(t)}{k} & \text{if } Q_r(t) - Q_{\text{eco}} \le N_{U1,\,\text{total}} Q_{U1,\,\text{turbine},\,\max}(t) \\ \frac{N_{U1,\,\text{total}} Q_{U1,\,\text{turbine},\,\max}(t) - l_{U2,\,\text{turbine}}(t)}{k} & \text{otherwise} \end{cases} \\ \max\left(\eta_{U1,\,\text{turbine}}(t)\right) \\ k \cdot P_{e,\,U1}(t) + l_{e,\,U2} \le P_{\text{installed}} \end{cases} \tag{10}$$

3 Results

An example using the previously described tools is presented below, through the study and optimization of an academic case: an existing power plant with two equivalent units of 50 MW. In France, the utilities authorize an increase up to 20 % of the powerhouse output with a simplified procedure. Thus, the case of the implementation of a new unit of 20 MW is studied.

- PROJ1 corresponds to the existing powerhouse with two Francis turbines U1;
- PROJ2 corresponds to the powerhouse with two Francis turbines U1 and the new Francis turbine U2.

For each case, unit sizing, transients' study, and annual energy production analysis are performed.

3.1 Unit Sizing and Characteristics Definition

Waterways head losses are calculated with dedicated HEC tool. They are then used for the waterways modeling and lead to the available net head. Then, DEMHY provides the sizing of the foreseen units. From this sizing, predictive performances (see Fig. 12) and transients' hill charts are issued from OUTPERF and TACTIC.

3.2 Transient Analysis

Many load cases must be investigated in order to help choose the submergence of the turbines, to compute overpressure in the penstock and overspeed of the machinery, and to help determine the dimensions of the surge shaft. In this chapter, only one of the load cases is presented. The surge shaft is initially sized to allow the prompt restart of the two units U1 but not the two units U1 and the unit U2. A transient analysis is performed to determine how to restart the new unit U2 without allowing air to be drawn into the tunnel.

The load case performed is:

- simultaneous load rejection of the three units;
- simultaneous restart of the two units U1 at the most unfavorable instant, that is, leading to the minimal surge shaft level;
- delayed restart of the unit U2 at the most favorable instant.

Figure 5 presents the numerical model of the hydraulic scheme to be evaluated in the transient study. Figures 6 and 7 present some results of the load case that allow fixing the best instant to restart the unit U2.

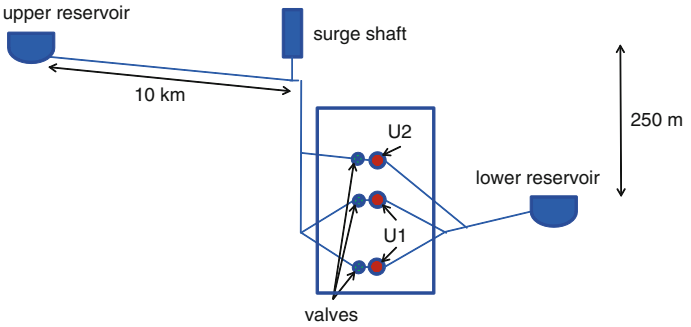

Fig. 5 BELIER numerical model of the project PROJ2 to be evaluated in the transient study

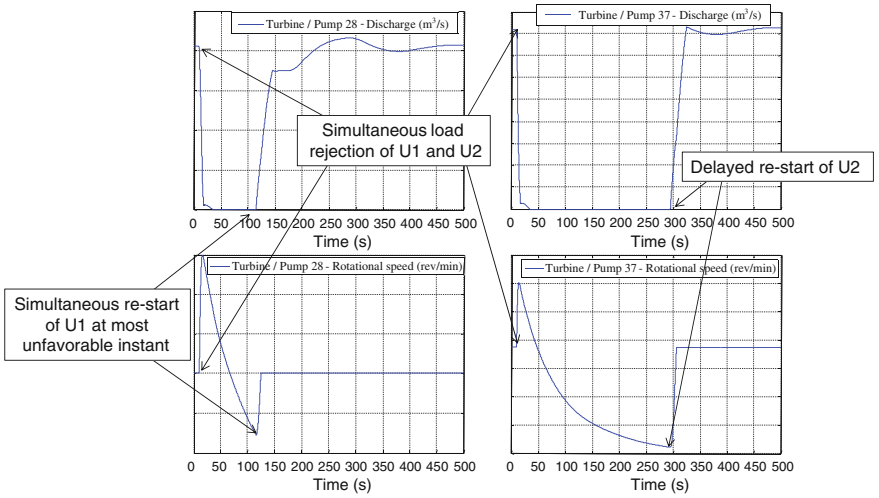

Fig. 6 Load case leading to the minimum surge shaft level: flow and speed of U1 and U2

3.3 Annual Energy Production

From HEC database, the flow of the river is defined by the flow duration curve Q_{River}, the blue line in the Fig. 8. The local utilities imposed an ecological flow $Q_e = 5\ \text{m}^3\text{s}^{-1}$ for an agricultural use. Thus, the total available flow used for the annual energy production is Q_{River}–Q_e.

3.3.1 PROJ1 with 2 Francis Turbines U1

The PROJ1 powerhouse consists of two existing Francis turbines U1 of 50 MW each for a total installed capacity of 98.5 MWe. The Table 1 presents the setup of units U1.

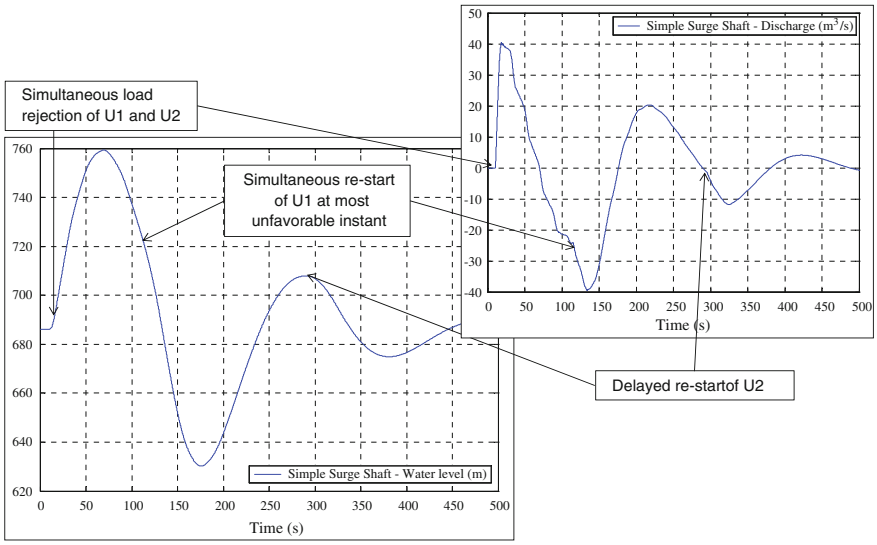

Fig. 7 Load case leading to the minimum surge shaft level: surge shaft water level and flow

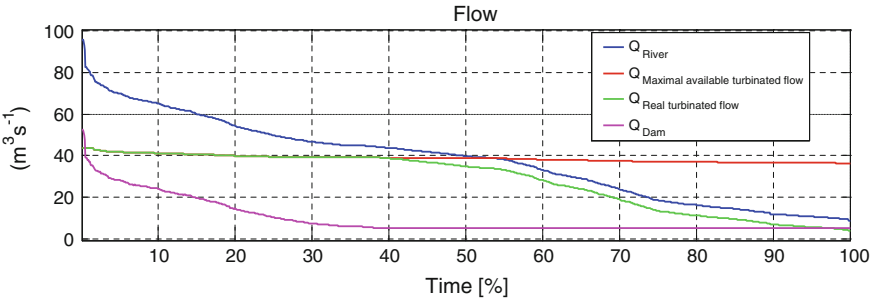

Fig. 8 Inflows for PROJ1

Table 1 Francis U1 turbine setup

Francis turbine	2 units U1
Runner diameter, *Dr* (m)	1.45
Synchronous speed (rpm)	600
Electrical output, *Pe* (MW)	49.25
Rated head, *Hn* (m)	250
Rated flow, Q (m^3s^{-1})	21.7
Turbine efficiency, $\eta_{turbine}$ (%)	94.6
Generator efficiency, η_g (%)	98.5

The river flow duration curves for the PROJ1 powerhouse are shown in Fig. 8 with the total river flow in blue, the maximal available turbinated flow in red, the real turbinated flow in green, and the spilled flow such as flow surplus and

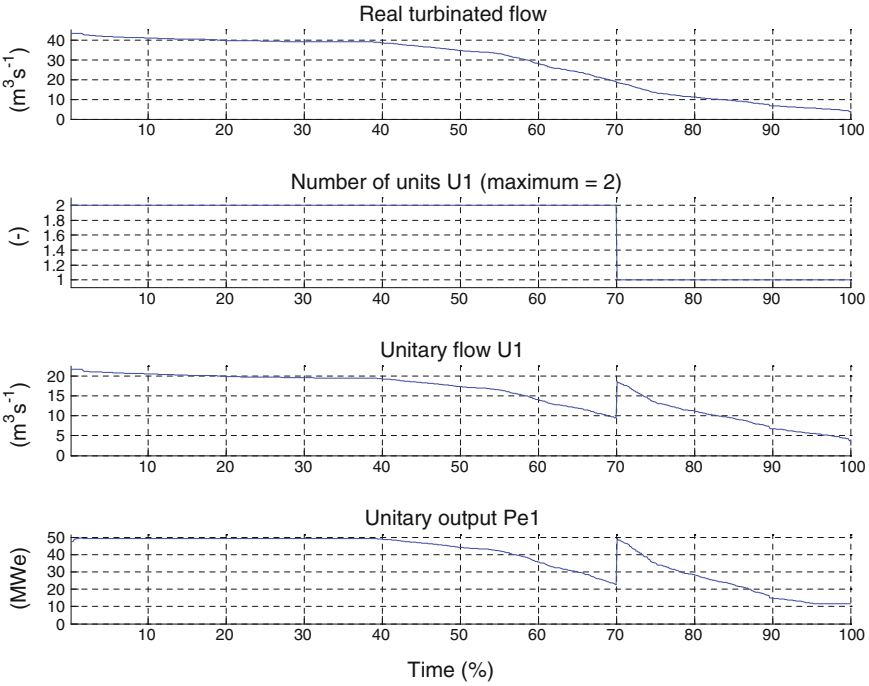

Fig. 9 Annual distribution of units, flow, and generated output for PROJ1

ecological flow in magenta. The flow surplus has been rejected for 40 % of the yearly time, and turbines U1 are working at their maximal operating range. Now, only focusing on the real turbinated flow, the number of units U1 only decreases from two to one unit after 70 % of the yearly time due to the variation in inflow. Due to the ST1 operating strategy, the unitary turbine flow slightly decreases during 70 % of the time when the powerhouse is operating with two units. Then, the flow increases at the shutdown of units and decreases in agreement with inflow, as shown in the Fig. 9.

Finally, in agreement with all the operating points and the formula (8), the annual energy production of the powerhouse PROJ1 with two units U1 is evaluated to 613 GWh for a total installed capacity of 98.5 MWe.

3.3.2 PROJ2 with 2 Francis Turbines U1 and 1 Francis Turbine U2

PROJ2 consists of increasing the total installed capacity by around 20 % to reach 118.2 MWe by adding a new unit with a lower output. This new PROJ2 powerhouse consists of two Francis turbines U1 of 50 MW and of 1 Francis turbine U2 of 20 MW. Table 2 presents the setup of unit U2.

Table 2 Francis U2 turbine setup

Francis turbine	1 Unit U2
Runner diameter, *Dr* (m)	1
Synchronous speed (rpm)	750
Electrical output, *Pe* (MW)	19.7
Rated head, *Hn* (m)	250
Rated flow, *Q* (m^3s^{-1})	8.7
Turbine efficiency, $\eta_{turbine}$ (%)	93.9
Generator efficiency, η_g (%)	98.5

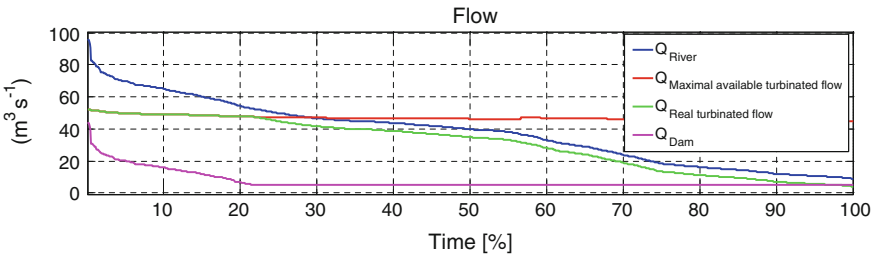

Fig. 10 Inflows for PROJ2

The river flow duration curves for the PROJ2 powerhouse are shown in Fig. 10. The flow surplus has been spilled for 22 % of the year.

Due to the ST2 operating strategy, the turbine U2 is working at maximum range during 39 % of the year before a shutdown due to a lack of inflow for all units of the PROJ2 powerhouse. All units U1 are operating in accordance with the inflow during 70 % of the time and, after that, one unit U1 is shutdown, as shown in the Fig. 11.

The corresponding operating points of units U1 and U2 during the yearly operation mode are represented in green circles in the Fig. 12. In the left figure for the units U1, the bottom circles' line consists of the operating points of the PROJ2 powerhouse operating with two units U1 and one unit U2. The mid-circles' line corresponds to the two units U1 in operating mode (unit U2 in standstill mode). The top green circles' line corresponds to only one unit U1 in operating mode. In the right figure for the unit U2, the green circle along the maximal path represents the operating range of the unit U2 during 39 % of the yearly time.

The annual energy production of the PROJ2 powerhouse with two units U1 and one unit U2 represents 662 GWh for a total installed capacity of 118.2 MWe.

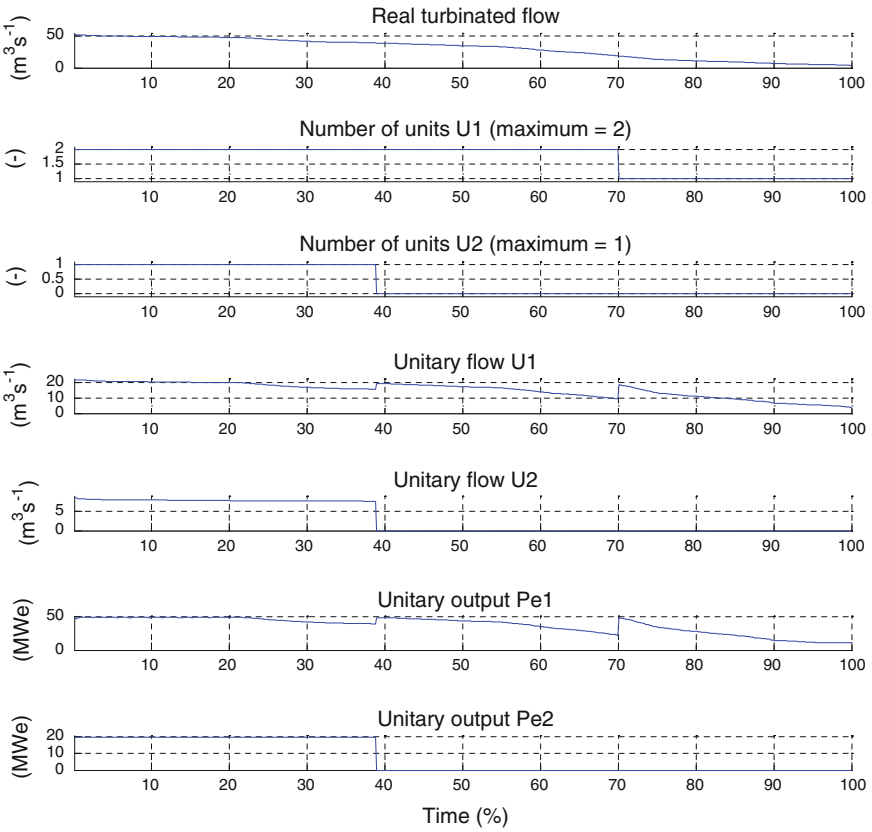

Fig. 11 Annual distribution of units, flow, and generated output for PROJ2

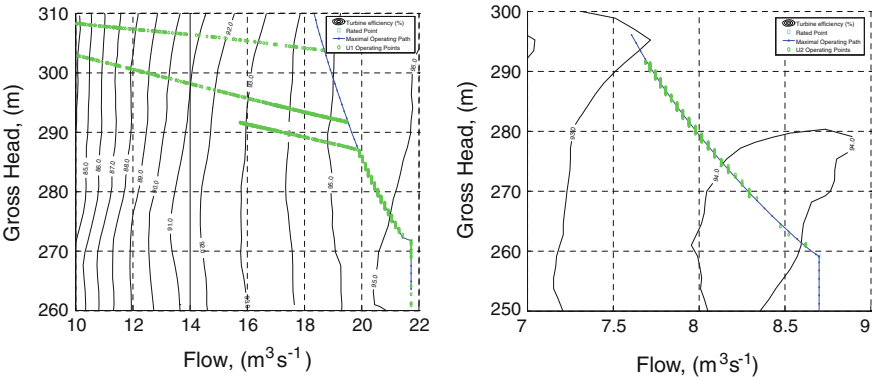

Fig. 12 Hill charts of U1 and U2 operating points with isolines of turbine efficiency for PROJ2

Table 3 Comparison between PROJ1 and PROJ2

	PROJ1	PROJ2	Difference
Total installed capacity (MW)	98.5	118.2	+20 (+20 %)
Time of flow surplus (%)	39	22	−17 (−56 %)
Annual energy (GWh)	613	662	+8 %

3.4 Synthesis

From safety point of view, the transient analysis confirms the need of the surge shaft modification and help to determine the operational flexibility of the units. It also permits to identify the needs of increasing the submergence of the new machine. These optimization results help to evaluate an accurate cost of civil work.

From the economical point of view, the comparison of the annual energy calculation shows that 8 % more energy is generated, for an increase of 20 % of total capacity (see Table 3). This increase in energy remains attractive. Moreover, considering water management, the time within which the surplus water is rejected is reduced by a factor of 2. Thus, 78 % of the river flow is effectively turbinated.

4 Conclusion

At HEC, considering main equipments criteria that are production and safety, useful numerical tools are developed to allow the modeling of hydraulic transients and the prediction of annual energy.

Those tools are applied for the development of a new runoff hydropower plant project on river where the maximum output is fixed to 120 MWe. The best electrotechnical solution consists of a powerhouse with two different capacities of units, which induces a significant increase in the annual energy production.

Furthermore, the transient optimization helps to implement a safety powerhouse regarding the behavior of the surge tank and to find realistic submergence of the units.

The next step of the decision-making process concerns an economical analysis according to the technical conclusions. By this way, a business plan should be elaborated and validated by the decision makers.

Acknowledgment The authors are very grateful for support of Process and Technology Department, in particular the help and advice from Nadine Pajean and Patrick Grillot.

References

1. Bellet, L., & Grillot, P. (1998). *IH.*.DT.1005 machines hydrauliques-logiciel demhy*, EDF internal note.
2. Winckler, V., & Lefebvre R. (1998). *EH.HDEC.ED.002 logiciel TACTIC version 3.4 notice de principes*, EDF internal note.
3. Calendray, J. F., Degrave, C., Ilaht, D., & Planchard, J. (1982). Belier: A computer code for the modeling of hydroelectric schemes. *Proceedings of IAHR 1982*, Moscow.
4. Huvet, P., & Chen, D. (1990). Particular features of hydraulic transient computations performed for the Guangzhou pumped storage power station. *Proceedings of International Symposium on Pumped Storage Development, 1990*. Beijing, China.
5. Maruzewski, P., Rogeaux, C., & Laurier, P. (2012). Hydraulic preliminary-sizing of hydropower plant. *Proceedings of IAHR 2012*. Beijing, China.

Information Handling in Interdisciplinary, Hydroenvironment Engineering Projects

Frank Molkenthin, Chi Yu Li and K. Vikram Notay

Abstract Information handling in water-related interdisciplinary engineering projects is a demanding challenge due to the mass of data from field work, laboratory experiments and numerical simulation. This chapter describes a general concept for information handling in an interdisciplinary research unit using a generalized information modelling approach for multi-scale physical state variables in combination with metadata and Web services–based information systems following the INSPIRE initiative. The research unit deals with the coupling of flow and deformation processes for modelling the movement of natural slopes and integrates data and models from different disciplines such as hydrology, hydrodynamics, geohydraulics, geophysics and soil mechanics. Key idea is a generalized information modelling concept for any kind of physical state variables on different spatial and timescales using tensor and set theory from mathematics as well as object-oriented information modelling techniques. Tensor objects are used for the full information handling process from field data acquisition and management via information analysis and model coupling to information archiving and storage. A hydroinformatics system so-called Turtle has been developed using standard IC technology such as XML schemes for tensor objects (TensorML) and ISO 19115 and 19119 for metadata and geoportal-based interdisciplinary collaboration and long-term archiving and reuse of the relevant information.

Keywords Hydroinformatics · Information systems · INSPIRE · Model coupling and integration

F. Molkenthin (✉) · C. Y. Li · K. V. Notay
BTU Cottbus, Chair Environmental Informatics Konrad-Wachsmann-Allee 1, 03046 Cottbus, Germany
e-mail: frank.molkenthin@tu-cottbus.de

C. Y. Li
e-mail: lichiyu@tu-cottbus.de

K. V. Notay
e-mail: vikram.notay@wahyd.tu-berlin.de

P. Gourbesville et al. (eds.), *Advances in Hydroinformatics*,
Springer Hydrogeology, DOI: 10.1007/978-981-4451-42-0_6,

1 Introduction

Water-related research and engineering projects are using mass of data originated from field measurements, laboratory experiments and numerical simulations. These giga/tera bytes of data, the related metadata and pre-processing activities lead to information—mass of information. The efficient handling and the useful utilization of such information pool require suitable information systems to support efficient interdisciplinary and distributed project collaboration as well as the integration of models and data on different scales.

Normally, information handling and management are not seen as critical core part of projects, assuming that the relevant information might be available on time. Efforts on these tasks pay off more on the medium- and long-term perspectives than on the short-term level. This leads to a lower level of efforts on information handling and management during the project preparation and the project performance. Simple, conventional solutions such as hierarchical file systems for ASCII data files, Excel sheet files and GIS files are applied to survive in the flood of incoming mass data. Results from data analysis and numerical simulation models are also handled in this way. Medium-term-oriented reporting and long-term-oriented archiving are considered by personal/internal "solutions" without standardization, without suitable metadata descriptions and incomplete documentation of the data collection process. This works in smaller projects with non-changing staff but not anymore on interdisciplinary projects, when mass of heterogeneous data are collected to be used by experts from different disciplines at any time over long time periods. Water management projects with long-term perspective (e.g. as defined by EU water-related directives) demand a more sophisticated and generalized information handling based on related IC technologies.

As the amount of available data by modern sensor, remote sensing and Web technology are increasing rapidly, there is a demand on suitable information management systems to deal with this problem on short-, medium- and long-term perspectives. As a vicious circle, no information management system is available when data are available, or if a sophisticated information management system is set up, nobody wants to use it [6]. Database systems and GIS software can be used as basic supporting tools, but did not consider as the different interdisciplinary aspects of water-related projects. To overcome this problem, hydroinformatics systems are requested as flexible solution considering different levels of project complexity, different spatial and timescales as well as the different, discipline-oriented view on the water-related project topics.

Interdisciplinary collaboration is based on standardizations such as ISO 19115 (geographical information—metadata) and ISO 19119 (geographical information—services) for GIS based data sharing and exchange. Hydroinformatics systems in this sense are not any more based mainly on numerical models; their main focus is to handle water-related information for engineering purpose. This indeed integrates numerical models but also information analysis, coupling components, reporting and documentation modules as well as any kind of Web-based services

for information handling. Hydroinformatics systems become a holistic approach to combine all computer-based information tools in an integrated manner in comparison with the conventional sequential combined set of tools. This chapter describes an approach for such a system, applied in an interdisciplinary hydroenvironmental research project.

2 Research Unit "Grosshang"

The interdisciplinary research unit "Grosshang—Natural Slopes" (web-page: http://www.grosshang.de, 2006–2011 [3]) deals with the "Coupling of Flow and Deformation Processes for Modelling the Movement of Natural Slopes" as described in [1, 2]. Target of the research unit is the modelling of the long-term deformation of large hillsides (Lindenmaier [4]). Extensive field measurements are taken to identify the relevant processes and belonging scenarios for the slope Heumöser in Ebnit/Austria. The measurements cover hydrometeorological, geohydrological and geophysical state variables on different timescales and spatial distribution. The quantity and heterogeneity of the measurement data have increased significantly during the project due to permanent measurements and additional short-period measurements. These mass data are used to identify the relevant natural processes and to specify suitable scenarios for further investigations. Simulation models from hydrology, hydrodynamic, multi-phase groundwater flow and soil mechanics are used and partially coupled towards interdisciplinary, multi-scale simulation components to get a better understanding of these processes and scenarios. Laboratory experiments have been performed for model parameter identification and verification. Both simulation models and laboratory experiments increased also significantly the amount of heterogeneous mass data to be handled in the research unit. All these lead to physical state variables on different scales in time and space. Scenarios of interest are defined by sets of physical state variables based on time series information analysis. Scenario simulation requires integration and coupling of different models. This task is based on the exchange or sharing of multi-scale physical state variables during simulation run-time or in a sequence of partial processes. The heterogeneity, complexity and interdisciplinarity of this research unit are a challenge for information modelling, management and engineering in hydroinformatics. The demands on information handling can be structured by time perspective in three types of support services:

- Information Acquisition and Management: This is a short-term task during and after field/laboratory measurement for data pre-processing to transform raw data to usable information.
- Information Analysis and Sharing: This is a medium-term task following the information acquisition running within the time window of the research unit. This task supports the core activities of the project partners and their collaboration based on information sharing.

- Information Archiving and Storage: This is a long-term task for the time after the research unit. It ensures the persistent availability of relevant information and allows an efficient information retrieval for future projects.

Information systems have to consider these three tasks with their different requirements and conditions. Section 3 shortly introduced a suitable information modelling concept, while in Sect. 4, the applied information handling concept of the research unit is described in detail.

3 Information Modelling Concept

Key idea of information management within the research unit is the generalized information modelling of all relevant physical state variables using the basics from mathematics (set theory, tensor algebra) and computer science (object-oriented modelling) in combination with metadata and Web services technology. All physical state variables are modelled by tensor classes and managed by sets. This modelling concept is called "TensorML" following other XML-based modelling concepts. The tensor classes are structured by tensor rank, tensor dimension and tensor structure (Molkenthin [5]). Examples for the tensor rank are scalar, vector and matrix. Physical state variables are depending on the different numbers of coordinates (such as space and time), defining the tensor dimension. For any tensor, dimension-related discretization structures are defined, such as regular and irregular topological structures based on points as known from grid modelling in numerical schemes. The physical state variable values and coordinates (space and time) are linked to these points within the topological structures. The tensor structure considers combination of tensors on the tensor object level or on the tensor value level. These set combinations include functional relationships between different tensor objects such as material laws, Q/h relationships and more complex dependencies described by AI or numerical models. Set operations on tensor sets enable the management of several physical state variables independent from their origin, scale and relationship.

The classifications by tensor rank, tensor dimension and tensor structure lead to several tensor classes covering all typical kinds of data for field/laboratory measurements and simulation models. Based on the object-oriented approach, the described tensor classes contain—besides the data for the physical state variable values—methods for management, manipulation and analysis such as tensor operations, tensor analysis and set operations. Tensor objects also contain metadata describing all relevant information about the origin (sensor, model), spatial and temporal coverage, contact person and so on. This tensor class–based information modelling concept is used for information handling in the research unit.

4 Information Handling Concept

The described information modelling approach has been used to develop a flexible information system with the code name Turtle. The system consists of tools for user interfaces (editor, analysis and visualization), report generator (interactive HTML report), information archiving, import/export as well as metadata management. It is linked with GIS systems such as Web GIS services for displaying maps within a browser and with metadata management systems/geoportal software for information retrieval. Turtle integrates the traditional separated pre- and post-processing, databases and simulation processors in a holistic but flexible hydro-informatics system. The basic concept of information handling in the system is shown in Fig. 1.

The raw data from field, laboratory and simulation are the input data as they are generated by the sensor device interfaces in the field and laboratory as well as by tools for information analysis and numerical simulation. They are collected, validated and pre-analysed in their original files (format, file system structure) in the raw data file base. Related metadata specifications—generated, analysed and manually defined—allow a complete description towards long-term persistent and accessible information. In a validation process, the raw data information is transferred into a generalized tensor base for physical state variables including several filter, interpolation, standardization and transformation methods to bring all information on a standardized level independent from their origin in the raw data file base.

As tensor objects are semantic independent units including data and methods, the tensor base can be used for any kind of information analysis in the research unit. Interactive Web reports are generated to access the tensor base in a distributed environment via the Internet and to ensure a long-term-oriented archiving and

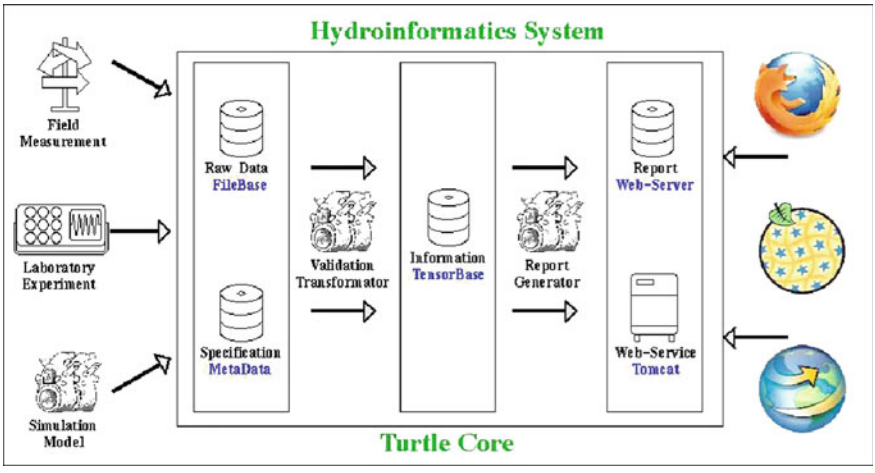

Fig. 1 Information handling concept in the research unit

storage of the information. Besides standard Web pages, Web/GIS services and metadata services are supporting this with modern functionality and Web interfaces to other systems such as spatial data infrastructures (SDI) and GIS systems. Some details of the introduced components of the information system Turtle are described in the next sections as an example of field measurements. Same principles are used for laboratory experimental data and results from simulation models but cannot be described in detail in this section with a limit of eight pages.

4.1 File Base: Information Acquisition and Handling

Turtle has been applied for the field measurements at the Heumöser in Ebnit/Austria. The related raw data are collected and stored in data files, using mainly proprietary ASCII formats, depending on the sensor/station configuration and technical equipment. Several permanent and temporal field measurements are available, and examples are as follows:

- meteorological stations operated by city of Dornbirn at 5 locations
- hydrological/meteorological station (21 sensors) operated by Karlsruhe Institute of Technology (KIT)
- creek water level/discharge measurements (weirs) by KIT
- tracer measurements by KIT
- 3 borehole measurements (pressure, displacements) by KIT
- nanoseismic network by University of Stuttgart
- geoelectric/-seismic investigations by UFZ Leipzig and University of Potsdam

The available data are handled in three steps:

- classification by metadata including filter and validation rules
- integration in the file base of the information system as original raw data
- transformation in the tensor base with flexible timescale using validation and transformation rules

The file base consists of a huge amount of raw data files with different data formats from the different sources. The files are analysed for format validation and measurement metadata such as time window, sampling rate, type and unit of the measured physical state variable and measurement gaps. The raw data itself are validated by rules. Examples are value ranges and filter methods. Value ranges define valid ranges of data, such as physical rules (e.g. air humidity: 0.0–100.0 %) or sensor-based limitations and specifications of the used sensors. Filter methods can be used to define specific operations for specific time windows such as NaN values for out of operation, or data offset for wind direction instrument shift and water level indicator vertical calibration. Time shift operations are used to transform all data from local measured time zone (CET, CEST, UTC) in one standard time coordinate system (UTC). Spatial coordinates are transformed in the Austrian national geospatial coordinate system (BMN).

The performed field measurements are described in a suitable information model and related metadata scheme based on ISO 19115. All measurements from one source (data service) are combined in one file model structured by stations. Each station consists of several sensors, and the sensor itself is linked to one or more measured physical state variables modelled as tensor objects. File, model, station, sensor and tensor do have metadata properties to describe all relevant properties, such as location, operation time windows, value range and tolerance, sampling rate, units, serial number. Time and location (spatial coordinates) are used as coordinates for the other attributes. This allows the description of time-depending calibration parameters, time windows of non-operations and maintenance as well as (e.g. seasonal) changing locations of sensors.

4.2 Tensor Base: Information Analysis and Sharing

The raw data are transformed into the tensor base using standard properties, for example for time, unit and location, to get a standardized set of physical state variables described by tensor objects ("TensorML"). Data from different sensors with the same physical state variable are combined into one time series. Gaps are filled by interpolation, where suitable and possible. The tensor base consists of tensors for a predefined project time window (1998–2012) and timescales for all physical state variables. Basic regular timestep is 600 s with the time origin of 01.01.1990 00:00:00 UTC. Further timescales can be specified, typically timestep resolution of 3600 s (1 h), 21600 s (6 h), 86400 s (1d) and 604800 s (7d) is used. The transformation between the timescales is part of the tensor base using typically mean value or sum-up methods. Separated measured state variables can be composed by tensor operations such as wind direction and speed towards wind vector or soil moisture at different depths towards a 2D (time, depth) scalar field. Exchanges of sensors during long-term measurements lead two different file sets in the raw data file base but are also handled in only one tensor object for the related physical state variable. The transformation of raw data in the tensor base considers the measured state variables. Further interesting physical state variables can be included as depending tensors. The relationship is again a tensor, which might be time dependent. Examples are discharge tensor within creeks. Measured physical state variable is the water level. Based on the weir geometry and instrument configuration, related Q/H relationships can be specified for specific time windows.

4.3 Web Report: Information Archiving and Storage

The information system generates an interactive Web report with the whole information content of the file base and the tensor base. The use of JavaScript and

JavaServlet technologies to generate any Web page dynamical on demand for any tensor object, tensor set or tensor operation allows flexible navigation through the existing information scheme. The Web report consists of three main parts:

- metadata-based structure report
- raw data file base report
- tensor base report and data (export) access

The metadata report represents the metadata specification of the raw data file base. Metadata-based information search functionality based on GeoNetwork (http://geonetwork-opensource.org) and GeoServer (http://www.geoserver.org) as GIS front-end provides a powerful interface for information retrieval. The raw data files are completely linked and reported in tables and diagrams of the raw data file base report. All data information can be found in the report and in the linked raw data files. The tensor base report is interactive to allow the reader to surf through the information base for different timescales and time windows. The Table Viewer reports all data in an alphanumeric manner. The Data Viewer is also based on tables but summarizes the physical state variables by hourly, daily, weekly, monthly, annual mean, min, max values as well as gaps, variance and standard deviation. The Image Viewer is the graphical report of the tensor base with all related diagrams of the physical state variable on every timescale for every suitable time window.

The access to the database via the Internet is realized by a JavaServlet component of the information system. User can ask for any physical state variable in any time resolution and duration as well as in any combination with other variables (e.g. rainfall data, creek discharge, soil moisture and borehole declination). Besides standard table and diagram presentation, the data can be downloaded as Excel, ASCII or XML file (data export) or be analysed in a tensor editor JavaApplet component or via Web/GIS interfaces in GIS (such as Web-based GeoPortal and GIS-Viewer, see Fig. 2) with full application functionality.

Long-term archiving of data is important for interdisciplinary projects to ensure data discovery and retrieval. In the research unit Großhang—"Natural Slope", such data archiving services are based on international standards such as ISO 19115 (geographical information—metadata) and ISO 19119 (geographical information—services). Information retrieval is implemented according to the INSPIRE ([7], http://inspire.jrc.ec.europa.eu) compatible GDI-DE technology (German spatial data infrastructure). This holds for the raw data in the file base as well as for the content of the tensor base. The interactive Web reports with metadata search functionality enable the full access to the tensor base and to the raw data file base. In this way, Turtle as information base combines all the three important tasks: short-term information acquisition and handling, medium-term information analysis and management and long-term information archiving and storage.

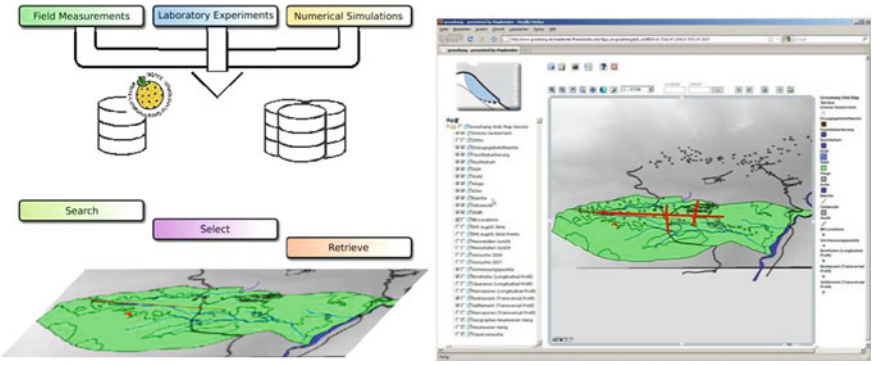

Fig. 2 Metadata application for information retrieval via GeoPortal

4.4 Time Series Knowledge Management for Event and Process Identification

Simulation models require input data such as boundary and initial conditions representing typical or specific scenarios of interest. These input data as physical state variables are based on measurements and can also be handled as tensor objects. Besides the direct use of measured physical state variables, specific events are identified and well-defined scenarios are specified for simulation. This task is supported by a sophisticated method of time series knowledge management part of the information handling concept. The method based on Mörchen [8] is also supporting process identification to identify relationships between events as sets of physical state variables. The method is developed for time series but will be extended for time/space systems as part of a PhD thesis work. Figure 3 shows the main working steps of the methods to identify events and their relationships towards an interactive scenario composition to generate initial and boundary condition time series for numerical simulation models. Details are described by Li [9].

4.5 Model Coupling and Integration

The research unit deals with investigations on complex physical processes: Coupling of Flow and Deformation Processes for Modelling the Movement of Natural Slopes. Several simulation tools for single processes (hydrological, hydraulic, soil mechanics) are available and have to be coupled and integrated in one system. Specification of well-defined initial/boundary conditions with a sequence of model runs and exchange of files is a suitable first attempt for this target. More sophisticated solutions such as OpenMI might be the next step. As OpenMI is (at the moment) not standard in all disciplines, such approach would require comparably high effort to develop required wrapper and functionality for all applied simulation models.

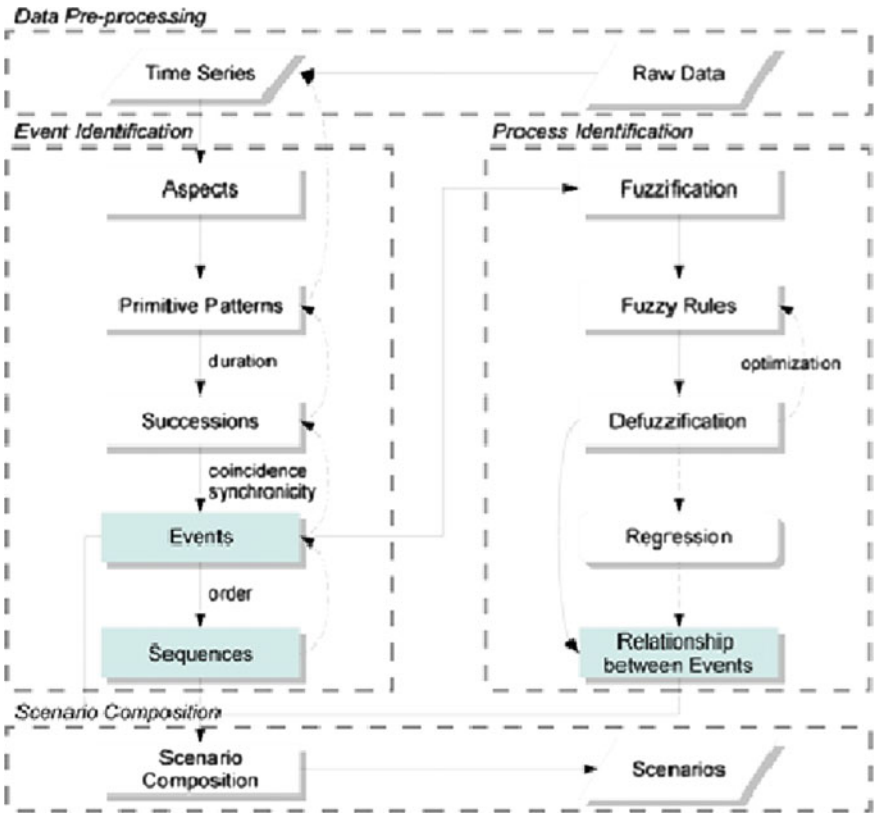

Fig. 3 Event and process identification—working steps

The applied information handling concept is based on tensor objects, which contain besides the physical state also methods to adapt themselves to any kind of spatial or temporal resolution and approximation. Relationships besides tensor objects can also be modelled as part of the information handling concept such as Q/h relationships or material laws. This allows a flexible and powerful model coupling and integration concept by a tensor object broker.

Models are requesting there input data and are offering their result data to the tensor object broker. Similar to OpenMI, this broker manages the exchange of the physical state variables between the involved models and offers timestep control support. The adaptation of the approximation of the requesting model (e.g. by interpolation) is completely covered by the tensor objects and not part of the simulation models. The broker can be also used to model "simple" physical behaviour by any kind of transformation rules of tensor object sets including integration, differentiation and algebraic operations. The broker has been developed for some first-test applications based on XML-RPC using TensorML and will

be extended for more complex systems as part of a PhD thesis work. Details are described by Notay [10].

5 Conclusions

Interdisciplinary water-related projects require a flexible handling of information from different disciplines on different time and space scales. This chapter described a holistic approach to handle mass information from field, laboratory and numerical simulation in one hydroinformatics system using a generalized modelling concept for physical state variables ("TensorML") in combination with metadata and Web/GIS techniques such as used by the INSPIRE initiative. The application in the research unit "Grosshang" demonstrates the suitability of this approach and the potential for further activities in this field. Two examples for ongoing activities are introduced: The tensor-based modelling concept is also used to couple different simulation model by an independent tensor exchange broker. This broker can support the exchange of information on demand including mapping and scaling but also using tensor object relationships to represent physical behaviour. Second example of future innovation is an event and process identification and scenario composition/generation component to feed simulation models based on natural observations.

Water is the base of human life. The challenge of a transparent, fair and sustainable water management on Earth in the age of the information society needs such kind of information system. Initiatives such as INSPIRE and the European Directives such as Water Framework Directive, Urban Waste Water Directive, Flood Directive, Drinking Water Directive are forcing these tasks on all levels. The importance of suitable, flexible information handling and management in water-related projects for short-, medium- and long-term perspectives is increasing, which demands innovative concepts and solutions.

Acknowledgments The work is partially funded by the Deutsche Forschungsgemeinschaft (DFG) within the Research Unit 581 "Grosshang". The presented work is based on a close collaboration within the subprojects of the research unit, and the special thanks go to all colleagues, in particular to Jan Wienhöfer, Falk Lindenmaier, Erwin Zehe and Reinhard Hinkelmann.

References

1. Hinkelmann, R., & Zehe, E. (2006). Kopplung von Strömungs- und Transportprozessen für die Modellierung von Großhangbewegungen. *Hydrologie und Wasserbewirtschaftung, Heft, 1*, 51–54.

2. Hinkelmann, R., Zehe, E., Ehlers, W., & Joswig, M. (2011). Special section on landslides: Setting the scene and outline of contributing studies. *Vadose Zone Journal,* May 2011, vol 10, 473–476, doi: 10.2136/vzj2011.0032.
3. DFG research unit FG 581 Großhang (2006–2011). http://www.grosshang.de.
4. Lindenmaier, F. (2008). Hydrology of a large unstable hillslope at Ebnit, Vorarlberg: identifying dominating processes and structures. Ph.D. thesis, University Potsdam, http://opus.kobv.de/ubp/volltexte/2008/1742/.
5. Molkenthin, F., Meienberg, C., & Hinkelmann, R., (2009). Information management of multi-scale physical state variables in an interdisciplinary research unit. DFG-Data Management Workshop, Cologne. http://www.tr32db.uni-koeln.de/workshop/workshop09.php.
6. Nelson, B. (2009). Empty archive. In Nature. Vol 461, 10 Sept 2009.
7. INSPIRE, Directive 2007/2/EC, http://inspire.jrc.ec.europa.eu/ (visited 31 March 2012).
8. Mörchen, F. (2006). Time series knowledge mining. Department of Mathematics and Computer Science, University of Marburg, Germany.
9. Li, C., Notay, K.V. & Molkenthin, F. (2012). Time series scenario composition framework in hydroinformatic systems. Proceedings Hydroinformatics Conference 2012, Hamburg.
10. Notay, K.V., Stadler, L., Simons, F., Molkenthin, F., Hinkelmann, R. (2012). Model coupling in hydroinformatics systems through the use of autonomous tensor objects. Proceedings Hydroinformatics Conference 2012, Hamburg.

Multivariable Model Predictive Control of Water Levels on a Laboratory Canal

Klaudia Horváth, Peter-Jules van Overloop, Eduard Galvis, Manuel Gómez and José Rodellar

Abstract Automatic control of irrigation canals can reduce the loss of water in considerable amounts; therefore, it is generating ecologic and economic benefits. There have been developed many different types of automatic controllers, but only a few of them had the opportunity of being tested on the field due to the long delay time and the inconveniences of interrupting the operation of the irrigation. Therefore, the automatic controllers developed for large irrigation canals should be tested before by means of numerical simulations and/or laboratory experiments. The Technical University of Catalonia possesses a laboratory irrigation canal with the length of 220 m, with 3 motorized gates and 11 level sensors that are connected to a SCADA system. This facility makes it possible to test controllers of any type, since all the instrumentation and real-time operation run within a flexible working environment running in MATLAB–Simulink. The canal can be configured from one pool to three pools, which allows the development of multivariable control. A numerical model of the canal has been developed using the 1D hydrodynamic model SIC. With the help of this software, it is possible to simulate the hydraulics of the canal and, due to the link between SIC and MATLAB, also to

K. Horváth (✉) · E. Galvis · M. Gómez · J. Rodellar
Technical University of Catalonia, Jordi Girona 1-3, 08034 Barcelona, Spain
e-mail: klaudia.horvath@upc.edu

E. Galvis
e-mail: eduard.galvis@upc.edu

M. Gómez
e-mail: manuel.gomez@upc.edu

J. Rodellar
e-mail: jose.rodellar@upc.edu

P.-J. van Overloop
Delft University of Technology, Postbus 5, 2600 AA Delft, The Netherlands
e-mail: p.j.a.t.m.vanoverloop@tudelft.nl

P. Gourbesville et al. (eds.), *Advances in Hydroinformatics*,
Springer Hydrogeology, DOI: 10.1007/978-981-4451-42-0_7,

test any controller developed previously in the MATLAB environment. In this work, a centralized multivariable model predictive controller for water levels has been developed and validated by means of numerical simulation.

Keywords Automatic control · Integrator delay model · Irrigation · Resonance · Filter

1 Introduction

Irrigation is one of the largest water consumers, while its efficiency is generally very low. In case of traditional operation, up to 40 % of the irrigation water can be lost. The reduction in this water loss is not only beneficial for economic reasons, but also for ecological needs. Part of the losses is caused by inappropriate management which can be reduced by introducing automation. The goal of automatic canal operation is to deliver the right amount of irrigation water at the right time, allowing on-demand operation of irrigation canals. This does not only make it more convenient for the users, but also allows them to use the least amount of water, just in the time and amount as they need it. Also, while discharges and water levels are regulated, construction and maintenance costs can be saved due to the lower fluctuations of the water levels.

2 The Laboratory Open Channel

The laboratory canal (UPC-PAC: Technical University of Catalonia—Control Algorithms Test Canal) is located in Barcelona, at the northern campus of the university. The facility occupies 22.5 × 5.4 m surface area: being 220 m long and having serpentine shape. It is 1 m deep and 0.44 m wide and contains 3 motorized vertical sluice gates, 9 water level sensors, and 4 rectangular weirs. With the help of the gates, it is possible to configure the canal as a single input/single output (SISO) or multiple input/multiple output (MIMO) system. It has been built with zero slope in order to achieve the largest possible time delay, which, in case of the normal operation discharge (70 l/s), is about 80 s. At the upstream end, there is a constant-level reservoir, and at the downstream end, there is a sharp-crested weir with variable height (Fig. 1).

The water level measurement and the gate-opening data are sent to the supervisory control and data acquisition (SCADA) system. It has been developed in MATLAB–Simulink environment; therefore, it is possible to test any control algorithms written in MATLAB. The discharges are calculated from the measured variables using the hydraulic relationships at the gates and the weirs.

In this work, the following configuration was used: (Fig. 2) the canal was set as three pools: at the upstream end of Reach 1, there is Gate 1, and at the downstream

Fig. 1 The UPC-PAC: the laboratory canal of the Technical University of Catalonia

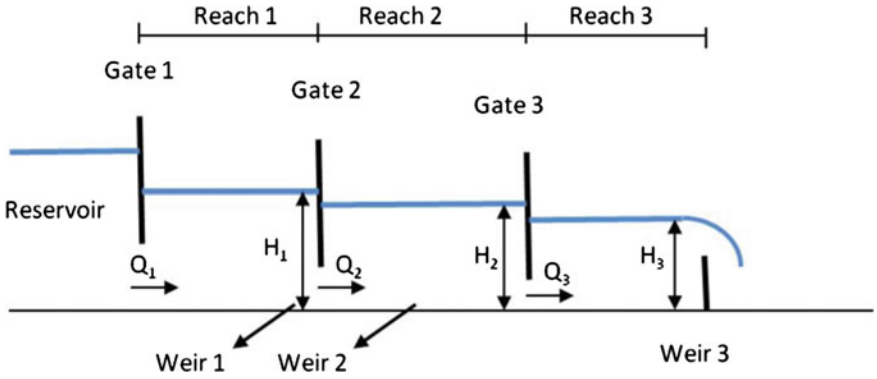

Fig. 2 The UPC-PAC: the laboratory canal of the Technical University of Catalonia

end, Level 1 is controlled (that is just upstream of Gate 2); Reach 2 is limited by Gate 2 at the upstream end and Gate 3 at the downstream end; and the last Reach 3 has a constant-height weir at the downstream end (W3). There are two offtakes in use (W1 and W2), both of which are gravity type, where the discharge varies with the water level.

Several control schemes had been developed and tested on the UPC-PAC before, like decentralized and centralized predictive control of water levels [1] and model predictive control for discharge [2].

3 Model for Control of the Canal UPC-PAC

3.1 Linear Model of a Canal Pool

Each reach of the canal is modeled using the integrator delay (ID) model. This simplified model was developed by Schuurmans [3] and is widely used for control purposes [4–6]. It is based on differentiating the approximation of the uniform flow and that of the backwater part. Hence, there are two parts: the uniform flow part and a downstream backwater flow part.

Due to the backwater part, the dynamics are complicated. Reflecting waves are traveling up and down the reach. However, in low frequencies, the water level integrates the discharge. Therefore, the water level can be approximated as the integral of the flow, and the gain is approximated by the reciprocal of the backwater surface (see Eq. 1).

In the uniform part, the downstream flow rate is assumed to be equal to the upstream flow rate some time before.

In this case, since the bed slope is zero, all the canal reaches are affected by backwater. Therefore, the model assumes that the canal reach behaves as a tank, the water level is the integral of the discharge, and the time it takes for the upstream discharge to arrive to the downstream water level is the time delay. This behavior can be described with the following equation in the Laplace domain:

$$h_i(s) = \frac{1}{A_e s} e^{-\tau s} q_i(s) \tag{1}$$

where $h_i(s)$ is the downstream water level relative to a steady-state water level in the ith reach, A_e is the backwater area, s is the Laplace's operator, τ is the time delay, and $q_i(s)$ is the upstream discharge relative to a steady-state discharge. The relative discharge and water level are defined as follows:

$$h_i = H_i - H_{0i} \tag{2}$$

$$q_i = Q_i - Q_{0i}, \tag{3}$$

where H_i and Q_i are the measured values of the discharge and the water level, respectively, and Q_0 and H_0 are the steady-state values. From now on, the steady-state values of the variables are noted with underscored zero.

The whole pool is supposed to be affected by backwater in this case; therefore, the surface area of each canal pool is used as backwater area. Since the water profile is very close to horizontal in case of the laboratory canal, the surface area is calculated as the length of the reach multiplied by the width:

$$A_e = H_0 L \tag{4}$$

The time delay is estimated as follows:

Table 1 Parameters of the ID model of the three canal reaches of the UPC-PAC

Reach	Length, L (m)	Water level, H_0 (m)	Backwater area, A_e (m^2)	Time delay, τ (s)
1	87	0.8	32.28	31
2	90.2	0.6	39.68	32
3	43.3	0.45	19.93	16

$$\tau = \frac{L}{V_0 + C_0} \tag{5}$$

where V_0 is the velocity (belonging to the reference discharge) and C_0 is the celerity (calculated from the reference water depth) using the formula:

$$C_0 = \sqrt{gH_0} \tag{6}$$

where h is the reference water level relative to the bed level and g is the gravitational acceleration. Values for the three canal pools are given in Table 1. All these values were calculated based on the chosen reference discharge and reference water level (H_0). The reference discharge in all the cases was 70 l/s.

After applying the z-transform, the model can be described with the following linear time-invariant discrete form:

$$h_i(k+1) = h_i(k) + A_d q_i(k-d+1) - A_d q_{i+1}(k) \tag{7}$$

where $h(k)$ is the downstream water level of the ith reach at instant k and $h(k+1)$ is the downstream water level at instant $k+1$, d is the delay steps, q_i is the inflow, and q_{i+1} is the outflow of the ith reach. A_d is calculated as follows:

$$A_d = \frac{T_d}{A_e} \tag{8}$$

where T_d is the sampling time and A_e is the backwater surface.

3.2 Filter Design

Due to the very small bed slope (actually horizontal), the test canal is sensitive to reflecting waves (resonances). In order not to excite these waves in the canal, appropriate filtering is required in the control system. Schuurmans [3] proposed to filter the resonance wave with a first-order low-pass filter. However, this introduces additional delay. In each canal pool, this is about 100 s; hence, it caused a significantly slower control loop. Therefore, in this work, for a sampling time of 10 s, 11 delay steps are used in the first two and 10 in the last pool. The filter is applied to the water level signals. The filter coefficient is calculated using the backwater surface (A_e), the frequency (ω_p), and the magnitude (M_p) of the first resonance peak according to [3]:

Table 2 The resonance frequency, the magnitude of the first peak, and the continuous filter coefficients for the three reaches of the UPC-PAC

Reach	Resonance frequency, ω_p (rad/s)	Magnitude of the resonance peak, M_p (s/m^2)	Filter coefficient, f_c (−)
1	0.1071	32.28	0.7795
2	0.0866	39.68	0.7549
3	0.1516	19.93	0.6308

$$T_f = \sqrt{\frac{A_e M_p}{\omega_p}} \tag{9}$$

The magnitude and the frequency of the first resonance peak are obtained from the Bode plots of the three pools. These plots are obtained using the geometric characteristics of the canal using the frequency model of Litrico [7]. The data and the calculated filter coefficients are summarized in Table 2.

The final discrete equation of the filter is given as follows:

$$h_{fil}(k) = f_c h_{fil}(k-1) + (1 - f_c) h_{\text{mes}}(k) \tag{10}$$

where $h_{fil}(k)$ is the filtered water level at instant k, $h_{fil}(k-1)$ is the filtered water level at instant $k-1$ (one sampling time step before the present), f_c is the discrete filter coefficient, and $h_{\text{mes}}(k)$ is the water level measured at the instant k (present time). The discrete filter coefficient is calculated from the continuous filter coefficient T_f using the following equation:

$$f_c = e^{-T_d/T_f} \tag{11}$$

The predictive controller takes into account the combination of the ID model and the first-order low-pass filter, which will be referred in the following as ID filter (IDF) model.

4 Controller Design

4.1 Control Strategy

Control strategies can be divided into two main groups: centralized and decentralized. The decentralized control strategy is normally based on simpler feedback control methods. There are separate controllers designed for each pool, not taking into consideration the interaction between pools. In some cases, a higher-level controller supervises the independent controllers. With this strategy, only suboptimal control is achievable. The disadvantage of this control strategy is that since the interactions between canal pools are not taken into account, the performance

can degrade considerably. The perturbation caused by one controller can spread throughout the whole canal system; hence, disturbance amplification can occur.

On the other hand, the centralized control strategy takes into account all the objectives that have to be fulfilled and a controller is designed using global information of the canal state. Compared to decentralized control, flows can be adjusted simultaneously at several gates, resulting in a mass transfer of water in less time. The best control performance can be obtained with this strategy; however, it is computationally more complicated and more expensive to implement in practice.

There are several examples in the literature of centralized control, some of which are implemented in the field. They can be categorized by the different types of controllers, for example downstream feedback with feedforward control [8], LQR [9], LQG [10], or model predictive control [4, 11]. In this work, centralized model predictive control is used.

4.2 Model Predictive Control

A centralized unconstrained model predictive controller has been developed. Equation (7) is used as an internal model for each reach. The control variables are the discharge under the gate, and then, a gate inverse formula is used to calculate each of the three gate openings as a function of submerged flow and the difference between upstream and downstream water levels. The controlled variables are the three water levels downstream in the reaches. The states of the system are the water level error, the discharge in the previous control steps, and the integral of the water level error. In order to design a multivariable MPC controller, a state-space description of the system is needed, so a linearized, discrete-time, state-space model of the canal is assumed in the general form:

$$\begin{aligned} x(k+1) &= Ax(k) + Bu(k) + B_d V(k) \\ y(k) &= Cx(k) \end{aligned} \tag{12}$$

where $x(k)$ is the state vector, $u(k)$ is the input control vector, $y(k)$ is the vector of measured outputs which are to be controlled, $V(k)$ is the disturbance vector, and A, B, B_d, C are matrices of appropriate dimension (see the Appendix). The index k counts time steps. By using a state-space model, the current information required for predicting ahead is represented by the state variable at the current time. The model is built using the following equations:

$$e_i(k+1) = e_i(k) + A_d q_i(k-d+1) - A_d q_{i+1}(k) \tag{13}$$

$$\Delta q_i(k+1) = q_i(k+1) - q_i(k) \tag{14}$$

$$e_{\text{int i}}(k+1) = e_{\text{int i}}(k) + e_i(k) \tag{15}$$

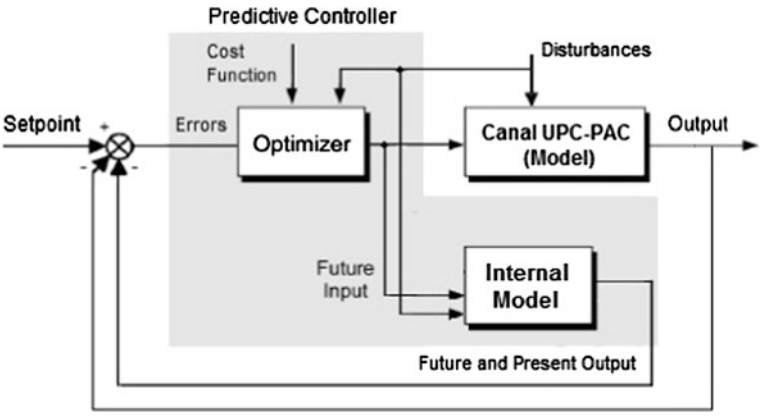

Fig. 3 MPC system applied to the test canal

where q_i is the discharge and e_i is the error of the downstream water level in the ith reach. Equation 13 is obtained by subtracting the set point from both sides of Eqs. 7 and 14 defines the incremental discharge variable Δq_i. Equation 15

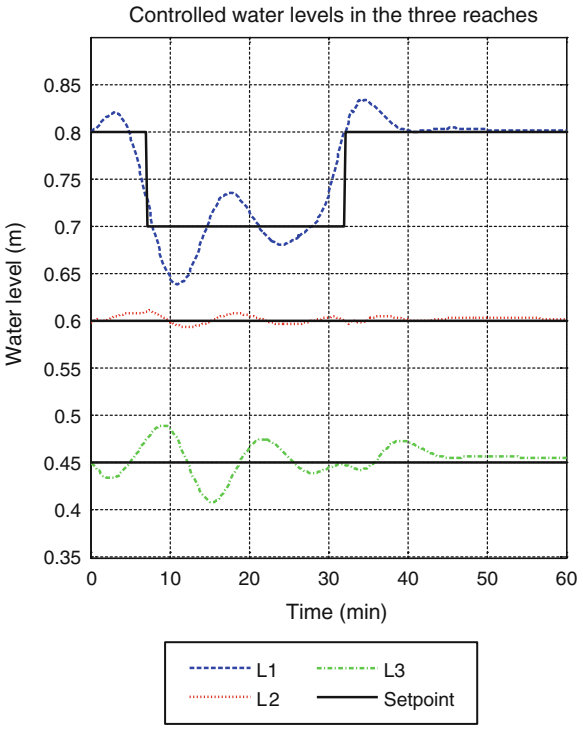

Fig. 4 Reach 1: discharge disturbance rejection

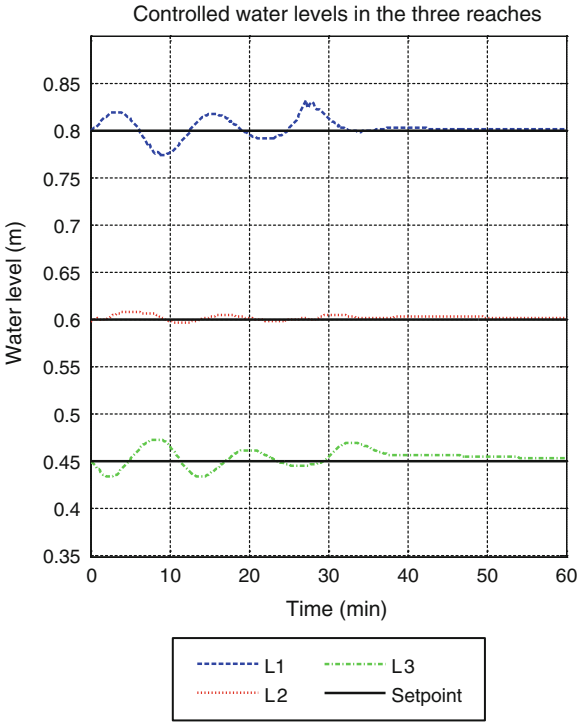

Fig. 5 Reach 2: flow disturbance rejection

describes an integral variable of the error ($e_{int\ i}$) that integrates the error in order to arrive zero steady-state error.

In case of the last reach, the output discharge was calculated by using the linearized equation of the weir at the downstream end of the canal pool, with a gain of k_h (see the Appendix).

Due to the extra time delay introduced by the filter, the delay steps are 11, 11, and 10, respectively, in the three reaches. Therefore, the overall number of the states [the length of the vector $x(k)$] is 38. The dimension of $u(k)$ is 3. The predictive controller output is obtained by minimizing the error and the integral error on the prediction horizon. The input variables are the measured water levels at the downstream end of each pool (Fig. 3).

The prediction horizon was set to be long enough to exceed all the delays of the system, 35 steps with a sampling time of 10 s. To obtain the control law, in order to keep the process as close as possible to a predefined reference, optimization process was carried out over the prediction horizon, minimizing the following cost function:

$$\min_{\Delta u} J = \sum_{j=0}^{\lambda} \left\{ x^T(k+j|k) Q x(k+j|k) \right\} + \sum_{j=0}^{\lambda} \left\{ \Delta q^T(k+j|k) R \Delta q(k+j|k) \right\} \quad (16)$$

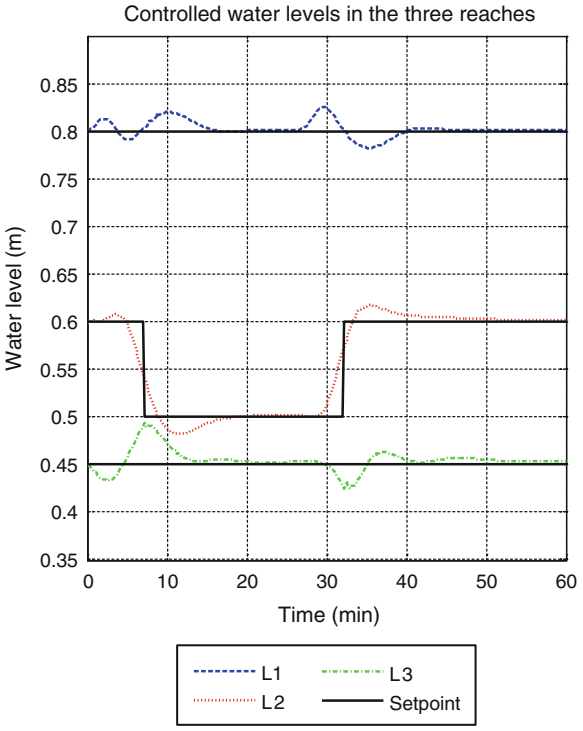

Fig. 6 Reach 3: flow disturbance rejection

where e is a vector containing the water level errors for the three pools for the whole prediction horizon, superscript T means transpose of the matrix, Q is the weighing matrix of the state, Δq is a vector containing the inputs (change in discharge) for the whole prediction horizon, and R is the weighing matrix for the input.

To minimize the function J, an optimizer predicts (calculates) output values as a function of past values of inputs and outputs and future control signals, making use of the internal model, and substitutes these in the cost function, obtaining an expression whose minimization leads to the looked-for values. The first control action $\Delta q(k|k)$ is sent to the gates, while the rest are neglected. This is because at the next sampling time, the output $y(k+1)$ is measured by the system, and then, the optimization process is repeated with new values from an updated control sequence. Details about the formulation of the controller can be found in [5] and [12].

The calculated control variable of the MPC is the change in the input discharges. From the three discharge changes, the new gate openings are calculated by using the inverse of the gate equation. In the simulation tests, these gate openings are sent to a 1D hydrodynamic model, included in the simulation of irrigation canals (SIC) software package [13].

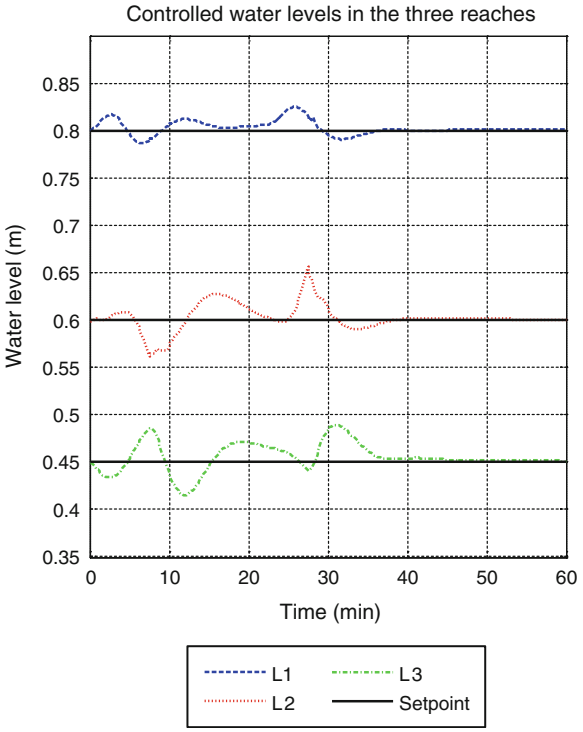

Fig. 7 Reach 1: level setpoint tracking

4.3 Controller Tuning

The tuning parameters are the weights in the matrices and the length of the prediction horizon. In the weighing matrices, the weights were normalized. The same weights were given to all the pools for the error and the same penalization for the integral of the error. For the input, the weight on the first input was increased proportional to the gain of the first gate, since the gain of the first gate is much higher due to the high water level in the upstream reservoir. The weighing matrices are as follows:

The weighing matrix for the input:

$$R = \begin{bmatrix} 8163 & 0 & 0 \\ 0 & 5102 & 0 \\ 0 & 0 & 5102 \end{bmatrix} \tag{17}$$

The weighing matrix for the integral of the error:

$$Q_{\text{int}} = \begin{bmatrix} 0.166 & 0 & 0 \\ 0 & 0.166 & 0 \\ 0 & 0 & 0.166 \end{bmatrix} \tag{18}$$

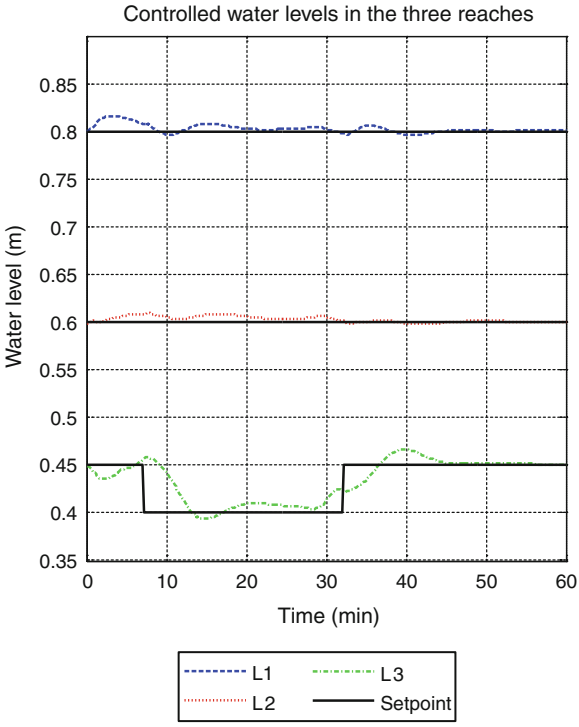

Fig. 8 Reach 2: level setpoint tracking

and the weighing matrix for the error:

$$Q_e = \begin{bmatrix} 69.4 & 0 & 0 \\ 0 & 69.4 & 0 \\ 0 & 0 & 69.4 \end{bmatrix} \tag{19}$$

5 Results

5.1 Numerical Tests

All tests were carried out using the 1D hydrodynamic model (SIC) [13]. The two different scenarios were tested: setpoint tracking and disturbance rejection. In case of setpoint tracking, the set point was changed at 7 min, and after 25 min, it was changed again to the original one. This test was carried out in all the three reaches with all the three set points.

The disturbance rejection was tested by using the lateral weirs (Figs. 4, 5 and 6). Initially, two lateral offtakes were in "open" position (Weir 1 in the downstream end of Reach 1 and Weir 2 in the middle of Reach 2), and the discharge

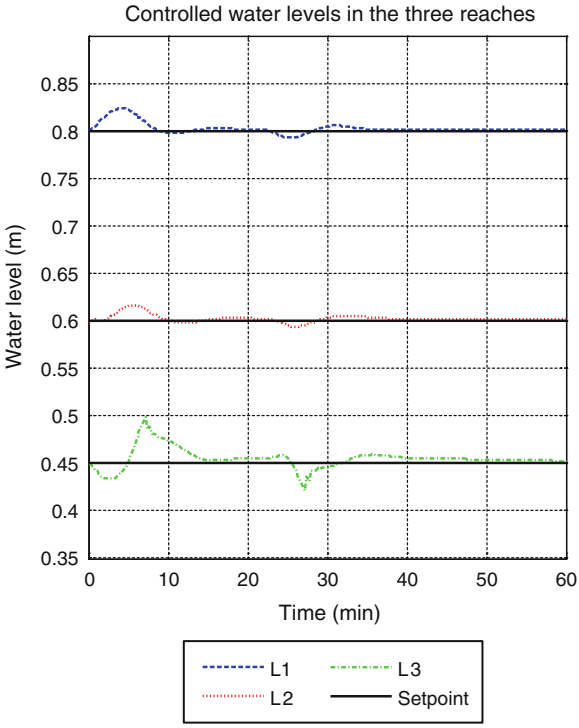

Fig. 9 Reach 3: level setpoint tracking

over these weirs was 10 and 40 l/s, respectively. In case of Reach 1, Weir 1 is located downstream of the reach. During the test for Reach 1, this offtake was "closed" from t = 7 min for 20 min, then opened again. In case of the test for Reach 2, the weir in the middle of the reach, Weir 2, was "closed" from t = 7 min for 20 min, then opened again. In case of the last test, the discharge in the downstream end of the last reach was increased at t = 7 min by 40 l/s for 20 min.

In case of the set point changes (Figs. 7, 8 and 9), the water levels returned to target level within 12 min. In case of the disturbances, the water levels recovered within 10 min. It can be seen how the controller starts the action before the change and arrives to the new state. The integrator action can be seen by the water level movements (oscillations), especially in the third reach. In all cases, the steady-state set point was reached.

6 Conclusion

Centralized model predictive controller is developed for a resonance-sensitive laboratory canal. The controller has been tested numerically. For both presented scenarios, setpoint tracking and rejection of known disturbances, the controller showed an acceptable performance.

Future work will be implementation of the controller on the laboratory canal.

Acknowledgment The authors wish to thank the support to Spanish Ministry of Education—Order EDU/2719/2011, to make possible the PhD students' internship at Delft University of Technology.

Appendix

The matrices for the state-space model

$$x(k) = \begin{bmatrix} q_1(k) & q_1(k-1) & q_1(k-2)\ldots q_1(k-10) & e_1(k) & & & & \\ q_2(k) & q_2(k-1) & q_2(k-2)\ldots q_2(k-10) & e_2(k) & & & & \\ q_3(k) & q_3(k-1) & q_3(k-2)\ldots q_3(k-10) & e_3(k) & e_{1\text{int}}(k) & e_{2\text{int}}(k) & e_{3\text{int}}(k) \end{bmatrix}^T$$

$$u(k) = \begin{bmatrix} \Delta q_1(k+1) \\ \Delta q_2(k+1) \\ \Delta q_3(k+1) \end{bmatrix} \qquad V(k) = \begin{bmatrix} q_{d1}(k+1) \\ \Delta h_{\text{ref}1}(k+1) \\ q_{d2}(k+1) \\ \Delta h_{\text{ref}2}(k+1) \\ q_{d3}(k+1) \\ \Delta h_{\text{ref}3}(k+1) \end{bmatrix}$$

$$B = \begin{bmatrix} 1 & 0 & 0 \\ 0 & 0 & 0 \\ 0 & 0 & 0 \\ 0 & 0 & 0 \\ 0 & 0 & 0 \\ 0 & -A_{d1} & 0 \\ 0 & 1 & 0 \\ 0 & 0 & 0 \\ 0 & 0 & 0 \\ 0 & 0 & 0 \\ 0 & 0 & 0 \\ 0 & 0 & -A_{d2} \\ 0 & 0 & 1 \\ 0 & 0 & 0 \\ 0 & 0 & 0 \\ 0 & 0 & 0 \\ 0 & 0 & 0 \\ 0 & 0 & 0 \\ 0 & -A_{d1} & 0 \\ 0 & 0 & -A_{d2} \\ 0 & 0 & 0 \end{bmatrix} \quad B_d = \begin{bmatrix} 0 & 0 & 0 & 0 & 0 & 0 \\ 0 & 0 & 0 & 0 & 0 & 0 \\ 0 & 0 & 0 & 0 & 0 & 0 \\ 0 & 0 & 0 & 0 & 0 & 0 \\ 0 & 0 & 0 & 0 & 0 & 0 \\ -A_{d1} & 1 & 0 & 0 & 0 & 0 \\ 0 & 0 & 0 & 0 & 0 & 0 \\ 0 & 0 & 0 & 0 & 0 & 0 \\ 0 & 0 & 0 & 0 & 0 & 0 \\ 0 & 0 & 0 & 0 & 0 & 0 \\ 0 & 0 & 0 & 0 & 0 & 0 \\ 0 & 0 & -A_{d2} & 1 & 0 & 0 \\ 0 & 0 & 0 & 0 & 0 & 0 \\ 0 & 0 & 0 & 0 & 0 & 0 \\ 0 & 0 & 0 & 0 & 0 & 0 \\ 0 & 0 & 0 & 0 & 0 & 0 \\ 0 & 0 & 0 & 0 & 0 & 0 \\ 0 & 0 & 0 & 0 & -A_{d3} & 1 \\ -A_{d1} & 1 & 0 & 0 & 0 & 0 \\ 0 & 0 & -A_{d2} & 1 & 0 & 0 \\ 0 & 0 & 0 & 0 & -A_{d3} & 1 \end{bmatrix}$$

$$A = \begin{bmatrix}
1 & 0 & 0 & 0 & 0 & 0 & 0 & 0 & 0 & 0 & 0 & 0 & 0 & 0 & 0 & 0 & 0 & 0 & 0 & 0 & 0 \\
1 & 0 & 0 & 0 & 0 & 0 & 0 & 0 & 0 & 0 & 0 & 0 & 0 & 0 & 0 & 0 & 0 & 0 & 0 & 0 & 0 \\
0 & 1 & 0 & 0 & 0 & 0 & 0 & 0 & 0 & 0 & 0 & 0 & 0 & 0 & 0 & 0 & 0 & 0 & 0 & 0 & 0 \\
0 & 0 & \dots & 0 & 0 & 0 & 0 & 0 & 0 & 0 & 0 & 0 & 0 & 0 & 0 & 0 & 0 & 0 & 0 & 0 & 0 \\
0 & 0 & 0 & 1 & 0 & 0 & 0 & 0 & 0 & 0 & 0 & 0 & 0 & 0 & 0 & 0 & 0 & 0 & 0 & 0 & 0 \\
0 & 0 & 0 & 0 & A_{d1} & 1 & -A_{d1} & 0 & 0 & 0 & 0 & 0 & 0 & 0 & 0 & 0 & 0 & 0 & 0 & 0 & 0 \\
0 & 0 & 0 & 0 & 0 & 0 & 1 & 0 & 0 & 0 & 0 & 0 & 0 & 0 & 0 & 0 & 0 & 0 & 0 & 0 & 0 \\
0 & 0 & 0 & 0 & 0 & 0 & 1 & 0 & 0 & 0 & 0 & 0 & 0 & 0 & 0 & 0 & 0 & 0 & 0 & 0 & 0 \\
0 & 0 & 0 & 0 & 0 & 0 & 0 & 1 & 0 & 0 & 0 & 0 & 0 & 0 & 0 & 0 & 0 & 0 & 0 & 0 & 0 \\
0 & 0 & 0 & 0 & 0 & 0 & 0 & 0 & \dots & 0 & 0 & 0 & 0 & 0 & 0 & 0 & 0 & 0 & 0 & 0 & 0 \\
0 & 0 & 0 & 0 & 0 & 0 & 0 & 0 & 0 & 1 & 0 & 0 & 0 & 0 & 0 & 0 & 0 & 0 & 0 & 0 & 0 \\
0 & 0 & 0 & 0 & 0 & 0 & 0 & 0 & 0 & 0 & A_{d2} & 1 & -A_{d2} & 0 & 0 & 0 & 0 & 0 & 0 & 0 & 0 \\
0 & 0 & 0 & 0 & 0 & 0 & 0 & 0 & 0 & 0 & 0 & 0 & 1 & 0 & 0 & 0 & 0 & 0 & 0 & 0 & 0 \\
0 & 0 & 0 & 0 & 0 & 0 & 0 & 0 & 0 & 0 & 0 & 0 & 1 & 0 & 0 & 0 & 0 & 0 & 0 & 0 & 0 \\
0 & 0 & 0 & 0 & 0 & 0 & 0 & 0 & 0 & 0 & 0 & 0 & 0 & 1 & 0 & 0 & 0 & 0 & 0 & 0 & 0 \\
0 & 0 & 0 & 0 & 0 & 0 & 0 & 0 & 0 & 0 & 0 & 0 & 0 & 0 & \dots & 0 & 0 & 0 & 0 & 0 & 0 \\
0 & 0 & 0 & 0 & 0 & 0 & 0 & 0 & 0 & 0 & 0 & 0 & 0 & 0 & 0 & 1 & 0 & 0 & 0 & 0 & 0 \\
0 & 0 & 0 & 0 & 0 & 0 & 0 & 0 & 0 & 0 & 0 & 0 & 0 & 0 & 0 & 0 & A_{d3} & 1 - A_{d3}K_n & 0 & 0 & 0 \\
0 & 0 & 0 & 0 & A_{d1} & 1 & -A_{d1} & 0 & 0 & 0 & 0 & 0 & 0 & 0 & 0 & 0 & 0 & 0 & 1 & 0 & 0 \\
0 & 0 & 0 & 0 & 0 & 0 & 0 & 0 & 0 & 0 & A_{d2} & 0 & -A_{d2} & 0 & 0 & 0 & 0 & 0 & 0 & 1 & 0 \\
0 & 0 & 0 & 0 & 0 & 0 & 0 & 0 & 0 & 0 & 0 & 0 & 0 & 0 & 0 & 0 & A_{d3} & 1 - A_{d3}K_n & 0 & 0 & 1
\end{bmatrix}$$

References

1. Sepúlveda, C. (2008). *Instrumentation, model identification and control of an experimental irrigation canal.* Ph.D. thesis, Barcelona, Spain: Technical University of Catalonia.
2. Horváth, K., Galvis, E., Gómez, M., & Rodellar, J. (2011). Pruebas de algoritmos de control automático en un canal de laboratorio y un canal simulado. *JIA 2011, II Jornadas del Ingeniería del agua, Modelos numéricos en dinámica fluvial*, Barcelona (Spain), October 5–6, 2011.
3. Schuurmans, J. (1997). *Control of water levels in open channels*, PhD thesis, Delft, The Netherlands: Delft University of Technology, Faculty of Civil Engineering.
4. van Overloop, P. J., Clemmens, A. J., Strand, R. J., Wagemaker, R. M. J., & Bautista, E. (2010). Real-time implementation of model predictive control on MSIDD's WM Canal. *Journal of Irrigation and Drainage Engineering, 136*(11), 747–756.
5. van Overloop, P. J. (2006). *Model predictive control on open water systems*. Doctoral Thesis, Delft, Netherlands: Delft University of Technology.
6. Litrico, X., Fromion, V. (2005). *Design of structured multivariable controllers for irrigation canals*, *Proceedings of the 44th IEEE Conference on Decision and Control and European Control Conference* (pp. 1881–1886). Seville.
7. Litrico, X., & Fromion, V. (2004). Frequency modeling of open-channel flow. *Journal of Hydraulic Engineering Division of the American Society of Civil Engineers, 130*(8), 806–815.
8. Montazar, A., Van Overloop, P. J., & Brouwer, R. (2005). Centralized controller for the Narmada main canal. *Irrigation and Drainage, 54*, 79–89.
9. Balogun, D., Hubbard, O. S., & De Vries, J. J. (1988). Automatic control of canal flow using linear quadratic regulator theory. *Journal of Hydraulic Engineering Division of the American Society of Civil Engineers, 114*(1), 75–101.
10. Begovich, O., Salinas, J., & Ruiz-Carmona V. (2003). *Real-time implementation of a fuzzy gain scheduling control in a multi-pool open irrigation canal prototype*. *Proceedings of the 2003 IEEE International Symposium on Intelligent Control* (pp. 304–309). Houston (USA), October 6–8 2003.
11. Malaterre, P.-O., & Rodellar, J. (1997). *Multivariable predictive control of irrigation canals. Design and evaluation on a 2-pool model*. *RIC97, International Workshop on the Regulation*

of Irrigation Canals: State of the Art of Research and Applications, Marrakech (Morocco), April 22–24, 1997.
12. Martín Sánchez, J.M., & Rodellar, J. (1995). *Adaptive predictive control, from the concepts to plant optimization.* New Jersey: Prentice Hall.
13. Malaterre, P. O., & Baume, J. P. (1997) *SIC 3.0, a simulation model for canal automation design*. *RIC97, International Workshop on the Regulation of Irrigation Canals: State of the Art of Research and Applications*, Marrakech (Morocco), April 22–24, 1997.

Estimation of Lateral Inflows Using Data Assimilation in the Context of Real-Time Flood Forecasting for the Marne Catchment in France

Johan Habert, Sophie Ricci, Andrea Piacentini, Gabriel Jonville, Etienne Le Pape, Olivier Thual, Nicole Goutal, Fabrice Zaoui and Riadh Ata

Abstract The present study describes the assimilation of discharge in situ data for operational flood forecasting. The study was carried out on the Marne River (France) catchment where lateral inflows' uncertainty is important due to karstic areas. This source of error was partly accounted for using an Extended Kalman Filter (EKF) algorithm built on the top of a mono-dimensional hydraulic model. The lateral inflows were sequentially adjusted over a sliding 48 h time window. The correction leads to a significant improvement in the simulated water level and

J. Habert (✉)
DREAL Champagne-Ardenne, Chalons-en-Champagne, France
e-mail: johan.habert@developpement-durable.gouv.fr

S. Ricci · A. Piacentini · G. Jonville
URA 1875/CERFACS, Toulouse, France
e-mail: ricci@cerfacs.fr

A. Piacentini
e-mail: piacentini@cerfacs.fr

G. Jonville
e-mail: jonville@cerfacs.fr

E. Le Pape
SCHAPI, Toulouse, France
e-mail: Etienne.lepape@developpement-durable.gouv.fr

O. Thual
URA1875/CERFACS and INPT, CNRS, IMFT, Toulouse, France
e-mail: thual@imft.fr

N. Goutal · F. Zaoui · R. Ata
LNHE EDF-R&D, Chatou, France
e-mail: nicole.goutal@edf.fr

F. Zaoui
e-mail: fabrice.zaoui@edf.fr

R. Ata
e-mail: riadh.ata@edf.fr

P. Gourbesville et al. (eds.), *Advances in Hydroinformatics*,
Springer Hydrogeology, DOI: 10.1007/978-981-4451-42-0_8,

discharge in re-analysis and forecast modes. These results pave the way for the operational use of the data assimilation (DA) procedure for real-time forecasting at the French flood forecasting service.

Keywords Flood forecasting · Data assimilation · Kalman filter · Karstic catchment

1 Introduction

In 2006, 9 % of the French population was exposed to flood risk, one of the greatest natural risks causing damage and human loss [1]. The French flood forecasting service (SCHAPI—Service Central d'Hydrométéorologie et d'Appui à la Prévision des Inondations), in collaboration with the 22 local flood forecasting centers (SPC—Service de Prévision des Crues), produces a twice-daily broadcast vigilance map available to governmental authorities and general public (http://www.vigicrues.gouv.fr).

In order to effectively support emergency management and decision making, it is essential to properly characterize the different sources of uncertainty in hydrologic forecasts [2, 3]. The reliability of flood forecasting strongly depends on the quality of the hydraulics model, its boundary conditions (upstream and lateral inflow), hydrologic initial conditions, and numerical parameters. Much effort has been directed toward the estimation of hydrologic and hydraulic model parameters especially for the statistical analysis of parameters' uncertainties usually using a historical batch of data, assuming time-invariant parameters [4, 5]. In practice, in addition to model simulation and batch calibration, the reliable operation of a watershed system requires a continuous correction of the forecast as observational data become available [6]. The application of data assimilation (DA) [7], which optimally merges information from model simulations and independent observations with appropriate uncertainty modeling, has proved promising in improving prediction accuracy and quantifying uncertainty [8–11]. Still, the use of such methods by operational agencies is rare and the need for implementing effective DA in the flood forecast process is increasing when flood frequency is likely to increase as a result of altered precipitation patterns triggered by climate change [12].

DA offers a convenient framework to overcome some of the limits of the calibration processes: observations and simulation outputs are combined to estimate an optimal set of model parameters and consequently reduce uncertainties in the simulation. With the increasing abundance of new in situ and remote sensing observations, DA was applied in several studies formulated in an operational framework. A great number of implementations were made on top of hydrologic models in order to improve soil moisture initial conditions. Thirel et al. [13, 14] assimilated past discharges to obtain a better initial soil moisture state and improve

ensemble streamflow simulations. Dechant and Moradkhani [15] used SNOTEL data to improve the estimation of snow water storage and consequently improve the ensemble streamflow prediction from the National Weather Service River Forecast System (USA). Seo et al. [16, 17] explored variational assimilation of hydrologic and hydrometeorological data into operational hydrologic forecast. The Kalman Filter (KF) [18] algorithm is the most commonly used sequential DA algorithm which results in the optimal estimation for linear dynamic models with Gaussian uncertainties. It was extended to nonlinear problems using a first-order approximation of Taylor series, namely Extended Kalman Filter (EKF), or an ensemble approach for the Ensemble Kalman Filter (EnKF) [19]. These algorithms are also now widely being used in hydrology and hydraulics for the estimation of model states [20, 21] as well as model parameters [22].

In the context of hydrodynamics modeling, Ricci et al. [23] showed that the EKF assimilation of water level observations on the Adour catchment with the 1D hydraulic model MASCARET [24] developed by Laboratoire National d'Hydraulique et d'Environnement (LNHE) from Electricité de France Recherche et Développement (EDF-R&D) enabled to improve flood forecasting of 60 % at a 1 h lead time and of 25 % at a 12 h lead time. In the present study, a similar approach is applied to flood forecasting in the Marne catchment where the presence of karstic areas makes it hard to correctly specify upstream and lateral inflows to the model. In the framework of operational flood forecasting, the Seine Amont Marne Amont (SAMA) SPC has developed two different models on two limited areas of the Marne catchment described in Fig. 1. On these limited areas, the batch calibration of the model was possible and the uncertainties due to lateral inflow were accounted for by artificially adjusting the Strickler coefficients. Still, in order to increase the forecast time on the Marne catchment, both models were recently merged into a global model far more difficult to calibrate. The need for a coherent estimation of the so far neglected inflows, which represent the dynamics of the karstic areas, and the unmodeled tributaries, which represent the dynamics of catchment areas, motivates the use of a DA procedure using in situ measurements. A realistic and time-varying estimation of the lateral inflows is then achieved using a sequential DA approach on 10 flood events over 2001–2010. It is shown that, in spite of certain limitations described further on, this approach provides a reliable estimate of the lateral inflows and leads to the improvement of the flood forecast at meaningful lead times for operational use.

The structure of the chapter is as follows: Sect. 2 provides a description of the Marne catchment. It also provides the arguments for building a DA scheme to estimate lateral inflows. The DA method is described in Sect. 3 along with the choices made for the implementation of the algorithm. Section 4 gives an overview of the results, highlighting the merits of the approach for flood forecasting along with its limitations on a representative flood event. Conclusions are given in Sect. 5.

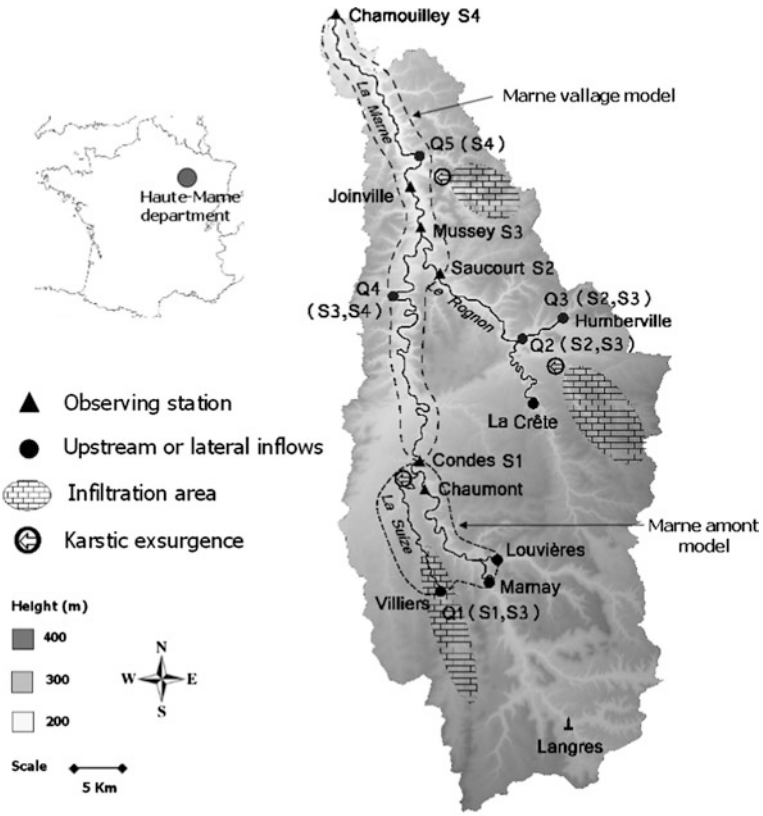

Fig. 1 The Marne catchment: the sub-models are *circled* with *dashed lines*. The hydrologic observing stations S_1, S_2, S_3, and S_4 are represented by *black triangles*. Lateral inflows Q_1, Q_2, Q_3, Q_4, and Q_5 are represented by *black dots* and the observing stations on which they depend are in *parentheses*

2 Modeling of the Marne Catchment

The Marne catchment is a karstic basin located east of the Paris Basin. The Marne River is a 525 km-long tributary of the Seine River, and its source is located in the Langres Plateau in the Haute-Marne Department (Fig. 1). The study is carried out on the upstream part of the river that is strongly sensitive to local precipitation and where flash floods (5–120 $m^3\ s^{-1}$ within a 24 h period in October 2006 at Condes) occur. The landscape of the catchment is defined by forested plateaus, incised valleys and presents numerous limestone outcrops. Therefore, the catchment area includes karstic areas and tributaries whose behavior is highly nonlinear and thus difficult to forecast.

As of today, the operational forecast relies on the integration of two sub-models on the Marne Amont and Marne Vallage areas (Fig. 1). These models are based on

the monodimensional numerical code MASCARET for hydraulics describing the Saint-Venant (shallow water) equations and developed by EDF-R&D and Centre d'Etudes Techniques Maritimes Et Fluviales (CETMEF). They were calibrated independently using water level in situ measurements from five hydrologic observing stations (Chaumont, Condes, Mussey, Joinville, and Chamouilley). The underestimation of the lateral inflow that leads to the underestimation of the simulated water levels and discharge was partly corrected by reducing the Strickler coefficients and thus artificially increasing the water level. These sub-models are used for operational forecast at SAMA SPC since 2008. They provide a satisfying water level signal, still discharges are usually underestimated and the maximum lead time for the forecast is 15 h.

In order to extend the maximum lead time and benefit from measurements at Saucourt, the sub-models were merged into a global model extending from Villiers to Chamouilley and including the karstic areas of the Rognon. The upstream flows are specified at five upstream stations (Marnay, Louvières, Villiers, La Crête, and Humberville). This global model underestimates the discharges of 50 % on average over ten significant events as presented in Fig. 2 for a representative event for Condes and Mussey observing stations (observations are in blue and simulations, denoted by Free Run, in black). Indeed, the global model area is about 2,250 km^2 when the area controlled by the five upstream stations is only about 755 km^2. Thus, it appears that the modeling of lateral inflows, despite the lack of hydrologic rainfall-runoff model on the area, represents a key step toward the use of the global model for the Marne catchment. Five lateral inflows were then added to the model to represent the exsurgences of the Suize (Q_1), the Seurre on the Rognon catchment (Q_2 and Q_3), and tributaries upstream Musey (Q_4) and Chamouilley (Q_5).

Given the homogeneous response of the catchment to an oceanic rainfall event, a water budget approach enables to describe a coherent, yet perfectible, behavior of the catchment. For instance, adding the lateral inflow $Q5$ estimated as eight

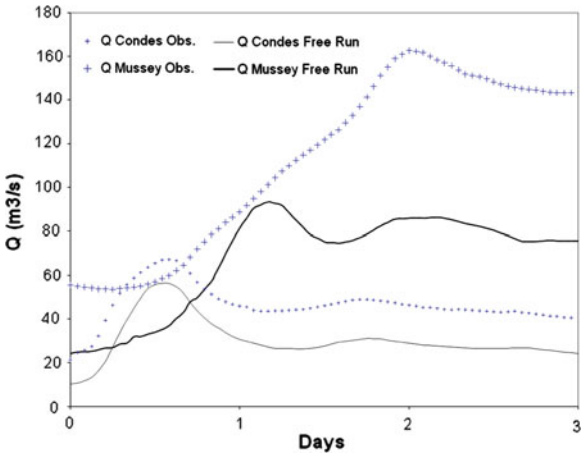

Fig. 2 Observed (*blue crossed curves*) and simulated discharges for Free Run (*black solid curves*) in Condes (*thin curves*) and Mussey (*thick curves*). March 2008 event

times bigger than the hydrograph at Villiers leads to a satisfying simulation of the discharge at Chamouilley as illustrated in Fig. 3 where observation is represented by the blue crossed curve, the Free Run simulation is in black and the Free Run simulation with the addition of the lateral inflow $Q5$ is represented in green by the dotted curve. Similar approach using Villiers and Humberville as elementary hydrographs to estimate each lateral inflow was used to identify multiplicative coefficients A_i [where $Q_{i,\text{new}}(t) = A_i Q_i(t)$], with $i \in [7, 12]$ and their statistics, from a batch calibration over the 10 flood events. These values presented in Table 1 can be greatly improved with a sequential method that allows for temporal variability of the coefficients, essential for instance for summer and early autumn events when the karst behavior is complex and the Villiers station may not be representative of the entire catchment's dynamics.

3 Sequential Data Assimilation Method

DA approaches aim at identifying the optimal estimate of the true value of the unknown variable $\mathbf{x}$ that includes, in this work, the set of corrective coefficients A_i with $i \in [7, 12]$. The a priori knowledge on these coefficients given in Table 1 describes the background vector $\mathbf{x}^b$. The observation vector $\mathbf{y}^o$ is composed of

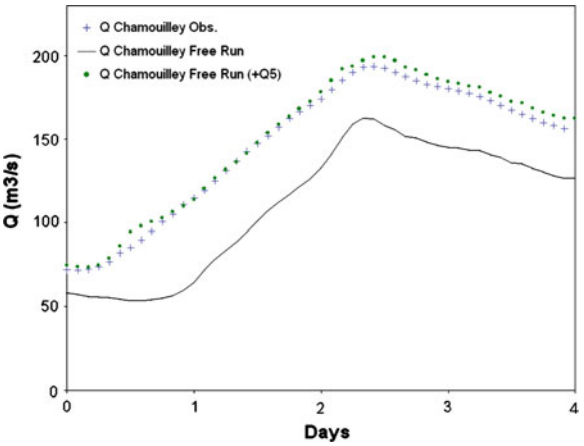

Fig. 3 Discharge at chamouilley, observation (*blue crossed curve*), Free Run (*black solid curve*), and Free Run with Q_5 (*green dotted curve*). March 2008 event

Table 1 Multiplicative corrective coefficients A_i for lateral inflows and standard deviations with $i \in [7, 12]$

Q_i	Elementary hydrograph	A_i	Std
Q_1	Villiers	3	0.8
Q_2	Villiers	4	1.3
Q_3	Humberville	3	1.8
Q_4	Villiers	2.5	1.4
Q_5	Villiers	5.5	2

hourly discharge measurements, a conservative variable, at Condes, Saucourt, Mussey, and Chamouilley (respectively, denoted by S_1, S_2, S_3, and S_4 in Fig. 1). The analysis is performed on a sliding time window, over which the A_i coefficients are assumed to be constant. Assuming that the background, the observation, and the analysis are unbiased, the analysis vector $\mathbf{x}^a$ for cycle k can be formulated as a correction to the background parameters:

$$\mathbf{x}_k^a = \mathbf{x}_k^b + \mathbf{K}_k\left(\mathbf{y}_k^o - H_k\left(\mathbf{x}_k^b\right)\right)$$

where $\mathbf{K}_k = \mathbf{B}_k\mathbf{H}_{k,b}^T\left(\mathbf{H}_k\mathbf{B}_k\mathbf{H}_k^T + \mathbf{R}_k^{-1}\right)$ is the gain matrix, B_k, R_k are the background and observation errors covariance matrixes, and $\mathbf{y}_k = H_k(\mathbf{x}_k)$ is the model equivalent of the observations, generated by the observation operator H_k.

The observation operator consists of two operations: the costliest of which is the nonlinear integration of the hydraulics model given the upstream and lateral flow conditions over the assimilation window. The second operation is the selection of the calculated discharges at the observation points and at the observation times. $H_k\left(\mathbf{x}_k^b\right)$ represents the discharges at the observation points and times computed by MASCARET using the background parameters $A_i = 1$.

The Jacobian matrix $\mathrm{H}_{k,b}$ is the tangent linear of the hydraulics model computed in the vicinity of $\mathbf{x}_k^b$ as follows:

$$H_k\left(\mathbf{x}_k^b + \Delta\mathbf{x}\right) = H_k\left(\mathbf{x}_k^b\right) + \mathrm{H}_{k,b}\Delta\mathbf{x}$$

and $\mathbf{H}_{k,b}^b$can be approximated using a finite differences scheme written as follows:

$$\mathbf{H}_{k,b} = \frac{\partial y}{\partial x} = \frac{\partial H_k\left(\mathbf{x}_k^b\right)}{\partial x} \approx \frac{H_k\left(\mathbf{x}_k^b + \Delta\mathbf{x}\right) - H_k(\mathbf{x}_k^b)}{\Delta x} = \frac{\Delta y}{\Delta x}$$

The local estimation of the tangent linear dynamics of the model with respect to the boundary conditions of the domain is a strong hypothesis. This method can be seen as an EKF algorithm without model errors (the model is considered as perfect). Since there is no propagation model for the parameters, the usual propagation steps of the KF algorithm are irrelevant; here, the background error covariance matrix is invariant between the cycles.

The analysis is cycled over the period covering the entire flood event, thus allowing A_i to vary between the cycles. For cycle k, the observations over the first 8 h (the re-analysis period) are used to estimate the optimal coefficients and a 24 h forecast is carried out. Each of the five lateral inflows $Q1$, $Q2$, $Q3$, $Q4$, and $Q5$ is controlled using downstream measurements from the hydrologic observing station as described in Fig. 1; $Q1$ is controlled by Condes and Mussey, $Q2$ and $Q3$ are controlled by Saucourt and Mussey, $Q4$ is controlled by Mussey and Chamouilley, and $Q5$ is controlled by Chamouilley only. A 5 $m^3\ s^{-1}$ standard deviation error is assumed on the discharge measurements to account for errors in misadjustment of pressure tube and extrapolation of water level-discharge rating curves. The background error covariance is described by a diagonal matrix with the same standard deviation error on every A_i estimated as the mean of those described in

Table 1. The DA algorithm was implemented using the Open-PALM dynamic coupler developed at CERFACS and designed to couple independent code components with a high level of modularity in the data exchanges while providing a straightforward parallelization environment [25].

4 Results

The benefits from the application of the sequential analysis over the 10 floods events for the Marne catchment are summarized in Table 2 presenting the Nash–Sutcliffe criteria computed with DA and without (Free Run) at the maximum lead time for the forecast at each observing station. It was shown that the assimilation of discharge measurements allows for a significant improvement of the simulated discharges in re-analysis (not shown) and forecast mode, with an average improvement of 0.91 at the maximum lead time.

For the major flood event in December 2010, the use of the DA procedure for real-time forecast would have improved both discharge peak forecasts of 15 % as illustrated in Fig. 4 (only the first peak is shown). The discharges are presented on the left vertical axis, and water levels are on the right vertical axis with solid thin and thick lines, respectively. Observations are represented by blue crossed curves, the Free Run 12 h forecast by black solid curves, and the analysis 12 h forecast by red dashed curves. For the discharge and water level, the area between observation and Free Run is shaded in red when the model underestimates the signal and in blue when it overestimates the signal. The corrective coefficients for Q_1, Q_2, Q_3, Q_4, and Q_5 represented in Fig. 5 are globally smaller than 1 when the Free Run overestimates the observed discharge and bigger than 1 where the Free Run underestimates the observed discharge. These values also depend on the sensitivity of the discharge at the observing station with respect to each A_i; this information is accounted for within the linearized observation operator **H**.

Still, the assumption of a constant correction of the lateral inflows over a DA analysis cycle can lead to an inappropriate correction as displayed in Fig. 4 for Day 3. The 12 h forecasted discharge at Day 3, resulting from the DA procedure (175 $m^3\ s^{-1}$ where the solid vertical line intersects the thick red dotted curve), is computed using the corrected inflows resulting from the assimilation of the difference between the Free Run and the observation during the 8 h period in Fig. 4

Table 2 Nash-sutcliffe criteria for Free Run and DA simulations averaged over 10 flood events over 2001–2010 at maximum lead time for each observing station

Observing station	Condes	Mussey	Joinville	Chamouilley	Saucourt
Forecast lead time	+6 h	+12 h	+13 h	+21 h	+10 h
Free Run	0.61	0.01	0.14	−1.38	−0.20
DA	0.87	0.78	0.55	0.47	0.80
Improvement	0.26	0.77	0.69	1.85	1.

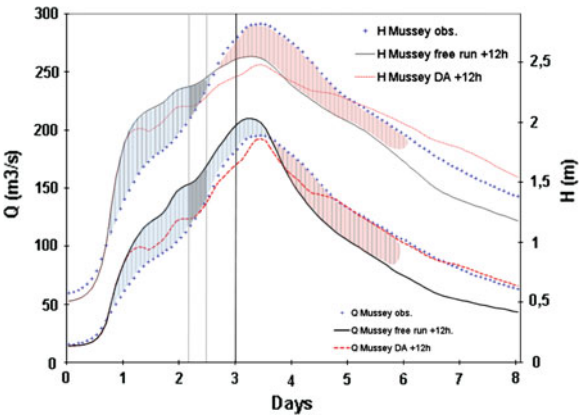

Fig. 4 Discharge (*thick curves*) and water level (*thin curves*) at +12 h, December 2010 (Mussey): observations (*blue crossed curves*), Free Run (*black solid curves*), DA analysis (*red dashed curves*)

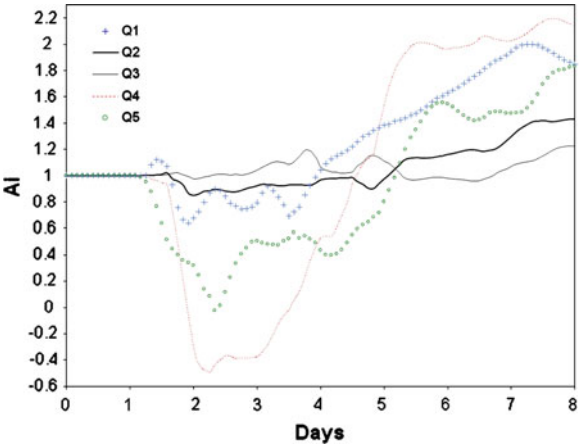

Fig. 5 A_i coefficients for Q_1, Q_2, Q_3, Q_4, and Q_5 during December 2010 event

represented in gray between the two thin vertical lines at Day 2 +2 h and Day 2 +10 h. Over this period, the average discharge (thick curves) difference is bigger than that at Day 3; thus, the DA procedure leads to an over correction of the discharge (an over decrease in this case): the solid red line at Day 3 is below the blue crossed line. To sum it up, if the model–observation error is not monotonous over the re-analysis and forecast period, the DA procedure can lead to an under or over correction. A possible leverage for this problem is to shorten the re-analysis period and thus allow for more temporal variability of the corrective coefficient.

Globally, in Fig. 4, the water level is also significantly improved (thin curves); still, the correction of the lateral inflows with assimilation of the discharge measurements does not improve the water level peak simulation, and it even degrades the first peak at Day 3 +12 h. Indeed, when the relation between water level and discharge in the model is not coherent with the relation between water level and discharge in the observation, the sign of model–observation error on discharge is different from the sign of the model–observation error on water level. This is the

case from Day 2.5 to Day 3.5; the Free Run simulation overestimates the discharge (blue area in Fig. 4) but underestimates the water level (red area in Fig. 4). Here, the DA correction tends to decrease the lateral inflow in order to decrease the simulated discharge, thus leading to the decrease in the simulated water level when the latter was already too small.

The friction coefficients (Ks) of the hydraulic model are mean values obtained from the calibration procedure using discharge data, over 10 flood events. The resulting values for the hydraulic section containing Mussey are 20 for the river channel and 13 for the flood plain. These values are potentially not well suited for high discharge events and might be responsible for a nonphysical local relation between discharge and water level. To account for uncertainty in the topography and bathymetry, a local correction of the Ks coefficient at Mussey is applied (over a 200 m section downstream of the observing station). As illustrated in Fig. 6, a change in Ks allows to improve the simulated water level, while the discharge is left unchanged by this local modification. Once the lateral inflows were corrected through the DA procedure, the simulated discharge is improved over the whole flood event; still, the water level is overestimated (red areas in Fig. 6) from Day 1–2.5 to 5–9 and underestimated at the flood peak (blue area in Fig. 6). An approximate calibration of the Ks coefficients is achieved to obtain the green curves in Fig. 6; the river channel and the flood plain coefficients are increased to 27 and 15, respectively, over the overestimation periods and decreased to 16 and 9 over the underestimation period. The local correction of the Ks coefficients improves water level forecasts without changing discharges. Based on these results, ongoing work aims at including the Ks coefficients within the DA control vector of the previously described procedure.

As the correction of lateral inflows, Ks coefficients must be corrected sequentially as observations become available. The linear approximation of the relation between the Ks coefficients and the simulated hydraulic state should be investigated. Figure 7 illustrates the nonlinear impact of the perturbation of the river channel Ks at the flood peak, at Mussey, around the reference value Ks = 20.

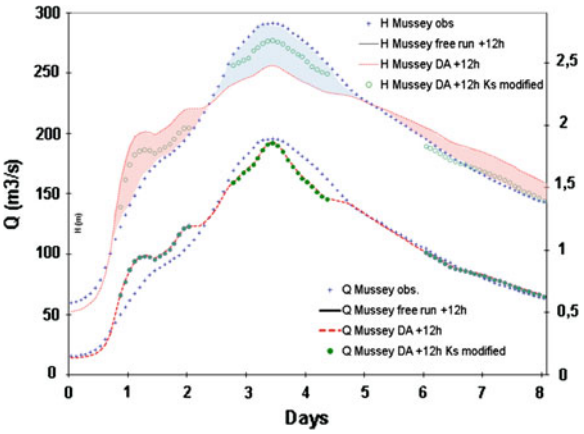

Fig. 6 Discharge (*thick curves*) and water level (*thin curves*) at +12 h, December 2010 (Mussey): observations (*blue crossed curves*), DA analysis (*red dashed curves*), and DA analysis with modified Strickler coefficient (*green dotted curves*)

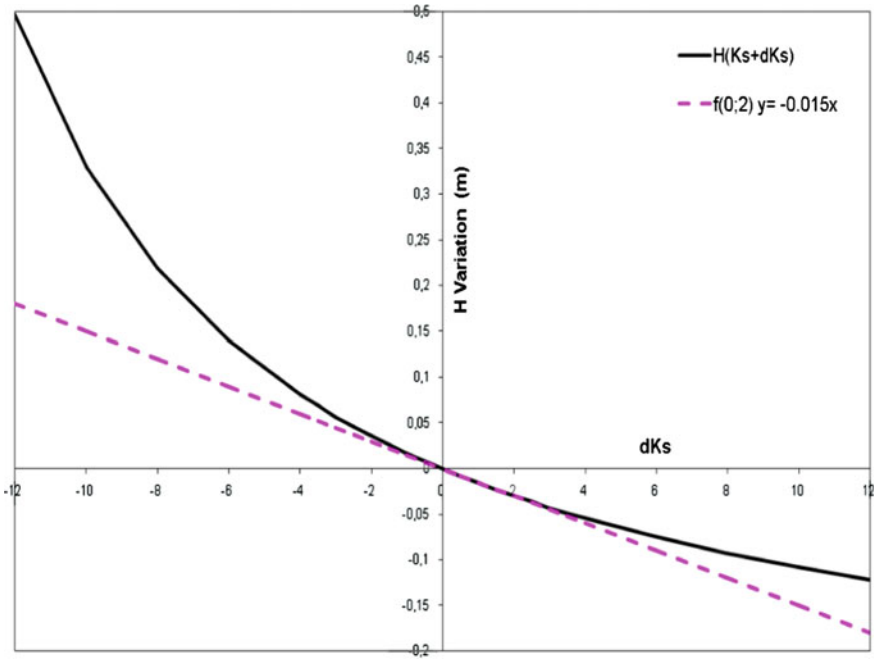

Fig. 7 Impact on the water level on the peak of the perturbation of the river channel Ks coefficient for dKs [−12; 12] (*black curve*) and dKs = 2 (*pink dashed line*)

For instance, a perturbation of 4 leads to a maximum discrepancy in water level of 2 cm with respect to the linear approximation computed for dKs = 2 (pink dashed line in Fig. 7). For a positive perturbation in Ks, the nonlinearity is significantly smaller than for negative perturbations with a water level difference of 6 cm when the Ks is increased from 20 to 32 and up to 33 cm when the Ks is decreased from 20 to 8. In order to keep the nonlinearity impact small on the EKF analysis, the correction to the Ks coefficient should remain in a limited interval such as [−5, 5].

5 Conclusion

The sequential assimilation of discharge measurements in real-time mode was presented in this chapter. The study focuses on the application of an EKF algorithm for the Marne catchment under the assumption that the relation between the lateral boundary conditions of the domain and the simulated discharge is fairly linear. It was shown that the estimation of the time-varying contributions of the karstic areas and the neglected tributaries can be achieved. This leads to the improvement of the hydraulic state forecast at meaningful lead time for operational use. Since the method developed here is not catchment dependent, it was

applied for other French catchments and it is currently being integrated in the real-time forecasting platform for operational use at SCHAPI. The reduced computational cost of the procedure is also a strong advantage. The extension of the control vector to model parameters such as the Strickler coefficients is one of the perspectives for further works as it will allow correcting the relation between water level and discharge within the model.

References

1. Service de l'Observation et des Statistiques—Commissariat Général au Développement Durable (SOeS—CGDD). (2009). Croissance du nombre de logements en zones inondables, Le point sur, 6, Février.
2. Coccia, G., & Todini, E. (2008). Recent developments in predictive uncertainty assessment based on the model conditional processor approach. *Hydrology and Earth System Sciences, 7*, 9219–9270.
3. Weerts, A. H. & Liu, Y. (2011). Advances in data assimilation for operational hydrologic forecasting. EOS Transactions of the AGU, *92*.
4. Duan, Q., Gupta, V., Sorooshian, S., Rousseau, A. N. & Turcotte, R. (2003). Preface in calibration of watershed Models. In Q. Duan et al. (Eds.), Water Science Appli Ser (vol. 6). Washington, DC: AGU.
5. Vrugt, J. A., Gupta, H. V., Bouten, W., & Sorooshian, S. (2003). A shuffled complex evolution metropolis algorithm for optimization and uncertainty assessment of hydrological parameters. *Water Resources Research, 39*(8), 1–14.
6. Schumann, G., Bates, P.D., Horritt, M.S., Matgen, P. & Pappenberger, F. (2009). Progress in integration of remote sensing derived flood extend and stage data and hydraulic models. Reviews of Geophysics, *47*.
7. Bouttier, F., & Courtier, P. (1999). Data assimilation concepts and methods. ECMWF Lecture Note.
8. Liu, Y., & Gupta, H. V. (2007). Uncertainty in hydrologic modeling: Toward an integrated data assimilation framework. *Water Resource Research, 43*, W07401.
9. Maclaughlin, D., & Townley, L. (1996). A reassessment of the groundwater inverse problem. *Water Resources Research, 32*, 1131–1161.
10. McLaughlin, D. (2002). An integrated approach to hydrologic data assimilation: interpolation, smoothing, and filtering. *Advances in Water Resources, 25*, 1275–1286.
11. Reichle, R. H. (2008). Data assimilation methods in the Earth sciences. *Advances in Water Resources, 31*, 1411–1418.
12. Drogue, G., Pfister, L., Leviandier, T., El Idrissi, A., Iffly, J. F., Matgen, P., et al. (2004). Simulating the spatio-temporal variability of streamflow response to climate change scenarios in a mesoscale basin. *Journal of Hydrology, 293*, 255–269.
13. Thirel, G., Martin, E., Mahfouf, J. F., Massart, S., Ricci, S., & Habets, F. (2010). A past discharges assimilation system for ensemble streamflow forecasts over France, Part 1: Description and validation of the assimilation system. *Hydrology and Earth System Sciences, 14*, 1623–1637.
14. Thirel, G., Martin, E., Mahfouf, J. F., Massart, S., Ricci, S., Regimbeau, F., et al. (2010). A past discharges assimilation system for ensemble streamflow forecasts over France, Part 2: Impact on the streamflow forecasts. *Hydrology and Earth System Sciences, 14*, 1639–1653.
15. Dechant, C. M., & Moradkhani, H. (2011). Radiance data assimilation for operational snow and streamflow forecasting. *Advances in Water Resources Research, 34*, 351–364.

16. Seo, D. J., Cajina, L., Corby, R., & Howieson, T. (2009). Automatic state updating for operational streamflow forecasting via variational data assimilation. *Journal of Hydrology, 367*, 255–275.
17. Seo, D. J., Koren, V., & Cajina, N. (2003). Real-time variational assimilation of hydrologic and hydrometeorological data into operational hydrologic forecasting. *Journal of Hydrometeorology, 4*, 627–641.
18. Gelb, A. (1974). *Applied optimal estimation*. Cambridge Mass.: MIT Press.
19. Evensen, G. (1994). Sequential data assimilation with a non linear quasi-geostrophic model using Monte Carlo methods to forecast error statistics. *Journal of Geophysical Research, 99*, 10143–10162.
20. Jean-Baptiste, N., Malaterre, P. O., Dorée, C., & Sau, J. (2009). Data assimilation for real-time estimation of hydraulics states and unmeasured perturbations in a 1D hydrodynamic model. *Mathematics and Computers in Simulation, 81*, 2201–2214.
21. Malaterre, P. O., Baume, J.P. & Jean-Baptiste, N. (2010). Calibration of open channel flow models: A system analysis and control engineering approach. SimHydro.
22. Moradkhani, H., Sorooshian, S., Gupta, H., & Houser, P. (2005). Dual-state parameters estimation of hydrological models using ensemble Kalman filter. *Advances in Water Resources, 28*, 135–147.
23. Ricci, S., Piacentini, A., Thual, O., Le Pape, E., & Jonville, G. (2011). Correction of upstream flow and hydraulics state with data assimilation in the context of flood forecasting. *Hydrology and Earth System Sciences, 15*, 1–21.
24. Goutal, N., & Maurel, F. (2002). A finite volume solver for 1D shallow water equations applied in an actual river. *International Journal for Numerical Methods in Fluids, 38*(2), 1–19.
25. Buis, S., Piacentini, A., & Déclat, D. (2006). PALM: A computational framework for assembling high performance computing applications. *Concurrency and Computation: Practice and Experience, 18*(2), 247–262.

Dam Break Flow Modelling with Uncertainty Analysis

Benjamin Dewals, Sébastien Erpicum, Michel Pirotton and Pierre Archambeau

Abstract Handling uncertainties in dam break flow modelling is of primary interest. Therefore, a procedure is presented here to conduct systematic analysis of the uncertainties resulting from the roughness coefficient, the breaching hydrograph and topographic data. The flow simulations have been conducted with the model WOLF 2D developed at the University of Liege. This two-dimensional flow model is computationally too costly to perform a high number of repeated runs, as needed for Monte Carlo simulations. Therefore, a "reduced complexity model" has been set up, in the form of multidimensional Hermite polynomials. This method, developed by Isukapalli et al. (2004) and first applied to dam break flow by Niemeyer (2007), involves a reduced number of runs of the complete model to calibrate the polynomials. This chapter shows the applicability and efficiency of the methodology, but it also discusses previously unreported shortcomings of the approach, together with hints to overcome them. Results of such uncertainty analysis for dam break flow modelling disclose crucial information for practical risk management. In particular, they reveal that the uncertainty ranges on maximum water depth and time of arrival of the front are not symmetric (overestimation vs. underestimation) and very unevenly distributed in space.

Keywords Risk analysis · Dam break · Flood risk · Uncertainty propagation · Sensitivity analysis

B. Dewals (✉) · S. Erpicum · M. Pirotton · P. Archambeau
HECE: Hydraulics in Environmental and Civil Engineering Chemin des Chevreuils, University of Liege, 1 Bat B52/3+1, 4000 Liege, Belgium
e-mail: b.dewals@ulg.ac.be

S. Erpicum
e-mail: hece@ulg.ac.be

P. Gourbesville et al. (eds.), *Advances in Hydroinformatics*, Springer Hydrogeology, DOI: 10.1007/978-981-4451-42-0_9,

1 Introduction

The failure of a large dam may result in catastrophic floods in the downstream valley. However, past experience has revealed that loss of life and damage can be drastically reduced if crisis management is planned in advance, including early warning systems, organized communication and structural measures. This requires a fairly good knowledge of the flood wave and inundation characteristics likely to be induced in case of a failure.

Predictions of flood waves induced by dam failure are affected by a considerable level of uncertainty. Due to the extreme nature of such events, numerical models can hardly be calibrated and validated. Flow resistance parameterizations are designed for ranges of flow properties which significantly differ from those occurring during dam break flows. Large amounts of debris may also be transported by the flow, and the details of the failure scenario remain usually unknown, such as sequence of dislodgement of dam wall fragments or breach formation time (e.g., Dewals et al. [1]). Nonetheless, most dam break flow studies so far have been conducted without systematic uncertainty nor sensitivity analyses. This is partly due to the high computational cost of the multidimensional flow models used to simulate dam break flows on natural topography.

A standard procedure to propagate uncertainties through models consists in the well-known Monte Carlo simulations. They are robust and flexible, but they lack efficiency because they require a high number of runs of the model. An alternative approach to propagate uncertainties through models relies on building an approximation of the complete model. For instance, a regression technique may be used based on the outputs of a limited number of runs of the complete model; and then, Monte Carlo simulations may be applied to the computationally more efficient approximation of the complete model.

In this chapter, we discuss one particular approximation of the complete hydraulic model, namely a polynomial expansion based on Hermite polynomials. This technique, called stochastic response surface method (SRSM), was first introduced by Isukapalli (e.g., [2]), in combination with environmental and biological models. The method was applied once to a real-world dam break flow by Niemeyer [3], but no validation data were available and the method was not comprehensively tested for a wide range of flow conditions. Here, we present results of tests we have conducted to evaluate the method in very different flow conditions, from simple ones up to a real-world application with validation data available. In particular, the procedure has been tested for a real dam break which occurred in Spain in 1982 [4] and for which a number of observations are available (mainly maximum water depths at different locations in a town).

2 Flow Model

All flow simulations have been performed using the model WOLF 2D, which has been developed by the research group Hydraulics in Environmental and Civil engineering (HECE) at the University of Liege. It solves the fully dynamic shallow water equations based on a shock-capturing finite-volume scheme and a self-developed flux–vector splitting) [5–7]. It handles multiblock regular grids, which routinely contain over 300,000 cells with a minimum of three unknowns per cell. Second-order accuracy is obtained in space and time. Various turbulence closures are available in the model, including a two-length-scale depth-averaged k-ε model [8]. WOLF enables sediment transport modelling, both bedload and suspended load, as well as morphodynamic modelling [9].

3 Setting Up of the Approximate Model

According to Isukapalli (e.g., [2]), a three-step procedure has been followed to set up the approximate model, also referred to as "reduced complexity model".

First, the uncertain input parameters have been expressed in terms of so-called *standard random variables*, which follow a normal distribution with zero mean and unit standard deviation. This step leads eventually to a numerically well-balanced approximation of the complete model. Simple mathematical transformations can be used to express variables following any kind of probability distribution functions as a standard random variable. Second, the outputs of the model, such as time of arrival of the front or maximum water depth, have been expressed as polynomials of the standard random variables.

Third, the coefficients of these polynomial expansions have been estimated based on a limited number of runs of the model. The so-called *co-location points*, where the complete model is run, are selected in such a way as to obtain a statistically representative approximation of the complete model. The number of terms in the expansion depends on the number of uncertain parameters and the order of the polynomial expansion. In turn, it directly affects the number of coefficients to be estimated and thus the number of necessary runs of the complete model. Usually a second- or third-order expansion leads to valuable results. In any case, the number of runs remains orders of magnitude lower than in the case of Monte Carlo simulations performed directly with the complete model.

4 Simple Test Cases

4.1 Uniform Flow and Backwater Curves

Uniform depths have been computed assuming uncertain discharge and Manning coefficient. Since the uniform flow computation relies simply on an algebraic equation, the Monte Carlo simulations could be applied both to the uniform flow equation and to its polynomial approximation, for validation and comparison purpose.

This has revealed that the second-order polynomial expansion was sufficient to represent the statistical behaviour of the model, as shown in Fig. 1a and b. It has also highlighted the need for a very high number of runs of the model used in the Monte Carlo simulation. This confirmed the relevance of using a computationally less-intensive approximation of the complete flow model. As can be seen in Fig. 1c, the output probability distribution has been found here to follow a normal distribution similar to the inputs.

Application of the method for the computation of backwater curves has enabled to quantify the relative sensitivity of the water depth with respect to different uncertain inputs, including discharge, roughness, slope and downstream water level. The method also reveals the spatial pattern of this sensitivity, providing, for instance, the distance up to which uncertainties on the downstream boundary condition affect the result, which is a result of utmost practical relevance.

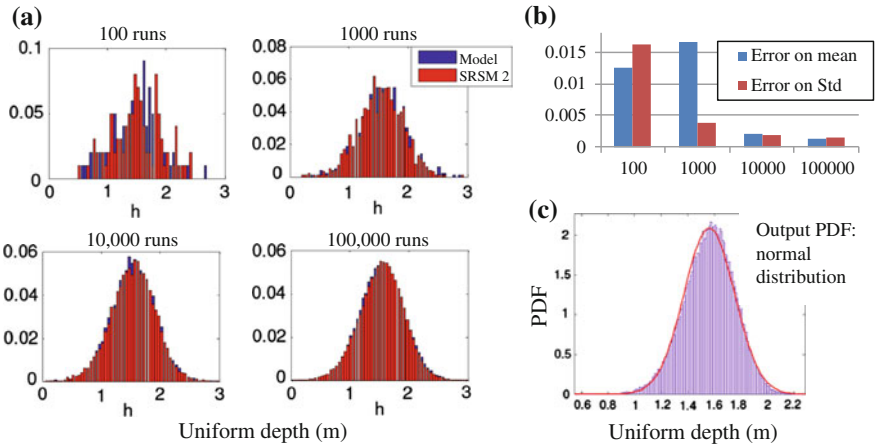

Fig. 1 Application of the uncertainty analysis procedure to the computation of uniform flow: (**a**) and (**b**) influence of the number of runs in the Monte Carlo simulations; **c** output probability distribution function

4.2 Transcritical Flow in a Frictionless Channel

The standard test case of a transcritical flow in frictionless channel with a parabolic bump has been considered, with the inflow discharge and the downstream water level as uncertain parameters. The method enables to deduce the probability distribution of the water level at any point along the channel, as displayed from upstream towards downstream in Fig. 2.

This reveals the parts of the channel in which each uncertain parameter has more influence: the discharge affects the water level only upstream of the hydraulic jump, whereas the downstream boundary condition influences the flow only downstream of the control section.

The probability distributions of the flow variables vary in space, with different relative standard deviations and skewness. They enable to deduce, for instance, a relative sensitivity index, which provides the spatial pattern of relative sensitivity of the output with respect to the uncertain inputs.

The second-order expansion has been found to be generally sufficient. Nonetheless, at some points, differences were found in the probability distributions of the output obtained from the second and third expansions. An example is provided in Fig. 3, in which the probability distribution obtained from the third order looked

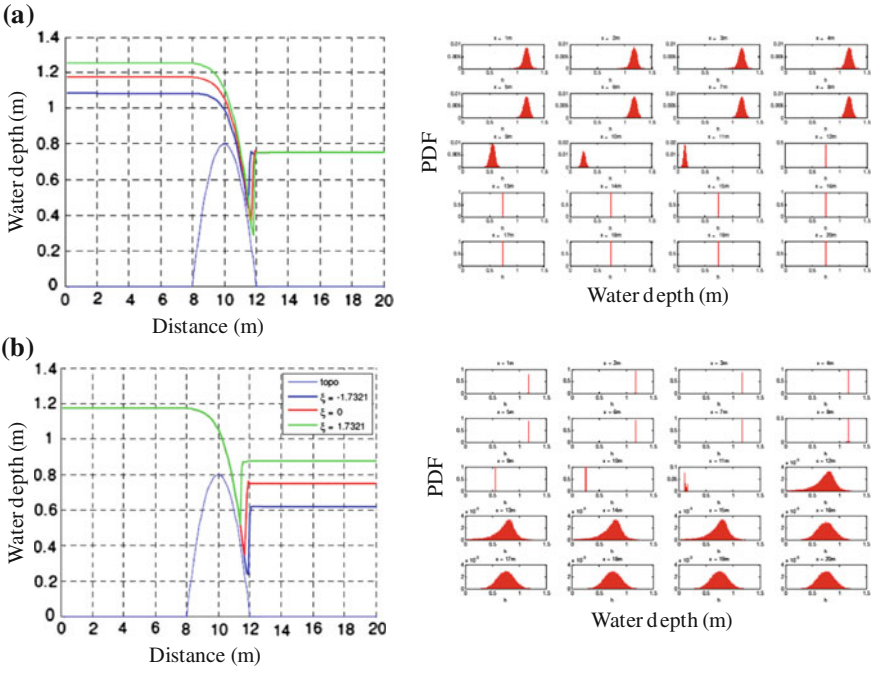

Fig. 2 The method provides the spatial pattern of the sensitivity of the outputs with respect to uncertainties in inputs (**a**) Uncertainty indischarge mainlyaffects the upperpart of the flow (**b**) Uncertainty in theboundary conditionmainly affects thelower part of the flow

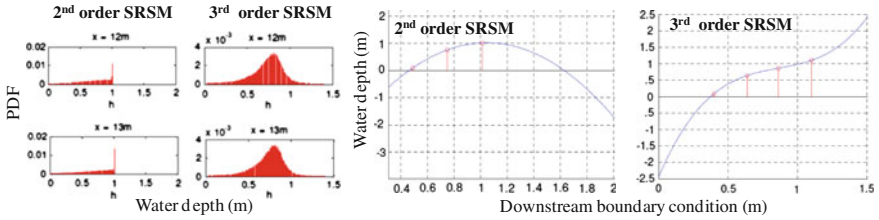

Fig. 3 Extrema in the polynomial expansion lead to artefacts in the probability distribution functions of the outputs

regular, while the probability distribution from the second-order expansion was bounded. Looking at the values of the output at the collocation points and the resulting polynomial approximations has disclosed that in the second-order approximation, a maximum of the quadratic polynomial was found near the co-location points. This has no physical meaning, and the third-order expansion is hence absolutely necessary in this case. In practical applications, attention should be paid to identify and correct such artefacts.

Similarly, in the transcritical region of the flow, each point may be located either upstream or downstream of the hydraulic jump depending on the uncertain input parameters, such as the downstream boundary condition. The local water depth varies thus discontinuously with the uncertain parameters. A polynomial approximation has no chance to properly reproduce such a discontinuous behaviour. Indeed, it would always lead to a continuous distribution of the output, contrarily to a distribution obtained by applying directly Monte Carlo simulations to the complete flow model. In such a case, an appropriate variable change can be used for the method to apply. For instance, the hydraulic jump location and/or strength may be used as output variable. Since these variables vary continuously with the uncertain inputs, they may be satisfactorily approximated by a polynomial expansion.

5 Idealized Dam Break Flow

The method for uncertainty analysis has been applied to idealized configurations of dam break flow, including Ritter and Dressler cases (Fig. 4). In the former case, characterized by a dry and frictionless flat bottom, the influence of the initial pool level (assumed normally distributed) on the maximum water depth and time of arrival of the front has been analysed. The computed maximum water depths follow a normal distribution, which is consistent with theory since in the analytical Ritter solution the water depth at any point scales with the initial pool level. In contrast, the time of arrival of the front does not follow a normal distribution. In addition, the sensitivity of the maximum water depth is found uniform along the valley, while the sensitivity of the time of arrival of the front increases towards

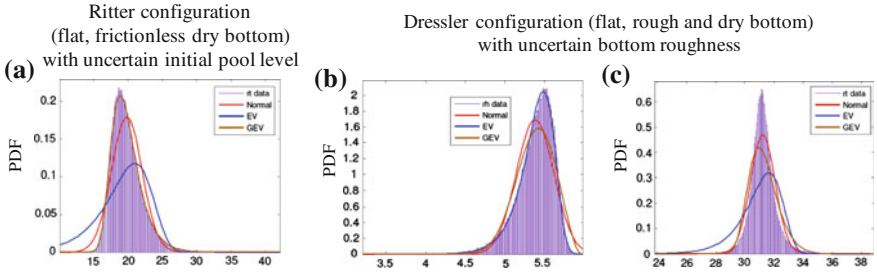

Fig. 4 Probability distribution of the maximal water depth and wave arrival time in Ritter and Dressler cases level (**a**) PDF of arrival time of the front (**b**) PDF of maximum water depth (**c**) PDF of arrival time of the front

downstream. Similar results have been found for the Dressler configuration, corresponding to a dry and rough flat bottom; but, in this case, even the probability distribution function of the maximum water depth shows a significant skewness.

6 Real-World Dam Break Flow

Finally, the procedure for uncertainty analysis has been applied to a real-world dam failure, which occurred in Spain in 1988 [4]. The *Tous dam* on river Jucar was breached following heavy rainfall, which lead to an estimated 600 million cubic metres of inflow compared to 120 million cubic metres storage capacity in the reservoir. The peak outflow was 300 times higher than the mean discharge of the river.

Two digital elevation models (DEM) of the valley are available. They were obtained, respectively, in 1982 shortly after the flood and in 1998 in the framework of the construction of a new dam. The former includes deposits induced by the dam break flood wave, while these deposits were dredged at the time of the later DEM. A number of observations of maximum water depth are available in a town located about 5 km downstream of the breached dam.

Three main sources of uncertainties may be identified in the computation of this real-world event:

- the topographic datasets
- the roughness coefficient, supposed to include locally the effect of high vegetation such as trees
- and the breach hydrograph.

The first one has been treated by means of sensitivity analysis: all simulations have been conducted based on each of the two available topographic datasets (Fig. 5). The other two uncertainty sources have been handled by the procedure for uncertainty propagation. For this purpose, the breach hydrograph has been parameterized and the corresponding parameters have been assumed to follow known normal distributions.

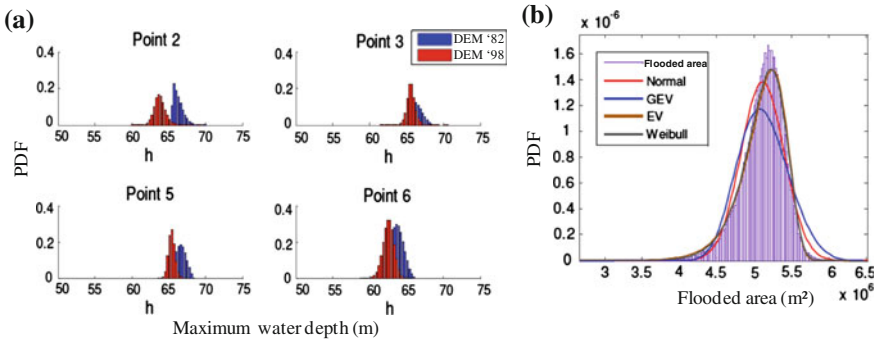

Fig. 5 Probability distributions obtained for the considered real-world dam break flow: **a** maximum water depth evaluated from the two digital elevation models (*DEM*) for uncertain roughness of the valley and **b** effect of uncertain breach hydrograph on the flooded area

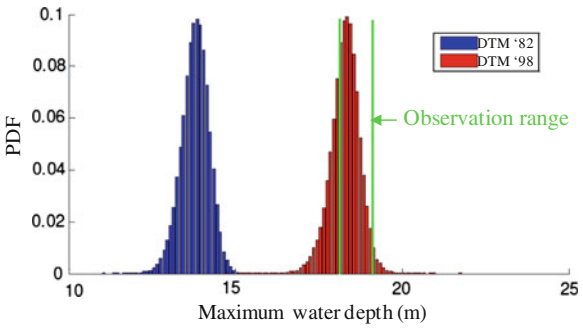

Fig. 6 Observation and probability distributions obtained for maximum water depth evaluated from the two digital elevation models (*DEM*) for uncertain roughness of the valley in the considered real-world dam break flow

Application of the procedure has enabled to quantify the relative influence of the different sources of uncertainty (Fig. 5) and provides results of very practical interest for risk analysis and management. Validation data, in particular observed water depth in the town, have shown that observations fall within the uncertainty range of the model; provided correct topographic data are used (Fig. 6). All these results have been deduced from a third-order polynomial expansion of the complete model, and the calibration of which has required just five runs of the two-dimensional flow model, confirming thus the efficiency of the procedure.

7 Conclusions

Real dam break flow modelling is probably one the hydraulic modelling problems in which uncertainties are the highest. It usually involves complex multiphase flow carrying debris and high concentrations of sediments. A complete knowledge of the failure scenario is also never available (failure mechanism, breach location, pool level and inflows at the time of failure), nor can the model be calibrated based

on a sufficient number of events since observations remain scarce. Therefore, handling scenario uncertainty and parameter uncertainty in dam break flow modelling is of primary importance.

In this chapter, a procedure has been discussed to propagate uncertainty through complex flow models. The method relies on the calibration of a polynomial expansion of the outputs as a function of the uncertain input parameters, expressed as standard random variables. The calibration requires a limited number of runs of the complete model.

For the purpose of evaluating the method, it has been tested on a range of simple hydraulic problems, including computation of uniform flow, backwater curves and transcritical flows in a smooth channel with a bump. These simple tests have revealed two potential pitfalls of the method, namely artefacts resulting from unphysical extrema in the polynomial expansion and the inability of the method to approximate discontinuous variations in the model outputs (e.g., water depth in hydraulic jumps). While care of the modeller is required in the former case, variable changes may be used to overcome the later.

Next, the method has been applied to an idealized and a real-world dam break flow analysis. The results turn out to be of high practical interest to estimate, for instance, the most relevant "safety factors" to be applied at the time of hazard mapping. These examples have demonstrated the applicability and efficiency of the methodology, which is readily available for real-world analyses.

Acknowledgments The authors gratefully acknowledge S. Kyabu for her contribution to part of the work presented in this chapter.

References

1. Dewals, B. J., Erpicum, S., Detrembleur, S., Archambeau, P., & Pirotton, M. (2011). Failure of dams arranged in series or in complex. *Natural Hazards, 56*, 917–939.
2. Isukapalli, S. S., Balakrishnan, S., & Georgopoulos, P. G. (2004). Computationally efficient uncertainty propagation and reduction using the stochastic response surface method. In *43rd IEEE Conference on Decision and Control*. Atlantis, Paradise Island, Bahamas (pp. 2 237–2243).
3. Niemeyer, M. (2007). Einfluss der Breschenbildung auf die Flutwellenausbreitung bei Damm- und Deichbrüchen. In *Institute of Hydraulic Engineering and Water Resources Management (IWW)*. (p. 224), RWTH Aachen: Aachen.
4. Alcrudo, F., & Mulet, J. (2007). Description of the Tous Dam break case study (Spain). *Journal of Hydraulic Research, 45*, 45.
5. Dewals, B. J., Kantoush, S. A., Erpicum, S., Pirotton, M., & Schleiss, A. J. (2008). Experimental and numerical analysis of flow instabilities in rectangular shallow basins. *Environmental Fluid Mechanics, 8*, 31–54.
6. Erpicum, S., Dewals, B. J., Archambeau, P., & Pirotton, M. (2010). Dam-break flow computation based on an efficient flux-vector splitting. *Journal of Computational and Applied Mathematics, 234*, 2143–2151.

7. Roger, S., Dewals, B. J., Erpicum, S., Schwanenberg, D., Schüttrumpf, H., Köngeter, J., et al. (2009). Experimental und numerical investigations of dike-break induced flows. *Journal of Hydraulic Research, 47*, 349–359.
8. Erpicum, S., Meile, T., Dewals, B. J., Pirotton, M., & Schleiss, A. J. (2009). 2D numerical flow modeling in a macro-rough channel. *International Journal for Numerical Methods in Fluids, 61*, 1227–1246.
9. Rulot, F., Dewals, B., Erpicum, S., Archambeau, P., & Pirotton, M. (2012). Modelling sediment transport over partially non-erodible bottoms. *International Journal for Numerical Methods in Fluids,*. doi:10.1002/fld.2684.

Coupling TOMAWAC and EurOtop for Uncertainty Estimation in Wave Overtopping Predictions

Nicolas Chini and Peter K. Stansby

Abstract An integrated model system has been implemented for downscaling from climate models, to wave climate and continental shelf models for tides and surge, to coastal models for waves and water levels and overtopping of sea defences and inundation. Within the system, the 3rd generation wave model TOMAWAC is applied to transfer inshore waves to the toe of the seawall, producing wave input for the predictive tool EurOtop that provides estimates of overtopping rates. This coupling is then used to assess the sensitivity of the overtopping predictions to uncertainty in offshore hydraulic conditions and beach levels for a case study on 7th November at Walcott in East Anglia, UK. The methodology used to transfer offshore conditions towards the nearshore allows estimation of the induced errors in nearshore wave heights by introducing small changes to offshore water level and significant wave height. Wave height uncertainty leads to an error in overtopping discharge rate less than 30 %. Errors induced by uncertainty in water levels are much higher. A + 10 % uncertainty in water level could increase the nominal overtopping discharge rate by a factor of 2.7. Thus, at least for this particular case, overtopping discharge predictions are mainly sensitive to water level. Uncertainty to beach profiles is also investigated showing that the overtopping is sensitive to low beach levels.

Keywords Uncertainty analyses · Coastal flood risk · Wave modelling

N. Chini (✉) · P. K. Stansby
School of MACE, University of Manchester, Sackville Street, Manchester M13 9PL, UK
e-mail: nicolas.chini@manchester.ac.uk

P. K. Stansby
e-mail: p.k.stansby@manchester.ac.uk

P. Gourbesville et al. (eds.), *Advances in Hydroinformatics*,
Springer Hydrogeology, DOI: 10.1007/978-981-4451-42-0_10,

1 Introduction

For coastal planning dealing with flood risk assessment, managers and stakeholders require robust and reliable flooding-related information enabling them to issue flooding alerts and to design coastal structures preventing inundation of low-lying lands. In the UK, the Environment Agency (EA) issues coastal flood alerts based on offshore wave and surge forecasts with a time horizon of up to several days in advance of an event. The forecasts are performed using operational regional numerical models for estimating waves and surges. These models are optimised to deliver an ensemble of simulations within a reasonable computational time (about 1 h). However, they miss the representation of the physical processes that take place in the nearshore where nonlinear interactions between water levels, currents, waves and the bathymetry constrain the wave overtopping occurrence and the loading experienced by the sea defences. In order to enhance the quality of wave overtopping predictions, a downscaling procedure was developed within the UK Flood Risk Management Research Consortium (FRMRC) Coastal Inundation Super Work Package. This downscaling proposes to include the nearshore processes while propagating the offshore conditions towards the seawall. Figure 1 presents the flow chart for data transfer from offshore conditions to wave overtopping discharge estimations.

The offshore waves and water levels are first simulated using regional models with a spatial resolution of about 12 km. POLCOMS [1], providing a coupling between waves and surge motion, is used here. This model provides the boundary conditions for a nested model with much smaller spatial resolution in order to capture the seabed features and to enhance the representation of the nearshore bathymetry. For this coastal modelling, the TELEMAC suite [2] is used. The module TELEMAC2D and TOMAWAC are applied on an unstructured grid with a spatial resolution varying from 2 km along the offshore boundary and 700 m along the coastline. The methodology proposed by Chini et al. [3] is applied to assess the wave data along the coastline. This methodology based on a look-up table with an interpolation scheme allows fast prediction of wave integrated

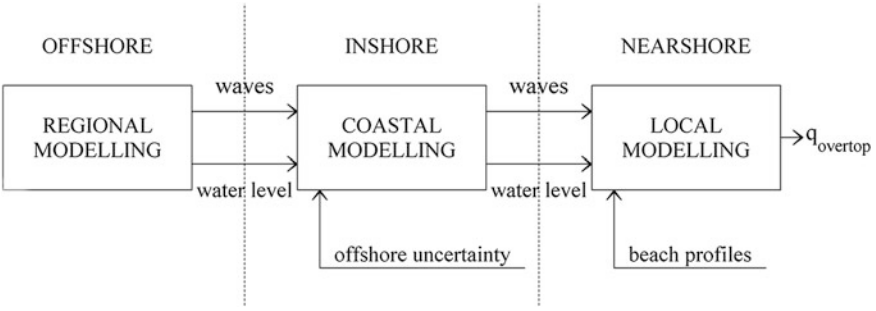

Fig. 1 Flow chart presenting data transfer in order to estimate overtopping discharge from regional modelling including uncertainties in offshore conditions and beach profiles

parameters, with inclusion of temporal water level variations. Ultimately, the water levels and wave integrated parameters at water depths of about 10 m are transferred towards the seawall using TOMAWAC on a smaller domain. This last nested model is employed to downscale the water levels and the wave parameters at the toe of a coastal structure which can be overtopped by waves. In order to estimate the wave overtopping discharge rates, the EurOtop neural network application [4] is eventually used. This downscaling procedure is only a part of the wider framework presented in detail in [5], in which other numerical methods for wave overtopping and inundation modelling are also considered.

The downscaling procedure (Fig. 1) is applied to a particular location where coastal flooding caused only by wave overtopping occurred in November 2007. Although the simulated highest water marks are in fair agreement with collected information about the flooding event, some uncertainty remains about the offshore conditions and the beach profile. As a matter of fact, comparison with field data showed that the offshore simulated water levels and significant wave heights were estimated with an uncertainty of about 10 %, with potential influence on the overtopping discharge predictions. In order to quantify the sensitivity of overtopping predictions, the uncertainty is propagated within the downscaling procedure. Another source of uncertainty on overtopping discharge simulation is the beach profile at the moment of the event. A healthy beach profile is often considered as a natural protection against overtopping by increasing wave energy dissipation by both bottom friction and wave breaking. In order to assess the influence of beach profile on wave overtopping discharge rates, historical beach profiles can be considered, and it is proposed to apply the downscaling procedure for these beach profiles. The sensitivity of the wave overtopping modelling to beach profiles can be therefore assessed.

Section 2 presents the case study and the available data used for the modelling of wave overtopping. In Sect. 3, the coupling between TOMAWAC and EurOtop is presented. The methodology applied to assess the uncertainty in wave overtopping due to offshore conditions and beach profiles is described in Sect. 4. The results are then presented in Sect. 5. Section 6 draws some conclusions about the offshore uncertainty analyses and implications of beach level on wave overtopping.

2 Case Study Presentation

The downscaling presented in Fig. 1 is here applied to a case study for the inundation that took place in Walcott on the Eastern coast of England (Fig. 2a). During the night between the 8th and the 9th of November 2007, severe atmospheric conditions generated wind waves and surge that travelled along the east coast of England. The measured surge levels, estimated after subtracting the predicted tidal levels to the tidal gauge measurements, at Lowestoft and Cromer (Fig. 2a) reached the values of 2.09 and 1.88 m, respectively. Offshore waves measured at the Dowsing wave buoy revealed that significant wave heights during the event reached

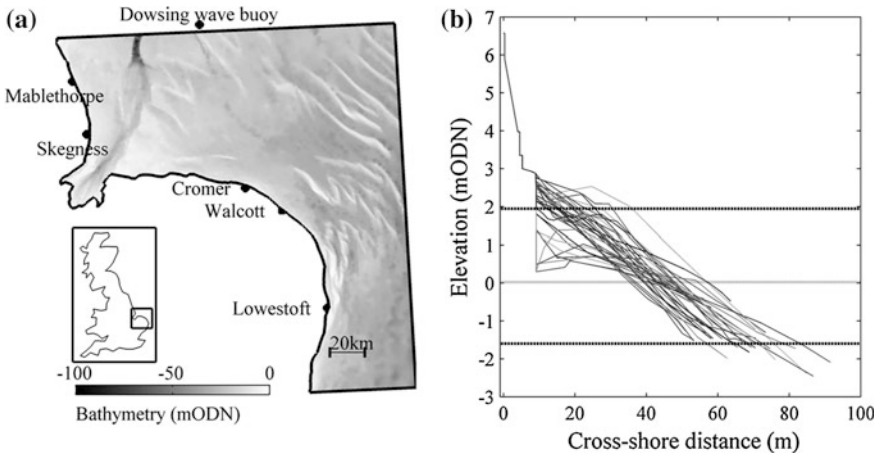

Fig. 2 Localisation map showing **a** the position of Walcott and the offshore bathymetry, and **b** the cross-profiles surveyed at Walcott

a maximum value of almost 6 m, associated with a direction from the north-north-west and a peak period of 12 s. These conditions led to almost £170,000 of damage in Norfolk [6], with the community of Walcott the most severely affected. In that particular location, wave overtopping caused flooding of the properties located along the seafront and agricultural fields. This community takes place in a low-lying land which separates two sections of soft cliffs constituting the shoreline of north-east Norfolk. This low-lying land is protected from waves and surges by a seawall whose crest level is 6.6 m Ordnance Datum Newlyn (ODN).

For that particular event in 2007, the highest nearshore wave heights and water levels at Walcott were estimated to reach 2.51 and 3.2 m, respectively. The event lasted for the upper part of the tidal cycle. Extreme event analyses qualified this event as a one in 100 years event.

At Walcott, the EA has undertaken beach profiles survey since 1991. These surveys are performed twice a year, one in late summer and another one in late winter, usually during low spring tides. Here, the data from 1992 to 2008 are considered, representing a set of 34 profiles. These profiles are represented on Fig. 2b. Table 1 presents statistics of the beach volumes and beach levels at the toe of the structure. Surveys with small resolution at the toe of structure are disregarded from the analyses. That happened for two surveys: in summer 1995 and winter 2000. Moreover, the profile surveyed in 1996 is not consistent with the other ones and is also removed from the analyses.

Beach volumes are computed for the section extending from the toe of the seawall to the lowest tidal mark. From the 34 profiles, only 13 covered this entire section. For the simulation of coastal inundation, the profile measured at the end of the summer 2007 was used. This measured profile was particularly low in comparison with other surveyed profiles. For this profile, the beach volume was 98.5 m^3/m and its elevation at the toe of seawall was 1.34 m ODN (Ordnance Datum Newlyn).

Table 1 Statistics of the beach profile at Walcott. Figures in brackets represent standard deviations

Volume (m^3/m)			Elevation at the seawall toe (m ODN)		
Min	Max	Mean	Min	Max	Mean
92.6	176.4	121.2 (23.2)	0.58	2.67	1.92 (0.54)

3 Coupling Procedure

3.1 TOMAWAC Presentation

Nearshore waves propagate towards the toe of the sea wall, potentially causing overtopping. A local wave model is embedded within the coastal domain, presented in Fig. 1, to simulate waves approaching the toe of the structure. This local model is shown in Fig. 3a for the coast at Walcott. TOMAWAC is used on an unstructured grid with 8,176 points and 16,032 elements. The spatial resolution varies from 0.1 m along the coastline to 80 m offshore at a distance of about 2 km. The spectral frequency is digitised as 25 frequencies, with a minimum frequency equal to 0.042 Hz, the frequency increments having a ratio of 1.1. Directional resolution is set to 15° over 360°. A JONSWAP-type spectrum with broad directional spreading [7] is imposed at the offshore boundary from the output of the coastal model at a point located on the outer boundary. The JONSWAP bottom friction coefficient of 0.038 m^2/s^3 [8] and the formulation for depth-induced wave breaking [9] were used. The time step is generally set at 2 s, with smaller values giving the same wave propagation. Mean water level is assumed spatially uniform, and it varies due to surges, tides and sea level rise. Dry areas are represented by a small water depth over which there is no wave propagation.

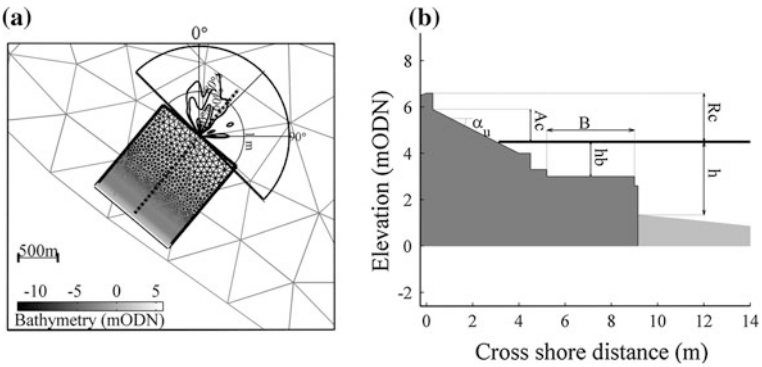

Fig. 3 **a** Computational grid for the local mesh, showing wave rose and the grid of the coastal model. **b** Seawall cross section at Walcott with definition of the parameter used for the EurOtop neural network

Normal wave incidence at the outer boundary is generally used with zero gradient along the lateral boundaries and the coastline. However, the wave rose on Fig. 3a shows that waves are approaching the coastline with oblique incidence [10] show that incidence up to 45° does not affect the extreme significant wave height at the toe of the structure.

At the toe of the structure, the water level can be increased due to set up h_s caused by wave breaking in the nearshore [11] provide a simple estimate as follows:

$$h_s = 0.19\, H_b, \tag{1}$$

where H_b is the wave height on the onset of depth-induced breaking. The wave set-up is added to water depth at the toe of the structure. The addition is not specifically recommended by the EurOtop manual [12]. However, comparison with other methods for overtopping prediction shows that considering the wave set-up improved the quality of the predictions [5].

3.2 EurOtop Neural Network Presentation

The seawall itself consists of a vertical wall, whose top is located 3.0 m above ODN, followed by a 2.75 m wide horizontal berm; the slope of the structure upward of the berm is 2:1. The seawall crest is at 6.6 m ODN, with a recurve. Figure 3b shows a sketch of the seawall, where h is the water level at the toe of the structure. Other relevant parameters are described in van Gent et al. [4].

During the CLASH and EurOtop projects [12, 13], overtopping predictors were developed. Several techniques are proposed in the EurOtop manual [12] dependant on the coastal structure. For the seawall geometry located at Walcott, the neural network approach is appropriate. The set-up of the model requires 15 different inputs describing both the hydrodynamic conditions and the geometry of the seawall (for details see [4]). Table 1 summarises the parameters describing the seawall.

For beach profiles levels reaching the berm height, the parameters in Table 1 are modified, so that the lower part of the seawall is removed. Consequently, for the EurOtop application, the vertical wall at the toe of the structure is removed and the berm becomes the toe of the structure.

Table 2 Neural network inputs: coastal structure geometry parameters

Ht (m)	Bt (m)	$\cot \alpha_d$	$\cot \alpha_u$	Rc (m)	B (m)	Hb (m)	$\tan \beta$	A_C (m)	gf	G_C (m)
h	0	0	1.78	6.6-h	3.72	*h*-3	0	5.9-h	1	0

4 Uncertainty Analyses

4.1 Propagating Offshore Uncertainties on Significant Wave Height and Water Levels

The ensemble runs are performed for an operational forecast of storm surges and waves. The use of perturbed physics ensembles assumes that the modified parameters belong to a domain where the model output is sensitive to input. Given the potentially large number of parameters, the ensemble should contain a large number of runs. In order to increase the computational efficiency of forecast, the use of adjoint modelling could be considered, since this modelling requires only one model integration to estimate model sensitivity. However, we propose here to test the sensitivity of the nearshore wave height to a small additive error on the input parameters:

$$y = f(x + \varepsilon), \tag{2}$$

where x represents the input vector (water level, offshore significant wave height, offshore peak wave period, offshore mean wave direction, ignoring the local wind forcing), ε is the additive error vector, f is the transfer function giving the nearshore wave parameter y.

Assuming ε to be small, the first-order Taylor expansion of f gives:

$$y = f(x) + \sum_{i=1}^{4} \frac{\partial f}{\partial x_i}(x)\varepsilon_i + o(\varepsilon) \tag{3}$$

The transfer of waves towards the shore of East Anglia is performed using a look-up table coupled with a linear interpolation scheme. This property means that (i) the partial derivative of f in the direction x_i can be analytically expressed and (ii) this derivative is, within each cell of the look-up table, independent of x_i and bounded by the maximum of the ensemble:

$$\left\{ \frac{\left| f\left(\bar{x}_1(a_k), \ldots, \bar{x}_i(a_2), \ldots, \bar{x}_4(a_j)\right) - f\left(\bar{x}_1(a_k), \ldots, \bar{x}_i(a_1), \ldots, \bar{x}_4(a_j)\right) \right|}{\Delta x_i}, (k,j) = 1,2 \right\}, \tag{4}$$

where $\bar{x}_j(a_k)$ represents one of the two vertices of the segment along the j coordinate of the cells of the look-up table to which x belongs.

For the look-up table presented by Chini et al. [3], an error in the offshore conditions will induce an error in the nearshore prediction bounded by

$$|y - f(x)| \leq 0.95\varepsilon_{Hm0} + 0.32\varepsilon_h + 1.18\varepsilon_{\mathrm{Tp}} + 0.035\varepsilon_\theta \tag{5}$$

This means that an error of 0.1 m in the offshore significant wave height will induce a maximum error of 0.095 m at Walcott. The relatively high sensitivity to the offshore peak wave period is misleading. In fact, this value is overestimated,

since the look-up table contains some relatively steep waves (with $H_{m0} = 8$ m and $T_p = 4$ s for instance). By considering only the situation where wave steepness is realistically limited (ka<= 0.07), the equation becomes

$$|y - f(x)| \leq 0.95\,\varepsilon_{Hm0} + 0.32\,\varepsilon_h + 0.52\,\varepsilon_{\mathrm{Tp}} + 0.035\,\varepsilon_\theta \tag{6}$$

4.2 Results

An uncertainty of 10 % is added to the values of offshore wave heights and water levels simulated during the 2007 event and then propagated towards the seawall to estimate the uncertainty on overtopping discharge predictions. This offshore 10 % error represents a maximum error on nearshore significant wave height of 0.47 m, that is, a maximum relative error of 18 %. For the water level, the 10 % error represents a variation of 0.3 m.

Figure 4 presents the error in overtopping discharge prediction for the 2007 event due to uncertainty in water levels and offshore significant wave heights. Wave height uncertainty leads to an error in overtopping discharge rate less than 30 %. Errors induced by uncertainty in water levels are much higher. A + 10 % uncertainty in water level could increase the nominal overtopping discharge rate by a factor of 2.7. Thus, for that particular event, overtopping discharge predictions are mainly sensitive to water level.

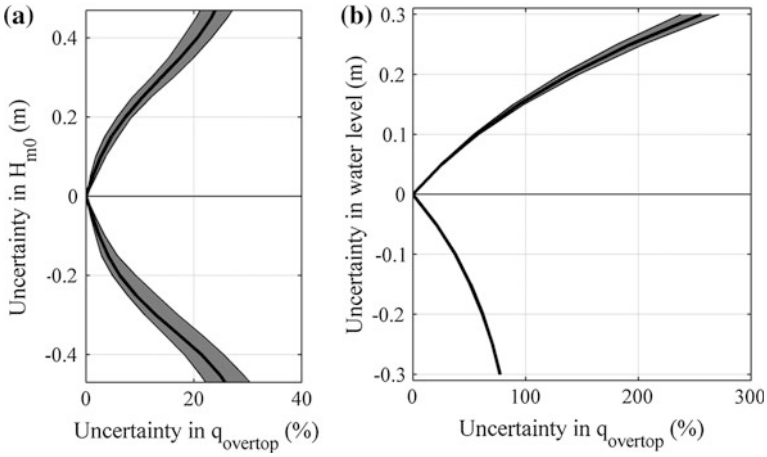

Fig. 4 Induced errors in overtopping discharge due to uncertainty in offshore wave height (**a**) and water level (**b**)

5 Sensitivity to Beach Profiles

5.1 Waves Conditions at the Toe of the Structure

The simulated water levels and wave integrated parameters for the 2007 event are used to drive the local model with the different beach profiles. Therefore, the influence of cross-shore profile can be assessed for extreme nearshore conditions. Emphasis is placed on the peak conditions that took place during the storm.

Figure 5 presents the significant wave height, H_{m0}, at the toe of the structure for the different beach profiles. Figure 5a shows that the predicted H_{m0} are correlated to the water depth at the toe of the structure, meaning that the lower the beach level, the higher the significant wave height. The lowest beach level at the toe of the seawall results to a H_{m0} almost 3 times higher than the one predicted for the highest beach level. Such dependence is less obvious when considering the beach volume. However, it could be stated that for beach volume higher than 120 m^3/m, the wave heights are constant. For smaller volume, a distinctive inverse correlation is, however, noticeable.

5.2 Overtopping Rates

Implications of the dependence of the significant wave height on beach profile to the prediction of wave overtopping discharge are investigated by using the EurOtop neural network presented in Sect. 3.2. Figure 6 presents the results for the wave overtopping discharge rates on the different beach profiles. Here, only the highest rates during the event are presented for different beach elevation at the toe of the structure and beach volumes.

For beach levels lower than 2 m ODN at Walcott, the coupling between TOMAWAC and EurOtop predicted wave overtopping. The rates of predicted overtopping discharge are sensitive to low beach level at the toe of the structure; the predictions increase with the lowering of the beach elevation. For beach

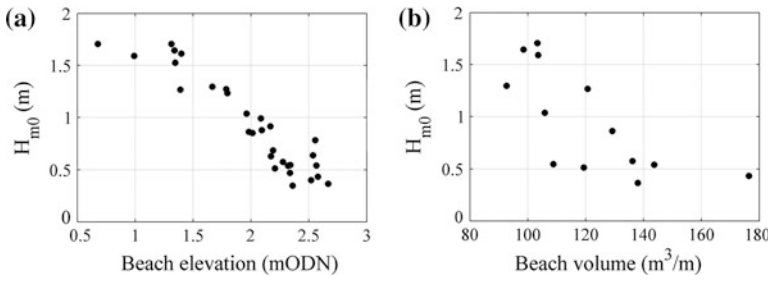

Fig. 5 Significant wave height (H_{m0}) at the toe of the seawall. **a** Scatter plot against beach elevation at the toe of the structure and **b** scatter plot against beach volume

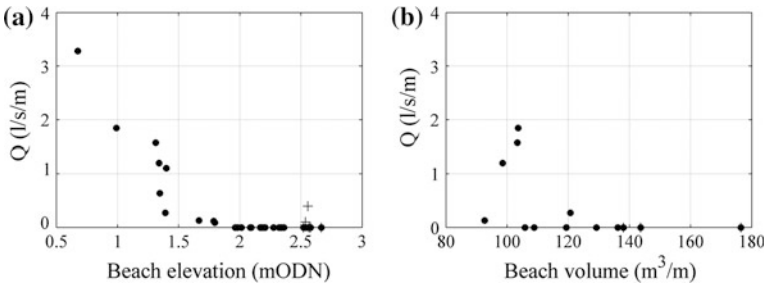

Fig. 6 Wave overtopping discharge (Q) predicted by EurOtop at Walcott. **a** Scatter plot of Q against beach elevation at the toe of the structure and **b** scatter plot of Q against beach volume. Crosses correspond to EurOtop configuration with no berm for the seawall

profiles higher than 2 m ODN, no overtopping is predicted. For these elevations, the configuration of the seawall is out of the bounds of the validity of EurOtop. For beach levels almost reaching the berm height of the seawall, the second configuration of EurOtop is used. In this case, some overtopping is predicted but much smaller than estimated for the lowest beach levels.

The influence of the beach volumes on the overtopping predictions is not as clear as the link between overtopping and beach levels. However, no overtopping is predicted for the highest volumes.

6 Conclusion

A coupling between TOMAWAC and EurOtop is proposed for the estimation of wave overtopping at a seawall located along the eastern coast of England. This coupling is part of a larger framework to transfer offshore conditions towards the seawall, in order to predict overtopping discharge rates and consequent coastal flooding. Sensitivity of the wave overtopping predictions to offshore conditions uncertainties and beach levels is considered. It is found that uncertainties in simulated water levels have a much higher impact on wave overtopping discharge prediction than uncertainties on wave heights. Using the proposed coupling, beach elevations are also found to induce large sensitivity in the wave overtopping modelling. Some restrictions to the proposed methodology could however be drawn. As described, different configurations of EurOtop should be used depending on the beach elevation, leading to more scattered results and less robust methodology. Moreover, the coupling does not include wave reflections at the toe of the structure, which could have an effect on the wave propagation towards the seawall. Therefore, to gain confidence in the above results, other numerical and experimental approaches should be undertaken and compared. If similar results are obtained with different methods, that could lead to the definition of policies based on beach replenishment to mitigate wave overtopping occurrence at Walcott.

Acknowledgments This work was funded through the Flood Risk Management Research Consortium. The FRMRC is supported by grant EP/F020511/1 from the Engineering and Physical Sciences Research Council, in partnership with the DEFRA/EA Joint Research Programme on Flood and Coastal Defence, UKWIR, OPW (Ireland) and the Rivers Agency (Northern Ireland). Their financial support is gratefully acknowledged.

References

1. Brown, J. M., & Wolf, J. (2009). Coupled wave and surge modelling for the eastern Irish Sea and implications for model wind-stress. *Continental Shelf Research, 10*, 1329–1342.
2. Hervouet, J.-M. (2007). *Hydrodynamics of free surface flows modelling with the finite element method*. NY: Wiley.
3. Chini, N., et al. (2010). The impact of sea level rise and climate change on inshore wave climate: A case study for East Anglia (UK). *Coastal Engineering, 57*, 973–984.
4. van Gent, M. R. A., van den Boogaard, H. F. P., Pozueta, B., & Medina, J. R. (2007). Neural network modelling of wave overtopping at coastal structures. *Coastal Engineering, 8*, 586–593.
5. P. K. Stansby et al. (2012). An integrated model system for coastal flood prediction with a case history for Walcott, UK. *Journal of Flood Risk Managemen*t, *45*, 9 Nov 2007.
6. Ellis, J. (2008). *Report on Norfolk County Council's Response to the East Coast High Tide and Storm Surge in Norfolk*. Norfolk County Council.
7. Kuang, C., & Stansby, P. (2004). Efficient modelling for directional random wave propagation inshore. *Maritime Engineering, MA3*, 123–131.
8. Hasselmann, K., et al. (1973). Measurements of wind-wave growth and swell decay during the joint north sea wave project (JONSWAP). *Ergnzungsheft zur Deutschen Hydrographischen Zeitschrift Reihe, 12*, 1–95.
9. J. A. Battjes & J. P. F. Janssen (1978). Energy loss and set-up due to breaking of random waves. In International Conference on Coastal Engineering (pp. 569–587).
10. Chini, N., & Stansby, P. K. (2012). Extreme values of coastal wave overtopping accounting for climate change and sea level rise. *Coastal Engineering, 65*, 27–37.
11. Thornton, E. B., & Guza, R. T. (1983). Transformation of wave height distribution. *Journal of Geophysical Research, C10*, 5925–5938.
12. Pullen, T. et al. (2007). EurOtop wave overtopping of sea defences and related structures—assessment manual.
13. De Rouck, J., Verhaeghe, H., & Geeraerts, J. (2009). Crest level assessment of coastal structures—General overview. *Coastal Engineering, 2*, 99–107.

Coupling 1-D and 2-D Models for Simulating Floods: Definition of the Exchange Terms

André Paquier and Pierre-Henri Bazin

Abstract During floods, the flows in the main channel and the floodplain have very different features. Thus, one can optimize the calculation time by using 1-D model for the main channel and 2-D model for the floodplain in which the flow is more complex. One solution to couple a 1-D model and a 2-D model is proposed. The two models are based on explicit finite volume schemes solving shallow water equations. Thus, the exchange terms are fluxes calculated on the edges that limit the 2-D model on the side of the 1-D model. For the 1-D model, these fluxes are lateral inputs, upstream, or downstream boundary conditions depending on the side of the coupling. This coupled model is tested on experiments in compound channels for a uniform flow and for a rapidly varied flow produced by an obstacle set on the floodplain. Numerical results are coherent with measurements. On uniform flow, energy losses due to the turbulence are missing, which provides too low water depths. On rapidly varied flow, the transfer velocity between main channel and floodplain is reduced if during the calculation of the exchange terms, the values of the 2-D variables on both sides of the boundary are not defined properly; moreover, the recirculation length is underestimated if the turbulent viscosity coefficient is not high enough.

Keywords Finite volume schemes · Compound channels · Hydraulic structure · Embankment · Numerical methods

A. Paquier (✉) · P.-H. Bazin
UR HHLY, Irstea, 5 rue de la Doua CS70077 69626 Villeurbanne, France
e-mail: andre.paquier@irstea.fr

P.-H. Bazin
e-mail: pierre-henri.bazin@irstea.fr

P. Gourbesville et al. (eds.), *Advances in Hydroinformatics*,
Springer Hydrogeology, DOI: 10.1007/978-981-4451-42-0_11,

1 Introduction

For calculating flood hazard, 2-D models are more and more often used instead of 1-D models because they permit to obtain a more detailed view of the flooding processes. However, a 2-D calculation on large areas can be time-consuming. Thus, one alternative strategy consists in coupling 1-D and 2-D models [1]. Generally, the 1-D model is dedicated to the areas such as river main channels in which the flow velocity direction can be assessed easily and is fixed all over the flood duration while the 2-D model is limited to areas such as floodplains in which the flow pattern evolves with time because:

1. at rising head, the flow goes from main channel to submerge the floodplain while the opposite is true after the peak of the flood
2. the topography of the floodplain is often irregular and several branches can be successively under water.

In such coupling of 1-D and 2-D models, the first question is the definition of the exchange terms at the boundaries between the two models [2]. These terms should be used in both models, which means that one of the difficulties stands in relating these exchange terms to the variables of both models at the locations and times in which they are used. To solve the problem more easily, it was decided that

1. the geographical boundary is selected as the location in which both models calculate the boundary conditions. Thus, the exchange terms are calculated only on this boundary.
2. the coupled models are two explicit finite volume schemes, respectively, solving 1-D de Saint–Venant equations and 2-D shallow water equations, which means that both physically and numerically the models are very similar.

Because of this latter similarity, the exchange terms are the fluxes (of mass and of momentum) through the boundaries between the areas dedicated to each model. The calculation of these fluxes should be performed taking into account the variables of both models. If the time of calculation is the same one in both models, the variables of both models are known at the previous time of calculation and an explicit scheme can be built straight forward. Then, the remaining difficulty stands in defining a calculation method of these fluxes that can represent the physical processes at the boundary and that is easy to implement starting from the variables of both models at the boundary or near the boundary.

Here below, after a short presentation of the numerical schemes for 1-D and 2-D models, the procedure for coupling and the calculation method of these “coupling” fluxes are provided for the various cases (1-D model located upstream or downstream, etc.). In a second part, two examples issued from a series of experiments in a compound channel are used to compare results between full 2-D model and coupled model. The first experiment for a quasi-uniform 1-D flow illustrates the small differences coming from the slight differences between the various sets of equations and from the inclusion of coupling in the numerical process. The second

experiment illustrates increasing differences in one case in which the flow in the main channel is no longer essentially 1-D because of a rapid transfer from floodplain to main channel.

2 Description of the Numerical Methods

2.1 1-D Numerical Scheme

The 1-D model (software Rubar 3 developed by Irstea [3]) is a classical one that relies on de Saint–Venant equations:

$$\frac{\partial A}{\partial t} + \frac{\partial Q}{\partial x} = q \tag{1}$$

$$\frac{\partial Q}{\partial t} + \frac{\partial}{\partial x}\left(\beta \frac{Q^2}{A} + P\right) = -gA\frac{\partial Z}{\partial x} - gA(J + J_s) + B + kq\frac{Q}{A} \tag{2}$$

which can be summarized by

$$\frac{\partial U}{\partial t} + \frac{\partial f(U)}{\partial x} = G(x, U) \tag{3}$$

in which U is the 2-D variable (A ,Q), A the wetted area, Q the discharge, Z the bottom elevation, K the Strickler coefficient, R the hydraulic radius, g the gravity acceleration, $P = \int_0^h g(h-y)L(x, y)\mathrm{d}y$ the pressure, $B = \int_0^h g(h-y)\frac{\partial L}{\partial x}\mathrm{d}y$ the lateral pressure, h the water depth, L the width, J_s local loss of quantity of movement, q the lateral discharge, k a coefficient (generally 0 or 1),

$$J = \frac{Q|Q|}{D^2} \text{ in which } D = K_m A_m C R_m^{2/3} + K_M\sqrt{A_M^2 + A_m A_M(1 - C^2)R_M^{2/3}} \tag{4}$$

and

$$\beta = \frac{A}{(1+H)^2}\left(\frac{1}{A_m} + \frac{H^2}{A_M}\right) \text{ in which } H = \frac{K_M\sqrt{A_M^2 + A_m A_M(1 - C^2)R_M^{2/3}}}{K_m A_m C R_m^{2/3}} \tag{5}$$

the index m corresponds to the main channel and M to the floodplain, C is a function of K_M, K_m, R_M, R_m, the simplest function being $C = 1$. Equations (4) and (5) constitute the Debord model used for compound channels [4].

The second-order explicit scheme built from the ideas of [5] and [6] includes 4 steps:

1. The slopes of the variables are computed from the values at the middle of the cell j by some kind of minmod relation:

$$\delta_j = \sigma \max\left(0,\ \min\left(\alpha\sigma\delta_j^1,\ \sigma\delta_j^2,\ \alpha\sigma\delta_j^3\right)\right) \tag{6}$$

in which δ_j^1, δ_j^2, δ_j^3 are, respectively, the slope between the left cell and the cell itself, between the left and the right cells, and between the right cell and the cell itself, σ is the sign of δ_j^2 and α a coefficient between 1 and 2. On each of the scalar variable Q discharge or h water depth, independently, the slope is computed. For h, a supplementary limitation through water level is imposed.

2. From these slopes and a time discretization of Euler type on one cell, the values on the limits of the cell (noted $j - 1/2$ or $j + 1/2$) are computed at an intermediate time $t_{n+1/2} = t_n + 0.5\Delta t$ by

$$U_{j-1/2}^{n+1/2} = U_{j-1/2}^n - 0.5\frac{\Delta t}{\Delta x}\left[f\left(U_{j+1/2}^n\right) - f\left(U_{j-1/2}^n\right)\right] + 0.5\Delta t\ G\left(x_j,\ U_j^n\right) \tag{7}$$

   Two values are thus obtained: one from the left cell and one for the right cell.

3. As values at the same limit are generally different when computed from the left cell and from the right cell, a Riemann problem is solved in an approximate way by a Roe-type linearization [7] in order to obtain the flux from one cell to the next one. Alternatively, the flux can be obtained using the equation providing the flow discharge of a hydraulic structure.
4. The value at the middle of the cell is computed from the difference of the fluxes for the conservative part of the equations and from an estimate $G_j^{n+1/2}$ of second member at the intermediate time $t_{n+1/2}$:

$$U_j^{n+1} = U_j^n - \frac{\Delta t}{\Delta x}\left[f\left(U_{j+1/2}^{n+1/2}\right) - f\left(U_{j-1/2}^{n+1/2}\right)\right] + \Delta t\, G_j^{n+1/2} \tag{8}$$

   Second member G is constituted of three terms:

1. the topographical term that is computed as a difference of pressures at constant water level;
2. the friction term that is computed in an implicit way;
3. the input from outside treated in an explicit way.

2.2 2-D Numerical Scheme

The finite volume scheme used (Rubar 20 software developed by Irstea [8]) is explicit and second-order accurate. It solves 2-D shallow water equations written as

$$\frac{\partial h}{\partial t} + \frac{\partial(hu)}{\partial x} + \frac{\partial(hv)}{\partial y} = 0 \tag{9}$$

$$\frac{\partial(hu)}{\partial t}+\frac{\partial\left(h_u^2+g\frac{h^2}{2}\right)}{\partial x}+\frac{\partial(huv)}{\partial y}=-gh\frac{\partial Z}{\partial x}-g\frac{u\sqrt{u^2+v^2}}{K_S 2_h 1/3}+v_t\left(\frac{\partial}{\partial x}\left(h\frac{\partial u}{\partial x}\right)+\frac{\partial}{\partial y}\left(h\frac{\partial u}{\partial y}\right)\right) \tag{10}$$

$$\frac{\partial(hv)}{\partial t}+\frac{\partial(huv)}{\partial x}+\frac{\partial\left(hv^2+g\frac{h^2}{2}\right)}{\partial y}=-gh\frac{\partial Z}{\partial y}-g\frac{v\sqrt{u^2+v^2}}{K_S 2_h 1/3}+v_t\left(\frac{\partial}{\partial x}\left(h\frac{\partial v}{\partial x}\right)+\frac{\partial}{\partial y}\left(h\frac{\partial v}{\partial y}\right)\right) \tag{11}$$

in which u and v are the velocities along x- and y-axes, respectively, h the water depth, Z the bottom level, g the acceleration due to gravity, K_s a Strickler coefficient, v_t a diffusion or turbulent viscosity coefficient.

The mesh consists of quadrilaterals or triangles having 0 or 1 (full) common edge. The mixing of these 2 kinds of cells provides various possibilities to adapt to any detail of topography.

The scheme includes 4 steps as follows:

1. computing slope of each one of the 3 variables h (or z water level), hu, and hv in every cell on x- and y-axes by the method of the least squares and applying limitations of slopes.
2. computing values of $W=(h, hu, hv)$ at the intermediate time $t_{n+1/2}=t_n+0.5\Delta t$ in the middle of the edge m_{ij} of cell i

$$W_{m_{ij}^L}^{n+1/2}=W_{m_{ij}^L}^n-0.5\Delta t\left[f_1'\left(W_t^n\right)\cdot W_{xi}^n+f_2'\left(W_i^n\right)\cdot W_{yi}^n\right]+0.5\Delta t\, S_i^n \tag{12}$$

in which f_1 (respectively f_2) are the fluxes on x (respectively y)-axis, S the second member, W_{xi}^n the slope of W along x-axis, index L (respectively R) means left (respectively right) side of the edge

3. at the intermediate time $t_{n+1/2}$, solving a 1-D Riemann problem in the direction normal to the edge [Eq. (13) similar to Eqs. (9) + (10) + (11) on x-axis because these last equations do not vary through a rotation] in order to estimate the fluxes through the edges. To avoid the full solving of this Riemann problem, the scheme either uses an approximate solution or uses a Roe-type linearization [7] which directly provides an estimate of the fluxes.

$$\begin{cases}\frac{\partial W}{\partial t}+\frac{\partial}{\partial x}\left(f_1(W)\right)=0\\ W\left(x,\, t_{n+1/2}\right)=W_{m_{ij}^L}^{n+1/2} & \text{if } x<0\\ W\left(x,\, t_{n+1/2}\right)=W_{m_{ij}^R}^{n+1/2} & \text{if } x>0\end{cases} \tag{13}$$

In specific cases (flow over an embankment, flow through a gate, etc.), this calculation of flux is replaced by the use of an equation typical from an hydraulic

structure, equation that will provide the flow discharge and then both fluxes using an estimate of the water depths upstream and downstream.

4. at the intermediate time $t_{n+1/2}$, integrating second member on the surface of the cell in order to obtain the final value of the 3-D variable W_i^{n+1} by adding the corresponding contribution for the second member $S_i^{n+1/2}$:

$$W_i^{n+1} = W_i^n + \sum_j \frac{\varepsilon_{ij} l_{ij}}{A_i} \Delta t f_1\left(W_{m_{ij}}^{n+1/2}\right) + S_i^{n+1/2} \Delta t \tag{14}$$

in which f_1 represents flux along x-axis, summing on j cells which have a common edge with cell M_i (of area A_i) and ε_{ij} equals 1 or -1 according the orientation of edge m_{ij} (length l_{ij}) common to the cells M_i and M_j.

The contribution of the second member S includes the gravity or slope terms $\left(-gh\frac{\partial Z}{\partial x} \text{ or } -gh\frac{\partial Z}{\partial y}\right)$ that are treated as fluxes in such a way as a horizontal water surface remains strictly horizontal as well as the bed friction terms that are more simply assessed at the center of the cell. The computation of these latter terms uses an implication in time in order to avoid numerical instabilities when a rapid change in water depth or velocity occurs. The diffusion term can be also added to this second member, for instance, in case turbulence influences the results.

2.3 Coupling Method

Coupling principle relies on the use of the Riemann problem of the 2-D model (Eq. 13) to calculate the flux at the 2-D edge that constitutes the boundary between 1-D and 2-D models. To simplify the method, it is assumed that the boundary on the 1-D side ("1-D edge") is constituted by one or several full 2-D edges, which implies an additional constraint on the building of the 1-D and 2-D meshes. Similarly, to what occurs in the 2-D model, this flux can be alternatively calculated starting from the flow discharge obtained using an equation for a hydraulic structure. Then, nine possibilities for coupling can be considered:

- 1. and 2. 1-D model upstream, 2-D model downstream, either solving Riemann problem or using hydraulic structure
- 3. and 4. 2-D model upstream, 1-D model downstream, either solving Riemann problem or using hydraulic structure
- 5. and 6. 1-D model at left side, 2-D model on the right bank of 1-D model, either solving Riemann problem or using hydraulic structure
- 7. and 8. 1-D model at right side, 2-D model on the left bank of 1-D model, either solving Riemann problem or using hydraulic structure
- 9. Hydraulic structure defining an other kind of coupling; for instance, 2-D model above 1-D model if the 1-D model represents an underground drainage network [9], but it can be also used for classical flood problems [2].

In the present chapter, we will only discuss of the cases 1, 3, and 5 in which the Riemann problem defined by Eq. (13) is used to calculate the fluxes at the edge of the 2-D model. Cases 5 and 7 are very similar and are different from cases 1 and 3 because the flow can be in one direction or the other one depending on time and because exchange terms are transferred into lateral inputs (or outputs) to the 1-D model instead of being boundary conditions. Thus, the variables are defined on that edge for both the 1-D and 2-D models. The values of the variables on the 2-D model side are defined as usual in the 2-D model and will only depend on the way the boundary is defined in the 2-D model because the type of boundary determining the calculation method of the slope in the adjacent cell. The values of the variables on the 1-D model side are defined as follows:

1. the water depth is equal to the 1-D free surface in the 1-D cell center (half distance of the cross sections in case of lateral coupling and upstream or downstream cross section in case of coupling through a 1-D model end) diminished by the bottom elevation of the edge middle,
2. one guesses the velocity of the 1-D cell center has the same direction as the 1-D model boundary (lateral coupling) or is normal to this boundary (end coupling). If the two models are based on the same mesh, this hypothesis will provide a direction equal or close to, respectively, the direction of the edge and the normal to the edge. Moreover, the velocity intensity can be set equal at the axis and at the boundary in agreement to the 1-D model assumption of quasi-uniform velocity inside one cross section. In case of lateral coupling with high transfer between the two models, this hypothesis will generally imply a too low (nearly zero) cross-velocity. Thus, an alternative method could consist in using the 2-D model velocity on both sides or to use an intermediate velocity introducing a weighting coefficient to average 1-D and 2-D models values; however, if some interpolations between 1-D and 2-D values are performed, it should be coherent to perform the same interpolation for the other variable that is water depth. Here below, the effect of such alternative methods are only briefly discussed for the second test case.

For building the algorithm, the hypothesis is that one or several 2-D time steps correspond to the 1-D time step although here below (Sect. 3), the basic assumption of equality of the time steps is used. During one 1-D time step, first, the 1-D model is calculated up to the intermediate time $t_{n+1/2}$: (steps 1 and 2 of the numerical scheme); then, the 2-D model is fully calculated using the 1-D predictions at intermediate time; finally, the 1-D time step is finished for the 1-D model (steps 3 and 4 of the numerical scheme). The stability of the coupling scheme is a priori similar to the one of the 1-D and 2-D schemes if the condition (Courant number below 1) on the 2-D cells adjacent to the 1-D model is also applied to the 1-D time step, which often will lead to the same time step for the two models.

3 Comparison of Numerical Results on Two Experiments

In order to test the coupling model, experimental test cases are selected. They permit to compare all the numerical results to measurements. In the selected cases of compound channel, they also offer a sharp variation of topography that can be also met in real flood problems at the boundary between main channel and floodplain.

3.1 Description of the Two Experiments

The experiments were performed in a prismatic flume located in the LMFA (Fluid Mechanics and Acoustics Laboratory) at INSA, Lyon, France [10]. The PVC-made flume is 8 m long and 1.2 m wide (Fig. 1). The cross section is asymmetric with a 0.8 m-wide floodplain. The longitudinal bed slope is 1.8 mm/m. The feeding system is shared in two inlets, which enables to inject an appropriate flow discharge distribution into each channel. Similarly, the downstream end is constituted by two separate tailgates which permits, for instance, to avoid transverse gradient of the water surface between the two channels and thus to satisfy one of the conditions for establishing uniform flow.

The two experiments selected are as follows:

1. a uniform flow for a flow discharge of 0.0247 m^3/s distributed between 0.0184 m^3/s for the main channel and 0.0063 m^3/s in the flood channel.
2. a rapidly varied flow due to a transverse embankment (length: 0.3 m, thickness: 0.02 m) set on the floodplain at a downstream distance of 2.5 m from the inlet tanks. The upstream inflow is the same one as in the experiment 1.

Water depths were measured with an ultrasonic probe. Mean flow and turbulence characteristics were measured using a micro-propeller and a micro-ADV (2-D/3-D side looking probe). The cross-flow distribution of the primary flow was integrated in each sub-section in order to get the discharges for, respectively, the main channel and the floodplain. The upstream inflows were monitored by electromagnetic flow meters. Large-scale particle imaging velocimetry (LSPIV) was used to get a detailed field of surface velocity and the shape of the recirculation zones.

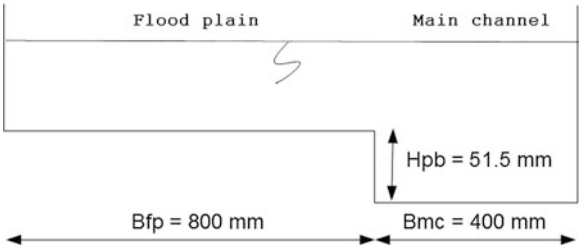

Fig. 1 Cross section of the LMFA flume (from [11])

3.2 Calculation Features

For the 2-D models, the mesh is constituted by rectangles with about 5-cm-long sides except at the interface for which the lateral space step is limited to 5 mm (Fig. 2). There, an inclined plane on one cell replaces the vertical plane of the experimental device. The vertices of the 2-D model are used as points of the 1-D cross sections. Thus, the cross section that is set perpendicular to the flume axis is at a distance of about 5 cm and, when coupling is performed, the 2-D edge at the interface corresponds exactly to the lateral side between two 1-D cross sections.

For the 2-D models, the upstream condition is constituted by the measured inflow in each channel (main channel or floodplain); inside one channel cross section, the flow is distributed by the calculation in order to obtain a distribution similar to the one in the downstream flow. A rating curve is set at every edge of the downstream boundary in order to obtain the average water elevation over the whole flume section: two curves are defined, one for the main channel and one for the floodplain. For the 1-D models, the upstream flow is defined for the whole flume and the downstream boundary condition is set as uniform flow.

A value of Strickler coefficient of 110 $m^{1/3}/s$ (Manning coefficient: 0.009) was obtained from flow measurement in a single channel and is used in the 1-D and 2-D models for both the main channel and the floodplain.

For the 2-D models, the diffusion coefficient is set to a value of 0.0002 m^2/s. This latter value was assessed using the Reynolds stresses measured by ADV in the case of uniform flow at the vertical interface between the main channel and the floodplain to calibrate the turbulence effects.

Both models are unsteady ones; thus, calculation is performed over 100 s with a time step of 0.001 s starting from initial conditions that correspond to a water depth of 7.4 cm in the main channel (2.2 cm in the floodplain) with the flow discharge defined for each channel and uniformly distributed in each channel cross section. This period of 100 s is enough to find a stabilized solution for all the calculation runs.

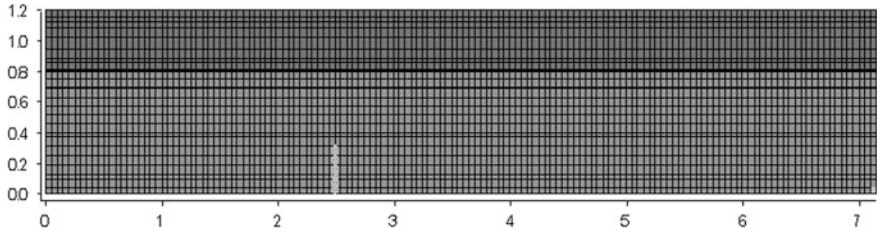

Fig. 2 Mesh for 2-D calculation (main channel is *darker*, location of obstacle is *clearer*). Distances along axis are in metres

3.3 Results on Uniform Flow

Five calculations are carried out: full 1-D calculation, full 2-D calculation, and coupling 1-D to 2-D with 1-D for the upstream half of the flume or 1-D for the downstream half of the flume or 1-D for the main channel.

The 1-D calculation shows a water depth of about 7.3 cm along the flume with some small variations linked to small variations of the bottom slope because the values of the bottom elevation are rounded up to the nearest 0.1 mm. Same feature is obtained for 2-D model but some flow is directed to the main channel at the upstream end and the water depth is slightly lower (down to 7.1 cm) with regular increase in the downstream end; this result shows that the energy losses are too weak (Strickler coefficient to lower and/or diffusion coefficient to increase). The model coupled by the interface shows same features but the water depth in the main channel (1-D model with downstream uniform flow) is also too low by about 0.5 cm at the upstream end. If one does not want to modify the roughness coefficient that corresponds to a physical value, additional energy losses at the interface should be added reminding the additional losses introduced in the 1-D calculation of a compound channel by the Debord equation.

Coupling with 1-D model upstream does not permit to obtain suitable results because the knowledge of the flow discharge and the mean water elevation does not permit to define a suitable upstream boundary condition for the 2-D model; the distribution of the discharge between the floodplain and the main channel is necessary; in that case, the velocity being equal in both channels, the flow discharge entering the floodplain in the 2-D model is too high and then, generates a transfer to the main channel along the whole 2-D model. However, note that this problem is specific to our test aiming at steady state with slightly wrong initial conditions and is not met in case of progressive flooding of floodplain.

Oppositely, there is no problem if the 1-D model is downstream the 2-D model because the coupling algorithm transforms the water depths and velocities of the 2-D model in the exact flow discharge at the upstream end of the 1-D model. In that case, as expected, results at the upstream end are intermediate between full 1-D and full 2-D models results.

3.4 Results on Flow with an Embankment on the Floodplain

The obstacle is set at $x = 2.5$ m from the upstream end letting no flow passes over a width of 0.3 m (to simplify, thickness of the obstacle is set to zero). Only full 2-D model and coupled model with 1-D for main channel were compared.

Both models provide a suitable picture of the experimental measurements. Upstream from the obstacle, some flow passes from the floodplain to the main channel and later goes back; a recirculation area is developing just downstream the obstacle of which the width is slightly higher than the length of the obstacle (Fig. 3).

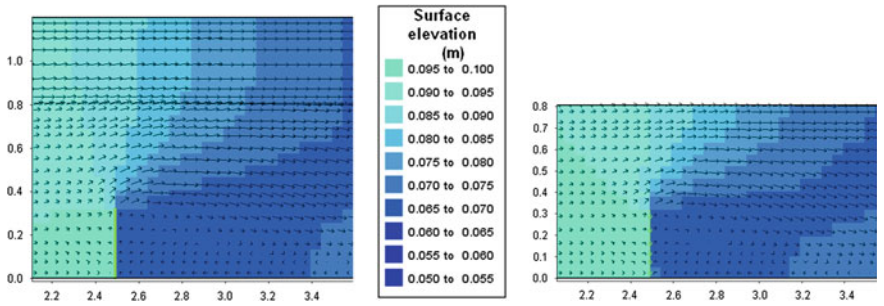

Fig. 3 Water surface elevation and velocity field calculated using full 2-D model (*left*) and coupled model (*right*)

However, both models predict a recirculation length too low (1.02 m for the coupled model and 1.22 m for the 2-D model to be compared with 2.94 m in the experiment). In order to obtain a longer recirculation area, the diffusion coefficient should be decreased in both models (such as in a single channel with such an obstacle). However, one can guess that it will be difficult to propose the same turbulent model for both the recirculation area and the interface between the two channels; thus, the representation of the interface as a boundary between two models can offer the opportunity to use an adapted model to represent the suitable head losses at the interface.

At the distance of the obstacle ($x = 2.5$ m), the discharge passed to the main channel is 1.13 l/s experimentally compared to 1.08 l/s in the coupled model and 1.34 l/s in the 2-D model. This result seems to agree with the hypothesis taken for transfer that minimizes the transfer velocity (Sect. 2.3). However, alternative methods to calculate the velocity at the interface did not change the results except that water depth is changed too. In the case of the values at the 1-D side equaled to half of the sum of the 1-D axis value and the 2-D side value, the transfer discharge increases to 1.19 l/s (but recirculation length decreases to 0.92 m). It seems that the observed differences between the numerical results are due to the differences in the calculation of the fluxes at the interface because all the variables (velocity and water depth) cannot be easily estimated at the boundary for the main channel represented by a 1-D model. Note also that it cannot be considered that coupled model predicts transfers in a better way than 2-D model: at 3 m from upstream, at the location in which transfer is maximum, the 2-D value is 2.1 l/s which is close to experimental value while coupled model (default option) transfers only 1.51 l/s.

4 Conclusions

A model coupling 1-D de Saint–Venant equations and 2-D shallow water equations is detailed. The exchange terms are calculated using the 2-D model method for fluxes between two cells and starting from the values extrapolated from the

nearest values of the same variables in each model at an intermediate time. These 2-D fluxes are then transformed to be applied as boundary conditions or lateral inputs to the 1-D model.

The model is tested on two experiments in a compound channel flume. Results of the coupling model are coherent with experimental measurements and similar to those using full 2-D model. The uniform flow test shows that additional losses are required if the interface between the two models is set at the boundary between floodplain and main channel. The second test of a rapid transfer confirms the capability of the coupled model to get the main hydraulic features in the floodplain as well as the 2-D model. One exception is the case of a boundary with 1-D model upstream and 2-D model downstream; in that case, simple assumptions could not permit to obtain a steady flow with the right flow distribution between floodplain and main channel at the upstream end of the 2-D model.

Extra research to define additional calculation methods for these exchange terms adapted to all the cases of hydraulic features is necessary in order to estimate transfer unit discharge (water depth and velocity) and energy losses at the interface. Other tests should also identify the limits of the coupled model, particularly when the main channel is no longer straight.

References

1. Chen, Y., Wang, Z., Liu, Z., & Zhu, D. (2012). 1D–2D coupled numerical model for shallow-water flows. *Journal of Hydraulic Engineering, 138*(2), 122–132.
2. Fernandez-Nieto, E. D., Marin, J., & Monnier, J. (2010). Coupling superposed 1D and 2D shallow-water model: Source terms in finite volume schemes. *Computers and Fluids, 39*, 1070–1082.
3. Paquier, A. (2012). *Rubar 3—RubarBE: Notice d'emploi*. Lyon: Irstea.
4. Nicollet, G., & Uan, M. (1979). Ecoulements permanents à surface libre en lits composés. *La Houille Blanche, 1*, 21–30.
5. Van Leer, B. (1979). Towards the ultimate conservative difference scheme. V. A second-order sequel to Godunov's method. *Journal of Computational Physics, 32*, 101–136.
6. Vila, J. P. (1984). Modélisation mathématique et simulation numérique d'écoulements à surface libre. *La Houille Blanche, 6*(7), 485–489.
7. Roe, P. L. (1981). Approximate Riemann solvers, parameter vectors and difference schemes. *Journal of Computational Physics, 43*, 357–372.
8. Paquier, A. (2012). *Logiciel Rubar 20: Notice d'emploi*. Lyon: Irstea.
9. Pathirana, A., Tsegaye, S., Gersonius, B., & Vairavamoorthy, K. (2011). A simple 2-D inundation model for incorporating flood damage in urban drainage planning. *Hydrology and Earth System Sciences, 15*, 2747–2761.
10. Peltier, Y. (2011). *Modélisation physique des écoulements débordants en présence d'épi placé dans la plaine d'inondation.* PhD thesis, Université Claude Bernard, Lyon, France.
11. Linde, F. (2011). *Représentativité de la modélisation 2D pour les écoulements en lit composé*. Master thesis. ENTPE, Vaulx en Velin, France.

Detection of Contamination in Water Distribution Network

Zineb Noumir, Kévin Blaise Guépié, Lionel Fillatre, Paul Honeine, Igor Nikiforov, Hichem Snoussi, Cédric Richard, Pierre Antoine Jarrige and Francis Campan

Abstract Monitoring drinking water is an important public health problem because the safe drinking water is essential for human life. Many procedures have been developed for monitoring water quality in water treatment plants for years. Monitoring of water distribution systems has received less attention. The goal of this communication is to study the problem of drinking water safety by ensuring the monitoring of the distribution network from water plant to customers. The system is based on the observation of residual chlorine concentrations which are provided by the sensor network. The complexity of the detection problem is due to the water distribution network complexity and dynamic profiles of water consumptions. The onset time and geographic location of water contamination are unknown. Its duration is also unknown but finite. Moreover, the residual chlorine concentrations, which are modified by the contamination, are also time dependent since they are functions of water consumptions Two approaches for detection are presented. The first one, namely the parametric approach, exploits the hydraulic model to compute the nominal residual chlorine concentrations. The second one, namely the nonparametric approach, is a statistical methodology exploiting

Z. Noumir · K. B. Guépié · L. Fillatre (✉) · P. Honeine · I. Nikiforov · H. Snoussi
Université de Technologie de Troyes, ICD—LM2S—STMR 12 rue Marie Curie BP2060 10010 Troyes, France
e-mail: lionel.fillatre@utt.fr

C. Richard
Université de Nice Sophia-Antipolis Parc Valrose, 06108 Nice Cedex 02, France
e-mail: cedric.richard@unice.fr

P. A. Jarrige
SAFEGE Ingénieurs Conseils, 15/27 rue du Port 92022 Nanterre Cedex, France
e-mail: pierre-antoine.jarrige@safege.fr

F. Campan
OndeoSystems, 38, rue du Président Wilson 78230 Le Pecq, France
e-mail: francis.campan@suez-env.com

P. Gourbesville et al. (eds.), *Advances in Hydroinformatics*,
Springer Hydrogeology, DOI: 10.1007/978-981-4451-42-0_12,

historical data. Finally, the probable area of introduction of the pollutant and the propagation of the pollution are computed and displayed to operational users.

Keywords Drinking water · Water pollution · Parametric detection · One-class classification · Field experiment · Sensor

1 Introduction

The quality and security of water supply systems are essential for public health: It is mandatory for drinking water infrastructure to prevent any intrusion in the supply systems and detect contamination being accidental or deliberate. The visible assets (plant, reservoirs, pumping station,…) are generally well protected using physical systems and perimeter protection systems. The water network is broad and difficult to protect against intrusive contamination and to monitor because of many entry points (hydrant, connection,…).

The protection of the network implies a continuous monitoring of the water quality in order to rapidly detect an abnormal situation. An abnormality can be based on measurement of indicator such as chlorine or turbidity. The proposed system is based on the detection of abnormal chlorine decay.

When an abnormal situation is detected, the reaction time must be minimized in order to operate in "real-time" corrective actions such as additional chlorine injection or isolation of the contaminated section of the network.

The article explains first the system from a technical point of view and then gives details about the methodologies proposed for detection.

2 Network Monitoring

The collection and treatment of data measured into the process are at the basis of the monitoring of an industrial process. From the data source to the decision support tool, there is a technical chain with several subsystems providing an end-to-end system. The target of the system is to give useful information for the operator to be able to take a decision in case of detection of an abnormality.

The monitoring system is based on a technical architecture with two subsystems: The first one includes any equipment installed on the field (sensor network) and the second one (information system) includes all the modules from data acquisition to the data presentation.

2.1 Sensor Network

The sensors have to be autonomous and able to communicate through a telecommunication network. The sensors are deployed along the network and have to provide two types of measurements:

- Quantitative: flow, pressure, level
- Qualitative: chlorine, conductivity, pH,…

The deployment of sensors has to face to different issues:

- There is no local energy source, thus, in order to avoid a main power supply, and the sensor is powered by a battery and needs to have a very low consumption to get a low frequency of battery's replacement.
- The communication device has also to be autonomous. Various wireless technologies are used in this context such as GSM/GPRS/3G or radio links in VHF or UHF bands.
- To dig a hole in a street is costly, so the hardware has to be compact to be easily installed.
- The placement of the sensors is optimized with the help of a hydraulic model. It is also important to take into account the amount of population downstream to the network.
- The placement and the number of chlorine sensors depend on the time in which an abnormality is expected to be detected.

2.2 Information System

The information system hosts the different modules displayed on the Fig. 1. The information system is based on a platform with the following main functionalities:

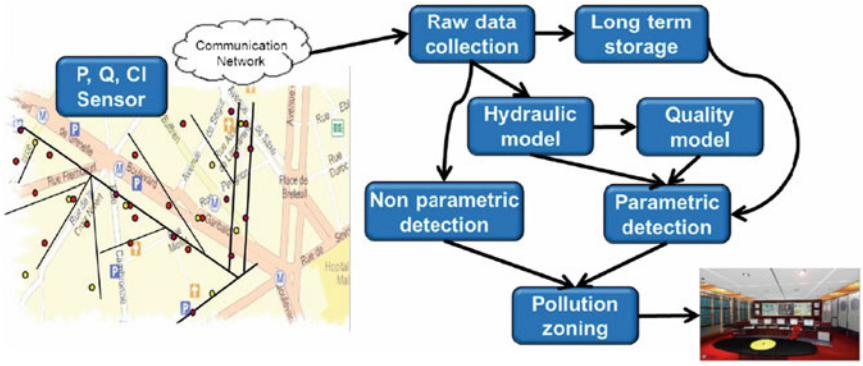

Fig. 1 Functional architecture of the monitoring system from sensor to decision tool

- Acquisition of all data from the field: Sensors and also status of equipment such as valve or pump,
- Data management and data treatment: A repository stores any data collected or produced by the platform and the hosted applications,
- Run time environment: Applications hosted on the platform need input data, may require synchronization with other IT processes, and should deliver a set of output data,
- Data presentation layer: The presentation layer is the unique interface with the data publication tools,
- Visualization tool: It is based on spatial analytical capabilities of GIS technology to display helpful information to users.

The technical architecture of the IS has taken into account several requirements:

- Scalability and flexibility to be able to gather an increasing number of data from different sources and by different means,
- Process management in "real time": The platform has to be able to run any of the modeling tools or detection modules when required by the processing of data in a time compatible with the expected time of detection of an abnormality,
- The global information system can be used locally or executed into a cloud.

3 Operational Modeling for Water Distribution Systems

The hydraulic modeling for the distribution system makes uses of a commercial software engine for solving both stationary hydraulic and chlorine concentration propagation and decay. The engine is encapsulated as a Web service that is launched by the integration platform at scheduled intervals.

The hydraulic engine solves stationary extended period simulation using an adaptive first- to fourth-order Runge–Kutta integration scheme, allowing detecting and simulating configuration changes at any intermediate time. The stationary state is obtained using a hybrid resolution method [1], modified in order to guarantee convergence in all cases, and also to efficiently detect initial fitting state and state transitions [2].

The water quality engine is the one that implemented in 1991 the "event driven method." It uses a Lagrangian method to solve separately the propagation of water and dissolved products and chemical reaction between components [3]. The commercial engine is focused on modeling travel time and chlorine residual and can currently handle single or dual parallel decay fractions, any decay order larger or equal to 1, multiple sources with individual variable decay coefficients, and a choice of parameterization of the pipe decay coefficients.

Lastly, the simulation engine has recently been completed with inverse problem-solving capabilities, allowing to identification of parameters such as the

elevation of pressure measurements, roughness per pipe material, friction coefficients, valve settings, multiple demand profiles, and chlorine decay coefficients per source and per type of material. This module explicitly computes sensitivity matrices, which has proved to be useful for locating hydraulic anomalies such as leakage [4].

In the project described in this article, the modeling has been implemented with direct simulation only; the simulation engine acts as a transfer function converting actual (gathered from the field) pump and valve states, flow and entry chlorine concentrations measurements, into chlorine patterns at chlorine sensor location. Raw data and simulated values are published to be used by the two statistical methods for anomaly detection.

4 Parametric Detection of Water Contamination

The goal of this section is to monitor the water distribution network through its parametric modeling. That is done by using some hydraulic and biochemical equations describing the flow of water in the network.

4.1 The Modeling of Normal Chlorine Decay

The residual chlorine concentration normally decreases in water network. That is due to both bulk flow (microbacteria) and pipe wall reaction (network components). Let $\delta_{ij}(t)$ be the water age (travel time) of one particle traveling from node N_i and arriving to node N_j at t time. The water age is defined as a function of water consumption profiles, and it is assumed to be known. The residual chlorine concentration $C_j(t)$ at node N_j is given by Castro and Neves [5]:

$$C_j(t) = C_0\big(t - \delta_{0j}(t)\big)e^{-\mu\delta_{0j}(t)}, \quad t = 1, 2, \ldots \tag{1}$$

where μ is the global kinetic of chlorine decay, $\delta_{0j}(t)$ the age of water going from the water tower N_0 and arriving to node N_j at time t, and $C_0(t)$ the water tower chlorine concentration. Let x_t^j be the residual chlorine concentration measured by the jth sensor at time t. Let $\tilde{y}_t^j$ be the logarithm of raw measurements x_t^j modeled by

$$\underbrace{\tilde{y}_t^j}_{\text{measured}} = \log\big(C_j(t)\big) + \varepsilon_t^j \tag{2}$$

The analyzed measurements are defined as

$$y_j^t \triangleq \underbrace{\log(C_0\big(t - \delta_{0j}(t)\big) - \mu\delta_{0j}(t)}_{\text{computable and known}} - \tilde{y}_j^t = \big(-\varepsilon_t^j\big), \tag{3}$$

where ε_t^j follows the zero mean Gaussian distribution $\mathcal{N}(0, \sigma^2)$ with the variance σ^2.

4.2 The Modeling of Abnormal Chlorine Decay

Let us assume that a contaminant is injected at node N_x. The contamination starts at time t_0. Its duration and kinetic value are, respectively, D and $\mu_1 > 0$. Hence, the kinetic of chlorine decay locally changes in the network. In fact, for all the nodes situated downstream from the node N_x, the chlorine decay is more rapid than in the nominal case. This rapid decay is explained by the change in local kinetic which takes the new value $\mu + \mu_1$. However, this abnormal chlorine decay only affects the water particles which left the contaminated node N_x between t_0 and $t_0 + D$. Similarly to the previous section, the analyzed measurements are given by

$$y_j^t = \begin{cases} -\varepsilon_t^j & \text{if} \quad t - \delta_{xj}(t) < t_0 \\ \theta_1 - \varepsilon_t^j & \text{if} \quad t_0 \le t - \delta_{xj}(t) < t_0 + D \\ -\varepsilon_t^j & \text{if} \quad t - \delta_{xj}(t) \ge t_0 + D \end{cases} \tag{4}$$

where $\theta_1 = \mu_1 \delta_{xj}$ is a constant value called the contamination intensity (strength). Let us explain the idea that θ_1 is a constant value. The consumption profiles are slowly varying functions of time that involves a quite similar variation in water age function. For detecting any contamination as quickly as possible, it is legitimate to consider the contamination duration as a short period of time even if it is really long. Hence, the water age function $\delta_{xj}(t)$ can be well approximated during this short contamination time by a constant value δ_{xj}.

4.3 Optimality Criterion and Detection Algorithm

From the statistical point of view, it is impossible, in principle, to detect a contamination without false alarms and missed detections. Hence, the best possible solution is to find a trade-off between these two antagonistic properties [6, 14]. Thus, it is necessary to fix one probability and to minimize the other one. An adapted optimality criterion for finite duration contamination detection is proposed. This criterion aims to minimize the probability of non-detection provided an acceptable detection delay and false alarm rate (see Guepie et al. [7])

$$\begin{aligned} &\overline{\mathbb{P}}(T) = \sup_{t_0 \ge L} \mathbb{P}_{t_0}(T - t_0 + 1 > D) \\ &\text{subject to } \mathbb{P}_0(L \le T < L + m_\alpha) \le \alpha \end{aligned} \tag{5}$$

where $\mathbb{P}_{t_0}$ is the probability associated with the distribution of $(y_j^1, y_j^2, \ldots y_j^{t_0}, \ldots y_j^{t_0+D-1}, \ldots)$ when the contamination onset time is t_0 and its duration is D, $\mathbb{P}_0$ is the probability associated with the distribution of $(y_j^1, y_j^2, \ldots)$ without contamination, L is the size of test sliding time window, α is the false alarm probability for a given period m_α and T the alarm time. Let us explain the meaning of criterion (5). The quantity α defines the probability of alarm when, in reality, the quality of drinking water is acceptable, per a unit of time m_α. The parameters α, m_α, and L are chosen by the water network supervisor. The following algorithm is proposed to detect a suddenly arriving contamination of a finite duration $L = D$

$$\begin{aligned} M_j &= \inf\left\{n \geq L, S_{n-L+1}^n \geq h_j\right\}, S_k^n = \sum_{t=k}^{n} \frac{f_{\theta_1}(y_j^t)}{f_0(y_j^t)}, h_j \\ &= \frac{\theta_1 \sqrt{L}}{\sigma} \Phi^{-1}\left((1-\alpha)^{1/m_\alpha}\right) - \frac{L\theta_1^2}{2\sigma^2}, \end{aligned} \tag{6}$$

where $\Phi(x)$ is the Gaussian normal distribution function, f_{θ_1} (respectively f_0) is the probability density function of y_j^1 under contamination hypothesis (respectively under no contamination hypothesis).

After the detection, the contamination intensity is provided. When a network is sufficiently equipped, it is possible to estimate the contamination zone and the kinetic of its chlorine decay. This can allowed us to get some information on the potential contamination. In addition, by using water management software like "Piccolo," the contamination propagation into network can be predicted. Therefore, the appropriate actions can be taken to stop the infection in the rest of the network.

5 One-Class Classification

5.1 Introduction

In this section, we propose to characterize the normal operation of a given chlorine sensor in a water supply network. Recently, machine learning research has been focused on a classification problem based on a single class information, that is, class of normal operation or the non-failure class. In one-class classification, one describes a single class of samples, in order to distinguish them from outlier samples [8, 9]. It has been applied successfully in many novelty detection and classification tasks [10]. In the following, we present a simple one-class classification approach, by combining a least-squares solution with a sparse model controlled by the coherence criterion. This criterion is based on the coherence

parameter, a fundamental quantity that describes the behavior of dictionaries in sparse approximation problems [11–13].

5.2 Proposed One-Class Method

Let $x_1 \ldots x_n$ be the set of training samples, where $x_i$is the ith residual chlorine concentration measured by the monitored sensor. Let $\phi(\cdot)$ be a nonlinear transformation applied on these samples, with inner product given by the kernel function $k(x_i, x_j) = \langle \phi(x_i), \phi(x_j) \rangle$. The principle idea of classical one-class support vector machines (SVM) is to find a sphere of minimum volume, containing most (or all) of the available samples. This sphere, characterized by its center $\mathbf{c}$ and its radius r, is obtained by solving a constrained quadratic optimization problem [8, 9]. We propose a new approach to solve the one-class classification problem, by separating the optimization into two stages. To this end, we write the sparse model of the center as

$$c_I = \sum_{i \in I} \alpha_i \Phi(x_i), \tag{7}$$

where the problem consists of properly identifying the subset $I \subset \{1, 2, \ldots, n\}$ and estimating the optimal coefficients α_i's. To solve this optimization problem, in the first stage, we identify the most relevant samples in the expansion (7), by using a sparsification rule, and in the second stage, we estimate the optimal coefficients α_i's, with optimality in the least-squares sense.

5.2.1 Identification of the Most Relevant Samples with Coherence Criterion

We consider the most relevant subset as the set of elements with the smallest coherence, the coherence being a measure of correlation between elements. The coherence of a set is defined by the largest absolute value of the off-diagonal entries of the Gram (kernel) matrix. We say that a set is μ-coherent if

$$\mu = \max_{\substack{i,j \in I \\ i \neq j}} |k(x_i, x_j)| \tag{8}$$

In our approach, the model order is fixed in advance, that is, the cardinality of the subset. Two of the authors of this paper (P. Honeine and C. Richard) have derived several properties of the resulting model [11–13].

5.2.2 Optimal Coefficients

The coefficients are estimated by minimizing the approximation error, $\|\mathbf{c}_n - \mathbf{c}_I\|^2$, where $\mathbf{c}_n = \frac{1}{n}\sum_{i=1}^{n} \Phi(x_i)$. By taking the derivative of this cost function with respect to these coefficients and setting it to zero, we obtain the final solution in matrix form

$$\boldsymbol{\alpha} = \mathbf{K}^{-1}\mathbf{k}$$

where $\boldsymbol{\alpha}$ is a column vector of the optimal coefficients $\alpha_k \psi$s for $k \in I$, $\mathbf{K}$ is the Gram (kernel) matrix, with entries $k(x_i, x_j)$ for $i, j \in I$, and $\mathbf{k}$ is a column vector with entries $\frac{1}{n}\sum_{i=1}^{n} k(x_k, x_i)$ for $k \in I$.

5.3 Experimentations

We conducted some experiments on a real-time series. It consists of the evolution in chlorine concentration at a given node in a water network. Chlorine is a highly efficient disinfectant, injected into water supplies to eliminate residual bacteria. These time series exhibit large fluctuations due to the variations in water consumption and operational constraints. These data, taken from a city network in France, were sampled at the rate of one sample every 3 min. We considered 4 days of chlorine concentration measures. See Fig. 2.

To capture the structure of the time series, a 10-length sliding window was used, where the Gaussian kernel of standard deviation σ was applied. Only the first day, that is 481 samples, was considered for training and estimating the optimal parameters using a 10-fold cross-validation configuration with $\sigma \in \{2^{-5}; 2^{-4}; \ldots\ldots; 2^{4}; 2^{5}\}$. To be comparable with the one-class SVM, we considered a model order of 55 for both methods, obtained from $\nu = 0.004$ in one-class ν-SVM.

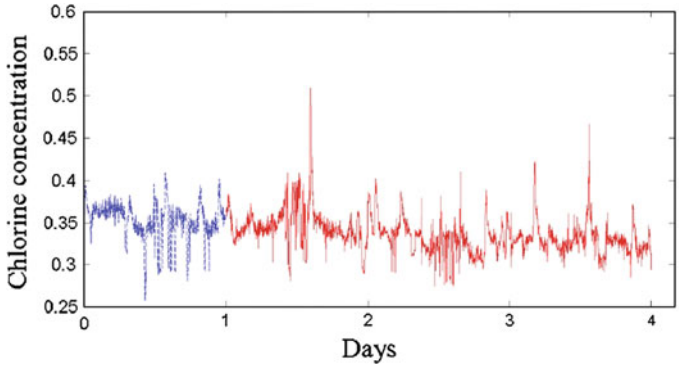

Fig. 2 Time series of the chlorine concentration, showing one day for training (*dashed line* in *blue*) and the next 3 days for error estimation (*full line* in *red*)

Table 1 Results obtained for the chlorine characterization problem

Experiment	Training error (%)	Time (m:ss)	Test error (%)
One-class SVM	8.9	1:16	63.7
Our method	0.20	0:02	1.9

Table 1 provides a comparative study, with training error given by the cross-validation and the test error estimated on the next 3 days.

6 Anomaly Propagation

The purpose of the anomaly propagation module is (i) to evaluate the envelop of potential contamination source (PCS) and (ii) to calculate the propagation of this potential contamination cloud throughout the system.

The module is activated when one or more alarms are raised. The envelope of PCS is spatially and temporally delimited from the sensor that raised the alarm back stream to the other sensors. The envelop is computed as the topological conic area formed by the backward propagation from each alarm sensor on the time interval the alarm is raised. When there are multiple alarm sensors, and the intersection from each individual envelope is not empty, then it is highlighted as the potential common cause.

The threatened area can then be anticipated. It is determined as the dynamic area of influence of the PCS envelop using the usual forward propagation engine. It provides a map of the delay before contamination, allowing the operator to prioritize emergency actions. Note that this module requires a prediction of the demand pattern over the next 12 to 24 h.

7 Conclusions

The monitoring of the drinking water distribution network from water plant to customers is considered in this paper. The first theoretical results show that it is possible to evaluate the minimum detectable level of contamination which can be detected in order to respect a required probability of correct detection. A second significant result concerns the efficiency of machine learning approaches to detect some outliers in residual chlorine concentrations. Perspectives include the use of this nonparametric approach to derive an online one-class algorithm for novelty detection.

The experimentation shows that the chlorine concentration must be known with accuracy, and furthermore, the spatial density of measurement has to be carefully addressed. Two axes could be explored: optimal placement of sensors and solving of inverse problem in the parametric methodology.

References

1. Hamam, Y., & Brameller, A. (1971). Hybrid method for the solution of piping networks. *Proc IEE, 118*(11), 1607–1612.
2. SAFEGE, Piccolo Modelling Guide. www.safege.fr.
3. Boulos, P., Altman, T., Jarrige, P. A., & Collevati, F. (1995). Discrete simulation approach for network water quality models. *Journal of Water Resources Planning and Management, 1996*, 49–60.
4. Jarrige, P. A. & Gancel, G. (2011). Inverse problem solving in water distribution networks. *Proceedings of Computer and Control in the Water Industry* (Vol. 11).
5. Castro, P., & Neves, M. (2003). Chlorine decay in water distribution systems case study-Lousada network. *Electronic Journal of Environmental, Agricultural and Food chemistry, 2*(2), 261–266.
6. Fillatre, L., & Nikiforov, I. (2010). A fixed size sample strategy for the sequential detection and isolation of non-orthogonal alternatives. *Sequential Analysis, 29*(2), 176–192.
7. Guepie, B., Fillatre, L. & Nikiforov, I. (2012). Sequential monitoring of water distribution network. In *The Proceeding of the SYSID 2012, 16th IFAC Symposium on System Identification*, Brussels, Belgium, 2012 July 11–13.
8. Tax, D. (2001). One-class classification. Ph. D Thesis, Delft University of Technology, Delft.
9. Schölkopf, B., Platt, J. C., Shawe-Taylor, J., Smola, A. J., & Williamson, R. C. (2001). Estimating the support of a high-dimensional distribution. *Neural Computation, 13*(7), 1443–1471.
10. Ratle, F., Kanevski, M., Terrettaz-Zufferey, A.-L., Esseiva, P. &Ribaux, O. (2007). A comparison of one-class classifiers for novelty detection in forensic case data. In *Proceedings 8th International Conference on Intelligent Data Engineering and Automated Learning (*pp. 67–76). Berlin, Heidelberg: Springer.
11. Honeine, P., Richard, C. & Bermudez, J. C. M. (2007). On-line nonlinear sparse approximation of functions. In *Proceedings IEEE International Symposium on Information Theory*, Nice, France (pp. 956–960).
12. Honeine, P., Richard, C., Bermudez, J. C. M. & Snoussi, H. (2008). Distributed prediction of time series data with kernels and adaptive filtering techniques in sensor networks. In *Proceedings 42nd Annual ASILOMAR Conference on Signals, Systems and Computers*, Pacific Grove, CA, USA, invited paper.
13. Richard, C., Bermudez, J. C. M., & Honeine, P. (2009). Online prediction of time series data with kernels. *IEEE Transactions on Signal Processing, 57*(3), 1058–1067.
14. Bakhache, B., & Nikiforov, I. (2000). Reliable detection of faults in measurement systems. *International Journal of Adaptive Control and Signal Processing, 14*(7), 683–700.

Water Planning and Management: An Extended Model for the Real-Time Pump Scheduling Problem

Louise Brac de la Perrière, Antoine Jouglet, Alexandre Nace and Dritan Nace

Abstract This work deals with the modeling of a water distribution system with a view to optimizing real-time pump schedules through the use of an integer linear programming (ILP) tool. We describe a number of different constraints that need to be modeled, and we provide mathematical models for each of them. Along with the more familiar capacity and demand satisfaction constraints, we consider specific constraints related to requirements such as water quality and maximum power consumption. Problems include taking the discrete behavior of pumps into account and modeling hydraulic phenomena. Solutions must be applicable to very large networks (about 100 pumps and 50 storage tanks in our example), and available computation time is limited in practice (30 min maximum in the application in hand) because of the real-time scheduling constraint. This problem is not new, but there are very few studies in the literature that address these various aspects of the problem at the same time, which implies a significant number of variables. We present as exhaustive a panorama as possible of the constraints and elements that have to be considered when modeling a water distribution system, and then describe our own model and computational work.

Keywords Real-time · Pump scheduling · Water distribution system · Integer linear programming

L. B. de la Perrière (✉) · A. Nace
Ondeo Systems, 38 rue du président Wilson 78230 Le Pecq, France
e-mail: louise.bracdelaperriere@suez-env.com

A. Nace
e-mail: alexandre.nace@suez-env.com

L. B. de la Perrière · A. Jouglet · D. Nace
Heudiasyc UMR CNRS 7253, BP 20529 60205 Compiegne cedex, France
e-mail: antoine.jouglet@hds.utc.fr

D. Nace
e-mail: dritan.nace@hds.utc.fr

P. Gourbesville et al. (eds.), *Advances in Hydroinformatics*,
Springer Hydrogeology, DOI: 10.1007/978-981-4451-42-0_13,

1 Introduction

Given a water distribution network and some forecasts about consumption at different nodes of the network over a specific time horizon, the problem addressed here is the scheduling of water pump jobs such that water demands are satisfied and conform to quality standards set by French and European legislation while minimizing operating costs (water treatment and electricity).

Among the approaches in the literature for solving this problem, we find linear programming (LP) [1], nonlinear programming [2], ant colony optimization [3], and genetic algorithms [4].

Each method has its own advantages and drawbacks, and a strategy may be more or less efficient, depending on the characteristics of any given network. The characteristics of the networks that concern us in particular are as follows:

- The considered networks are very large (about 100 pumps and 50 storage tanks).
- The computation time available for devising optimized solutions is relatively short (30 min maximum) because of the real-time scheduling constraint.
- The discrete behavior of pumps needs to be expressed through the model. The pumping stations work at some defined level of pumping depending on the type and the power of the station and changes in the pumping regime can take place only periodically.

We chose to use LP for several reasons. First, our intention is to enhance an existing tool that is based on LP. Secondly, LP provides an appropriate modeling tool for most of the constraints encountered in drinking water distribution networks, including some related pressure constraints (known to be difficult to handle within an LP framework but that we have managed to express in a linear form). Finally, efficient solvers are already available.

The starting point is an existing software tool, Saphir [5], which already models the pump-scheduling problem with LP. Our aim is to enhance this tool so as to achieve the following:

- Modeling, through the use of LP, new constraints that have not been expressed before.
- Expressing in a linear form the hydraulic phenomena in the system.
- Placing a limit on computation time while dealing with integer LP models of large dimensions.

The first difficulty is to model new elements of the network (such as pumps with variable flow) and to take into account the discrete behavior of pumps. This discrete behavior makes the optimization problem more difficult to handle: while the continuous problem can be solved with a polynomial algorithm, the mixed integer linear programming (MILP) problem is NP-hard and requires a branch and price procedure [6], but it represents the real-life operation of the pumps much better than a continuous approach. We therefore included in this formalization new constraints that have not been expressed before. The second difficulty is to respect

or even reduce the limits placed on computation time, and to this end, we have looked at a number of different strategies.

In this chapter, we describe the previous existing formalization of a water network with MILP, we describe the new constraints, we provide some results, and we show how these results allow a better choice of parameters in the optimization.

2 Water Distribution System Modeling

In this section, we present the main elements of a water distribution network, and we list the associated structural constraints.

2.1 Elements

A water distribution system can be described by nodes and edges; each element in the network implies the creation of a set of constraints. The time horizon is divided into different time slots. The aim of the optimization is to determine whether each element, and in particular each pump, should operate or not operate within each time slot.

Let us consider the nodes and their associated constraints. We consider four different kinds of node:

- *Production points* must respect the maximum flow production and the discrete behavior of the pumps. Some of these production points have a semi-discrete behavior, as their flow can vary between two fixed values. Each production point has only one outgoing pipe in our model.
- *Storage tanks* must respect the maximum and minimum volumes of water they can contain. The level of each storage at the end of the day also has a required value, and the non-respect of this constraint penalizes the objective function (the penalty is commensurate with the difference observed).
- *Consumption points* have only one input pipe in our model.
- *Connection nodes* represent points where several pipes are connected.

Each node in the model needs to respect an additional constraint, namely continuity of flow. For every connection node and storage tank, the volume of water entering the node during a given time slot is equal to the outgoing volume (with an acceptable gap corresponding to the variation of volume inside the storage tank).

The volume produced during a time slot by a production element is equal to the volume of water carried by the outgoing pipe during this time slot. Finally, the volume required by a consumption point during a given period is equal to the volume carried by its input pipe.

Let us now consider the different pipes to be found in the network model:

- Non-gravitational pipes have exactly the same constraints as for production points, because both are composed of pumps.
- Gravitational pipes have a continuous behavior: They only need to respect the maximum volume they are able to carry during a given time slot.

Each element of the network has to respect this basic set of structural constraints, to ensure continuity of flow and the coherence of the model. A large network therefore implies a large number of variables and constraints to be taken into account, which is one of the difficulties of our problem. Because of the discrete behavior of the pumps, we have to employ integer variables, which means using integer linear programming (ILP) models. The larger the network, the larger the number of these integer variables, which seriously impacts computation time.

2.2 Mathematical Formulation

We now introduce the mathematical formulation for the main elements of the network.

- For a production element p:

$$q_{p,t} = f_{p,t} \times Q_{p,t} \tag{1}$$

$$q_{p,t} = q_{k,t} \tag{2}$$

where parameter t represents the index of the considered time slot; element p is the index of the production node. Parameter $Q_{p,t}$ is the water volume that can be produced if element p operates during time slot t.

Element k is the index of the single output pipe from production node p.

Variable $f_{p,t}$ is a binary variable that represents the operation ($f_{p,t} = 1$) or non-operation state ($f_{p,t} = 0$) of element p. Variable $q_{p,t}$ is the volume of water actually produced by production node p during time slot t.

Variable $q_{k,t}$ is the volume of water carried by pipe k during time slot t.

Constraint 1 represents the flow of element p at each time slot.

Constraint 2 is the flow continuity constraint, which gives a flow value to element k.

Most of the time production elements have a discrete behavior as described above. But some production elements have a partial continuous behavior, which means that operation is discrete between 0 and a first flow value, and continuous between this value and the maximum flow. To take this behavior into account in the model, two variables $f_{p,t}$ are created and the equations rearranged.

$$q_{p,t} = f_{p,t} \times Q_{p,t} + f'_{p,t}\left(Q'_{p,t} - Q_{p,t}\right) \tag{3}$$

$$f'_{p,t} \leq f_{p,t} \tag{4}$$

$$0 \leq f'_p,\ t \leq 1 \tag{5}$$

where $f_{p,t}$ still represents the operation or non-operation of pump, $Q_{p,t}$ is the first acceptable flow value, $Q'_{p,t}$ is the maximum flow, and $f'_{p,t}$ is a continuous variable that allows the flow to fluctuate between the first flow value and the maximum flow.

- For a consumption element c:

$$q_{k,t} = q_{c,t} \tag{6}$$

where k is the index of the single input pipe into consumption point c, variable $q_{k,t}$ represents the volume transported by pipe k during time slot t, and variable $q_{c,t}$ represents the consumption demand of node c during time slot t.

- For each connection node o, the flow continuity constraint can be expressed as follows:

$$\sum_{k \in U_0^+} q_{k,t} = \sum_{k \in U_0^-} q_{k,t} \tag{7}$$

where set U_o^+ is the set of successors of element o, and set U_o^- is the set of predecessors of element o.

- Finally, a very similar expression can be obtained for a storage point l:

$$\sum_{k \in U_l^+} q_{k,t} = \sum_{k \in U_l^-} q_{k,t} + \Delta(n_{l,t}) \tag{8}$$

where variable $\Delta(n_{l,t})$ represents the variation in the volume held in storage tank l during time slot t.

3 Operational Constraints

In addition to these structural constraints that describe the functioning network, a number of operational constraints have to be considered. We first provide an exhaustive list of the operational constraints to be taken into account and then focus on two of them in particular.

3.1 Operational Constraints

Constraints are more or less hard to express. The following are qualified as "simple" because they can be expressed through LP using conventional tools.

The constraints to be found already in the previous LP model are as follows:

- The maximum or minimum volume to be pumped in a day for a given production element.
- The maximum electricity power levels defined by the electricity supplier's contractual obligations.
- The list of elements that must work only in cases of emergency.
- The maximum incremental rate for the flow in some elements of the network.

The constraints added in our new ILP model are as follows:

- Simultaneity and exclusion constraints (pumps that cannot work at the same time or that are required to work at the same time).
- A maximum inactivity period length for some pumps.
- Ensuring a required water quality level through the mixing of water from different sources in some storage tanks (for instance by guaranteeing a percentage from different water sources).
- Avoiding stagnation in storage tanks to ensure water quality.
- Taking account of transfer delays when using very long pipes.

We now focus on the stagnation avoidance constraint and on a specific constraint that does not appear in the list.

To maintain a high quality of distributed water, stagnation has to be avoided. Most of the time water renewal occurs naturally, but in some areas with low consumption, a constraint needs to be added in relation to storage.

We denote as δ the maximum time water may remain in the tank. For each time slot t, we can write:

$$n_{l,t} \leq \sum_{t}^{t+\delta} \sum_{k \in U_l^+} q_{k,t} \tag{9}$$

where $n_{l,t}$ represents the volume held in tank l at time slot t, and set U_l^+ is the set of pipes leading out of tank l. In other words, the volume held in the tank at a given time slot may not exceed the outgoing volume over the following δ hours, in order to force a water turnover.

Because of the diversity of existing networks, highly specific constraints may sometimes be encountered. The constraint described below was encountered in only one network and required particular modeling. Two tanks are connected by both a gravitational and a non-gravitational pipe. The use of a gravitational pipe is possible only when the difference in levels is sufficiently large (Fig. 1).

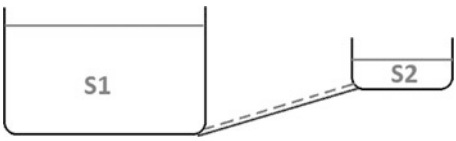

Fig. 1 Two tanks connected by a gravitational and a non-gravitational pipe

We expressed this constraint with ILP as follows:

$$h_{t+1} \geq m\left(1 - f_{g,t}\right) \tag{10}$$

$$h_t \geq m\left(1 - f_{g,t}\right) \tag{11}$$

$$0 \leq q_{g,t} \leq f_{g,t} \times Q^{+}_{g,t} \tag{12}$$

where variable h_t represents the difference in levels between tanks S1 and S2 at the beginning of time slot t (h_{t+1} represents this difference at the beginning of the next time slot following t, that is to say $t+1$).

Parameter m is the minimum value possible for variable h_t.

Parameter $Q^{+}_{g,t}$ is the greatest possible volume that can be transported by gravitational pipe during time slot t.

As before, the binary variable $f_{g,t}$ stands for the operation or non-operation of gravitational pipe g during time slot t.

These equations represent the possibility or the impossibility of using gravitational pipe g; the same equations can be used to represent the availability of pipe g', by changing variable h_t.

If the difference in levels is negative at the beginning of the time step (represented by h_t) or at the end of the time step (represented by h_{t+1}), then the variable $f_{g,t}$ is equal to zero. It is therefore impossible to use the gravitational pipe because the flow $q_{g,t}$ will be null.

3.2 Production-Related Constraints and Simplification

As explained above, expressing the problem through ILP increases computation time, which is a problem when seeking real-time solutions. To improve the solving process, we propose the aggregation of some pumps in a "super-pump" structure, in order to keep track of only the feasible flows. For example, having three identical pumping stations linked to the same connection node means that to obtain the same flow on this node, three pump combinations are possible, and so we have more variables than are needed to represent the same information, that is feasible flow. Therefore, under certain conditions, it will be more efficient to aggregate these three pumping stations into a single one.

The delicate aspects of this are as follows:

- Deciding when pumps cannot be aggregated (for example, if a particular constraint affects only one of the pumping stations).
- Transferring constraints from the previously separate pumps to the new aggregate one.

Conversely, in order to express certain constraints, it may be helpful to separate a pumping station with several allowed flows into different "simple pumps".

For example, consider four pumps in the same pumping station. One of them can send water in two different directions, and only three pumps out of the four can work at the same time because of the maximum power consumption allowed by the electricity supply contract. To simplify, we separate the first pump into two (with an exclusion constraint meaning that they cannot operate during the same time slot), and express the constraints on the five pumps (Figs. 2, 3).

Depending on the constraint difficulty, two strategies may be helpful:

Dividing a complex production element into "pump units" may be helpful if there is no other simple way to express particular constraints, but this means increasing the number of variables.

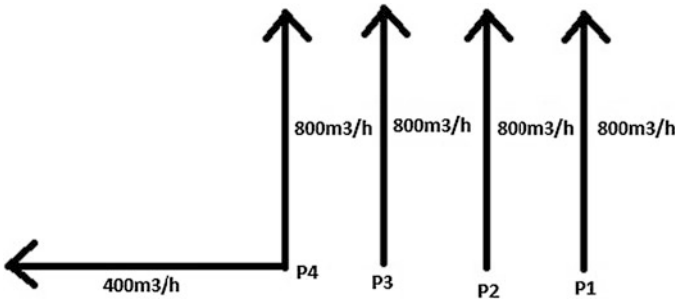

Fig. 2 Initial real configuration of pumps

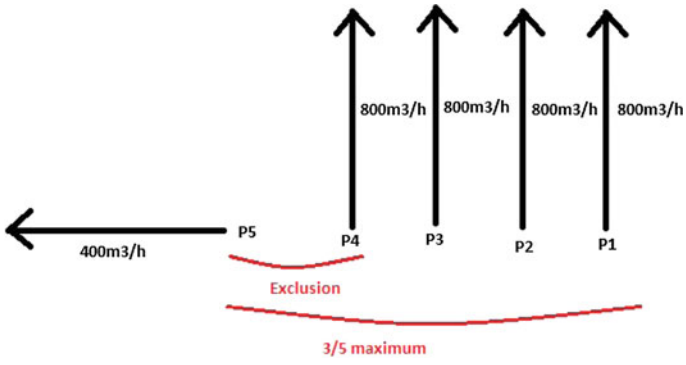

Fig. 3 New configuration and constraints associated

Where possible we aggregate pump units, in order to limit the number of variables and equations. For instance, situation involving only the pumps P1, P2, and P3 can led to a simple case of aggregation of pumps.

3.3 Hydraulic Phenomena

The hardness of modeling hydraulic phenomena is the first reason cited in the literature to disqualify the use of LP for the pump-scheduling problem. It was therefore especially important for us to show that hydraulic phenomena can be taken into account with a simplification precise enough for our needs. If the linearization of the hydraulic behavior of components is not possible, or unsatisfactory—as a result, for example, of an unacceptable increase in the number of constraints and the length of computation time—an alternative strategy may be to work with a hydraulic module during the optimization, in order to obtain the real flow values. This is already done in some applications such as the Derceto software [7].

A situation involving hydraulic phenomena arises when there are different gravitational pipes that bring water to or from a particular location, while the water distribution depends on pressure. The equations representing this situation are clearly nonlinear.

Another problem with pressure is water exchanges between storage tanks that supply the same consumption area. Given the difference in pressure between them their water levels tend to become balanced. To understand this phenomenon, we studied experimentally the behavior of two tanks supplying the same consumption area, with and without consumption.

The two storage tanks provide a certain amount of water to satisfy demand, and when consumption is low or null the water in the two of them will move toward the same level (Fig. 4). The equations above (obtained with Kirchhoff's nodal rule and Kirchhoff's mesh rule) represent the mathematical formalization of the flows

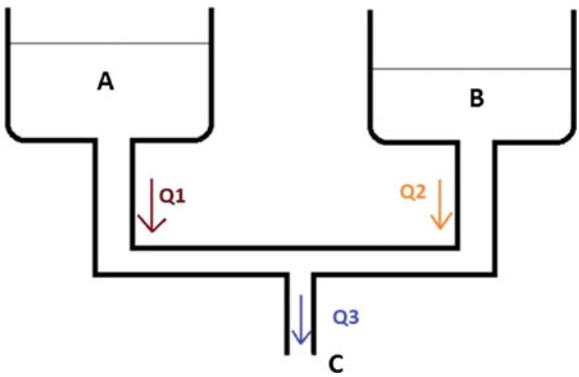

Fig. 4 Parallel tanks supplying the same consumption area *C*

$$\begin{cases} Q_1 + Q_2 - Q_3 = 0 \\ \frac{P_A}{\rho} + z_A + \frac{8Q_A^2}{\pi^2 g D_A^4} - \frac{P_C}{\rho} - z_C - \frac{8Q_C^2}{\pi^2 g D_C^4} - \frac{8f_1 L_1 Q_1^2}{\pi^2 g D_1^5} - \frac{8f_3 L_3 Q_3^2}{\pi^2 g D_3^5} = 0 \\ \frac{P_B}{\rho} + z_B + \frac{8Q_B^2}{\pi^2 g D_B^4} - \frac{P_C}{\rho} - z_C - \frac{8Q_C^2}{\pi^2 g D_C^4} - \frac{8f_2 L_2 Q_2^2}{\pi^2 g D_2^5} - \frac{8f_3 L_3 Q_3^2}{\pi^2 g D_3^5} = 0 \end{cases}$$

Fig. 5 Hydraulic behavior equations

Q_1, Q_2, and Q_3 between points A, B, and C (Fig. 5). We shall not explain the notation here, as our aim is simply to show the nonlinearity of the equations.

We attempted to model experimentally the movements using the hydraulic software tool EPANET. We found that the curve representing the exchanges between A and B when there is no demand can be linearized (Fig. 6).

We performed other experiments with nonzero consumption and for different pipe parameters, and we concluded that in the case of two parallel storage tanks, the different flows can be calculated from the experimental curves, based only on knowledge of consumption and water levels.

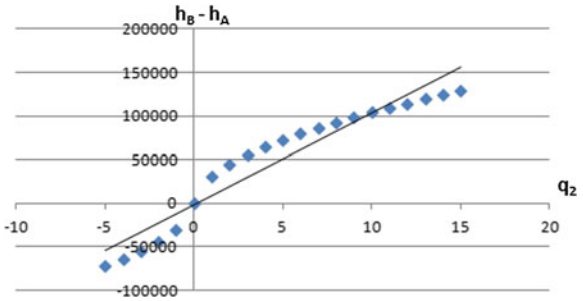

Fig. 6 Flow from storage B to A with respect to the difference in levels between B and A

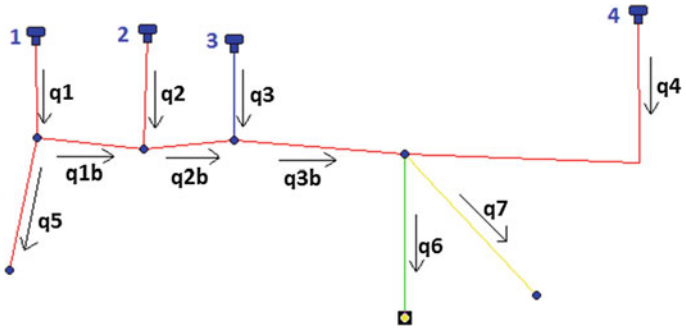

Fig. 7 New test network modeled with EPANET

We generalized this approach to a slightly more complicated case with 4 tanks, 10 pipes, and 3 consumption points (Fig. 7).

In addition to the flow values in the pipes, we add a pressure value on the nodes. On each pipe, we add a linear equation of the following form, where f is a linear function:

$$q_{k,t} = f\left(h_{i,t}, h_{f,t}, H_k\right) \tag{13}$$

The flow through a pipe q_k depends on the pressure $h_{i,t}$ in its initial node, in the pressure $h_{f,t}$ in its final node, and on certain known parameters of the pipes H_k (such as diameter and length).

For 19 different combinations of storage level values, we calculated the flow and pressure values on this small network, both with our linear model and with the hydraulic software tool EPANET (Table 1).

Table 1 Comparison in percentages between the results from EPANET and from our linear model

Levels	Test 1	Test 2	Test 3	Test 4	Test 5	Test 6	Test 7	Test 8	Test 9	Test 10	Test 11	Test 12	Test 13	Test 14	Test 15	Test 16	Test 17	Test 18	Test 19
l1	10	1	1	1	10	1	10	1	1	10	1	10	10	10	5	2	2	7	5
l2	1	13	1	1	13	1	1	13	13	13	13	1	13	13	13	1	2	2	5
l3	1	1	7	1	1	7	7	1	7	7	7	7	1	7	4	5	5	0	5
l4	1	1	1	10	1	10	1	10	1	1	10	10	10	10	2	6	10	8	5
Results																			
Δq1	19.92	119.04	6.92	0.91	3.30	2.19	19.14	109.25	68.79	8.58	48.83	16.87	13.92	17.04	182.44	2.34	0.04	4.47	5.93
Δq2	680.91	10.84	125.54	106.24	3.56	39.11	4.52	6.20	12.42	2.26	8.28	1.32	29.59	18.16	0.18	62.52	27.38	332.53	46.66
Δq3	41.42	35.77	25.76	24.30	43.48	77.00	34.99	57.50	5386.11	0.00	0.00	100.00	60.93	0.00	58.64	79.68	1513.00	32.71	66.35
Δq4	2.36	36.44	59.66	14.08	50.05	12.57	5.85	16.87	11.76	12.22	11.30	8.03	22.59	18.91	40.27	5.30	9.50	7.61	3.77
Δq1b	50.11	23.55	12.84	1.96	6.71	3.52	51.39	27.31	18.09	10.08	16.49	47.93	18.45	9.86	14.44	8.80	0.07	17.61	17.19
Δq2b	28.74	1.87	49.69	486.97	5.66	20.81	91.82	52.42	3.39	1.10	38.78	33.21	47.40	29.76	11.50	43.40	9.29	91.22	61.99
Δq3b	20.59	79.50	37.01	39.11	75.98	49.54	7.63	71.04	3.60	1.10	38.78	33.59	119.01	29.76	51.25	39.62	31.96	25.73	43.32
Δh1	25.87	13.47	7.82	5.68	2.59	6.20	20.84	16.20	12.94	4.29	12.74	18.34	2.12	4.36	1.42	4.22	5.64	14.39	4.40
Δh2	10.08	9.65	1.10	2.39	1.68	2.57	5.64	9.83	4.63	0.79	0.44	4.77	3.53	1.44	5.33	0.86	1.56	6.04	0.74
Δh3	5.14	19.48	0.11	19.69	20.89	2.87	1.37	23.86	2.24	4.27	2.82	5.05	22.13	4.61	13.40	2.10	10.62	14.51	0.13
Δh4	0.31	3.71	7.23	30.22	4.26	12.47	6.65	22.00	4.85	2.14	4.25	12.62	18.71	6.22	0.82	8.07	19.55	24.06	0.90
Δz5	38.85	21.82	8.09	4.99	1.72	5.64	30.96	25.28	20.84	3.70	19.99	27.06	1.11	3.87	3.73	2.74	5.05	22.93	3.59
Δz6	0.26	3.79	7.29	30.25	4.34	12.46	6.61	22.01	4.89	2.18	4.22	12.61	18.71	6.25	0.79	8.15	19.55	24.07	0.94
Δz7	2.16	2.00	9.94	31.07	2.69	11.90	9.22	22.10	6.98	4.01	5.49	12.07	18.58	7.49	0.85	7.00	19.47	24.37	2.58

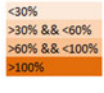

We know that our results cannot be exactly the same as those calculated from a real hydraulic model, owing to the simplifications we introduced. Regarding the margins of error calculated, we conclude that they are acceptable for our needs. Moreover, the largest differences in percentages correspond to only small differences in absolute values.

We now have to test this linear model on a real network. The most significant concern is the likely increase in computation time as a result of the new equations added. It may be possible to address this problem by reducing the number of integer time steps, as shown in Sect. 3.2.

4 Solution Strategies

The model as it is formalized can provide the network manager with a pumping schedule for the day. But the efficiency and the speed of the search for a solution can still be improved, as we see in this section. First, we discuss the formulation of the objective function. Then, we describe the optimization parameters that can help to improve the efficiency of the search for a solution.

4.1 Two-Stage Optimization Strategy

The objective function is formulated as follows:

$$f = \sum_{t=1}^{H} \sum_{x} C_{x,t} f_{x,t} + \sum_{t=1}^{H} \sum_{y} K_y k_{y,t} \tag{14}$$

where parameter H is the time horizon (the number of time slots in the optimization). Parameter $C_{x,t}$ represents economic cost penalties, and variable $f_{x,t}$ represents the operation or non-operation of the corresponding element x during time slot t. Parameter $K_{y,t}$ is the penalty for not respecting constraint y; variable $k_{y,t}$ is different from 0 only if constraint y is not respected at time slot t.

One problem of this objective function is its heterogeneity. Penalties $C_{x,t}$ represent real economic costs, while penalties K_y are set arbitrarily to enforce the respect of some constraints if possible.

Introducing these two goals into the objective function (to ensure that operational constraints are met as far as possible while minimizing the economic cost) is not the most efficient way to proceed. It might even be counterproductive, in that it can lead to aberrations if the arbitrary penalty is not well chosen (for example, failure to respect a particular constraint, because this is a less expensive option, whereas optimization of economic cost should only begin once all operational constraints have been met).

A two-stage optimization might be an answer to this problem. First, we optimize taking into account only the constraint penalties. At the end of this step, we

are able to set the maxim penalties allowed for the non-respect of each constraint. For example, we know the smallest deficit value for the storage tanks that will still allow us to reach a feasible solution.

Once these new constraints have been established, we can start to optimize in the second step, taking into account only the economic penalties.

We tested this approach with a time limit of 1,800 s (30 min). We compared a direct optimization with a two-stage resolution. After a few trials, we decided to devote the largest amount of available computation time to the first stage (1,790 s) and only 10 s to the second stage (Fig. 8).

The cost of the objective function is always less for direct optimization, but most of the time (except for five instances out of twelve) two-stage optimization better respects the constraints of the problem.

Our test showed us that the most difficult part of the optimization problem was emphatically not the economic aspect, but the respect of all constraints (as stated above, we had to set the first step of the optimization to 1,790 s, and the second step to only 10 s). Two-stage optimization is therefore relevant to our problem, but might be refined to obtain better results. The values of the penalties, in particular, have to be chosen very carefully.

4.2 Partially Continuous Relaxation Strategy

Another idea for reducing computation time is to reduce the number of integer time steps. As we are periodically recalculating the pump scheduling because consumption predictions are constantly being updated, it is possible to use integer time steps during an initial phase only, before switching to continuous time steps for the remainder of the solution process.

The correct schedule obtained in this fashion for the first time steps can be implemented directly. For subsequent time steps, we will have continuous values

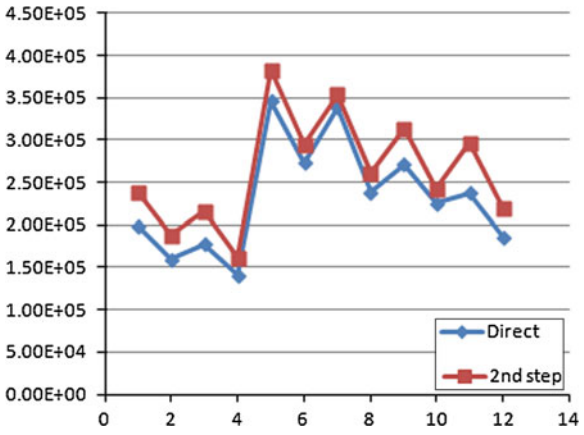

Fig. 8 Comparison between economic costs of a direct or two-stage optimization

(somewhere between 0 and 1) for the pump operation. It will not be possible to use these values directly, but they will give us an idea of the volumes to be exchanged.

We tested the computation time for 20, 12, and 4 initial integer time steps, followed by continuous time steps (Table 2, Fig. 9).

Reducing the number of integer time steps considerably increases the efficiency of the solution process. For the test with only four integer time steps, we obtained an optimal solution in less than 10 s for each instance.

But we have to determine the smallest number of time steps necessary to guarantee the quality of the solution.

Table 2 Gap between best bound and best feasible solutions for different numbers of integer time steps

Instance	All integer time steps (24)				20 integer time steps			
	CPU	Solution	Bound	Gap (%)	CPU	Solution	Bound	Gap (%)
1	60	–	2.27E+06	–	60	2.17E+06	2.17E+06	0.04
2	60	–	2.23E+06	–	60	2.13E+06	2.13E+06	0.06
3	60	1.75E+06	8.15E+05	53.54	60	7.35E+05	7.34E+05	0.11
4	60	1.22E+07	7.75E+05	93.64	60	6.95E+05	6.93E+05	0.19
5	60	2.98E+06	7.76E+06	40.99	60	1.32E+06	1.32E+06	0.10
6	60	2.79E+06	1.93E+06	30.83	60	1.24E+06	1.24E+06	0.04
7	60	–	1.73E+06	–	60	1.29E+06	1.29E+06	0.13
8	60	–	1.89E+06	–	60	1.21E+06	1.21E+06	0.02
9	60	–	1.45E+06	–	60	9.79E+05	9.78E+05	0.03
10	60	–	1.39E+06	–	60	9.20E+05	9.19E+05	0.05
11	60	1.82E+07	1.41E+06	92.24	60	9.49E+05	9.48E+05	0.03
12	60	–	1.34E+06	–	60	8.88E+05	8.88E+05	0.02
12 integer time steps					4 integer time steps			
1	60	2.09E+06	2.09E+06	0.02	1.15	2.05E+06	2.05E+06	0.01
2	60	2.05E+06	2.05E+06	0.02	1.95	2.01E+06	2.01E+06	0.01
3	60	6.64E+05	6.63E+05	0.06	0.7	6.26E+05	6.26E+05	0.01
4	60	6.18E+05	6.18E+05	0.04	0.89	5.80E+05	5.79E+05	0.01
5	60	1.21E+06	1.21E+06	0.05	4.52	1.13E+06	1.13E+06	0.01
6	60	1.13E+06	1.13E+06	0.04	4.56	1.05E+06	1.05E+06	0.00
7	60	1.18E+06	1.18E+06	0.07	6.36	1.11E+06	1.11E+06	0.00
8	60	1.09E+06	1.09E+06	0.06	1.78	1.02E+06	1.02E+06	0.01
9	60	8.82E+05	8.82E+05	0.01	0.81	8.29E+05	8.29E+05	0.01
10	60	8.23E+05	8.23E+05	0.04	1.9	7.67E+05	7.67E+05	0.00
11	60	8.53E+05	8.53E+05	0.02	1.09	8.02E+05	8.02E+05	0.00
12	60	7.92E+05	7.92E+05	0.02	1.01	7.39E+05	7.39E+05	0.00

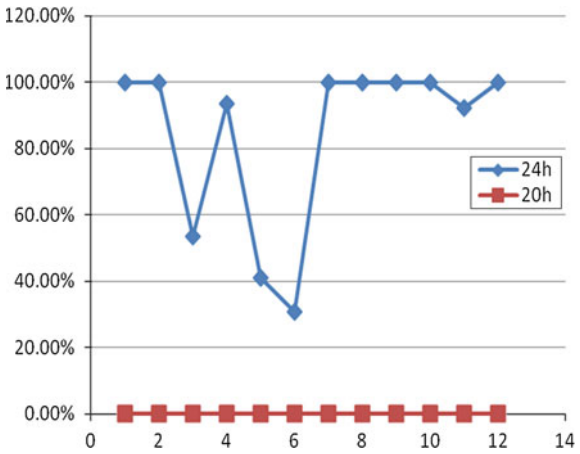

Fig. 9 Comparison of gap for 20 and 24 integer time steps

4.3 Enlarging the Horizon Time

Another problem is planning for the final time slots of the day. Some constraints are hard to take into account unless we have some knowledge concerning the following periods. For example, in the case of the constraint designed to avoid stagnation in the storage tanks, we need to know if consumption will be low or high just after the end of the optimization.

To overcome this difficulty, we planned to extend the optimization horizon: If the requested planning was over 24 h, the optimization would be over a period of 48 h so as to avoid the problem of non-visibility affecting the final periods. But extending the optimization horizon increases the computation time, which is a serious drawback in a real-time context. We therefore retained the principle while slightly modifying the model for the following 24 h in order to have no more than an overall vision of the volume and constraints present the following day, thus avoiding a large increase in computation time.

We tested the differences between a 24-hour and a 48-hour optimization. A computation time limit of 30 min was specified in advance, and we compared the final discrepancy between the feasible solution and the best bound found. The storage tanks were required to be full at the end of the optimization, and the first time slot was fixed at 6 a.m. The different instances tested had different initial water levels in the tanks and the tests concerned different periods of the year or week, which impacts the level of consumption and certain energy-related constraints (price and maximum authorized power) (Tables 3, 4).

The first column indicates the instance tested: the initial level in the tanks, the season, the consumption prediction used for the first 24 h, and the consumption prediction for the latest 24 h (because the consumption is different during the week and during the week end). There are more instances for the 48-hour optimization because there are a larger number of possibilities when we are dealing with two

Table 3 24-hour optimization

Characteristics	Solution	Best bound	Gap (%)
Full storages–summer–week/week	2.81E+06	2.81E+06	0.05
Full storages–summer–week/Sunday	2.62E+06	2.62E+06	0.05
Full storages–summer–Sunday/week	2.77E+06	2.77E+06	0.05
Full storages–winter–week/week	1.36E+06	1.36E+06	0.11
Full storages–winter–week/Sunday	1.30E+06	1.30E+06	0.12
Full storages–winter–Sunday/week	1.32E+06	1.32E+06	0.13
Low storages–summer–week/week	1.86E+06	1.86E+06	0.15
Low storages–summer–week/Sunday	1.63E+06	1.63E+06	0.13
Low storages–summer–Sunday/week	1.79E+06	1.79E+06	0.07
Low storages–winter–week/week	1.82E+06	1.82E+06	0.18
Low storages–winter–week/Sunday	1.76E+06	1.75E+06	0.24
Low storages–winter–Sunday/week	1.75E+06	1.75E+06	0.12
Half-full storages–summer–week/week	1.58E+06	1.58E+06	0.04
Half-full storages–summer–week/Sunday	1.36E+06	1.36E+06	0.07
Half-full storages–summer–Sunday/week	1.52E+06	1.52E+06	0.08
Half-full storages–winter–week/week	1.53E+06	1.53E+06	0.08
Half-full storages–winter–week/Sunday	1.47E+06	1.47E+06	0.09
Half-full storages–winter–Sunday/week	1.48E+06	1.47E+06	0.08

Table 4 48-hour optimization

Characteristics	Solution	Best bound	Gap (%)
Full storages–summer–week/week	2.41E+06	2.27E+06	5.98
Full storages–summer–week/Sunday			
Full storages–summer–Sunday/week	2.32E+06	2.23E+06	4.03
Full storages–winter–week/week	9.45E+06	8.16E+06	13.67
Full storages–winter–week/Sunday			
Full storages–winter–Sunday/week	9.11E+06	7.75E+06	14.98
Low storages–summer–week/week	2.31E+06	1.77E+06	23.22
Low storages–summer–week/Sunday			
Low storages–summer–Sunday/week	2.20E+06	1.93E+06	12.30
Low storages–winter–week/week	2.27E+06	1.73E+06	23.57
Low storages–winter–week/Sunday			
Low storages–winter–Sunday/week	2.16E+06	1.89E+06	12.64
Half-full storages–summer–week/week	1.76E+06	1.45E+06	17.18
Half-full storages–summer–week/Sunday			
Half-full storages–summer–Sunday/week	1.69E+06	1.42E+06	16.03
Half-full storages–winter–week/week	1.75E+06	1.41E+06	19.30
Half-full storages–winter–week/Sunday			
Half-full storages–winter–Sunday/week	1.54E+06	1.35E+06	12.55

separate days. The three other columns respectively show the final feasible solution obtained, the best bound, and the difference between these two values. These results are presented in the following graphic (Fig. 10):

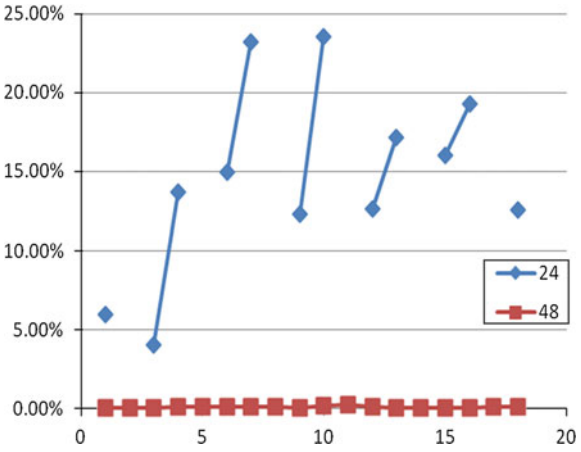

Fig. 10 Comparison of gap for a 24-hour and a 48-hour optimizations concerning 18 different instances

We can see that the 48-hour optimization converges faster on the best bound than the 24-hour solution. This is encouraging and will enable us to reduce the 30-min limit on computation time.

5 Conclusions

The aim of this study is to build a realistic mathematical model giving rise to pertinent, feasible solutions, where computation time has been reduced as much as possible and the solutions are of a high quality.

The use of integer variables in our model takes into account the discrete behavior of pumps, and the solutions obtained are therefore easy to implement. We also take new constraints into account. The next important step for us will be to increase the relevance of our model by taking fully into account a number of hydraulic phenomena that can be observed in the network.

We succeeded in reducing computation time and the discrepancy between the best bound and feasible solutions by changing some parameters in our optimization. Our intention is now to refine our optimization techniques and to introduce new ways of reasoning with the aim of reducing the solution space and the computation time. We also plan to look at other optimization tools (such as constraint programming) that may be able to solve the same model more efficiently.

References

1. Guhl, F. (1999). *Gestion optimale des réseaux d'eau potable*. Ph.D. thesis, Université Louis Pasteur.
2. Ulanicki, B., Kahler, J., & See, H. (2007). Dynamic optimization approach for solving an optimal scheduling problem in water distribution systems. *Journal of Water Resources Planning and Management, 133*, 23–32.

3. Lopez-Ibanez, M., Prasad, T. D., & Paechter, B. (2008). Ant colony optimization for optimal control of pumps in water distribution networks. *Journal of Water Resources Planning and Management, 134*, 337–346.
4. Nicklow, J. (2010). State of the art for genetic algorithms and beyond in water resources planning and management. *Journal of Water Resources Planning and Management, 136*, 412–432.
5. Nace, D., Demotier, S., Carlier, J., Daguinos, T., & Kora, R. (2001). Using linear programming methods for optimizing the real-time pump scheduling. World Water and Environmental Resource Congress.
6. Wosley, L. A. (1998). *Integer linear programming*. New York: Wiley.
7. Pegg, S. (2001). An online optimised pump scheduling system. *Proceedings of the ORSNZ Conference Twenty Naught One*.

Study of Flow in a Staircase at Subway Station

Walid Bouchenafa, Nassima Mouhous-Voyneau, Philippe Sergent and Jacques Brochet

Abstract The flooding service of the Régie Autonome des Transports Parisiens (RATP) initiated hydrodynamic modeling of flows in its metro network in order to improve its Plan of Flood Risk Prevention. The modeling was performed using the software mike urban (MU), software developed by the Danish Hydraulic Institute (DHI) for open channel flows normally dedicated to the modeling of sewage network. The selected event to check this model is the exceptional flood in 1910. Modeling the RATP network in MU requires to introduce boundary conditions as time series of flows for each water inlet (staircase, ventilation grille, trap, etc.). The estimated flow represents a major element of the modeling process, and its quality can significantly influence the calibrated parameters and therefore the model output. This document details and discusses the assumptions that determine the flow rate Q entering in a staircase at subway station as a function of water level taking into account the presence of a facing wall on three of the four sides of the entrance to the metro. Three approaches will be discussed for this problem: theoretical, numerical, and experimental. The objective here is to present the results of the first two approaches and their limitations and to clarify the contributions of the experimental approach. The numerical approach has been able to model

W. Bouchenafa · N. Mouhous-Voyneau (✉)
Equipe AVENUES-GSU, EA7284, Université de Technologie de Compiègne (UTC), Rue Roger Couttolenc, CS 60319, Compiègne CEDEX 60203, France
e-mail: nassima.voyneau@utc.fr

W. Bouchenafa
e-mail: walid.bouchenafa@utc.fr

P. Sergent
Centre d'Etudes Techniques Maritimes et Fluviales (CETMEF), 2 Boulevard Gambetta, BP 60039, Compiègne Cedex 60321, France
e-mail: philippe.sergent@developpement-durable.gouv.fr

J. Brochet
RATP (Régie Autonome des Transports Parisiens), LAC VBE6 50 rue Roger Salengro, Fontenay-Sous-Bois Cedex 94724, France
e-mail: jacques.brochet@ratp.fr

P. Gourbesville et al. (eds.), *Advances in Hydroinformatics*, Springer Hydrogeology, DOI: 10.1007/978-981-4451-42-0_14,

stationary flow through a staircase although some geometric shapes such as stairs are not fully represented. Tests by this software showed that the flow discharge through a staircase corresponds to the theoretical values.

Keywords Flood of 1910 · Modeling · Urban flooding · Weir · Fudaa-Reflux · Physical model

Abbreviation

Fr	Froud number
CETMEF	Centre d'Études Techniques Maritimes et Fluviales
EDF	Électricité de France
RATP	Régie Autonome des Transports Parisiens
UTC	Université de Technologie de Compiègne

1 Introduction

The flood of 1910 that affected Paris region has had a direct impact on the functioning of different networks (electric, wastewater, transport, and drinking water). The RATP subway has been particularly disturbed. In the context of the climate changes, this event has strong chances to recur and the damage that it would generate may be even higher since the network today is 212 km and is much more vulnerable due to electrical and computing equipment that it contains. The majority of the emergences (the entrances of water: trapdoors, subway entrances, aeration grids, etc.) of the subway network are located in flood risk area. During an overflow of the Seine river, the flow spreads directly in the underground and the central part of the network (Metro and RER) through these emergences. The consequences of such a flood for the RATP and the economy of the Ile-de-France would be devastating with consequences at the national level [1].

To improve its Plan for Flood Risk Prevention (PFRP) and to understand how the network is affected the overflowing of the Seine, the RATP initiated a hydrodynamic modeling of flows in the subway system using the software mike urban (MU) developed by the Danish Hydraulic Institute (DHI), normally dedicated to the modeling of sewer systems. The simulation of the flow in the RATP network using this software requires to introduce, for every emergence, a time series of flow variation as a boundary condition. However, only the temporal variation of water levels around these emergences is available. It is thus necessary to establish a flow equation for every entrance of water.

The objective of this work is studying the flow in an outlet of staircase in a subway station in order to approach the real volumes and ultimately establishes a flow rate law for this complex structure. The first and quickest approach is to consider that the outlet of staircase consists of four weirs; three of them will work

only when the water level exceeds the level of the walls. The entering flow is then obtained by summing the four flow discharges. The second approach which will be tested is the numerical modeling of flow around the subway entrance. We will then show the limits of this approach and the interest of using a physical model.

2 Presentation of the Encountered Problem

In the initial model, developed by DHI, all emergences were modeled in the same way. The equation of free-fall spillway in a channel has been applied to transform the height of water in discharge entering in the outlets of staircase subway.

$$Q = L \cdot \sqrt{g}(H)^{3/2} \tag{1}$$

where L is the width of the weir (here, equal to the entrance perimeter) (Fig. 1), g is the acceleration due to gravity. H is the water height. This equation was applied for all types of emergence.

The use of this equation for the case of staircase outlet, illustrated in the following figure, ignores the wall on three edges of the subway entrance even when the water level is lower than this wall.

The method proposed by the DHI office for estimating discharge accelerates the simulation, and this simplification allows to use a single-spillway equation for all types of outlet staircases only by changing the value of the perimeter of each structure. However, it introduces errors on real assessment of discharge and overestimates the entrance volumes because it ignores the presence of the walls.

To obtain accurate estimation of flow, we will study the flow in a subway entrance depending on water depth, taking into account the presence of a wall on three of the four edges of the subway entrance.

Fig. 1 Schematic representation of the configuration of the spillway formula for emergence of type outlet staircase by DHI office

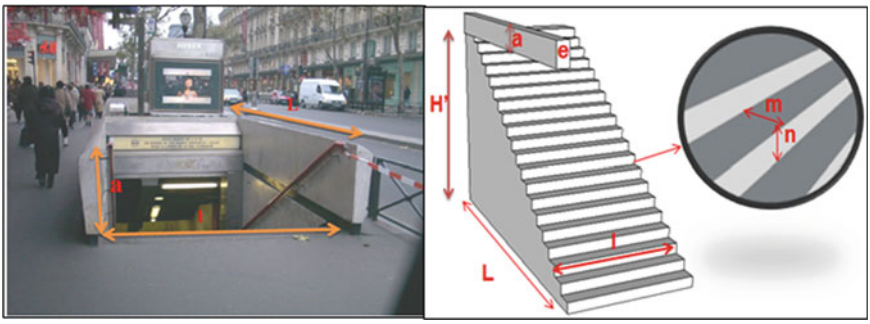

Fig. 2 Outlet staircase studied: Havre Caumartin station

Table 1 Geometrical characteristics of the studied outlet staircase

	Definition	Dimension (cm)
L	Length of wall	550
l	Length of stair	270
a	Height of wall	100
e	Thickness of wall	20
H′	Depth of stairs	400
m	stair horizontal	30
n	stair vertical	20
Number of stair = 20		

3 Characteristics of the Studied Outlet Staircase

The properties of the flow in an outlet staircase depend on the geometric shape of this one. The most widespread shape of staircase is represented in Fig. 1. The fluid is characterized by its density ρ and a kinematic viscosity υ, g is the acceleration due to gravity, and H is the water height around the structure. The other parameters are related to the geometry of the outlet staircase and are presented in Fig. 2 and Table 1.

4 Approaches of Calculation of the Flow in an Outlet of Staircase

Three approaches are discussed for the study of water entry into an outlet of staircase: theoretical, numerical, and experimental. Initially, the interest of this work is focused on theoretical and numerical resolutions of this problem.

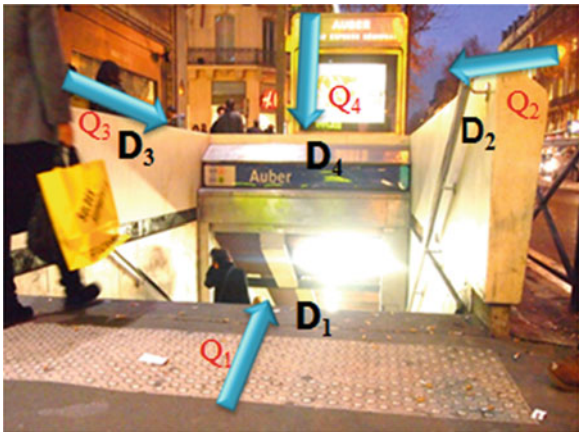

Fig. 3 Schema of the flow rates for the different edges of the outlet of staircase of subway

4.1 Theoretical Approach

One can assimilate the flow on a staircase outlet as an overflow spillway. However, it is easily seen that a single-spillway formula is not representative of the shape of our structure. The assumption used to calculate the flow is to decompose the staircase outlet into four weirs: $D1$, $D2$, $D3$, and $D4$, to calculate the flow produced by each wall by applying adapted spillway equation: Q_1, Q_2, Q_3, and Q_4. The total flow is then obtained by adding the four flow rates (Fig. 3)..

4.1.1 First Case: Water Depth is Less Than the Height of Walls

When the water level is lower than the height of the walls, $H < a$, the water flows exclusively through the staircase, the adapted equation is the spillway $D1$, and the total flow in this case is equal to Q_1. The flow characteristics in a staircase are considered the same as the flow in steep chute spillway [2] (Fig. 4).

Upstream of the fall section, in an area where there is still parallelism of the streamlines, the flow occurs in the critical regime and is described by the following equation (2):

$$Q = Q_1 = C_d \cdot l \cdot \left(2gH^3\right)^{1/2}. \tag{2}$$

The flow coefficient C_d depends essentially on the dimensionless charge $\xi = H/(H + Le)$ where Le is the length of the staircase. An average value of C_d is 0.37 [2]. H is the initial height far from outlet of staircase; Eq. (1) takes into account the water height near the staircase; however, the Eq. (2) considers a water height far from the spillway, and this explains the difference between the two equations.

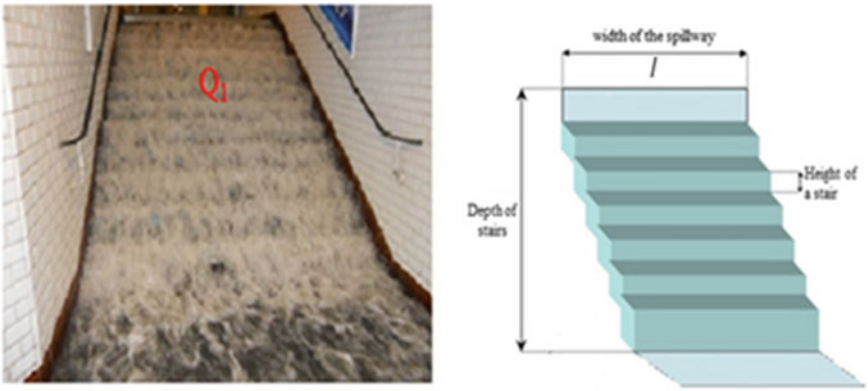

Fig. 4 Flow through the staircases

4.1.2 Second Case: Water Depth is Greater Than the Height of the Wall

When the water level exceeds the height of the wall: $H > a$, the flow rate is the sum of the four flow rates: $Q = Q_1 + Q_2 + Q_3 + Q_4$.

Flow through the spillways $D2$, $D3$, and $D4$ is identical to a flow of a rectangular spillway without lateral contraction. If we take as the Coriolis coefficient $\alpha = 1$, we have [3]:

$$Q_i = \mu \cdot l_i \sqrt{2g} H'^{3/2} \tag{3}$$

where l_i is the width of the i wall, H' is the height of water above the wall. μ is the flow coefficient calculated using the following formula [4]:

$$\mu = 0.401 + 0.05H'/a \tag{4}$$

Since spillways $D2$ and $D3$ have the same geometrical dimensions, the estimated total flow is simplified as follows:

$$QT = Q_1 + 2Q_2 + Q_4 \tag{5}$$

If the hypothesis of summation of the four flows finds some justification for the calculation of the flow rate for a water level greater than wall height, it remains necessary to specify the detailed behavior of the flow around outlet of staircase. This study will be achieved through a numerical modeling of flow around the structure.

4.2 Numerical Approach

Different numerical codes solving the equations of Barre de Saint–Venant 2D are proposed in the literature [5]. Nevertheless, these equations have limitations like the representation of certain physical processes [6], in particular met at intersections of flows entering on four sides of an outlet of staircase.

The computer code Fudaa-Reflux jointly developed by UTC and CETMEF, for the modeling of horizontal bi-dimensional flows proved capable of modeling steady flow around an outlet staircase although some geometric shapes such as stairs are not fully represented.

A staircase has a complex geometry that is difficult to deal with this computer code; flows are constrained by stairs and velocity, and direction of propagation of the flow is strongly influenced by the stairs (their form and their orientation) and the location of the outlet of staircase. The geometry of the stairs is not represented in this study.

The flow is considered stationary, a water depth H is imposed on the outer contour. The resolution method chosen is that of Newton–Raphson with a maximum number of iterations of 10. The calculation provides the flow rate Q entering the subway station.

Two cases of modeling are performed. The first is to simulate the flow when the water level is smaller than the wall height. In this case, the flow passes only through the staircase. The second case of modeling deals with the overflow above the walls.

The OASIS mesh generator is used to mesh the input domain. In our case, the contour located around the outlet of staircase is limited by 8 points forming its profile, and simulations are performed on a uniform mesh of a step of space $\Delta x = \Delta y = 0.1$ m. The schema below represents the geometry of the contour and mesh performed.

For our example, we have no field data and we consider that the bottom contour is flat, and the geometry of the structure is entered by hand directly into the OISIS mesh generator.

The method used to mesh the contour depends largely on the density of urbanization around the structure. In our case, events to represent take place at the surface in areas without urban density. The considered study aims to check if the model is able to adequately represent the flow structures that occur around an outlet of staircase placed in the center of a flow (Fig. 5a).

Subsequently, a second experimental study will be conducted to simulate flows similar to those that may arise during the urban floods whose flows around outlet of staircase are less spaced, and a typology of these flows will be proposed depending on the location of structure.

After making the mesh by OASIS, three steps are necessary in order to start modeling by the Fudaa-Reflux:

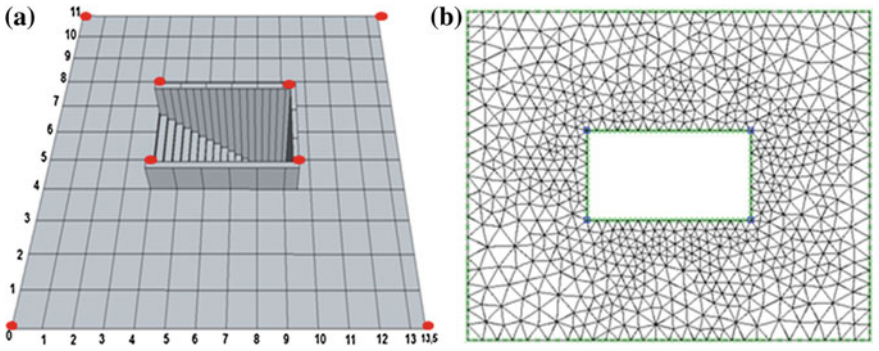

Fig. 5 Geometry and mesh of the structure, **a** schematic geometry of the contour and the outlet of staircase, **b** contour mesh by OASIS

(a) Definition of the characteristics of the flow

For this example, we will choose 2D as nature of background, a roughness of 70 (cement), a viscosity of 0.1 m^2s^{-1}, and a null pressure drop.

(b) Border definition

This step allows to inform Fudaa-Reflux on the properties of borders of the study area. In our example, and for the first case of modeling, we have three closed borders (three walls of the metro entrance) and two open borders; the first is an open border around the contour, and the second is an open border with flow in entrance of the staircase of the subway. There is no closed border for the second case of modeling (Fig. 6).

(c) Boundary conditions

This step is to define the characteristics of open borders. The first open border around the contour is characterized by water depth chosen. For the first case of

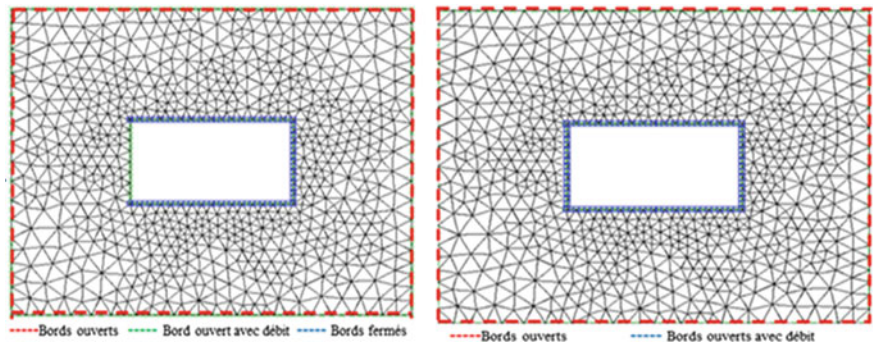

Fig. 6 Definitions of borders for the first and second case of modelings

modeling, when the water level is less than the height of the walls of the outlet of staircase, the flow passes through only the staircase. Upstream of the gravity section, in an area where there is still parallelism of the streamlines, the flow occurs in the critical regime. If we take as a Froude number $Fr = 1$, the flow rate for this regime is estimated by the following formula [7]:

$$Qc = \left(g \cdot l \cdot S^3\right)^{0.5} \tag{6}$$

where S is the wetted surface, $S = l \times hc$, and hc is the critical height and l is the spillway width. For a free-fall spillway, and when flow occurs in the critical regime, we have [3] $hc = 2/3\ H$, knowing that H is the height of water far upstream to the spillway.

1. First case of modeling: Flow without overflow: $H < a$

The objective for the first case of modeling is to calculate the water level and flow velocity field in the subway entrance staircases.

Nine different tests were conducted using nine different water depths with constant flow conditions (steady flow). The results are compared with the theoretical solution and the results calculated by the DHI office.

The following figure compares the flow rate theoretically obtained using Eq. (2) with the flow rate imposed as boundary conditions for the code Fudaa-Reflux and the flow rate estimated by DHI.

The numerical solutions computed with the code Fudaa-Reflux come closer to the theoretical solution (see Fig. 7). Figure 8 presents the modeling results obtained for a water depth of 0.2 m. The flow rate estimated numerically for this height is 0.45 m^3s^{-1} and that calculated by the formula (2) is 0.44 m^3s^{-1}.

The Fig. 8a shows the field of the free surface around the outlet of stairs. The flow is homogeneous and the water level remains constant along the contour, upstream of the access to the staircase, the water level begins to decrease, the flow

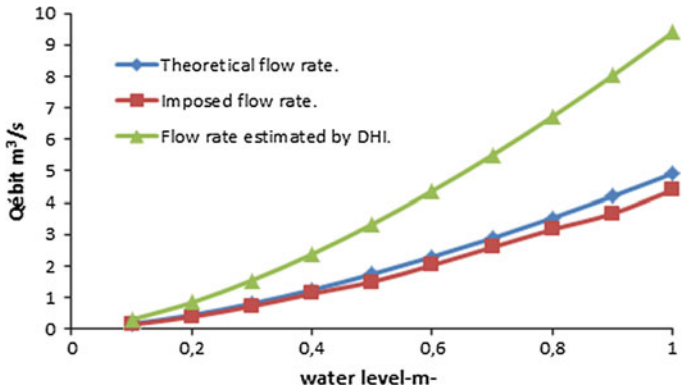

Fig. 7 Graph of different flow rates for $H < a$

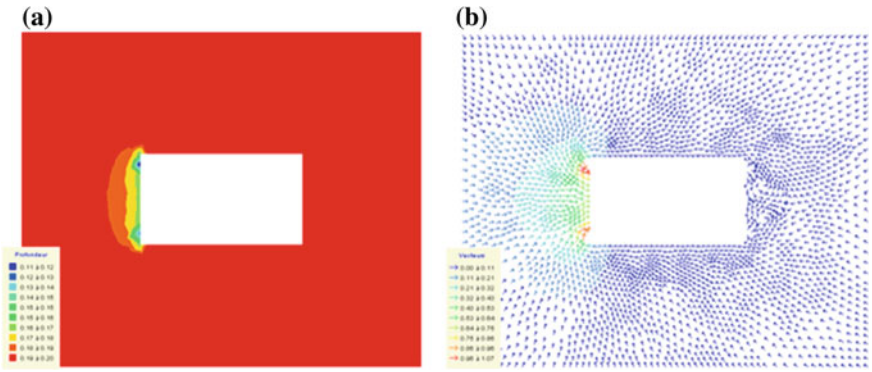

Fig. 8 Free surface (**a**) and numerical velocity field (**b**) around an outlet of staircase when $H < a$

rate Q causes a transition from stream flow in the upstream of the entrance of the outlet of staircase to a supercritical flow downstream, flow between these two regimes is critical; the water height hc is equal to 0.14 m. This height is of the order of 70 % of the initial height.

The numerical tests showed that the flow rate through an outlet of the staircase when $H < a$ corresponds to the theoretical value obtained by applying the equation of spillway with inclined wall.

2. Second case of modeling: Flow with overflow $H > a$

The results of flow modeling with overflow are correctly estimated. The flow get around the outlet of staircase leads interactions with its walls; different zones of complex flow appear.

The code shows areas of acceleration around the walls of outlet of staircase. The flows that take place are shown in Fig. 10. Around the subway station, the water level gradually decreases, the flows are more uniform around the contour. The flow tends to get around the subway station with a different height to the initial height. Longitudinal velocity and water depth tend to re-homogenize around the subway station. Figure 9 compares the flow rate obtained theoretically using Eq. (3) with the flow rate imposed as boundary conditions for the code Fudaa-Reflux and the flow rate estimated by DHI.

For clarity, only two out of ten illustrations are shown in Fig. 10. The calculation results obtained for a water depth of 2.1 and 2.5 m are summarized in the following illustration. The flow rates estimated by the formula (5) for these two heights are, respectively, 47.6 and 73.66 m^3/s.

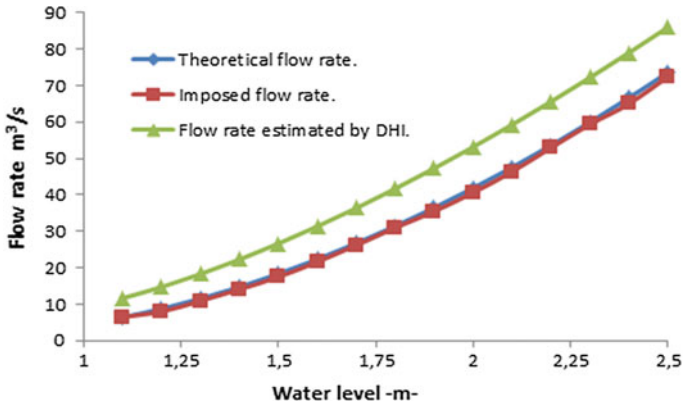

Fig. 9 Graph of different flow rates after overflow

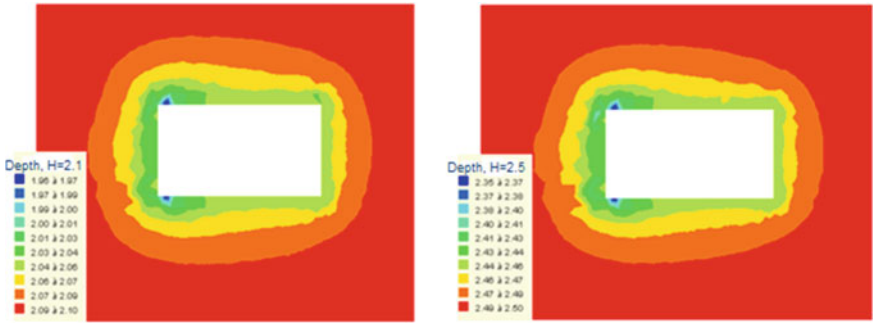

Fig. 10 Forms of the free surface around an outlet of staircase for the second case of modeling

5 Conclusion

This study helps to accumulate a good knowledge of process and the typology of flow through the outlets of staircase in a subway station. We developed an equation for flow rate entering in outlet of staircase of access to a subway station as a function of water depth taking into account the presence of a wall on three of the four edges of the subway entrance.

The theoretical approach based on the summation of flows finds a certain justification. The results of calculation using the code Fudaa-Reflux for the first case of modeling helped to define the characteristics of the flow around an outlet of staircase. Upstream of the gravity section, the flow occurs in the critical regime and the water height is 70 % of the initial height.

Numerical modeling of flow for the second case requires to introduce the value of flow rate entering on four edges of outlet of staircase and to verify the critical regime of each spillway. This is a simplified approach that gives a first estimation

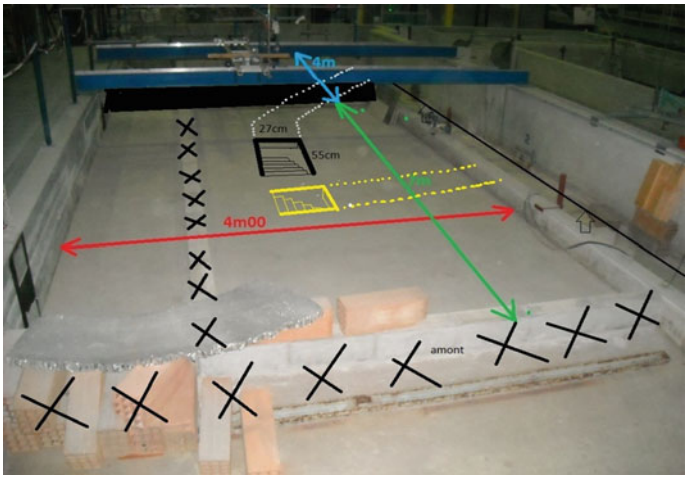

Fig. 11 Mock-up in progress of realization

of flow rates. It is usable when the heights are homogeneous on each edge as is the case here. This approach allows to define the nature of flow and to specify the detailed behavior of the flow around the outlets of staircase.

The use of physical model tests is, however, necessary to check whether this 2D approach is sufficient and to test more complex configurations with lateral confinement. These tests will definitively validate the theoretical approach and determine its limits.

An experimental study is in preparation to better understand the flow processes that develop around of an outlet of staircase. The experimental resolution of this flow problem is based on the reproduction of flow conditions appropriate to the problem studied on a model produced in laboratory with a small scale. This model has to satisfy the principles of geometrical and physical similarity compared to the initial problem. The laboratory model is likely to be built in an experimental channel of EDF (Fig. 11).

References

1. Brochet, J., & Guillois, R. (2010). Crue centennale, la position d'un maître d'ouvrage particulièrement expose : la RATP. Colloque SHF ≪ Risques d'inondation en Ile de France, 100 ans après les crues de 1910, *9*, 177–185.
2. Hager, W.H., & Schleiss, A.J. (2009). Constructions hydrauliques. Ecoulements stationnaires. Traité de Génie Civil de l'Ecole polytechnique fédérale de Lausanne. *15*, 597.
3. Lencastre, A. (1999). Hydraulique générale. Edition EYROLLERS, 633.
4. Benis, S. (2009). Hydraulique et hydrologie. 2e édition revue et augmentée. Presses de l'Université du Québec, 451.

5. Mignot, E. (2005). Etude expérimentale et numérique de l'inondation d'une zone urbanisée : cas des écoulements dans les carrefours en croix. Thèse de doctorat, Ecole Centrale de Lyon, 333.
6. Ghostine, R. (2009). Contribution à la résolution numériques des équations de Barrée de Saint Venant bidimensionnelles par une méthode de type éléments finis discontinus : application à la simulation des écoulements au sein des carrefours dans la ville. Thèse de doctorat, Université de Strasbourg, 258.
7. Degoute, G. Aide-mémoire d'hydraulique à surface libre. Université de Paris VI, ENGREF, [En ligne], http://www.agroparistech.fr/coursenligne/hydraulique/hydraulique.html.

Part II
New Numerical Methods and Approaches for Modeling Systems

Introduction to Part II

Philippe Gourbesville, Jean Cunge and Guy Caignaert

1 New Numerical Methods and Approaches for Modelling Systems

At first glance, the reader interested in computational hydraulics might be disappointed from the number of chapters of this part of the book. Indeed, the title seems to promise a lot, and then the number of chapters and the content of some of them seem to be limited. One should keep in mind, however, that the subject of this part was not the main corpus of the conference. This explains the limited number of papers. On the other hand, more general and more important comments are to be taken into account.

The flow modelling, especially free surface flow modelling, is the area that became so much everyday industrial practice that research efforts and the development of new methods, not being driven any more by needs of applications, decreased considerably. Indeed, algorithmic methods in solving hydrodynamics and hydraulics equations that have been integrated in the industrial codes are sufficient for most of the current engineering applications. This situation does not mean that everything is perfect and understood. There are still very wide areas in numerical domain of computational hydraulics to be developed and researched along several main tracks.

One is the development of equations taking into account the physical phenomena that have been neglected originally by researchers because of complexity

P. Gourbesville (✉)
University of Nice-Sophia Antipolis, 930 Route Des Colles, Sophia Antipolis 06903, France
e-mail: Philippe.Gourbesville@unice.fr

J. Cunge
31 Rue Doyen Gosse, La Tronche 38700, France
e-mail: jacunge@orange.fr

G. Caignaert
Society Hydrotechnique of France, 25 Rue des Favorites, Paris F 75015, France
e-mail: guy.caignaert@ensam.eu

P. Gourbesville et al. (eds.), *Advances in Hydroinformatics*,
Springer Hydrogeology, DOI: 10.1007/978-981-4451-42-0_15,

of physical situations, complexity of possible mathematical formulation and clear impossibility to find their solutions at that time; for example, unsteady rapidly varying flows beyond De Saint–Venant hypotheses such as discontinuity of dependent variables (bores) or hydrostatic repartition of pressures.

Another is to ensure coherence of mathematical approach and widely spread quasi-experimental use of computer power without always knowing anything more about obtained results than "it seems that they are physically correct"; for example, most of 3D modelling of free surface flows that includes turbulence modelling, all based on approximate solutions of equations for which the theorems of existence of solutions in function of boundary and initial conditions do not exist. Thus, one does not know if the problems are well posed or ill posed at the step of setting up equations and even less at the step of numerical solutions. We have the theory that was developed for 1D linear systems of equations and we "feel" that this is enough for 2D and 3D nonlinear systems! In a way, one may think that we are subservient to the developments of technology (computers) at expense of physics.

Still another area concerns the very concept of formulation of physical phenomena when compared with engineering needs; for example, it is obvious from engineering point of view that detailed 2D modelling of flooding of urban areas, implying thousands of computational grid points is not very useful approach except if one is interested in local situations. Approach such as heat diffusion analogy with propagation of the flood across urban agglomeration (already elaborated at its bases but so far not really applied in engineering practice) is certainly something to be developed further and to find its place in panoply of the modelling tools.

Then, talking about "approaches" we must think of new trends in developing tools available to engineering community; for example open software, Software as a Service (SaaS), namely how these new trends can be used on our field in *integrated* way and not just following the philosophy of using the ICT as they are because obviously the latter is neither optimal nor creative approach but rather and certainly the very negation of what is called hydroinformatics.

Chapters of the following part are belonging to the above-mentioned areas and trends without any ambition to cover all or even fully one of them. Their very presence in a conference content devoted rather to engineering applications than developments is significant and important by underlining the fact that behind the applications there are unexplored territories.

A Non-Hydrostatic Non-Dispersive Shallow Water Model

Didier Clamond and Denys Dutykh

Abstract An improvement of the nonlinear shallow water (or Saint-Venant) equations is proposed. The new model is designed to take into account the effects resulting from the large spatial and/or temporal variations of the seabed. The model is derived from a variational principle by choosing the appropriate shallow water ansatz and imposing suitable constraints. Thus, the derivation procedure does not explicitly involve any small parameter.

Keywords Varying bathymetry · Steep bottom · Modified Saint-Venant equations.

1 Introduction

The celebrated classical nonlinear shallow water (Saint-Venant) equations were derived for the first time in 1871 by Saint-Venant [1]. Currently, these equations are widely used in practice and the literature counts many thousands of publications devoted to the applications, validations, or numerical solutions of these equations.

Some important attempts have been also made to improve this model from physical point of view. The main attention was paid to various dispersive

D. Clamond (✉)
Laboratoire J.-A. Dieudonné Parc Valrose, Université de Nice – Sophia Antipolis, Nice 06108 Nice Cedex 2, France
e-mail: didier.clamond@gmail.com

D. Dutykh
Université de Savoie, Laboratoire de Mathématiques Appliquées Campus Scientifique, LeBourget-du-Lac Cedex 73376, France
e-mail: denys.dutykh@univ-savoie.fr

P. Gourbesville et al. (eds.), *Advances in Hydroinformatics*, Springer Hydrogeology, DOI: 10.1007/978-981-4451-42-0_16,

extensions of shallow water equations. The inclusion of dispersive effects resulted in a big family of the so-called Boussinesq-type equations (c.f., e.g., [2, 3]).

However, there are a few studies which attempt to include the bottom curvature effect into the classical Saint-Venant. One of the first studies in this direction is perhaps due to Dressler [4]. Much later, this research was pursued almost in the same time by Keller [5] and by Bouchut et al. [6]. We note that all these authors used some variant of the asymptotic expansion method. The present study is a further attempt to improve the classical Saint-Venant equations by including a better representation of the bottom shape. As a general derivation procedure, we choose a variational approach based on a relaxed Lagrangian principle [7].

In the next section, we present the derivation and discussion of some properties of the improved Saint-Venant equations. Then, we detail the hyperbolic structure in Sect. 3 and give a numerical example in Sect. 4. Finally, we underline some main conclusions of this study in Sect. 5.

2 Modified Saint-Venant Equations

Consider an ideal incompressible fluid of constant density ρ. The horizontal independent variables are denoted by $\boldsymbol{x} = (x_1, x_2)$ and the upward vertical one by y. The origin of the Cartesian coordinate system is chosen such that the surface $y = 0$ corresponds to the still water level. The fluid is bounded below by an impermeable bottom at $y = -d(\boldsymbol{x}, t)$ and above by an impermeable free surface at $y = \eta(\boldsymbol{x}, t)$. Usually, we assume that the total depth $h(\boldsymbol{x}, t) = d(\boldsymbol{x}, t) + \eta(\boldsymbol{x}, t)$ remains positive $h(\boldsymbol{x}, t) \geq h_0 > 0$ for all times t. Traditionally, in water wave modeling, the assumption of flow irrotationality is also adopted. The assumptions of fluid incompressibility and flow irrotationality lead to the Laplace equation for a velocity potential $\phi(\boldsymbol{x}, y, t)$.

It is well known that the water wave problem possesses several variational structures [8–10]. Recently, we proposed a relaxed Lagrangian variational principle which allows much more freedom for constructing approximations in comparison with classical formulations, namely the water wave equations can be derived as the critical point of the functional $\iiint \mathscr{L}\, d^2\boldsymbol{x}\, dt$ involving the Lagrangian density [7]:

$$\begin{aligned} \mathscr{L} \;&= (\eta_t + \tilde{\boldsymbol{\mu}}\cdot\nabla\eta - \tilde{v})\,\tilde{\phi} \;+\; (d_t + \check{\boldsymbol{\mu}}\cdot\nabla d + \check{v})\,\check{\phi} \;-\; \tfrac{1}{2} g\,\eta^2 \\ &+ \int_{-d}^{\eta} \big[\, \boldsymbol{\mu}\cdot\boldsymbol{u} - \tfrac{1}{2}\boldsymbol{u}^2 \;+\; v v - \tfrac{1}{2} v^2 \;+\; (\nabla\cdot\boldsymbol{\mu} + v_y)\,\phi \,\big]\, dy, \end{aligned} \tag{1}$$

where g is the acceleration due to gravity force, and $\nabla = (\partial_{x_1}, \partial_{x_2})$ denotes the gradient operator in horizontal Cartesian coordinates. Other variables $\{\boldsymbol{u}, v, \boldsymbol{\mu}, v\}$ are the horizontal velocity, the vertical velocity, and the associated Lagrange multipliers, respectively. The last two additional variables $\{\boldsymbol{\mu}, v\}$ are called *pseudo-velocities*. They formally arise as Lagrange multipliers associated with the

constraints $\boldsymbol{u} = \nabla\phi$, $v = \phi_y$. However, once these variables are introduced, the ansatz can be chosen regardless to their initial definition. The over 'tildes' and 'wedges' denote, respectively, a quantity traces computed at the free surface $y = \eta(\boldsymbol{x}, t)$ and at the bottom $y = -d(\boldsymbol{x}, t)$. We shall also denote below with 'bars' the quantities averaged over the water depth. Note that the efficiency of the relaxed variational principle (1) relies on the extra freedom for constructing approximations.

In order to simplify the full water wave problem, we choose some approximate, but physically relevant, representations of all variables. In this study, we consider very long waves in shallow water. This means that the flow is mainly columnar [11] and that the dispersive effects are negligible. In other words, a vertical slice of the fluid moves like a rigid body. Thus, we choose a simple shallow water ansatz, which is independent of the vertical coordinate y, and such that the vertical velocity v equals the one of the bottom, i.e.,

$$\phi \;\approx\; \bar{\phi}(\boldsymbol{x}, t), \qquad \boldsymbol{u} \;=\; \boldsymbol{\mu} \;\approx\; \bar{\boldsymbol{u}}(\boldsymbol{x}, t), \qquad v \;=\; v \;\approx\; \check{v}(\boldsymbol{x}, t), \tag{2}$$

where $\check{v}(\boldsymbol{x}, t)$ is the vertical velocity at the bottom. In the above ansatz, we take for simplicity the pseudo-velocity to be equal to the velocity field $\boldsymbol{\mu} = \boldsymbol{u}$, $v = v$. Note that in other situations, they can differ (see [7] for more examples). With this ansatz, the Lagrangian density (1) becomes

$$\mathscr{L} \;=\; (h_t + \bar{\boldsymbol{u}}\cdot\nabla h + h\nabla\cdot\bar{\boldsymbol{u}})\,\bar{\phi} \;-\; \tfrac{1}{2} g\,\eta^2 \;+\; \tfrac{1}{2} h\,(\bar{\boldsymbol{u}}^2 + \check{v}^2), \tag{3}$$

where we introduced the total water depth $h = \eta + d$.

Now, we are going to impose one constraint by choosing a particular representation of the fluid vertical velocity $\check{v}(\boldsymbol{x}, t)$ at the bottom, namely we require fluid particles to follow the bottom profile:

$$\check{v} \;=\; -d_t \;-\; \bar{\boldsymbol{u}}\cdot\nabla d. \tag{4}$$

This last identity is nothing else but the bottom impermeability condition within ansatz (2). Substituting the relation (4) into Lagrangian density (3), the Euler–Lagrange equations yield

$$\delta\bar{\phi} \;:\quad 0 \;=\; h_t \;+\; \nabla\cdot[\,h\,\bar{\boldsymbol{u}}\,], \tag{5}$$

$$\delta\bar{\boldsymbol{u}} \;:\quad \boldsymbol{0} \;=\; \bar{\boldsymbol{u}} \;-\; \nabla\bar{\phi} \;-\; \check{v}\,\nabla d, \tag{6}$$

$$\delta\eta \;:\quad 0 \;=\; \bar{\phi}_t \;+\; g\,\eta \;+\; \bar{\boldsymbol{u}}\cdot\nabla\bar{\phi} \;-\; \tfrac{1}{2}(\bar{\boldsymbol{u}}^2 + \check{v}^2). \tag{7}$$

Taking the gradient of (7) and eliminating $\bar{\phi}$ from (6) gives us this system of governing equations

$$h_t \;+\; \nabla\cdot[\,h\,\bar{\boldsymbol{u}}\,] \;=\; 0, \tag{8}$$

$$\partial_t \left[\bar{\boldsymbol{u}} - \check{v} \nabla d \right] + \nabla \left[g\eta + \tfrac{1}{2}\bar{\boldsymbol{u}}^2 + \tfrac{1}{2}\check{v}^2 + \check{v}\, d_t \right] = 0, \tag{9}$$

together with the relations

$$\bar{\boldsymbol{u}} = \nabla\bar{\phi} + \check{v}\nabla d, \qquad \check{v} = -d_t - \bar{\boldsymbol{u}}\cdot\nabla d = -\frac{d_t + \nabla\bar{\phi}\cdot\nabla d}{1 + |\nabla d|^2}.$$

Further details on these equations and their variants can be found in [12].

3 Hyperbolic Structure

From now on, we consider Eqs. (8, 9) posed in 1D space for simplicity:

$$\partial_t h + \partial_x \left[h\bar{u} \right] = 0, \tag{10}$$

$$\partial_t \left[\bar{u} - \check{v}\,\partial_x d \right] + \partial_x \left[g\eta + \tfrac{1}{2}\bar{u}^2 + \tfrac{1}{2}\check{v}^2 + \check{v}\,\partial_t d \right] = 0. \tag{11}$$

In order to make appear conservative variables, we will introduce the potential velocity variable $U = \partial_x\bar{\phi}$. From Eq. (6) it is straightforward to see that U satisfies the relation $U = \bar{u} - \check{v}\partial_x d$. Depth averaged and vertical bottom velocities can be also easily expressed in terms of the potential U. Consequently, using this new variable Eqs. (10, 11) can be rewritten as a system of conservation laws

$$\partial_t w + \partial_x f(w) = 0, \tag{12}$$

where the vector of conservative variables w and the advective flux $f(w)$ are

$$w = \begin{pmatrix} h \\ U \end{pmatrix}, \qquad f(w) = \begin{pmatrix} h\dfrac{U - (\partial_t d)(\partial_x d)}{1 + (\partial_x d)^2} \\[2ex] g(h-d) + \dfrac{U^2 - 2U(\partial_x d)(\partial_t d) - (\partial_t d)^2}{2\left[1 + (\partial_x d)^2\right]} \end{pmatrix}.$$

The Jacobian matrix of the advective flux $f(w)$ can be easily computed:

$$\mathbb{A}(w) = \frac{\partial f(w)}{\partial w} = \frac{1}{1 + (\partial_x d)^2} \begin{bmatrix} U - (\partial_t d)(\partial_x d) & h \\ g\left(1 + (\partial_x d)^2\right) & U - (\partial_t d)(\partial_x d) \end{bmatrix}.$$

The matrix $\mathbb{A}(w)$ has two distinct eigenvalues:

$$\lambda^{\pm} = \frac{U - (\partial_t d)(\partial_x d)}{1 + (\partial_x d)^2} \pm c = \bar{u} \pm c, \qquad c^2 \equiv \frac{g\,h}{1 + (\partial_x d)^2}.$$

Physically, the quantity c represents the phase celerity of long gravity waves. In the framework of the Saint-Venant equations, it is well known that $c = \sqrt{gh}$. Both expressions differ by the factor $1/\sqrt{1 + (\partial_x d)^2}$. In our model, the long waves are slowed down by strong bathymetric variations since fluid particles are constrained to follow the seabed.

4 Numerical Experiment

The equations are solved numerically with a spacial finite volume scheme together with a high-order adaptive time stepping. In order to obtain a higher-order scheme in space, we use a piecewise polynomial representation. This is achieved by various so-called reconstruction procedures, such as MUSCL TVD [13–15], UNO [16], ENO [17], WENO [18], and many others. In order to solve numerically the last system of equations, we apply a third-order Runge–Kutta scheme with four stages, with an embedded second-order method which is used to estimate the local error and, thus, to adapt the time step size. The model details and its performance can be found in [19]. Here, we focus of an illustrative example of the new modified Saint-Venant model: Wave generation by a sudden bottom uplift. This simple situation has some important implications to tsunami genesis problems.

The bottom is given by the following function:

$$d(x,t) \;=\; d_0 \;-\; a\,T(t)H(b^2 - x^2)\left[\left(\frac{x}{b}\right)^2 - 1\right]^2, \qquad T(t) \;=\; 1 \;-\; e^{-\alpha t},$$

where $H(x)$ is the Heaviside step function, a is the deformation amplitude, and b is the half-length of the uplifting sea floor area. The function $T(t)$ provides a complete information on the dynamics of the bottom motion. In tsunami wave literature, it is called a *dynamic scenario*. Initially, the free surface is undisturbed and the velocity field is taken to be identically zero. The values of various parameter are given in Table 1, where one should note that the quantities are normalized such that the water depth and the acceleration due to gravity are equal to one.

Table 1 Values of various parameters used for the wave generation by a moving bottom

Slow uplift parameter α_1:	$2.0\ s^{-1}$
Fast uplift parameter α_2:	$12.0\,\mathrm{s}^{-1}$
Gravity acceleration g:	$1\,\mathrm{m}\,s^{-2}$
Final simulation time T:	$5\,\mathrm{s}$
Undisturbed water depth d_0:	$1\,\mathrm{m}$
Deformation amplitude a:	$0.25\,\mathrm{m}$
Half-length of the uplift area b:	$2.5\,\mathrm{m}$

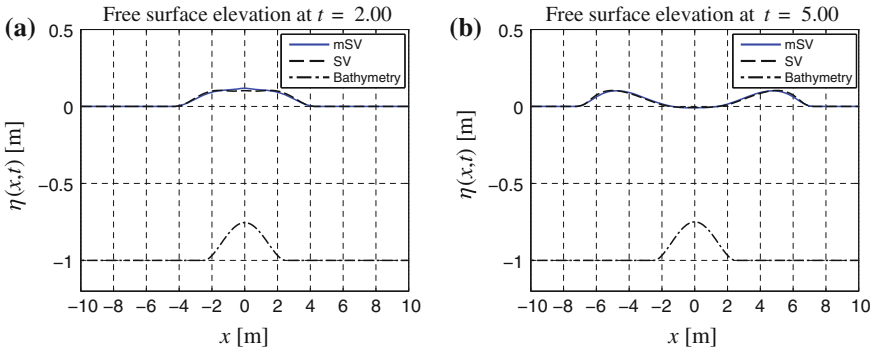

Fig. 1 Slow *bottom* uplift test case ($\alpha_1 = 2$). **a** $t = 2.0\,\mathrm{s}$. **b** $t = 5.0\,\mathrm{s}$

The numerical results of the moving bottom test case are shown on the figures below. On all these figures, the blue solid line corresponds to the modified Saint-Venant equations (mSV), while the black dashed line refers to its classical counterpart (SV). The dash-dotted line shows the bottom profile which evolves in time as well.

First, we present numerical results (see Fig. 1) corresponding to a relatively slow uplift of a portion of the bottom ($\alpha_1 = 2.0\,\mathrm{s}^{-1}$). There is a very good agreement between the two computations. We note that the amplitude of the bottom deformation $a/d = 0.25$ is big which explains some small discrepancies on Fig. 1a between two models. This effect is rather due to the bottom shape than to its dynamic motion.

Second, we test the same situation but the bottom uplift is fast with the inverse characteristic time $\alpha_2 = 12.0\,\mathrm{s}^{-1}$. In this case, the differences between two models are very flagrant. As it can be seen on Fig. 2 that the modified Saint-Venant equations give a wave with almost two times higher amplitude. Some differences

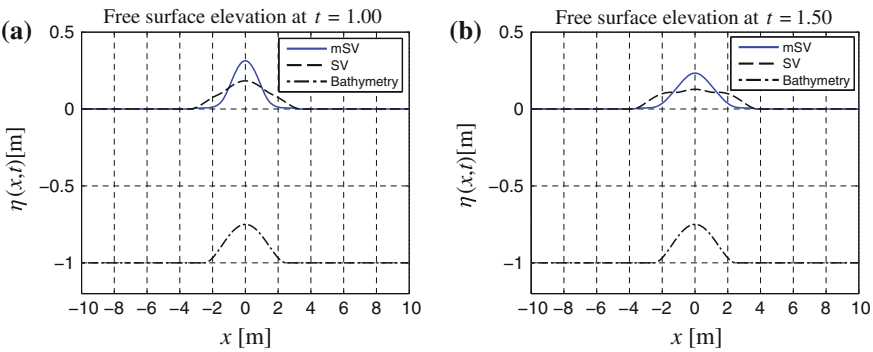

Fig. 2 Fast *bottom* uplift test case ($\alpha_2 = 12\,\mathrm{s}^{-1}$). **a** $t = 1.0\,\mathrm{s}$. **b** $t = 1.5\,\mathrm{s}$

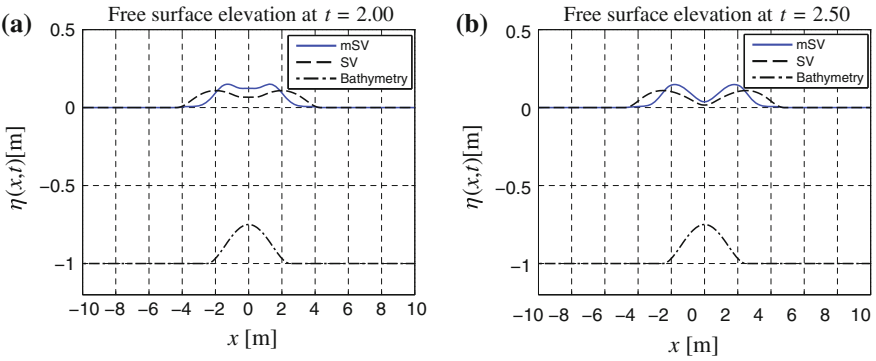

Fig. 3 Fast *bottom* uplift test case ($\alpha_2 = 12\,\mathrm{s}^{-1}$). **a** $t = 2.0\,\mathrm{s}$. **b** $t = 2.5\,\mathrm{s}$

in the wave shape persist even during the propagation (see Fig. 3). This test case clearly shows another advantage of the modified Saint-Venant equations in better representation of the vertical velocity field.

5 Conclusion

We derived a non-hydrostatic non-dispersive model of shallow water type which takes into account large bathymetric variations. Previously, some attempt was already made in the literature to derive shallow water systems for arbitrary slopes and curvature [4–6]. However, our study contains a certain number of new elements with respect to the existing state of the art, namely our derivation procedure relies on a generalized Lagrangian principle of the water wave problem [7]. Moreover, we do not introduce any small parameter, and our approximation is made through the choice of a suitable constrained ansatz. Resulting governing equations have a simple form and physically sound structure. Another new element is the introduction of arbitrary bottom time variations.

The proposed model is discretized with a finite volume scheme with adaptive time stepping to capture the underlying complex dynamics. The performance of this scheme is then illustrated on several test cases. Some implications to tsunami wave modeling are also suggested at the end of this study.

Among various perspectives, we would like to underline the importance of a robust run-up algorithm development using the current model. This research should shift forward the accuracy and our comprehension of a water wave runup onto complex shores [20, 21].

References

1. de Saint-Venant, A. J. C. (1871). Théorie du mouvement non-permanent des eaux, avec application aux crues des rivières et à l'introduction des marées dans leur lit. C. R. Academic Science Paris, 73, 147–154.
2. Peregrine, D. H. (1967). Long waves on a beach. *Journal of Fluid Mechanics*, *27*, 815–827.
3. Serre, F. (1953). Contribution à l'étude des écoulements permanents et variables dans les canaux. *La Houille blanche*, *8*, 374–872.
4. Dressler, R. F. (1978). New nonlinear shallow-flow equations with curvature. *Journal of Hydraulic Research*, *16*(3), 205–222.
5. Keller, J. B. (2003). Shallow-water theory for arbitrary slopes of the bottom. *Journal of Fluid Mechanics*, *489*, 345–348.
6. Bouchut, F., Mangeney-Castelnau, A., Perthame, B., & Vilotte, J.-P. (2003). A new model of Saint-Venant and Savage-Hutter type for gravity driven shallow water flows. *C. R. Academic Science Paris*, *I*(336), 531–536.
7. Clamond, D., & Dutykh, D. (2012). Practical use of variational principles for modeling water waves. *Physica D: Nonlinear Phenomena*, *241*(1), 25–36.
8. Petrov, A. A. (1964). Variational statement of the problem of liquid motion in a container of finite dimensions. *Prikladnaia Mathematics Mekhanika*, *28*(4), 917–922.
9. Luke, J. C. (1967). A variational principle for a fluid with a free surface. *Journal of Fluid Mechanics*, *27*, 375–397.
10. Zakharov, V. E. (1968). Stability of periodic waves of finite amplitude on the surface of a deep fluid. *Journal of Applied Mechanical Technology Physics*, *9*, 190–194.
11. Miles, J. W., & Salmon, R. (1985). Weakly dispersive nonlinear gravity waves. *Journal of Fluid Mechanics*, *157*, 519–531.
12. Dutykh, D., & Clamond, D. (2011). Shallow water equations for large bathymetry variations. *Journal of Physics A: Mathematical Theory*, *44*, 332001.
13. Kolgan, N. E. (1975). Finite-difference schemes for computation of three dimensional solutions of gas dynamics and calculation of a flow over a body under an angle of attack. *Uchenye Zapiski TsaGI [Science Notes Central Institute Aerodyn]*, *6*(2), 1–6.
14. van Leer, B. (1979). Towards the ultimate conservative difference scheme V: a second order sequel to Godunov' method. *Journal of Computer Physics*, *32*, 101–136.
15. van Leer, B. (2006). Upwind and high-resolution methods for compressible flow: From donor cell to residual-distribution schemes. *Communications in Computational Physics*, *1*, 192–206.
16. Harten, A., & Osher, S. (1987). Uniformly high-order accurate nonoscillatory schemes. *I. SIAM Journal of Numerical Analytical*, *24*, 279–309.
17. Harten, A. (1989). ENO schemes with subcell resolution. *Journal of Computer Physics*, *83*, 148–184.
18. Xing, Y., & Shu, C.-W. (2005). High order finite difference WENO schemes with the exact conservation property for the shallow water equations. *Journal of Computer Physics*, *208*, 206–227.
19. Dutykh, D., & Clamond, D. (2012). *Modified shallow water equations for significantly varying bottoms*. Submitted.
20. Dutykh, D., Katsaounis, T., & Mitsotakis, D. (2011). Dispersive wave runup on non-uniform shores. In J. Fort, et al. (Eds.), Finite Volumes for Complex Applications VI - Problems & Perspectives (pp. 389–397). pp Prague: Springer Berlin Heidelberg.
21. Dutykh, D., Labart, C., & Mitsotakis, D. (2011). Long wave run-up on random beaches. *Physics Review Letter*, *107*, 184504.

Finite Volume Implementation of Non-Dispersive, Non-Hydrostatic Shallow Water Equations

Vincent Guinot, Didier Clamond and Denys Dutykh

Abstract A shock-capturing, finite volume implementation of recently proposed non-hydrostatic two-dimensional shallow water equations, is proposed. The discretization of the equations in conservation form implies the modification of the time derivative of the conserved variable, in the form of a mass/inertia matrix, and extra terms in the flux functions. The effect of this matrix is to slow down wave propagation in the presence of significant bottom slopes. The proposed model is first derived in conservation form using mass and momentum balance principles. Its finite volume implementation is then presented. The additional terms to the shallow water equations can be discretized very easily via a simple time-stepping procedure. Two application examples are presented. These examples seem to indicate that the proposed model does not exhibit strong differences with the classical hydrostatic shallow water model under steady-state conditions, but that its behavior is significantly different when transients are involved.

Keywords Shallow water model · Non-hydrostatic pressure distribution · Bottom acceleration

V. Guinot (✉)
Université Montpellier—HSM UMR 5569, Place Eugène Bataillon, CC 057, Montpellier Cedex 5, 34095, Montpellier, France
e-mail: guinot@msem.univ-montp2.fr

D. Clamond
Université de Nice-Sophial Antipolis—Laboratoire J. A, Dieudonné UMR 7351, Parc Valrose, Nice Cedex 02, 06108, Nice Cedex, France
e-mail: didierc@unice.fr

D. Dutykh
LAMA UMR 5127, Campus Scientifique, Le-Bourget-du-Lac Cedex 73376 Marseilles Cedex, France
e-mail: Denys.Dutykh@univ-savoie.fr

P. Gourbesville et al. (eds.), *Advances in Hydroinformatics*,
Springer Hydrogeology, DOI: 10.1007/978-981-4451-42-0_17,

1 Introduction

Among the many available tools for water wave model formulation (see [1] for an overview), the variational formulation has proved a powerful one [2, 3]. Recently, the Lagrangian variational approach has been used to derive a family of free surface flow models [1, 4]. This approach allows the classical shallow water equations, the Serre equations, the Boussinesq equations, and many others, to be derived as particular cases [1].

The purpose of this communication is to show how a non-hydrostatic shallow water model, presented in [4] under the assumption of non-negligible flow vertical acceleration, can be implemented in a simple way within a classical, Godunov-type algorithm. This model has the interesting property that the system of governing equations remains hyperbolic, thus making standard numerical techniques easily applicable.

In Sect. 2, the governing equations are derived in conservation form, not using the variational approach, but using the more classical integral form for mass and momentum balances that are more widely accepted by the hydraulic community. In Sect. 3, an overview of the numerical implementation is given. Section 4 is devoted to computational examples and Sect. 5 to the conclusions.

2 Assumptions and Governing Equations

2.1 Notation—Assumptions

The following notation is used (Fig. 1). The water depth is denoted by h, and the vertical averages of the x- and y-components of the flow velocity are denoted, respectively, by u and v. The bottom and free surface elevations are denoted, respectively, by z_b and z_s, and $z_s = z_b + h$. The unit discharge in the x- and y-directions is denoted, respectively, by $q = hu$ and $r = hv$. The bottom slopes in the x- and y- directions are denoted, respectively, by $S_{0,x}$ and $S_{0,y}$. $\mathbf{u} = [u, v, w]^T$ is the flow velocity vector. The restriction of the velocity vector to the horizontal plane is defined as $\mathbf{u}_h = [u, v]^T$.

The classical shallow water equations are based on the following assumptions:

(A1) the water in incompressible,

(A2) the flow velocity is uniform over the depth,

(A3) the pressure distribution is hydrostatic over the vertical,

(A4) the bottom slope is negligible.

In the modified shallow water equations, assumptions (A1–3) are retained, but assumption (A4) is replaced with the following one:

(A5) the bottom slope may not be negligible, and the flow velocity vector is collinear to the bottom tangent vector.

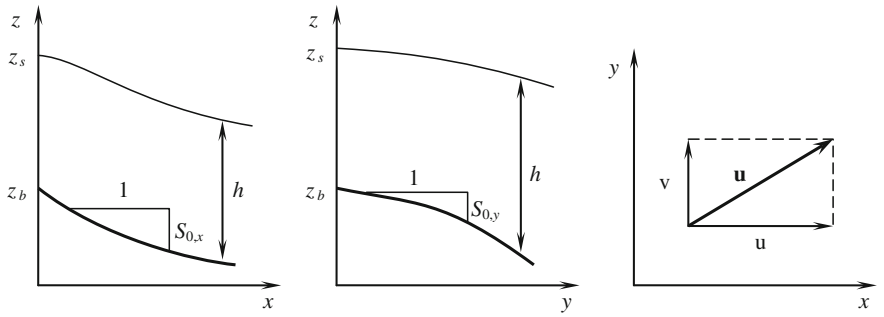

Fig. 1 Notation vertical cross-section in the (x, z) plane (*left*), in the (y, z) plane (*middle*), and in the (x, y) plane (*right*)

Assumption (A4) may be translated mathematically as follows:

$$\tilde{w}(x,y,z,t) = w(x,y,t) = \mathbf{u}_h(x,y,t).\nabla z_b = -u(x,y,t)S_{0,x} - v(x,y,t)S_{0,y} \ \forall z \in [z_b; z_s] \tag{1}$$

where $\tilde{w}(x,y,z,t)$ is the vertical component of the flow velocity vector. Equation (1) has important consequences on the momentum source term in the conservation form of the equations.

2.2 Conservation Form

In [1, 4], the governing equations are derived using variational principles. Owing to the non-uniqueness of weak solutions (see [5] for the example of the shallow water equations), it is not clear whether the conservation form established in [1, 4] using variational principles remains valid in the presence of flow discontinuities. For this reason, the governing equations are derived using the integral form of mass and momentum balances over a control volume hereafter.

The continuity equation is derived by carrying out a mass balance over a cylindrical control volume Ω, extending from the bottom to the free surface (Fig. 2).

The boundary Γ of the control volume being vertical, its normal unit vector $\mathbf{n}$ (oriented outwards) lies in the (x, y) plane. Mass conservation with assumption (A1) gives, after simplification by the (constant) water density,

$$\partial_t \int_{\Omega} \mathrm{d}\Omega + \int_{\Gamma} \mathbf{u}.\mathbf{n}\, d\Gamma = 0 \tag{2}$$

Since the boundary is vertical, $\mathrm{d}\Gamma = h\,\mathrm{d}s$, where s is the curvilinear coordinate along the boundary, and $\mathrm{d}\Omega = h\,\mathrm{d}A$, where $\mathrm{d}A$ is the infinitesimal area in plan view. Introducing these definitions into (2) yields

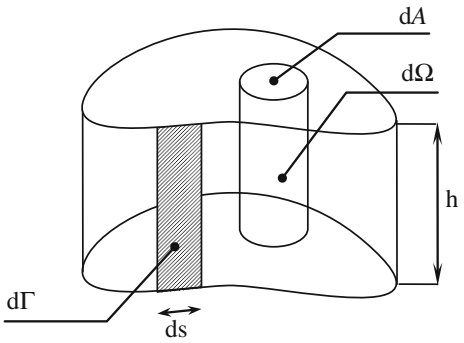

Fig. 2 Definition sketch for the integration control volume

$$\partial_t \int_\Omega h \, \mathrm{d}A + \int_\Gamma h\mathbf{u}.\mathbf{n} \, \mathrm{d}s = 0 \tag{3}$$

which yields the well-known differential form

$$\partial_t h + \nabla.(h\mathbf{u}_h) = 0 \tag{4}$$

where $\mathbf{u}_h$ is the restriction of $\mathbf{u}$ to the horizontal plane.

The momentum equation is obtained from Euler's theorem:

$$\partial_t \int_\Omega h\mathbf{u}\mathrm{d}A + \int_\Gamma (\mathbf{u}.\mathbf{n})h\mathbf{u} \, \mathrm{d}s = \int_\Omega \mathbf{g}h\mathrm{d}A - \int_\Gamma \frac{g}{2}h^2\mathbf{n} \, \mathrm{d}s + \mathbf{R} \tag{5}$$

where $\mathbf{g} = [0, 0, -g]^T$ is the gravitational acceleration and $\mathbf{R} = [R_x, R_y, R_z]^T$ is the reaction of the bottom. A major difference with the classical shallow water equations is that owing to assumption (A5), the terms R_x and R_y in Eq. (5) are modified. Projecting (5) onto the three axes, using the fact that $\mathbf{R}$ is collinear to the normal unit vector to the bottom yields:

$$\partial_t \int_\Omega hu\mathrm{d}A + \int_\Gamma q_n u \, \mathrm{d}s = -\int_\Gamma \frac{g}{2}h^2 n_x \, \mathrm{d}s + R_z S_{0,x} \tag{6}$$

$$\partial_t \int_\Omega hv\mathrm{d}A + \int_\Gamma q_n v \, \mathrm{d}s = -\int_\Gamma \frac{g}{2}h^2 n_y \, \mathrm{d}s + R_z S_{0,y} \tag{7}$$

$$\partial_t \int_\Omega hw\mathrm{d}A + \int_\Gamma q_n(\mathbf{u}_h.\nabla z_b) \, \mathrm{d}s = \int_\Omega -gh \, \mathrm{d}A + R_z \tag{8}$$

where q_n is the normal unit discharge to the boundary. Equations (1) and (8) lead to the following expression for R_z:

$$R_z = \int_\Omega \left(\partial_t(hw) + gh\right) \mathrm{d}A + \int_\Gamma q_n(\mathbf{u}_h.\nabla z_b)\ \mathrm{d}s$$
$$= \int_\Omega \left(gh + \partial_t(h\mathbf{u}_h).\nabla z_b\right) \mathrm{d}A + \int_\Gamma q_n(\mathbf{u}_h.\nabla z_b)\ \mathrm{d}s \tag{9}$$

It is easy to see from Eq. (9) that the assumption of a non-negligible bottom slope introduces an additional vertical acceleration, thus yielding a modification in the apparent gravitational acceleration. Substituting Eq. (9) into (6–7) leads to

$$\partial_t \int_\Omega h\left(u + \mathbf{u}_h.\nabla z_b S_{0,x}\right) \mathrm{d}A + \int_\Gamma \left(u + \mathbf{u}_h.\nabla z_b S_{0,x}\right) q_n\ \mathrm{d}s$$
$$= -\int_\Gamma \frac{g}{2} h^2 n_x\ \mathrm{d}s + \int_\Omega ghS_{0,x}\mathrm{d}A \tag{10}$$

$$\partial_t \int_\Omega h\left(v + u + \mathbf{u}_h.\nabla z_b S_{0,y}\right)\mathrm{d}A + \int_\Gamma \left(v + \mathbf{u}_h.\nabla z_b S_{0,y}\right) q_n\ \mathrm{d}s$$
$$= -\int_\Gamma \frac{g}{2} h^2 n_y\ \mathrm{d}s \int_\Omega ghS_{0,y}\mathrm{d}A \tag{11}$$

thus yielding the following system in differential conservation form:

$$\partial_t \mathbf{M}\mathbf{U} + \partial_x \mathbf{F}_x + \partial_y \mathbf{F}_y = \mathbf{S} \tag{12}$$

$$\mathbf{U} \equiv \begin{bmatrix} h \\ q \\ r \end{bmatrix}, \mathbf{F}_x \equiv \begin{bmatrix} q \\ q^2/h + gh^2/2 + \left(\mathbf{u}_h.\nabla z_b S_{0,x}\right)q \\ qr/h + \left(\mathbf{u}_h.\nabla z_b S_{0,x}\right)r \end{bmatrix}, \mathbf{F}_y \equiv \begin{bmatrix} r \\ qr/h + \left(\mathbf{u}_h.\nabla z_b S_{0,y}\right)q \\ r^2/h + gh^2/2 + \left(\mathbf{u}_h.\nabla z_b S_{0,y}\right)r \end{bmatrix},$$
$$\mathbf{S} \equiv \begin{bmatrix} 0 \\ ghS_{0,x} \\ ghS_{0,y} \end{bmatrix}, \mathbf{M} \equiv \begin{bmatrix} 1 & 0 & 0 \\ 0 & 1 + S_{0,x}^2 & S_{0,x}S_{0,y} \\ 0 & S_{0,x}S_{0,y} & 1 + S_{0,y}^2 \end{bmatrix} \tag{13}$$

The appearance of the mass (or inertia) matrix $\mathbf{M}$ and two additional flux terms is worth noting. It is responsible for the modification in the wave propagation speeds as identified in [1, 4].

3 Shock-Capturing Finite Volume Discretization

The governing equations in conservation form (12–13) were implemented into a shock-capturing, finite volume-based computational code for shallow water simulations, the SW2D platform. This platform may be used to solve the shallow water equations with single porosity [6, 7] and multiple porosity [8], as well as the

two-dimensional shallow water sensitivity equations [9]. The Godunov-based solution techniques implemented in this implementation use MUSCL-based reconstructions [10] over unstructured grids. For the sake of computational rapidity, the eigenvector-based reconstruction [11] is used. It allows second-order time integration within a single timestep. The fluxes are computed using a modified HLLC [12] solver [7].

In a first step, the classical shallow water equations are solved:

$$\partial_t \mathbf{U} + \partial_x \mathbf{F}_x^{\mathrm{SW}} + \partial_y \mathbf{F}_y^{\mathrm{SW}} = \mathbf{S} \tag{14}$$

where $\mathbf{F}_x^{\mathrm{SW}} = [q, q^2/h + gh^2/2, qr/h]^T$ and $\mathbf{F}_y^{\mathrm{SW}} \equiv [r, qr/h, r^2/h + gh^2/2]^T$ are the classical shallow water fluxes. The discretization technique is a standard one and will not be described here for the sake of conciseness (see e.g., [13] for an overview).

In a second step, the additional terms in the fluxes are accounted for

$$\partial_t \mathbf{U} + \partial_x \mathbf{F}_x^{\mathrm{NH}} + \partial_y \mathbf{F}_y^{\mathrm{NH}} = 0 \tag{15}$$

where $\mathbf{F}_x^{\mathrm{NH}} = \left[0, \mathbf{u}_h.\nabla z_b S_{0,x} q, \mathbf{u}_h.\nabla z_b S_{0,x} r\right]^T$ and $\mathbf{F}_y^{\mathrm{NH}} = \left[0, \mathbf{u}_h.\nabla z_b S_{0,y} q, \mathbf{u}_h.\nabla z_b S_{0,y} r\right]^T$ are the additional fluxes arising from the non-hydrostatic assumption. Since these fluxes account for advection of the scalar quantity $\mathbf{u}_h.\nabla z_b$, a simple upwind flux formula is used, with the mass flux computed in step 1 using the modified Riemann solver.

In a third step, the influence of the inertia matrix is incorporated. This is done as follows: denoted by $\mathbf{U}_i^n$ the average cell value of $\mathbf{U}$ over the cell i at the time level n. Solving Eqs. (14–15) over the timestep Δt yields a provisional solution $\mathbf{U}_i^{n+1,(1)}$ at the time level n. The final solution $\mathbf{U}_i^{n+1}$ at the end of the timestep (thus, at time level $n + 1$) is given by

$$\mathbf{U}_i^{n+1} \approx \mathbf{U}_i^n + \Delta t\, \partial_t \mathbf{U} \approx \mathbf{U}_i^n + M^{-1}\left(\mathbf{U}_i^{n+1,(1)} - \mathbf{U}_i^n\right) \tag{16}$$

4 Application Examples

4.1 Steady-State Simulation

A steady-state experiment was carried out using the experimental facilities at the SupAgro'Montpellier engineering school. A Venturi flume with variable bottom was placed in a channel, and a constant discharge was prescribed upstream (Fig. 3).

The Venturi flume was operated under undrowned conditions, so that the flow velocity (hence the accelerations) be maximum. A constant discharge $Q = 40$ L s^{-1} was prescribed, and the free surface elevation was measured every

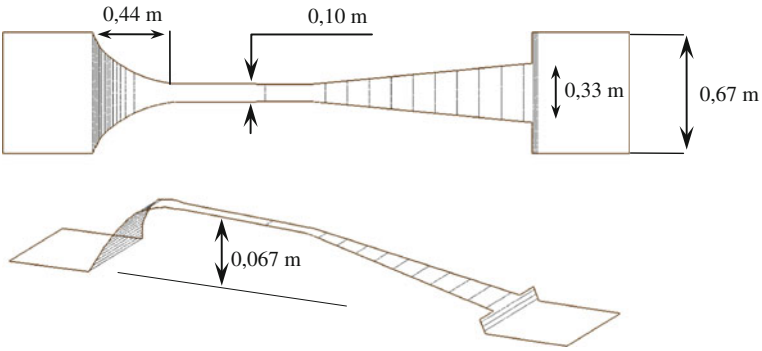

Fig. 3 Geometry of the Venturi flume used in the experiment. *Top* plan view. *Bottom* bird's eye view with a vertical scale magnified by a factor 5

5 cm along the Venturi flume and up to 50 cm upstream (the free surface elevation was measured horizontally upstream of this distance).

Figure 4 (left) shows the longitudinal profile of the spectral radius of M, that is, $1 + S_{0,x}^2$ (because $S_{0,y} = 0$). Note that this profile, which is computed using an approximation of the Venturi bottom slope between two measurement points, is an experimental profile. It can bee seen that $1 + S_{0,x}^2$ is significantly larger than unity upstream of the narrow section. The free surface elevation profile may thus be expected to be significantly different from that given by the classical shallow water equations in the upstream part of the Venturi flume, while no significant difference should be expected in the narrow and downstream parts.

The numerical solutions computed by solving both the classical and modified shallow water equations are compared to the experimental free surface profiles in Fig. 4 (right). It can be seen that under steady conditions, very little difference is observed between the two numerical solutions. The difference between the simulated and computed free surface elevations in the narrow section of the Venturi

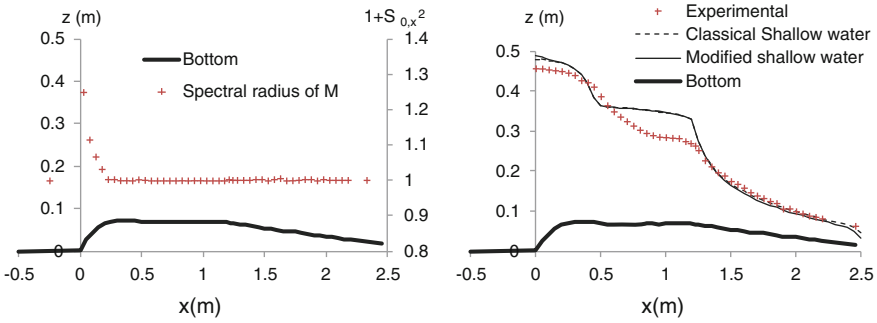

Fig. 4 Venturi flume. *Left* spectral radius of the mass/inertia matrix M as a function of the longitudinal coordinate. *Right* bottom and free surface profiles for a steady discharge $Q = 40$ L s^{-1}

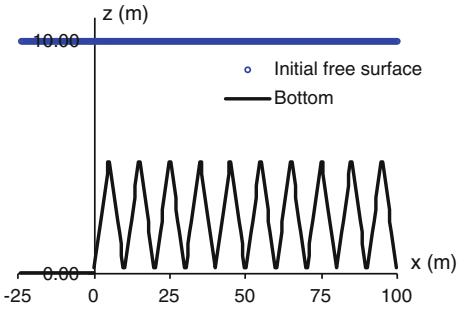

Fig. 5 Transient propagation over undulated *bottom*. Longitudinal profile of the *bottom* and initial free surface

flume is clearly due to non-hydrostatic pressure distribution stemming from the strong vertical accelerations. However, these accelerations are mainly due to the curvature of the free surface, not to the bottom gradient.

4.2 Transient Propagation over Undulated Bottom

In this test, a transient propagates into still water over a sawtooth-shaped bottom (Fig. 5). The length and height of the bottom undulations are, respectively, 10 and 5 m, which means that the bottom slope is $\pm$ 45°. At $t = 0$, $z_s = 10$ m and $u = v = 0$ m s^{-1}. At $t > 0$, a constant unit discharge $q_b = 1$ m^2 s^{-1} is injected at the left-hand boundary of the model. This creates a moving bore that propagates to the right along the x-direction. When the bore reaches the sawtooth-shaped bottom, part of the transient continues to the right, while part of it is reflected back to the left. In simulating this type of transient (shock wave), a proper formulation of the equations in conservation form is essential.

Figure 6 shows the simulated free surface elevations at various times using the classical, hydrostatic, and non-hydrostatic shallow water Eq. (11). As predicted in [1, 4], the two models are equivalent as long as the transient propagates over zero bottom slopes (which is the case for $x < 0$ m and $t < 5$ s), while the non-hydrostatic model exhibits slower wave propagation speeds when the bottom slope is non-zero; hence; the larger free surface elevations are observed compared to the hydrostatic shallow water model.

5 Conclusions

A shock-capturing, finite volume implementation, has been presented for the non-hydrostatic shallow water equations of [1, 4]. The governing equations in conservation form are easy to implement in the framework of classical time-stepping procedures.

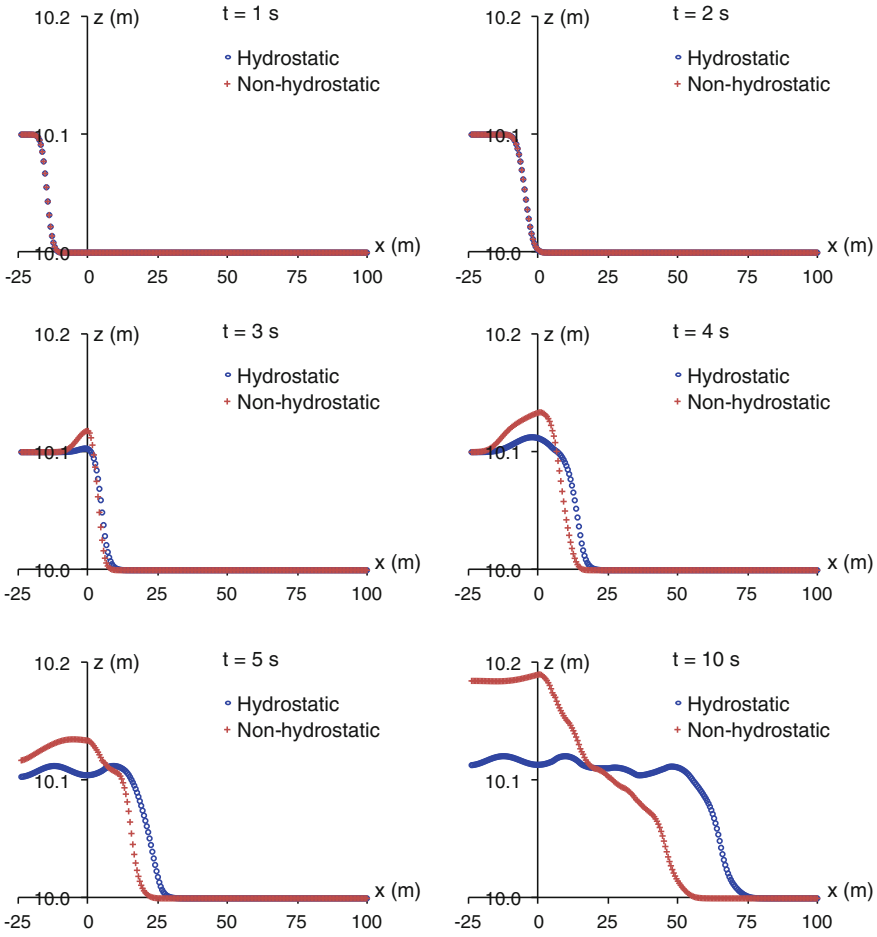

Fig. 6 Transient propagation over sawtooth-shaped *bottom*. Simulated water depths at various times

Computational applications seem to indicate that the non-hydrostatic model does not bring significant differences compared to the hydrostatic model when steady flows are involved. In contrast, transient propagation seems to be more strongly influenced by the hydrostatic/non-hydrostatic assumption. Experimental validation is obviously needed to confirm the added value brought by this model.

References

1. Clamond, D., & Dutykh, D. (2012). Practical use of variational principles for modelling water waves. *Physica D: Nonlinear Phenomena, 241*, 25–36.
2. Radder, A. C. (1999). Hamiltonian dynamics of water waves. *Advances in Coastal and Ocean Engineering, 4*, 21–59.
3. Salmon, R. (1988). Hamiltonian fluid mechanics. *Annual Review of Fluid Mechanics, 20*, 225–256.
4. Dutykh, D., & Clamond, D. (2011). Shallow water equations for large bathymetry variations. *Journal of Physics A: Mathematical and Theoretical, 44*, 332001.
5. Stoker, J.J. (1957). Water waves. Interscience.
6. Finaud-Guyot, P., Delenne, C., Lhomme, J., Guinot, V., & Llovel, C. (2010). An approximate-state Riemann solver for the two-dimensional shallow water equations with porosity. *International Journal for Numerical Methods in Fluids, 62*, 1299–1331.
7. Guinot, V., & Soares-Frazão, S. (2006). Flux and source term discretization for shallow water models with porosity on unstructured grids. *International Journal for Numerical Methods in Fluids, 50*, 309–345.
8. Guinot, V. (2012). Multiple porosity shallow water models for macroscopic modelling of urban floods. *Advances in Water Resources, 37*, 40–72.
9. Guinot, V., Delenne, C., & Cappelaere, B. (2009). An approximate Riemann solver for sensitivity equations with discontinuous solutions. *Advances in Water Resources, 32*, 61–77.
10. Van Leer, B. (1977). Toward the ultimate conservative difference scheme. IV. A new approach to numerical convection. *Journal of Computational Physics, 23*, 276–299.
11. Soares-Frazão, S., & Guinot, V. (2007). An eigenvector-based linear reconstruction scheme for the shallow water equations on two-dimensional unstructured meshes. *International Journal for Numerical Methods in Fluids, 53*, 23–55.
12. Toro, E. F., Spruce, M., & Speares, W. (1994). Restoration of the contact surface in the HLL-Riemann solver. *Shock Waves, 4*, 25–34.
13. Guinot, V. (2010). *Wave propagation in fluids. Models and numerical techniques*. 2nd edition. Wiley-ISTE.

Modeling Flood in an Urban Area: Validation of Numerical Tools Against Experimental Data

Quentin Araud, Pascal Finaud-Guyot, Fabrice Lawniczak, Pierre François, José Vazquez and Robert Mosé

Abstract Flooding events in urban area are known to generate expensive damages. Nowadays, numerical tools are frequently used to simulate flows in urban area during extreme events, in order to be able to forecast and to reduce flood impacts. However, most of the computational softwares currently used in engineering studies were initially developed for river flows. The lack of accurate data during real events and the few experimental data specific to the urban flood at the district scale leads to no or few validations of the existing numerical tools. This paper presents experimental results of an urban flood physical model at the Fluid and Solid Mechanics Institute of Strasbourg (IMFS), and the comparison with both 2D and 3D numerical results. The presented experimental configurations are in steady flow on a flat bottom. Numerical results are provided using the commercial software Ansys-Fluent®, that solves the Reynolds-averaged Navier–Stokes equations, and Neptune 2D, a research software that solves the two-dimensional shallow water equations with an Eigenvector Reconstruction—Discontinuous Galerkin (EVR-DG) scheme. The experimental water height in particular locations and outflows at each outlet are compared to the numerical results. The comparison validates the use of Fluent at the scale of the street (differences with experimental results under 10 %). The 2D and the 3D approaches are validated at the scale of the district (differences on the side of the district discharges are around 1 %). The non-hydrostatic pressures profiles in some crossroads and the turbulence modeling could explain the high differences (up to 30 %) of the discharges calculated in some streets by Neptune 2D.

Keywords Urban flooding · Physical model · Ansys-Fluent · Eigenvector reconstruction—discontinuous Galerkin (EVR-DG) scheme · Shallow water modeling · Experimental/numerical comparison · Neptune 2D

Q. Araud (✉) · P. Finaud-Guyot · F. Lawniczak · P. François · J. Vazquez · R. Mosé
IMFS (CNRS/UdS/INSA/ENGEES), 2 rue Boussingault, Strasbourg 67000, France
e-mail: araud@etu.unistra.fr

P. Gourbesville et al. (eds.), *Advances in Hydroinformatics*,
Springer Hydrogeology, DOI: 10.1007/978-981-4451-42-0_18,

1 Introduction

The urbanization of floodplains raises vulnerability of urban area. Consequences of floods in high-density populated area can become calamitous with losses of human lives and expensive damage. Urban flooding has recently become an important issue and a main interest for research. In the field of urban flood engineering, numerical tools are frequently used. Most of the time, these tools were designed for other purposes: river, sea, or fluid dynamic modeling. These numerical tools should therefore be validated in urban flood configurations, and the accuracy of these softwares has to be established.

Experimental studies [1–3] and numerical approaches [4–6] are carried out to understand flows in urban area and to develop numerical tools able to predict the water level and the discharge repartition during an urban flood. Van Emelen [7] recently studied on a scale model the 2005 New Orleans flood and shown that a finite volume scheme solving the two-dimensional depth-averaged shallow water equations could lead to accurate simulation of urban floods.

In order to confirm this fact and to overcome to the lack of experimental data, a physical model of an urban district was built in the Fluid and Solid Mechanical Institute of Strasbourg (IMFS). At the present time, not enough data were collected on the experimental setup to fully understand the behavior of the flow through the district. Nevertheless, experimental results can be used as a reference for a comparison and the validation of numerical tools. Therefore, the water height and the outflows were measured during three steady flow experiments and compared to the numerical results. The inflow and outflow conditions lead to subcritical flows inside the district. The experimental setup is presented in the Sect. 2.

The numerical simulations were carried out with two numerical tools:

1. Ansys-Fluent which solves the three-dimensional Reynolds equations and simulates the turbulence.
2. Neptune 2D, a discontinuous Galerkin scheme solving the two-dimensional shallow water equations.

Numerical models are detailed in the Sect. 3. The Sect. 4 presents the comparison of the numerical results and the experimental data. The Sect. 5 is devoted to the conclusion.

2 Experimental Investigation

2.1 Experimental Setup and Measuring Techniques

The experiments are carried out over a 5 × 5 m physical model representing an eight by eight blocks district (see Fig. 1). This particular geometry was chosen in the RIVES project [8] to represent a dense European urban area. The street width

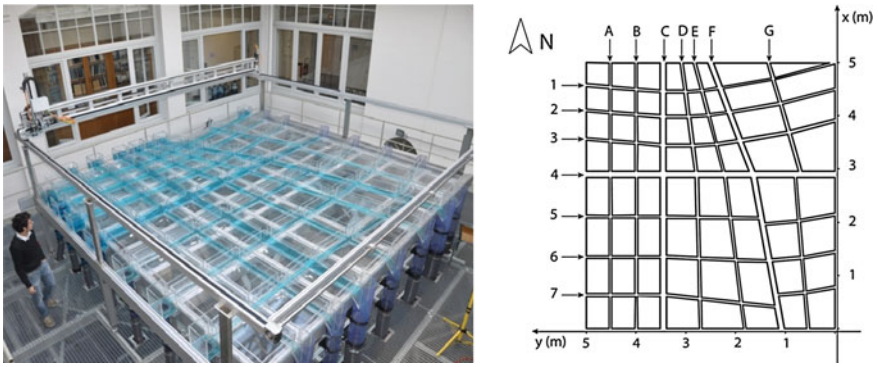

Fig. 1 *Left* figure of the physical model. *Right* sketch of the district

varies from 4.5 cm for narrow streets to 12.5 cm for the broader ones (see http://www-imfs.u-strasbg.fr/content/Pilote-inondation for more details). The physical model is flooded by fourteen screw pumps allowing to independently control the discharge in each upstream street. A 2 % error on the inflow was evaluated. This particular feature allows for an accurate management of the boundary conditions. The water height is measured in different points using an automatic vertical moving system controlated by a phase sensor. This system enables measurements even in narrow streets and measurements are ± 1 mm accurate. The water height was measured in 600 points all over the district, with eight measuring points per crossroad, and two to three measuring points per street.

The outflows are collected at each downstream end of the street and measured using fourteen channels equipped with weirs. The water height in each channel is monitored using doppler, which enables accurate free-surface measurements, with an error smaller than a percent. Nevertheless, the error on the outflows is estimated around 1 %.

2.2 Experimental Configurations

The experiments were conducted under steady states. The bottom slope of the model is equal to zero, which generates a subcritical flow over the whole district. The boundary conditions for each experiment are summarized in Table 1. The total inflow is divided into two equal contributions injected in west and north sides. The unit discharge calculated in the transversal direction of each upstream street is constant for each face. Since the total inflow width is not the same on each side, the unit discharge is different on both sides. In the downstream streets, water leaves the district in a waterfall. It can be considerate as a critical outflow condition, characterized by a Froude number equal to unity.

Table 1 Inlet boundary conditions for each experiment

Experiment	Unit discharge (m^2/h)		Total discharge injected (m^3/h)
	North side	West side	
Case 1	61.34	73.17	60
Case 2	81.87	97.56	80
Case 3	102.33	121.95	100

Detailed inflows for each street and for each experiment are available http://www-imfs.u-strasbg.fr/content/Pilote-inondation

3 Numerical Tool

3.1 Neptune 2D: A Two-Dimensional Approach Solved with an EVR-DG Scheme

Under the assumption of a hydrostatic pressure, the Navier–Stokes equations can be depth averaged leading to the shallow water equations. This hyperbolic system can be written in conservation form as

$$\frac{\partial \mathbf{U}}{\partial t} + \frac{\partial \mathbf{F}}{\partial x} + \frac{\partial \mathbf{G}}{\partial y} = \mathbf{S} \tag{1a}$$

$$\mathbf{U} = \begin{pmatrix} h \\ q \\ r \end{pmatrix} \mathbf{F} = \begin{pmatrix} q \\ \frac{q^2}{h} + \frac{1}{2} g h^2 \\ \frac{qr}{h} \end{pmatrix} \mathbf{G} = \begin{pmatrix} r \\ \frac{qr}{h} \\ \frac{r^2}{h} + \frac{1}{2} g h^2 \end{pmatrix} \mathbf{S} = \begin{pmatrix} 0 \\ gh\left(S_{0,x} - S_{f,x}\right) \\ gh\left(S_{0,y} - S_{f,y}\right) \end{pmatrix} \tag{1b}$$

where **U** is the conserved vector variable, **F** (and **G**) are the fluxes in the x- (and y-) directions, and **S** represents the source terms. h is the water depth, g is the gravity acceleration, q and r are the unit discharge in the x- and y-directions, respectively, defined as $q = h.u$ and $r = h.v$ where u and v are the velocities in x- and y-directions, respectively. The source terms takes into account the bottom slope ($S_{0,x}$ and $S_{0,y}$ in the x- and y-directions, respectively) and the friction effects ($S_{f,x}$ and $S_{f,y}$ in the x- and the y-directions, respectively) using the classical Strickler formula. A sensibility study was realized to determine the most appropriate Strickler coefficient for the numerical simulation. Even though the usual Strickler coefficient for Plexiglas surfaces is about $K = 100\ \mathrm{m}^{1/3}\mathrm{s}^{-1}$, the best results were obtained by using a Strickler coefficient $K = 80\ \mathrm{m}^{1/3}\mathrm{s}^{-1}$. This coefficient is therefore used for all numerical simulations.

The 2D shallow water equations are solved using a discontinuous finite element method on an unstructured triangular mesh presented in [9]. This yields the following scheme:

$$\frac{\partial \mathbf{U}_i^{(k)}}{\partial t} = \frac{A_i}{3}\left(\sum_{k=1}^{3}\left[\mathbf{F}\left(m_i^{(k)}\right)\frac{\partial \varphi_i^{(k)}}{\partial x} + \mathbf{G}\left(m_i^{(k)}\right)\frac{\partial \phi_i^{(k)}}{\partial y} + \mathbf{S}\left(m_i^{(k)}\right)\right] + \oint_{\Gamma_i} \mathbf{F}_{\xi}^{*}\varphi_i^{(k)}\mathrm{d}\Gamma_i\right. \tag{2}$$

where $\mathbf{U}_i^{(k)}$ is the conserved variable at $m_i^{(k)}$ the middle point of the kth edge of cell i; A_i is the area of cell i, $\varphi_i^{(k)}$ the shape function defined on cell i so that $\varphi_i^{(k)} = \delta_{kl}$ where δ_{kl} is the Kronecker symbol (*i.e.* $\delta_{kl} = 1$ if $k = 1$ and $\delta_{kl} = 0$ if $l \neq k$). $\mathbf{F}(m_i^{(k)})$ and $\mathbf{G}(m_i^{(k)})$ are the fluxes at $m_i^{(k)}$ and $\mathbf{F}_{\xi}^{*}$ the numerical fluxes projected on cell i interfaces Γ_i. Those numerical fluxes are approximated using the classical Lax-Friedrich Riemann solver [10]. Equation (2) is discretized using an EVR approach presented in [11]. All the numerical simulations are carried out over a 2D regular mesh of 15,000 triangular cells. A sensibility study was carried out to choose this mesh.

3.2 A Three-Dimensional Approach with ANSYS-Fluent

3.2.1 Governing Equations

Fluent solves the Navier–Stokes equations time averaged using the Reynolds approach. Each instantaneous variable u can be considered as the sum of its time average U and its fluctuating part u'. The time-average equation of the continuity therefore becomes

$$\frac{\partial \rho}{\partial t} + \mathrm{div}(\rho \mathbf{U}) = 0 \tag{3}$$

and the three momentum equations in any x_i-direction becomes

$$\frac{\partial(\rho U_i)}{\partial t} + \mathrm{div}(\rho U_i \mathbf{U}) = \frac{\partial P}{\partial x_i} + \mathrm{div}[\mu \mathbf{grad}(U_i)] - \frac{\partial(\overline{u_i' u'})}{\partial x} - \frac{\partial(\overline{u_i' v'})}{\partial y} - \frac{\partial(\overline{u_i' w'})}{\partial z} - \rho g_{x_i} \tag{4}$$

where ρ is the phase density, μ the phase molecular viscosity, g_x the gravity acceleration contribution in the x-direction, P the pressure, $\mathbf{U}$ the velocity vector, U_i being the component of the velocity vector in the x_i-direction, U, V and W are the velocities, respectively, in the x-, y-, and z-directions The Reynolds stresses (the time average of velocity fluctuation product) are approximated using a classical k-ε model [12].

The equations are solved in steady flow using a finite volume scheme associated to a volume of fluid approach to modelized the free surface at the interface between the water and the air [12, 13]. All the numerical simulations are carried out over a 3D regular mesh of 700,000 cells, with 15,000 cells in the plan xy. The friction effect is taken into account by the boundary layer condition affected to all walls.

4 Results and Comparison

The comparison of the three experiments against numerical results leads to the same conclusion. Therefore, only results for the case 3 are fully described hereafter.

4.1 The Outflows Distribution

Even though the same unit discharge is injected in all the inlets, flows are distributed at each crossroad. Therefore, the comparison of experimental outflow discharges and the numerical ones gives important information on the accuracy of the softwares. One interesting experimental result is that the outflows distributions are independent of the total discharge injected in the district, represented in Fig. 2. Each outlet evacuates, for the three different cases, the same proportion of the total discharge.

All the outflows distribution results for case 3 are presented in Table 2. The differences observed with numerical simulations for other cases are in the same order. The Ansys-Fluent numerical results are much more close to the experiments than the Neptune 2D ones. Indeed, the difference between Fluent and the experimental results are frequently under 10 %, excepted for the streets 7 and G located at the southeast corner, characterized by small discharges. Errors made by using Neptune 2D appears to be more significants, as half of the differences with the experiments are over 10 %. Differences can reach −36 % in street G.

The outflow distribution has also to be considerated at the district scale. Indeed, the sum of the discharges for each side has also been compared to experimental

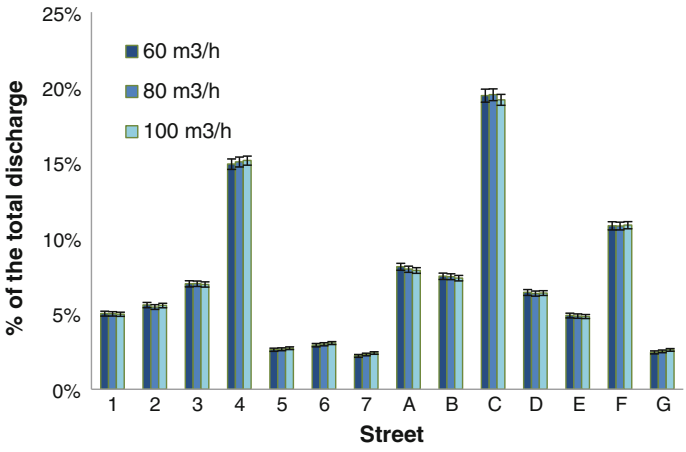

Fig. 2 Outflow distribution for the three experiments

Table 2 Outflows distribution by side for the three cases

Outflow	Exp. (m^3/h)	Fluent (m^3/h)	Difference (%)	Neptune 2D (m^3/h)	Difference (%)
1	4.9	4.6	−6	4.8	−3
2	5.5	5.4	0,2	5.7	3
3	6.9	7.3	4	7.4	8
4	15	16	5	16	7
5	2.7	2.8	7	2.3	−16
6	3.0	2.7	−11	2.4	−22
7	2.4	1.9	−19	1.8	−26
A	7.8	8.2	4	8.7	11
B	7.3	7.0	−5	7.4	0.5
C	19	20	4	22	13
D	6.3	5.6	−11	5.8	−8
E	4.8	4.2	−12	4.4	−8
F	11	11	0,7	10	−7
G	2.6	2.1	−18	1.7	−36

The discharges are in m^3 /h and the differences in %

data. They are presented for the three configurations in Table 3 and in Fig. 3. The total amount of the outflows is not the same for east side and south side. It is more important for the south, which is in agreement with the sum of the width of every street which is more important for this side. One can noticed that at the district scale, Neptune 2D and Ansys-Fluent calculations of the discharge on the sides are almost the same and accurate. Indeed, differences with experimental results are, for both softwares, around 1 %.

4.2 The Water Height

The water height was measured and compared to the numerical simulation in 600 points (see the Part 2.1). A top view of the water height in the experimental district is represented in Fig. 4. It can be noticed that it is maximal on the northwest corner at 14.1 cm for the case 3. It decreases in the district until the downstream streets are reached. The water height is transformed from potential energy to velocity as the flow rapidly accelerates. Some complex static waves appear. As water height was measured in only three points per streets, those static waves cannot show through.

The water-level evolution, represented in Fig. 5 for the street B, displays singular patterns: water level is almost constant in many streets but rapidly decreases at every crossroad. This particularity was observed for every street and for all experiments.

The differences of the free surface computed with both softwares with the experimental results are shown in Fig. 6. It can be noticed that qualitatively, the main feature of the water height repartition is correctly calculated. Fluent results

Table 3 Outflows comparison for the case 3

	Case 1					Case 2					Case 3				
Side	Exp.	3D	Dif.	2D	Dif.	Exp.	3D	Dif.	2D	Dif.	Exp.	3D	Dif.	2D	Dif.
East	24.35	24.53	−0.74	24.22	0.56	32.24	32.38	−0.45	32.26	−0.05	40.55	40.45	0.23	40.42	0.32
South	36.07	35.37	1.96	35.58	1.37	47.38	46.68	1.47	47.46	−0.17	58.71	58.29	0.71	59.71	−1.70

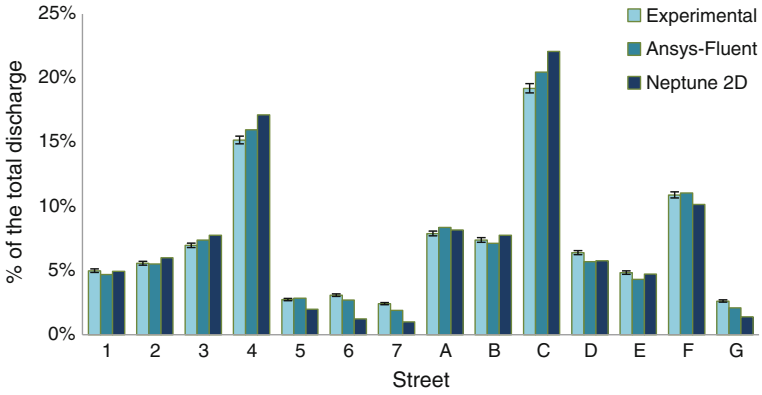

Fig. 3 Outflow distribution in every outflow street comparison with experimental results for case 3

Fig. 4 Water height measured for case 3

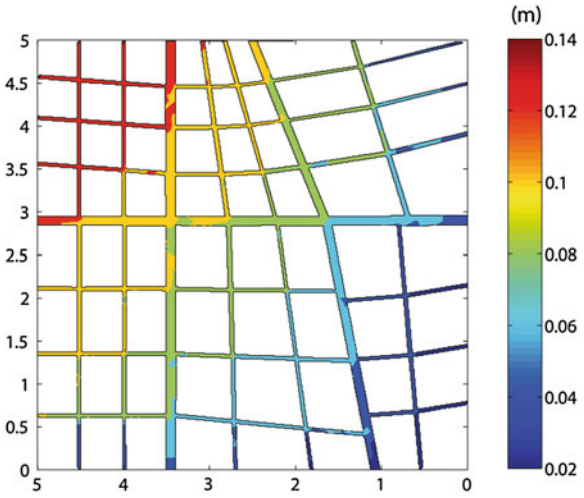

are more accurate with a difference with experimental results globally under 10 %. Neptune 2D software overestimates the water height in the upstream area of the district (with differences around 10 %) and underestimates the water height in the downstream area. The computed water level in the southeast corner is particularly low, with differences superior to 20 %. Figure 7 presents the comparison of the measured and the simulated water height at each measuring point for both softwares. It can be noticed for both softwares that the differences with experimental data are increasing as the water depth decreases. This can be explained by the complex static wave observed that are not correctly reproduced by the softwares. Moreover, the uncertainty of the measures is larger when the flow is faster and the free surface oscillates as it was observed in the downstream streets.

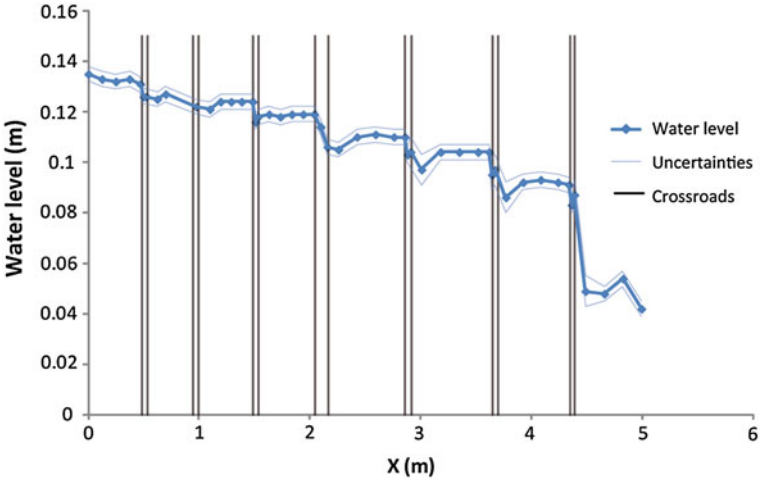

Fig. 5 Water-level evolution in street B for case 3

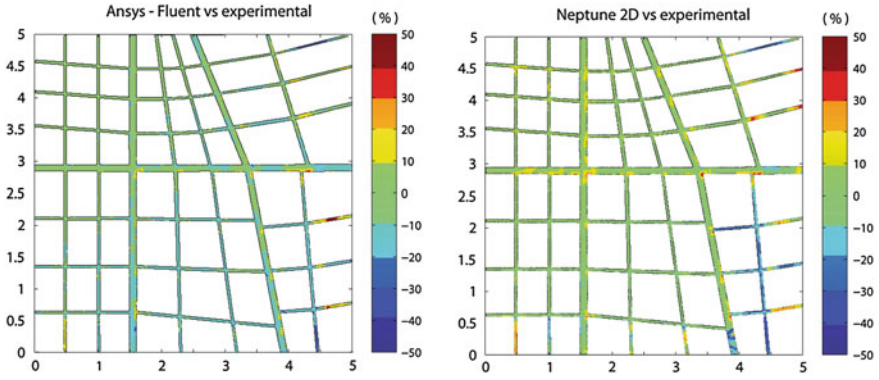

Fig. 6 Comparison of the experimental free surface with the one calculated with Ansys-Fluent (*left*) and the one calculated with Neptune 2D (*right*)

Figure 7 compares the experimental water-level evolution in street 4 to numerical simulations. The differences between experimental results and Ansys-Fluent and the uncertainties have the same order of magnitude. The water level computed by Neptune 2D in this street confirms previous observations. The sudden drop of the water level in the crossroads is computed as well as the constant water level between two crossroads, which shows the flow is qualitatively reproduced. Quantitatively, however, differences are observed. Water heights at the upstream of the street are overestimated.

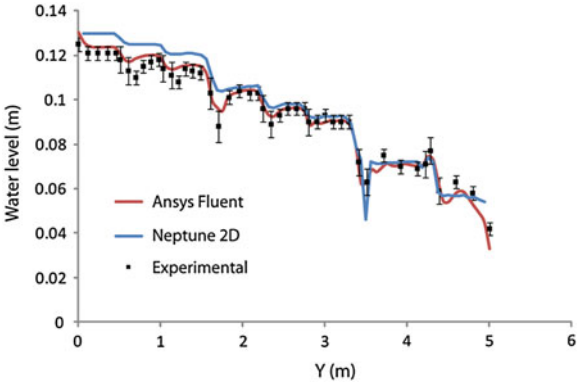

Fig. 7 Comparison of the experimental free surface in street 4 with the one calculated with Ansys-Fluent and the one calculated with Neptune 2D in case 3

4.3 Discussion

Ansys-Fluent results appear to be more accurate than the ones of Neptune 2D, especially regarding the discharge distribution at the street scale. The key differences between the softwares that could explain this observation are listed and require further exploration.

4.3.1 Turbulence

Ansys-Fluent takes into account the turbulence by using a k-ε model whereas the Eigenvector Reconstruction—Discontinuous Galerkin (EVR-DG) scheme only considers the friction using the Strickler formula. The turbulence may have a significant importance for the discharge distribution and the head loss at each crossroad. Therefore, the importance of these phenomena has to be more deeply studied at the crossroad scale, as well as the impact of the implementation of a turbulence model in the 2D software.

Moreover, the use of a turbulence model induces the modelization of turbulence diffusion. This enables the numerical software to homogenize the flow velocities downstream each crossroad. The absence of any diffusion term in the solved shallow water equations creates underestimation of natural diffusion which generates asymmetrical velocity profiles downstream each crossroad. Figure 8 represents the velocity profile downstream the crossroad between street C and 4. This assumption could also explain the shape of the recirculation zone calculated with Neptune 2D which is longer than the one calculated with Ansys-Fluent.

4.3.2 Hydrostatic Assumption

The shallow water equations assume the vertical pressure profile to be hydrostatic, which neglect vertical phenomena. This assumption has not been confirmed by the

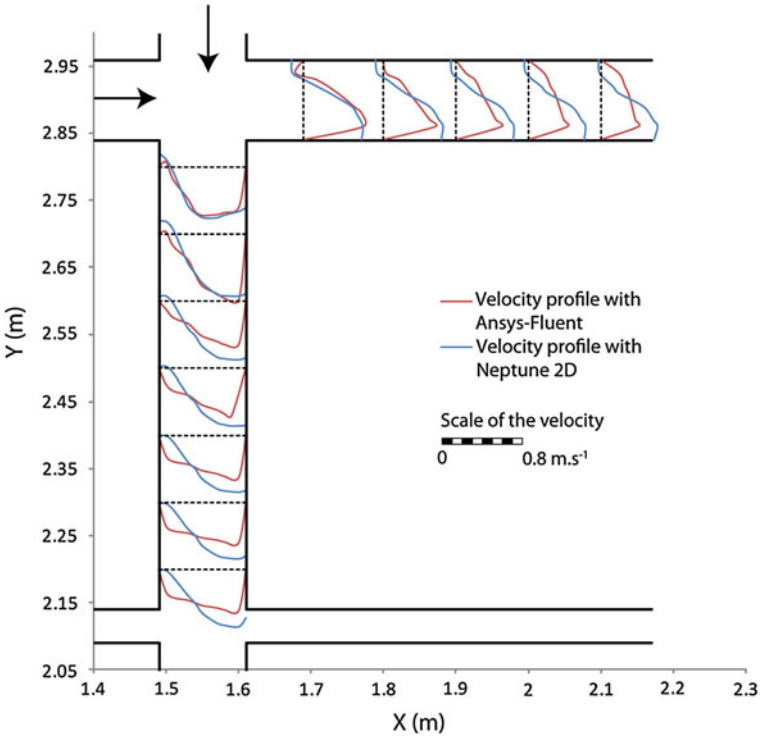

Fig. 8 Comparison of the velocity profiles computed with Ansys-Fluent and Neptune 2D at the crossroad between street 4 and C in case 3

experiments, as the pressure has not been measured on the district yet. However, the observation of the free-surface elevation at the crossroad indicates a rapid evolution that highlights a priori non-hydrostatic pressures. Fluent is a 3D software, taking into account z-direction velocities and therefore vertical phenomena. The comparison of the pressure field on the bottom calculated with Fluent and the hydrostatical pressure field (calculated using Ansys-Fluent water level) is presented in Fig. 9. It appears that the assumption of hydrostatic pressure seems to be verified almost everywhere, excepted in some crossroads of the larger streets. This observation may explain the poor Neptune 2D results regarding flow modelization of the southeast corner of the district. As pressures on the bottom in crossroads are not hydrostatics, particularly in the street F, the flow distributions computed with Neptune 2D (or any software solving the shallow water equations) can poorly match the experimental data. This could lead to underestimations of water discharges entering the southeast area. This could explains the low water level computed by Neptune 2D in this area as well as the under estimation of outflow water discharges of streets 5, 6, 7, and G.

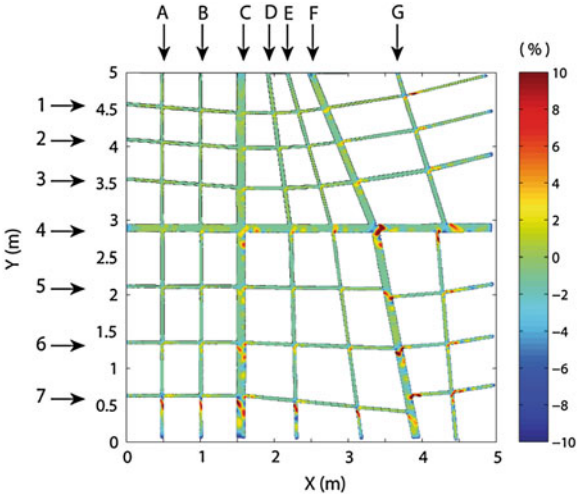

Fig. 9 Difference in percentage between the pressure field at the *bottom* and the hydrostatic pressure field calculated by Ansys-Fluent in case 3

5 Conclusion

The experimental results of steady flows in an urban physical model enabled the comparison with numerical tools. Two softwares, Ansys-Fluent® and Neptune 2D, were used to calculate the flows on the studied district. The comparison of the results in the same configuration leads to several conclusions:

1. Ansys-Fluent results allow for accurate results at 10 %. The differences on the water level between the numerical and the experimental results are under 10 %, excepted in the downstream streets, where the measure uncertainties are the most important. Regarding the water discharge in the streets, the differences are frequently under 10 %.
2. Neptune 2D results are less accurate than Ansys-Fluent ones, even though the water level computed appears to be generally under 10 %. Regarding the flow discharges at the streets scale, Neptune 2D differences with experimental results can reach up to 30 %. Two main assumptions are suggested to explain the software results. The lack of turbulence model may explain the asymmetries in the velocity profiles computed by Neptune 2D. Indeed, turbulence model usually generates turbulence diffusion which homogenized velocities in each street. Secondly, the pressure profile in some crossroad computed by Ansys-Fluent is not hydrostatic. This could highlight the shallow water equations limits, as they are built on this particular assumption. At the district scale, the side discharges calculated by Neptune 2D is very accurate, around 1 %.

The first experimental data presented in this paper suggests a global behavior of the district, at the district scale. The particular distribution of the water level, as well as the sides, discharges repartition is some interesting features that require further investigations.

Acknowledgments We would like to thank the Alsacian Network of Laboratory in Engineering and Environmental Sciences (REALISE) for the funding of the physical model as well as the numerous colleagues and PhD students fellows that worked hard on this project.

References

1. Mignot, E., Paquier, A., & Rivière, N. (2008). Experimental and numerical modeling of symmetrical four-branch supercritical. *Journal of Hydraulic Research, 46*, 723–738.
2. Nania, L., Gómez, M., & Dolz, J. (2004). Experimental study of the dividing flow in steep street crossings. *Journal of Hydraulic Research, 42*, 406–412.
3. Testa, G., Zuccala, D., Alcrudo, F., Mulet, J., & Soares-Frazão, S. (2007). Flash flood flow experiment in a simplified urban district. *Journal of Hydraulic Research, 45*, 37–44.
4. Ghostine, R., Kesserwani, G., Vazquez, J., Rivière, N., Ghenaim, A., & Mose, R. (2009). Simulation of supercritical flow in crossroads: Confrontation of a 2D and 3D numerical approaches to experimental results. *Computers and Fluids, 38*, 425–432.
5. Sanders, B., Schubert, J., & Gallegos, H. (2008). Integral formulation of shallow-water equations with anisotropic porosity for urban flood modeling. *Journal of Hydrology, 362*, 19–38.
6. Soares-Frazão, S., Lhomme, J., Guinot, V., & Zech, Y. (2008). Two-dimensional shallow-water model with porosity for urban flood modelling. *Journal of Hydraulic Research, 46*, 45–64.
7. Van Emelen, S., Soares-Frazão, S., Riahi-Nezhad, C., Chaudhry, M., Imran, J., & Zech, Y. (2012). Simulations of the New Orleans 17th street canal breach flood. *Journal of Hydraulic Research, 50*, 70–81.
8. Kouyi, G., Fraisse, D., Rivière, N., Guinot, V. & Chocat, B. (2008). 1D modelling of the interactions between heavy rainfall-runoff in urban area and flooding flows from sewer network and river. *11th International Conference on Urban Drainage.* Edinburgh, Scotland, UK.
9. Cockburn, B., & Shu, C.-W. (1998). The Runge-Kutta discontinuous Galerkin method for conservation laws V: multidimensional systems. *Journal of Computational Physics, 141*, 199–224.
10. Toro, E. (2001). *Shock-capturing methods for free-surface shallow flows*. New York: Wiley.
11. Araud, Q., Finaud-Guyot, P., Guinot, V., Mosé, R., & Vazquez, J. (2011). An Eigenvector-based linear reconstruction approach for time stepping in Discontinuous Galerkin scheme used to solve shallow water equations. *International Journal for Numerical Methods in Engineering, Accepted,*. doi:10.1002/fld.3645.
12. Fluent, I. (2002). *Fluent user's guide*. USA: Fluent Inc.
13. Dufresne, M., Vazquez, J., Terfous, A., Ghenaim, A., & Poulet, J. (2009). Experimental investigation and CFD modelling of flow, sedimentation, and solids separation in a combined sewer detention tank. *Computers and Fluids, 38*, 1042–1049.

FullSWOF: A Software for Overland Flow Simulation

Olivier Delestre, Stéphane Cordier, Frédéric Darboux, Mingxuan Du, François James, Christian Laguerre, Carine Lucas and Olivier Planchon

Abstract Le ruissellement sur les terres agricoles peut avoir des effets indésirables tels que l'érosion des sols, les inondations et le transport de polluants. Afin de mieux comprendre ce phénomène et d'en limiter les conséquences, nous avons développé un code à l'aide de méthodes numériques récentes : FullSWOF (Full Shallow Water equations for Overland Flow), un code orienté objet écrit en C++. Il est libre et peut

O. Delestre (✉)
Laboratoire J.A. Dieudonné & Polytech Nice – Sophia, UMR CNRS 7351 UNSA, 06108 Nice Cedex 02, France
e-mail: delestre@unice.fr

S. Cordier · F. James · C. Laguerre · C. Lucas
Laboratoire MAPMO—Fédération Denis Poisson, UMR CNRS 7349, Université d'Orléans, B.P. 6759 45067 Orléans Cedex 2, France
e-mail: stephane.cordier@math.cnrs.fr

F. James
e-mail: Francois.James@math.cnrs.fr

C. Laguerre
e-mail: christian.laguerre@math.cnrs.fr

C. Lucas
e-mail: carine.lucas@univ-orleans.fr

F. Darboux
Institut National de la Recherche Agronomique (INRA), UR 0272 Science du sol, Centre de recherche Val de Loire, CS 40001 45075 Orléans Cedex 2, France
e-mail: Frederic.Darboux@orleans.inra.fr

M. Du
Polytech Nice—Sophia, 930 Route des Colles, BP 145 06903 Sophia Antipolis Cedex, France
e-mail: mingxuanism@gmail.com

O. Planchon
Institut de Recherche pour le Développement (IRD), UMR Lisah, 2 Place Viala 34060 Montpellier Cedex 1, France
e-mail: olivier.planchon@gmail.com

P. Gourbesville et al. (eds.), *Advances in Hydroinformatics*, Springer Hydrogeology, DOI: 10.1007/978-981-4451-42-0_19,

être téléchargé à partir de http://www.univ-orleans.fr/mapmo/soft/FullSWOF/. Le modèle résout le système de Saint–Venant. Les difficultés numériques viennent des nombreuses transitions sec/mouillé et de la topographie très variable rencontrée sur le terrain. Le code intègre le ruissellement, les précipitations, l'infiltration (modèle de Green-Ampt), la friction (les lois de Darcy-Weisbach et de Manning). Nous présentons d'abord la méthode numérique pour la résolution des équations en eaux peu profondes integrée dans FullSWOF_2D (la version en deux dimensions). Cette méthode repose sur le schéma de reconstruction hydrostatique, couplée à un traitement semi-implite du terme de friction. FullSWOF_2D a déjà été validé à l'aide des solutions analytiques de la bibliothèque SWASHES. FullSWOF_2D est exécuté sur des données de terrain acquises sur une parcelle située à Thiès (Sénégal). Les résultats de la simulation sont comparés avec les données mesurées. Ce banc d'essai expérimental permet de démontrer les capacités de FullSWOF à simuler l'écoulement de surface. FullSWOF pourrait également être utilisé pour d'autres problèmes environnementaux, tels que les inondations fluviales et les ruptures de barrage.

Keywords Rainfall runoff · Shallow water system · Well-balanced scheme · Hydrostatic reconstruction · Finite volumes · Dry/wet transition · Green-Ampt model

1 Introduction

Rain on agricultural fields can yield to the occurrence of overland flow. At field scale, overland flow may have some undesirable effects such as soil erosion and pollutant transport. Downstream the watersheds, roads and houses may be damaged. Some control measures can be taken such as using grass strips. We have to know how the water is moving in order to put these developments. In overland flow prediction, several methods are used from black box models to physically based models. Two physical models are often used to model overland flow: kinematic (KW) and diffusive wave (DW) Eqs. [14, 15]. But following [1–3], we choose to use the shallow water (de Saint–Venant [4]) physical model. Indeed, KW and DW models may give poor results in terms of water heights and velocities in case of mixed subcritical and supercritical flow. In spite of computational time, SW is mandatory. MacCormack scheme is widely used to solve SW equations [1–3]. But it neither guarantees the positivity of water depths at the wet/dry transitions, nor preserves steady states (not well-balanced [5]) as noticed in [6]. In industrial codes (ISIS, Canoe, HEC-RAS, MIKE11…), SW equations are often solved under non-conservative form [7] with either Preissmann scheme or Abbott-Ionescu scheme. Thus, transcritical flows and hydraulic jumps are not solved properly. In order to cope with all these problems, we choose to use the hydrostatic reconstruction [8, 9]. This positive preserving well-balanced finite volume scheme is integrated in FullSWOF_2D. In what follows, we present the physical model,

and then the numerical methods. In the end, FullSWOF_2D is applied on a real event measured in Thiès by IRD [10].

2 The Model

2.1 The Shallow Water Equations

As in [1, 2], we consider the 2D shallow water equations (SW2D) which write (see Fig. 1a)

$$\begin{aligned} \partial_t h + \partial_x(hu) + \partial_y(hv) &= R - I \\ \partial_t(hu) + \partial_x\left(hu^2 + gh^2/2\right) + \partial_y(huv) &= gh\left(S_{0x} - S_{fx}\right) \\ \partial_t(hv) + \partial_x(huv) + \partial_y\left(hv^2 + gh^2/2\right) &= gh\left(S_{0y} - S_{fy}\right) \end{aligned} \tag{1}$$

where the unknowns are the velocities $u(x, y, t)$ and $v(x, y, t)$ [m/s] and the water height $h(x, y, t)$ [m]. The subscript x and y stands for the x-direction and y-direction, respectively: $S_{0x} = -\partial_x z(x, y)$ and $S_{0y} = -\partial_y z(x, y)$ are the ground slopes, S_{fx} and S_{fy} are friction terms. $R(x, y, t)$[m/s] is the rainfall intensity, and $I(x, y, t)$[m/s] is the infiltration rate. As in [1], we use the Darcy-Weisbach friction law which writes

$$S_{fx} = f\frac{u\sqrt{u^2+v^2}}{8gh}, \quad S_{fy} = f\frac{v\sqrt{u^2+v^2}}{8gh} \tag{2}$$

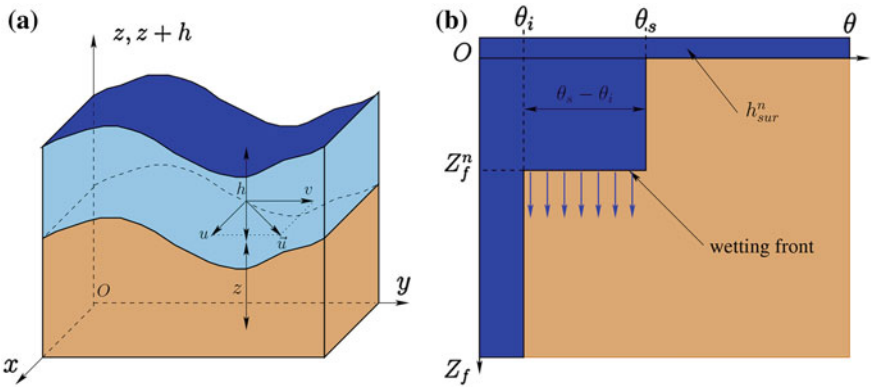

Fig. 1 Illustration of variables of **a** shallow water equations (SW2D) and **b** Green-Ampt infiltration model

2.2 The Green-Ampt Infiltration Model

Infiltration is computed at each cell using a modified version of the Green-Ampt model [1, 11, 12]. With this model, the movement of water in soil is assumed to be in the form of an advancing wetting front (located at Z_f^n[m]) that separates a zone still at the initial soil moisture θ_s (see Fig. 1b). At the moment $t = t_n$, the infiltration capacity I_C^n[m/s] is calculated thanks to

$$I_C^n = K_s\left(1 + \frac{h_f - h_{\text{sur}}^n}{Z_f^n}\right) \quad \text{where} \quad Z_f^n = \frac{V_{\text{inf}}^n}{\theta_s - \theta_i}, \tag{3}$$

where h_f is the wetting front capillary pressure head, K_s the hydraulic conductivity at saturation, h_{sur}^n the water height, and V_{inf}^n the infiltrated water volume. Thus, we have the infiltration rate

$$I^n = \frac{\min\left(h_{\text{sur}}^n, \Delta t \cdot I_C^n\right)}{\Delta t} \tag{4}$$

and the infiltrated volume

$$V_{\text{inf}}^{n+1} = V_{\text{inf}}^n + \Delta t \cdot I^n, \tag{5}$$

where Δt is the time step. In the case of a two-layer soil, we consider a modification of this model (see [1, 13]).

3 The Numerical Method

The scheme is presented in one dimension (SW1D)

$$\begin{aligned} \partial_t h + \partial_x(hu) &= R - I \\ \partial_t(hu) + \partial_x\left(hu^2 + gh^2/2\right) &= gh\left(S_{0x} - S_{fx}\right). \end{aligned} \tag{6}$$

This is the one integrated in FullSWOF_1D. The one-dimensional version of FullSWOF has been developed for teaching, academical research, and numerical development purposes. The extension of the 1D numerical method to SW2D on structured grid is straightforward and is integrated in FullSWOF_2D. The two codes FullSWOF_1D and FullSWOF_2D are an object-oriented C++ codes (free software and GPL-compatible license CeCILL-V2, source code available at http://www.univ-orleans.fr/mapmo/soft/FullSWOF/) developed in the framework of the project ANR METHODE (for details about the codes see [13, 14]). FullSWOF is structured in order to ease the implementation of new numerical methods and physical models.

In what follows, we note the discharge $q = hu$ [m^2/s] and the vector of conservative variables $U = {}^t(h \quad hu)$.

3.1 Convective Step

A finite volume discretization of SW1D writes

$$U_i^* = U_i^n - \frac{\Delta t}{\Delta x}\left[F_{i+1/2L}^n - F_{i-1/2R}^n - Fc_i^n\right] \tag{7}$$

with Δx the space step, Δt the time step, and

$$\begin{aligned} F_{i+1/2L}^n &= F_{i+1/2}^n + S_{i+1/2L}^n \\ F_{i-1/2R}^n &= F_{i-1/2}^n + S_{i-1/2R}^n \end{aligned} \tag{8}$$

the left and right modifications of the numerical flux Fl for the homogeneous problem, respectively (see the Sect. 3.3), with

$$F_{i+1/2}^n = Fl\Big(U_{i+1/2L}^n, U_{i+1/2R}^n\Big). \tag{9}$$

The values $U_{i+1/2L}$ and $U_{i+1/2R}$ are obtained thanks to two consecutive reconstructions. Firstly, a MUSCL reconstruction [9, 13] is performed on u, h and $h+z$ in order to get a second-order scheme in space. This gives us the reconstructed values (U_-, z_-) and (U_+, z_+). Secondly, we apply the hydrostatic reconstruction [8, 9] on the water height which allows us to get a positive preserving well-balanced scheme (in the sense that it preserves at least steady states at rest)

$$\begin{aligned} h_{i+1/2L} &= \max\big(h_{i+1/2-} + z_{i+1/2-} - \max\big(z_{i+1/2-}, z_{i+1/2+}\big), 0\big) \\ U_{i+1/2L} &= {}^t\big(h_{i+1/2L}, h_{i+1/2L}u_{i+1/2-}\big) \\ h_{i+1/2R} &= \max\big(h_{i+1/2+} + z_{i+1/2+} - \max\big(z_{i+1/2-}, z_{i+1/2+}\big), 0\big) \\ U_{i+1/2R} &= {}^t\big(h_{i+1/2R}, h_{i+1/2R}u_{i+1/2+}\big) \end{aligned}. \tag{10}$$

We introduce

$$S_{i+1/2L}^n = \begin{pmatrix} 0 \\ \frac{g}{2}\left(h_{i+1/2-}^2 - h_{i+1/2L}^2\right) \end{pmatrix}, \quad S_{i-1/2R}^n = \begin{pmatrix} 0 \\ \frac{g}{2}\left(h_{i-1/2+}^2 - h_{i-1/2R}^2\right) \end{pmatrix} \tag{11}$$

and a centered source term is added to preserve consistency and well-balancing (see [8, 9])

$$Sc_i = \begin{pmatrix} 0 \\ -g\frac{h_{i-1/2+}+h_{i+1/2-}}{2}\left(z_{i+1/2-} - z_{i-1/2+}\right) \end{pmatrix}. \tag{12}$$

We have to insist on the positivity and the robustness of this method. But, let us mention that such method requires some condition on the mesh size compared with mean water height (see [15]). The rain and the infiltration are treated explicitly (for details see [13]).

3.2 Friction Treatment

In this step, the friction term is taken into account with the following system

$$\partial_t U = \begin{pmatrix} 0 \\ -ghS_f \end{pmatrix}. \tag{13}$$

This system is solved thanks to a semi-implicit method (as in [2, 16])

$$\begin{aligned} h^{n+1} &= h^* \\ q^{n+1} &= \frac{q^*}{1 + \Delta t \frac{f}{8} \frac{|q^n|}{h^n h^{n+1}}}. \end{aligned} \tag{14}$$

where h^*, q^* and u^* are the variables from the convective step. This method allows to preserve stability (under a classical CFL condition) and steady states at rest. Finally, these two steps are combined in a second-order TVD Runge–Kutta method which is the Heun's predictor–corrector method. It writes

$$\begin{aligned} U^* &= U^n + \Delta t \Phi(U^n) \\ U^{**} &= U^* + \Delta t \Phi(U^*) \\ U^{n+1} &= \frac{U^n + U^{**}}{2} \end{aligned}, \tag{15}$$

where Φ is the right part of (7).

3.3 Numerical Flux

We use the HLL flux [9, 13] which writes

$$Fl(U_L, U_R) = \begin{array}{ll} F(U_L) & \text{if} \quad 0 < c_1 \\ \dfrac{c_2 F(U_L) - c_1 F(U_R)}{c_2 - c_1} + \dfrac{c_1 c_2}{c_2 - c_1}(U_R - U_L) & \text{if} \quad c_1 < 0 < c_2 \\ F(U_R) & \text{if} \quad c_2 < 0 \end{array}, \tag{16}$$

with two parameters $c_1 < c_2$ given by

$$c_1 = \min_{U=U_L,U_R} \left(\min_{j\in\{1,2\}} \lambda_j(U) \right), \quad c_2 = \max_{U=U_L,U_R} \left(\max_{j\in\{1,2\}} \lambda_j(U) \right), \tag{17}$$

where $\lambda_1(U) = u - \sqrt{gh}$ and $\lambda_2(U) = u + \sqrt{gh}$ are the eigenvalues of SW1D. In practice, we use a CFL condition $n_{\text{CFL}} = 0.5$ at second order and $n_{\text{CFL}} = 1$ at first order, with

$$\Delta t \leq n_{\mathrm{CFL}} \frac{\Delta x}{\max\limits_{i \in 1,\mathrm{Nx}} (|u_i| + \sqrt{\mathrm{g}h_i})}, \tag{18}$$

where Nx is the number of space cells. At second order, variables (h_i, u_i) in (18) are replaced by the reconstructed values $\left(h_{i+1/2-}, u_{i+1/2-}\right)$ and $\left(h_{i+1/2+}, u_{i+1/2+}\right)$ (detailed in the next section).

3.4 MUSCL Reconstruction

We define the MUSCL reconstruction of a scalar function $s \in \mathrm{R}$ [17] by

$$s_{i-1/2+} = s_i - \tfrac{\Delta x}{2} Ds_i, \quad s_{i+1/2-} = s_i + \tfrac{\Delta x}{2} Ds_i\,, \tag{19}$$

with the operator

$$Ds_i = \mathrm{minmod}\Big(\frac{s_i - s_{i-1}}{\Delta x}, \frac{s_{i+1} - s_i}{\Delta x}\Big), \tag{20}$$

and the minmod limiter

$$\mathrm{minmod}(x,y) = \begin{array}{lll} \min(x,y) & if & x,y \geq 0 \\ \max(x,y) & if & x,y \leq 0 \\ 0 & & \text{else} \end{array} \tag{21}$$

As mentioned previously, the MUSCL reconstruction is performed on u, h and $h + z$ then we deduce the reconstruction of z. In order to keep the discharge conservation, the reconstruction of the velocity has to be modified as what follows

$$u_{i-1/2+} = u_i - \frac{h_{i+1/2-}}{h_i} \frac{\Delta x}{2} Du_i, \quad u_{i+1/2-} = u_i + \frac{h_{i-1/2+}}{h_i} \frac{\Delta x}{2} Du_i\,. \tag{22}$$

4 Validation

FullSWOF_2D has already been validated on analytic solutions integrated in Shallow Water Analytic Solutions for Hydraulic and Environmental Studies (SWASHES) a free library of analytic solutions written in object-oriented ISO C++ [18, 19]. The purpose of this section is to confront FullSWOF_2D to a real system: the plot of Thiès, Senegal [10]. The results presented below are the results preliminary to a more detailed study. They simply aim at illustrating the ability of FullSWOF_2D to simulate a dynamic runoff on real data without any preprocessing.

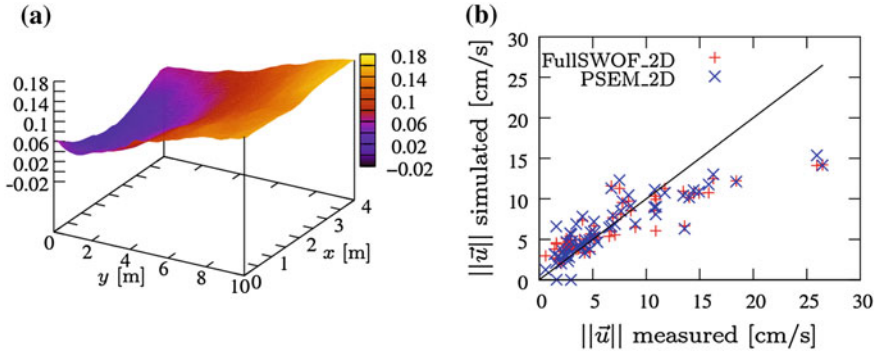

Fig. 2 **a** The topography of the experimental plot of land and **b** comparison between measured and simulated velocities

4.1 Experimental Data

Thiès (Senegal) is the location of a plot of land equiped with an experimental system instrumented by IRD [10] in the project PNRH RIDES. The experiment consisted of a two-hour artificial rainfall on a sandy-soil plot of 4-by-10 m^2 (Fig. 2a). The plot had the classical configuration of Wooding's open book, with 1 % slope along (Ox) and (Oy) axes. Several experiments have been carried out to test the salt velocity gauge [20] (a new measurement technique) and to study the dynamics of runoff and erosion. The set of measures considered consists of flow measurements at the outlet and flow velocities measured at 63 locations in the plot. These data have been used to compare different computer codes: NCF and MAHLERAN (based on KW), RillGrow (based on DW) and PSEM_2D (based on SW2D with MacCormack scheme). The data set is freely available at http://www.umr-lisah.fr/Thies_2004/. In the following, we have used the set of parameters obtained with PSEM_2D and we have observed the sensitivity to infiltration parameters.

4.2 Numerical Results

For all the simulations, we have used $\Delta x = \Delta y = 0.1\,\text{m}$ as space steps and $f = 0.26$ as Darcy-Weisbach friction coefficient. The average rain intensity was 70 mm/h during two hours. Infiltration parameters used with PSEM_2D [10] were $h_f = 0.06\,\text{m}$, $\theta_s - \theta_i = 0.12$ and $K_s = 4.4e^{-6}$ m/s. We tried this set of parameters. We noticed that the simulated velocities with FullSWOF_2D are close to those obtained with PSEM_2D (Fig. 2b). Small flow-velocities are well caught, contrary to the bigger values. In the latter case, values are underestimated both by FullSWOF_2D and PSEM_2D. This means that the friction law is not adapted to this

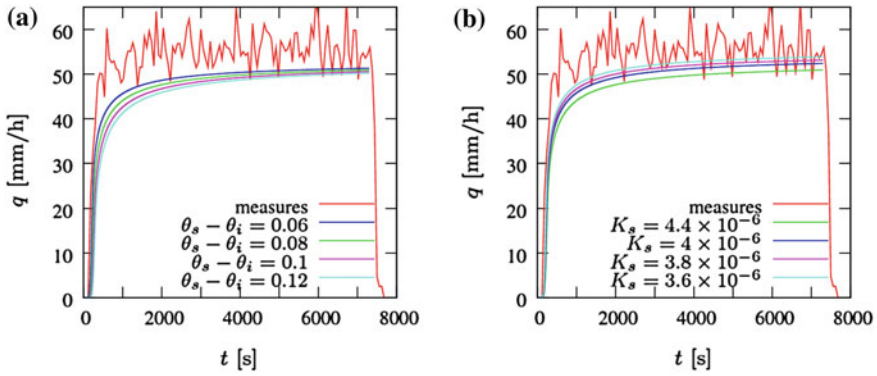

Fig. 3 Comparison between simulated hydrographs and measures **a** for several values of $\theta_s - \theta_i$ and **b** K_s

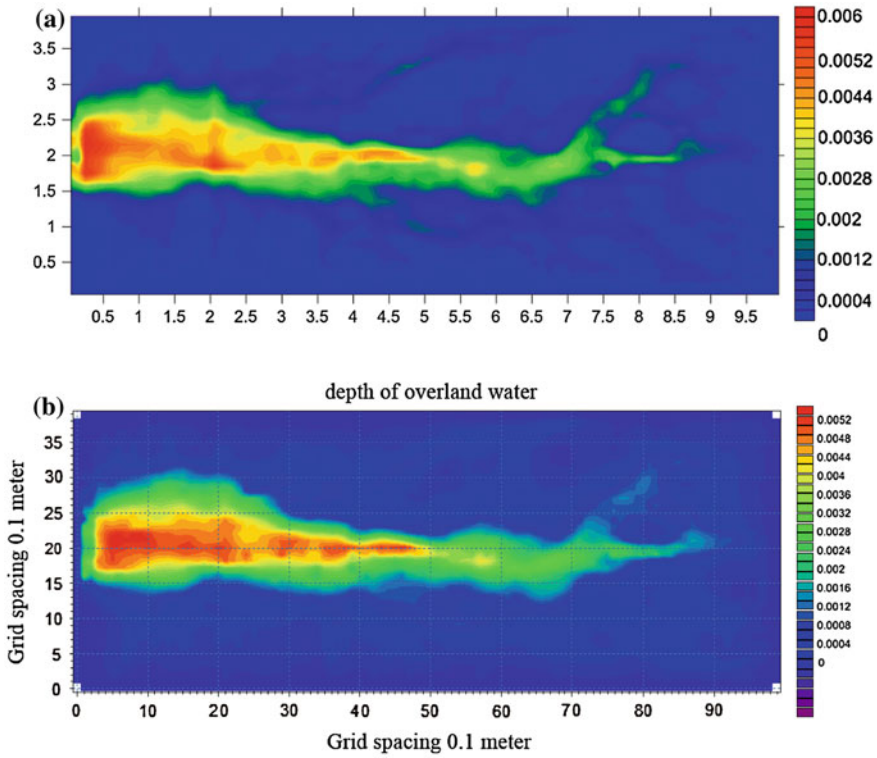

Fig. 4 Comparison between the water heights obtained with **a** FullSWOF_2D and **b** MIKE SHE

simulation. Moreover, we noticed that the simulated hydrographs are below the measured one. Thus, we have tried other values for $\theta_s - \theta_i$ and K_s. We kept H_f unchanged. We tried different values of K_s without changing $\theta_s - \theta_i$, and vice-versa. We noticed that decreasing $\theta_s - \theta_i$ improved mainly the beginning of the hydrograph (Fig. 3a), while decreasing K_s improved the entire hydrograph (Fig. 3b). We noticed that the saturated hydraulic conductivity K_s is the most influent parameter, as observed in [21], which is on the impact of this parameter on the surface runoff.

Moreover, we have performed the simulation of this event on the integrated hydrological modeling system: MIKE SHE by DHI. This software is widely used for overland flow simulation; thus, it might be used as a reference. In this software, the overland flow is calculated using a finite difference method using the DW approximation coupled with the one-dimensional Richards' equation [22] for the infiltration. Thus, it is an approximation of the physical model included in FullSWOF_2D. We notice that FullSWOF_2D gives water heights very close to those obtained with MIKE SHE (Fig. 4).

This work is still in progress, and we will have to do more complete comparison between FullSWOF, measured data, and other software.

5 Conclusions

FullSWOF is a freely available object-oriented code designed to simulate overland flow on agricultural fields. This code is based on the shallow water system. The numerical difficulties such as dry/wet transitions and steady states are dealt with using up-to-date numerical methods. FullSWOF gave good results on real data. Nevertheless, the physical model has to be improved to catch more accurately the measured velocities.

Acknowlegments This work was partially supported by ANR grant "METHODE" #ANR-07-BLAN-0232.

REFERENCES AND CITATIONS

1. Esteves, M., Faucher, X., Galle, S., & Vauclin, M. (2000). Overland flow and infiltration modelling for small plots during unsteady rain: numerical results versus observed values. *Journal of Hydrology, 228*, 265–282.
2. Fiedler, F. R., & Ramirez, J. A. (2000). A numerical method for simulating discontinuous shallow flow over an infiltrating surface. *International Journal of Numerical Methods in Fluids, 32*, 219–240.
3. Zhang, W., & Cundy, T. W. (1989). Modeling of two-dimensional overland flow. *Water Resources Research, 25*, 2019–2035.
4. de Saint-Venant, A. J.-C. (1871). Théorie du mouvement non-permanent des eaux, avec application aux crues des rivières et à l'introduction des marées dans leur lit. *Comptes Rendus de l'Académie des Sciences, 73*, 147–154.

5. Greenberg, J. M., & LeRoux, A.-Y. (1996). A well-balanced scheme for the numerical processing of source terms in hyperbolic equation. *SIAM Journal on Numerical Analysis, 33*, 1–16.
6. Rousseau, M., Cerdan, O., Delestre, O., Dupros, F., James, F., & Cordier, S. (submitted). Overland flow modelling with Shallow Water Equation using a well balanced numerical scheme: Adding efficiency or just more complexity ?, Available on http://hal.archives-ouvertes.fr/hal-00664535.
7. Novak, P., Guinot, V., Jeffrey, A., & Reeve, D.E. (2010). Hydraulic modelling—an Introduction. Spoon Press.
8. Audusse, E., Bouchut, F., Bristeau, M.-O., Klein, R., & Perthame, B. (2004). A fast and stable well-balanced scheme with hydrostatic reconstruction for shallow water flows. *Journal on Scientific Computing, 25*(6), 2050–2065.
9. Bouchut, F. (2004). *Nonlinear stability of finite volume methods for hyperbolic conservation laws, and well-balanced schemes for sources*. Frontiers in Mathematics: Birkhauser.
10. Tatard, L., Planchon, O., Wainwright, J., Nord, G., Favis-Mortlock, D., Silvera, N., et al. (2008). Measurement and modelling of high-resolution flow-velocity data under simulated rainfall on a low-slope sandy soil. *Journal of Hydrology, 348*, 1–12.
11. Green, W. H., & Ampt, G. A. (1911). Studies on soil physics. *The Journal of Agricultural Science, 4*, 1–24.
12. Rousseau, M. (2008). *Modélisation des écoulements à surface libre : étude du ruissellement des eaux de pluie*. Master thesis Université de Nantes, available on http://dumas.ccsd.cnrs.fr/dumas-00494243/fr/.
13. Delestre, O. (2010). *Simulation du ruissellement d'eau de pluie sur des surfaces agricoles*. (PhD thesis, Université d'Orléans, 2010). Available on http://tel.archives-ouvertes.fr/INSMI/tel-00531377/fr.
14. Delestre, O. (2008). *Ecriture d'un code C++ pour la simulation en hydrologie*. (Master thesis Université d'Orléans, 2008). Available on http://dumas.ccsd.cnrs.fr/dumas-00446163/fr/.
15. Delestre, O., Cordier, S., Darboux, F. & James, F. (2012). A limitation of the hydrostatic reconstruction technique for Shallow Water equations, *C. R. Acad. Sci. Paris,Ser. I*, http://dx.doi.org/10.1016/j.crma.2012.08.004.
16. Bristeau, M.-O., & Coussin, B. (2001). Boundary conditions for the shallow water equations solved by kinetic schemes. Inria report RR-4282.
17. van Leer, B. (1979). Towards the ultimate conservative difference scheme. V. A seond-order sequel to Godunov's method. *Journal of Computational Physics, 32*(1), 101–136.
18. Delestre, O., Lucas, C., Ksinant, P.-A., Darboux, F., Laguerre, C., Vo, T.N.T., James, F., & Cordier, S. (2013). SWASHES: a compilation of Shallow Water Analytic Solutions for Hydraulic and Environmental Studies. *International Journal of Numerical Methods in Fluids*, *72*(3), 269–300. doi: 10.1002/fld.3741.
19. Delestre, O., Lucas, C., Ksinant, P.-A., Darboux, F., Laguerre, C., James, F., & Cordier, S. (2014). SWASHES: a library for benchmarking in hydraulics/SWASHES : Une bibliothèque de bancs d'essai en hydraulique. To be published in *Proceedings of SimHydro 2012,* Polytech'Nice Sophia, Sophia-Antipolis: France, 2012. Advances in Hydroinformatics—SimHydro 2012: Springer. doi: 10.1007/978-981-4451-42-0_20.
20. Planchon, O., Silvera, N., Gimenez, R., Favis-Mortlock, D., Wainwright, J., Le Bissonnais, Y., et al. (2005). An automated salt-tracing gauge for flow-velocity measurement. *Earth Surface Processes and Landforms, 30*, 833–844.
21. Rousseau, M., Cerdan, O., Ern, A., Le Maître, O., & Sochala, P. (2012). A study of overland flow with uncertain infiltration using stochastic tools. *Advances in Water Resources, 38*, 1–12.
22. Richards, L. A. (1931). Capillary conduction of liquids through porous mediums. *Physics, 1*, 318–333.

SWASHES: A Library for Benchmarking in Hydraulics

Olivier Delestre, Carine Lucas, Pierre-Antoine Ksinant, Frédéric Darboux, Christian Laguerre, François James and Stéphane Cordier

Abstract De nombreux codes sont en cours d'élaboration pour résoudre les équations de Saint–Venant. Parce qu'elles sont utilisées dans les études hy-drau-li-ques et environnementales, leur capacité à simuler correctement les flux en eau est indispensable afin de préserver les infrastuctures et la sécurité humaine. Par conséquent, la validation de ces codes et des méthodes numériques associées est un problème essentiel. Des solutions analytiques de référence constitueraient une excellente réponse à ces questions. Toutefois, les solutions analytiques aux équations de Saint–Venant sont rares. Et surtout, elles ont été publiées sur une période de plus de cinquante ans, ce qui fait qu'elles sont dispersées à travers la

O. Delestre (✉)
Laboratoire J.A. Dieudonné & Polytech Nice–Sophia, UMR CNRS 7351 UNSA, 06108 Nice Cedex 02, France
e-mail: delestre@unice.fr

C. Lucas
Laboratoire MAPMO–Fédération Denis Poisson, UMR CNRS 7349, Université d'Orléans, B.P. 6759 45067 Orléans Cedex 2, France
e-mail: carine.lucas@univ-orleans.fr

P.-A. Ksinant · F. Darboux
Institut National de la Recherche Agronomique (INRA), UR 0272 Science du sol, Centre de recherche d'Orléans, CS 40001 45075 Orléans Cedex 2, France
e-mail: Pierre-Antoine.Ksinant@orleans.inra.fr

F. Darboux
e-mail: Frederic.Darboux@orleans.inra.fr

C. Laguerre · F. James · S. Cordier
Laboratoire MAPMO–Fédération Denis Poisson, UMR CNRS 7349 Université d'Orléans, B.P. 6759 45067 Orléans Cedex 2, France
e-mail: christian.laguerre@math.cnrs.fr

F. James
e-mail: Francois.James@math.cnrs.fr

S. Cordier
e-mail: stephane.cordier@math.cnrs.fr

P. Gourbesville et al. (eds.), *Advances in Hydroinformatics*,
Springer Hydrogeology, DOI: 10.1007/978-981-4451-42-0_20,

littérature. Dans cet article, un nombre important de solutions analytiques aux équations de Saint–Venant est décrit dans un formalisme unifié. Elles englobent une grande variété de conditions d'écoulement (supercritique, sous-critique, choc…), en une ou deux dimensions d'espace, avec ou sans frottement, pluie et topographie, pour des écoulements transitoires ou à l'état stationnaire. Une caractéristique originale est que les codes source correspondants sont mis gratuitement à disposition de la communauté (http://www.univ-orleans.fr/mapmo/soft/SWASHES), afin que les utilisateurs de modèles en eaux peu profondes puissent facilement trouver un banc d'essai adaptable pour valider leurs méthodes numériques.

Keywords Shallow water equation · Saint–Venant system · Analytic solutions · Benchmarking · Validation of numerical methods · Steady-state flow · Transitory flow · Source terms

1 Introduction

Nowadays, shallow water equations are widely used to model flows in various contexts, such as overland flow [1, 2], rivers [3, 4], flooding [5, 6], dam breaks [7, 8], near shore [9, 10], tsunami [11–13]. This system of partial differential equations (PDEs), proposed by Adhémar Barré de Saint–Venant in 1871 to model flows in a channel [14], consists in a system of conservation laws describing the evolution of the height and mean velocity of the fluid.

In real situations (realistic geometry, sharp spatial or temporal variations in the parameters), it is impossible to give an analytic formula for the solutions of this system of PDEs. Thus, there is a necessity to develop specific numerical schemes to compute approximate solutions for these PDEs [15–17]. Implementation of such methods implies a subsequent step of code validation.

Validation of a model (that is, the equations, the numerical methods and their implementation) is essential to know if it describes suitably the considered phenomena. At least three complementary kinds of numerical tests help us ensure that a numerical code is suitable for the considered system of equations. First, we can perform convergence or stability analysis (e.g. by refining the mesh). But this validates only the numerical method and its implementation. Second, approximate solutions can be compared with analytic solutions available for some simplified or specific cases. Finally, numerical results can be applied on experimental data, produced indoor or outdoor. This step should be done after the previous two; it is the most difficult one and must be validated by a specialist of the domain. In [18], we have focused on the second approach.

In numerical code validation, analytic solutions seem to be underused. We think that there are two possible reasons. First, each analytic solution has a limited scope in terms of flow conditions. Second, as they are dispersed through the literature, they are difficult to find. However, an important number of published analytic solutions allow us to embrace a wide range of flow conditions. Thus, overall, the existing analytic solutions have a large potential for numerical code validation. In the literature, we can find benchmarks for hydraulic river modelling software [19]. But they are too specific (weirs, pump, culverts… treatment validation), and there are too few tests available for numerical methods for shallow water equations.

In Ref. [18], we have tried to overcome these problems both by gathering a significant set of analytic solutions and by providing the corresponding source codes. Reference [18] describes the analytic solutions and gives some comments about their use and advantage. The source codes are freely available through the Shallow Water Analytic Solutions for Hydraulic and Environmental Studies (SWASHES) library. With SWASHES software, we do not pretend to list all existing analytic solutions. Indeed, SWASHES is a framework to which users are invited to contribute by sending other analytic solutions together with the dedicated code.

The chapter is organized as follows: in Sect. 2, we briefly present the notations we use and the main properties of shallow water equations. In Sect. 3, we will focus on stationary solutions which are well known by the hydraulics community but much less by mathematicians, that is, "backwater curves". Lastly, in Sect. 4, we will present SWASHES and the interest of solutions described in [18].

2 Equations, Notations and Properties

In the first section, we give the "complete" shallow water system in two space dimensions, that is, with topography, rain, infiltration, soil friction and viscous term. Then, we give this system in one space dimension and its main properties are recalled.

2.1 General Settings

The Shallow-Water equations in two space dimensions take the following form:

$$\begin{aligned}
\partial_t h + \partial_x(hu) + \partial_y(hv) &= R - I \\
\partial_t(hu) + \partial_x\left(hu^2 + \frac{gh^2}{2}\right) + \partial_y(huv) &= gh\left(S_{O_x} - S_{f_x}\right) + \mu S_{d_x} \\
\partial_t(hv) + \partial_x(huv) + \partial_y\left(hu^2 + \frac{gh^2}{2}\right) &= gh\left(S_{O_y} - S_{f_y}\right) + \mu S_{d_y}
\end{aligned}, \qquad (1)$$

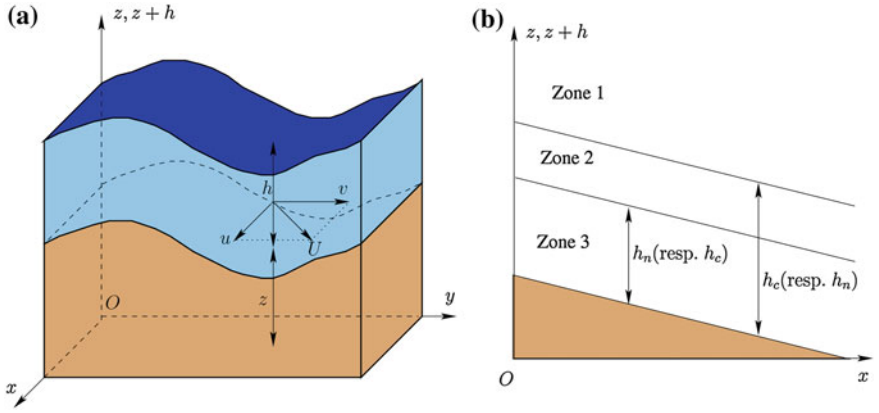

Fig. 1 Illustration of variables of **a** shallow water equations and **b** zones for classification of free surface profiles

where the unknowns of the model are the water height ($h(t,x,y)$[L]) and $u(t,x,y)$, $v(t,x,y)$ the horizontal components of the vertically averaged velocity $[L/T]$ (Fig. 1a) and $g = 9.81\,\mathrm{m/s^2}$ is the gravity constant. The first equation is the mass conservation equation. The other two equations are the momentum conservation equations; they involve forces such as gravity and friction. We give now a short description of all the terms with their physical dimensions.

- z is the topography $[L]$, since erosion is not considered here, it depends only on space, $z(x,y)$, and S_{O_x} (resp. S_{O_y}) is the opposite of the slope in the x (resp. y) direction, $S_{O_x} = -\partial_x z(x,y)$ (resp. $S_{O_y} = -\partial_y z(x,y)$);
- $R \geq 0$ is the rain intensity $[L/T]$, and it is a given function $R(t,x,y) \geq 0$. In [20], it is considered uniform in space;
- I is the infiltration rate $[L/T]$. It is given by another model (such as Horton, Philip, Green-Ampt, Richards …) and is not taken into account in the following;
- $S_f = \left(S_{f_x}, S_{f_y}\right)$ is the friction force/law and may take various forms, depending on both soil and flow properties. In the formulas below, U is the velocity vector, $U = (u,v)$ with $|U| = \sqrt{u^2+v^2}$ and Q is the discharge $Q = (hu, hv)$. In hydrological models, two families of friction laws are encountered based on empirical considerations. On the one hand, we have the family of Manning–Strickler's friction laws

$$S_f = C_f \frac{U|U|}{h^{4/3}} = C_f \frac{Q|Q|}{h^{10/3}} \tag{2}$$

$C_f = n^2$, where n is the Manning's coefficient $\left[L^{-1/3}T\right]$.
On the other hand, the laws of Darcy–Weisbach's and Chézy's family write

$$S_f = C_f \frac{U|U|}{h} = C_f \frac{Q|Q|}{h^3} \tag{3}$$

With $C_f = f/(8g)$, f a dimensionless coefficient (resp. $C_f = 1/C^2, C\left[L^{1/2}/T\right]$), we get the Darcy–Weisbach's (resp. Chézy's) friction law. Notice that the friction may depend on the space variable, especially for large areas. In the following this will not be considered.

- finally, $\mu S_d = \left(\mu S_{d_x}, \mu S_{d_y}\right)$ is the viscous term with $\mu \geq 0$ the viscosity of the fluid $[L^2/T]$.

2.2 Properties

In this section, some properties of the shallow water model are recalled. These properties are useful to the flow description. To simplify, we consider the one-dimensional model, but extensions to two dimensions are straightforward. The 2D shallow water system (1) rewrites

$$\begin{aligned} \partial_t h + \partial_x(hu) &= R - I \\ \partial_t(hu) + \partial_x\left(hu^2 + \frac{gh^2}{2}\right) &= gh\left(S_{O_x} - S_f\right) + \mu\partial_x(h\partial_x u) \end{aligned}. \tag{4}$$

The left-hand side of this system is the transport part of the model. It corresponds to the flow of an ideal fluid in a flat channel, without friction, rain or infiltration. It is in fact the model introduced by Saint–Venant in [14]. Several important properties of the flow are included in this model. The one-dimensional equations are rewritten using vectors' form, in order to highlight these properties:

$$\partial_t W + \partial_x F(W) = 0, \text{ where } W = \begin{pmatrix} h \\ hu \end{pmatrix}, F(W) = \begin{pmatrix} hu \\ hu^2 + \frac{gh^2}{2} \end{pmatrix}, \tag{5}$$

with $F(W)$ the flux of the equation. With the following nonconservative form, where $A(W) = F'(W)$ is the jacobian matrix or the matrix of transport coefficients

$$\partial_t W + A(W)\partial_x W = 0, \text{ with } A(W) = F'(W) = \begin{pmatrix} 0 & 1 \\ -u^2 + gh & 2u \end{pmatrix}, \tag{6}$$

the transport is more clearly evidenced. More precisely, when the matrix turns out to be diagonalizable, with eigenvalues

$$\lambda_1(W) = u - \sqrt{gh} \leq u + \sqrt{gh} = \lambda_2(W). \tag{7}$$

If the water height is strictly positive, lambda_1(W) < lambda_2(W), the system is said to be strictly hyperbolic (see among others [21]). The eigenvalues (7) are the velocities of surface waves on the fluid. For dry zones (*i.e.* if $h = 0$ m),

the eigenvalues coincide. In that case, the system is no longer hyperbolic, and this induces difficulties at both theoretical and numerical levels, such as negative water depths. Designing numerical schemes that preserve positivity for h is very important in this context.

With these formulas we recover a useful classification of flows. Indeed, if $|u| < \sqrt{gh}$, the characteristic velocities (of the fluid u and of the waves $\sqrt{gh}$) have opposite signs and information propagates upwards as well as downwards the flow. The flow is said to be subcritical or fluvial. In the other case, when $|u| > \sqrt{gh}$ the flow is supercritical, or torrential, all the information goes downwards. A transcritical regime exists when some parts of a flow are subcritical, other supercritical.

Since we have two unknowns h and u (or equivalently h and $q = hu$), a subcritical flow is therefore determined by one upstream and one downstream value, whereas a supercritical flow is completely determined by the two upstream values. Thus, for numerical simulations, we have to impose one variable for subcritical inflow/outflow. For supercritical inflow, we impose both variables and free boundary conditions are considered (see for example [22–24]).

Two quantities allow us to determine the type of flow. The first one is a dimensionless parameter called the Froude number

$$Fr = \frac{|u|}{\sqrt{gh}}. \tag{8}$$

Its analogue in gas dynamics is the Mach number. If $Fr < 1$ (resp. $Fr > 1$), the flow is subcritical (resp. supercritical). The other essential quantity is the critical height h_c which writes

$$h_c = \left(\frac{q}{\sqrt{g}}\right)^{2/3}, \tag{9}$$

for a given discharge $q = hu$. It is a very readable criterion for criticality: the flow is subcritical (resp. supercritical) if $h > h_c$ (resp. $h < h_c$).

In the presence of additional terms, we have to consider other properties, such as the occurrence of steady-state (or equilibrium) solutions. In Sect. 3, we will focus on backwater curves which are specific steady-state solutions.

3 Backwater Curves

By considering system (4) at steady state ($\partial_t h = \partial_t u = \partial_t q$), without rain and diffusion ($R = 0$ and $\mu = 0$), it rewrites

$$\begin{aligned} q &= q_0 \\ \partial_x h &= \frac{S_0 - S_f}{1 - Fr^2}. \end{aligned} \tag{10}$$

In hydraulics, Eq. (10) is used as a base for theoretical analysis of the water surface profiles obtained for different flow conditions in open channels [25–27]. It is called the gradually varied flow equation [25, 26]. Water surface profiles can be deduced theoretically and drawn qualitatively by studying the relative position of the profile (h) with respect to the critical-depth line (h_c) and the normal-depth line (h_n, the height solution of equation $S_0 - S_f = 0$). We notice that the normal height h_n depends on the slope S_0, while the critical height h_c does not depend on S_0. Bottom slopes are classified into five categories (designated by the first letter of the name): mild M if $h_n > h_c$, critical C if $h_n = h_c$, steep S if $h_n < h_c$, horizontal H if $S_0 = 0$ and adverse A if $S_0 < 0$. Now, we have to designate the relative position of the free surface. In the cases of the mild and steep slopes, the space above the topography is divided into three regions by the normal height and the critical height (Fig. 1b). For the adverse, horizontal and critical slopes, there are only two regions because the normal height does not exist for the first two slopes and is the same as the critical one for the critical slope. The region between the lower line and the topography is designated as "zone 3", and the region between the upper and lower lines is designated as "zone 2" and that above both lines is designated as "zone 1". Thus, we have 13 different types of water height profiles. This technique allows us to make qualitative observations about various types of free surface profiles. These observations allow us to draw the profile without any detailed calculations. For example, we know if the water height increases or decreases with distance, how the profiles end at downstream and upstream limits. It is possible to put end-to-end several backwater curves to obtain a complete profile. In some cases, it is possible to generate this method to section average model (i.e. to take into account the shape of the cross-section).

For engineering applications, it is necessary to compute the flow conditions. But the gradually varied flow equation (10) is nonlinear, and the dependence on h is complicated, so the obtention of a general analytic solution is not possible: we have to use higher-order numerical methods [24]. We start the computations from downstream if the flow is subcritical and from upstream otherwise (see [25–27]). Some computer programs such as HEC-RAS are based on this method. In the next section, we will describe SWASHES library.

4 Advanced Analytic Solutions

SWASHES is freely available to the community through the SWASHES repository hosted at http://www.univ-orleans.fr/mapmo/soft/SWASHES. It is distributed under CeCILL-V2 (GPL compatible) free software licence. When running the software, the user must specify the choice of the solution as well as the number of cells for the discretization of the chosen analytic solution. The solution is calculated and is redirected in a gnuplot-compatible ASCII file. SWASHES is written in object-oriented ISO C++ that allows us to easily implement a new solution.

We claim that SWASHES can be a useful tool for developers of shallow water codes to evaluate the performances and properties of their own code. Indeed,

SWASHES has been created because we have been developing a free software for the resolution of shallow water equations, namely FullSWOF [28, 29], and we wanted to validate it against analytic solutions. With SWASHES, a wide range of flow conditions are available as developed in the following subsection: steady-state solutions and transitory solutions.

4.1 Steady-State Solutions

In case of steady states ($\partial_t h = \partial_t u = \partial_t q = 0$), the one-dimensional shallow water Eq. (4) is reduced in the following system

$$\begin{aligned} q &= Rx + q_0 \\ \partial_x z &= \frac{1}{gh}\left(\frac{q^2}{h^2} - gh\right)\partial_x h - S_f(h,q) + \frac{\mu}{gh}\partial_x\left(h\partial_x \frac{q}{h}\right). \end{aligned} \tag{11}$$

System (11) enables us to produce an infinity of analytic solutions. For these solutions, the strategy consists in choosing either a topography and getting the associated water height or a water height and deducing the associated topography. With the first approach, we can get, for example, the well-known solutions for flow over a bump [30, 31], the backwater curves (Sect. 3)… With the second approach, we get the MacDonald's solutions (which are section-averaged) [32, 33] and all their one-dimensional variants [20, 28].

Since [34] it is well known that the topography source term treatment is a crucial point in preserving steady states. Thanks to the steady-state solutions gathered in [18], one can check whether the steady state at rest and dynamic steady-state solutions are satisfied by the considered schemes. These solutions, integrated in SWASHES, cover a wide variety of flow conditions (fluvial, torrential, transcritical, with shock…). Moreover, different source terms (topography, friction, rain and diffusion) are taken into account, which allow us to validate each source term treatment.

4.2 Transitory Solutions

In previous subsection, we dealt with the steady-state solutions of SWASHES. These solutions can be used to check whether the numerical methods are able to keep/catch steady-state flows. But even if the initial conditions differ from the expected steady state, we do not have information about the transitory behaviour. Thus, transitory solutions are also included in SWASHES, such as the dam-break solutions of increasing complexity [35–37, 42], 1D and 2D Thacker's and variants solutions [38–40, 41]. These solutions allow us to test moving wet/dry transitions, moving shock, moving wet/dry transitions with friction…

5 Conclusions

We have developed SWASHES, a free tool for benchmarking in hydraulics. It is open to user's contributions. We think that it might be useful for codes/numerical testing.

Acknowlegments This study is part of ANR METHODE project ANR-07-BLAN-0232 granted by the French National Agency for Research. The authors wish to thank V. Caleffi and A. -C. Boulanger for their collaboration.

References

1. Esteves, M., Faucher, X., Galle, S., & Vauclin, M. (2000). Overland flow and infiltration modelling for small plots during unsteady rain: numerical results versus observed values. *Journal of Hydrology, 228*(3–4), 265–282.
2. Tatard, L., Planchon, O., Wainwright, J., Nord, G., Favis-Mortlock, D., Silvera, N., et al. (2008). *Measurement and modelling of the high-resolution flow-velocity data under simulated rainfall on a low-slope sandy soil*. *Journal of Hydrology, 348*(1–2), 1–12.
3. Burguete, J., & Garcia-Navarro, P. (2004). Implicit schemes with large time step for non-linear equations : Application to river flow hydraulics. *International Journal for Numerical Methods in Fluids, 46*(6), 607–636.
4. Goutal, N., & Maurel, F. (2002). A finite volume solver for 1D shallow-water equations applied to an actual river. *International Journal for Numerical Methods in Fluids, 38*(1), 1–19.
5. Caleffi, V., Valiani, A., & Zanni, A. (2003). Finite volume method for simulating extreme flood events in natural channels. *Journal of Hydraulic Research, 41*(2), 167–177.
6. Delestre, O., Cordier, S., James, F., & Darboux, F. (2009). Simulation of rain-water overland-flow. In E. Tadmor., J.G. Liu. & A. Tzavaras (Eds), *Proceedings of the 12th International Conference on Hyperbolic Problems, Proceedings of Symposia in Applied Mathematics,* (Vol 67, pp. 537–546). USA: Amer. Math. Soc., University of Maryland, College Park.
7. Alcrudo, F. & Gil, E. (1999). The Malpasset dam break case study. *Proceedings of the 4th Concerted Action on Dambreak Modelling Workshop* (pp. 95–109). Zagaroza, Spain.
8. Valiani, A., Caleffi, V., & Zanni, A. (2002). *Malpasset dam-break simulation using a two-dimensional finite volume method*. *Journal of Hydraulic Engineering, 128*(5), 460–472.
9. Borthwick, A.G.L., Cruz Leon, S., & Jozsa, J. (2001). The shallow flow equations solved on adaptative quadtree grids. *International Journal for Numerical Methods in Fluids, 37*, 691–719.
10. Marche, F. (2005). Theoretical and numerical study of shallow water models, applications to nearshore hydrodynamics. (PhD Thesis, Laboratoire de mathématiques appliquées, Université de Bordeaux 1, France, 2005).
11. George, D.L. (2006). Finite volume methods and adaptative refinement for tsunami propagation and inundation. (PhD Thesis, University of Washington, USA, 2006).
12. Kim, D.H., Cho, Y.S., & Yi, Y.K. (2007). Propagation and run-up of nearshore tsunamis with HLLC approximate Riemann solver. *Ocean Engineering, 334*(8–9), 1164–1173.
13. Popinet, S. (2011). Quadtree-adaptative tsunami modelling. *Ocean Dynamics, 61*(9), 1261–1285.
14. Barré de Saint-Venant, A.J.C. (1871). Théorie du mouvement non-permanent des eaux, avec application aux crues des rivières et à l'introduction des marées dans leur lit. Comptes Rendus de l'Académie des Sciences, 73, 147–154.

15. Bouchut, F. (2004). Nonlinear stability of finite volume methods for hyperbolic conservation laws, and well-balanced schemes for sources. In *Frontiers in Mathematics* (Vol. 4). Birkhauser: Basel Boston Berlin.
16. LeVeque, R.J. (2002). *Finite volume methods for hyperbolic problems.* Cambridge: Cambridge University Press.
17. Toro, E.F. (1997). *Riemann solvers and numerical methods for fluid dynamics. A practical introduction*. Berlin and New York: Springer.
18. Delestre, O., Lucas, C., Ksinant, P.-A., Darboux, F., Laguerre, C., Vo, T.N.T., James, F., & Cordier, S. (2013) SWASHES: a compilation of shallow water analytic solutions for hydraulic and environmental studies. *International Journal for Numerical Methods in Fluids*, 72(3): 269–300.
19. Defra, E.A. (2004). *Flood & Coastal Defence R&D Programme, Benchmarking Hydraulic River Modelling Software Packages.* R&D Study: W5-105/TR1.
20. Delestre, O., & Marche, F. (2010). A numerical scheme for a viscous shallow water model with friction. *Journal of Scientific Computing*, 1–11.
21. Godlewski, E., & Raviart, P.A. (1996). Numerical approximations of hyperbolic systems of conservation laws. *Applied mathematical sciences* (Vol. 118). New York: Springer.
22. Bristeau, M.-O., & Coussin, B. (2001). Boundary conditions for the shallow water equations solved by kinetic schemes. *Technical Report 4282*, INRIA.
23. Cunge, J., Holly, F.M., Jr, & Verwey, A. (1980). *Practical Aspects of Computational River Hydraulics*. London: Pitman.
24. Novak, P., Guinot, V., Jeffrey, A., & Reeve, D.E. (2010). *Hydraulic modelling—an Introduction.* Spoon Press.
25. Chaudhry, M.H. (2008). *Open-Channel flow.* New York: Springer.
26. Chow, V.T. (1959). *Open-Channel hydraulics*. New-York: McGraw-Hill.
27. Henderson, F.M. (1966). *Open channel flow.* In G. Nordby (Ed.), *Civil engineering*, New-York: MacMilan.
28. Delestre, O. (2010). Simulation du ruissellement d'eau de pluie sur des surfaces agricoles (PhD Thesis, MAPMO—Université d'Orléans, France, 2010). Available on http://tel.archives-ouvertes.fr/INSMI/tel-00531377/fr.
29. Delestre, O., Cordier, S., Darboux, F., Du, M., James, F., Laguerre, C., Lucas, C., & Planchon, O. (submitted). FullSWOF: A software for overland flow simulation/FullSWOF : un logiciel pour la simulation du ruissellement. To be published in *Proceedings of SimHydro 2012,* Polytech'Nice Sophia, Sophia-Antipolis: (France), Advances in Hydroinformatics—SimHydro 2012: Springer.
30. Goutal, N., & Maurel, F. (1997). *Proceedings of the 2nd workshop on dam-break wave simulation.* Technical Report HE-43/97/016/B, Electricité de France, Direction des études et recherches.
31. Houghton, D.D., & Kasahara, A. (1968). Nonlinear shallow fluid flow over an isolated ridge. *Communications on Pure and Applied Mathematics, 21*, 1–23.
32. MacDonald, I. (1996). Analysis and computation of steady open channel flow. (PhD Thesis, Department of Mathematics, University of Reading, GB,1996).
33. MacDonald, I., Baines, M.J., Nichols, N.K., & Samuels, P.G. (1997). Analytic benchmark solutions for open-channel flows. *Journal of Hydraulic Engineering, 123*(11), 1041–1045.
34. Bermudez, A., & Vazquez, M.E. (1994). Upwind methods for hyperbolic conservation laws with source terms. *Computers & Fluids, 23*(8), 1049–1071.
35. Dressler, R.F. (1952). Hydraulic resistance effect upon the dam-break functions. *Journal of Research of the National Bureau of Standards., 49*(3), 217–225.
36. Ritter, A. (1892). Die Fortpflanzug der Wasserwellen. *Zeitschrift des Vereines Deuscher Ingenieure., 36*(33), 947–954.
37. Stoker, J.J. (1957). *Water Waves: The mathematical theory with applications*. *Pure and Applied Mathematics.* New York: Interscience Publishers.
38. Miles, J.W., & Ball, F.K. (1963). On free-surface oscillations in a rotating paraboloid. *Journal of Fluid Mechanics, 17*, 257–266.

39. Sampson, J., Easton, A., & Singh, M. (2006). Moving boundary shallow water flow above parabolic bottom topography. In A. Stacey., B. Blyth., J. Shepherd., & A. J. Roberts (Eds), *Proceedings of the 7th Biennal Engineering Mathematics and Applications Conference. EMAC-2005, vol 47 of ANZIAM Journal, Australian Mathematical Society* (pp. 666–680).
40. Thacker, W.C. (1981). *Some exact solutions to the nonlinear shallow-water wave equations*. *Journal of Fluid Mechanics, 107*, 499–508.
41. Ball, F.K. (1963). Some general theorems concerning the finite motion of a shallow rotating liquid lying on a paraboloid. *Journal of Fluid Mechanics, 17*(2), 240–256.
42. Whitham, G.B. (1955). The effects of hydraulic resistance in the dam-break problem. *Proceedings of the Royal Society of London, Ser. A*, *227*(1170), 399–407.

Correct Boundary Conditions for Turbulent SPH

Martin Ferrand, Damien Violeau, Arno Mayrhofer and Omar Mahmood

Abstract We present unified and consistent boundary conditions for the 2D smoothed particle hydrodynamics (SPH) weakly compressible numerical method, including (1) pressure (wall impermeability), (2) wall shear stress (for laminar and turbulent flows), (3) wall turbulent conditions (k–ε model) and (4) inlet–outlet open boundaries. The first three conditions (wall conditions) are based on modified discrete differential operators, using a proper renormalising function at the wall, which is calculated by solving a governing equation. The last condition (inlet/outlet) is prescribed through the Riemann invariants of Euler equations, leading to absorbing conditions which avoid spurious waves. Validations (fish pass, open and closed channels, hydraulic jump, Creager weir) proved that the proposed models perform well.

Keywords SPH · Lagrangian model · Boundary conditions · Turbulence

Nomenclature

A_a	Value of A at the point occupied by the particle a
A_{ab}	Difference A_a–A_b
c, c_0	Speed of sound and reference speed of sound

M. Ferrand · D. Violeau (✉)
MFEE and LNHE Departments, EDF R&D, Chatou, France
e-mail: damien.violeau@edf.fr

M. Ferrand
e-mail: martin.ferrand@edf.fr

A. Mayrhofer
School of MACE, The University of Manchester, Manchester, England
e-mail: arno.m@gmx.at

O. Mahmood
Ecole des Ponts ParisTech, Paris, France
e-mail: mahmoodo@eleves.enpc.fr

P. Gourbesville et al. (eds.), *Advances in Hydroinformatics*,
Springer Hydrogeology, DOI: 10.1007/978-981-4451-42-0_21,

$\mathbf{g}$	Gravity acceleration
k	Turbulent kinetic energy
P	Production of turbulent kinetic energy
p	Pressure
$\mathbf{r}_a$	Particle position vector
R^+, R^-	Riemann invariants
$\mathbf{S}$	Rate-of-strain tensor
$\mathbf{U}$, u	Velocity vector and longitudinal velocity
$\mathbf{u}_\tau$	Shear velocity vector
w	SPH kernel
γ_a	Renormalising factor
ε	Dissipation of turbulent kinetic energy
ξ	Exponent of the state equation
μ, μ_T	Molecular viscosity and eddy viscosity
ρ, ρ_0	Density and reference density
$\boldsymbol{\tau}$	Wall shear stress

1 Introduction

Smoothed Particle Hydrodynamics (SPH) is now a well-established numerical technique, and its Lagrangian properties have proved their efficiency in simulating highly deformable flows. However, boundary treatment in SPH is still an issue although it has been widely addressed in the literature during the past decade, especially regarding wall treatment. Up to a recent past, indeed, no clear model has proved its ability to handle arbitrary boundary conditions for all differential operators in SPH. The question of open boundaries is also a key issue in SPH.

In this paper, we extend the concept of wall renormalisation to derive a consistent boundary treatment for gradient, divergence and Laplacian discrete operators. We then apply this method to solve the Reynolds-averaged Navier–Stokes (RANS) equations together with a standard k–ε model for turbulent closure. Then, we consider the Riemann invariants of the Euler equations in order to specify correct inflow/outflow boundary conditions for open domains.

2 Governing Equations

2.1 Continuous Model

We consider a turbulent weakly compressible free surface flow. The velocity vector, density, pressure, turbulent kinetic energy and energy dissipation rate are denoted by $\mathbf{u}$, ρ, p, k and ε, respectively. Velocities and pressure are Reynolds-

averaged, and the effects of turbulent fluctuations are modelled through the concept of eddy viscosity μ_T, estimated from the k–ε model [1].

The Lagrangian form of the RANS and k–ε equations reads

$$\begin{aligned}
\frac{d\rho}{dt} &= -\,\rho\,\mathrm{div}\,\mathbf{u} \\
\frac{d\mathbf{u}}{dt} &= -\,\frac{1}{\rho}\mathbf{grad}\,\tilde{p} + \frac{1}{\rho} div(\mu_m \mathbf{grad}\,\mathbf{u}) + \mathbf{g} \\
\frac{dk}{dt} &= P - \varepsilon + \frac{1}{\rho} div(\mu_k \mathbf{grad}\,k) \\
\frac{d\varepsilon}{dt} &= \frac{\varepsilon}{k}(C_{\varepsilon 1}P - C_{\varepsilon 2}\varepsilon) + \frac{1}{\rho} div(\mu_\varepsilon \mathbf{grad}\,\varepsilon)
\end{aligned} \tag{1}$$

where $\mathbf{g}$ is the gravitational acceleration. In these equations, the modified pressure $\tilde{p}$ and production of turbulent energy P are given by

$$\begin{aligned}
&\tilde{p} = p + \tfrac{2}{3}\rho k \qquad p = \tfrac{\rho_0 c_0^2}{\xi}\left[\left(\tfrac{\rho}{\rho_0}\right)^{\xi} - 1\right] \\
&P = \tfrac{2\mu_T}{\rho}\mathbf{S} : \mathbf{S} \quad \mathbf{S} = \tfrac{1}{2}\left[\mathbf{gradu} + (\mathbf{gradu})^T\right]
\end{aligned} \tag{2}$$

c_0 being the speed of sound at the reference density ρ_0, $\xi = 7$ and $\mathbf{S}$ being the (mean) rate-of-strain tensor. Lastly, the dynamic viscosities are given by

$$\begin{aligned}
\mu_m &= \mu + \mu_T \quad & \mu_T &= C_\mu \rho \tfrac{k^2}{\varepsilon} \\
\mu_k &= \mu + \tfrac{\mu_T}{\sigma_k} \quad & \mu_\varepsilon &= \mu + \tfrac{\mu_T}{\sigma_\varepsilon}
\end{aligned} \tag{3}$$

where μ is the dynamic molecular viscosity. The model constants C_μ, $C_{\varepsilon 1}$, $C_{\varepsilon 2}$, σ_k and σ are given in Table 1.

Equations (1) are subject to the following set of boundary conditions at the walls:

$$\begin{aligned}
\left[\tfrac{\partial}{\partial \mathbf{n}}\left(\tfrac{p}{\rho} - \mathbf{g}\cdot\mathbf{r}\right)\right]_{\partial\Omega} &= 0 \quad & \left(\mu_k \tfrac{\partial k}{\partial \mathbf{n}}\right)_{\partial\Omega} &= 0 \\
\left(\mu_m \tfrac{\partial \mathbf{u}}{\partial \mathbf{n}}\right)_{\partial\Omega} &= \mathbf{Q}^{\mathbf{u}} = \tau \quad & \left(\mu_\varepsilon \tfrac{\partial \varepsilon}{\partial \mathbf{n}}\right)_{\partial\Omega} &= Q^{\varepsilon}
\end{aligned} \tag{4}$$

where $\mathbf{Q}^{\mathbf{u}}$ and Q^{ε} are wall fluxes of momentum and energy dissipation, respectively. The first one is equal to the wall shear stress vector τ and can be related to the shear velocity vector $\mathbf{u}_\tau$ (with modulus u_τ). Under turbulent conditions, from the theory of turbulent boundary layer [1], we can write

Table 1 Model constants [1]

C_μ	$C_{\varepsilon 1}$	$C_{\varepsilon 2}$	σ_k	σ	κ
0.09	1.44	1.92	1.0	1.3	0.41

$$\begin{aligned} \mathbf{Q}^u &= \tau = -\rho u_\tau \mathbf{u}_\tau \\ \mathbf{u}_\tau &= \frac{\kappa \mathbf{u}(z)}{\ln(\rho u_\tau z/\mu)} \\ Q^\varepsilon &= \frac{\rho u_\tau^4}{\sigma_\varepsilon z} \end{aligned} \tag{5}$$

where κ is given in Table 1 and z is the (relatively small) distance to the wall, still larger than the viscous sublayer. All fluxes are assumed to be zero at the free surface, which is a crude approximation.

In the next sections, we will present two SPH models to discretise the previous set of equations: the first one (Sect. 2.2) is the traditional SPH with fictitious (or ghost) particles for wall treatment; the second one (Sect. 3.1) is a renormalised SPH with appropriate boundary fluxes.

2.2 Discrete Model Without Boundary Conditions

The SPH method is based on discrete interpolations of the required fields and differential operators. The fluid domain is constituted of particles a, b, etc., making a discrete set F, with positions $\mathbf{r}_a$, $\mathbf{r}_b$, etc. (see Fig. 1), and moving with velocities $\mathbf{u}_a = d\mathbf{r}_a/dt$. In the standard SPH method, the following discrete forms of the operators, gradient, divergence and Laplacian, are generally used:

$$\begin{aligned} (\nabla A)_a &\approx \mathbf{G}_a\{A_b\} \equiv \rho_a \sum_{b\in F} m_b \left(\frac{A_a}{\rho_a^2} + \frac{A_b}{\rho_b^2}\right) \nabla w_{ab} \\ (\nabla \mathbf{A})_a &\approx \tilde{\mathbf{G}}_a\{\mathbf{A}_b\} \equiv -\frac{1}{\rho_a} \sum_{b\in F} m_b \mathbf{A}_{ab} \otimes \nabla w_{ab} \\ (\nabla \cdot A)_a &\approx D_a\{\mathbf{A}_b\} \equiv -\frac{1}{\rho_a} \sum_{b\in F} m_b \mathbf{A}_{ab} \cdot \nabla w_{ab} \\ (\nabla \cdot (B\nabla \mathbf{A}))_a &\approx \mathbf{L}_a\{B_b, \mathbf{A}_b\} \equiv \sum_{b\in F} V_b (B_a + B_b) \frac{\mathbf{A}_{ab}}{r_{ab}^2} \mathbf{r}_{ab} \cdot \nabla w_{ab} \end{aligned} \tag{6}$$

where A (resp. $\mathbf{A}$) is an arbitrary scalar (resp. vector) field, m denotes the particle masses, V denotes their volumes, and w is the SPH kernel (see [2] for more details). In the above equations, the subscripts a and b denote all quantities relative to a particle; we define $\mathbf{A}_{ab} = \mathbf{A}_a - \mathbf{A}_b$, where ∇w_{ab} is the gradient of $w(r_{ab})$ with respect to $\mathbf{r}_a$, and $r_{ab} = |\mathrm{r}_{ab}|$. The governing Eq. (1) then take the following discrete form:

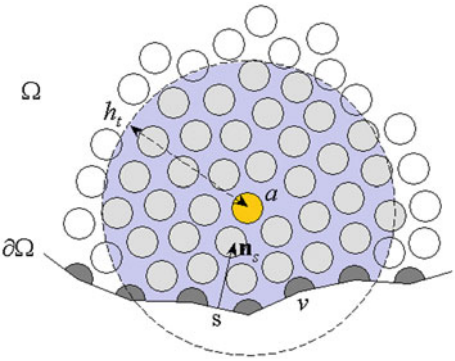

Fig. 1 The discretisation used in this work is based on fluid particles (*a* or *b*), vertex particles (*v*) and wall segments (*s*) (in two dimensions). The truncation of the kernel is considered through the integral γ (*coloured area*)

$$\begin{aligned}
\frac{d\rho_a}{dt} &= -\rho_a D_a\{\mathbf{u}_b\} \\
\frac{d\mathbf{u}_a}{dt} &= -\frac{1}{\rho_a}\mathbf{G}_a\{\tilde{p}_b\} + \frac{1}{\rho_a}\mathbf{L}_a\{\mu_{m,b}, \mathbf{u}_b\} + \mathbf{g} \\
\frac{dk_a}{dt} &= P_a - \varepsilon_a + \frac{1}{\rho_a}\mathbf{L}_a\{\mu_{k,b}, k_b\} \\
\frac{d\varepsilon_a}{dt} &= \frac{\varepsilon_a}{k_a}(C_{\varepsilon 1}P_a - C_{\varepsilon 2}\varepsilon_a) + \frac{1}{\rho_a}\mathbf{L}_a\{\mu_{\varepsilon,b}, \varepsilon_b\}
\end{aligned} \tag{7}$$

As for the definition of the rate-of-strain tensor [last formula of (2)], it now reads

$$\mathbf{S}_\mathrm{a} = \frac{1}{2}\left[\tilde{\mathbf{G}}_a\{\mathbf{u}_b\} + \left(\tilde{\mathbf{G}}_a\{\mathbf{u}_b\}\right)^T\right] \tag{8}$$

The other Eq. of (2) are unchanged, as well as (3), with particle labels. Equation (7) is solved with a time integration scheme, which can be of arbitrary order, with CFL-type stabilising conditions [2]. We use here a first-order symplectic scheme.

Although the standard SPH method proved its efficiency in several flow regimes (see e.g. [3]), it is known to have some drawbacks, among which the question of boundary conditions is one of the most important. For wall boundary conditions, the ghost particle technique is often used [3], but it leads to results with poor accuracy and can hardly tackle the question of prescribing the correct fluxes at the wall. We will now address this issue.

3 Boundary Conditions

3.1 Modified Operators for Wall Conditions

We now present a modified SPH model accounting for the presence of walls in a more appropriate way, concentrating on 2D. The fluid domain is still constituted of particles a, b, etc., but we also consider 'vertex' particles v, while the walls are now discretised with segments s (in 2D), making a discrete set S (see Fig. 1). As depicted in Fig. 1, the effects of walls are firstly to truncate the kernel. In order to account for this effect, we proposed in [4] the following modified discrete form of the differential operators:

$$\begin{aligned}
(\nabla A)_a &\approx \mathbf{G}_a^{\gamma}\{A_{b,s}\} \equiv \frac{\rho_a}{\gamma_a}\sum_{b\in F} m_b\left(\frac{A_a}{\rho_a^2}+\frac{A_b}{\rho_b^2}\right)\nabla w_{ab} - \frac{\rho_a}{\gamma_a}\sum_{s\in S}\rho_s\left(\frac{A_a}{\rho_a^2}+\frac{A_s}{\rho_s^2}\right)\nabla\gamma_{as}\\
(\nabla \mathbf{A})_a &\approx \tilde{\mathbf{G}}_a^{\gamma}\{\mathbf{A}_{b,s}\} \equiv -\frac{1}{\gamma_a\rho_a}\sum_{b\in F} m_b\mathbf{A}_{ab}\otimes\nabla w_{ab} + \frac{1}{\gamma_a\rho_a}\sum_{s\in S}\rho_s\mathbf{A}_{as}\otimes\nabla\gamma_{as}\\
(\nabla\cdot A)_a &\approx D_a^{\gamma}\{\mathbf{A}_{b,s}\} \equiv -\frac{1}{\gamma_a\rho_a}\sum_{b\in F} m_b\mathbf{A}_{ab}\cdot\nabla w_{ab} + \frac{1}{\gamma_a\rho_a}\sum_{s\in S}\rho_s\mathbf{A}_{as}\cdot\nabla\gamma_{as}\\
(\nabla\cdot(B\nabla\mathbf{A}))_a &\approx \mathbf{L}_a^{\gamma}\left\{B_b,\mathbf{A}_b,\mathbf{Q}_{b,s}^{\mathrm{A}}\right\} \equiv \frac{1}{\gamma_a}\sum_{b\in F} V_b(B_a+B_b)\frac{\mathbf{A}_{ab}}{r_{ab}^2}\mathbf{r}_{ab}\cdot\nabla w_{ab} - \frac{1}{\gamma_a}\sum_{s\in S}\left(\mathbf{Q}_a^{\mathrm{A}}+\mathbf{Q}_s^{\mathrm{A}}\right)\cdot\nabla\gamma_{as}
\end{aligned} \tag{9}$$

where $\mathbf{Q}_a^{\mathrm{A}} = (B\nabla\mathbf{A})_a$ is the flux of the quantity A and γ_a is the integral of the kernel:

$$\gamma_a = \int_{\Omega} w(|\mathbf{r}_a - \mathbf{r}\prime|)d^n\mathbf{r}\prime \tag{10}$$

n being the spatial dimension. This integral extends over the entire physical domain Ω. Due to the compactness of the kernel support, however, it is restricted to the coloured area on Fig. 1. In the above equations, the subscripts s refer to wall segments and $\mathbf{A}_{as} = \mathbf{A}_a - \mathbf{A}_s$. $\nabla\gamma_{as}$ is the contribution of the segment s to the boundary effect, defined by

$$\nabla\gamma_{as} = \int_s w(|\mathbf{r}_a - \mathbf{r}_s|)\mathbf{n}_s d^{n-1}\Gamma_s = |\nabla\gamma_{as}|\mathbf{n}_s \tag{11}$$

where $\mathbf{n}_s$ is the unit inward normal vector of the segment (see Fig. 1). The system (7), together with (8), now reads

$$\begin{aligned}
\frac{d\rho_a}{dt} &= -\rho_a D_a^{\gamma}\{\mathbf{u}_{b,s}\} + L_a^{\gamma}\{v_{\rho,b}, \rho_b, 0\} \\
\frac{d\mathbf{u}_a}{dt} &= -\frac{1}{\rho_a}\mathbf{G}_a^{\gamma}\{\tilde{p}_{b,s}\} + \frac{1}{\rho_a}\mathbf{L}_a^{\gamma}\{\mu_{m,b}, \mathbf{u}_b, \boldsymbol{\tau}_{b,s}\} + \mathbf{g} \\
\frac{dk_a}{dt} &= P_a - \varepsilon_a + \frac{1}{\rho_a}\mathbf{L}_a^{\gamma}\{\mu_{k,b}, k_b, 0\} \\
\frac{d\varepsilon_a}{dt} &= \frac{\varepsilon_a}{k_a}(C_{\varepsilon 1}P_a - C_{\varepsilon 2}\varepsilon_a) + \frac{1}{\rho_a}\mathbf{L}_a^{\gamma}\left\{\mu_{\varepsilon,b}, \varepsilon_b, Q_{b,s}^{\varepsilon}\right\} \\
\mathbf{S}_a &= \frac{1}{2}\left[\tilde{\mathbf{G}}_a^{\gamma}\{\mathbf{u}_{b,s}\} + \left(\tilde{\mathbf{G}}_a^{\gamma}\{\mathbf{u}_{b,s}\}\right)^T\right]
\end{aligned} \tag{12}$$

As can be seen, we considered a smoothing term in the continuity equation [first line of (12)], initially recommended in [5] to avoid unphysical density (and thus pressure) variations. The latter term is based on a numerical (volume conserving) diffusion coefficient for densities here denoted by ν_ρ. The boundary terms $\nabla\gamma_{as}$ are calculated exactly from the positions of the particles and wall segments [4]. The renormalising factors γ_a are then calculated from the following dynamic equation:

$$\frac{d\gamma_a}{dt} = \sum_{s\in S}\nabla\gamma_{ab}\cdot\mathbf{u}_{as} \tag{13}$$

where $\mathbf{u}_{as} = \mathbf{u}_a - \mathbf{u}_s$ is the velocity of the particle a with respect to the segment s. The latter equation is solved through a second-order time integration scheme [4] with a stabilising criterion:

$$\begin{aligned}
\gamma_a^{m+1} &= \gamma_a^m + \frac{\delta t}{2}\sum_{s\in S}\left(\nabla\gamma_{as}^m + \nabla\gamma_{as}^{m+1}\right)\cdot\mathbf{u}_{as} \\
\delta t &\le \frac{C_{t,\gamma}}{\max\limits_{a\in F, s\in S}|\nabla\gamma_{as}\cdot\mathbf{u}_{as}|}
\end{aligned} \tag{14}$$

The von Neumann boundary conditions (4) are now specified through the following procedure. As depicted in Fig. 1, each segment is bounded by two vertex particles v (included in the set F), which are truncated by the wall. The value of an arbitrary quantity at the place of a segment is then averaged over its respective vertex particles. The latter are estimated from an SPH discrete interpolation [4]. As for the fluxes appearing in (12), as well as for the friction velocities, they are defined from (5), that is,

$$\begin{aligned}
\boldsymbol{\tau}_a &= -\rho_a u_{\tau,a}\mathbf{u}_{\tau,a} \\
\mathbf{u}_{\tau,a} &= \frac{\kappa\mathbf{u}_a}{\ln\left(\rho_a u_{\tau,a}\delta r_{as}/\mu_a\right)} \\
Q_a^{\varepsilon} &= \frac{2\rho_a u_{\tau,a}^4}{\sigma_\varepsilon \delta r_{as}}
\end{aligned} \tag{15}$$

where $\delta r_{as} = \max(r_{as}; \delta r)$, δr being the particle size. Several applications of the present model were presented in [4 and 6]. Figure 2 shows the comparison of the present SPH model with finite volume software (*Code_Saturne*) in the case of a quasi-steady turbulent flow in a vertical slot fish pass (periodic flow). As can be seen, the comparisons regarding the distributions of velocity magnitude, turbulent kinetic energy and eddy viscosity are excellent. On the one hand, the traditional boundary conditions' method (i.e. the ghost particle technique, not presented here) was not capable of obtaining acceptable results in that case [4].

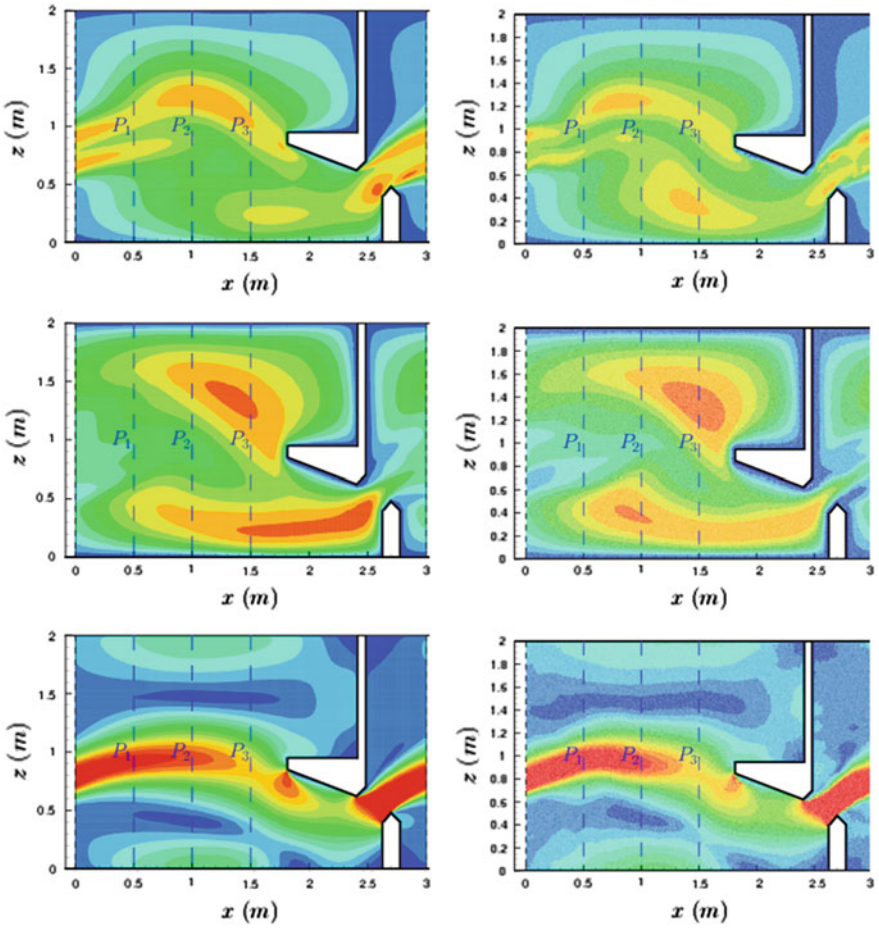

Fig. 2 Turbulent flow in a *vertical slot* fish passage simulated with the k–ε model. Comparison between a finite volume model (*left*) and the presently modified SPH method (*right*). Distributions of the turbulent kinetic energy, the eddy viscosity and the velocity magnitude (*from top to bottom*)

3.2 Inflow/Outflow Boundary Conditions

In order to prescribe inflow and outflow boundary conditions, we will consider the simplified case of a straight open boundary where the velocity is everywhere orthogonal to it. Moreover, we will neglect the effect of diffusion terms in the equations. Under these assumptions, the first two equations of the original system (1) can be written in the well-known quasi-linear form of the Euler equations, that is,

$$\frac{\partial \mathbf{X}}{\partial t} + \mathbf{A}\frac{\partial \mathbf{X}}{\partial x} = 0 \tag{16}$$

where

$$\mathbf{X} \equiv \begin{pmatrix} \rho \\ u \end{pmatrix} \quad \mathbf{A} \equiv \begin{pmatrix} u & \rho \\ c^2/\rho & u \end{pmatrix} \tag{17}$$

u being the longitudinal velocity and the speed of sound c being defined by

$$c \equiv c_0 \left(\frac{\rho}{\rho_0}\right)^{\frac{\xi-1}{2}} \tag{18}$$

As it is already known, the latter system can be written as a set of two transport equations:

$$\frac{\partial R^\varepsilon}{\partial t} + \lambda^\varepsilon \frac{\partial R^\varepsilon}{\partial x} = 0, \quad \varepsilon = \pm 1 \tag{19}$$

where we have defined the Riemann invariants R and the propagation speeds λ^ε:

$$\begin{aligned} R^\varepsilon &\equiv u + \varepsilon r \\ \lambda^\varepsilon &\equiv u + \varepsilon c \end{aligned} \tag{20}$$

with

$$r \equiv \frac{2c}{\xi - 1} \tag{21}$$

Equation (19) means that the Riemann invariant R^+ propagates downstream with the velocity λ^+, while R^- propagates upstream with the velocity λ^-. Thus, we may consider that a particle a located on an inflow boundary is characterised by an R^+ equal to the desired (i.e. prescribed) value, that is, coming from outside of the fluid domain, while its R^- is equal to the corresponding value immediately downstream of the inflow boundary, inside the domain. Here, the latter is interpolated using an SPH approximation:

$$\begin{aligned} R_a^+ &= R_p^+ \\ R_a^- &= \mathbf{I}_a\{R_b^-\} \end{aligned} \tag{22}$$

where the label p stands for 'prescribed' and $\mathbf{I}_a$ is a renormalised SPH discrete interpolation operator:

$$\mathbf{I}_a\{A_b\} = \frac{1}{\gamma_a}\sum_{b\in F} V_b A_b w_{ab} \tag{23}$$

with $w_{ab} = w(r_{ab})$. Rearranging (22), and accounting for the linearity of the latter operator, we can write the values of the longitudinal velocity u and the quantity r corresponding to the particle a:

$$\begin{aligned} r_a &= \frac{r_p + \mathbf{I}_a\{r_b\}}{2} + \frac{u_p - \mathbf{I}_a\{u_b\}}{2} \\ u_a &= \frac{u_p + \mathbf{I}_a\{u_b\}}{2} + \frac{r_p - \mathbf{I}_a\{r_b\}}{2} \end{aligned} \tag{24}$$

Thus, the prescribed values u_p and r_p [in relation with ρ_p through (18) and (21)], as well as the definition (23), give the values to impose to the entering particles through (24). Conversely, for an outflow boundary, we have

$$\begin{aligned} R_a^+ &= \mathbf{I}_a\{R_b^+\} \\ R_a^- &= R_p^- \end{aligned} \tag{25}$$

or after rearranging:

$$\begin{aligned} r_a &= \frac{r_p + \mathbf{I}_a\{r_b\}}{2} - \frac{u_p - \mathbf{I}_a\{u_b\}}{2} \\ u_a &= \frac{u_p + \mathbf{I}_a\{u_b\}}{2} - \frac{r_p - \mathbf{I}_a\{r_b\}}{2} \end{aligned} \tag{26}$$

As a first test case, we consider an infinite horizontal closed channel in steady laminar regime. Although the present work is mainly devoted to turbulent flows, which are predominant in the environment and industry, it can easily be applied for laminar regimes, by ignoring the k and ε equations [or setting the eddy viscosity μ_T to zero in (3)] [5]. The known solution in the present case is then a parabolic vertical velocity profile, while pressure decreases linearly with the horizontal distance and remains constant on the vertical. We can easily deduce the prescribed values at the open boundaries:

$$\begin{pmatrix} r_p \\ u_p \end{pmatrix} = \begin{pmatrix} \frac{2c_0}{\xi - 1}\left(1 + \frac{\xi p}{\rho_0 c_0^2}\right)^{\frac{\xi-1}{2\xi}} \\ 6U\frac{z}{H}\left(1 - \frac{z}{H}\right) \end{pmatrix} \tag{27}$$

where U is the averaged inflow velocity, H the distance between the two walls of the channel and p the pressure. We choose the latter differently at inlet and outlet,

in order to set a fluid motion. The pressure gradient is $\Delta p/\Delta x = -12\mu U/H^2$. Figure 3 depicts the pressure distribution along the channel as well as the velocity profile at the entrance [prescribed profile u_p (z)] and in the middle of the channel. The vertical coordinate z and the velocities are non-dimensionalised using H and the maximum velocity, and the pressure is non-dimensionalised by the pressure drop Δp. It can be seen that, as expected, the pressure decreases linearly, while the velocity remains parabolic.

In order to apply the present model to a simple turbulent flow, we now consider an infinite open channel with a gentle slope, generating a logarithmic velocity profile and a hydrostatic pressure:

$$\begin{pmatrix} r_p \\ u_p \end{pmatrix} = \begin{pmatrix} \frac{2c_0}{\xi-1}\left[1+\frac{\xi g}{c_0^2}(H-z)\right]^{\frac{\xi-1}{2\xi}} \\ u_\tau\left(\frac{1}{\kappa}\ln\frac{\rho z u_\tau}{\mu}+C_\tau\right) \end{pmatrix} \tag{26}$$

where $C_\tau = 5.2$ [1]. The turbulent conditions (i.e. k and ε) at the inflow and outflow are specified according to the theory of turbulent channel flows [6]. The flow, here generated by the gravity, is depicted in Fig. 4, where it can be seen that the velocity profile remains logarithmic, as expected (the velocities were non-dimensionalised with the depth-averaged velocity). It should be emphasised that the present model for prescribing inflow/outflow conditions was necessary to obtain such a result. As an illustration, with a cruder approach, where the inflow particles are simply introduced inside the domain with the desired velocity and density, that is, $u_a = u_p(z)$ and $\rho_a = \rho_0$ instead of (24), the velocity profile does not keep the correct shape, as it can be seen from the same figure.

Finally, we consider two cases close to real flows, although still two-dimensional: a hydraulic jump and a flow over a Creager weir. Figure 5 shows that the hydraulic jump develops well and stays steady, as required under the present conditions (inflow Froude number $Fr = 2$). Additional investigations proved that the profile of the free surface, as well as the distributions of velocity and turbulent kinetic energy,

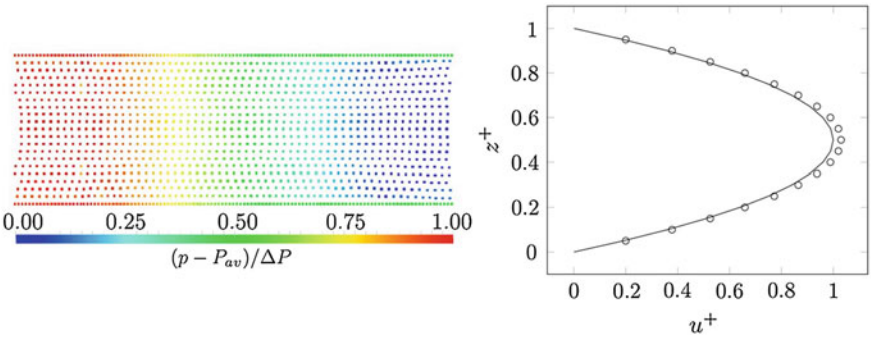

Fig. 3 Laminar flow in an infinite closed channel. Distribution of pressure (*left*) and vertical dimensionless velocity profiles (*right*). *Continuous line* prescribed velocity at the channel inflow; *symbols* computed velocity in the middle of the channel

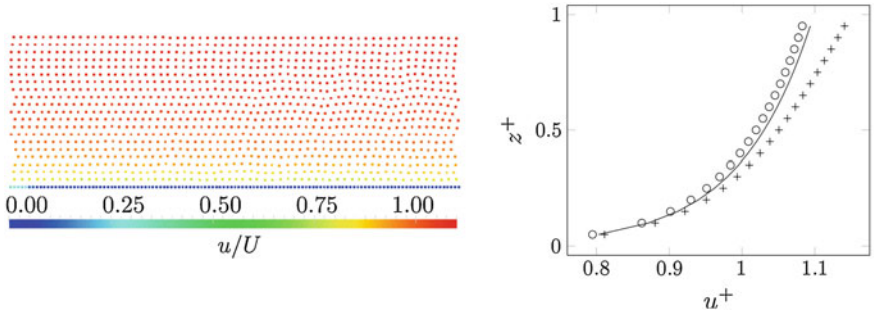

Fig. 4 Turbulent flow in an infinite open channel. Distribution of pressure (*left*) and vertical dimensionless velocity profiles (*right*). *Continuous line* prescribed velocity at the channel inflow; *circles* computed velocity in the middle of the channel with the present inflow/outflow model; *crosses* same profile with a coarser approach, where the inflow particles are simply injected with the prescribed velocity profile

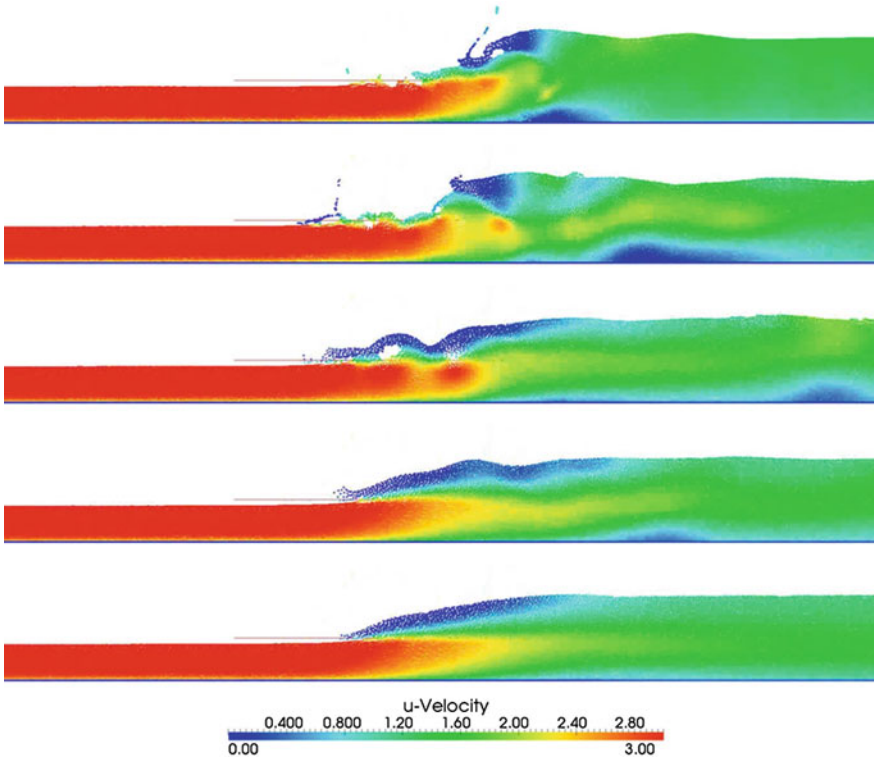

Fig. 5 Hydraulic jump simulated with SPH

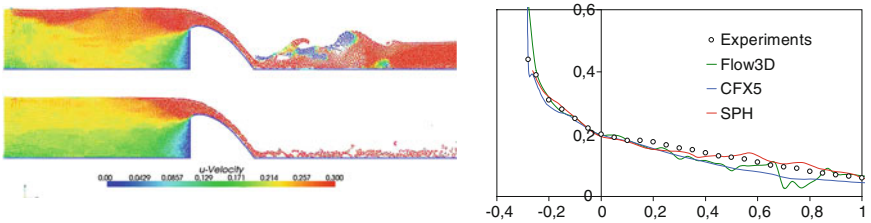

Fig. 6 Flow over a Creager weir. The pressure distribution along the weir crest is well predicted, as depicted in the *right side*

is fairly well reproduced [6]. This is mainly due to the appropriate wall boundary treatment, since it was not possible to keep the jump steady with the traditional ghost particle technique (not presented here, see [6]).

Figure 6 shows that the fluid slides along the weir as expected, without any spurious void. As a consequence, the pressure profile along the crest of the weir is fairly well predicted, as can be seen in the same figure. SPH even performs slightly better than two commercial codes based on grid computations. Again, this is the benefit of the newly developed wall boundary technique, since with the ghost particle method (not presented here) the flow is not properly sliding and the pressure at the wall is almost zero [6].

4 Conclusions

The question of boundary conditions in the SPH Lagrangian numerical method has been addressed here with success. Wall boundary conditions were improved in comparison with the traditional ghost particle technique, on the basis of renormalised discrete differential operators. The validations (fish pass, Creager weir) show a good distribution of pressure and turbulent quantities. On the other hand, inlet/outlet boundary conditions have been developed from the theory of the Riemann invariants of the Euler equations and proved efficient in the case of channel flows and hydraulic jump. An extension to 3D flows is under progress.

References

1. Pope, S. B. (2000). *Turbulent flows*. Cambridge: Cambridge University Press.
2. Monaghan, J. J. (1992). Smoothed Particle Hydrodynamics. *Annual Review of Astronomy and Astrophysics, 30*, 543–574.
3. Lee, E.-S., Moulinec, C., Xu, R., Violeau, D., Laurence, D., & Stansby, P. (2008). Comparisons of weakly compressible and truly incompressible SPH algorithms for 2D flows. *Journal of Computational Physics, 227*, 8417–8436.

4. Ferrand, M., Violeau, D., Rogers, B. D., Laurence, D. (2011). Consistent wall boundary treatment for laminar and turbulent flows in SPH. *Proceedings of 6th Spheric International Workshop* (pp. 275–282). Hamburg, Germany.
5. Ferrari, A., Dumbser, M., Toro, E. F., & Armanini, A. (2009). A new 3D parallel SPH scheme for free surface flows. *Computers and Fluids, 38*, 1203–1217.
6. Mahmood, O., Kassiotis, C., Violeau, D., Ferrand, M., Denis, C. (2011). Effect of wall boundary treatment in SPH for modelling turbulent flows with inlet/outlet. *Proceedings of 6th Spheric International Workshop* (pp. 333–339), Hamburg, Germany.

Integrated Water Quality Modelling of the River Zenne (Belgium) Using OpenMI

Olkeba Tolessa Leta, Narayan Kumar Shrestha, Bruno de Fraine, Ann van Griensven and Willy Bauwens

Abstract The modelling of the different catchment processes is key for integrated water resources management. Constructing a single model for all the catchment processes may not always be a feasible option, and it does not make appropriate use of existing models. The Open Modelling Interface (OpenMI), which allows time-dependent models to exchange data at run-time, might just be useful for such proposes. We used the Soil and Water Assessment Tool (SWAT) and the Storm Water Management Model (SWMM) for simulating rural and urban catchment processes, respectively. We also used SWMM to model the river processes. To link these models in OpenMI, both models were migrated to the OpenMI platform. As the water quality processes in SWAT are based on the QUAL2E process description, a new OpenMI compliant water quality module that is based on the same principles was developed to simulate the water quality processes in the river. The latter model, which uses a river network that is similar to that of the SWMM river model, is then also linked to the SWMM model using OpenMI. We tested this integrated model for the river Zenne in Belgium. The integrated model results show that such integration can be very useful as a decision support tools for integrated river basin management approach.

Keywords OpenMI · SWAT · SWMM · Water quantity model · Water quality model · Integrated modelling

O. T. Leta (✉) · N. K. Shrestha · A. van Griensven · W. Bauwens
Department of Hydrology and Hydraulic Engineering, Vrije Universiteit Brussel, Pleinlaan 2, 1050 Brussels, Belgium
e-mail: otolessa@vub.ac.be

B. de Fraine
Department of Computer Science, Vrije Universiteit Brussel, Pleinlaan 2, 1050 Brussels, Belgium

A. van Griensven
UNESCO-IHE Institute for Water Education, Core of Hydrology and Water Resources, Delft, The Netherlands

P. Gourbesville et al. (eds.), *Advances in Hydroinformatics*, Springer Hydrogeology, DOI: 10.1007/978-981-4451-42-0_22,

1 Introduction

The awareness of water quality issues and the environmental policy has gained increased importance in recent years. For example, in 2000, the European Union has launched the Water Framework Directive (EU-WFD) which calls to achieve a good water quality and a good ecological status by 2015 through integrated river basin management [1]. In this framework, integrated modelling of the water quantity and quality processes is essential to assess the present and future quality of the water bodies. Apart from water quantity and quality assessment, integrated modelling can help decision makers to better understand environmental problems and to design appropriate mitigation measures [2, 3]. In the realm of integrated modelling, different water quantity and quality processes need to be considered without neglecting the most important physical phenomena: the upland rural catchment processes, the hydraulics of the river and the in-stream transport and conversion processes of water quality constituents.

There exist numerous environmental simulators for the modelling of the upland catchment processes. These models differ in terms of complexity for the representation of the physical processes, in temporal and spatial scales and regarding the input data requirements. For example, hydrological models such as the Soil and Water Assessment Tool (SWAT) [4] and SHE [5] are widely used for upland catchment modelling and also contain water quality modules. In general, the hydrological models provide a detailed representation of the upland processes but use simplified routing techniques for the receiving water bodies [3].

As a typical example of a hydrological simulator, SWAT considers the interactions between water, soil and plants—the latter being quite important in view of the modelling of the nutrient processes—in the upland catchments in a quite detailed way [6–11], but its river routing modules—the variable storage method [12] or the Muskingum method [13]—are just simplified approximations of the kinematic wave equation and cannot take backwater effects into consideration [2]. In addition, hydraulic structures such as weirs, locks, orifices, pumps and gates cannot be implemented in SWAT. Hence, to be generally applicable for integrated catchment modelling, SWAT needs an improvement of its routing modules by replacing these modules by a dynamic wave routing approach or it should be coupled with a hydraulic model that uses such an approach.

As opposed to most hydrological simulators, the hydraulic simulators generally consider the full dynamic wave equation for river routing and are thus able to account for backwater effect and to represent various hydraulic structures. Some of these simulators also consider the in-stream transport and conversion of water quality constituents in a more or less detailed way. Examples of such simulators are the Storm Water Management Model (SWMM) [14], HEC-RAS [15] and MIKE11 [16]. The weak point of these simulators is that they generally represent the upland catchment processes in a simplified way [2]. Therefore, the hydraulic models also need to be complemented by more detailed hydrological models.

An optimal solution to the problem consists of integrating various types of models, thereby making use of one's strength over the other's weakness. Brandmeyer and Karimi [17] provide an overview of various coupling techniques for environmental modelling. Recently, the Open Modelling Interface (OpenMI) [18]—based coupling is getting more and more attention for integrated modelling because (1) it makes use of existing models [18], (2) it ensures dynamic linking of data between time-dependent models at run-time and thereby eliminates the time-consuming and error-prone task of data extraction and conversion [17, 19], (3) it offers flexibility and a generic model integration [2], and (4) it allows for the reuse of models [19]. Hence, we also used the OpenMI coupling method.

In this paper, we present an OpenMI-based fully integrated modelling approach to simulate the in-stream water quality process applied to the river Zenne, Belgium. For the rural catchments of our study case, we used SWAT to simulate both flow and water quality variables. To represent the river processes, as well as the processes in the major sewer systems, we selected SWMM. In addition, as SWMM lacks a detailed representation of the water quality processes, we developed a new water quality simulation tool. The latter is based on the QUAL2E [20] principles. Although the QUAL2E approach has some clear shortcomings [21], the approach was chosen because of its wide applicability and simplicity. More important, as the representation of the water quality processes in SWAT is based on the same principles, the same state variables could be used for both models. Finally, to address the temperature effects on the kinetic parameters of water quality simulator, we developed a new model code to calculate the stream water temperature. The temperature simulator assumes a nonlinear relationship between air and stream water temperature, as suggested by Mohseni et al. [22].

To be able to link these different components in the OpenMI platform, we migrated the existing modelling tools (SWAT and SWMM) to the OpenMI standard by rearranging the engine core, while the new model codes were directly conceived in an OpenMI compliant way. The main objective of this paper is to test the applicability and usefulness of OpenMI-based integrated water quality modelling.

A brief description of the study basin and the used different models for integrated water quality modelling are given in Sect. 2. Section 2 also provides details on the data used including the calibration strategy, and the structure for integrated water quality modelling. Results of the application for the integrated models are shown and discussed in Sect. 3. Final conclusions are formulated in Sect. 4.

2 Materials and Methods

2.1 Description of the Models

SWAT is a physically based, semi-distributed, hydrological and water quality simulator that operates on different time steps at a basin scale. SWAT was originally developed to predict the impact of watershed management on water,

sediment, nutrients and agricultural and chemical yields at basin scale [4]. Additionally, SWAT can integrate complex watersheds with varying land use, weather, soils, topography and management conditions over a long period of time. The model is interfaced with a geographic information system (GIS) to integrate various spatial and hydro-meteorological data [23]. A watershed is divided into a number of subbasins that have homogeneous climatic conditions [24]. Subbasins are further subdivided into hydrological response units (HRUs) based on a homogenous combination of land use, soil type and slope [25]. The water balance equation includes precipitation, surface runoff, actual evapotranspiration, interflow and return flow components profile [26]. The simulator uses a modification of the Soil Conservation Service Curve Number (SCS-CN) method [27], which determines the surface run-off based on the antecedent moisture content for each HRU, or alternatively, it uses the Green and Ampt method as modified by Mein and Larson [28] if subdaily precipitation data are provided. The percolation through each soil layer is estimated using a storage routing techniques [29]. SWAT offers three options to estimate the potential evapotranspiration (PET) from climatic data: the Penman-Monteith method [30], the Hargreaves method [31] and the Priestley-Taylor method [32]. River routing can be performed by the variable storage method [12] or by the Muskingum method [13].

SWAT simulates the nutrient cycles for nitrogen and phosphorous in the soil profile and in the shallow aquifer by considering mineralization, decomposition and immobilization processes from different pools. For the nitrogen cycle, the model considers five pools: two inorganic forms (ammonium and nitrate) and three organic forms (fresh, stable and active). Similarly, the phosphorous cycle is monitored at six different pools: three inorganic and three organic forms. The river water quality module, which is incorporated into the SWAT, is based on the concepts of QUAL2E [20]. Variables that can be simulated include nutrients, biochemical oxygen demand, dissolved oxygen and microorganisms [6, 26].

SWMM is a dynamic rainfall runoff and conduit or channel flow simulation model, aiming at computing the run-off quantity and quality primarily from urban areas. SWMM can be used for both continuous and single event modelling. A drainage system in the SWMM is modelled as a series of water and material flows between four major subunits: the atmosphere compartment, the land surface compartment, the groundwater compartment and the transport compartment [14]. The latter takes care of the flow routing, based on the dynamic wave routing approach (or approximations of the latter). It allows also for the representation of many types of hydraulic structures in the system and the definition of their operation rules.

The developed in-stream water quality model incorporates the water constituents interactions based on the principles and concepts of QUAL2E [20]. The stoichiometric matrix with the process rates for the water quality model is shown in Table 1. The model contains 9 state variables and 15 processes.

The temperature model uses a regression model between air and stream temperature. Such model has lesser calculation overhead and proved to be quite accurate too. A nonlinear fit of the type as suggested by Mohseni et al. [22] is used. Besides, thermal discharges—for example, from WWTPs—can be considered.

Table 1 Stoichiometric matrix of the water quality model with different components, processes and rates [33]

Component	1	2	3	4	5	6	7	8	9	Process rate
Process	DO	BOD	ABM	ORG-N	NH4	NO2	NO3	ORG-P	DIS-P	[$ML^{-3}T^{-1}$]
1. Reaeration	1									K2.(DOsat-DO)
2. Biodegradation	−1	−1								K1.BOD
3. BOD sedimentation		−1								K3.BOD
4. Sediment DO demand	−1									K4/d
5. Photosynthesis	$\alpha 3$		1		−0.07.FNH4		−0.07.(1-FNH4)		−0.01	μmax.ABM.F(L,N,P)
6. Respiration	$-\alpha 4$		−1	0.07				0.01		ρ.ABM
7. Algae sedimentation			−1							$\sigma 1$/d.ABM
8. Nitrogen hydrolysis				−1	1					$\beta 3$.ORG-N
9. Nitrification 1st step	−3.43				−1	1				$\beta 1$.NH4.f(DO)
10. Nitrification 2nd step	−1.14					−1	1			$\beta 2$.NO2.f(DO)
11. N sedimentation				−1						$\sigma 4$.ORG-N
12. N sediment release					1					$\sigma 3$/d
13. P hydrolysis								−1	1	$\beta 4$.ORG-P
14. P sedimentation								−1		$\sigma 5$.ORG-P
15. P sediment release									1	$\sigma 2$/d

where *DO* dissolved oxygen [ML^{-3}]; *DOsat* saturation concentration [ML^{-3}]; *BOD* biochemical oxygen demand [ML^{-3}]; *ABM* algal biomass [ML^{-3}]; *OPG-N* organic nitrogen [ML^{-3}]; NH_4 ammonia-N [ML^{-3}]; NO_2 nitrite-N [ML^{-3}]; NO_3 nitrate–N [ML^{-3}]; *ORG-P* organic phosphorus [ML^{-3}]; *DIS-P* dissolved phosphorus [ML^{-3}]; $K1$ deoxygenating coefficient [T^{-1}]; $K2$ reaeration coefficient [T^{-1}]; $K3$ BOD settling rate [T^{-1}]; $K4$ sediment oxygen demand rate [$ML^{-2}\ T^{-1}$]; d mean steam depth [L]; μmax maximum algal growth rate [T^{-1}]; ρ algal respiration rate [T^{-1}]; $\sigma 1$ algal settling rate [LT^{-1}]; $\sigma 2$ benthos source rate for P [$ML^{-2}\ T^{-1}$]; $\sigma 3$ benthos source rate for N [$ML^{-2}\ T^{-1}$]; $\sigma 4$ N settling rate [T^{-1}]; $\sigma 5$ P settling rate [T^{-1}]; $\beta 1$ ammonia oxidation rate [T^{-1}]; $\beta 2$ nitrite oxidation rate [T^{-1}]; $\beta 3$ N hydrolysis rate [T^{-1}]; $\beta 4$ P hydrolysis rate [T^{-1}]; $\alpha 3$ oxygen production per unit algal growth

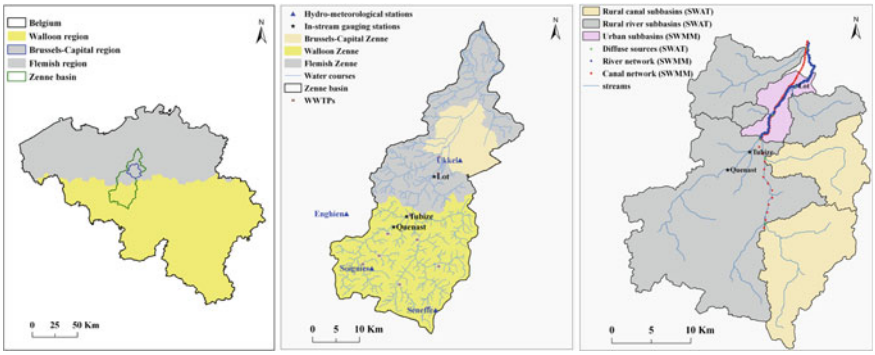

Fig. 1 Location of the Zenne basin in Belgium (*Left*), the three regions in the Zenne river basin with water courses, locations of WWTPs and hydro-meteorological stations (*middle*), and the study area upstream of the Brussels-capital region (*right*)

2.2 The Study Area

The Zenne River basin drains an area of 1,162 km^2 and runs through the three administrative regions of Belgium (Fig. 1): the Walloon Region (574 km^2), the Brussels-Capital Region (162 km^2) and the Flemish Region (426 km^2). After a length of about 103 km, it finally meets the river Dijle, where it is subject to the tidal influence of the river Scheldt. About 1.5 million people discharge to the river. Almost parallel to the river runs the canal Brussels-Charleroi that interacts with the river; especially in the southern part of the basin, the flow of some of the tributaries is diverted to the canal, while also several exchange points are established between the river and the canal, to prevent Brussels from flooding. As a consequence, the canal has to be integrated in the modelling of the system.

This paper is limited to the upstream of Brussels region, as a first step towards the integrated modelling of water quality processes in the river Zenne. The upstream basin has an area of ca. 747 km^2 and a population density of 470 inhabitants per km^2.

The upstream basin elevation ranges from 18 to 171 m above mean sea level. It is dominated by agricultural land use (56 %) followed by pasture (22 %) and mixed forest (11 %), whereas the remaining area is covered by other land uses (urban, rangeland and water bodies). The upstream basin is mainly covered by loam soils (79 %), while the other soils (anthropogenic, sandy loam, sand, loamy sand and clay) account 21 % (Table 2).

2.3 The Data

We developed the SWAT model based on 30 × 30 m digital elevation models (DEM) obtained from OC GIS-Vlaanderen and ASTER GDEM (http://www.gdem.aster.ersdac.or.jp/search.jsp), on 20 × 20 m soil and land use maps

Table 2 Land use and soil characteristics of the upstream Zenne basin

Land use			Soil		
Type	Area (km^2)	%	Type	Area (km^2)	%
Agriculture	416	56	Loam	590	79
Pasture	167	22	Anthropogenic	87	12
Forest	82	11	Sandy loam	46	6
Urban	72	10	Sandy	13	2
Rangeland	5	1	Loamy sand	6	1
Water	5	1	Clay	4	1

from OC GIS-Vlaanderen and the Carte Numérique des Sols de Wallonie (http://cartographie.wallonie.be/NewPortailCarto/) and on Corrine data from Ministère de la Région Wallonne- Générale de l'Aménagement du Territoire, du Logement et du Patrimoine (MRW- DGATLP).

For the SWMM river and canal model, we used the geometric data of the river sections with an approximate spatial resolution of 100 m, in combination with data of the hydraulic structures, as provided by Flanders Hydraulic Research-Waterbouwkundig Laboratorium (http://www.watlab.be/en).

We obtained daily precipitation data for 3 stations (Enghien, Soignies, Seneffe) of the Direction Générale Opérationnelle de la Mobilité et des Voies Hydrauliques of the Walloon Region (DGVH) (http://voies-hydrauliques.wallonie.be/opencms/opencms/fr/hydro/Archive/annuaires/index.html) and for one station (Ukkel) of the Royal Meteorological Institute of Belgium. Daily maximum and minimum temperatures, wind speed, solar radiation and relative humidity were also available for the Ukkel station.

We estimated the point sources from households and industry based on the assessment of the inhabitant equivalents (IE) and considering a water consumption of 150 l/day.IE, 60 g BOD/day.IE, 10 g Kjeldahl nitrogen/day.IE and 2.2 g total phosphorous/day.IE. We considered the wastewater treatment efficiencies based on data for the different wastewater treatment plants (WWTPs) design capacity (Table 3). For the assessment of the diffuse pollution by SWAT, we used the following annual average application of fertilizers: 125 kg ha^{-1} mineral N, 12 kg ha^{-1} mineral P and 79 kg ha^{-1} organic N (OrgN), as obtained from Direction Générale Opérationnelle Agriculture, Ressources Naturelles et Environnement (DGARNE) (http://aqualim.environnement.wallonie.be). As data for organic P (OrgP) were not available, we used a ratio of OrgN to OrgP of 2.2, based on data for the Flemish Region.

For the calibration of the flow models, we used daily flow data at Tubize (DGVH) and at Lot (Vlaamse Milieu Maatschappij, VMM) (http://www.hydronet.be). Pollutant concentrations were available at Quenast (DGARNE) and at Lot (VMM) for the calibration of the water quality models (Fig. 1).

Table 3 WWTPs design capacity of the upstream Zenne Basin

WWTP					
Name	Design capacity (IE)	Region	Name	Design capacity (IE)	Region
Av.Behault	5,400	Walloon	R. Pont Demeur	25,000	Walloon
Itrre/Catala	5,600	Walloon	St. Pt. Leeuw	30,000	Flemish
Ruc de L'ave del	7,300	Walloon	Monstreux	44,450	Walloon
Braine-le-Comte	11,500	Walloon	Beersel	50,000	Flemish
Biamont	14,000	Walloon	Soudromont	65,000	Walloon

Sources Société Publique de la Gestion de l'Eau, SPGE (http://www.spge.be) of Walloon region and Aquafin (http://www.aquafin.be) of Flemish region

2.4 Model Set-Up

We built the SWAT model for the upstream basin based on the DEM, the land use map, the soil map and the hydro-meteorological data sets of the basin. The model consists of 33 subbasins and 214 HRUs. We set up the SWAT model for the period 1985–2008. The WWTPs in the Walloon Region were considered as explicit in Sect. 2.3.

A SWMM network has been developed for the reach between the border of Walloon–Flemish Region and the Brussels-Capital Region. Hereby, the river and the canal are segmented in intervals of ca. 100 m or less. In addition, the information on special structures on the river such as weirs, orifice and locks and their control rules has been implemented. A diversion structure between the river and the canal is implemented a few km downstream of the Walloon–Flemish border. The WWTPs of Beersel and St. Pt. Leeuw were considered as explicit in Sect. 2.3, and a simplified representation of its sewer system was implemented in SWMM. The SWMM gets its in-flow boundaries from the SWAT model during run-time.

The SWMM network is further also used to represent the system for the water quality and the temperature models.

2.5 Model Integration

The integrated model consists of 4 OpenMI compliant models (SWAT, SWMM, the water quality model and the temperature model) as summarized in Fig. 2. The SWAT model provides the run-off from the rural catchments to the SWMM model that calculates the hydraulic variables in the river reaches and provides them to the temperature and the water quality models. SWMM is also used to simulate the flows in the (simplified) sewer networks. The temperature model provides stream

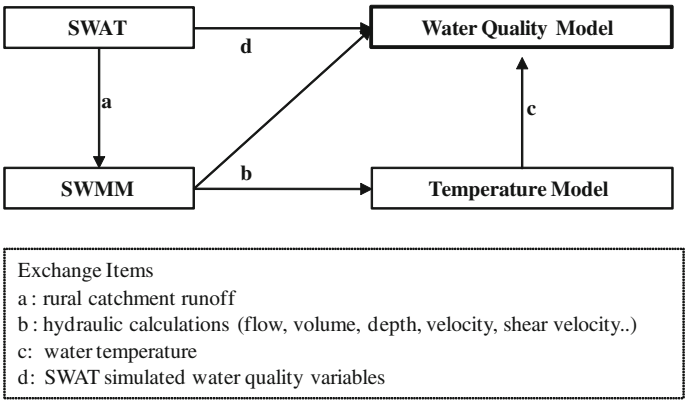

Fig. 2 OpenMI data flow diagram for the integrated water quality model

water temperature to the water quality model to assess the temperature dependence on the kinetic parameters. The SWAT model also provides diffuse pollution concentrations from the rural catchments to the water quality model. The latter model then simulates the in-stream conversion processes of the water quality variables along the river.

2.6 Model Calibration and Validation

For the SWAT model, we used three years (1985–1987) for warming up of the model and the years 1998–2008 to calibrate the model both for water quantity and quality. The model was then validated for the years 1988–1997. Before calibration, we carried out a sensitivity analysis to determine the most important parameters of the model with respect to the water quantity, using the sensitivity analysis tool of SWAT [34]. Then, we calibrated the model at Tubize by considering the most important parameters, using the auto-calibration tool of SWAT [35]. The water quality component of the SWAT model also calibrated for the years 1998–2008 and validated for the period 1994–1997. For water quality calibration, we followed a heuristic approach due to limited amount of sampling data. We validated the integrated model in terms of water quantity using the observed stream flows of 2007–2008 at Lot. Similar to SWAT, we used a heuristic approach to calibrate the integrated water quality model for the years 2007–2008. The same water quality parameters were optimized both for SWAT model and integrated water quality model.

We used the Nash–Sutcliffe Efficiency, NSE [36], and time series plots for evaluating the performance of the models.

3 Results and Discussion

3.1 SWAT Standalone Results

A good representation of the hydrological processes is crucial for pollution transport modelling [37]. Hence, we first calibrated and validated the SWAT model for the water quantity simulation. Then, the model was calibrated for the water quality variables. To illustrate the results of SWAT with respect to the water quantity from the rural areas, the results at Tubize will be shown. The SWAT results with regard to the water quality will be shown for Quenast, as for this upstream station, the residence times in the river—and thus the impact of the in-stream processes—are small.

3.1.1 Water Quantity

The sensitivity analysis results show that CN2, ALPHA_BF, GWQMN and GW_DELAY are the most sensitive parameters with respect to the flow. Apart from these sensitive parameters, additional parameters were also calibrated (Table 4). The table also includes the calibrated values of the parameters.

Figure 3 depicts the observed and simulated stream flows both for the calibration (1998–2008) and validation (1988–1997) periods at Tubize. The observed and predicted stream flows are reasonably matched for the calibration period (NSE = 0.79), but a lower efficiency is noted for the validation period (NSE = 0.48). The low efficiency during validation could be partly explained by the use of only one rain gauge station (Ukkel) from outside the catchment, while four stations were used during the calibration period. It is also observed that the model is performing well for the low flows, which are important in view of water quality modelling.

Table 4 Optimized water quantity parameters for the SWAT model

Parameters	Description	Unit	Calibrated values
CN2	Curve number	–	69–92*
ALPHA_BF	Groundwater recession constant	day	1
GW_DELAY	Groundwater delay	day	3
ESCO	Soil evaporation compensation factor	–	0.8
GW_REVAP	Groundwater revap coefficient	–	0.12
REVAPMN	Threshold depth in shallow aquifer for revap	mm	47
GWQMN	Depth for groundwater flow occurrence	mm	73
SOL_AWC	Soil water availability capacity	–	0.14–0.34**
SURLAG	Surface runoff lag coefficient	day	1.5

*Varies with land use, soil and slope, **Varies with soil type

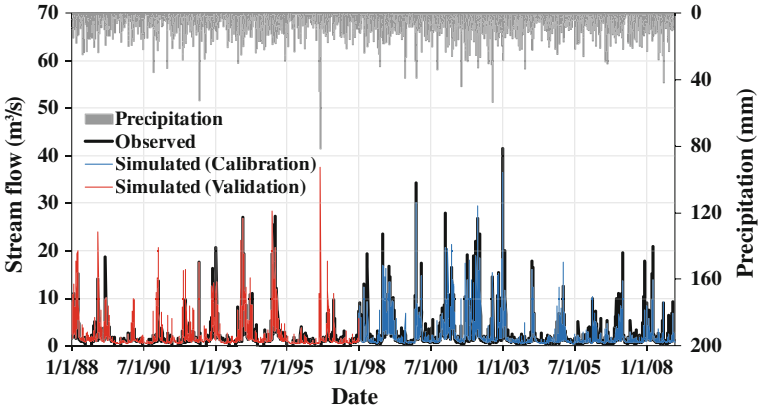

Fig. 3 Observed and simulated daily stream flows at Tubize

3.1.2 Water Quality

The measured and simulated water quality variables (dissolved oxygen (DO), biochemical oxygen demand (BOD), nitrate (NO_3-N) and mineral P) are shown in Fig. 4. The temporal patterns of the simulated BOD and DO are generally in good agreement with the measured values. The simulated DO is closely fitting the observed values. Extreme depletion of oxygen (<5 mg l^{-1}) is noticed during the summer period.

Overall, the trends of the simulated mineral nutrients are fairly following the evolution of observed values, except for the overprediction of some peak values of nitrate and mineral P, particularly during validation and for the years 2003–2008

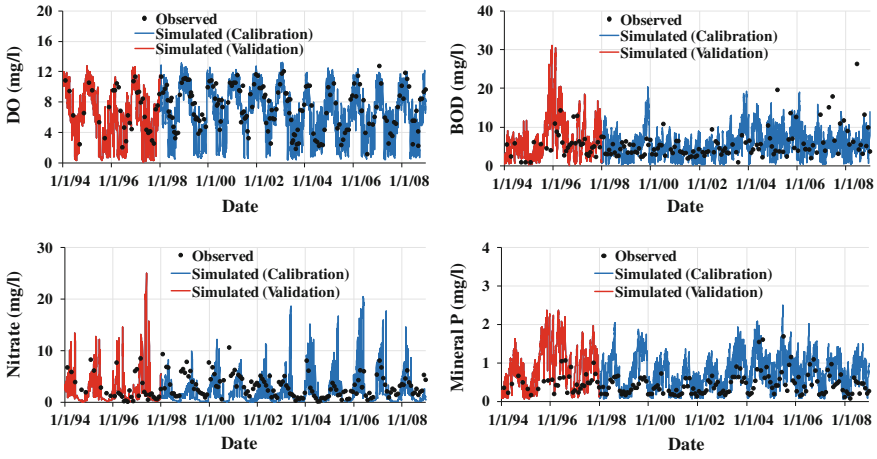

Fig. 4 Observed and simulated DO (*top left*), BOD (*top right*), nitrate (*bottom left*) and mineral P (*bottom right*) at Quenast

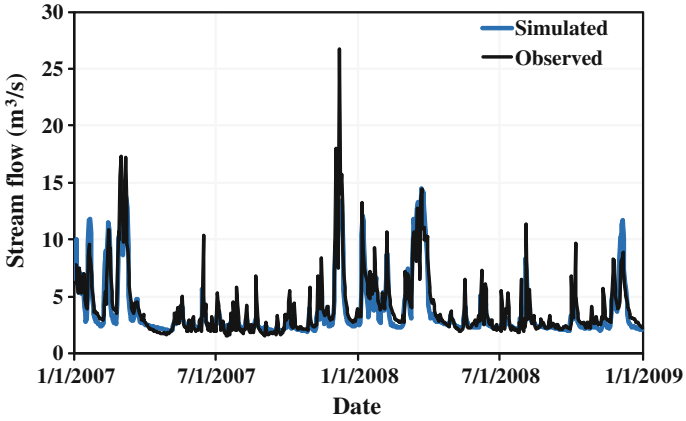

Fig. 5 Observed and simulated daily stream flows at lot for the integrated model

during calibration. This may be partly due to limited information on land management and fertilizer data in the upstream basin, but also the representation of the related processes in SWAT might be questioned.

3.2 Integrated Model Results

In what follows, the results of the integrated model (see Sect. 2.5) are discussed. Figure 5 shows the observed and simulated daily stream flows at Lot. The NSE value of 78 % indicates a good overall performance of the integrated model in terms of the flows, but it is clearly noted that some peak flows are underestimated in 2007.

The calibrated water quality parameters for the in-stream water quality model are shown in Table 5. The parameters are optimized manually considering the ranges and realistic values of the basin.

The results of the integrated water quality model at Lot in terms of DO, BOD, NO_3-N and mineral P are shown in Fig. 6. It can be observed that—while the general trend of DO is reasonably well represented—the model tends to overestimate DO concentrations during the dry periods. Oppositely, the BOD concentrations are underestimated during this period. The model predicted NO_3-N reasonably but it has a tendency to simulate high concentrations of NO_3-N during the storm periods. Similar trends can be observed for the mineral P; however, the model seems systematically overestimated mineral P. This could be partly linked to the overestimation of nitrate and mineral P by SWAT model (Fig. 4). Generally, although further calibration is still needed, the water quality variables are well predicted by the integrated model.

Table 5 Calibrated parameter values for the water quality model

Parameters	Description	Unit	Ranges	Calibrated values
K1	BOD deoxygenation rate coefficient	day^{-1}	0.02–3.4	0.21
K2	Oxygen recreation rate	day^{-1}	0–100	1
K3	Rate loss of BOD due to settling	day^{-1}	−0.36–0.36	0.36
K4	Sediment oxygen demand rate	mgO_2m^{-2} day^{-1}	Variable	2
$\beta 1$	Rate constant for biological oxidation of NH_4 to NO_2	day^{-1}	0.1–1	0.25
$\beta 2$	Rate constant for biological oxidation of NO_2 to NO_3	day^{-1}	0.2–2	0.2
$\beta 3$	Rate constant for hydrolysis of OrgN to NH_4	day^{-1}	0.02–0.4	0.05
$\beta 4$	Rate constant for mineralization of organic P to mineral P	day^{-1}	0.01–0.7	0.1
$\sigma 1$	Rate coefficient for organic N settling	day^{-1}	0.5–6	0.08
$\sigma 2$	Benthic source rate for mineral P	$mgPm^{-2}$ day^{-1}	Variable	1.5
$\sigma 3$	Benthic source rate for NH_4	$mgNH_4m^{-2}$ day^{-1}	Variable	0.01
$\sigma 4$	OrgN settling rate	day^{-1}	0.001–0.1	0.08
$\sigma 5$	Rate coefficient for organic P settling	day^{-1}	0.001–0.1	0.1
μmax	Maximum algal growth rate	day^{-1}	1.0–3.0	2.2
ρ	Algal respiration rate	day^{-1}	0.05–0.5	0.2

While the results of this study seem promising with respect to the potential of OpenMI, it should be mentioned that the approach involves a significant calculation time overhead. When compared to a standalone SWMM simulation of the considered system, the calculation time for the integrated model is increased by a factor of 3–4. The latter is due to the chain of request–reply calls between the models. Hereby, it should be kept in mind that the parallel application of the different models, whereby information has to be exchanged between several models for each of the model reaches/junctions, is an extreme case with regard to the application of OpenMI. The latter is indeed most often used to link models at a limited number of junctions only.

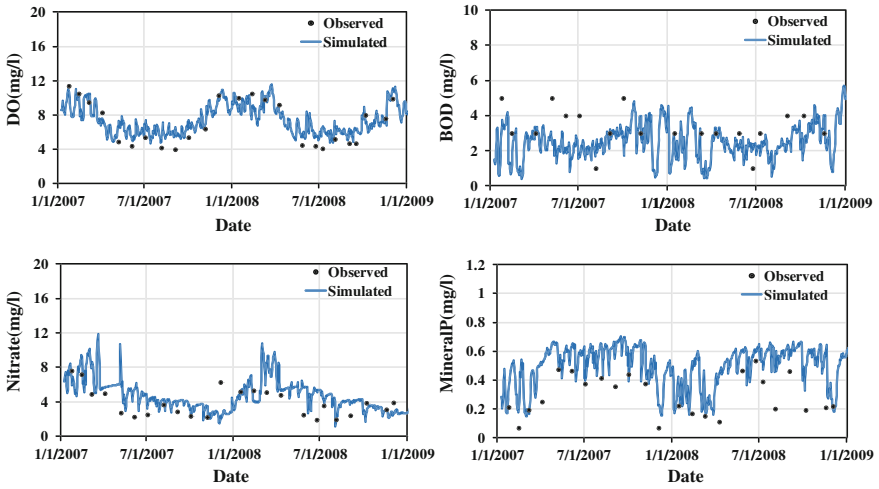

Fig. 6 Observed and simulated DO (*top left*), BOD (*top right*), nitrate (*bottom left*) and mineral P (*bottom right*) at lot for the integrated model

4 Conclusions

An integrated modelling chain for the simulation of the water quality of the river Zenne was presented. In the integrated models, SWAT simulates the flows and the water quality variables from the rural upstream basin(s) and provides them as input to the SWMM model and the water quality model. SWMM routes the flow along the river and supplies the hydraulic variables to the in-stream water quality and the temperature models. The water quality model then simulates the in-stream water quality conversion processes. In the mean time, the temperature model provides the river water temperature to the in-stream water quality model.

It was shown that the integrated model simulates the flow and water quality variables with reasonable accuracy, although further calibration of the models with regard to some of the water quality variables should be performed.

Hereby, the usefulness and the feasibility of using OpenMI to perform a parallel simulation, using SWAT, SWMM, a water quality model and a temperature model, have been demonstrated for a complex river basin. We believe that such an integration can be very useful as a decision support tool for integrated river basin management.

The calculation time overhead of the OpenMI-based integrated models is the major drawback of the presented approach.

Acknowledgments The study was carried out in the framework of the project "Towards a good ecological status of the River Zenne (GESZ)", as funded by INNOVIRIS, the Brussels Institute for Research and Innovation. We also thank all the institutes and administrations mentioned in this paper for providing the necessary data.

References

1. EU (2000). *Directive 2000/60/EC of the European parliament and of the council of 23 Oct 2000 establishing a framework for community action in the field of water policy*. EU-WFD.
2. Betrie, G. D., van Griensven, A., Mohamed, Y. A., Popescu, I., Mynett, A. E., & Hummel, S. (2011). Linking SWAT and SOBEK using open modeling interface (OpenMI) for sediment transport simulation in the Blue Nile river basin. *Trans. Am. Soc. Agric. Biol Eng, 54*, 1749–1757.
3. Debele, B., Srinivasan, R., & Parlange, J. Y. (2008). Coupling upland watershed and downstream waterbody hydrodynamic and water quality models (SWAT and CE-QUAL-W2) for better water resources management in complex river basins. *Env. Model. Assess., 13*, 135–153.
4. Arnold, J. G., Srinivasan, R., Mukundan, R. S., & Williams, J. R. (1998). Large area hydrologic modeling and assessment part I: model development. *J. Am. Water Res. Ass., 34*, 73–78.
5. Refsgaard, J. C. (1997). Parameterisation, calibration and validation of distributed hydrological models. *J. Hydrol., 198*, 69–97.
6. Jha, M. K., Gassman, P. W., & Arnold, J. G. (2007). Water quality modeling for the Raccoon river watershed using SWAT. *Trans. Am. Soc. Agric. Biol. Eng., 50*, 479–493.
7. Lam, Q. D., Schmalz, B., & Fohrer, N. (2010). Modelling point and diffuse source pollution of nitrate in a rural lowland catchment using the SWAT model. *Agr. Water Manag., 97*, 317–325.
8. Santhi, C., Arnold, J. G., Williams, J. R., Dugas, W. A., Srinivasan, R., & Hauck, L. M. (2001). Validation of the SWAT model on a large river basin with point and nonpoint sources. *J. Am. Water Res. Ass., 37*, 1169–1188.
9. Srinivasan, R., Ramanarayanan, T. S., Arnold, J. G., & Bednarz, S. T. (1998). Large area hydrologic modeling and assessment part II: Model application. *J. Am. Water Res. Ass., 34*, 91–101.
10. White, K. L., & Chaubey, I. (2005). Sensitivity analysis, calibration, and validations for a multisite and multivariable SWAT model. *J. Am. Water Res. Ass., 41*, 1077–1089.
11. Gassman, P. W., Reyes, M. R., Green, C. H., & Arnold, J. G. (2007). The soil and water assessment tool: Historical development, applications, and future research directions. *Trans. Am. Soc. Agric. Biol. Eng., 50*, 1211–1250.
12. Williams, J. R. (1969). Flood routing with variable travel time or variable storage coefficients. *Trans. Am. Soc. Agric. Biol. Eng., 12*, 0100–0103.
13. Chow, V. T. (1959). *Open channel hydraulics*. New York: McGraw-Hill Book Company.
14. Rossman, L. A. (2010). *Storm water management model user's manual*. Cincinnati: National risk management research laboratory. 45268.
15. Brunner, G. W. (2008). *HEC-RAS River analysis system user manual, version 4.0*. Davis: Institute for Water Resources.
16. Havno, K., Madsen, M. N., & Dorge, J. (Eds.). (1995). *MIKE-11: A generalized river modeling package, Highlands Ranch*. Colo: Water Resources Publications.
17. Brandmeyer, J. E., & Karimi, H. A. (2000). Coupling methodologies for environmental models. *Environ. Model. Softw., 15*, 479–488.
18. Gregersen, J. B., Gijsbers, J. A., & Westen, S. J. P. (2007). OpenMI: Open modelling interface. *J. Hydroinformatics, 9*, 175–191.
19. Reubner, F., Alex, J., Bach, M., Schutze, M., & Muschalla, D. (2009). Basin-wide integrated modelling via OpenMI considering multiple urban catchments. *Water Sci. Technol., 60*, 1241–1248.
20. Brown, L. C., & Barnwell, T. O. (1987). *The enhanced stream water quality models QUAL2E and QUAL-UNCAS: Documentation and user manual*. EPA.

21. Masliev, I., Somlyody, L. & Koncsos, L. (1995). *On reconciliation of traditional water quality models and activated sludge models*. Working paper WP-95-18, IIASA, Laxenburg, Austria.
22. Mohseni, O., Stefan, H. G., & Erickson, T. R. (1998). A nonlinear regression model for weekly stream temperatures. *Water Resour. Res., 34*, 2685–2692.
23. Winchell, M., Srinivasan, R., & Luzio, M. D. (2010). *ArcSWAT interface for SWAT2009 user's guide*. Blackland: Soil and Water Research Laboratory Agricultural Research Service.
24. van Liew, M. W., Arnold, J. G., & Bosch, D. D. (2005). Problems and potential of autocalibrating a hydrologic model. *Trans. Am. Soc. Agric. Biol. Eng., 48*, 1025–1040.
25. Arnold, J. G., Kiniry, J. R., Srinivasan, R., Williams, J. R., Haney, E. B., & Neitsch, S. L. (2011). *Soil and water assessment tool. Input/output file documentation, Version 2009*. Temple: Agrilife Blackland Research Center. 76502.
26. Neitsch, S. L, Arnold, J. G, Kiniry, J. R, Williams, J. R. (2011). *Soil and water assessment tool. Theoretical documentation, Version 2009*. Grassland, Soil and Water Research Laboratory, Agricultural Research Service Blackland Research Center-Texas AgriLife Research.
27. USDA-SCS. (1986). *US Department of Agriculture-Soil Conservation Service (USDA-SCS): Urban hydrology for small watersheds*. Washington, DC: USDA.
28. Mein, R. G., & Larson, C. L. (1973). Modeling infiltration during a steady rain. *Water Resour. Res., 9*, 384–394.
29. Arnold, J. G., Williams, J. R., & Maidment, D. R. (1995). Continuous-time water and sediment-routing model for large basins. *J. Hydraul. Eng., 121*, 171–183.
30. Monteith, J. L. (1995). Evaporation and environment. *Symp. Soc. Exp. Biol., 19*, 205–234.
31. Hargreaves, G. L., Hargreaves, G. H., & Riley, J. P. (1985). Agricultural benefits for Senegal River basin. *J. Irrig. Drainage Eng., 111*, 113–124.
32. Priestley, C. H. B., & Taylor, R. J. (1972). On the assessment of surface heat flux and evaporation using large-scale parameters. *Mon. Weather Rev., 100*, 81–92.
33. Reichert, P., Borchardt, D., Henze, M., Rauch, W., Shanahan, P., Somlyody, L., et al. (2001). *River water quality model no. 1*. London: IWA Publishing.
34. van Griensven, A., Meixner, T., Grunwald, S., Bishop, T., Di Lluzio, M., & Srinivasan, R. (2006). A global sensitivity analysis tool for the parameters of multi-variable catchment models. *J. Hydrol., 324*, 10–23.
35. Green, C. H., & Van Griensven, A. (2008). Autocalibration in hydrologic modeling: Using SWAT2005 in small-scale watersheds. *Environ. Model. Softw., 23*, 422–434.
36. Nash, J. E., & Sutcliffe, J. V. (1970). River flow forecasting through conceptual models part I: A discussion of principles. *J. Hydrol., 10*, 282–290.
37. Kannan, N., White, S. M., Worrall, F., & Whelan, M. J. (2007). Hydrological modelling of a small catchment using SWAT-2000: Ensuring correct flow partitioning for contaminant modelling. *J. Hydrol., 334*, 64–72.

Part III
3D CFD and Applications

Introduction to Part III: 3D CFD and Applications

Philippe Gourbesville, Jean Cunge and Guy Caignaert

The third part refers to the efficient use of CFD in two application domains:

- Industrial problems relating to hydraulic machinery and systems or to specific problems;
- Free surface problems with mainly environmental purposes.

The difficulties of CFD approaches that appear in the papers are due to:

- the geometry complexity and the associated meshing, with the management of various reference frames and of the necessity of mesh refinements, for example in the vicinity of surfaces limiting the calculation domain;
- the management of time and scale resolutions to attain;
- the management of boundary conditions;
- the management of multiphase flows and associated interfaces.

Most applications use 3D CFD, with a lot of experimental validations that are still necessary, especially to validate the models that are chosen by the authors in order to have a good description of physical phenomena of interest.

Two papers show how 1D models can be useful to study large-scale problems with transient considerations. One of them combines 1D and 3D calculations in order to solve efficiently and accurately an engineering problem. One-dimensional simulations refer to SIMSEN package.

P. Gourbesville (✉)
University of Nice-Sophia Antipolis, 930 Route Des Colles, Sophia Antipolis 06903, France
e-mail: Philippe.Gourbesville@unice.fr

J. Cunge
31 Rue Doyen Gosse, La Tronche 38700, France
e-mail: jacunge@orange.fr

G. Caignaert
Society Hydrotechnique of France, 25 Rue des Favorites, Paris 75015, France
e-mail: Guy.CAIGNAERT@ENSAM.EU

P. Gourbesville et al. (eds.), *Advances in Hydroinformatics*,
Springer Hydrogeology, DOI: 10.1007/978-981-4451-42-0_23,

Three types of numerical methods are mainly proposed in the papers for 3D CFD:

- Finite volume method with either commercial CFD software packages (ANSYS CFX, FLOW3D, FLUENT), free open-source CFD software packages (code_SATURNE, OpenFOAM,), or academic code (SSIIM for Sediment Simulation In Intakes with Multiblock option from Norwegian University of Science and Technology), used to solve either shallow water or Navier–Stokes equations according to the kind of application. Multiphase flow problems are solved within these codes using the volume of fluid approach.
- Finite element method with freeware and open-source code TELEMAC-MASCARET where shallow water equations are solved
- Smoothed Particle Hydrodynamics (SPH) method and extensions as SPH-ALE (SPH—Arbitrary Lagrange Euler) and SPH-FPM (SPH-finite particle method), that appear to be useful to model multiphase flows with surface tension.

The large variety of applications in that chapter demonstrate that methods such as Reynolds-averaged Navier–Stokes (RANS), unsteady RANS (URANS), or transient RANS (TRANS) are now of common use in industry even if the appropriate choice of turbulence model has still to be validated with reference to the objectives of the simulation and the accuracy target. One paper shows how such a method can be efficiently used in order to optimize the design of an industrial component: of course, this necessitates a very large amount of calculations, but the use of cloud computing makes it now reasonable for the user.

The reader of that chapter will find a large number of practical examples, covering a large spectrum of methods. It is clear that research is going on for the development of more accurate numerical methods. Chapters using Detached Eddy Simulation (DES) or Large Eddy Simulation (LES) will probably become more common in the next SimHydro events. A need for more discussions about the uncertainties of such numerical methods is also clearly established and will be required for next SimHydro conferences.

Use of Numerical Modeling to Optimize the Placement of Data-Gathering Equipment in Low-Head Hydro Production Structures

Julien Schaguene, Olivier Bertrand, Eric David, Pierre Roumieu, Gilles Pierrefeu, Karine Pobanz, Xavier Cornut and Laurent Tomas

Abstract In 2010, rivers in France provided 12 % of the country's electricity. However, as locations for new hydraulic power plants are no longer plentiful, the efficiency of the existing ones has to be increased. The aim of the PENELOP2 project is to study the influence of different factors contributing to the disturbance of low-head turbine function, in order to develop ways in which to optimize sites and production methods and thus increase production rates. For the purposes of the project, it is planned to install a significant quantity of instrumentation (current meters, ADCP sensors, and ASFM) on a generating set at the Vaugris power station on the Rhône. Owned by CNR, the Vaugris plant is equipped with 4 bulb turbines supplied by Alstom in the 1970s. These have runner diameters of 6.25 m and deliver 18 MW each under 5.65 m net head. Data collected from Vaugris test sites will be used for calibrating and adjusting several different physical and numerical models. Although a normal study schedule foresees the calibration of numerical models in line with data recorded on site, local constraints have led to the development of an initial 3D numerical model that will allow flow to be determined, thus allowing equipment to be optimally positioned. In this case, it is therefore a matter of using the preliminary results to optimize the use of site data, to find the optimum location for placing equipment and to obtain the most coherent data possible to inform a posteriori calibration of the physical and numerical models.

Keywords Hydraulic power plant · Data-gathering · Low-head turbine · 3D numerical modeling · ADCP · Propeller · Discharge measurement

J. Schaguene (✉) · O. Bertrand · E. David
Artelia, Echirolles, France
e-mail: Julien.schaguene@arteliagroup.com

P. Roumieu · G. Pierrefeu · K. Pobanz
CNR, Lyon, France

X. Cornut · L. Tomas
Alstom Power Hydro, Grenoble, France

P. Gourbesville et al. (eds.), *Advances in Hydroinformatics*,
Springer Hydrogeology, DOI: 10.1007/978-981-4451-42-0_24,

1 Introduction

In the framework of applying the various "climate change plans" in France and Europe since the start of the 2000s, France is required to reduce its energy expenditure while increasing the share of renewable energy in its consumption.

In 2010, hydraulic energy represented 80 % of renewable energy production in France. It has the advantage of being highly adaptable to the demand placed on the network, in contrast to solar and wind energy. However, most potential production sites are already equipped, and so it is necessary to improve their operation in order to increase their productivity.

This is the aim of the project known as PENELOP2 (Performance ENergétiques, Economiques, et environnementaLes des Ouvrages de Production hydroélectrique de basse-chute—Energy, economic, and environmental performance of low-head hydro production structures), a collaborative research project involving major players in the area of hydraulics in France (Compagnie Nationale du Rhône (CNR), Alstom Hydro France, Artelia Eau & Environnement, In Vivo Environnement, Actoll, JKL Consultants, and Grenoble INP). PENELOP2 is approved by the Tenerrdis competetiveness cluster, with funding granted in the framework of the 9th *Fonds Unique Interministériel* (FUI) programme.

PENELOP2 concentrates on low-head turbines. Because they operate on a run-of-river basis, the turbines (which are generally of the bulb type) are vulnerable to flow disturbances, especially upstream. The aim is to devise a method for optimizing the shape of the built structure around the turbine, depending on inflow and outflow conditions. Several stages are scheduled with this in view: instrumentation of unit G4 at Vaugris on the River Rhone, in order to obtain the maximum amount of data that can be exploited in the numerical and physical models built subsequently. The models will then test the various possible modifications for improving the uniformity of flow along the flow path. Finally, a more general optimization method must be introduced by extrapolating the results obtained on the numerical model of Vaugris, and by constructing other conceptual models.

In view of the quantity and cost of using the measuring equipment deployed during the campaign, it was decided to build a preliminary 3D CFD model in order to maximize the efficiency of the in situ measurements and prepare for processing the expected results. This approach which is contrary to the usual method used (where a numerical model is calibrated by means of measurements) is the subject of this article.

2 Presentation of the 3D Numerical Model

In order to prepare the in situ measurement campaign as efficiently as possible and place the various sensors in the best possible positions, Artelia built an initial 3D numerical model of the hydraulic passage for a unit in the Vaugris plant (project

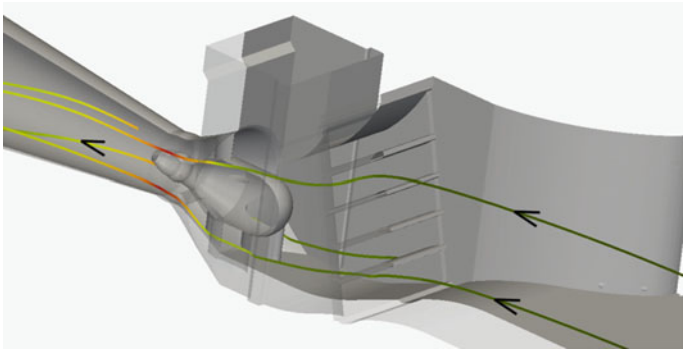

Fig. 1 Longitudinal section of the 3D model

pilot site). This model runs from 70 m upstream of the inlet to unit G4 (on which instrumentation was placed during the PENELOP2 project), to the outlet from the draft tube downstream of the plant.

This model was built with the OpenFOAM CFD software. The grid consists mainly of cubic cells, the size of which varies from 10 cm to 1 m depending on the area modeled. The grid is refined near the walls and in potentially highly turbulent areas. The grid consists of a total of over a million cells.

The aim of this preliminary model was to produce results rapidly, even without having any calibration data available in order to analyze flows in the plane of the measurement frame (positioned at the level of the stop-log grooves upstream of the water chamber), where instruments would then be placed. It was therefore decided to take into account only the fixed components of the bulb unit. The rotating blades and their effects, which are in principle negligible in an area so far upstream of the bulb, were therefore not represented. The Fig. 1 showing a longitudinal section gives a clearer idea of the components taken into account in an upstream–downstream direction. These include the roundhead separating the power plant and the dam (visible on the left side of this section), the floor, the main supports of the inlet screen, the water chamber, the bulb and its supports, and finally the draft tube.

Still with a view to ensuring simplicity, it was decided not to take into account the free surface at the entrance to the model or in the water chamber. This was therefore fixed by the upper boundary of the model, to which a slip boundary condition was applied. A discharge was imposed uniformly at the upper boundary on the assumption that the distance to the inlet was sufficient for the major structures of the flow, constrained in particular by the geometry of the roundhead, would have enough time to be established. The model will then be coupled with a much larger one (covering the width of the Rhône) in order to take into account any elements (adjacent units, dam gates, etc.) disturbing flow at the upstream boundary. A uniform pressure was applied at the outflow from the draft tube.

A k-ε type model was used for these simulations, with a turbulent intensity of 10 % at the entrance to the model and a stilling length of 10 % of the depth of water, that is, 1.5 m.

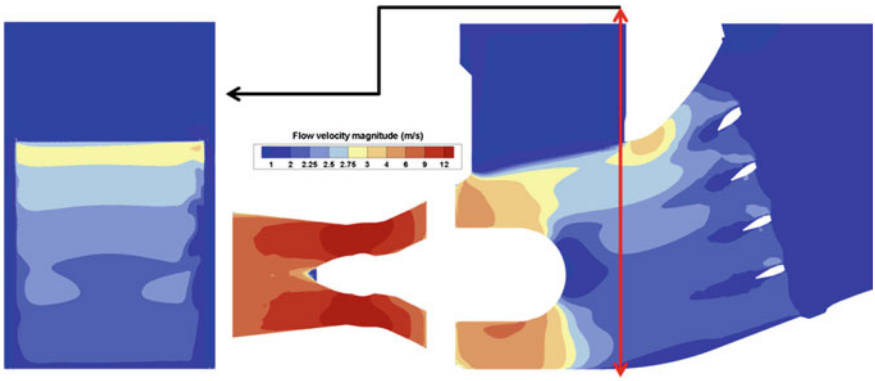

Fig. 2 Flow velocity in the plane of the measurement frame (*left*)—view of flow in the axial longitudinal plane (*right*)—the position of the frame plane is indicated by the *red line*

The test schedule called for the study of three main flow rates: 110, 220, and 350 m^3/s. These three flow rates were therefore simulated, with two additional simulations being run for ±10, 20, and 25 m^3/s.

As an example, the results obtained for a flow rate of 350 m^3/s are presented in the Fig. 2.

The following can be observed from this result in the plane of the measurement frame: flow is slightly asymmetrical between the left and right walls (this result can be explained by the shape of the roundhead upstream); detachment in the lower part due to the shape of the floor; higher velocity in the upper part linked directly with the upstream inlet; little impact of the stoppage point observed on the upstream part of the bulb and main supports of the inlet screen; and boundary layers of varying thickness at the stop-log grooves.

Finally, the model gives a 3D representation of the velocity intensities and directions in the entire hydraulic passage through the unit and an indication of the usefulness of placing measurement sensors in the plane situated at the stop-log grooves. This information should guide the experimenters in choosing the location and orientation of the sensors.

3 Presentation of the Instrumented Measurement Frame

A measurement frame was built for the purposes of the project and fitted with instruments. It is 18 m high and 12 m wide. It was placed in the grooves intended to hold the stop log for closing off unit G4. In view of its dimensions and the handling equipment available on site, the frame had to be built in several sections that were then assembled on site.

Finally, the measurement frame was designed in two parts: one fixed inside the stop-log slot, carrying the ADCP (acoustic Doppler current profiler) and ASFM

Fig. 3 *Upper part* of the measurement frame prior to immersion—the *white part* is the sliding support for the propellers

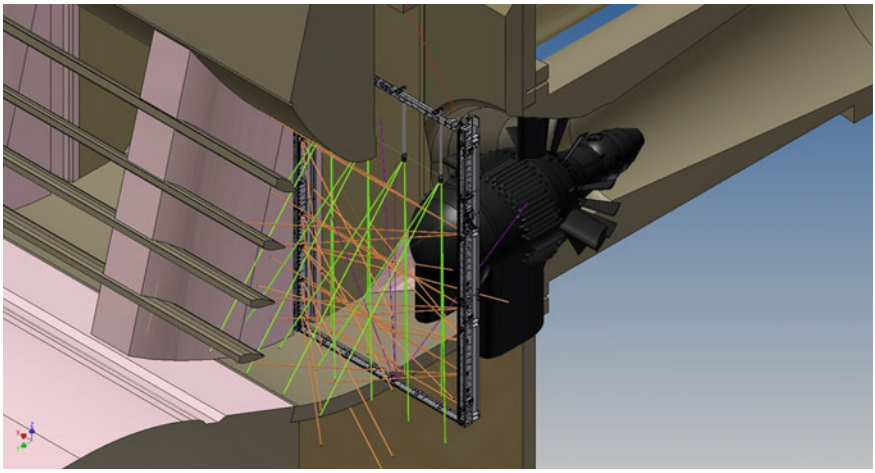

Fig. 4 View of the position of the frame inside the unit and of the ADCP beams upstream of the turbine

(acoustic scintillation flow meter) sensors, and the second sliding inside the first one and carrying the discharge measurement propellers (Fig. 3). This movable chassis is made of teardrop profiles to limit flow perturbations. It was also designed carefully from a structural point of view to remain stiff enough so as not to bend under the flow or to produce vibrations which would have spoiled the quality of the ASFM measurement.

The Fig. 4 shows a theoretical layout and the situation of the frame with respect to the various components of the turbine.

3.1 Current Meter Measurement

The current meter method has been successfully used by Alstom for discharge measurement in power plants for decades. The main drawback of the method is the cost related to preparing the tests and the time taken for the measurements. However, the current meter method offers several advantages even today: the velocity is measured directly and not deduced from other physical values, it targets an area in the section that we are particularly interested in and it allows an appreciation of changes in the velocity field with respect to the height and width of the measurement section.

The propeller bodies used are of Dumas-Neyrpic type, with 50 mm propellers for those closest to the wall and 120 mm auto-compensating propellers for the others. They ensure a resolution of three tops per revolution and were calibrated for a velocity range of 0.4–3.2 m/s according to the preliminary CFD studies conducted for the PENELOP2 project.

Throughout the measurement process, the method was based on standard ISO 3354:1998 "Measurement of fluid flow in closed conduits," which defines the necessary rules to ensure accurate measurement. As stated in this standard, even though some of the standard requirements were not met, such as the minimum length between the measurement section and any channel irregularity, the method can be used, though with slightly greater uncertainty.

3.2 ADCP Measurement

An ADCP is a current profiler based on the Doppler effect. It is one of the techniques used to measure discharges by exploring velocity fields. Frequently implemented to measure discharges in rivers, it was used in a confined environment in the framework of the PENELOP2 project. Thirteen Workhorse Rio Grande–type ADCPs with frequencies of 600 and 1,200 kHz and one V-ADCP with a frequency of 2,400 kHz were used for this project. Several sensors were lent by government services and the manufacturer, completing those of CNR and In Vivo to ensure the project was carried out satisfactorily.

The Workhorse Rio Grande ADCPs are equipped with four beams located in orthogonal planes in pairs at an angle of 20° in relation to the axis of the ADCP. The V-ADCP sensor is also equipped with four beams: three set at an angle of 20° in relation to the axis of the ADCP to measure radial speeds; the fourth, in the axis of the ADCP, measures the height of the water only.

The ADCP measures velocity components as a function of the axes of the beams. These radial velocities can be used with simple trigonometric formulae to estimate flow velocity in three dimensions, Vx, Vy, and Vz, provided that the flow detected by the beams of the ADCP at a given distance (in a plane perpendicular to the axis of the ADCP) is homogenous.

4 Results: Interaction Between Simulations and Measurements

4.1 Model and Current Meter Measurements

The propeller locations on the frame (Fig. 5) were chosen in such a way that the mesh becomes thinner in places where high-velocity gradients are expected and computed by CFD simulations, such as the near wall ends and the middle of the measurement section because of the proximity of the bulb nose. Again, the tests on site confirmed the results of the preliminary study. Taking into account the fact that the frame holds 2 rows of 11 propellers each, an overall mesh of 88 nodes is obtained.

As part of the frame design study, it was necessary to determine the propeller angle on each row since it has a crucial influence on the measurement results. Once again, the results of the CFD study were used to position the current meters at a 15° angle with respect to the horizontal, as shown in the picture above. Later on, the on-site ASFM measurements confirmed this trend.

Before and after each ASFM and ADCP measurement, Alstom performed a current meter measurement of the "same" operating point (same position of blades and guide vanes with almost the same upstream and downstream levels) to double-check. The results showed good repeatability of the measurements. In addition, in terms of random uncertainty, most of the time, more than 95 % of the measurement population was kept within the average plus or minus two times the standard deviation, which is a criterion of measurement reliability, according to standard IEC 60041:1991.

Fig. 5 Position of the propellers on the transverse axis

Fig. 6 Workhorse Rio Grande ADCP placed on vertical position on measurement frame

4.2 Model and ADCP Measurement

The 3D numerical model was used to determine the positioning and orientation of the ADCPs on the frame as a function of the flow characteristics.

The longitudinal velocity field was used to define the orientation of the vertical ADCPs attached to rods (Fig. 6). These values were used to calculate the angle of the flow in relation to the horizontal in the plane (Oyz), noted β. It was then possible to check the angle of the flow relative to each beam in the same plane, denoted θ (Fig. 7). This analysis was performed for discharges of 110, 220, and 350 m^3/s. The aim was to obtain flow not perpendicular to the beam.

By considering an ADCP fixed to a rod oriented at 0°, that is, so that the axis of the ADCP was vertical, the average angle θ_{B3} was very close to 90° whatever the discharge considered (Table 1). This provided an average flow almost perpendicular to the upstream beam *B3*, and thus a radial velocity on *B3* close to nil, making it very difficult to attempt reconstituting elementary velocities as a function of each component. Angle θ_{B4} could be used, although downstream beam *B4* is disturbed by the bulb turbine (Fig. 8, top).

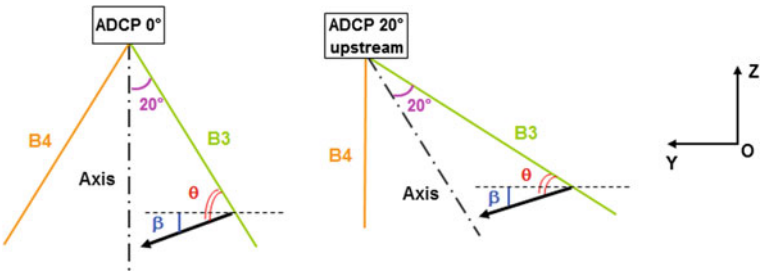

Fig. 7 On the *left*, the *vertical* ADCP (0°). On the *right*, the ADCP-oriented 20° upstream

Table 1 Angle of the average flow resulting from the 3D numerical model for discharges of 110, 220, and 350 m^3/s

Orientation of ADCPs	0°			20° upstream		
Beam	B4	Axis	B3	B4	Axis	B3
θ average (°)	122	102	86	102	86	69

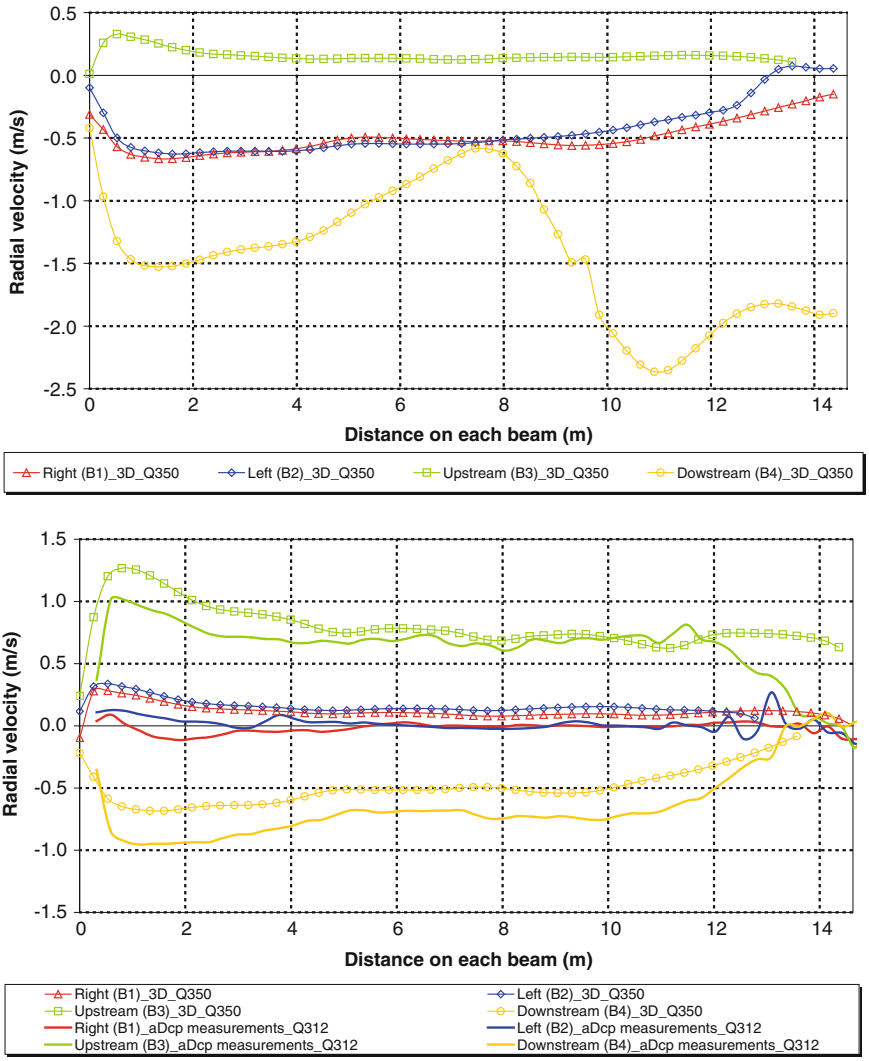

Fig. 8 *Top*: radial velocities resulting from the 3D numerical model for the vertical ADCP PV2 (0°). *Bottom*: comparison between radial velocities measured on site and those resulting from the 3D numerical model for the ADCP PV2–oriented 20° upstream

Orienting the ADCPs vertically 20° upstream resulted in a satisfactory flow angle θ on the upstream beam *B3* and downstream beam *B4*, making it possible to determine components *Vy* and *Vz* used afterward to determine the discharge. In addition, downstream beam *B4*, in the plane of the frame, was not disturbed by the bulb turbine and made it possible to measure vertical velocities *Vz* directly. This configuration was chosen for the project.

Therefore, four Workhorse ADCPs profiling top down (vertical ADCPs: PV1 to PV4) and oriented 20° upstream were installed on rods fixed on the upper cross-beam of the frame.

The graphs in Fig. 8 illustrate the results of the analysis presented in Table 1 and highlight the good general representativeness of the 3D numerical model in terms of the form of the flow. However, the intensity must still be refined.

The lateral velocities in the plane of the frame (cross section of flow at the stop-log recess) resulting from the 3D numerical model proved the soundness of positioning the horizontal ADCPs. Therefore, nine Workhorse ADCPs profiling laterally were fixed on the left (5) and right (4) uprights of the frame. Another ADCP, smaller than the thirteen other sensors and profiling bottom upwards (vertical ADCP), was installed on the lower beam of the frame.

ASFM measurements, referred to but not presented here, were also taken during the measurement campaign. The various measurement acoustic paths could be placed and their exploitation prepared in advance thanks to the results obtained by the 3D simulation.

5 Conclusions

The consistency of the measurement results with the preliminary results provided by the 3D model confirms the effectiveness of the procedure.

By using the 3D results, it was possible to choose strategic positions for the various sensors (propellers, ADCP, and ASFM) and the results obtained following the measurements confirm the model predictions. Certain differences between the results obtained can be explained by geometric elements not taken into account in the model (measurement frame in the stop-log groove and profile of the frame placed on the floor) or by hydraulic simplifications, particularly in the boundary conditions.

The 3D simulations indicated that the theoretical error in the discharge measurements taken with the ADCP was about 9 % (underestimation). In practice, the discharges measured by the ADCP method are about 4 % lower than the reference discharges measured by the propellers. However, when the uncertain measurements are removed, the discharges estimated by the ADCP method are about 7 % lower than the reference discharges measured by the propellers, which is consistent with the theoretical error.

Using the preliminary model meant it was possible not only to place the propellers judiciously on the mobile part of the measurement frame but also to rate them in order to obtain the most reliable measurement possible.

Acknowledgments This work was carried as part of the PENELOP2 project approved by the Tenerrdis competitiveness cluster, with funding granted in the framework of the 9th Fonds Unique Interministériel (FUI) programme. The project partners are Alstom Power, CNR, Artelia, LEGI (Grenoble INP), In Vivo, Actoll, and JKL.

Optimization of a Shared Tailrace Channel of Two Pumped-Storage Plants by Physical and Numerical Modeling

Giovanni De Cesare, Martin Bieri, Stéphane Terrier, Sylvain Candolfi, Martin Wickenhäuser and Gaël Micoulet

Abstract Pump and turbine operations lead to head losses in the tailrace channel. Pumping discharge may be limited due to potential air entrainment into the pump shaft when the downstream reservoir is at its lowest level and the head losses are too high. Regarding turbine operations, the limit is given by the maximum level in the Pelton turbine chamber due to high water level in the downstream reservoir and head losses. The rapid starting and stopping of turbines and pumps lead to highly unsteady flow in the tailrace channel system of the two connected hydropower plants. Negative and positive surges may lead to similar consequences as for stationary operations such as sudden air entrainment into the pump shaft and submerging of the Pelton runner under operation. Therefore, flow and head losses test were conducted on a physical model at 1:30 scale together with numerical

G. De Cesare (✉) · S. Terrier
Laboratoire de Constructions Hydrauliques (LCH), Ecole Polytechnique Fédérale de Lausanne (EPFL), Station 18 CH-1015 Lausanne, Switzerland
e-mail: giovanni.decesare@epfl.ch

S. Terrier
e-mail: stephane.terrier@epfl.ch

S. Candolfi
Université Laval, Québec G1V 0A6, Canada
e-mail: sylvain.candolfi.1@ulaval.ca

M. Wickenhäuser
Stucky Ltd, Rue du Lac 33 CH-1020 Renens, Switzerland
e-mail: mwickenhaeuser@stucky.ch

G. Micoulet
Alpiq Suisse SA, Ch. de Mornex 10, CP 570 CH-1001 Lausanne, Switzerland
e-mail: gael.micoulet@alpiq.com

M. Bieri
Pöyry Energy Ltd, Hardturmstrasse 161 CH-8037 Zürich, Switzerland
e-mail: martin.bieri@a3.epfl.ch; martin.bieri@poyry.com

P. Gourbesville et al. (eds.), *Advances in Hydroinformatics*,
Springer Hydrogeology, DOI: 10.1007/978-981-4451-42-0_25,

simulations using FLOW-3D. On-site measurement of the existing power plant allows validating the results. Representative and extreme operational scenarios have been simulated; the main results are discussed and presented.

Keywords Hydropower · Pumped-storage · Surge waves · Transient flow · Head losses · Free-surface flow · Intake/outlet structure

1 Introduction

The existing Hongrin-Léman pumped-storage scheme, located in western Switzerland, commissioned in 1971 and operated by Forces Motrices Hongrin-Léman SA (FMHL), exploits a maximum head of 878 m between the upper Hongrin reservoir (1′255 m a.s.l.) and Lake Geneva (372 m a.s.l.) at the Veytaux 1 underground powerhouse. The powerhouse contains four horizontal axis pump–turbine units with a total installed power of 240 MW. During off-peak periods, water from Lake Geneva is pumped at a maximum rate of 24 m^3/s to be turbined during periods of high demand with a discharge up to 32 m^3/s. The connection between the powerhouse and Lake Geneva is made by a 200 m long underground straight free-surface channel. The Hongrin reservoir is formed by a twin-arch dam of 125 and 90 m height, respectively (Fig. 1). It has an active storage volume of 52×10^6 m^3.

The objective of the FMHL+ enhancement project is to double the today's plant capacity by constructing a new underground cavern adjacent to the existing one at Veytaux (Fig. 1). Two additional vertical axis pump–turbine groups of 120 MW each will be installed. The total power will be 480 MW, with 420 MW for operating mode and 60 MW as reserve. The increased flexibility, generating peak electricity, will allow the plant to play an important role in supplying electricity to western Switzerland and to meet the growing demand for balancing energy which is mainly due to the extension new renewable energies in Europe and Switzerland.

Fig. 1 Hongrin reservoir with the twin-arch dam (*left*) and view of the existing 170 m long Veytaux 1 powerhouse (*source* www.alpiq.ch)

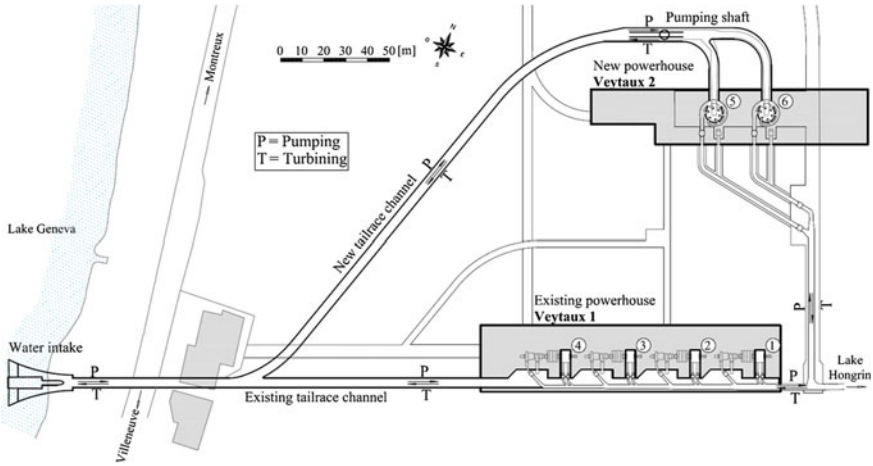

Fig. 2 Plan view of the existing and new Veytaux underground pump-turbine plants

The new plant will mainly use the existing upstream (headrace tunnel and penstock) and downstream (tailrace channel and intake/outlet work) hydraulic system. Figure 2 shows the shared downstream channel system. Special attention has to be paid on the combined operation of the two plants.

This paper presents the results of head loss investigations and wave propagation experiments in the open tailrace channel. The study has been conducted both on a physical model and with numerical 3D simulation. The numerical simulation provided mainly input to the optimization process of the project, before modifying the physical model.

2 Physical and Numerical Model

In order to study the unsteady flow behavior, both a physical model and a numerical model were built at the Laboratory of Hydraulic Constructions (LCH) of the *Ecole Polytechnique Fédérale de Lausanne* (EFPL), Switzerland [1, 2].

2.1 Physical Model

The physical model was operated according to Froude similarity with a length-scale ratio of 1:30, replicating the downstream part of the existing Veytaux 1 powerhouse with its 200 m long tailrace channel to the Lake Geneva as well as the new Veytaux 2 powerhouse with the new 300 m long tailrace channel connected to the existing one. The two pumps of Veytaux 2 are fed by a single pumping shaft, where only its inlet structure was modeled. All hydraulic elements were built with transparent PVC. Lake Geneva was modeled with a 8 m^3 steel tank (Figs. 3, 4).

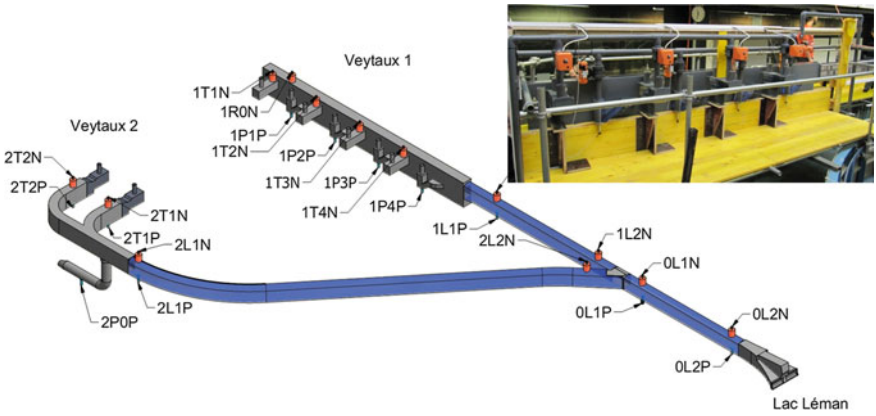

Fig. 3 3D view of the physical model showing the positions of water level (*N*) and pressure (*P*) sensors for water supply by turbines (*T1–T6*), and sinks by pumps (*P1–P6*) as well as Lake Geneva (*Léman*) with water intake; photograph of the modeled Veytaux 1 powerhouse with the four turbines and pumps

Fig. 4 Overview of the physical model with Lake Geneva tank on the *right*, Veytaux 1 powerhouse in the background, and Veytaux 2 powerhouse on the far *left*

2.2 Numerical Model

The numerical simulations were carried out using the software FLOW-3D, version 10 from Flow Science Inc. in New Mexico, USA [3]. FLOW-3D numerically solves the continuity and momentum equations using finite-volume approximation. The flow region is subdivided into a mesh of fixed rectangular cells. Within each cell, there are associated local average values of all dependent variables. All variables are located at the center of the cells except for velocities, which are located at cell faces (staggered grid arrangement). Curved obstacles, wall boundaries, or other geometric features are embedded in the mesh by defining the fractional face areas and fractional volumes of the cells that are open to flow (the Fractional Area/Volume Obstacle Representation—FAVOR method). Most terms in the equations are evaluated using the current time-level values of the local

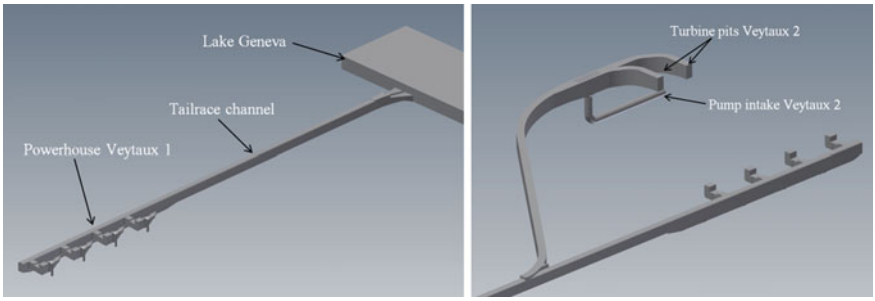

Fig. 5 Numerical FLOW-3D model of the existing Veytaux 1 powerhouse, tailrace channel, and Lake Geneva (*left*) for the calibration simulation and (*right*) the added Veytaux 2 branch with the two turbine pits and the pump intakes below

variables explicitly. This produces a simple and efficient computational scheme for most purposes but requires the use of a limited time step size to maintain computationally stable and accurate results. For the simulations, the RNG turbulence model is used, which is similar to the k-ε. The RNG model is better adapted for lower Reynolds numbers as it dynamically evaluates the turbulence length all along the simulation domain (Fig. 5).

The numerical model is built using one mesh block per turbine, respectively, pump unit, the tailrace channel, and Lake Geneva. The splitting into one mesh block per each supply by turbines (T1–T6) and sinks by pumps (P1–P6) is necessary in order to introduce correctly the individual discharges both in steady und unsteady states.

The main calibration parameters of the numerical model are the mesh size, the lake-level boundary condition, and the surface roughness of the concrete tailrace channel. Uniform mesh size of 0.5, 1.0, and 1.5 m have been tested. The mesh size choice influences largely the duration of the simulation, without any major difference in the obtained results both in space and time for the two smaller ones. Finally, a mesh size of 1 m has been selected.

As the lake-level boundary condition, a hydrostatic pressure distribution with fixed water level has been selected, giving the most stable results compared to a simple outflow condition, where due to very low flow velocities flow disturbances at the outflow boundary may affect the entire computational domain.

Two k_s roughness values (1 and 2 cm) of the concrete surface in the tailrace channel have been tested based on observation of the real surface irregularities. Their influence is negligible, as the head losses occur as linear head losses for quasi-hydraulically smooth surfaces (due to the very small k_s over hydraulic radius R ratio) and as in general, head losses due to surface roughness can be neglected in local head losses due to geometry effects, such as section changes in the water intake.

3 Validation Tests

In a first step, the numerical and physical models were validated for steady-state head losses in pump and turbine mode as well as waves consecutive to the pump or turbine operations in the Veytaux 1 powerhouse. Thanks to on-site measurements taken over several month with an immersed pressure gauge placed in the Veytaux 1 tailrace channel (type Rittmeyer MPB) between the outlets of turbine 1 and 2 (position 1R0 N in Fig. 2), combined with lake-level measurements at an nearby official gauging station and exploitation data over the same period, several typical events have been selected for the validation of the models.

The measurement interval is 10 s for the 1R0N probe, a minimum of 2 s for the discharge, and 10 min for the lake gauging station. The accuracy of the on-site-level measurements is in the order of 0.2 % of full scale (according to Rittmeyer MPB datasheet), giving some mm exactness. No information is available on the discharge accuracy, but as discharge gradients are of interest, the absolute precision is not so relevant.

The discharge measurements in the physical model (using Endress + Hauser Flowtec Promag 50 W) have a precision better than 0.5 % full scale (converted to prototype, less than 0.5 m^3/s), the water levels are measured with US gauges (Type Baumer Ultrasonic sensors UNAM 30) with a resolution better than 0.5 mm (prototype 1.5 cm) at an acquisition frequency of 50 Hz.

3.1 Steady-State Head Losses in Pump and Turbine Mode

The steady-state validation tests have been conducted with the same prototype boundary conditions as follows:

Lake Geneva water surface elevation:	372.18–372.22 m a.s.l.
Discharge of pumping events:	12.7, 20.0, and 27.1 m^3/s
Discharge of turbining events:	11.8, 19.7, 25.1, and 33.0 m^3/s

Due to exploitation reasons, where only the total energy output (or consumption in pumping mode) of the powerhouse is registered, only the sum of the considered pumping or turbining discharge is known, without the distribution between the four groups of the existing Veytaux 1 powerhouse. This may have a certain impact, as the on-site water level gauge is placed between the outlets of turbine 1 and 2. The different combinations have been tested to see their impact.

Figure 6 gives an overview of the total head losses ΔH between Lake Geneva and the water level in the powerhouse outlet channel for the considered discharges and water levels from the prototype, physical, and numerical models for both generating and pumping modes. Regarding these results, the physical model seems to be slightly too smooth, underestimating the total head losses. The numerical model, independent of the chosen surface roughness k_s, overestimates slightly the

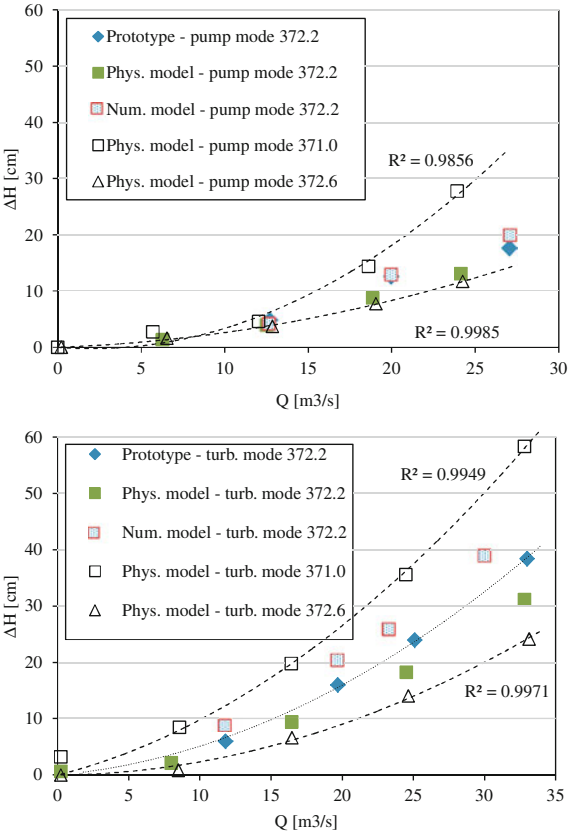

Fig. 6 Head losses in function of the discharge between Lake Geneva and the powerhouse outlet channel (1R0N) for the numerical and physical model in both pumping (*left*) and generating (*turbine, right*) mode. The approximated minimum and maximum head loss curves are as well positioned

total head losses in turbining mode, but reproducing them trustfully in pumping mode. In conclusion, both approaches give a consistent estimate of the total head losses. For the optimization, mainly the reduction in head losses between two geometrical alternatives is of importance, meaning that both model approaches can be reliably used.

In addition to the validation tests, the physical model has been used to evaluate the minimum and maximum head loss curves taking into account the extreme low and high lake water levels. Both relations follow a parabolic curve (proportional to Q^2), that is in concordance with the general relations for local and linear head losses.

3.2 Unsteady Waves Due to Pump and Turbine Start

The on-site measured start and stop of pumps and turbines in the Veytaux 1 powerhouse have been simulated as well during the validation phase. The numerical simulations were carried out in order to test the mesh size, the

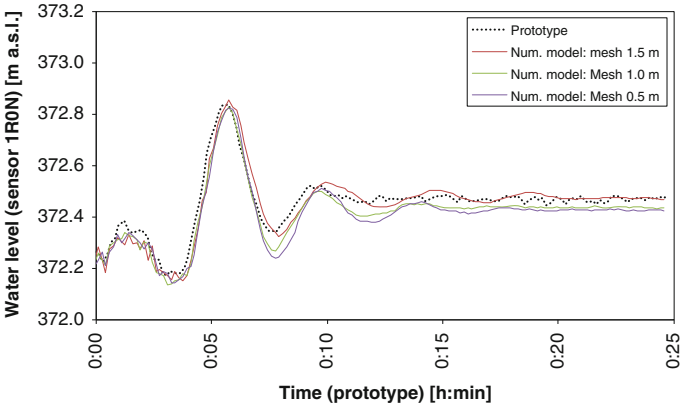

Fig. 7 Start of three turbine groups in the numerical model: influence of the mesh size on the variation of the water level in the Veytaux 1 plant (1R0N), and comparison to prototype measurements. The simulation results show a very good agreement

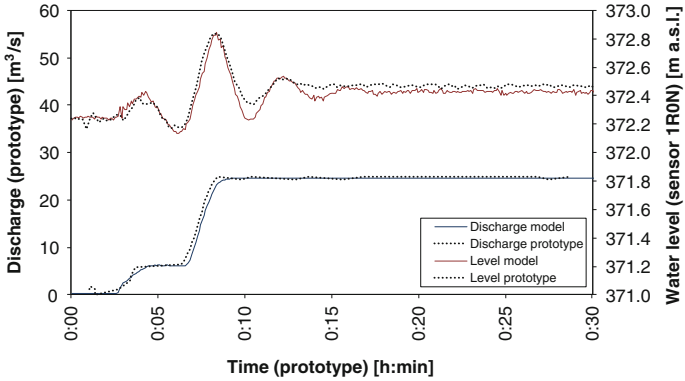

Fig. 8 Results of the physical model test of the same case than for Fig. 6 showing the water level registered at the 1R0N probe, located in the Veytaux 1 plant, compared to prototype measurements as well as the discharge variation registered in prototype and physical model. The simulation results show again a very good agreement, and the physical model reproduces identical results to the numerical model

roughness, the turbulence model, the time step size, and the boundary conditions. Figure 7 shows the influence of the start of three turbine groups on the water level fluctuations in the powerhouse outlet channel. The numerical simulation allows a correct representation of the prototype behavior in unsteady stage as well. The rise and fall of the water level and the amplitudes are all well reproduced.

Identical simulations were carried out on the physical model. Figure 8 shows again the influence of the start of three turbine groups on the water level fluctuations in the powerhouse outlet channel, this time from the physical model. The

discharge changes are overlapped to illustrate the ability of the physical model to reproduce correctly any discharge fluctuations coming from the powerhouse operations, both in turbine and pumping mode. As the exact sequence of turbine start is unknown, all possibilities have been run through, and all showed quasi-identical results from the physical and numerical model.

4 Simulation Taking into Account Both Powerhouses

The impact on the head losses as well as on minimum and maximum water levels in the downstream channel, turbine pits, and pump sinks were investigated with a systematic test program. In the physical model, a total of 142 stationary and 85 unsteady tests were conducted, including repetition of typical boundary conditions for the optimized model. The numerical model was mainly used to simulate and optimize the remediation measures on the geometry of particular structures such as the junction, pump sink inlet or outlet/inlet structure into Lake Geneva. Thus, only the final optimized geometry needed to be built and put into the physical model, allowing substantial time and cost savings on the physical model.

4.1 Steady-State Head Losses in Pump and Turbine Mode and Remedial Measures

The physical model was used in order to analyze the head losses in the combined operation of the new and old powerhouse for a large range of pumping and turbining discharges as well as lake water levels [4]. The critical conditions are low lake water level with maximum pumping actions as well as high lake water level with maximum turbining discharge. Figure 9 illustrates the case of Lake Geneva's water surface elevation at 371.80 m a.s.l. for a Veytaux 2 discharge of 24 m^3/s and Veytaux 1 of 19 m^3/s using three existing pumps only. Supercritical flow with shock waves occurs from the intake to hydraulic jumps at the bifurcation, leading to large head losses. These head loses lower significantly the water level above the Veytaux 2 pump shaft and entrains air into the shaft. The numerical simulations showed the same behavior and position of the hydraulic jump (Fig. 10).

To remediate the unfavorable head losses, the following four main modifications were proposed. They were at first optimized with the numerical model, then build and installed, and finally tested in the physical model:

1. Partial removal of the central pillar in the intake/outlet structure and reshaping of the remaining pillar like a bridge pier to reduce flow contraction and expansion losses.

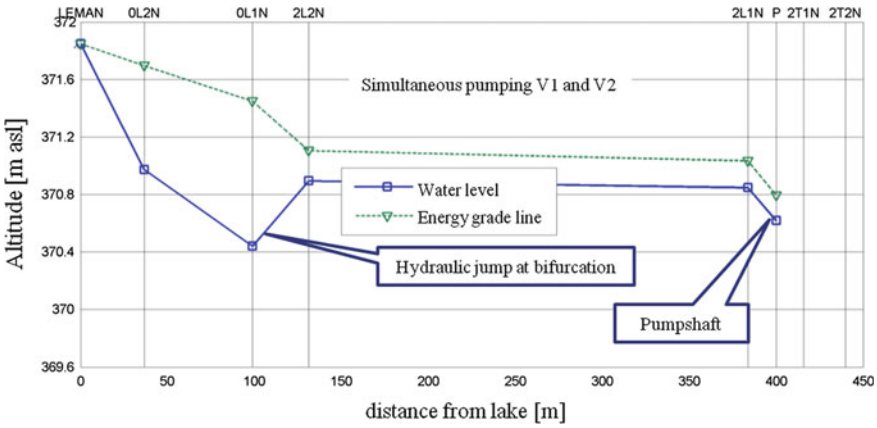

Fig. 9 Head losses and water level lines along the common tailrace channel and Veytaux 2 branch obtained in the physical model. Lake Geneva water surface elevation at 371.80 m asl for a Veytaux 2 discharge of 24 m^3/s and Veytaux 1 of 19 m^3/s using three pumps. The hydraulic jump at the bifurcation is clearly visible, producing undesirable local head losses

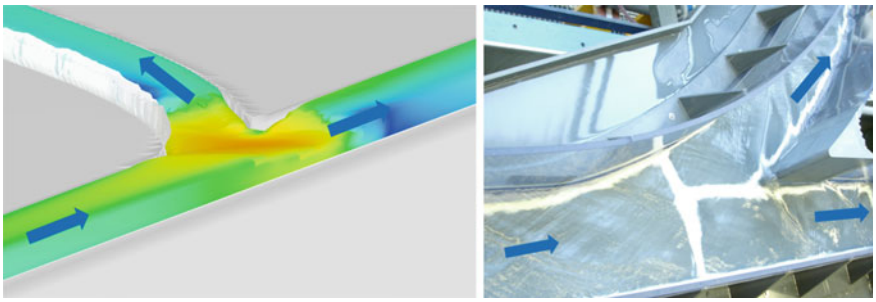

Fig. 10 3D hydraulic jump formation at the bifurcation in pumping mode resulting from the numerical simulation (*left*) and in the physical model (*right*) for low Lake Geneva water surface elevation at 371.80 m a.s.l. for Veytaux 2 discharge of 24 m^3/s and Veytaux 1 of 19 m^3/s using three pumps

2. Lowering of the common tailrace channel section by 1 m to increase wetted flow perimeter and section to prevent supercritical flow and the hydraulic jump at its end. The bottom transitions have a slope of 10 % to join the original levels on both sides.
3. Reshaping of the bifurcation (angle, bottom transition, chamfer of the edge with a series of increasing radii to have an optimum flow separation between the two channels.
4. Reshaping of the Veytaux 2 pump shaft transition (chamfer of the edges, lengthening and widening of the channel, anti-vortex wall prolongation).

All those modifications, once implemented allowed an accurate functioning of the existing and new powerhouse together for almost any boundary condition. The reshaping of the bifurcation and its results are presented in more details in the section below.

4.1.1 Reshaping of the Bifurcation

To reduce the head losses in the bifurcation in pumping mode, two main designs of the junction have been studied (Fig. 11). In the original design, the new tailrace channel is connected laterally to the existing channel with an angle of 35°. The aim of the new design is to soften the change of direction of the flow in the new channel. For that purpose, the new channel makes a turn and is connected tangentially to the existing channel.

For each geometry, numerical simulations in pumping mode were carried out for two levels of Lake Geneva at 371.8 and 371.6 m a.s.l. and the discharge at Veytaux 2 of 24 m^3/s and at Veytaux 1 of 19 m^3/s. The corresponding head losses between the common channel and the channels leading to the Veytaux 1 and Veytaux 2 powerhouses are given in Table 1.

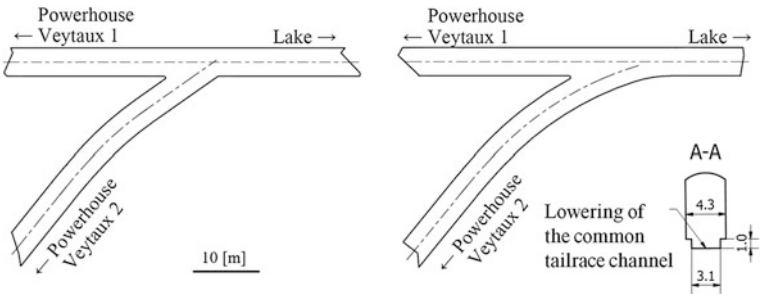

Fig. 11 Plan view of the lateral original bifurcation (*left*) and the tangential bifurcation (*right*) with the lowered common channel (*bottom*)

Table 1 Comparison of the head losses for the lateral and the tangential bifurcation with a level of Lake Geneva at 371.9 and 371.6 m a.s.l. in pumping mode

Level of Lake Geneva (m a.s.l.)	Type of bifurcation	Head losses to Veytaux 1 (cm)	Head losses to Veytaux 2 (cm)
371.8	Lateral bifurcation	5	20
	Tangential bifurcation	11	3
371.6	Lateral bifurcation	29	68
	Tangential bifurcation	88	83

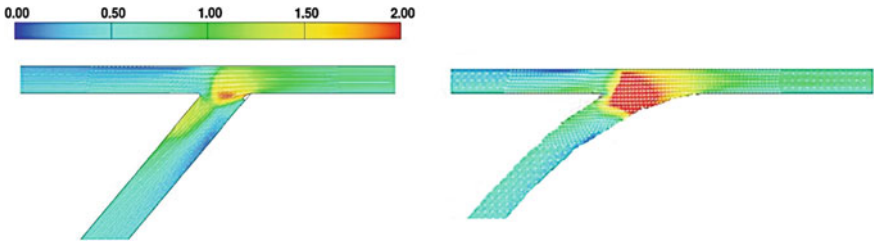

Fig. 12 Froude number in the lateral bifurcation (*left*) and tangential bifurcation (*right*) with Lake Geneva at 371.6 m a.s.l

In the case of the Lake Geneva with a level of 371.8 m a.s.l., the tangential bifurcation reduces the head losses toward Veytaux 2 powerhouse by a factor of almost 7 but doubles the head losses toward Veytaux 1. The flow is more equally divided between the two channels for the tangential bifurcation; the head losses are more equally distributed.

With a low level of Lake Geneva (371.6 m a.s.l.), the head losses are increased due to the higher kinetic energy. The head losses are equally divided (88 for Veytaux 1 and 83 cm for Veytaux 2) with the tangential bifurcation. The hydraulic jump is stronger in the case of the tangential bifurcation due to the widening of the channel at the bifurcation (Fig. 12). To counteract this, the bottom of the common channel will be lowered by 1 m in its central section (3.1 m wide) with a gradual slope at the bifurcation, reducing considerably Froude number and therefore the intensity of the hydraulic jump.

4.2 Unsteady Waves Due to Pump and Turbine Start

The main objectives of the unsteady wave tests were to identify critical exploitation scenarios that may endanger the safe operation of both power plants. Due to the complex wave behavior with reflection of the surface waves at each channel end, at the Lake Geneva boundary and at the bifurcation, the physical model was used to conduct these tests [5, 6]. Typical start and stopping situations of turbines and pumps were simulated, taking into account the most critical sequences as well as the synchronization with the grid.

Figure 13 shows the water level evolution above the Veytaux 2 pump shaft for a typical operation scenario with the start of three pumps of the Veytaux 1 powerhouse and Veytaux 2. It also shows the identification of the most critical combination sequence. The results illustrate that it is not possible to overlap the minimum water level produced by each powerhouse for a combined powerhouse operation, thus reducing restrictions in grid regulation operation. The same

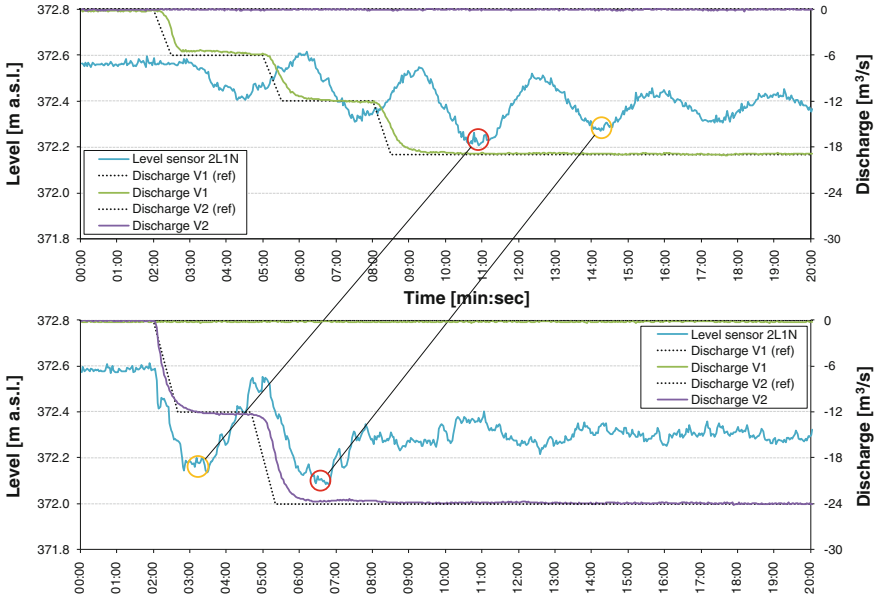

Fig. 13 Local wave evolution in the downstream tailrace channel of the Veytaux 2 plant (probe 2L1N, see Fig. 3) for sequential pump start with three pumps for Veytaux 1 (*top*) and two pumps for Veytaux 2 (*bottom*) plants. The minimum water levels cannot be overlaid due to the length of the connection channel

statement is valid for turbine operation, where the surge waves will not rise in the turbine pits to an extend that may endanger their safe operation.

5 Conclusions

The existing Hongrin-Léman pumped-storage scheme, 240 MW with four pump–turbine units, is currently under power extension work to double the current plant's capacity by constructing a new powerhouse adjacent to the existing one with two additional vertical axis pump–turbine groups of 120 MW each. Both power plants share the intake and outlet structures and part of the existing tailrace channel at Lake Geneva which is the downstream reservoir. A physical model at a scale of 1:30 and a numerical model at prototype scale were built at the Laboratory of Hydraulic Constructions of the *Ecole Polytechnique Fédérale de Lausanne* with the aim of studying the future stationary and transient behavior of the two plants. Stationary pump and turbine operations lead to head losses in the tailrace channel that have to be minimized to allow the envisaged flexible operation. Power generation or storage by pumping as well as grid stabilization and frequency

regulation leads to highly transient bidirectional flows in the tailrace channel system that have to be understood.

At the beginning, the numerical and physical models were validated for steady-state head losses in pump and turbine mode as well as for waves consecutive to the pump or turbine start in the existing powerhouse. Both approaches give consistent values for the head losses in the tailrace channel as well as for level variation in the powerhouse. Both model approaches can be reliably used for the optimization of geometrical elements to reduce local head losses. Thanks to its fast and simple geometrical adaption, the numerical model has mainly been used to optimize the geometry before constructing and implementing the modified elements in the physical model. The final goal of having a tailrace channel giving satisfactory low head losses was achieved and tested in the physical model after several required modifications.

In order to understand the negative and positive surge waves due to characteristic start and stopping situations of turbines and pumps, some 85 unsteady tests were conducted. The tests confirmed that envisaged flexible operation scenarios should not lead to negative consequences such as vortices and air entrainment into the pump shaft and submersion of the turbine pits under operation. The physical and numerical models allowed optimizing and rendering of the downstream hydraulic system viable. The enhanced scheme was tested in detail in order to analyze critical stationary and transient scenarios and to define the operation limits of two power plants together.

Physical modeling and experimental research is more than 100 years old and is a proven tool for hydraulic engineering. Most of today's created or transformed dams, hydroelectric, or flood control projects pass over one or more phases of physical modeling in their specification phase. These models are more and more endorsed by numerical simulations, giving another very powerful, complementary tool for an insight view on hydraulics and hydraulic works [7].

Acknowledgments This study has been conducted on behalf of the plant owner FMHL. We address our gratitude having retained the LCH for this model study and for allowing the LCH to exploit the model for scientific research. A part of the numerical study has been conducted during an alternative civilian service.

References

1. LCH (2011). Augmentation de la puissance de l'aménagement Hongrin-Léman—Essais sur modèle numérique 3D. LCH Report (unpublished) 06/2011, EPFL Lausanne (in French).
2. LCH (2012). Augmentation de la puissance de l'aménagement Hongrin-Léman—Etude sur modèle physique. LCH Report (unpublished) 03/2012, EPFL Lausanne (in French).
3. Flow Science (2011). Flow-3D® user manual, Flow Science Inc., Santa Fe, USA
4. Blevins, R. D. (1984). *Applied fluid dynamics handbook* (p. 558). New York: Van Nostrand Reinhold Co.
5. Faure, J., & Nahas, N. (1961). Etude numérique et expérimental d'intumescences à forte courbure du front. *Intumescences—Société hydrotechnique de France, 5*, 579–587.

6. Soares-Frazao, S., & Zech, Y. (2002). Undular bores and secondary waves—Experiments and hybrid finite—volume modelling. *Journal of Hydraulic Research, 40*(1), 33–43.
7. De Cesare, G., Pfister, M., Daneshvari, M. Bieri, M. (2012). Herausforderungen des heutigen wasserbaulichen Versuchswesens mit drei Beispielen. WasserWirtschaft, 7–8, ISSN: 0043–0978 (in German).

Influence of the Hydraulic System Layout on the Stability of a Mixed Islanded Power Network

Christian Landry, Christophe Nicolet, Silvio Giacomini and François Avellan

Abstract Numerical simulation and stability analysis of an islanded power network comprising 40 MW of hydropower, 20 MW of wind power, and 60 MW of gas-fired power plants are investigated. First, the modeling of each power plant is fully described. The wind farm is modeled through an aggregated model approach of 10 wind turbines of 2 MW and comprises a stochastic model of wind evolution with wind gust. The hydraulic power plant comprises the upstream reservoir, a 1,000 m gallery, a surge tank, the 500 m-long penstock feeding a low-specific-speed pump turbine and connected to the downstream tank through a 70 m-long tailrace water tunnel. The model of gas-fired power plant includes an upstream rotating compressor coupled to a downstream turbine and a combustion chamber in-between. To predict the performance of the gas turbine engine, both at design and off-design conditions, performance maps are integrated in the modeling. Then, the capability of the hydraulic power plant to compensate wind power variations or load rejections is investigated using the EPFL simulation software SIMSEN to perform time domain simulation of the entire mixed islanded power network. This study shows the evolution of the response time of the hydraulic part as function of the penstock length and highlights the influence of the hydraulic layout on the power system stability. The dynamic performances of such hydraulic power plants are of highest interest for improving stability of mixed islanded power network, but require reliable simulation model of the entire network for safety and optimization purposes.

C. Landry (✉) · S. Giacomini · F. Avellan
EPFL, Laboratory for Hydraulic Machines, Av. de Cour 33 bis 1007 Lausanne, Switzerland
e-mail: christian.landry@epfl.ch

S. Giacomini
e-mail: silvio.giacomini@epfl.ch

F. Avellan
e-mail: Francois.Avellan@epfl.ch

C. Nicolet
Power Vision engineering sàrl, Ch. des Champs-Courbes 1 1024 Ecublens, Switzerland
e-mail: christophe.nicolet@powervision-eng.ch

P. Gourbesville et al. (eds.), *Advances in Hydroinformatics*,
Springer Hydrogeology, DOI: 10.1007/978-981-4451-42-0_26,

Keywords Stability analysis · Pump turbine · Modeling · Power network · Simulation

Nomenclature

A	Cross-sectional area [m^2]
a	Wave speed [m/s]
C	Hydraulic capacitance [m^2]
C_{inf}	Wind velocity [m/s]
D	Diameter [m]
g	Gravity [m/s^2]
f	Frequency [Hz]
H	Head [m]
L	Hydraulic inductance [s^2/m^2]
N	Rotational speed [1/min]
Q	Discharge [m^3/s]
R	Hydraulic resistance [s/m^2]
Re	Reynolds number [-]
R_{ve}	Viscoelastic resistance [s/m^2]
y	Guide vanes opening [-]
T	Torque [Nm]
λ	Local loss coefficient [-]
μ	Dynamic viscosity [Pa s]
μ'	Expansion viscosity [Pa s]
ν	Specific speed [-]
ρ	Density [kg/m^3]

1 Introduction

Electricity generated from intermittent energy resources is developing rapidly worldwide. Earlier studies have found that energy storage can compensate for the stochastic nature of the variable energy sources by storing the excessive energy when generation exceeds predicted levels and providing it back to the grid when generation levels fall short. For instance, islanded power networks featuring high level of wind power penetration are subjected to undesired perturbation jeopardizing the power network stability [1]. Consequently, pumped storage plants are a proven solution for storing electricity at large scale and offering flexibility to the power management. The high dynamic performances of such pumped storage plants are of highest interest for improving stability of mixed islanded power network, but require reliable simulation model of the entire power network for safety and optimization purposes [2].

This paper presents the modeling, numerical simulations, and stability analysis of an islanded power network comprising 40 MW of hydropower, 20 MW of wind

power, and 60 MW of gas-fired power plant. First, the modeling of each power plant is fully described. The wind farm is modeled through an aggregated model approach of 10 wind turbines of 2 MW and comprises a stochastic model of wind evolution with wind gust. The hydraulic power plant comprises the upstream reservoir, a 1,000 m gallery, a surge tank, the 500 m-long penstock feeding a low-specific-speed pump turbine ($\nu = 0.217$) and connected to the downstream tank through a 70 m-long tailrace water tunnel. The model of gas-fired power plant includes an upstream rotating compressor coupled to a downstream turbine, and a combustion chamber in-between. To predict the performance of the gas turbine engine, both at design and off-design conditions, performance maps are integrated in the modeling.

The power plants are connected to a passive consumer load via a 500 kV electrical network. Then, the capability of the hydraulic power plant to compensate wind power variations or load rejections is investigated using the EPFL simulation software SIMSEN to perform time domain simulation of the entire mixed islanded power network. This study shows the evolution of the response time of the hydraulic part as function of the penstock length and highlights the influence of the hydraulic layout on the power system stability.

2 Modeling of Hydraulic Power Plant

The modeling of the hydraulic components based on equivalent scheme representation is presented in this section. The following set of hyperbolic partial differential equations describes the one-dimensional momentum and continuity balances for an elementary pipe of length dx and wave speed a. Moreover, we assume uniform pressure and velocity distributions in the cross section A and we neglect the convective terms [3].

$$\begin{cases} \dfrac{\partial h}{\partial t} + \dfrac{a^2}{gA} \cdot \dfrac{\partial Q}{\partial x} = 0 \\ \dfrac{\partial h}{\partial x} + \dfrac{1}{gA} \cdot \dfrac{\partial Q}{\partial t} + \dfrac{\lambda |Q|}{2gDA^2} \cdot Q = 0 \end{cases} \tag{1}$$

The system (1) is solved using the finite difference method with first-order centered scheme discretization in space and a scheme of Lax for the discharge variable. This discretization leads to a system of ordinary differential equations that can be represented as a T-shaped equivalent scheme [4] as presented in Fig. 1.

The RLC parameters of the equivalent scheme are given by

$$R = \frac{\lambda |\overline{Q}| dx}{2gDA^2}, \quad L = \frac{dx}{gA}, \quad C = \frac{gA\mathrm{d}x}{a^2}, \tag{2}$$

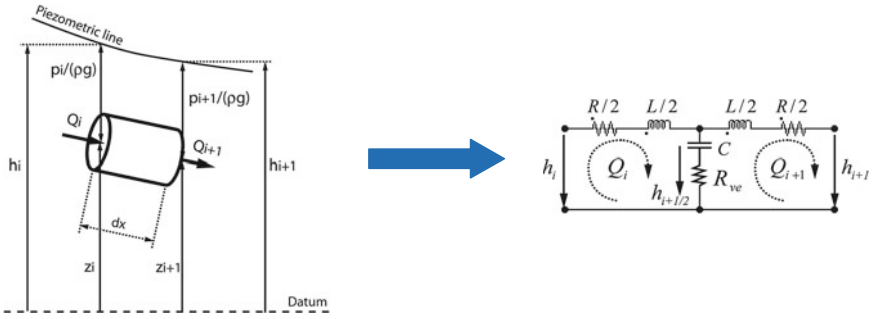

Fig. 1 Representation of an elementary hydraulic pipe of length dx and its equivalent circuit

where λ is the local loss coefficient and D is the diameter of the elementary pipe. The hydraulic resistance R, the hydraulic inductance L, and the hydraulic capacitance C correspond, respectively, to energy losses, inertia, and storage effects. Moreover, in order to predict accurately pressure fluctuation amplitudes and system stability, it is necessary to take into account the viscoelastic behavior due to energy dissipation during the wall deflection. This additional dissipation leads to a resistance in series with the capacitance. This viscoelastic resistance is accounting for both fluid and pipe material viscoelasticity and can be expressed as

$$R_{\text{ve}} = \frac{\mu_{\text{equ}}}{A\rho g \mathrm{d}x} \tag{3}$$

with μ_{equ} the equivalent viscoelastic damping of both the fluid and the wall. The model of a pipe with a length L is made of a series of elements based on the equivalent scheme illustrated in Fig. 1, the system of equations being set up using Kirchhoff laws. This modeling approach based on equivalent electrical schemes of hydraulic components is extended to all the standard hydraulic components such as valves, surge tanks, air vessels, cavitation development, Francis pump turbines, Kaplan turbines, pumps, and provides a high level of abstraction allowing for a rigorous formalism. This modeling approach is also extended to all electrical components such as transmission lines, transformers, synchronous machines. Finally, models of all those components are implemented in the EPFL software SIMSEN, developed for the simulation of the dynamic behavior of hydroelectric power plants [5].

The layout of the hydraulic power plant is presented in Fig. 2. In this case study, the influence of two different penstocks will be highlighted: a 500 m-short penstock and a 2,000 m-long penstock. The power plant is constituted of an upstream reservoir, a 1,000 m-long gallery, a short or a long penstock connected to a 40 MW pump turbine. Moreover, the hydraulic machine is connected to the downstream reservoir by a tailrace water tunnel of 70 m long. Finally, the turbine is equipped with a PID turbine speed governor including a rate limiter and the generator is controlled by ABB Unitrol voltage regulator. Table 1 gives the main characteristics of the hydraulic power plant.

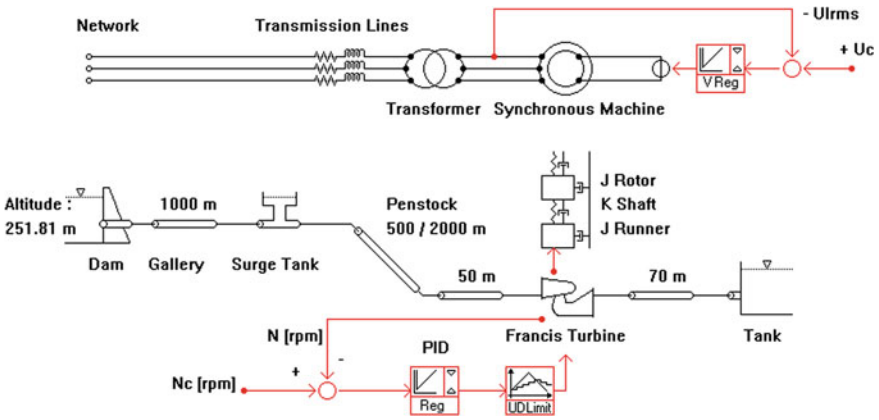

Fig. 2 Hydraulic power plant model

Table 1 Hydraulic power plant characteristics

Gallery			Penstock		
Length	$L_G = 1{,}000$	m	Length	$L_p = 500/2{,}000$	m
Diameter	$D_G = 3$	m	Diameter	$D_p = 2.02/2.64$	m
Wave speed	$a_G = 1{,}200$	m/s	Wave speed	$a_p = 1{,}200$	m/s
Pump turbine			**Generator**		
Rated mechanical power	$P_r = 40$	MW	Rated apparent power	$S_n = 42.88$	MVA
Rated speed	$N_r = 500$	rpm	Rated phase to phase voltage	$V_n = 17.5$	kV
Rated discharge	$Q_r = 17.7$	m^3/s	Frequency	$f = 50$	Hz
Rated head	$H_r = 242$	m	Inertia	$J_t = 10^5$	kg m^2
Specific speed	$v = 0.217$		Number of poles pairs	$P = 6$	
Reference diameter	$D_{ref} = 2.6$	m	Stator windings	Y	
Surge tank			**Coupling shaft**		
Mid-tank section	$A_{st} = 15$	m^2	Stiffness	$K = 10^8$	Nm/rad
			Viscous damping	$\mu = 10^3$	Nm s/rad

For completeness, the electrical system of the hydraulic power plant model is a synchronous machine of 43 MVA and is connected to the islanded network through 17.5/500 kV Yd5 transformers. The synchronous machine is laminated rotor type and is modeled according to a model with transient and subtransient characteristic quantities.

3 Modeling of the Wind Farm

The model of a 2 MW wind turbine is presented in Fig. 3. The turbine can adjust the blade pitch angle θ to provide the highest power coefficient for different tip ratio U_t/C_{inf}, where U_t is the blade tip velocity and C_{inf} is the wind velocity. But, for tip speed ratio below 8, the pitch angle is selected to generate the 2 MW output power limit. Finally, the characteristic of the shaft stiffness, the gear box, and the synchronous generator of 2 MVA with voltage regulator is given in Table 2.

The turbulent wind model is composed of a wind mean value and a wind gust, as suggested by Slootweg et al. [6]. The turbulent gust is modeled by a pseudo-random binary sequence, PRBS, obtained by a shift register method, see [7]. The mechanical power P transmitted by the fluid to the wind turbine can be expressed as

$$P = \frac{1}{2}\rho A_{\text{ref}} C_p(\lambda, \theta) \cdot C_{\text{inf}}^3 \tag{4}$$

where A_{ref} is the swept area, C_p is the power coefficient, ρ is the air density, and λ is the tip speed ratio given by

$$\lambda = \frac{U_t}{C_{\text{inf}}} = \frac{D_w \omega}{C_{\text{inf}}} \tag{5}$$

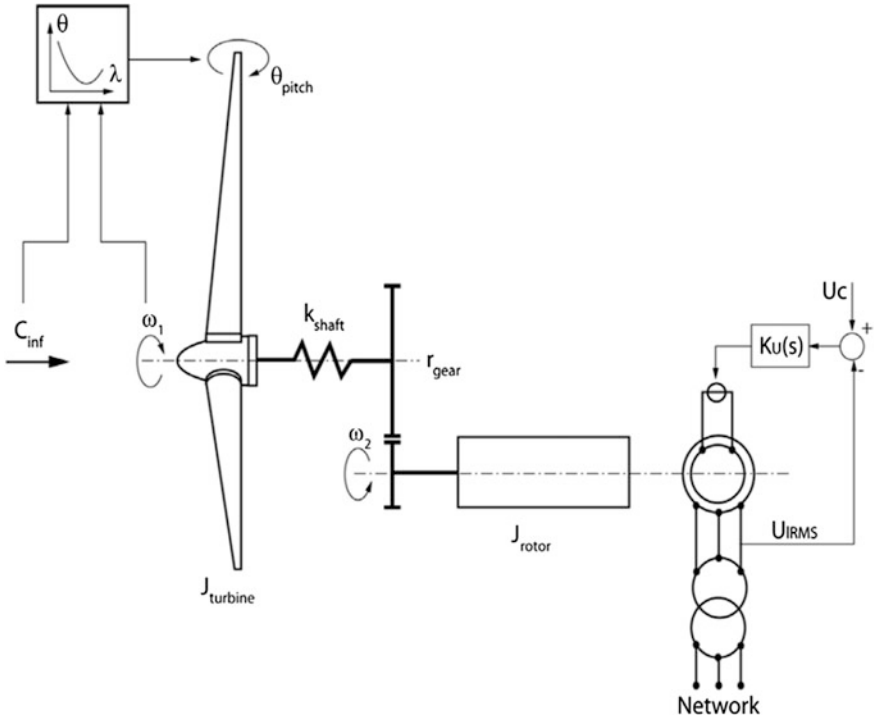

Fig. 3 Wind turbine model

Table 2 Wind turbine characteristics

Wind turbine			Generator		
Number of blades	$N_b = 3$		Rated apparent power	$S_n = 2.2$	MVA
Diameter	$D_W = 75$	m	Rated phase to phase voltage	$V_n = 400$	V
Rotational speed	$n_W = 24.75$	rpm	Frequency	$f = 50$	Hz
Inertia	$J_W = 3.15 \times 10^6$	kg m^2	Inertia	$J_{GW} = 6.48 \times 10^4$	kg m^2
			Number of poles pairs	$P = 40$	
			Stator windings	Y	
Operating data			Coupling shaft		
Cut-in wind velocity	$C_{\text{cut-in}} = 3.5$	m/s	Stiffness	$k_{\text{shaft}} = 2.2 \times 10^8$	Nm/rad
Cut-out wind velocity	$C_{\text{cut-out}} = 20$	m/s	Viscous damping	$\mu_W = 5 \times 10^5$	Nm s/rad
Rated wind velocity	$C_w = 13$	m/s	Gear ratio	$r_{\text{gear}} = 3.032$	

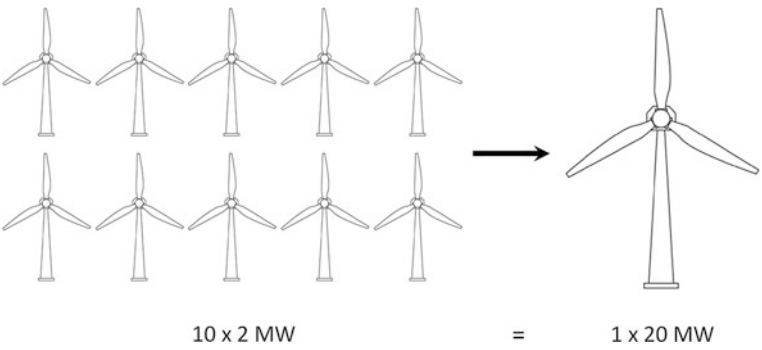

Fig. 4 Wind turbine farm of 10 × 2 MW modeled as an equivalent wind turbine of 20 MW

For power grid stability purposes, it is possible to use an aggregated wind farm model, consisting of one wind turbine equivalent to n single-wind turbines as presented in Fig. 4. Then, according to the energy conservation and in order to keep the same torsional mode eigenfrequency, the active power P_n, rotating inertias J, the shaft stiffness k_{shaft}, and the swept area A_{ref} are multiplied by the number of wind turbine n.

For completeness, the electrical system of the aggregated wind farm model is a synchronous machine of 22 MVA and is connected to the islanded network through 400/500 kV Yd5 transformers. The synchronous machine is laminated rotor type and is modeled according to a model with transient and subtransient characteristic quantities.

4 Modeling of Gas-Fired Power Plant

The gas turbine engine is a complex assembly of a variety of components that are designed on the basis of thermodynamic laws. The design and operation theories of these individual components are complicated. Therefore, to simplify the modeling, the following assumptions are taken into account:

1. The compressor shaft speed N_c equals the turbine shaft speed N_t,

$$N_c = N_t = N \tag{6}$$

2. The gas mass flow through turbine $\dot{m}_g$ is the sum of the air mass flow through compressor $\dot{m}_a$ and the fuel mass flow $\dot{m}_f$,

$$\dot{m}_g = \dot{m}_a + \dot{m}_f \tag{7}$$

3. We assume that the pressure loss in the combustion chamber is a constant small percentage ξ_{cc} of the combustion chamber inlet pressure P_{02},

$$P_{03} = (1 - \xi_{cc})P_{02} \tag{8}$$

4. We assume that the pressure loss in the compressor inlet is a constant small percentage ξ_c of the atmospheric pressure.

$$P_{04} = (1 - \xi_c)P_{02} \cong P_{01} \tag{9}$$

5. The fuel was assumed to be pure methane and the combustion model was taken from Keating [8] and Turns [9], considering a complete combustion of the fuel without dissociation (Fig. 5).

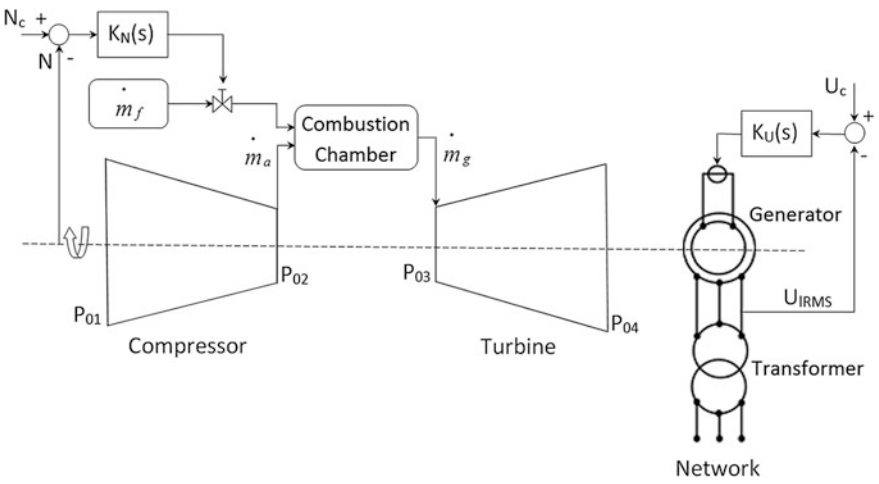

Fig. 5 Gas-fired turbine model

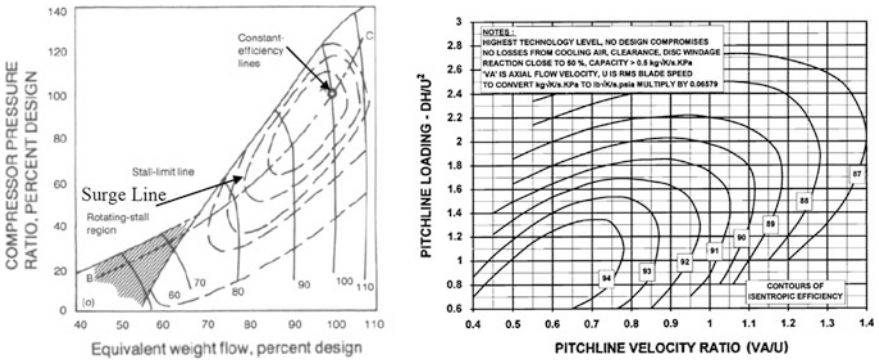

Fig. 6 Performance maps of a compressor (*left*) [11] and a turbine (*right*) [12]

Moreover, the gas turbine design and off-design model presented in this paper aims both at computational simplicity and at the ability to deal with plants having large variations in the operating parameters. Thus, some tools were needed to predict the performance of gas turbine engines especially at off-design conditions where its performance was significantly affected by the load and the operating conditions.

A solution to define the off-design behavior of the compressor and turbine is to use performance maps for each gas turbine component. Starting from known maps, such as those shown in Fig. 6, the evaluation of the off-design performance of different gas turbines can be investigated.

For completeness, the electrical system of the gas-fired power plant model is a synchronous machine of 66.6 MVA and is connected to the islanded network through 17.5/500 kV Yd5 transformers. The synchronous machine is solid iron rotor type. Finally, Table 3 gives the main characteristics of the gas-fired power plant.

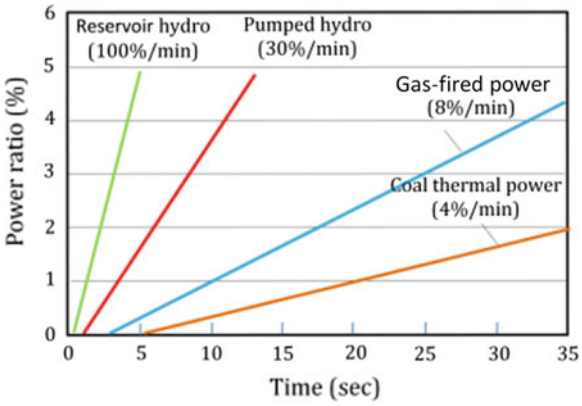

Fig. 7 Comparison of the adjustable load rates of four power plants [10]

Table 3 Gas-fired power plant characteristics

Compressor			Turbine		
Specific heat capacity	$C_{p,c}$ = 1,004	J/kg K	Specific heat capacity	$C_{p,T}$ = 1,156	J/kg K
Individual gas constant	R = 287	J/kg K	Individual gas constant	R = 287	J/kg K
Specific heat ratio	K_c = 1.4		Specific heat ratio	K_T = 1.35	
Pressure ratio (nominal)	$\pi_{c,nom}$ = 20		Rotational speed	N_T = 1,500	rpm
Rotational speed	N_c = 1,500	rpm	Inertia	$J_T = 3.16 \times 10^5$	kg m^2
Inertia	$J_c = 2.4 \times 10^4$	kg m^2			
Gas-fired turbine			**Generator**		
Power	P = 60	MW	Rated apparent power	S_n = 66.6	MVA
Efficiency	η_{nom}= 37	%	Rated phase to phase voltage	V_n = 17.5	k
Exhaust gas flow	Q_{ex} = 182.3	kg/s	Frequency	f = 50	Hz
Exhaust gas temperature	T_{ex} = 480	°C	Inertia	$J_{GT} = 1 \times 10^4$	kg m^2
			Number of poles pairs	P = 2	
			Stator windings	Y	

5 Transient Behavior of Mixed Islanded Power Network

The full SIMSEN model of the mixed power network is presented in Fig. 8 based on the hydraulic, gas-fired, and wind power plant models described above. The model includes the 500 kV transmission lines and the passive consumer load. Moreover, in order to make the system behavior more realistic, response times of the power plants are modeled. Figure 7 compares the adjustable load rates of several types of power plants. Overall, general hydro plants have the fastest response times, able to change from full power to zero and vice versa within 1 min. However, coal thermal power plants respond comparatively slowly [10].

For the analysis of the dynamic behavior of the mixed islanded power network, two different cases are considered and described:

- The first case consists of the compensation of the wind power variation due to wind velocity evolution,
- The second case is carried out for the power network subjected to a load rejection corresponding to the tripping of the 10 MW consumer.

In the first case, the wind velocity increases from a mean value of C_{inf} = 7.5–15 m/s in 40 s. Then, after 220 s, the wind velocity decreases from a

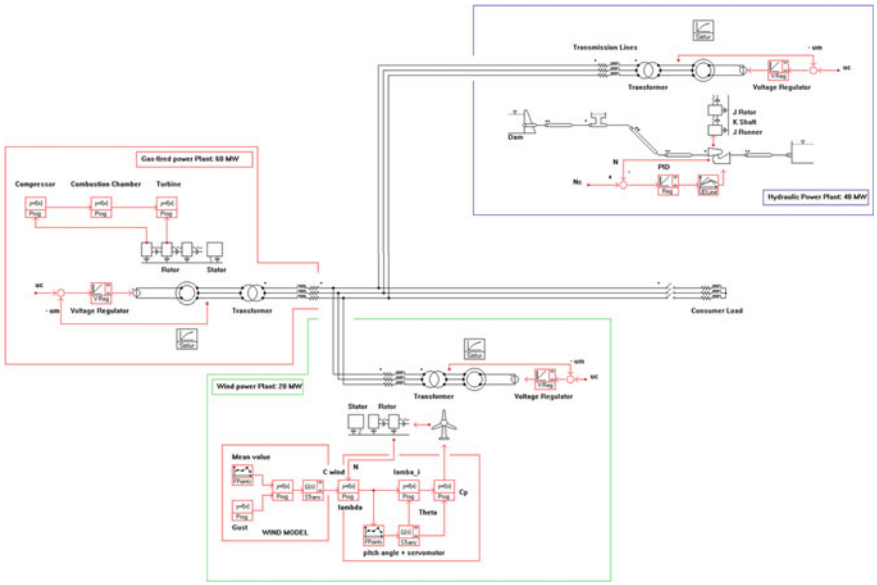

Fig. 8 Mixed islanded power network SIMSEN model

Table 4 Initial power flow before the wind increase

Element	Active power P [MW]	Network power level [%]	Power flow
Wind farm	−2.94	2.54 %	Production
Gas-fired power plant	−77.30	66.76 %	Production
Hydropower plant	−35.54	30.70 %	Production
Consumer load	115.38	–	Consumption

mean value of $C_{inf} = 15–7.5$ m/s. The initial conditions of the power flow of the islanded power network are summarized in the Table 4.

The difference between production and consumption corresponds to the energy losses in both the transmission lines and the transformers. The Fig. 9 describes the time history of the main parameter of the wind farm during the simulation. During the first 10 s, the wind velocity modeled by a PRBS fluctuates around a mean value of 7.5 m/s. Then, it can be noticed that the wind increase induces output power increase and therefore the blade pitch angle is constantly adapted to maximize the power coefficient. However, after 40 s, the pitch angle is selected to generate the 2 MW output power limit of each wind turbine unit.

After 10 s, the wind power increase causes both an overproduction and a network frequency increase involving consequently an acceleration of different turbines. Thus, to ensure the stability of the islanded power network, the turbine speed governors stabilize the network frequency by closing the hydraulic guide vanes and by reducing the gas consumption of the gas-fired turbine and therefore

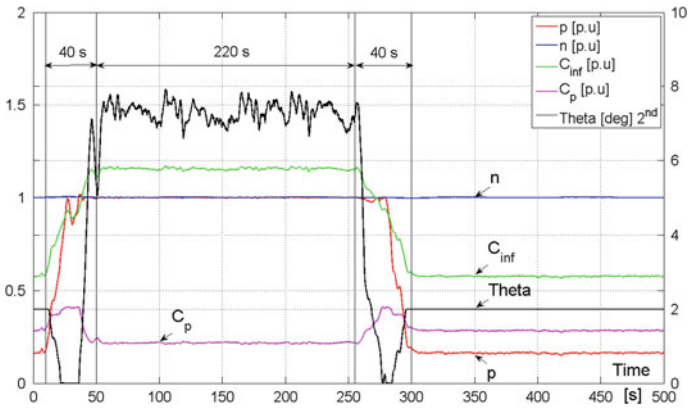

Fig. 9 Time history of the wind farm parameters during the wind evolution

the electrical output of the hydraulic and thermal parts are reduced. To better visualize the time history of generation and consumption on the grid, the Figs. 10, 11 show the time history of the active power of the hydro, gas-fired, and wind power plants and of the consumer load during the wind evolution, respectively, with a short and a long penstock.

Overall, a long penstock emphasizes dynamic phenomena, such as water hammer, surge tank water-level oscillation, and turbine operation instabilities. Indeed, the increase in the penstock length causes an increase in the response time of the hydraulic system. Thus, when the turbine speed governors impose a closure of the guide vanes to reduce output power and therefore stabilize the network, the hydraulic system requires a period of 3.33 s before the torque begins to decrease. However, during this period, the power continues to increase and the regulator has to overreact to avoid too much change in the network frequency (see Fig. 12).

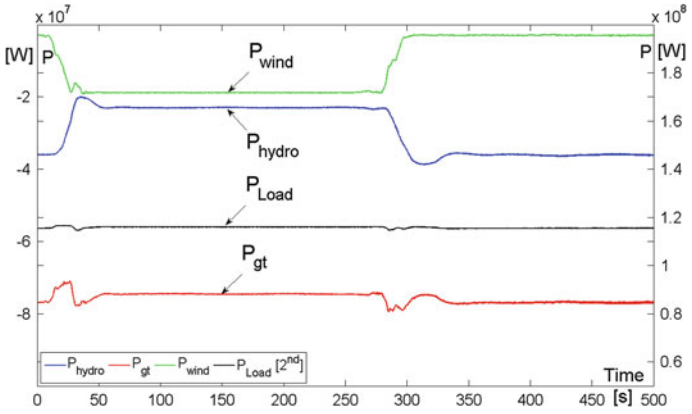

Fig. 10 Transient behavior of the active power during the wind evolution for a short penstock

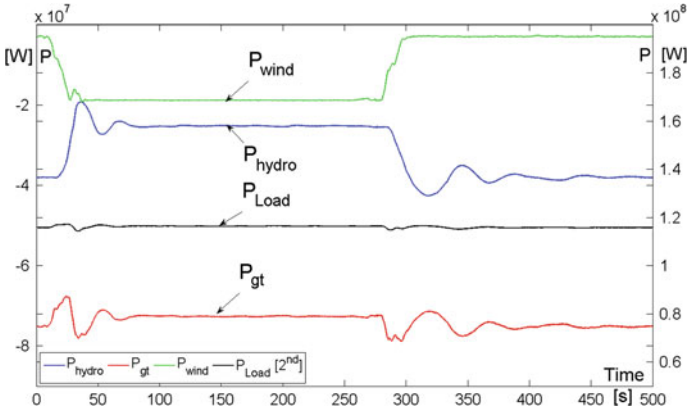

Fig. 11 Transient behavior of the active power during the wind evolution for a long penstock

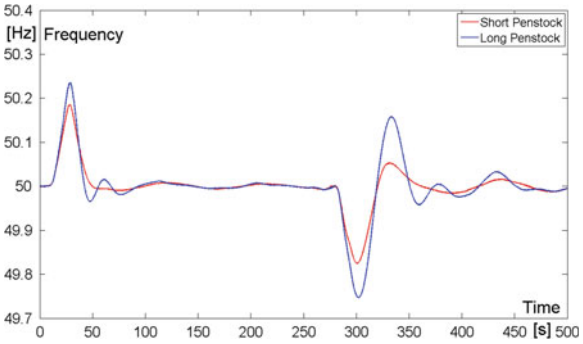

Fig. 12 Time history of the network frequency for a long and a short penstock

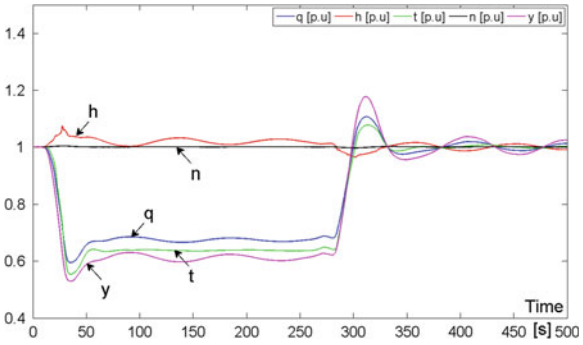

Fig. 13 Transient behavior of the hydraulic turbine parameters during the wind evolution for a short penstock

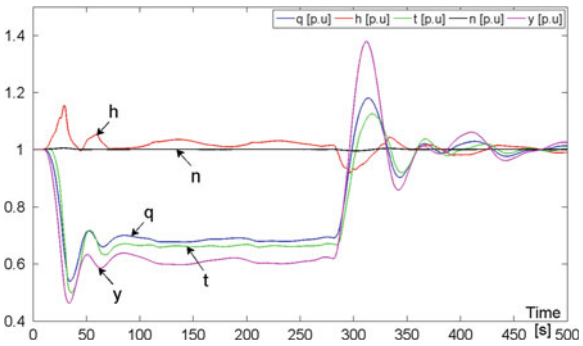

Fig. 14 Transient behavior of the hydraulic turbine parameters during the wind evolution for a long penstock

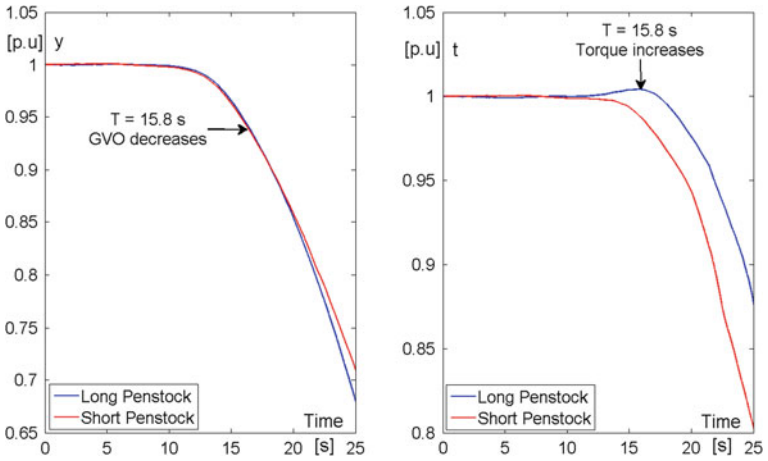

Fig. 15 Time history of the guide vane opening y and the torque T for the hydraulic turbine

Therefore, larger amplitudes of piezometric pressure H, discharge Q, and power P appear that could lead to unstable behavior of the turbine; all these specific aspects are highlighted in the Figs. 13, 14.

More precisely, at time $t = 15.8$ s, the torque reaches its maximum value while the guide vane opening (GVO) decreases for a reaction time equal to 3.33 s (see Fig. 15). This reaction time corresponds to the so-called reflection time of the penstock given by 2L/a. This long reaction time causes an overpressure of 116.1 % at the bottom of the penstock instead of 108.7 % for a configuration with a short penstock. In addition, greater mass oscillations amplitudes between the surge tank and the dam appear and so a larger time is necessary to stabilize the system.

For the second case, the investigation is carried out for the power network subjected to a load rejection corresponding to the tripping of 10 % of the consumer

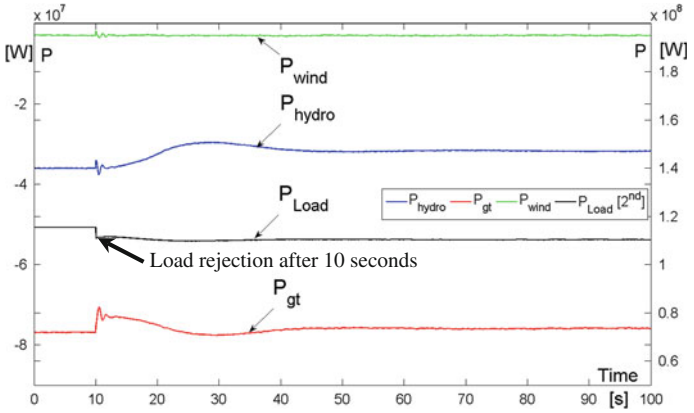

Fig. 16 Transient behavior after a load rejection for a short penstock

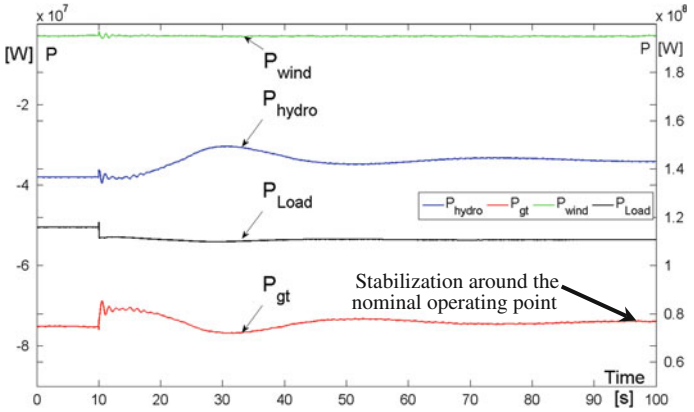

Fig. 17 Transient behavior after a load rejection for a long penstock

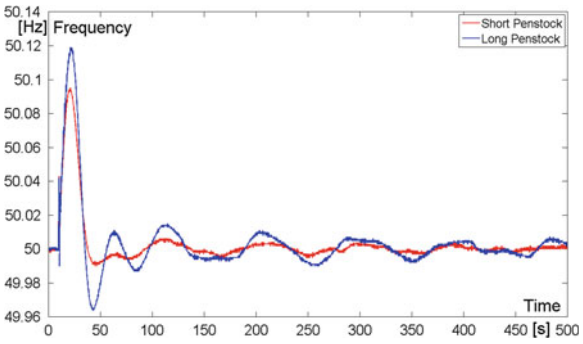

Fig. 18 Time history of the network frequency for a long and a short penstock

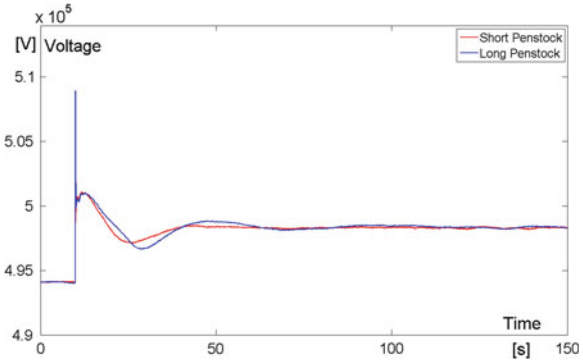

Fig. 19 Time history of the network voltage frequency for a long and a short penstock

load. After 10 s, the power consumption drops instantaneously of 10 MW, changing the voltage on the network (see Fig. 19). Therefore, the electromagnetic torque decreases causing an increase in the rotational speed of different synchronous machines. Thus, to avoid too large variations in network frequency, speed governors must act quickly and reduce mechanical torque. Initially, the hydraulic part compensates very quickly the power reduction imposed by the load rejection and the sharp drop in the thermal torque. Then, as the gas turbine performance is not very high at partial load, it will tend to stabilize around its nominal operating point forcing the hydraulic part to compensate for the gradual increase in production (see Figs. 16, 17, 18).

Finally, as for the case of the wind variation, the system takes longer time to stabilize when the length of the penstock increases. Thus, a long penstock can lead to longer response time of the hydropower plant and reduces the power stability. Therefore, the hydraulic layout needs to be included in the stability assessment to study the nonlinear behavior of a mixed islanded power network.

6 Conclusion

The modeling, numerical simulations, and stability analysis of an islanded power network comprising 40 MW of hydropower, 20 MW of wind power, and 60 MW of gas-fired power plant were presented in this paper. The wind farm is modeled through an aggregated model approach of 10 wind turbines of 2 MW and comprises a stochastic model of wind evolution with wind gust. The model of gas-fired power plant includes an upstream rotating compressor coupled to a downstream turbine, and a combustion chamber in-between. To predict the performance of a gas turbine engine, both at design and off-design conditions, performance maps are integrated in the modeling.

The high dynamic performances of pumped storage plants are of highest interest for improving stability of mixed islanded power network, but require reliable simulation model of the entire power network for safety and optimization purposes. This study shows the evolution of the response time of the hydraulic part as function of the penstock length and highlights the influence of the hydraulic layout on the power system stability. Thus, a long penstock can lead to longer response time of the hydropower plant and reduces the power stability. Therefore, the hydraulic layout needs to be included in the stability assessment to study the nonlinear behavior of a mixed islanded power network.

Acknowledgments The authors would like to thank Swisselectric Research and the Energy Program of The Ark and the Foundation for Innovation of Valais Canton, for their financial support.

References

1. Wiik, J., Gjerde, J.O., Gjengedal, T. (2000). Impacts from large scale integration of wind farms into weak power systems. IEEE.
2. Nicolet, C., Vaillant, Y., Kawkabani, B., Allenbach, P., Simond, J.-J., Avellan, F. (2008). *Pumped storage units to stabilize mixed islanded power network: A transient analysis, proceedings of HYDRO*. Ljubljana.
3. Wylie, E. B., & Streeter, V. L. (1993). *Fluid transients in systems*. Englewood Cliffs: Prentice Hall.
4. Nicolet, C., Alligné, S., Kawkabani, B., Koutnik, J., Simond, J.J., & Avellan, F. (2009). Stability study of Francis pump-turbine at runaway. *3th IAHR International Meeting of the Workgroup on Cavitation and Dynamic Problems in Hydraulic Machinery and Systems.*
5. Nicolet, C., Greiveldinger, B., Hérou, J.-J., Kawkabani, B., Allenbach, P., Simond, J.-J., et al. (2007). High-order modeling of hydraulic power plant in islanded power network. *IEEE Transactions on Power Systems, 22*(4), 1870–1880.
6. Slootweg, J. G., De Haan, S. W. H., Polinder, H., & Kling, W. L. (2003). General model for representing variable speed wind turbines in power system dynamics simulations. *IEEE Transactions on Power Systems, 18*(1), 144–151.
7. Godfrey, K. (1991). Design and application of multifrequency signals. *Computing and Control Engineering Journal, 2*(4), 187–195.
8. Keating, E.L. (1993). Applied combustion. In M. Dekker, Inc., New York.
9. Turns, S. R. (1996). *An introduction to combustion*. New York: Mc Graw-Hill.
10. Inage, S. (2009). Prospects for large-scale energy storage in decarbonised power grids. International Energy Agency, OECD/IEA, Paris.
11. Boyce, MP. (2006). 2.0 Axial-flow compressors, *The gas turbine handbook*. Houston: NETL.
12. Walsh, P. P., & Fletcher, P. (2004). *Gas turbine performance* (2nd ed.). Oxford: Blackwell.

Determination of Surge Tank Diaphragm Head Losses by CFD Simulations

Sébastien Alligne, Primoz Rodic, Jorge Arpe, Jurij Mlacnik and Christophe Nicolet

Abstract At early stage of a hydroelectric project, 1D transient simulations are performed to determine the basic layout of power plant. In this phase, the design of surge tanks is decisive to achieve good dynamic performances of the power plant, with respect to water hammer and mass oscillations induced by the hydraulic machines for normal, exceptional, and accidental operation. As the head losses between the gallery and the surge tank have strong influence on the transient behavior of the hydraulic system, they are usually optimized by means of 1D transient simulation to avoid low pressure in gallery or surge tank overflow. An asymmetric diaphragm is often placed at the surge tank inlet to achieve the optimum inlet and outlet head losses. Thus, the design of such diaphragm is a challenging task usually performed through an iterative process on reduced-scale model. In this context, 3D CFD simulations can significantly improve the design process to select the appropriate geometry of the diaphragm. In this chapter, head losses coefficients of a surge tank scale model are derived from CFD simulations performed with ANSYS CFX. Results are compared with measurements on reduced-scale physical model and analytical approach. The good agreement of CFD computations with measurements demonstrates that a design optimization

S. Alligne (✉) · C. Nicolet
Power Vision Engineering sárl, Chemin des Champs-Courbes 1,
CH1024 Ecublens, Switzerland
e-mail: sebastien.alligne@powervision-eng.ch

C. Nicolet
e-mail: christophe.nicolet@powervision-eng.ch

P. Rodic · J. Mlacnik
Hidroinstitut, Hajdrihova 28, SI-1115 Ljubljana, Slovenia
e-mail: primoz.rodic@hidroinstitut.si

J. Mlacnik
e-mail: jurij.mlacnik@hidroinstitut.si

J. Arpe
AF-Consult Switzerland Ltd, Täfernstrasse 26, 5405 Baden-Dättwil, Switzerland
e-mail: jorge.arpe@afconsult.com

P. Gourbesville et al. (eds.), *Advances in Hydroinformatics*,
Springer Hydrogeology, DOI: 10.1007/978-981-4451-42-0_27,

with 3D flow simulations can be performed preliminary to scale model tests in order to reduce the number of geometries to be tested to achieve the expected head losses.

Keywords Surge tank · Diaphragm · Head losses · CFD · Transient analysis

Nomenclature

f	Darcy- Weisbach loss coefficient, [–]
g	Gravitational acceleration, [m.s^{-2}]
$\overrightarrow{n}$	Normal vector to surface, [–]
p	Pressure, [Pa]
q	Non-dimensional flow rate, [–]
y^+	Y plus, [–]
Δh_{ij}	Non-dimensional head losse from i to j, [-]
A	Cross section area, [m^2]
$\overrightarrow{C}$	Velocity vector [m.s^{-1}]
D	Diameter, [m]
H_i	Total head, [m]
K_{ij}	Head loss coefficient, [–]
L	Length, [m]
Pz_i	Piezometric head, [m]
Q	Flow rate, [m^3.s^{-1}]
Re	Reynolds number, [–]
ΔH_{ij}	Total head loss from i to j, [m]
α_q	Relative flow rate, [–]
λ	Length scale, [–]
ρ	Density, [kg.m^{-3}]

1 Introduction

The design process of a hydroelectric power plant layout includes 1D transient simulations aiming to avoid undesirable fluid transients during specific operational procedures. Many methods for controlling transients are available, and the appropriate surge control devices are deduced from the transient simulations. For long pipeline systems, surge tanks are usually integrated in order to protect the headrace tunnel from water hammer induced by exceptional or accidental operations of the hydraulic machines. However, mass oscillations between surge tank and reservoir are experienced. Since the head losses between the headrace tunnel and the surge tank drive the transient behavior of this mass oscillation [1], they are usually optimized by adding a singular loss through a diaphragm at the entrance of the surge tank.

The design of such diaphragm is a challenging task usually performed through an iterative process on reduced-scale model. In this context, 3D CFD simulations can significantly improve the design process to select the appropriate geometry. Such numerical investigations have been performed previously by Huber [2] and Klasinc et al. [3] where they computed head losses coefficients of a diaphragm located in a T-shaped junction. Richter et al. [4] focused on the velocity field induced by the incoming jet into the surge tank and compared to PIV measurements. Regarding the optimization process of the diaphragm geometry, Gabl et al. [5] used CFD simulations and showed that theoretical approach gives different results. Similar investigations on geometries without diaphragm, such as simple T-junction [6] or trifurcation [7], have been carried out to compute head losses coefficients.

This chapter presents the design process of a surge tank diaphragm to be integrated into a pumped-storage power plant. First of all, the required head loss coefficients determined by 1D transient simulations for safety operating conditions are given. Then, physical model tests of the optimized geometry are presented with the head loss coefficients' measurements. Finally, comparison with CFD simulations is performed in order to assess whether 3D flow simulations can be used preliminary to scale model tests to reduce the number of geometries to be tested.

2 Surge Tank Design by 1D Transient Simulations

The design of the surge tank of a pumped-storage power plant is carried out by 1D transient simulations of the entire power plant as shown in Fig. 1. This optimization procedure aims to find the surge tank geometry with the minimum volume and comply with the safety requirements of the waterways for normal, exceptional, and accidental load cases. For this purpose, the optimization of the head losses at the surge tank inflow and outflow could significantly contribute to minimize the size and thus the cost of the surge tank, see [8]. Figure 2 shows simulation results of the transient behavior of the pumped-storage power plant of Fig. 1 obtained with the EPFL simulation software SIMSEN, see [9] for turbine and pump emergency shutdown which are usually one of the most critical cases to be considered in the design phase. It could be noticed that optimum head losses coefficients are achieved when maximum and minimum head, H, in the headrace tunnel at the surge insertion, corresponds to the maximum and minimum water level, Hc,

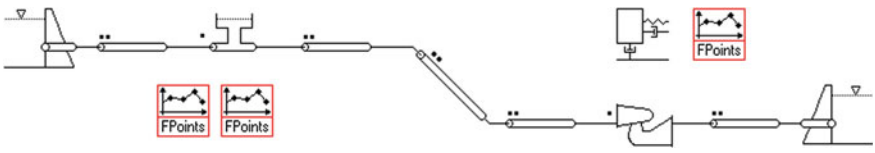

Fig. 1 SIMSEN model of typical pumped-storage power plant with upstream surge tank

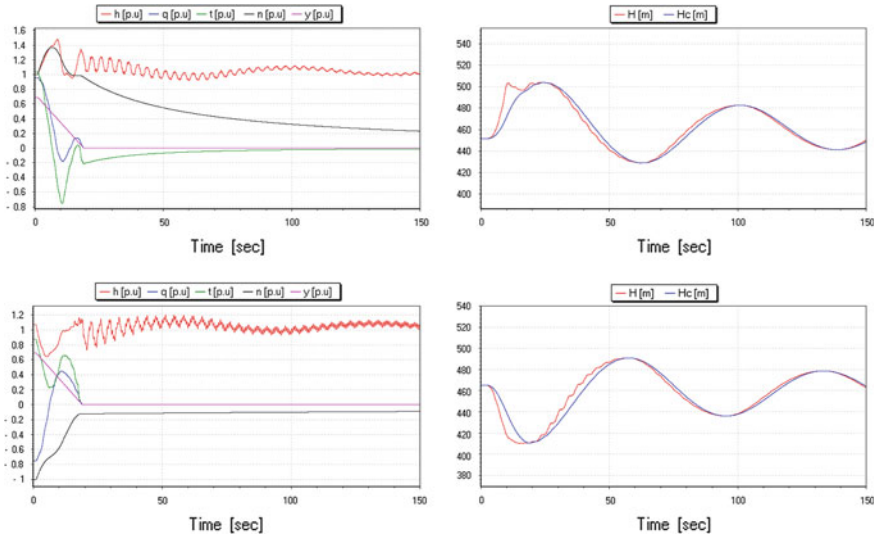

Fig. 2 Simulation results of emergency shutdown of pumped storage in generating mode (*top*) and pumping mode (*down*) and transient behavior of the pump-turbine (*left*) and of the surge tank (*right*)

in the surge tank, see Stucky [1]. The final surge tank design should at least ensure (1) to avoid empting the surge tank and related risk of entrapped air the waterways, (2) prevent from water column separation in the gallery and top of the penstock, (3) prevent from cavitation in the surge tank diaphragm if any, (4) ensure sufficient mass oscillation damping, (5) comply with the turbine governor stability, see Thoma, [10], and (6) prevent from overflow, if not permitted. Finally, the 1D transient simulation performed for the pumped storage of interest leads to an optimal inlet and outlet surge tank loss coefficient, respectively, equal to $K_{12} = 5$ and $K_{21} = 2.5$.

3 Surge Tank Diaphragm Design by Physical Model Tests

3.1 Reduced-Scale Model Geometry

After optimization of a pumped-storage power plant surge tank by 1D transient analysis, experiments have been conducted at the Hydraulic Laboratory of Hidroinstitut, Ljubljana, to define the diaphragm geometry, enabling us to reach the specified surge tank head losses. Figure 3 shows the optimized geometry of the reduced-scale model of the surge tank considering a length scale of $\lambda = 1{:}13.2$.

The pipe between the headrace tunnel and the surge tank features three singularities: a 90° T-junction, a change in direction, and a diaphragm inducing

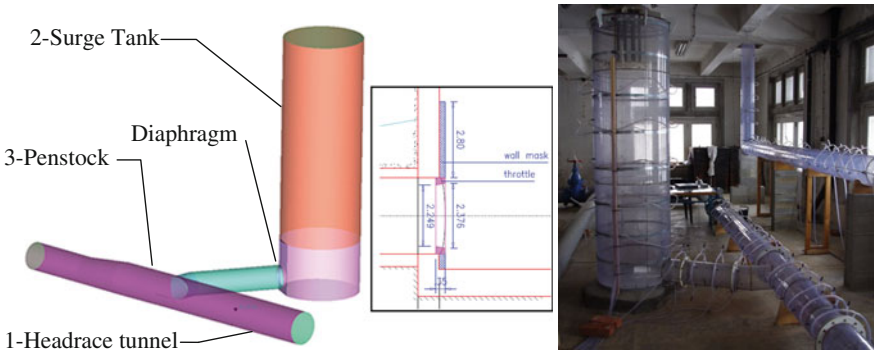

Fig. 3 3D reduced-scale model geometry (*left*), drawing of the prototype diaphragm geometry (*center*) and experimental apparatus (*right*)

sudden change in cross section. All these singularities contribute to the global head losses of the surge tank combined with the friction losses on the walls. For convenience, the headrace tunnel, the surge tank, and the penstock are numbered, respectively, by 1, 2, and 3.

3.2 Investigated Operating Conditions

In this chapter, four cases are investigated. These cases correspond to different operating conditions which differ according to the flow configurations in the system. Table 1 summarizes the investigated cases. Moreover, the distribution of the flow rates in each branch is mentioned by the flow rate ratio $\alpha_q i$ which is defined by the ratio between the flow rate in the considered branch i and the total flow rate. The flow configurations described in Table 1 correspond to the following cases:

- Case #1: The flow is going from the headrace tunnel to the surge tank ($\alpha_q 1 = \alpha_q 2 = 1$), and the flow rate in the penstock is equal to zero ($\alpha_q 3 = 0$);

Table 1 Investigated operating conditions

Case	#1	#2	#3	#4
Scheme	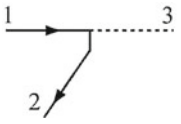	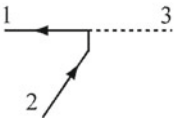	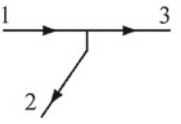	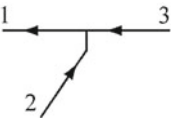
Symbol	1 > 2	2 > 1	1 > 2,3	2,3 > 1
$\alpha_q 1 = Q1/Qtot$	1	1	1	1
$\alpha_q 2 = Q2/Qtot$	1	1	0.5	0.25
$\alpha_q 3 = Q3/Qtot$	0	0	0.5	0.75

this flow configuration is experienced during the mass oscillations between headrace tunnel and surge tank consecutive to a turbine emergency shutdown;
- Case #2: The flow is going from the surge tank to the headrace tunnel ($\alpha_q 2 = \alpha_q 1 = 1$), and the flow rate in the penstock is equal to zero ($\alpha_q 3 = 0$); this flow configuration is experienced during the mass oscillations between surge tank and headrace tunnel consecutive to a pump emergency shutdown;
- Case #3: The flow coming from the headrace tunnel is equally divided into the penstock and into the surge tank ($\alpha_q 2 = \alpha_q 3 = 0.5$); this flow configuration is experienced in turbine mode just after an emergency shutdown;
- Case #4: The flows coming from the surge tank and from the penstock are going to the headrace tunnel; for this case, most of the incoming flow comes from the penstock ($\alpha_q 2 = 0.25$, $\alpha_q 3 = 0.5$); this flow configuration is experienced in pump mode just after an emergency shutdown.

Respecting the Froude similitude with a length scale of the model λ, the scale factor for the Reynolds number transposition to prototype is equal to $\lambda^{3/2} = 48$. The involved Reynolds numbers are set in a range to ensure experimental head losses coefficients representative to the prototype conditions.

3.3 Experimental Setup

The reduced-scale model of the surge tank is manufactured with clear PVC material. The headrace tunnel and the penstock in the vicinity of the T-junction are included in the reduced-scale model geometry. The experimental setup is shown in Fig. 4.

The model was equipped with electromagnetic flow meters, and measurements of piezometric heads were taken in 25 cross sections: 8 in the headrace tunnel (Pz11–Pz18), 8 in the penstock (Pz31–Pz38), and 9 in the connecting pipe and the surge tank (Pz21–Pz29). To compute the head losses coefficients, reference cross

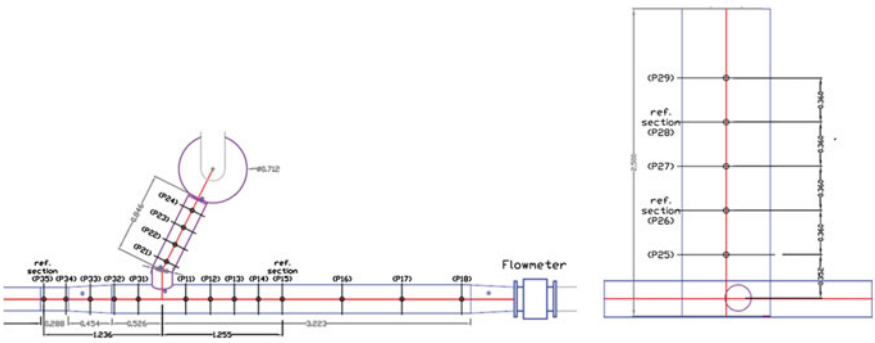

Fig. 4 Experimental setup with top view (*left*) and side view (*right*) of the surge tank and related pressure taps

sections, located far from flow disturbances, are selected: Pz15 in the headrace tunnel, Pz35 in the penstock, Pz28 in the surge tank for inflow conditions, and Pz26 in the surge tank for outflow conditions.

3.4 Loss Coefficients

Head losses between sections i and j include both friction and singular losses. Hence, to derive the contribution of the singular part, the friction losses $\delta H_{\mathrm{ij\_friction}}$ must be subtracted from the total head difference $\Delta H_{\mathrm{ij}} = H_i - H_j$, see Gardel [11]. The resulting singular head loss coefficient is defined by

$$K_{\mathrm{ij}} = \left(H_i - H_j - \delta H_{\mathrm{ij\_friction}}\right) \Big/ \left(Q_2^2 \Big/ 2gA_{\mathrm{ref}}^2\right) \tag{1}$$

where Q_2 is the reference flow rate and A_{ref} the reference cross-sectional area corresponding to the connecting pipe between the surge tank and the headrace tunnel. The friction losses are estimated with the Darcy–Weisbach friction factor f as follows:

$$\delta H_{\mathrm{ij\_friction}} = f \frac{L}{D} \frac{Q^2}{2gA^2} \tag{2}$$

Preliminary measurements to derive the friction factor of the different pipe components are taken. The methodology consists in measuring the total head difference in a straight part of the considered pipe for several flow rates. Assuming a constant friction factor in the turbulent regime, a fitting function with the square of the flow rate is found to derive the coefficients. The friction factors f are given in Table 2.

Finally, to derive the singular head losses coefficients, the same methodology as for the computation of the friction factors is used. Total head differences are measured for several flow rates, and a fitting function is derived from raw data. The head losses coefficients are given in Table 3 for all the investigated cases.

Table 2 Experimental Darcy-Weisbach friction factor f

Pipe	1-Headrace tunnel	2-Connecting pipe	3-Penstock
f	0.015	0.014	0.017

Table 3 Experimental singular head losses coefficients K obtained by physical model tests

Case	Symbol	K_{12}	K_{21}
#1	1 > 2	5.047	–
#3	1 > 2, 3	5.274	–
#2	2 > 1	–	2.543
#4	2, 3 > 1	–	1.370

4 CFD Computations of Diaphragm Head Losses Coefficients

4.1 Numerical Setup

For the present application, ANSYS CFX 14.0 version is used for the flow computation in the surge tank reduced-scale model. Steady Reynolds-averaged Navier-Stokes equations are solved, and the set of equations is closed with an eddy viscosity turbulence model: the shear stress transport (SST) model which gives highly accurate predictions of the onset and the amount of flow separation. For this typical investigated geometry, flow separations are expected in the T-junction and at the outlet diaphragm. The computational domain is in adequacy with the reduced-scale model and includes the reference cross sections used experimentally to compute the head losses. It is discretized with a structured mesh of 1.9 million nodes, generated with ANSYS ICEM 14.0. Influence of the mesh refinement was carried out in order to check the mesh independency on the head losses coefficients. Taking into account this spatial discretization, the "high resolution" advection scheme is used to solve the set of equations.

The inlet boundary condition is a prescribed velocity profile corresponding to a turbulent flow fully developed and obtained by a preliminary computation in a long straight pipe. Moreover, a non-slip wall condition is set up with a specified roughness. The roughness value is derived from the experimental Darcy–Weisbach factor f. Finally, for the outlet boundary condition, an opening condition is used. If the numerical model includes only one outlet, the "static pressure for entrainment" is set up. However, if the model features two outlets, for dividing flow conditions, one is set up as previously, whereas for the other one, a specified velocity field is used to impose the flow rate.

4.2 Mesh Quality

Accuracy computation of head losses coefficients requires solving properly the boundary layer to predict wall friction and flow separations. Instead of using a very fine near-wall grid and a low Reynolds model, the wall function solution is used. The idea is to set the first computational node outside the viscous sublayer and make suitable assumptions about the near-wall velocity profile. This meshing requirement is a decisive issue for the turbulence model performance. To set up the first computational node away from the wall, a non-dimensional wall distance from the wall y + is introduced. This distance should be between 20 and 200 to obtain a resolved boundary layer at least with 10 computational nodes. The y+ area average is reported in Table 4 for the different simulated cases.

Table 4 Mesh quality analysis with y+ values

Case	Q_{tot}/Q_{ref}	$\overline{y^+}$
#1	1.53	84
#2	1.54	55
#3	1.56	63
#4	1.53	27

4.3 Loss Coefficients

Gravity being not applied in the numerical setup, total head in a given cross section is computed as follows:

$$H_i = \frac{1}{Q_i}\int_{S_i}\left(\frac{p}{\rho g} + \frac{\overrightarrow{C}^2}{2g}\right)\overrightarrow{C}.\overrightarrow{n}\cdot dS \tag{3}$$

In the total head difference ΔH_{ij} derived from numerical simulations, part of the head losses are due to friction phenomena. Hence, to derive the singular head losses, the estimated experimental friction losses are subtracted. Indeed, the roughness value specified in the numerical setup has been calibrated with respect to experiments. For convenience, non-dimensional head losses Δh_{ij} are presented in the following charts:

$$\Delta h_{ij} = \frac{\Delta H_{ij} - \delta H_{ij\_friction}}{\frac{Q_{2\_ref}^2}{2gA_2^2}} \tag{4}$$

To define this non-dimensional value, the singular head losses are divided by reference kinetic energy defined in the connecting pipe between the surge tank and the headrace tunnel with the nominal flow rate value of $Q_{2\_ref} = 0.063\ m^3.s^{-1}$, which is relevant for our investigations. In Fig. 5, head losses Δh_{ij} are plotted as function of the square of the non-dimensional flow rate of the connecting pipe $q_2 = Q_2/Q_{2\_ref}$ for each investigated case.

The experimental methodology that allows us to derive the singular head losses coefficients K_{ij} is used for the numerical approach. The head losses are computed for three flow rate values and are plotted as a function of the square flow rate in order to fit numerical results with a linear function. The slope of this linear function gives the head loss coefficients K_{ij}. The comparison between experimental and numerical coefficients is given in Table 5,

For the three first cases, good agreement is observed between experiments and flow simulations. However, a large relative error of 29 % is observed for the case #4 where low Reynolds number in the connecting pipe is experienced with a value of $Re_2 = 1.10^5$. In that case, the experienced head losses are very small. Indeed, regarding the absolute error for case #4, it corresponds to 0.9 cm of head losses, whereas for case #1, the absolute error is 11.2 cm. In Fig. 5, streamlines projected

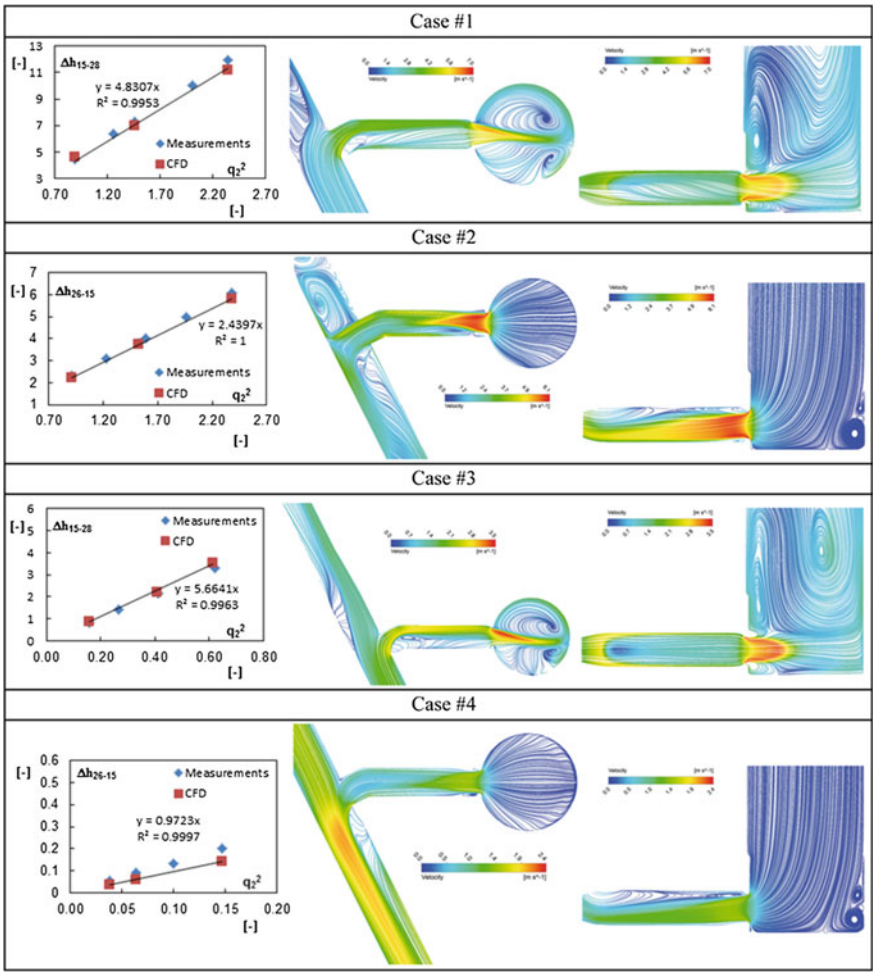

Fig. 5 Head losses as a function of the square flow rate (*left*), surface streamlines in the horizontal plane (*center*) and in the vertical plane (*right*)

Table 5 Comparison between experimental and numerical head losses coefficients K

Case	Symbol	Experimental		Numerical		Relative error
		K_{12}	K_{21}	K_{12}	K_{21}	
#1	$1 > 2$	5.047	–	4.830	–	−4.3 %
#3	$1 > 2, 3$	5.274	–	5.664	–	+7.4 %
#2	$2 > 1$	–	2.543	–	2.440	−4.0 %
#4	$2, 3 > 1$	–	1.370	–	0.972	−29 %

Table 6 Comparison between experimental, numerical, and theoretical head losses coefficients K

Case	Symbol	Experimental	Numerical	Theoretical
#1	$1 > 2$	5.047	4.830	5.16
#2	$2 > 1$	2.543	2.440	2.65

on the horizontal and the vertical planes are shown for each investigated case at the highest simulated flow rate. These visualizations allow us to identify flow separations, swirling flow, or large recirculations inducing the head losses in the system.

5 Comparison with Theoretical Approach

A comparison for cases #1 and #2 with theoretical approach can be performed with the Idel'cik handbook [12], taken as reference. For convenience, analytical formula is not written in this chapter, but the used diagrams are referenced. For case #1, the head loss coefficients for the T-junction and the diaphragm are derived, respectively, from the diagrams 7.21 and 4.11, whereas for case #2, diagrams 4.12 and 7.16 are used. The obtained theoretical coefficients are given in Table 6 and compared to experimental and numerical results.

The theoretical approach gives as good results as numerical investigations contrary to Gabl et al. [5]. It can be concluded that the distance between the T-junction and the diaphragm allows us to compute separately the head loss coefficients with analytical models. However, when the layout of the power plant imposes a design far away from the analytical models such as diaphragm in T-junction [2] or sudden expansion downstream to a bend [5], the 3D flow simulations can be useful for preliminary design.

6 Conclusions

The present work shows the ability of steady RANS simulations to derive the head loss coefficients of a surge tank diaphragm under turbulent flow regimes. Hence, a design optimization with 3D flow simulations can be performed preliminary to scale model tests. Moreover, it is shown that theoretical approach gives as good results as numerical investigations when each component constituting the surge tank geometry can be considered separately. However, for complex geometries, the 3D flow simulations should be more accurate compared to the analytical models.

Acknowledgments Authors would like to thank particularly Mr. Roberto Rosseti from CAD-FEM company who placed test license of ANSYS products at our disposal to check feasibility of such study.

References

1. Stucky, A. (1958). Chambres d'équilibres. EPFL, Cours d'aménagement des chutes d'eau, Sciences et Technique.
2. Huber, B. (2009). Physical model tests and CFD simulation of an asymmetrical Throttle in a T-Shaped Junction of a High Head Power Plant. 33rd IAHR Congress: Water Engineering for a sustainable Environment, pp. 5013–5021.
3. Klasinc, R., Bilus, I. (2009). Experimental and numerical approach to surge tank improvements. international symposium on water management and hydraulic engineering.
4. Richter, W., Dobler, W., Knoblauch, H. (2012). Hydraulic and numerical modelling of an asymmetric orifice within a surge tank. 4th IAHR international symposium on hydraulic structures. Porto, Portugal.
5. Gabl, R., Achleitner, S., Neuner, J., Götsch, H., Aufleger, M. (2011). 3D numerical optimisation of an asymmetric orifice in the surge tank of a high head power plant. 34th IAHR world congress, Brisbane, Australia.
6. Huber, B. CFD simulation of a T-junction. Institute of hydraulic and water resources engineering, department of hydraulic engineering, Vienna University of Technology.
7. Basara, B., Grogger, H. A., Klasinc, R., Mayr, D. Experimental and numerical study of the flow through a trifurcation.
8. Steyrer, P. (1999). *Economic surge tank design by sophisticated hydraulic throttling, proceedings of the 28th IAHR congress*. Austria: Graz.
9. Nicolet, C. (2007). Hydroacoustic modelling and numerical simulation of unsteady operation of hydroelectric systems, Ph.D. Thesis, EPFL N 3751, Lausanne, (http://library.epfl.ch/theses/?nr=3751).
10. Thoma, D., (1910). Zur Theorie des Wasserschlosses bei selbsttätig geregelten Turbinenanlagen, Munich (Oldenbourg).
11. Gadel, A., Rechsteiner, G. D. (1970). Les pertes de charge dans les branchements en Té des conduites de section circulaire. Bulletin technique de la Suisse Romande, N 25, pp. 363–391.
12. Idel'cik, I. E. (1960). *Memento des pertes de charges*. Paris: Edition Eyrolles.

Study of the Hydrodynamic Phenomena and Fluid–Structure Interactions of a Bypass Butterfly Valve with Double Disc

Julien Large, Jérôme Fouque and David Reungoat

Abstract Bypass system is used to balance the pressure of the fluid between upstream and downstream of the valve before the opening of the main valve in order to achieve the rated capacity. They also reduce the fluid velocity in the early stages of operation. Conventional bypass system is made of a main valve of large diameter, a secondary valve and additional piping. Based on more than 30 years in developing and manufacturing butterfly valves from 1″ up to 150″, KSB developed a new product to integrate a bypass valve within a double disc. Main advantages are reduction of piping, joints, and tightness improvement. This study concerns the mechanical and hydraulic behaviour of a bypass butterfly valve with double disc to replace the conventional bypasses. A numerical model was performed (ANSYS CFX©) to study the flow around the double butterfly valve through hydraulic pressure loss and hydrodynamic torque coefficients. With computational fluid dynamics, it is possible to predict the hydrodynamic torque versus opening angle characteristic. One of the key parameter of butterfly valves design is to master the hydrodynamic torque that has great impact on actuator size. With this new design, actuator sizing is improved by about 30 %. This model is also used to design the configurations studied in the experimental approach. The tests carried out on the test facility of CETIM concerned the measurement of static pressure upstream and downstream of the prototype and the flow rate in order to know the pressure losses. The hydrodynamic torque measurements were performed using strain gauge inserted between the actuator and the valve neck. This experimental phase was used to validate the numerical model. It will allow KSB to size new system with virtual prototype.

J. Large (✉) · J. Fouque
KSB, Bordeaux, France
e-mail: julien.large@ksb.com

J. Fouque
e-mail: jerome.fouque@ksb.com

D. Reungoat
I2M, University Bordeaux I, Bordeaux, France
e-mail: david.reungoat@u-bordeaux1.fr

P. Gourbesville et al. (eds.), *Advances in Hydroinformatics*,
Springer Hydrogeology, DOI: 10.1007/978-981-4451-42-0_28,

Keywords Hydrodynamic · Fluid–structure interaction · Pressure loss · Butterfly valve · Bypass

Nomenclature

C [N.m] operating torque of valve
C_d [N.m] hydrodynamic torque
C_f [N.m] friction torque of bearings
C_h [N.m] hydrostatic torque
C_g [N.m] offset torque of gravity
C_s [N.m] seat torque
C_m [.] hydrodynamic torque coefficient (aerodynamic)
d [m] internal diameter of secondary valve
d_i [.] fluid density by density of water
D [m] internal diameter of main valve and penstock
K_v [m^3/h/bar½] coefficient of flow reduces
K_h [.] coefficient of hydrodynamic torque
Q_v [m^3/s] flow
U [m/s] velocity of flow

Greek Letter

α [°] angle of main disc
β [°] angle of secondary disc
Δ_P [Pa] head loss
Ψ [°] relative angle
ρ [Kg/m^3] density of water

1 Introduction

In piping system, butterfly valves of large diameters (called main valve) are commonly used with bypasses. This association makes possible two functions. The first one appears when the main valve is closed. In this state, the bypass is used to balance the fluid pressure from each side of the butterfly valve (upstream to downstream flow). This balance is necessary before the full opening of the main valve to obtain the nominal capacity of the installation. This pressure balancing decreases speeds of the fluid at the beginning of the opening to preserve the gasket against erosion and cavitation. Moreover, the advantage of bypass is to limit the efforts to open the main valve. To fulfil this function, conventional bypass is made

of a derivation piping from upstream to downstream connections by a piping of smaller diameter with a secondary valve.[1]

The second function appears when the main valve is normally in a fully open position. When the valve is triggered by either an abnormally high flow rate, or a remote controlled signal, a locking mechanism disengages. For example, hydro-electric power schemes require safety valves to stop water flow from the tanker to the turbine. Turbines that operate under significant head and have a long penstock tunnel usually need a valve near the upstream tanker to isolate flow to the penstock tunnel. Butterfly valves are often chosen for this purpose since they have simple mechanical construction, fast closing time, and, more importantly, give a low head loss when fully opened. The size of these valves will depend on the size of the section of penstock in which they are housed. The design of such valve is one of KSB 30 years' fields of expertise.

The presence of butterfly valve in a piping causes a restriction of section which disturbs the flow and may generate disturbances downstream. Thus, it is necessary to study and quantify the previous phenomena in order to design the installation.

The pressure loss is a function of the mode of flow described by Reynold number (R_e).

We will limit the study to usual configuration with incompressible and turbulent fluids ($R_e > 10^5$, see [1]). When the main valve is opened, it generates pressure drop that are characterized with flow coefficient K_v or C_v as a function of opening and flow value. The opening diameter depends of the opening angle of the valve. Flow coefficients are given by the following equation:

$$K_v = Q_v \sqrt{\frac{d_i}{\Delta_P}} \tag{1}$$

where d is the density of flow, and Δp is the loss of head under flow Q_v.

The torque acting on the valve is then estimated from the measured pressure and the mechanical arrangement of the valve. For a closing valve, this torque is defined from several components (see American water works association (AWWA) [2]):

$$C = C_s + C_f + C_h + C_g, \text{ phase (A) } 0^\circ \textit{ to } 7^\circ \tag{2}$$

$$C = C_s + C_f + C_g, \text{ phase (B)} 7^\circ \text{ to } 15^\circ \tag{3}$$

$$C = C_s + C_f + C_d + C_g, \text{ phase (C)} 15^\circ \text{ to } 90^\circ \tag{4}$$

[1] CETIM: Technical Center for Mechanical Industry was created in 1965, upon request from mechanical industry companies in order to provide companies with means and competences to improve their competitiveness, take part in standardization, establish a relationship between scientific research and industry, promote technical progress, provide assistance to improve performance and guarantee quality.

where C_f is bearing torque, C_g is torque given by an offset centre of gravity of the valve, C_d is hydrodynamic torque, C_s is the torque due to packing torque, and C_h is torque due to hydrostatic pressure. The sign convention used in this study is to be positive when acting in the closing direction. Components C_f and C_s always act in the opposite direction to the valve closing direction. Components C_d and C_g will depend on the valve geometry and may act in the either direction.

It is common to express the hydrodynamic torque C_d in the form of a dimensionless torque coefficient from K_v. The two most common definitions are as follows:

$$C_m = \frac{C_d}{0.5\rho U^2 D^3} \tag{5}$$

and

$$K_h = \frac{C_d}{\Delta_P D^3} \tag{6}$$

It must be noticed that Solliec and Danbon [3] compared torque coefficient results presented as Eqs. (5) and (6) and found Eq. (5) to be less sensitive to effects of other system losses, such as bends and elbows, and thus more useful definition for comparing valve torque characteristics for different valves (Eq. (6).

2 Valve Geometry

A schematic diagram of valve geometry at mid-section is shown in Fig. 1. The main parameters of the prototype are as follows: D = 900 mm and d = 300 mm.

In order to define the relative position of discs, we will introduce the following notation: $A_\alpha P_\psi$ where α is the angular position of main disc, and ψ is the angular position of the secondary disc relative to the main disc.

We will study the six relative positions of the secondary disc compared to the main disc, which are $A_\alpha P_\psi, where\, \psi = 0°,\ 30°,\ 60°,\ 90°,\ 120°,\ 150°$.

This method privileges the angular evolution of the main disc that is supposed to have more influence on the flow. The absolute position of secondary disc is obtained by the following relation:

$$\Psi = \alpha - \beta \tag{7}$$

3 Flow Condition

The valve is located in a long straight circular section of pipeline. All simulations were carried out with water and the mode of flow was supposed to be steady. We imposed boundary conditions representative of the average conditions of the test.

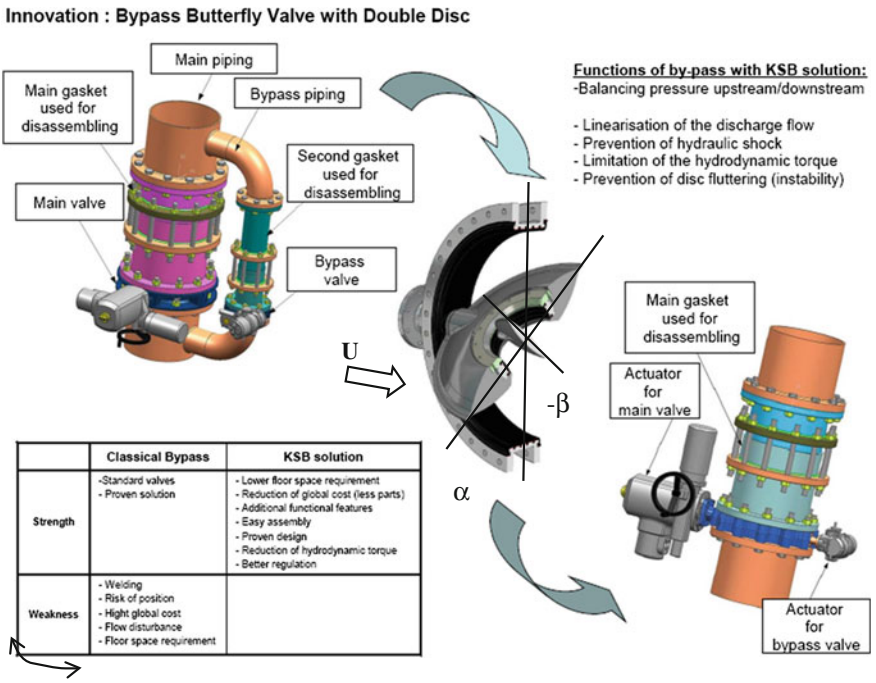

Fig. 1 KSB solution, bypass butterfly valve

A common method of determining the valve torque characteristic of a butterfly valve is by a constant-head test as described in AWWA [2]. In that test, the valve is located in a long horizontal section of pipe that is fed by a constant-head source. Measurements of torque and head loss are then made at various valve angles. The dynamic pressure reduces as the valve closes, which can give very high values of C_m at low valve angles ($\alpha < 30°$). However, maximum hydrodynamic torque occurs at much higher angles and is better reflected by Eq. (6) as the static pressure does not vary significantly during the test.

This study uses ANSYS CFX© software to predict the hydrodynamic torque acting on a butterfly valve. The aim is to establish an accurate model for predicting the valve loads and torques that would occur in the event of a penstock burst or turbine failure, as the increased flow rate would lead to increase hydrodynamic forces and moment acting on the valve.

4 Numerical Approach

A quasi-steady modelling approach was used in this study. This was considered to be acceptable given the long valve closing time of several minutes relative to the flow transit time.

The valve geometry was created using Unigraphics© software and imported into ANSYS Design Modeller©. A rubber seal around the rim of the valve was not included in the model to avoid problems associated with meshing very small sliver volumes. The flow was assumed to be symmetrical about the valve *Y–Z* centre plane, and thus only half of the flow field was modelled by applying a symmetry boundary condition.

The modelling aimed to simulate a constant-head test commonly used to determine valve characteristics [2]. Since defining a velocity profile at the model inlet would set the flow rate and the head loss across the valve, it was decided to model a long downstream section of penstock and to specify the static pressure at outlet, thereby allowing the velocity profile to develop before reaching the valve. This distance required for the flow to develop may be estimated using an empirical formula for entry length given by Munson [4]. In practice, we decided with CETIM, to comply with the test procedure proposed by the standard NF EN1267. Following, the upstream section of penstock 2D is located upstream the valve axis and the downstream section 10D is located downstream the valve axis.

The computational domain was divided into three main sections: upstream penstock, near valve section, and the downstream penstock. Upstream and downstream penstock sections were meshed using an inflated layer of hexahedral elements on the walls, with triangular-based prism elements in the centre. A layer of inflated elements was used on the valve face to improve modelling of the boundary layer. The surrounding mesh consisted of tetrahedral elements. Meshes were generated for valve angles between 10 and 90° by steps of 10°. The total number of elements contained in each mesh varied between 6.10^5 and $2,3.10^6$ elements, and Fig. 2 shows the mesh on the valve symmetry plane with $\alpha = 30°$ and $\beta = -60°$ (A30P90).

Surfaces of the two discs in contact with the fluid are the subject of a detailed attention. In order to collect the maximum information on the field of pressure close to surfaces, the grid is finer close to the walls. Theses surfaces are used to

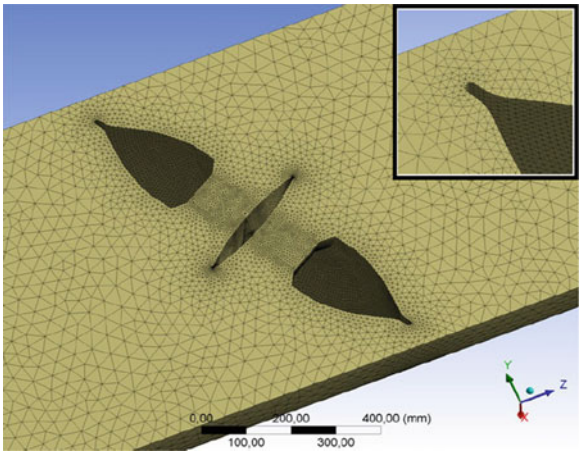

Fig. 2 CFD mesh on the symmetry plane for valve angle $\alpha = 30°$ and $\beta = -60°$

calculate the fluid–structure interactions, in order to determine the hydrodynamic torque coefficients, see [5].

Studies from Lin and Schohl [6] and Leutwyler and Dalton [7] found that the SST model produced best agreement with experimental measurements of hydrodynamic loading and torques acting on butterfly valves. However, according to study of Danbon [3] which showed the robustness of *k*-epsilon turbulence model and its large industrial application, the *k*-epsilon turbulence model was used for this study.

A convergence criterion for maximum RMS residual of 10^{-4} was set, which is two orders of magnitude below the default level used by the solver [8]. An automatic timescale with a conservative length scale and automatic time factor was used to improve stability at the expense of a slightly longer solution time.

5 Results

5.1 Mesh Resolution

A mesh refinement study was completed for the valve shown in Fig. 2. The number of elements in the inflated wall layer was changed to maintain an acceptable aspect ratio. However, the first element height and expansion ratio of the inflated wall layers were not changed to avoid modification of the boundary layer model. These results suggested that sufficient resolution was provided by the mesh of around 7.10^5 elements used for the purposes of this study.

5.2 Description of Flow Field

A sequence of plots showing the *Y*–*Z* symmetry plane is shown in Fig. 3. The analysis of the field velocity between the two configurations $A_\alpha P_0$ and $A_\alpha P_{90}$ highlights the phenomenon of reduction in hydrodynamic torque. Traditional butterfly valve can be compared to the $A_\alpha P_0$ configuration. The opening of the bypass valve allows the passage of a large quantity of flow for angles close to the closing of the large valve. In fact, it is to decrease the rate of flow around the main disc and to reduce the hydrodynamic torque. The three-dimensional trajectories occur on the section of the disc and around the passages of axis. It is necessary to notice the importance of the socket of measurement to 10D downstream from the valve. This makes it possible to limit the fluctuations during the measurement. Upstream, the flow is disturbed very little by the discs acting as an obstacle and the fluctuations seem to be relatively low.

Increasing the valve angle increases the extent of the downstream flow separation. Despite this, the downstream length of flow domain was sufficiently long to

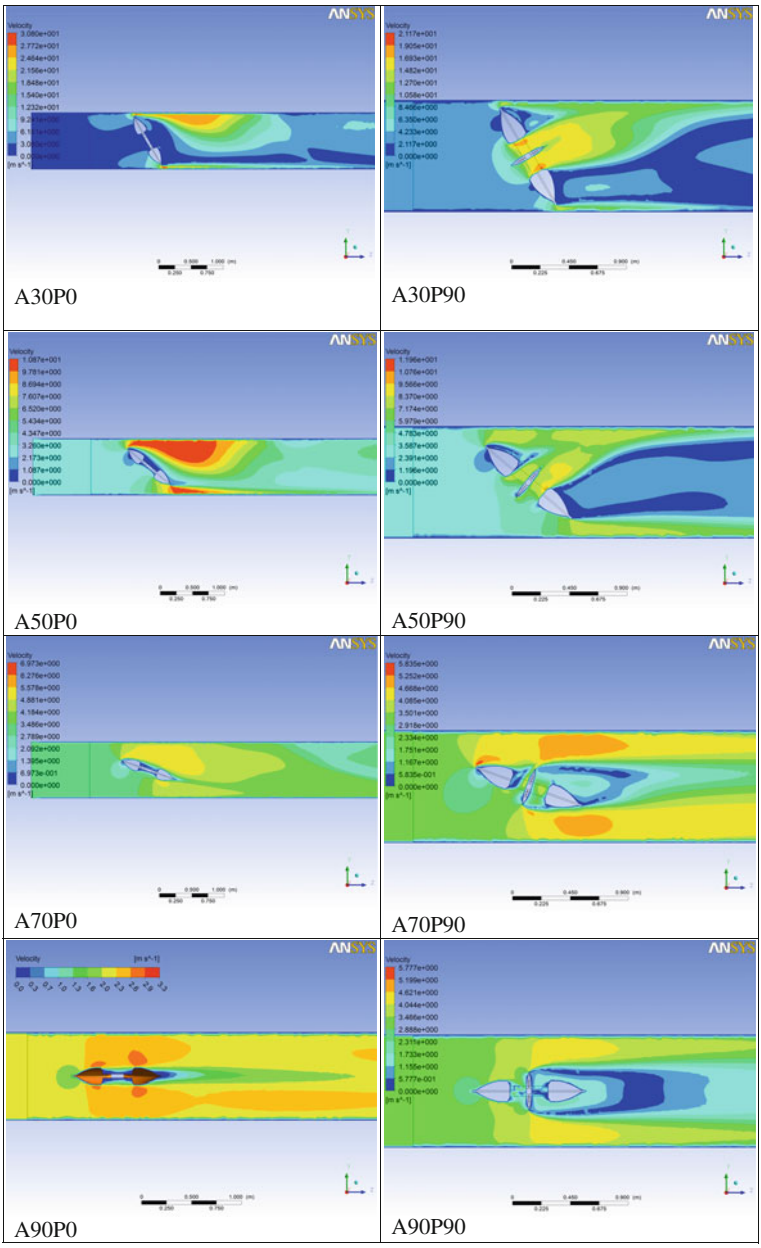

Fig. 3 Valve flow field on symmetry plane

prevent reverse flow at the outlet. A dominant feature of the downstream flow is a counter-rotating stream wise vortex pair that develops at all non-zero valve angles, see [3]. With the opening angle increasing, a swirling flow is created for several

diameters. The strong vortex flow persists throughout the whole downstream flow domain. This also implies the existence of a lift force perpendicular to the pipe axis. The main flow of fluid circumvents the valve of DN900 of the full opening until approximately 30° of closing. Then, the valve of bypass has authority on the flow. In this case below (A30P90), flow passing around the two discs is appreciably equivalent. The complexity of the structure of the flow is clearly highlighted. The secondary flow of bypass comes to disturb the structure of the main flow to the downstream from the valve.

5.3 Comparison with Test Measurements

In order to determine the hydrodynamic torque component from the global torque estimate, the global torque was corrected using data from a test done with water. This approach aimed to remove most of the torque components common to both the water and flow closure tests. The results showed good agreements with theory.

The reduction in the hydrodynamic torque coefficient is significant. The coefficient C_m is representative of the evolution of the torque. For an incidence close to 30° of the main valve, the opening of the bypass valve plays a major role in the evolution of the hydrodynamic torque. By taking into account the results presented above, we can estimate a reduction of approximately 30 % of the hydrodynamic torque for configuration A30P90 compared to configuration A30P0.

The coefficient K_h also shows the reduction in the hydrodynamic torque for incidences relatively weak near to the full opening, see Fig. 4. The capacity of regulation of one bypass is related to the knowledge of flow coefficients, see Fig. 5.

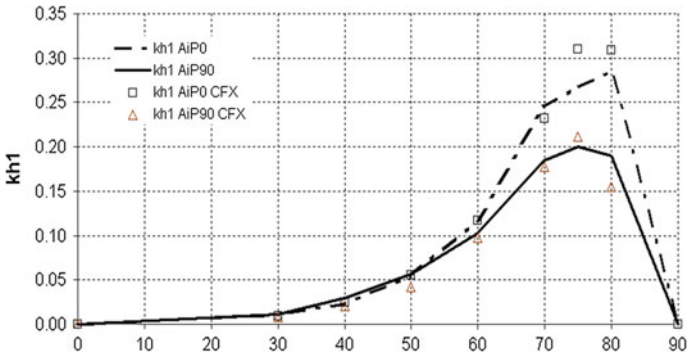

Fig. 4 Coefficient of hydrodynamic torque Kh $f(\alpha)$

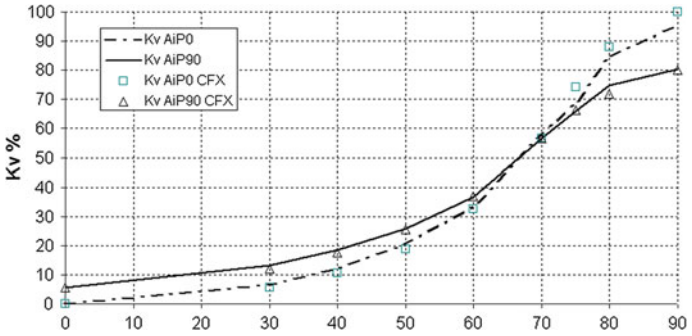

Fig. 5 Flow coefficient K_v $f(\alpha)$

6 Conclusions

KSB introduced a new concept of integrated butterfly bypass valves with double disc. We showed the following significant cost advantages for customer: reduction in piping, joints, and tightness improvement. Due to the huge range of application of bypass system, it is impossible to test and qualify all range of bypass system.

The CFD was an opportunity for KSB to evaluate virtual prototype. The first key parameter is the flow coefficient. The test showed excellent agreement with CFD calculation. One of the key parameter of butterfly valves design is to master the hydrodynamic torque that has great impact on size actuator. With this new design, actuator sizing is improved about 30 %.

By the correlation of the results obtained, we can be confident on the extrapolation of a CFD study in order to quantify the flow coefficients and the hydrodynamic torque according to conditions of use of the system in customer real configuration.

As a conclusion, the numerical approach makes it possible to predict the average behaviour of a bypass butterfly valve with double disc.

References

1. Henderson, A.D., Sargison, J.E., Walker, G.J., Haynes, J. (2007). A numerical study of the flow through a safety butterfly valve a hydro-electric power scheme. In: A.D.H., 16th Australasian fluid mechanics conference, 2–7/12/07.
2. American water works association (2001), Butterfly valves: Torque, head loss and cavitation analysis, Technical report M49.
3. Danbon, F., & Solliec, C. (2000). Aerodynamic torque of a butterfly valve—influence of an elbow on time-mean and instantaneous aerodynamic torque. *ASME Journal of Fluids Engineering, 122*, 337–344.
4. Munson, B. R., Young, D.F., Okiishi, T. H. (2002). Fundamentals of fluid mechanics, John Wiley, fourth edition.

5. Large, J. (2012). Study of the hydrodynamic phenomena and fluid structure interactions of bypass butterfly valve with double disc, EICNAM/KSB.
6. Lin, F., Schohl, G. A. (2004). CFD prediction and validation of butterfly valve hydrodynamic forces. In: Conference proceedings of world water and environmental resources congress, Salt Lake City, USA.
7. Leutwyler, Z., & Dalton, C. (2006). A computational study of torque and forces due to compressible flow on a butterfly valve disk in mid-stroke position. *ASME Journal of Fluids Engineering, 128*, 1074–1088.
8. ANSYS Europe Ltd, (2007) ANSYS CFX solver modelling guide, V11, Technical report, ANSYS Europe Ltd.

Simulations of Rotor–Stator Interactions with SPH-ALE

Magdalena Neuhauser, Francis Leboeuf, Jean-Christophe Marongiu, Etienne Parkinson and Daniel Robb

Abstract Smoothed particle hydrodynamics (SPH) is known to be well adapted for the simulation of dynamic free surface flow. This paper examines the applicability of a weakly compressible SPH Arbitrary Lagrange Euler (ALE) method to the simulation of transient flows in hydraulic machines. The novelty of the approach is to use the properties of SPH-ALE in order to simulate rotor–stator interactions without a rotor–stator interface. Due to the ALE formalism, the particle velocity is a free parameter and can be chosen independently of the flow velocity. Instead of a rotor–stator interface, we have blocks of particles with different particle velocities. To validate the results, the flow field around a static airfoil and the pressure coefficient on the profile are compared with the results of an in-house Euler solver which is an inviscid finite volume code. Results of transient simulations prove the capability of the method to detect unsteady pressure waves and emphasize its applicability to study global phenomena in multistage machines.

Keywords Mesh-less · Particle method · Transient flow · NACA · Internal flow

M. Neuhauser (✉) · F. Leboeuf
Laboratory of Fluid Mechanics and Acoustics, Ecole Centrale de Lyon,
36 Avenue Guy de Collongue, Ecully, France
e-mail: Magdalena.Neuhauser@ec-lyon.fr

J.-C. Marongiu · E. Parkinson
Hydraulic Research Department ANDRITZ Hydro,
Rue des Deux-Gares 6, Vevey, Switzerland
e-mail: Jean-Christophe.Marongiu@andritz.com

D. Robb
Department of Civil Engineering and Applied Mechanics , McGill University,
817 Sherbrooke Street West, Montreal, QC, Canada
e-mail: Daniel.Robb@mail.mcgill.ca

P. Gourbesville et al. (eds.), *Advances in Hydroinformatics*,
Springer Hydrogeology, DOI: 10.1007/978-981-4451-42-0_29,

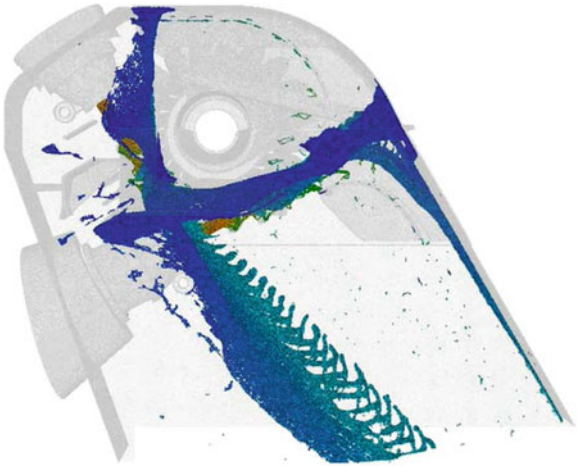

Fig. 1 Free surface flow in a Pelton casing computed with an SPH-ALE code. The fluid is colored by the velocity: *red* is high velocity and *blue* is low velocity

1 Introduction

In the past years, a weakly compressible SPH-ALE code was developed with the original purpose of simulating the free surface flow in a hydraulic Pelton turbine. It is now applied in the industrial process within the ANDRITZ HYDRO R&D department for a coupled CFD finite element stress analysis on Pelton buckets [1] and simulations of complex free surface flows in Pelton casings as shown in Fig. 1. The code was further extended to multiphase flow with surface tension to capture surface deformations of jets from a Pelton turbine nozzle [2]. In addition, there are ongoing developments for solid transport in open-channel applications like in Fig. 2.

The present work aims at showing the potential of the SPH-ALE method for rotor–stator systems. The simulation of transient flow configurations in hydraulic

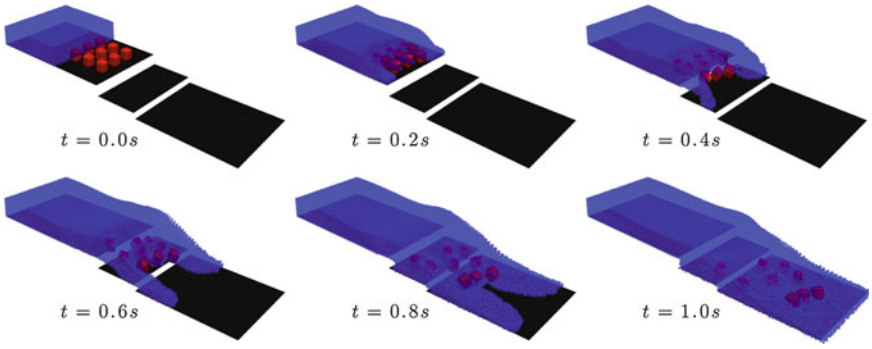

Fig. 2 Solids transported by a water stream in a stepped channel computed with SPH-ALE. Each solid's motion is governed by the hydraulic force of the stream and by rigid body collisions between solids

machines is still a challenge for standard numerical methods, especially at off-design conditions as start-up and shutdown of units. In particular, mesh-based methods face difficulties at mesh interfaces between rotating and static parts of the machine. SPH on the contrary is a mesh-less method and does not have the problem of mesh interfaces. The presented approach is illustrated on the basis of a 2D test case of two symmetric NACA airfoils, where one (the rotor) is moving with a given velocity and the other (the stator) is static.

2 The SPH-ALE Formalism

Smoothed particle hydrodynamics (SPH) is a mesh-less Lagrangian particle method which was first described in 1977 by Lucy [3], Gingold and Monaghan [4]. It replaces the fluid by a finite set of particles which carry their own mass, velocity, and pressure. A continuous field f is calculated by integrating over the neighboring particles weighted by a kernel or smoothing function W with a compact support D_x. Integration by parts yields an SPH approximation of the field gradients,

$$\nabla f(x) = \sum_{j \in D_x} \omega_j f_j \nabla W\big(x_j - x, h\big),$$

where h is the smoothing length and ω_j the volumetric integration weight of the particle. This formula is only valid far away from the boundaries of the computational domain, where the kernel support is not truncated.

We consider the inviscid compressible Euler equations

$$\frac{\partial \rho}{\partial t} + \nabla \cdot (\rho v) = 0,$$

$$\frac{\partial \rho v}{\partial t} + \nabla \cdot (\rho v \otimes v) + \nabla \cdot (pI) = S,$$

together with the so-called Tait's equation of state for weakly compressible fluids, which links the pressure p to the density ρ,

$$p(\rho) = \frac{\rho_0 c_0^2}{\gamma} \left[\left(\frac{\rho}{\rho_0} \right)^{\gamma} - 1 \right],$$

as described in [5], so that the system of equations is closed without considering the energy equation. Here, c_o denotes the reference speed of sound, ρ_0 the reference density, and $\gamma = 7$. In contrast to classical SPH methods, Vila proposed in [6] to write a weak form of the conservation equations in an arbitrarily moving frame of reference. Discretizing the equations by the SPH operators leads to the following discrete set of SPH equations in Arbitrary Lagrange Euler (ALE) formalism for a particle i,

$$\begin{cases} \frac{d}{dt}(x_i) = v_0(x_i,t) \\ \frac{d}{dt}(\omega_i) = \omega_i \sum_{j\in D_i} \omega_j \left(v_0(x_i,t) - v_0(x_j,t)\right) \nabla_i W_{ij} \\ \frac{d}{dt}(\omega_i \rho_i) + \omega_i \sum_{j\in D_i} \omega_j 2\rho_{ij}^E \left(v_{ij}^E - v_0(x_{ij},t)\right) \cdot \nabla_i W_{ij} = 0 \\ \frac{d}{dt}(\omega_i \rho_i v_i) + \omega_i \sum_{j\in D_i} \omega_j 2\left[\rho_{ij}^E v_{ij}^E \otimes \left(v_{ij}^E - v_0(x_{ij},t)\right) + p_{ij}^E\right] \cdot \nabla_i W_{ij} = \omega_i \rho_i g \end{cases}$$

where $\left(\rho_{ij}^E, v_{ij}^E\right)^T$ is the upwind solution of the moving Riemann problem at the midpoint between pairs of particles. In order to calculate this solution of the Riemann problem, the field variables are extrapolated at the interface following the MUSCL procedure. Then, a linearized approximate Riemann solver calculates a mean of these extrapolated states and expresses the corresponding solution analytically. For the MUSCL procedure, gradients of the field variables are needed, whose accuracy has an influence on the numerical diffusion of the scheme. More details on the formalism can be found in [7].

SPH-ALE formalism has some similarities to finite volume methods like the solution of Riemann problems, and it has some important differences compared to classical SPH methods. Mass can be exchanged between calculation points which are still called particles but should be rather seen as moving control volumes. The frame of reference moves with an arbitrary particle velocity v_0. Until now, this particle velocity v_0 was mainly set equal to the flow velocity to obtain free surface simulations in Lagrangian description, but it can be chosen independently of the fluid velocity. This property of the SPH-ALE formalism will be used in the following for the simulations of rotor–stator systems.

3 Flow around a Static Airfoil

Before simulating rotor–stator systems, the flow around a two-dimensional symmetric airfoil developed by the National Advisory Committee for Aeronautics (NACA) was computed and validated. The solid geometry is a four-digit NACA airfoil [8] with a chord length of 0.1 m and a thickness of 20 % of the chord length. Non-reflecting boundary conditions at infinity inspired by [9] are applied to the inlet situated on the left-hand side and the outlet on the right-hand side. In the z-direction, periodicity is applied. The blade channel distance is one chord length.

Since the particle velocity can be chosen freely, all simulations are conducted in an Eulerian frame of reference. In consequence, the particles have to be distributed regularly in the fluid domain at the beginning of the simulation. As the particles do not move, this distribution remains the same throughout the simulation and the initial positions can be chosen in a way that discretization errors are reduced. Using Colagrossi's packing algorithm [10], $\nabla\Gamma = \sum_{j\in D_i} \omega_j \nabla W_{ij}$ is minimized. This

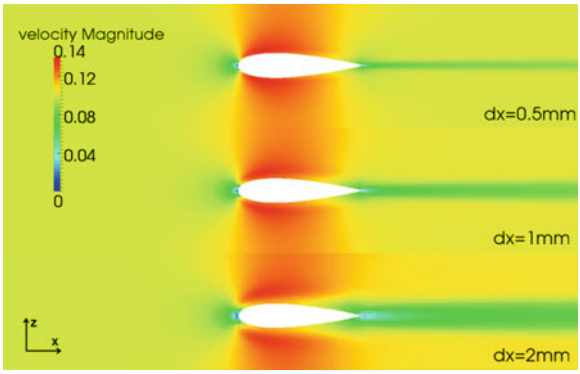

Fig. 3 Velocity field around a symmetric NACA airfoil computed with SPH-ALE for different particle sizes

term $\nabla\Gamma$ plays an important role in the accuracy of the SPH scheme. It should be zero in order to reproduce correctly the gradients of a constant field.

Simulations with three different particle sizes with $\Delta x = 2\,\text{mm}$ (15,958 fluid particles), $\Delta x = 1\,\text{mm}$ (63,728 fluid particles), and $\Delta x = 0.5\,\text{mm}$ (254,714 fluid particles) are compared. Figure 3 shows the velocity field for these three simulations, which changes considerably according to the discretization size. All three show the expected stagnation point attached to the leading edge and the acceleration of the flow around the profile.

3.1 Validation and Comparison with a Finite Volume Solution

For the validation of the SPH results, a reference solution has been computed with an in-house finite volume solver for inviscid flows [11]. The scheme uses a linearized Riemann solver which is very similar to the one used in the SPH-ALE code. Figure 4 shows that the pressure field computed with SPH is in good

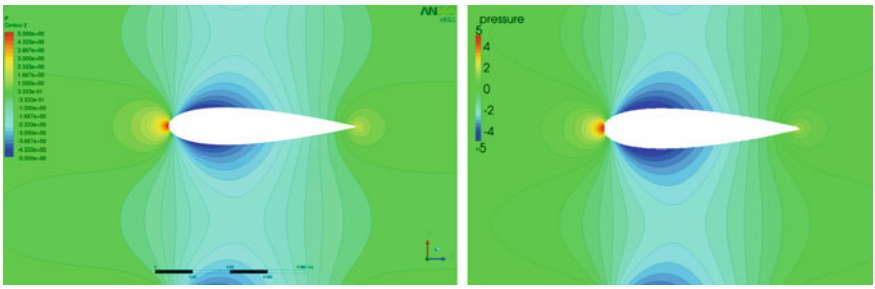

Fig. 4 Pressure field around a symmetric NACA airfoil in [Pa] computed with an in-house finite volume solver (*left*) and SPH-ALE (*right*). The particle size for the SPH simulation is $\Delta x = 0.5\,\text{mm}$

agreement with the reference solution, especially around the blades. However, the velocity field in Fig. 3 shows a wake and a deceleration of the flow in a zone close to the airfoil which should not appear when the inviscid Euler equations are solved. The size of the wake and the decelerated area reduce with the particle size (also see Fig. 5) and further decrease with the artificial speed of sound. This corresponds to what can be found in literature about the numerical diffusion introduced by Riemann solvers, especially in the low Mach number limit [12, 13]. In consequence, the results are further improved by the choice of either a preconditioned Riemann solver which is known to be less diffusive [14] or the AUSM + Up Riemann solver which is especially well suited for low Mach number regimes [15]. In addition, a more accurate estimation of the gradients for the MUSCL procedure reduces the numerical diffusion of the scheme. This can be achieved by applying an SPH technique, renormalization [16], to the computation of the gradients.

In the considered SPH-ALE code, wall boundaries are taken into consideration by partial Riemann problems between fluid particles and surface elements, see [7] for more details. In the case of the NACA airfoil, fluid particles at the trailing edge have both sides of the profile inside their kernel support area, but only the boundary elements with the normals pointing in the direction of the fluid particle should be considered for the surface integration at the boundaries. A similar problem arises between fluid particles which "see" each other through the walls. To avoid this, a visibility criterion was implemented which decreases the amplitude of the artificial wake considerably as can be observed in Fig. 5.

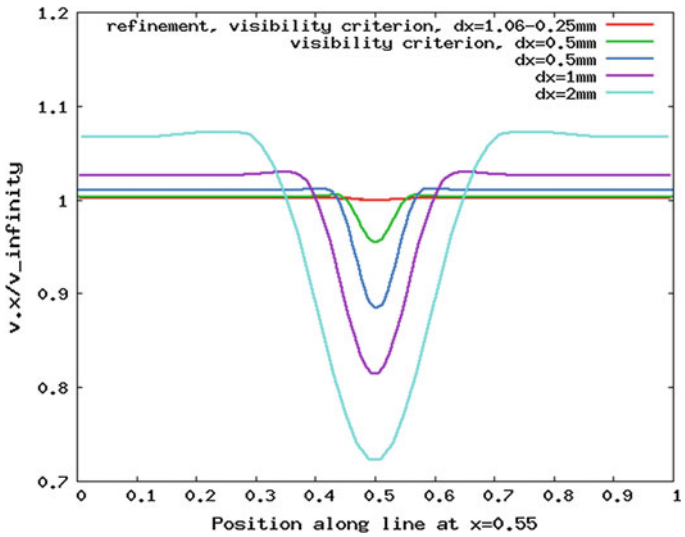

Fig. 5 The x component of the velocity divided by the inlet velocity, plotted along a line at $x = 0.55$ m which goes through the wake, perpendicular to the flow direction

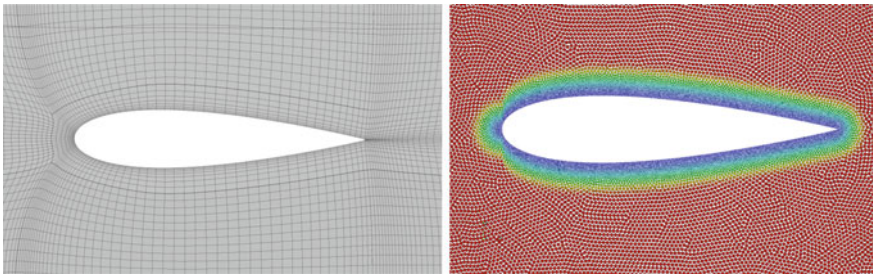

Fig. 6 *Left* Mesh used for the computation of the reference finite volume solution. It is strongly refined in the direction normal to the wall geometry. *Right* Distribution of the fluid particles around the NACA airfoil. The particles are colored by the particle size ranging from $\Delta x = 1.06$ to 0.25 mm.

However, all these modifications do not lead to a result of the same quality as the finite volume solution. To better understand the cause of this, the velocity of the reference solution was analyzed along a streamline close to the stagnation point, where it was found that the velocity is at least of order four, but the SPH scheme with MUSCL has no higher order than two. This is the reason for numerical errors which decelerate the flow field in a boundary-layer-like manner and generate the numerical wake downstream. The finite volume solver is also affected by this rapid evolution of the flow around the stagnation point. Common practice with finite volume solvers consists in strongly refining the mesh around the profiles in the direction normal to the wall (see Fig. 6). Using a mesh without refinement close to walls yields very similar results as the ones obtained by SPH.

3.1.1 Refinement of the Particles Close to the Wall

As a consequence of this, the particle size is reduced close to the wall according to a smooth function while displacing the particles by Bouscasse's algorithm. Since the particles are not moving, the distribution remains constant throughout the whole simulation with the advantage that there is no sharp transition between particles of different sizes. After the refinement, the computational domain contains fluid particles with a size Δx between 1.06 and 0.25 mm, see Fig. 6.

Figure 7 shows the comparison of the velocity field obtained by the finite volume solver and SPH-ALE using refinement around the NACA profile as well as a visibility criterion at the trailing edge. The SPH solution is in good agreement with the reference solution, and almost no artificial wake occurs as seen in Fig. 5. However, the flow is still slightly decelerated near the wall.

Figure 8 shows the pressure coefficient,

$$c_p = \frac{p - p_{\text{stag}}}{\frac{1}{2}\rho_\infty v_\infty^2}$$

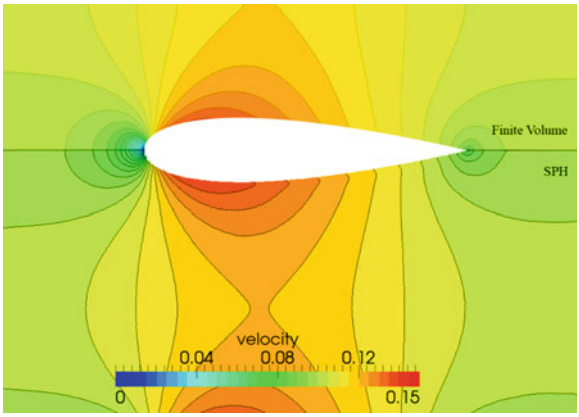

Fig. 7 Comparison of the velocity field obtained with a finite volume euler code (*top*) and SPH-ALE (*bottom*)

where p_{stag} denotes the stagnation pressure and $\rho_\infty = 1000\,\text{kg}/\text{m}^3$ and $v_\infty = (0.1, 0)\,\text{m}/\text{s}$, for both a zero angle of attack and an angle of attack of 2°. Again, the SPH-ALE solution is consistent with the one computed by the finite volume method.

4 Simulation of a Rotor–Stator System

The above sections show that the SPH-ALE method is capable of reproducing the Euler solution obtained by a finite volume solver. In the following, we take use of the mesh-less nature of SPH for the simulation of rotor–stator interactions. Classical mesh-based methods are usually confronted with a rotating mesh around the rotating geometry (the rotor) and a static mesh around the static parts of the geometry (the stator). Between these parts, there is a mesh interface, where the field variables have to be interpolated with possible interpolation errors.

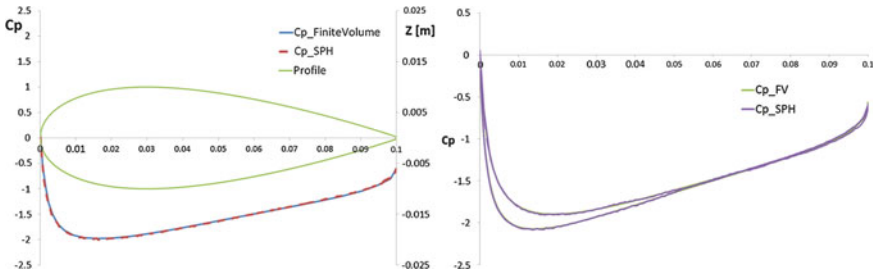

Fig. 8 Comparison of the pressure coefficient on the NACA profile computed with an SPH-ALE and a finite volume method, computed for an NACA airfoil with zero angle of attack (*left-hand side*) and an angle of attack of 2° (*right-hand side*)

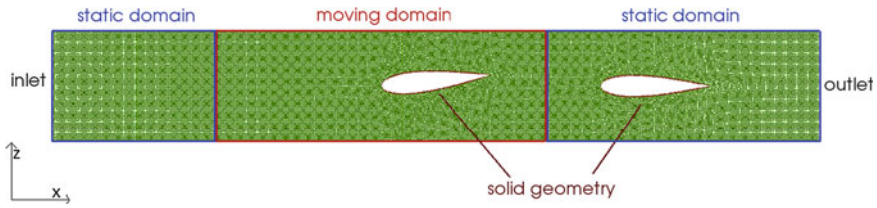

Fig. 9 Computational domain of the simulation with three blocks of particles with different particle velocities

Here, we use the property of SPH-ALE that the particle velocity is a free parameter and we choose it in accordance with the movement of the geometry. Figure 9 shows the computational domain. Again, the inlet and outlet are situated at the two extremities of the domain, and again, they are boundary conditions at infinity [9]. The other boundaries are periodic. There are three blocks of particles with different particle velocities, where the ones next to the inlet and the outlet do not move, while the one around the first airfoil moves with the rotation speed of the rotor. The same symmetric four-digit NACA profiles are used for the geometry of the airfoils, but the first one is rotated by 5.71° in order to have zero angle of attack for both NACA profiles.

In rotor–stator interactions, the physical wake plays an important role for the flow and our future aim will be the simulation of viscous flow. In the following, results with a numerical wake are presented even if we are well aware that it does not represent a physical phenomenon but is created by numerical errors. However, it illustrates the possible use of this method for these physical phenomena once the code is improved for viscous and turbulent flow. In this case, the methods described above such as mesh refinement and the application of a visibility criterion will be indispensable.

4.1 Simulation of a Rotor with a Constant Rotation Speed

Figure 10 shows the velocity field obtained by SPH with a particle size of $\Delta x = 1\,\text{mm}$, no visibility criterion, and no refinement of the particles. The rotor moves with a velocity of $v_0 = (0, -0.01)^T\,\text{m/s}$. The artificial wake passes through the blocks of different particle velocities without being disturbed or deviated. The wake of the first airfoil changes the velocity field around the second airfoil, and the stagnation point of the leading edge is propagated upstream like it is expected in turbomachines.

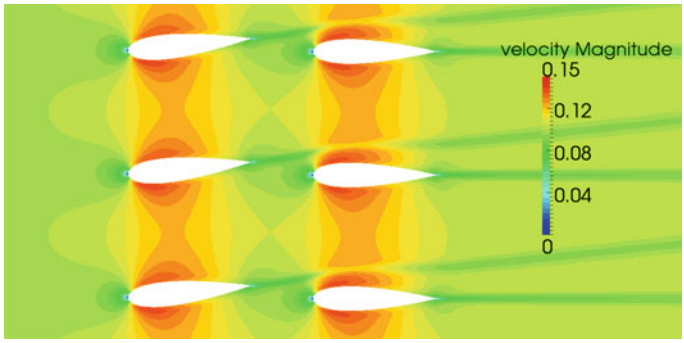

Fig. 10 Velocity field for a moving blade row (*left-hand side*) and a static blade row (*right-hand side*) obtained by an SPH-ALE code with three blocks with different particle velocities

4.2 Simulation of an Accelerating Rotor

Usually, hydraulic turbines are operated by a constant rotation speed that is synchronized with the electricity network. However, at the start-up or shutdown, the rotor is accelerated or decelerated. We launched a simulation that has the same computational domain and blocks of particles as mentioned above, but the rotor is accelerated by a smooth function to a maximum velocity of $v_0^{\text{end}} = (0, -0.1)^T$ m/s which is reached after 22 s and afterward the rotating velocity is kept constant. The geometry was constructed to have a zero angle of attack for $v_o = (0, -0.01)^T$ m/s; hence, the angle of attack is far away from zero for both blade rows after the maximum velocity is reached. Figure 11 shows the pressure and velocity of the dynamic flow field at three different positions of the rotor. The pressure and the velocity around the stator are strongly influenced by the position of the rotor. At $t = 85.6$ s, we clearly see the zone of high pressure at the stagnation point of the rotor, while the leading edge of the stator is situated in the wake of the rotor. A big part of the channel between the stator blades is blocked by a zone of very low velocity, and in the middle of the channel, an almost jet-like structure of high velocity occurs. As the rotor blades move forward ($t = 86.1$ s), the channel is almost completely blocked which creates pressure waves upstream. At $t = 86.55$ s, the wake of the rotor moves to the stator again and a zone of high velocity is created again. Placing a pressure probe upstream of the rotor, as indicated in Fig 11, detects a pressure signal of a frequency of 1 Hz that corresponds to the time the rotor needs for one passage of the stator and is explained by the phenomena described above.

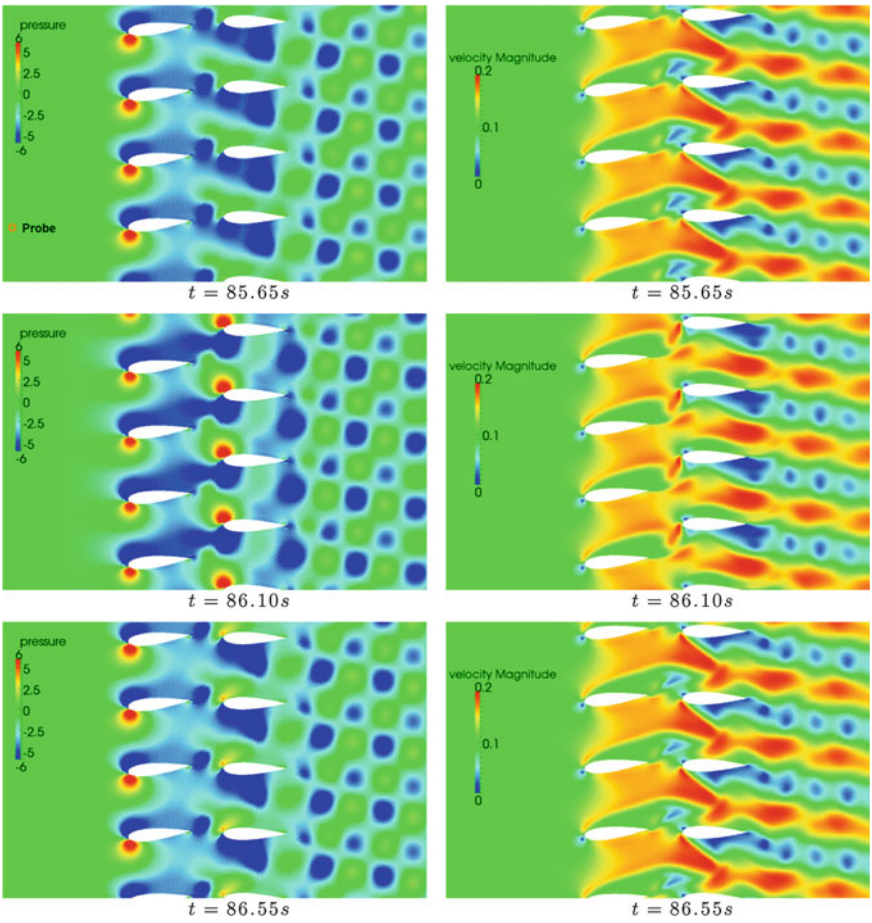

Fig. 11 Pressure (*left-hand side*) and velocity field (*right-hand side*) for a moving blade row and a static blade row obtained with by an SPH-ALE code with three blocks with different particle velocities

5 Conclusions

A thorough validation of the presented SPH-ALE method was carried out for an inviscid flow around a symmetric airfoil with zero and non-zero angles of attack. A comparison to an established finite volume code showed the necessity of implementing a visibility criterion near the trailing edge and refining the particles close to walls because of higher-order fields around the profile. The presented SPH-ALE method proved to be applicable to the simulations of rotor–stator systems. Even if no viscous simulations were carried out, it has been shown that a wake is able to be

propagated downstream and pressure waves upstream which both are typical rotor–stator interactions in turbomachines. The next step will be the implementation of a physical viscosity model and its careful validation.

Acknowledgments The authors would like to thank the Association Nationale Recherche Technologie (ANRT), These 1120/2010, the Consortium Industrie-Recherche en Turbomachines (CIRT), and the ERG (No. 267072). Many thanks to Dr. Arno Gehrer from ANDRITZ Pumps R&D Graz for providing the inviscid reference solution with an in-house finite volume code and to Dr. Martin Rentschler from ANDRITZ Hydro R&D Vevey for the result of the Pelton casing simulation. We further wish to thank Alexandre Dodier for the generation of the NACA geometry and his help with the preparation of the test cases.

References

1. Marongiu, J.-C., Leboeuf, F., Parkinson, E. (2011). On the use of the SPH-ALE meshless method to simulate free surface flows in Pelton hydraulic turbines. Proceeding of the 9th European turbomachinery conference, Istanbul.
2. Leduc, J., Leboeuf, F., Lance, M., Parkinson, E., & Marongiu, J.-C. (2010). A SPH-ALE method to model multiphase flows with surface tension. Proceeding 7th international conference on multiphase flow, Tampa.
3. Lucy, L. B. (1977). A numerical approach to the testing of the fission hypothesis. *Astronomical Journal, 82*, 1013–1024.
4. Gingold, R. A., & Monaghan, J. J. (1977). Smoothed particle hydrodynamic: Theory and application to non-spherical stars. *Monthly Notices of the Royal Astronomical Society, 181*, 375–389.
5. Batchelor, G. (1967). *An introduction to fluid dynamics*. Cambridge: Cambridge University Press.
6. Vila, J. P. (1999). On particle weighted methods and smooth particle hydrodynamics. *Mathematical Models and Methods in Applied Sciences, 9*, 161–209.
7. Marongiu, J.-C., Leboeuf, F., & Parkinson, E. (2008). Riemann solvers and efficient boundary treatments: An hybrid SPH-finite volume numerical method. Proceeding 3rd international SPHERIC workshop, Lausanne.
8. Abbot, I., & von Doenhoff, A. (1949). *Theory of wing sections. Including a summary of airfoil data*. New York: Dover Publications.
9. Ghidaglia, J.-M., & Pascal, F. (2005). The normal flux method at the boundary of multidimensional finite volume approximations in CFD. *European Journal of Mechanics B/ Fluids, 24*, 1–17.
10. Colagrossi, A., Bouscasse, B., Antuono, M., & Marrone, S. (2012). Particle packing algorithm for SPH schemes. *Computer Physics Communications, 183*, 1641–1653.
11. Gehrer, A. (1999). Entwicklung eines 3D-Navier-Stokes Codes zur numerischen Berechnung der Turbomaschinenstroemung, PhD Thesis, Technical University Graz. http://www.ttm.tugraz.at/arno/.
12. De Leffe, M. (2011). Modelisation d'ecoulements visqueux par methode SPH en vue d'application à l'hydrodynamique navale, PhD Thesis, Ecole Centrale de Nantes.
13. Guillard, H., & Murrone, A. (2004). On the behavior of upwind schemes in the low Mach number limit II: Godunov type schemes. *Computers & Fluids, 33*, 655–675.
14. Marongiu, J.-C., Leboeuf, F., Caro, J., & Parkinson, E. (2009). Low Mach number numerical schemes for the SPH-ALE method. Application in free surface flows in Pelton turbines. Proceeding 4th international SPHERIC workshop, Nantes.

15. Liou, M.-S. (2006). A sequel to AUSM, Part II: AUSM + -up for all speeds. *Journal of Computational Physics, 214*, 137–170.
16. Randles, R. W. (1996). Libertsky, smoothed particle hydrodynamics, some recent improvements and applications. *Computer Methods in Applied Mechanics and Engineering, 139*, 375–408.

Numerical Simulations of a Counter-Rotating Micro-Turbine

Cécile Münch-Alligné, Sylvain Richard, Bastien Meier, Vlad Hasmatuchi and François Avellan

Abstract A counter-rotating hydraulic micro-turbine has been developed to recover the energy lost in release valves of water supply network. This compact two-stage axial turbine could be installed in line with the conduit, reducing the infrastructure investments, which is a crucial point for small power plant. The two stages of the turbine allow to use this axial turbine in case of high head conditions. Steady numerical simulations of the flow in the turbine have been carried out using ANSYS CFX to develop the design of the turbine and assess its performance. The influence of numerical set up such as the mesh size and the type of interface between the stator and the two rotating parts has been studied. The influence of the elbow and the honeycomb on the inflow conditions was also assessed. A best efficiency of 85 % is reached when the two runners counter-rotate at the same nominal speed. When the turbine operates under part and full load conditions, the relative rotational speed between the two runners will allow optimizing the efficiency.

Keywords Small hydro · Axial turbine · Water supply network · Numerical simulations

C. Münch-Alligné (✉) · S. Richard · B. Meier · V. Hasmatuchi
University of Applied Sciences Valais, Route du Rawyl 47 CH-1950 Sion, Switzerland
e-mail: cecile.muench@hevs.ch

S. Richard
e-mail: sylvain.richard@hevs.ch

B. Meier
e-mail: bastien.meier@hevs.ch

V. Hasmatuchi
e-mail: vlad.hasmatuchi@hevs.ch

F. Avellan
EPFL Laboratoire de machines hydrauliques, 1015 Lausanne, Switzerland
e-mail: francois.avellan@epfl.ch

P. Gourbesville et al. (eds.), *Advances in Hydroinformatics*,
Springer Hydrogeology, DOI: 10.1007/978-981-4451-42-0_30,

1 Introduction

Hydropower, small and large, remains the most important source of renewable energy for electrical power production providing more than 15 % of the world's electricity. The top five countries for "new" renewable power capacity in 2009 considering only small hydro, modern biomass, wind, solar, geothermal, and biofuels were China, the United States, Germany, Spain, and India. Small-scale energy hydropower is distinct from traditional hydropower by generating less than 10 MW per site; the term mini-hydro being generally used below 2 MW, micro-hydro below 500 kW, and pico-hydro below 10 kW.

In Switzerland, 56.6 % of the electricity is provided by hydropower, 5.7 % coming from small hydro. Indeed, there are more than 1,300 small-scale hydropower plants in operation, with an installed capacity of approximately 860 MW and an output of 3,770 GWh per year. The Swiss government aims now to increase the total amount of electricity produced by renewable energy sources between 2010 and 2020, see [1].

In this chapter, the development of a new multi-stage axial turbine is presented. The counter-rotating micro-turbine will recover the energy lost in release valve of water supply network. The design of the turbine considered in this paper has been performed by the EPFL Laboratory for Hydraulic Machines. Numerical simulations of the flow have been carried out using ANSYS CFX 13.0 to assess the performance of the turbine. A test rig has been built to measure the performance of this turbine and validate the numerical results.

After a description of the case study, the numerical setup is presented. The numerical methods are shortly described as well as the computation domain, mesh, and boundary conditions. The numerical results are then discussed. Finally, concluding remarks are given.

2 Case Study

Axial turbines are generally used in case of low head and high specific speed. The concept of multi-stage runners allows to work under high head operating conditions, each stage recovering a fraction of the available head. For this one-stage design, two counter-rotating runners compose the turbine: a five-blade runner and seven-blade runner (see Fig. 1).

The main characteristics of turbine geometry are presented in Table 1.

The turbine has been engineered for a head of 20 m and a discharge of 8.7×10^{-3} m^3 s^{-1}, each runner recovering 10 m at the best efficiency point. The characteristics of the hydraulic conditions are presented in Table 2. For these conditions, the expected efficiency of the turbine is equal to 85 % with a rotational speed of 3,000 rpm. The specific speed of the turbine for this case study is equal to $\nu = 0.313$, which is not conventional for a head of 20 m, according to Fig. 2.

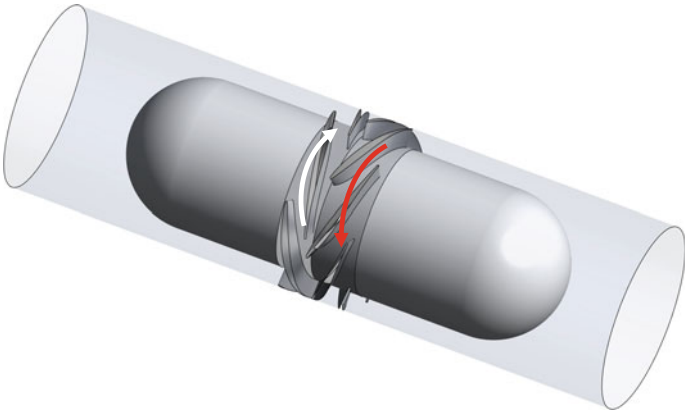

Fig. 1 Geometry of the turbine

Table 1 Turbine geometry

Components	Variable	Value
Shroud radius	R_s	50 mm
Hub radius	R_h	40 mm
Number of blades: runner A	z_A	5
Number of blades: runner B	z_B	7

Table 2 Operating conditions for the turbine design

Quantity	Symbol	Value
Head	H	20 m
Mass flow	Q	8.7×10^{-3} $m^3\ s^{-1}$
Specific energy	E	196 J kg^{-1}
Hydraulic power	P_h	1,700 W
Expected efficiency	η_h^{desgin}	0.85
Expected mechanical power	P_{mec}	1,446 W
Nominal rotational speed	$\lvert n_A' \rvert = \lvert n_B' \rvert$	3,000 min^{-1}
Turbine mass flow coefficient	$\varphi = \frac{Q}{\omega R_s^3 \pi \left(R_s^2 - R_h^2\right)}$	0.196
Turbine energy coefficient	$\psi_T = \frac{2E}{\omega^2 R^2}$	1.59
Runner energy coefficient	$\psi_R = \frac{E}{\omega^2 R^2}$	0.795
Turbine-specific speed	$\nu_T = \frac{\varphi^{\frac{1}{2}}}{\psi^{\frac{3}{4}}}$	0.313
Runner-specific speed	$\nu_R = \frac{\varphi^{\frac{1}{2}}}{\psi^{\frac{3}{4}}}$	0.526

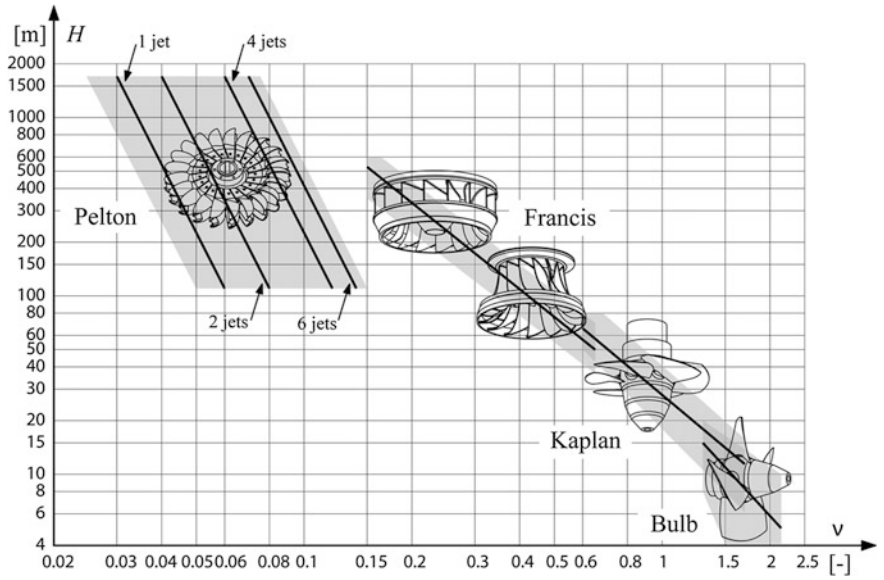

Fig. 2 Classification of hydraulic runners as a function of head and specific speed. [2]

However, each runner of the turbine has a specific speed of 0.526 for a head of 10 m, which is acceptable for an axial runner.

3 Numerical Setup

3.1 Numerical Scheme

Steady numerical simulations were carried out with the commercial software, ANSYS CFX 13.0, based on the finite volume method; the software solves both the incompressible unsteady reynolds-averaged navier–stokes (URANS) equations in their conservative form and the mass conservation equation, see [3]. The set of equations is closed-formed and solved using a two-equation turbulence model and the shear stress transport (SST) model Menter [4]. The SST model uses the $k - \omega$ model [5] close to surfaces and the $k - \varepsilon$ model [3] far away from the surfaces. The steady equations were discretized by an advection scheme with a specified blend factor equal to one corresponding to a second order in space. The numerical parameters are summarized in Table 3.

Table 3 Parameters for the numerical simulations

Simulations type	Steady
Spatial scheme	second-order-specified blend factor 1
Temporal scheme	none
Time step	none
Turbulence model	SST
Convergence criteria	Max RMS $< 10^{-6}$

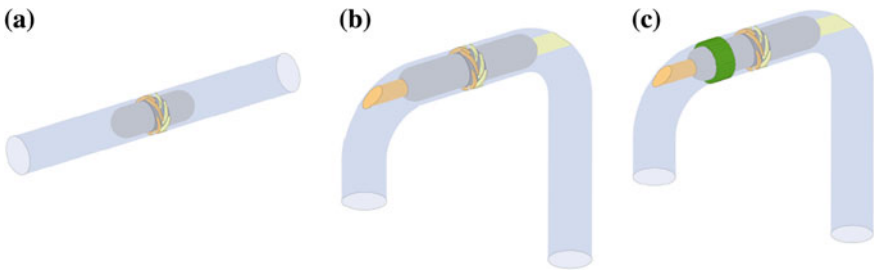

Fig. 3 Computation domains. **a** *Case 1* in-line turbine. **b** *Case 2* turbine with two elbows and shafts. **c** *Case 3* turbine with honeycomb, two elbows, and shafts

3.2 Computational Domains

Three different computational domains have been considered. The turbine in a straight duct composes the first one, two elbows and a shaft are then added in the second one, and a honeycomb is considered as well in the third one, see Fig. 3. The third computational domain is the closest to the experimental test rig.

3.3 Mesh

The three computational domains are discretized with structured meshes except for the honeycomb, see Fig. 4. The characteristics of the three computational domains are presented in Tables 4, 5, and 6.

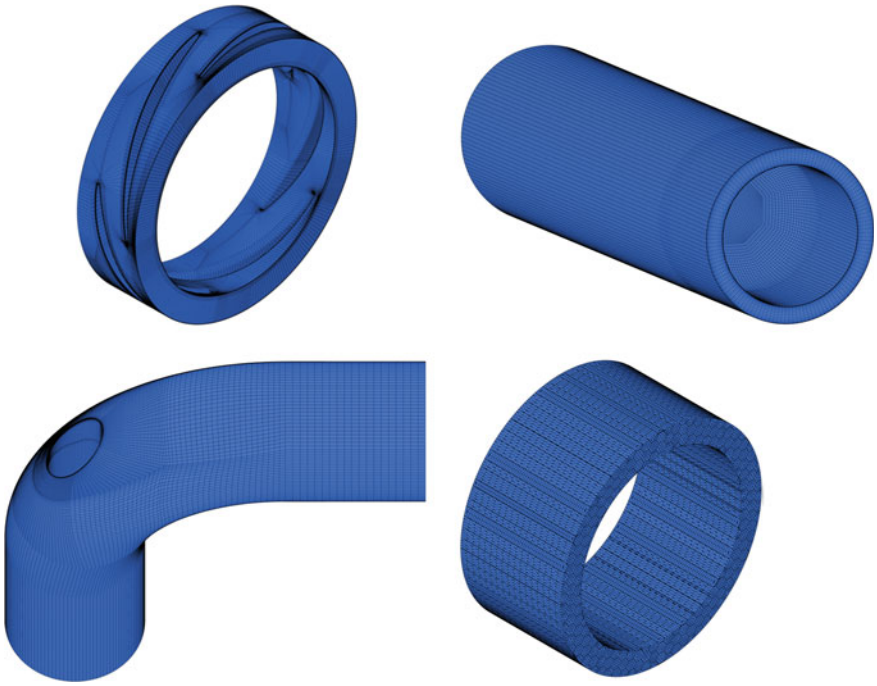

Fig. 4 Meshes of the different parts of computation domains

Table 4 Characteristics of the computational domain in *case 1* in-line turbine

	Number of nodes	y^+_{min}	y^+_{mean}	Angle
Runner A	838,440	2.38	56.26	20.63
Runner B	966,504	2.07	55.84	25.55
Inlet hub "in-line"	730,711	0.62	7.58	28.16
Outlet hub "in-line"	730,711	0.45	10.45	28.16
Total	3,266,366	–	–	–

Table 5 Characteristics of the computational domain in *case 2*: turbine with elbows and shafts

	Number of nodes	y^+_{min}	y^+_{mean}	Angle
Runner A	838,440	2.43	56.30	20.63
Runner B	966,504	2.43	56.03	25.55
Inlet elbow	1,258,608	0.09	6.95	28.04
Outlet elbow	1,481,808	0.42	11.03	28.04
Total	4,545,360			

Table 6 Characteristics of the computational domain in *case 3* turbine with honeycomb, elbows, and shafts

	Number of nodes	y^+_{min}	y^+_{mean}	Angle
Runner A	838,440	2.84	56.32	20.63
Runner B	966,504	2.38	55.88	25.55
Inlet elbow	790,384	0.11	7.56	28.04
Duct between elbow and honeycomb	72,000	4.31	5.83	85.00
Honeycomb	91,296	6.49	67.80	x
Outlet elbow	1,481,808	0.42	11.03	28.04
Total	4,240,432	–	–	–

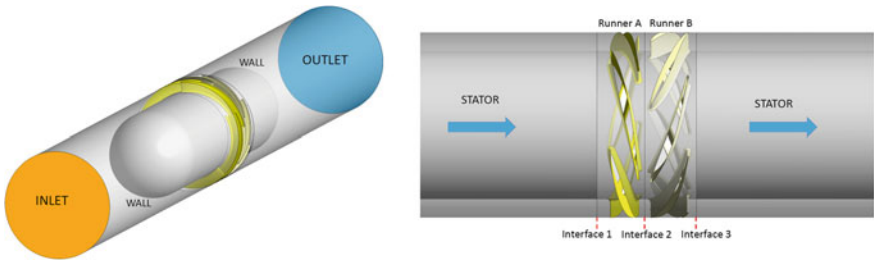

Fig. 5 Boundary conditions

3.4 Boundary Conditions

The discharge is set at the inlet of the computational domain, while at the outlet, the pressure is taken equal to the atmospheric pressure. No slip conditions are imposed for the velocity on the different walls of the domain.

The computational domain is split in four parts connected by three interfaces; see on the left of Fig. 5. There are two stator parts and two rotating parts. For all the simulations, the interfaces 1 and 3 between stator parts and runners are stage conditions. Between the two runners, a frozen condition is applied. These types of interfaces are available in the software ANSYS CFX 13.0 used for the simulations.

4 Results

4.1 Influence of the Computational Domain

As shown in Fig. 3, three different configurations of the turbine have been considered. The simplest one is the in-line configuration, Fig. 6a. This configuration will be the one installed in water supply network, the electric generator being like the one in straflo turbine. The test rig, which has been built in EPFL Laboratory for

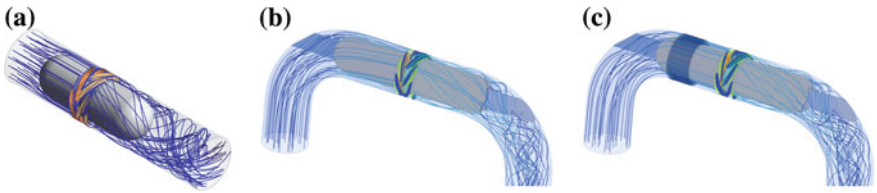

Fig. 6 Streamlines in the three computational domains

Hydraulic Machines, is closest to the Fig. 6c. Numerical simulations in the three computation domains have been carried out to evaluate the influence of the configuration on the turbine efficiency and the losses.

In the three cases, a strong swirl develops at the outlet of the turbine behind the bulb. An optimization of the second runner must be performed to mitigate this phenomenon. At the inlet of the runner, in cases with elbow, see Fig. 6b, the flow is not perfectly lined up with rotation axis of the turbine. This deviation is due to the secondary flow generated by the upstream elbow. Using a honeycomb allows to straighten out the flow, as observed in Fig. 6c. For the measurements on the EPFL test rig, the honeycomb will ensure an axial flow at the inlet of the turbine.

The specific energy in the different part as well as the hydraulic power, mechanical power, and efficiency has been calculated in the three cases at the expected design point for a discharge of 8.7×10^{-3} m^3 s^{-1} and a rotation speed $|\omega_A| = |\omega_B| = 314.16$ rad $\cdot$ s^{-1}, see Table 7.

The following notations are introduced:

- gH_I and $gH_{\bar{I}}$ are, respectively, the specific energy at the high-energy side and the low-energy side of the machine, corresponding to the inlet and the outlet of the turbine.
- $gH_{\bar{1}}^{A}$ and $gH_{\bar{\bar{1}}}^{B}$ are, respectively, the specific energy at the runner A inlet and the runner B outlet.

The elbows, the shafts, and the honeycomb generate losses inducing a decrease in the turbine efficiency. Two percentage is lost in the case with elbows and honeycomb compared with the in-line configuration. In other words, the simulations in the in-line turbine will overestimate the measured efficiency on the test rig of 2 %. To reduce the computational costs, the in-line configuration will be considered for this study.

Table 7 Specific energy in different parts of the turbine, powers, and efficiencies in the three configurations

Components	$gH_I - gH_{\bar{1}}^{A}$ $[\mathrm{J \cdot kg^{-1}}]$	$gH_{\bar{I}}^{B} - gH_{\bar{I}}$ $[\mathrm{J \cdot kg^{-1}}]$	$gH_I - gH_{\bar{I}}$ $[\mathrm{J \cdot kg^{-1}}]$	P_h $[W]$	P_m $[W]$	η [%]
In-line turbine	1.576	1.581	141.2	1,229	975	79.3
Turbine with elbows	1.846	2.872	147.4	1,2836	1,009	78.7
Turbine with elbows and honeycomb	3.168	2.855	145.2	1,263	976.2	77.3

4.2 Operating Conditions and Performances

To describe the operating conditions and the performances of the turbine, three coefficients are used:Energy coefficient:

$$\psi = \frac{2E}{U^2} \tag{1}$$

Discharge coefficient:

$$\phi = \frac{Q}{A \cdot U} \tag{2}$$

Efficiency:

$$\eta = \frac{P_m}{P_h} \tag{3}$$

with U the peripheral velocity $U = \omega_A \cdot R_s$, A the surface defined as $A = \pi\left(R_S^2 - R_H^2\right)$, and P_m and P_h, the mechanical and hydraulic powers.

Numerical simulations of the flow in the micro-turbine for a large range of discharge and rotation speed have been carried out to assess the efficiency of the turbine. The absolute value of the two runner's rotation speeds $\alpha = |\omega_B/\omega_A|$ is kept equal to 1 and the in-line configuration is considered, see Fig. 3a. The results are presented on Fig. 7. The best efficiency point is obtained for a discharge coefficient of 0.235 corresponding to an efficiency of 88 % and an energy coefficient of 2.38. The turbine will produce 2.65 kW for a discharge of 10.42×10^{-3} m^3 s^{-1} and a head of 29.9 m. According to the numerical results, the best efficiency point does not exactly correspond to the design point expected. The discharge and energy coefficient are higher.

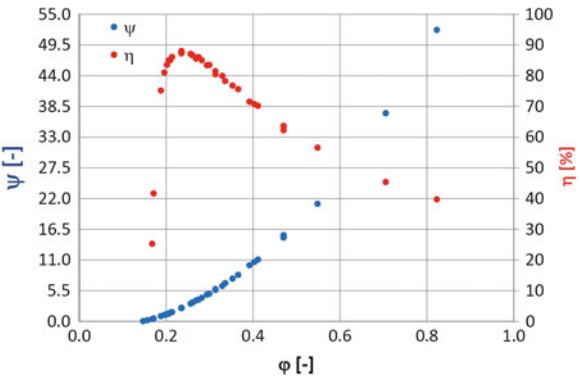

Fig. 7 Efficiency of the turbine and energy coefficient as a function of the discharge coefficient for $\alpha = 1$

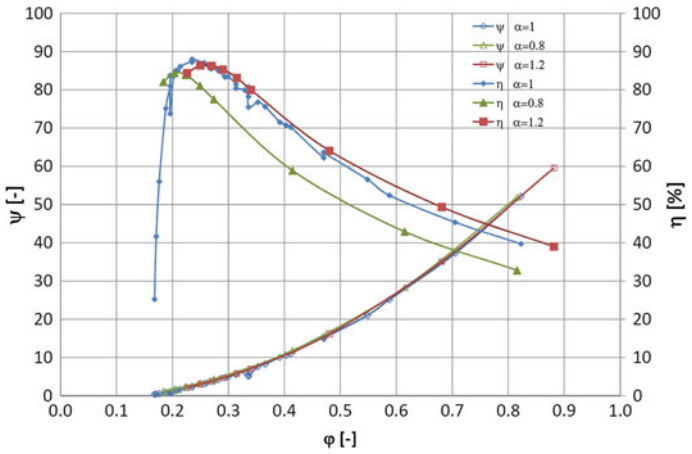

Fig. 8 Efficiencies of the turbine and energy coefficients as a function of the discharge coefficient for $\alpha = 0.8$, 1 and 1.2

4.3 Influence of the Relative Rotational Speed

The absolute value of the ratio between the two rotation speeds may be a degree of freedom to regulate the turbine performances when the discharge fluctuates in the fresh water duct. To investigate this possibility, numerical simulations of the flow in the turbine for three values of $\alpha = |\omega_2/\omega_1|$ have been performed. The results are presented on Fig. 8. The value of the energy coefficient ψ as a function of the discharge coefficient φ seems to be independent of α, for α varying between 0.8 and 1.2. However, a translation of the efficiency is observed. For $\alpha = 0.8$, in other words when the rotation speed of the second runner is lower in absolute value than the first one, the best efficiency point is moved to lower values of the discharge coefficient φ. The efficiency reaches 84.3 % for $\varphi = 0.204$. When the rotation speed of the second runner is higher in absolute value than the first one, the best efficiency point is moved to higher values of the discharge coefficient φ. The efficiency of the turbine, for $\alpha = 1.2$, reaches 86.4 % for $\varphi = 0.250$. The result shows that the absolute value of the ratio between the two rotation speeds can allow to move the characteristic of the turbine. It means that the running of the turbine can be optimized when the discharge of fresh water fluctuates in order to increase the production of electricity.

5 Conclusions

A new axial counter-rotating turbine for small hydro applications has been developed to recover the energy lost in release valves of water supply network. This compact axial turbine could be installed in line with the conduit, reducing the

infrastructure investments, which is a crucial point for small power plant. The two runners of the turbine allow to use this axial turbine in case of high head conditions which is not conventional. Two or three turbines can even be set up in series in order to recover higher head.

Numerical simulations of the flow in this counter-rotating micro-turbine have been carried out with ANSYS CFX 13.0 to assess the performance of the turbine and investigate a way to regulate the turbine in case of fluctuations of the discharge in the fresh water duct.

An efficiency of 88 % has been reached for the turbine providing 2.65 kW for a discharge of 10.42×10^{-3} m^3 s^{-1} and a head of 29.9 m. The influence of the ratio $\alpha = |\omega_B/\omega_A|$ on the efficiency and the energy has been investigated. It has been shown that when $\alpha < 1$, the best efficiency point is reached for lower value of the discharge coefficient. When $\alpha > 1$, the best efficiency point is moved to higher value of the discharge coefficient. The absolute value of the ratio between the two runner's rotation speeds can thus be a degree of freedom of the system to optimize the production of electricity following the discharge fluctuations of the fresh water network.

The next step of this study will be to compare the numerical results with measurements taken on the test rig built in the EPFL Laboratory for Hydraulic Machines.

Acknowledgments The investigation reported in this paper is part of the work carried out for the HYDRO VS project whose partners are the HES SO Valais and the EPFL. This project is financially supported by the Ark Energy. The staff of the Laboratory for Hydraulic Machines should be thanked for their support in the numerical work.

References

1. Crettenand, N. (2012). The facilitation of mini and small hydropower in Switzerland. Ecole Polytechnique Fédérale de Lausanne (EPFL). Thèse N° 5356.
2. Avellan, F. (2010). *Courses of hydraulic machines*. Suisse: Ecole Polytechnique Fédérale de Lausanne.
3. Launder, B. E., & Spalding, D. B. (1974). The numerical computation of turbulent flow. *Computer Methods in Applied Mechanics and Engineering, 3*(2), 269–289.
4. Menter, F. R. (1994). Two-equation eddy-viscosity turbulence models for engineering application. *AIAA Journal, 32*(8), 1598–1605.
5. Wilcox, D. (1993). Comparison of two-equation turbulence models for boundary layers with pressure gradient. *AIAA Journal*, *31*(8), 1414–1421.

CFD-Based Mathematical Optimization of Hydroturbine Components Using Cloud Computing

Albert Ruprecht, Andreas Ruopp and Jakob Simader

Abstract Hydropower plants are usually individually designed according to the local discharge and head. Accordingly, there is a rather large engineering effort for each project. Especially, the hydraulic design of the turbine components requires a great amount of engineering effort. Therefore, an automatic optimization tool is developed in order to optimize the hydraulic shape of the different turbine components by means of a mathematical algorithm. This implies that the shape of each component is parameterized, and these parameters are optimized by the mathematical optimization algorithm. For the assessment of the quality of the shape for each set of parameters, a CFD simulation has to be carried out. Since an accurate CFD simulation requires rather fine grids, the computational time is rather large (in the range of hours for each simulation). In order to optimize a set of 15–20 parameters, many hundreds or even thousands sets of parameters have to be evaluated. This leads to an enormous requirement of computer resources. Consequently, an optimization tool is developed which can be applied in a computational grid or cloud environment. This requires a robust, fault tolerant, asynchronous optimizer. The developed optimizer is based on a combination of genetic algorithm with a discrete simplex-type algorithm and a randomly chosen distribution of the parameters. As examples, this optimizer is applied to the shape optimization of a turbine draft tube and to the optimization of the blading of a tidal current turbine.

A. Ruprecht (✉) · A. Ruopp · J. Simader
Institute of Fluid Mechanics and Hydraulic Machinery,
Pfaffenwaldring 10, Stuttgart 70550, Germany
e-mail: ruprecht@ihs.uni-stuttgart

A. Ruopp
e-mail: ruopp@ihs.uni-stuttgart.de

J. Simader
e-mail: simader@ihs.uni-stuttgart.de

P. Gourbesville et al. (eds.), *Advances in Hydroinformatics*,
Springer Hydrogeology, DOI: 10.1007/978-981-4451-42-0_31,

Keywords Parallel optimization · Genetic algorithm · High performance computing · Draft tube · Tidal current turbine blade

1 Introduction

In many engineering applications, the optimization of a hydrodynamic shape is necessary. For example, hydroturbines are individually designed according to their local situation (discharge, head etc.). This requires a rather large engineering effort for each project. As a consequence, there is a tendency to automate the design process. Today, the design process is based on computational fluid dynamics (CFD). Since an accurate CFD simulation requires rather fine computational grids, the computational time for a simulation run is quite large (in the range of hours for each simulation).

In order to automate the process, a tool is developed, which allows an automatic optimization of the hydraulic shape of the different turbine components by mathematical algorithms. This means that the shape of each component is parameterized and these parameters are optimized by the mathematical optimization algorithm. The typical number of parameter for a component is in the range of 15–30. For the assessment of the quality of the shape for each set of parameters, a CFD simulation has to be carried out. In order to optimize such a set of parameters, many hundreds or even thousands of sets of parameters have to be simulated and evaluated. As already mentioned, each CFD run is rather computational and time-consuming. This leads to an enormous requirement of computer resources, which are usually not available on a single computer or a cluster. Consequently, an optimization tool is developed which can be applied in a computational grid or cloud environment. This means that the various CFD runs are distributed into the grid or the cloud. Working in a cloud environment, however, means that there is no guarantee that results for each CFD run are really obtained. Also, wrong (or uncertain) results can be delivered, and finally, the answer times for getting the results are completely unpredictable. This means that applying the optimization process to the cloud requires a robust, fault tolerant, and asynchronous optimization strategy.

The developed optimizer is based on a combination of genetic algorithm with a discrete simplex-type algorithm. In order to ensure the finding of the global optimum and not to stick in a local optimum, some sets of parameters per generation are randomly chosen, and additionally, also a ‘parallel universe’ approach is introduced. This means that the optimizer works independently on several sets until all ‘universes’ converge to the same optimum.

In the following, this optimizer is described in detail and its behavior is discussed on complex test functions. Finally, the optimizer is applied to two real applications: the design of a current turbine blade and the design of a turbine draft tube.

2 The Optimizer

The optimization algorithm is based on a genetic procedure, which uses several individuals per generation. In terms of this evolutionary process, one individual represents one design with a given parameter setup. If one generation was calculated, the optimizer retrieves back the solution of each single design, sorts out all bad designs, and creates a new set of individuals for the next generation. This action is repeated until convergence is reached.

First, the optimizer reads in the number of parameters n_p, the limits of each parameter

$$l_{i,\min} < p_i < l_{i,\max} \tag{1}$$

the number of individuals n_{ind}, the number of survivors n_{sur}, the maximum number of generations n_{gen}, and the radius of convergence r_k. The centroid of each parameter is calculated according to

$$c_i = \frac{\sum_{j=1}^{n_{\text{sur}}} \frac{p_{i,j} - l_{i,\min}}{l_{i,\max} - l_{i,\min}}}{n_{\text{sur}}} \tag{2}$$

The radius of convergence is checked using the following relation after each generation:

$$r_k = \sqrt{\sum_{i=1}^{n_{\text{par}}} \left(\frac{p_{i,j} - l_{i,\min}}{l_{i,\max} - l_{i,\min}} - c_i \right)^2} \tag{3}$$

2.1 The Optimization Algorithm

In detail, the optimizer is based on a combination of three different methods to calculate the parameters of its individuals. The method of reproduction, two combined simplex algorithms, and a random function are utilized. The method of reproduction uses a random number

$$x_{r,i} = f_{\text{rand}} \tag{1}$$

where the subscript i denotes the control variable for the parameter and $0 \leq x_{r,i} \leq 1$. Using this random number, the best individuals are combined together by the following formulation:

$$x_{i,j} = x_{r,i} \times \frac{p_{i,j} - l_{i,\min}}{l_{i,\max} - l_{i,\min}} + \left(1 - x_{r,i}\right) \times \frac{p_{i,j+1} - l_{i,\min}}{l_{i,\max} - l_{i,\min}} \tag{2}$$

If $0 \leq x_i \leq 1$, the new parameters of one individual are calculated with

$$P_{i,j} = l_{i,\min} + \left(l_{i,\max} - l_{i,\min}\right) \times x_{i,j} \tag{3}$$

where $p_{i,j}$ denotes the parameter of each new individual j. In case of an overrun of one parameter, the appropriate limit is taken into account.

The second method of designing the individuals is divided into two procedures. First, a standard simplex algorithm is used corresponding to

$$p_{i,j} = l_{i,\min} + \left(l_{i,\max} - l_{i,\min}\right) \times \left(2 \times c_i - \frac{p_{i,j} - l_{i,\min}}{l_{i,\max} - l_{i,\min}}\right) \tag{4}$$

Second, a modification of the simplex algorithm is implemented. Here again, a random number is used with

$$x_{r,i} = (f_{\text{rand}} - 0.5) \times 2 \tag{5}$$

resulting in the following relation

$$x_{i,j} = \frac{p_{i,j} - l_{i,\min}}{l_{i,\max} - l_{i,\min}} + 2r_{k,\min} \times x_{r,i} \times \sqrt{x_{r,i}} \tag{6}$$

The final parameter setup is performed by

$$p_{i,j} = l_{i,\min} + \left(l_{i,\max} - l_{i,\min}\right) \times x_{i,j} \tag{7}$$

The last method is the random function which generates its designs totally stochastically. This approach reduces the risk of finding a local minimum. The number of designs created by each method is one-third of the whole new generation except for the starting generation. For this first initial step, the random function is used for all individuals, assuring an adequate starting solution. With the new total set of parameters, one generation is processed and the best n_{sur} individuals are sorted out, survived, and provided the basis for the next generation, which has $n = n_{\text{ind}}$–n_{sur} new individuals. This is repeated until convergence or the maximum number of generations is reached. Convergence is reached, if the convergence radius of the current generation, denoted by $r_{k,\max}$, is smaller then a desired number.

In addition, the optimizer can detect bad designs and vary the number of survivors. This strategy is beneficial for some cases in the beginning of the optimization. For those cases, the new parameter setup is calculated using the random function instead. In order to test the performance of the optimization algorithm, another random number is implemented, modifying the stochastic creation of the initial generation.

Hence, the optimization algorithm is based on an evolutionary procedure; one civilization is used in a run normally. In addition, the code can also vary the number of civilizations in one run. In the beginning, the optimizer reads in the number of civilizations n_{ziv} and treats every civilization completely independently as described in the section before. At the time when one civilization finds a

minimum and convergence is reached, the minimum is compared with the values of the other competing civilizations. If it is, so far, a global minimum, the civilization is stopped and the best design is copied to the other civilizations. The remained civilizations share the number of individuals so that the total number of individuals stays constant during the run. If the best design appears to be a local minimum (compared with the other civilizations), the civilization starts from the beginning with a complete set of new individuals using a random distribution.

In total, this procedure can reduce the risk of finding only a local minimum instead of the global one. Therefore, two different stopping criteria are defined. First, the optimization run can stop, if one civilization has finished and reached convergence. This strategy can be very fast. Second, the finished civilization shares its best design with the other remaining civilizations and, by doing so, reduces the number of civilizations step by step. This surely slows down the optimization but can significantly reduce the risk of finding only a local minimum. In the following, the two 'multicivilization' strategies are denoted with 'slow mode' (SM) or 'fast mode' (FM), respectively.

3 Verification of the Genetic Algorithm

3.1 The Sphere Function of De Jong's Test Set

The sphere function of De Jong's first test set is a simple benchmark illustrated in Fig. 2 (left), whose function is continuous, convex, and unimodal [1]. It has the following general definition:

$$f(\vec{x}) = \sum_{i=1}^{n} \left(x_i^2\right) \tag{8}$$

The test area is restricted to $-1 \leq x_i \leq 1$ for $i = 1, \ldots, n$ parameters. The global minimum $f(\vec{x}) = 0$ is centered at $\vec{x} = 0$.

The number of individuals per generation with one civilization is kept constant while varying the number of parameters. The ratio $n_{\text{ind}}/n_{\text{sur}} = 3$ performs best in terms of calculation time in all cases and is independent of number of parameters. In total, each run is calculated ten times with different initial generations, and therefore, the ordinate of the graphs indicates the average number of the ten runs. The convergence criterion is varied and depicted in the legend of the graphs in Fig. 1. The number of $n_{\text{ind}} = 30$ or $n_{\text{ind}} = 60$ is not optimal in terms of calculation time. Hence, the number of individuals is decreased step by step for each number of parameter in order to find the 'optimal setting' curve. This curve shows the best performance while finding the minimum within the range of the convergence criterion (this criterion is valid for all runs).

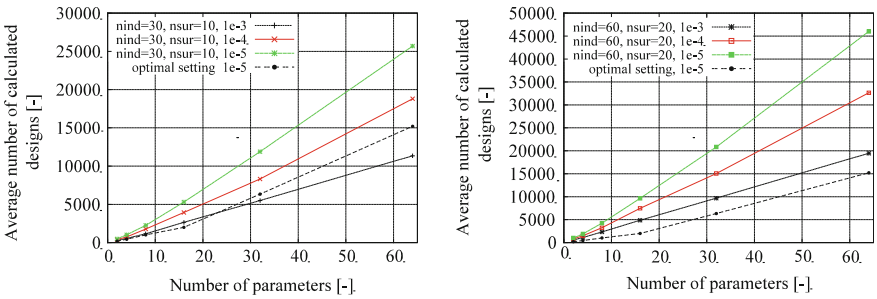

Fig. 1 Total average number of individuals for De Jong's test set, $n_{\text{ind}} = 30$ *left graph*, $n_{\text{ind}} = 60$ *right graph*

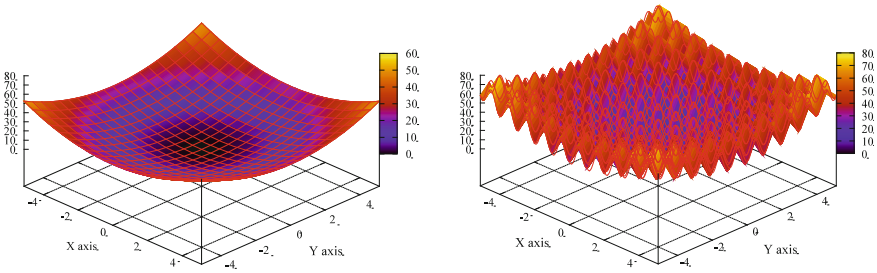

Fig. 2 The De Jong's test function [1] (*left figure*) and the generalized Rastrigin's function [2] with the full range and global minimum at $\vec{x} = 0$ (*right figure*)

3.2 The Rastrigin's Test Function

The generalized Rastrigin's function [2] is given by the following relation:

$$f(\vec{x}) = 10n + \sum_{i=1}^{n} \left(x_i^2 - 10\cos(2\pi x_i)\right) \tag{9}$$

The Rastrigin's function, illustrated in Fig. 2 (right), is used in the full range of ± 5.12, has a cosine modulation and is therefore highly multimodal with a high number of local minima. The global minimum $f(\vec{x}) = 0$ is located in the center at $\vec{x} = 0$. The function can be used for $i = 1, \ldots, n$ parameters. This test function is appropriate to check the performance of the optimization algorithm and to determine the behavior of the possible settings.

Two different cases are calculated and compared. The first case uses two parameters and different settings of the optimizer, and the second case tests a four-parameter setup. Hence, the optimizer is based on random numbers in the beginning; each setting was tested with 100 different random numbers. If one run did find a local minimum instead of the global one, the error was counted. The two and four parameters are always calculated with the same ratio of $n_{\text{ind}}/n_{\text{sur}} = 5$ and

Table 1 Overview over Rastrigin's function test runs for two and four parameters with identifiers

$n_{par} = 2$		
Identifier	Mode	n_{ziv}
x-1-2	–	1
0-2-2	SM	2
1-2-2	FM	2
0-4-2	SM	4
1-4-2	FM	4
x-1-4	–	1
0-2-4	SM	2
1-2-4	FM	2
0-4-4	SM	4
1-4-4	FM	4

a maximum number of $n_{gen} = 200$ generations. The number of individuals was increased constantly by a factor ($n_{ind} = 60f$ with $f = 1,\ldots,15$). This reduces the total error but increases the amount of processed individuals. In total, five different basic settings are compared for each parameter test, summarized in Table 1. If the case '*x*-1-4' uses, for example, 120 individuals and 24 survivors, the equivalent runs are mode '0-2-2 or 1-2-2' with 2 civilizations, 60 individuals, and 12 survivors per civilization (declaration of identifier: SM/FM-n_{ziv}-n_{par}). Hence, the total number of individuals per generation is kept the same.

The convergence criterion is always set to 10^{-5}. The performance of the algorithm testing two and four parameters is shown in Fig. 3. The two-parameter setup shows a decrease in errors with increased number of individuals per generation. The total amount of needed individuals in average performs the same. The '*x*-1-2' run with one civilization does not perform better than the fast run mode with four civilizations, if the total number of individuals $n_{ind} = 60f$ is set to low values. The algorithm shows a slightly better behavior with more civilizations in total.

The four-parameter run behaves differently. The runs with one civilization perform better in most of the cases. The '*x*-1-4' curve appears in the right subfigure of Fig. 3 in most instances below the multicivilization runs. The set ratio of individuals to survivors shows to be suboptimal for the multicivilization runs in the case with four parameters.

4 Cloud Computing Strategies

The basic advantage of an evolutionary algorithm is the presence of many designs or individuals at the same time. The step-by-step approach to the optimum can remain, and many designs can be processed at the same time. Hence, a parallel approach is introduced to accelerate the optimization process, since CFD calculations of a complex problem are time-consuming. The principle configuration is

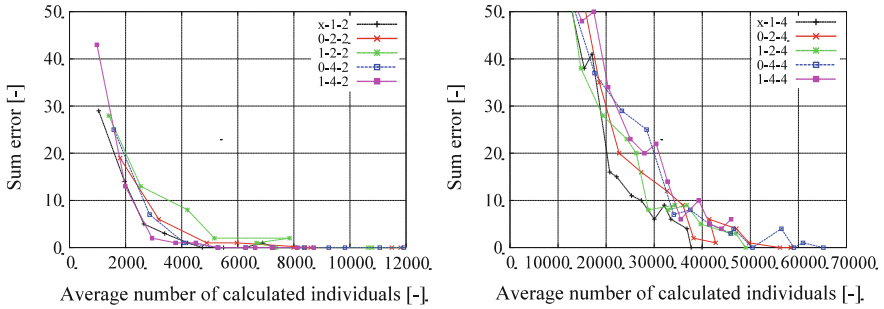

Fig. 3 Number of errors over calculated individuals. Two parameters *left figure* and four parameters *right figure*

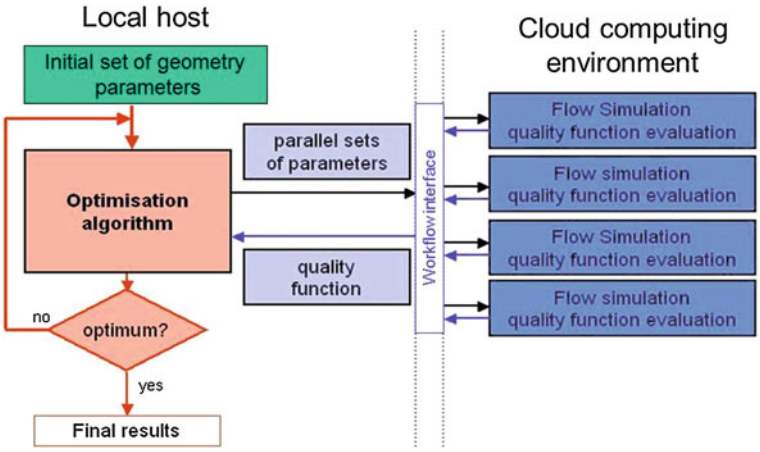

Fig. 4 Workflow for the optimization

illustrated in Fig. 4 and is divided into three major parts. The optimizer provides a set of individuals and hands over the designs to the workflow interface. The interface manages the work distribution for one generation and starts single threads on a master node, which treat each individual or design on a node. Each thread has a specific PID number (i.e., process identification number) and controls one work flow. Each work flow is started and contains the same working procedure; hence, every individual of a generation has to be executed similarly.

In terms of a robust optimization procedure, not every individual or run has to finish successfully. If one design fails due to a meshing or simulation error, a predefined trivial solution will be linked with this design. This prevents the mechanism to stop when a design fails. The standard work flow is divided into five different steps, including the case setup, the meshing, the CFD computation, the convergence check, and the solution processing.

The workflow interface has implemented two blocking routines. First, it starts the maximum possible number of threads at the same time, until all available nodes in a network are busy. Second, it waits until one design finishes and starts on this specific node the next thread. If all individuals in one generation are running, the interface waits until all designs have finished and pass back the quality criteria to the optimizer. If the network provides enough nodes, all individuals or one generation is processed at the same time.

5 CFD Optimization Cases

5.1 Case 1: Tidal Current Turbine Blade

The parallel optimization method is utilized on a tidal current turbine blade. The horizontal-axis tidal current turbine uses the kinetic energy and transforms it into electricity. The power output P at the rotor shaft and the power coefficient c_p are defined as follows:

$$P = \omega \times M \tag{10}$$

$$c_p = \frac{P}{\frac{\rho}{2} v_\infty^3 A_t} \tag{11}$$

The power coefficient is used as the quality criterion in the optimization process at a certain design tip speed ratio of

$$\lambda_{\text{opt}} = \frac{\omega \times r_{\text{tip}}}{v_\infty} \tag{12}$$

In addition, the thrust coefficient at design tip speed is used as a limiter

$$c_t = \frac{T}{\frac{\rho}{2} v_\infty^2 A_t} \tag{13}$$

where $T$is the thrust of the blades. If the thrust coefficient is exceeded, the individual is treated as a bad design.

The blade chord length and angle distribution over span are discretized with polynomial and linear function. The chord length parameterization uses a linear segment in the middle, linked with to quadratic polynomial functions at the tip and the hub. In total, six parameters vary the chord length distribution over span. The blade angle distribution utilizes three quadratic polynomials which are linked together and use in total 8 parameters. In this test case, the standard profiles of the NACA four-digit series [3] are applied. The absolute thickness distribution was given and kept constant for all individuals.

The meshing algorithm provides a block-structured hexahedral mesh setup. The domain consists of one rotor blade and has a periodic setup, the domain setup, and

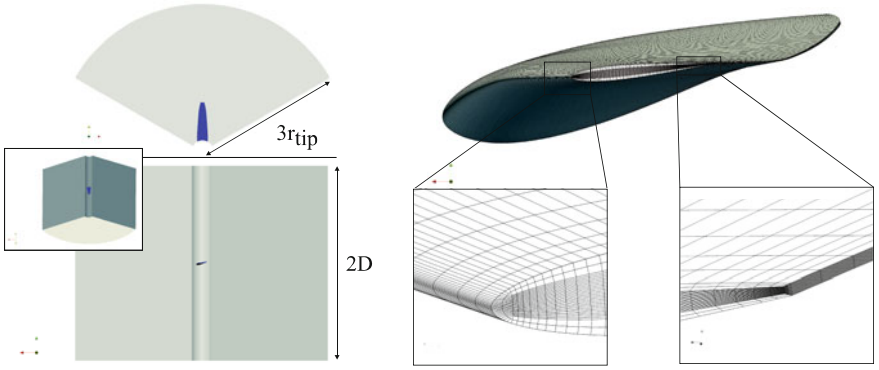

Fig. 5 Domain setup of the tidal current turbine blade, *left figure*. Mesh of blade, *right figure*

size, which are illustrated in Fig. 5. The hub is continuous through the whole domain. The total mesh size has 1,440,000 nodes and performs adequate in terms of computing time and relative comparison between the individuals. The flow around the blade is resolved using an O-grid.

The CFD code OpenFOAM® is used with the standard k-ω-SST model. A convergence check evaluates the characteristics of power coefficient and thrust coefficient. Each design uses an initial flow field ensuring a faster convergence.

In total, 972 designs are calculated and the best design was found after 500 individuals. The 14-parameter setup used 70 individuals in one generation with 10 survivors. The power coefficient over the thrust coefficient is shown in the left graph of Fig. 6, with two groups of individuals. The 'good designs' are below the artificial thrust limit, and the 'bad designs' exceeded this limit. The red line highlights the path of the best design with proceeded generation number. The limitation of the parameter range for the construction angle over span is shown in

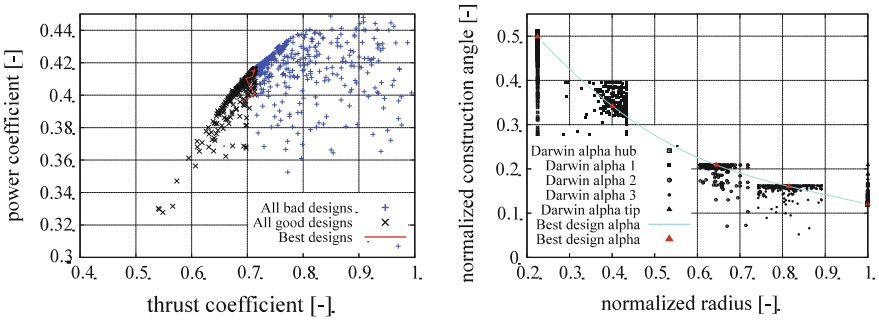

Fig. 6 Power coefficient over thrust, *left graph*. Variation in construction angles over normalized radius, *right graph*

the right graph of Fig. 6. This is one major reason that the optimizer could not find a better design after approximately 500 individuals in total, although the algorithm calculated 470 individuals more after the last best design.

5.2 Case 2: Draft Tube

The second case is the optimization of an elbow-type draft tube which is shown in the right side of Fig. 7. This kind of diffuser is a standard element in hydraulic power plants and transforms the kinetic energy downstream the turbine runner into a pressure-head increase. Even though it is standard, an efficient draft tube can significantly raise the overall plant performance, especially for low-head power plants. The pressure recovery coefficient c_p is commonly used to determine the draft tube efficiency and is defined as follows:

$$c_p = \frac{p_{s,\text{out}} - p_{s,\text{in}}}{\frac{1}{2}\bar{v}_{\text{in}}^2} \tag{14}$$

where $p_{s,\text{out}} - p_{s,\text{in}}$ is the static pressure difference through the draft tube and $^1/_2\rho\bar{v}_{\text{in}}^2$ the dynamic pressure at inlet region. As quality criterion, the pressure recovery coefficient is taken into account. For geometry discretization, the draft tube is split into eight linear sections defined by nine cross sections as indicated in Fig. 7. Each cross section is positioned by an x- and y-value of the center point corresponding to the red line in Fig. 7. Furthermore, the cross sections are rotated by an angle to the horizontal and can vary in width and height. The last parameter is given by the radius, rounding the corners of each cross section. In total, 48 parameters are introduced for eight liner sections and the parameters of the inlet cross section are fixed.

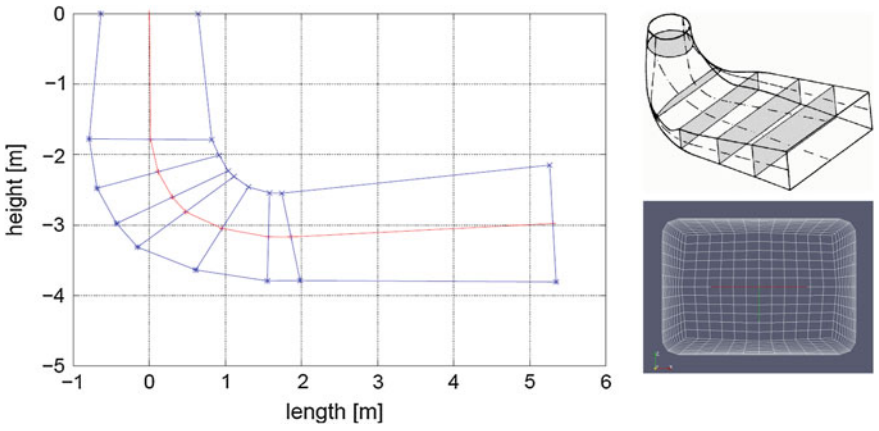

Fig. 7 Geometry definition and mesh layout of the draft tube

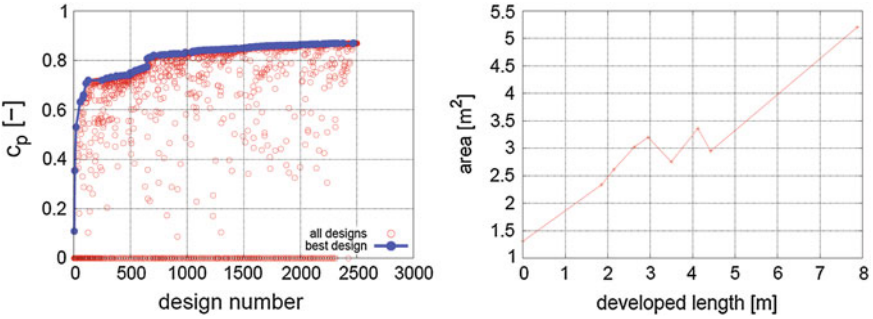

Fig. 8 Pressure recovery over design number, *left graph.* Area distribution of the best design, *right graph*

The meshing algorithm provides a block-structured hexahedral mesh and consists of about 90,000 nodes. The flow inside the tube is resolved using an O-grid. As in case 1, OpenFOAM® solves the RANS equations with the standard k-ω-SST model. Also, the same convergence check evaluates the characteristics of the absolute mass flow-averaged pressure values at draft tube inlet and outlet. As inlet boundary data, a measured flow field downstream a Francis impeller for BEP is implemented.

The optimization run is set up by $n_{\text{ind}} = 30$ individuals in one generation, consisting of one civilization with a $n_{\text{ind}}/n_{\text{sur}} = 5$ surviving rate. The convergence is chosen to 10^{-4}. Due to time restriction, the optimization run was terminated before reaching this convergence criterion. Nevertheless, the pressure recovery of the best design equals 0.87 and there is no bigger increase expected as shown in Fig. 8. In total, 2,502 designs are calculated, wherein 449 designs are marked as 'bad designs' with a value of $c_p = 0$. The geometry discretization can create unphysical designs, for example overlapping of cross sections. These unphysical designs will be treated as 'bad designs.' The right graph of Fig. 8 shows the area distribution of the best design. It is similar to the expected pattern known in the literature except for the short increase in area at 4 m length during the end part of the elbow section. It has a positive impact on secondary flow phenomena, helping to avoid flow separation after the elbow.

6 Conclusion

For the optimization of the hydrodynamic shape of hydroturbine components, a mathematical optimization procedure is developed. This optimizer is robust, fault tolerant, and asynchronous. It allows the use of a complete heterogeneous computational environment. This makes the tool usable for applications or practical relevance. This has been proven by the design of a tidal current turbine and of a turbine draft tube.

References

1. De Jong, K.A., (1975). An analysis of the behavior of a glass of genetic adaptive systems. Ph D thesis, University of Michigan.
2. Mühlenbei, D., Schomisch, H., & Born, J. (1991). The parallel genetic algorithm as function optimizer. *Parallel Computing, 17*(6), 619–632.
3. Abbott, I. H., & von Doenhoff, A. E. (1959). *Theory of wing sections: Including a summary of Airfoil data*. New York: Dover Books on Physics.

Numerical Simulation of Pressure Pulsations in Francis Turbines

M. V. Magnoli and R. Schilling

1 Introduction

For more than 150 years, hydraulic power plants have been strongly contributing to energy generation. At present, with the expanding participation of other non-storable renewable energy sources in the electrical market composition, water turbines can importantly contribute to the electrical grid stability and to energy storage.

With the increasing demand for such services, new procedures have to be developed, in order to allow the hydraulic turbines to operate in critical load conditions, as part load, for example. The technique proposed here, based on pitching guide vanes, was numerically tested with instationary CFD models and delivered possibly promising results, concerning the machine performance and stability, at part load conditions.

The extension of the operating range of hydraulic power plants, through the turbine active flow control, yields even greater flexibility to them, in providing regulation services to the electrical grid. This technique has also the potential to extend the operational life of main turbine components and may lead to the increase in the annual energy output in some cases.

The active flow control may, in principle, be employed for Francis machines and pump turbines with different specific speeds. At Francis turbines with high specific speeds, the benefits concern mainly the reduction in the pressure pulsations and extension of the operating range. At pump turbines, the active flow control might most notably contribute to the reduction in the "S" instability in turbine mode.

M. V. Magnoli (✉)
Voith Hydro Holding GmbH & Co. KG, Alexanderstr. 11, 89522 Heidenheim, Germany
e-mail: marcelo_vinicius.magnoli@voith.com

R. Schilling
TU München Institute of Fluid Mechanics, Boltzmannstr. 15, Garching 85748, Germany

P. Gourbesville et al. (eds.), *Advances in Hydroinformatics*,
Springer Hydrogeology, DOI: 10.1007/978-981-4451-42-0_32,

2 Background

Water power corresponds to one of the earliest sources of renewable energy in commercial use. Still current days, it corresponds to an important part of the installed energy generation facilities, ranging from small complexes with less than 1 MW up to Itaipu, in Brazil, and Three Gorges, in China, with rated capacity of, respectively, 14.0 and 18.2 GW and annual energy output of, respectively, 91.6 and 79.4 TWh in 2009.

Most recently, with the increasing demand for clean energy sources, hydraulic energy appears once again as an interesting solution. In the current context of the energy market, where other renewable energy sources, such as wind and solar energy, enjoy increasing market shares, the hydraulic power plants offer a very attractive solution for grid stabilization and energy storage.

The energy output of wind and solar energy parks is influenced by variations of the weather conditions, sometimes producing more or less energy as in the moment needed and introducing a strong dynamic component in the electrical grid. With their increasing importance, their impact on the grid tends to be even greater, as well as the need for regulation and storage services. Hydraulic turbines can efficiently supply this dynamic balance to the electrical grid and in a faster way than traditional thermal plants. However, with the increasing need for such services, water turbines must also offer increasing flexibility.

At this point, it comes to the current challenge in the design of water turbines. The operating range of the hydraulic plants must be extended, in order to offer more possibilities in the regulation of energy generation as whole. It means that the turbines must be able to be smoothly operated along a larger portion of their hill chart than in the past. Common customer requirements for modern water turbines are, for example, that they shall be capable to operate at deep part load, sometimes even considerably below the half of their rated power.

At deep part load in hydraulic turbines, with less than 60 % of the optimal flow, $Q < 0.60\ Q_{opt}$, strong pressure pulsations, with amplitudes up to 10 % of the nominal head, may arise in the machine, typically due to the formation of an oscillating vortex rope in the draft tube cone. The pressure pulsations are diffused through the hydraulic active parts of the turbine. In the case of strong pressure oscillations, they may affect the stability of the energy output at the generator, due to possibly strong torque oscillations, as well as they may cause structural damages to turbine components, especially to the turbine runner.

This critical condition turns out to be even more challenging, if considered that the power density of water turbines has got much larger during the last decades, in order to satisfy economical and competitive needs.

There are different approaches to overcome the pressure oscillation problem. Common actions to reduce the amplitude of the pressure pulsations at part load, which are normally employed and which have been empirically established, are the air injection in the turbine or the installation of fins at the walls of the draft tube cone. Both solutions often impact negatively at the turbine efficiency and rely on

weak theoretical backgrounds. Another solution would be to better understand the dynamical behaviour of the turbine at highly transient operating conditions, as done by Magnoli and Schilling [1], and adapt its mechanical design accordingly, including it, in the future, in the design process.

The solution proposed in this study, to reduce the pressure oscillation amplitude, and thereby increase the turbine operating range and flexibility, is to control the flow in an active manner, with kinematic energy supply, obtained through the controlled pitching movement of the guide vanes. This procedure can reduce the pressure oscillation amplitude at critical operating conditions, allowing the machine to operate in part load more smoothly and increasing the operating range, with the advantage of low or even beneficial impact on the turbine efficiency, as discussed by Wunderer and Schilling [2]. If the required guide vanes pitching frequency is low, the movement can be provided by the servomotors of the operating ring. In case of high pitching frequencies, especially designed actuators have to be employed.

This technique of active flow control could also avoid the flow separation and the associated fixed limit cavitation at the runner inlet edges, in the case of off-design water heads, as in the case of early take into operation of the machine, when the reservoir is still not completely filled in, or at unexpected flood conditions.

The reduction in the pressure oscillation amplitude can also reduce the plant maintenance costs and outage periods, thanks to the consequently extended fatigue life of the mechanical components.

Besides the benefits of grid regulation offered by the extension of the operating range of hydraulic turbines, the possibility to operate at deep part load can, in some cases, especially in plants with a reduced number of generator units, lead to an additional annual energy output from approximately 5 up to 10 %.

3 Numerical Simulations

To develop and investigate the technique of active flow control, through the pitching movement of the turbine guide vanes, a complete Francis turbine, with $n_q \approx 80\ \text{min}^{-1}$, was numerically simulated with computational fluid dynamics (CFD). This particular machine, denominated FT 80, was chosen, since Francis machines with high specific speeds are especially affected by the adverse operating conditions at part load. The numerical simulation offered an economic possibility to test the new control technique at this early development stage, prior to actual model testing, which might require complicated and expensive experimental devices, with the additional advantage of offering practical visualization and measuring tools.

The simulated operating points were taken from real operating conditions from an existing prototype turbine, already in operation and built with exact the same geometry as the turbine model FT 80. The considered operating points comprise the optimum, full load, normal operation, part load at low and high heads and

extreme part load. For the objective of this study, that is, to extend the machine operating range, the last three load conditions are the most interesting and belong to the critical portion of the hill chart, in terms of pressure oscillations.

The computational model is only suitable for the investigations, if it can accurately reproduce the real behaviour of the physical flow through the turbine, qualitatively as well as quantitatively. Therefore, after the preparation of the numerical model, it was preliminary verified with stationary simulations, whose results were compared to the experimental head, flow, power and efficiency measurements available from the model test. As long as the main interest of the simulations was in reproducing the transient phenomena, the instationary calculations were also verified with the observations and pressure oscillation values from the experimental data.

3.1 Stationary Simulations

The numerical simulations were carried out with the finite volume method (FVM), applied to the complete turbine, with all its hydraulic components: spiral case, stay vanes, guide vanes, runner and draft tube. The calculations were conducted in a coupled manner, that is, considering all the turbine components and interfaces between them, as long as the dynamic effects in the fluid flow through the turbine arise from the interaction between its components, caused by the rotating runner and the stationary parts.

Different computational mesh densities were tested and optimized to deliver accurate results with acceptable computation times. The final computational mesh counted with more than 6 million cells and part of it can be seen in Fig. 1. The employed FVM made use of second-order interpolation schemes.

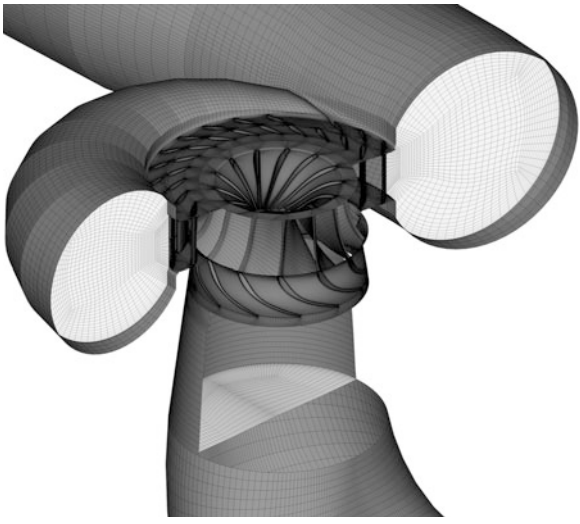

Fig. 1 Computational mesh for the fluid flow simulation

With the preliminary stationary simulations, different turbulence models were tested: standard k-ε, k-ε LCL, k-ε and k-ω SST, and no significant influence on the results was noticed. However, the standard k-ε model achieved the best agreement with the available experimental results. The comparison between the results from the computational simulation and from the model test is reproduced in Table 1. The accuracy provided by the numerical model offers a maximum deviation under 2 %.

3.2 Transient Simulations

For the simulation of the instationary effects in the fluid flow through the turbine, like the rotor–stator interaction and the flow instabilities in the draft tube, adequate time resolution and turbulence models were needed.

Approximately 400 time-steps were calculated for each machine revolution, in order to capture the effects not only from the draft tube instabilities, but also from the rotor–stator interaction.

Considering the turbulence modelling, the unsteady averaged Navier–Stokes equations (URANS) model introduced excessive artificial dissipation in the flow simulation, as expected, and turned out to be unable to reproduce the highly transient effects in the turbine, especially in the draft tube. Therefore, adequate and more sophisticated turbulence models had to be employed.

The detached eddy simulation (DES), for example, attempts to resolve the turbulent eddies, which are larger then the mesh resolution, as it would be done in a strict large eddy simulation (LES). On the other hand, the eddies smaller than the grid resolution are modelled, as done in URANS. This hybrid behaviour is achieved with the modification of the turbulence dissipation, ε, with the limiter F_{DES}, which accounts for the local mesh size. Strelets [3] modified the k-ω SST model with the DES approach, coming to the modified turbulence transport equations below.

$$\frac{\partial(\rho k)}{\partial t}+\frac{\partial\left(\bar{u}_j\rho k\right)}{\partial x_j}=\tau_{ij}\frac{\partial\bar{u}_i}{\partial x_j}-\beta^*\rho\omega k F_{\mathrm{DES}}+\frac{\partial}{\partial x_j}\left[(\mu+\sigma_k\mu_T)\frac{\partial k}{\partial x_j}\right]$$

$$\frac{\partial(\rho\omega)}{\partial t}+\frac{\partial\left(\bar{u}_j\rho\omega\right)}{\partial x_j}=\frac{\gamma}{\nu_T}\tau_{ij}\frac{\partial\bar{u}_i}{\partial x_j}-\beta\rho\omega^2+\frac{\partial}{\partial x_j}\left[(\mu+\sigma_\omega\mu_T)\frac{\partial\omega}{\partial x_j}\right]+2(1-F_1)\rho\sigma_{\omega2}\frac{1}{\omega}\frac{\partial}{\partial x_j}\frac{\partial}{\partial x_j}$$

The influence of the mesh resolution appears in the dissipation term, $\beta^*\ \rho\ \omega\ k\ F_{\mathrm{DES}}$, in the turbulence kinetic energy transport equation. The last term in the transport equation of the specific dissipation rate is the normal SST modification of the original k-ω model.

The interpolation scheme has also to be modified for the application of the DES model. In the regions where DES assumes the LES characteristic, the interpolation

Table 1 Experimental results obtained at the model test and numerically simulated results

Operating point	Model test				Simulation				Deviation			
	$n'_1/n'_{1,opt}$ (%)	$Q'_1/Q'_{1,opt}$ (%)	$T'_1/T'_{1,opt}$ (%)	$\eta/\eta_{,opt}$ (%)	$n'_1/n'_{1,opt}$ (%)	$Q'_1/Q'_{1,opt}$ (%)	$T'_1/T'_{1,opt}$ (%)	$\eta/\eta_{,opt}$ (%)	$\delta n'_1$ (%)	$\delta Q'_1$ (%)	$\delta T'_1$ (%)	$\Delta\eta$ (%)
Optimum	100	100	100	100	99.4	100	100.3	100.2	−0.6	−0.6	0.3	0.2
Full load	110.3	122.9	108.3	97.2	109.6	122.2	110	98.7	−0.6	−0.6	1.6	1.5
Normal	107	110.2	102.2	99.3	106	109.2	102.4	99.4	−1.0	−1.0	0.2	0.1
High head	107.8	79.7	69.3	93.8	106.7	78.9	69.3	93.8	−1.0	−1.0	0	0
Low head	119.9	84.8	64.4	91	119	84.2	65.1	91.9	−0.7	−0.7	1	1

function must reproduce the CDS scheme. While, in other regions, where the URANS behaviour is dominant, the interpolation function must be second-order UDS. This blend between these two interpolations schemes is based on local flow characteristics and is described by Travin [4].

The transient numerical simulation was also verified with experimental data. The calculated and measured pressure fluctuation amplitudes at four measuring points at the draft tube cone were compared and are presented in Table 2. The shape of the vortex rope in the draft tube could also be accurately predicted by the numerical simulation, as seen in Fig. 2.

The transient simulation required approximately 30 machine revolutions, depending on the operating point and on the prescribed initial solution, until the instationary flow patterns were established. The computation of one machine revolution took, in average, 15 h in a Linux cluster with 8 Intel Q6600 processors, each with 4 kernels, 2.4 GHz and 2 GB memory.

The numerical simulations were also able to capture the higher part load phenomenon. This effect has been experimentally observed by Nicolet et al. [5], as seen in Fig. 3. At part load, the vortex rope rotates around the turbine axial axis, with the angular velocity ω_{rope}. At the same time, the vortex rope rotates around itself, with the angular velocity, ω^*. At higher part load, the vortex rope cross section assumes an elliptical shape, as illustrated in Fig. 3. The elliptical shape associated with the self-rotation can increase the pressure pulsation amplitude.

To the authors' knowledge, in no published work until now, there has been an attempt to numerically simulate the higher part load phenomenon. The first successful numerical simulation of this effect in Francis turbines has been reported by Schilling and Magnoli [6], as part of their research work. Figure 4 shows the numerical simulated streamlines and vector field at a selected draft tube cone section at higher part load. As graphically seen, the developed numerical model was able to reproduce the self-rotation of the vortex rope as well as its elliptical shape.

The time signals of the pressure pulsations in the draft tube cone and their Fourier transforms, obtained experimentally and numerically predicted, can be found in Figs. 5 and 6. The second amplitude peak, present in the frequency spectrum, is caused by the higher part load effect and is related to the vortex rope self-rotation, ω^*. The visual comparison of the experimental and numerical results shows the capability of the numerical model to qualitatively reproduce the higher part load phenomenon.

3.3 Pitching Guide Vanes

The active control of the flow through the turbine was reached with the pitching movement of the guide vanes. To the stationary opening angle of the guide vanes, $\Delta\gamma$, a harmonic oscillating component was added, $\delta(\Delta\gamma)$, in which the control parameters are the pitching angle amplitude, $\Delta\tilde{\gamma}$, and the pitching frequency, $\Delta\tilde{f}$.

Table 2 Experimental results obtained at the model test and numerically simulated with DES

Operating point	Model test				f/f_n	Simulation				f/f_n	Deviation				$\delta f/f_n$
	$\Delta p/\rho\ g\ H$					$\Delta p/\rho\ g\ H$					$\delta\ \Delta p$				
	HW (%)	90° (%)	TW (%)	270° (%)	(−)	HW (%)	90° (%)	TW (%)	270° (%)	(−)	HW (%)	90° (%)	TW (%)	270° (%)	(%)
High head	4.70	3.65	4.28	5.25	0.302	4.31	3.23	3.85	4.52	0.298	−8.3	−11.5	−10.0	−13.9	−1.3
Low head	5.29	4.51	5.71	6.78	0.282	5.04	4.44	5.94	6.40	0.315	−4.7	−1.6	4.0	−5.6	11.7

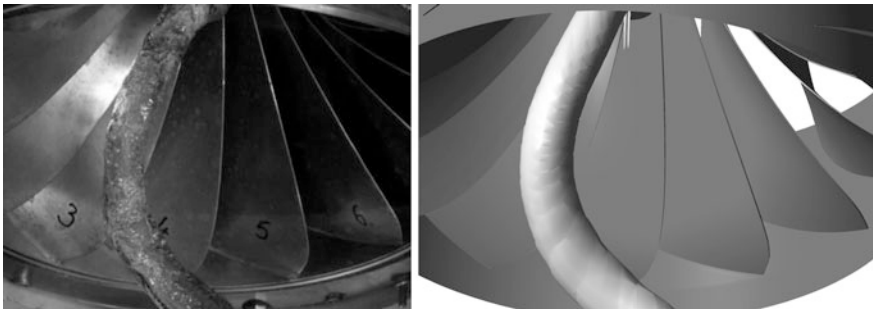

Fig. 2 Comparison of the vortex rope shape observed at the model test and numerically simulated at part load and high head

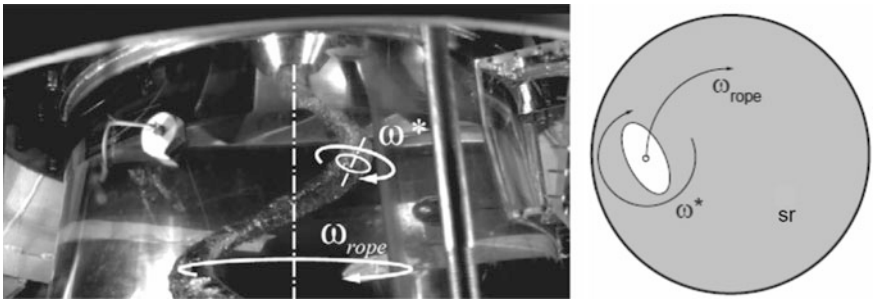

Fig. 3 Vortex rope shape at higher part load, experimentally observed at the model. Reproduced from Nicolet et al. [5]

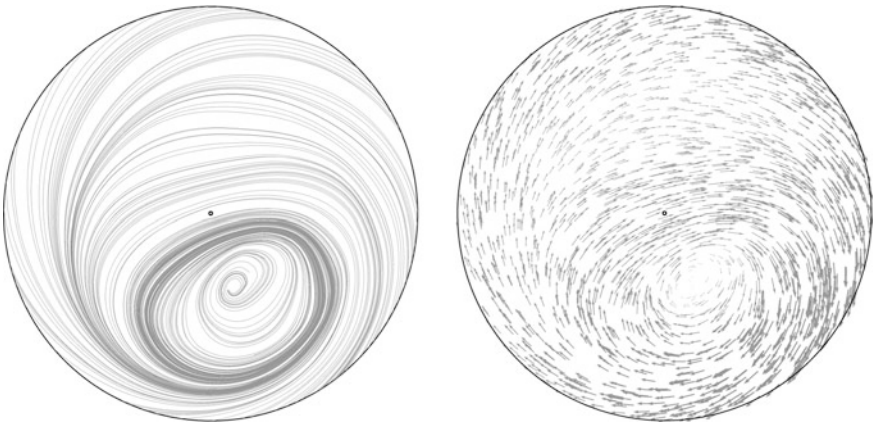

Fig. 4 Numerical simulated streamlines and vector field at a selected draft tube cone section at higher part load

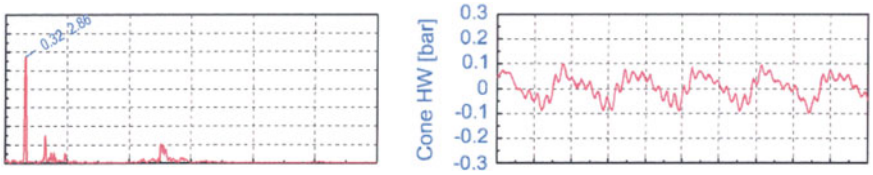

Fig. 5 Experimentally measured time signal (*right*) and Fourier transform (*left*) of the pressure pulsation in the draft tube cone at higher part load

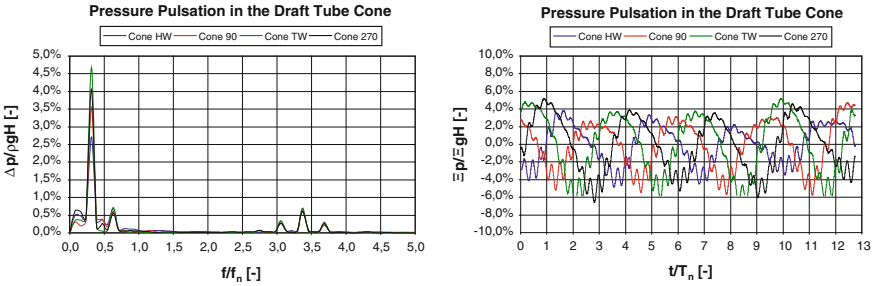

Fig. 6 Numerically predicted time signal (*right*) and Fourier transform (*left*) of the pressure pulsations in the draft tube cone at higher part load

$$\delta(\Delta\gamma) = \Delta\tilde{\gamma}\sin\left[\tilde{f}(t - t_0)\right]$$

At the beginning of the simulation, the fluid volume in the distributor was meshed with the original stationary position of the guide vanes. With the pitching movement of the guide vanes, the mesh boundaries, which correspond to the guide vane walls, must be accordingly modified, to simulate the motion effect in the numerical computations. Still, the displacement of the mesh boundaries, associated with the guide vane walls, had to be followed by mesh adjustments in the surrounding region, in order to preserve the computational grid quality.

Here, the mesh deformation was specified, based on the displacement diffusion principle, which counts with a diffusion transport equation for the displacement in the computation field and assumes the prescribed movement of the guide vanes walls as the boundary conditions.

$$\frac{\partial}{\partial x_i}\left(\Gamma_\delta \frac{\partial \delta}{\partial x_i}\right) = 0$$

This equation involves the local displacement diffusion parameter, Γ_δ, which specifies how fast the displacement of the mesh boundaries is diffused into the computational grid. Its importance is limited to the numerical simulation and does not reflect any physical property of the real problem.

To limit the mesh deformation near to the wall boundaries and preserve the mesh resolution and quality in the boundary layer, the local diffusion is inversely

proportional to the distance to the moving boundary, $\Gamma_\delta = (1/d)^K$, $K > 0$. It has the effect that the mesh near to the moving wall remains almost undeformed, while the stream region absorbs the most part of the mesh deformation caused by the displacement of the mesh boundaries.

4 Application

4.1 Pressure Oscillation Amplitude

After the verification of the numerical model accuracy and its application to the simulation of several turbine operating points, with stationary guide vanes, it was used for the simulation of the effect of pitching guide vanes on the fluid flow.

Figure 7 shows the massive vortices in the runner blades channel on the suction side of the blades at extreme part load. This critical operating point results in strong pressure pulsations, which would prevent the runner from being operated at this condition. The objective with the introduction of the active flow control, though the pitching guide vanes, is to reduce the pressure pulsations at operating conditions, such as the one just mentioned, in order to extent the turbine operating range, increasing the annual energy output.

Wunderer [7] commented on the possibility to successfully employ this kind of active flow control to reduce the pressure pulsations in Francis turbines with high specific speed. However, his numerical experiments were limited to extremely simplified models and very singular operating points and blade geometry configurations. To test the actual effectiveness of this technique in real turbines, different control parameters $\Delta\tilde{\gamma}$ and $\Delta\tilde{f}$, for the pitching movement of the guide vanes, were

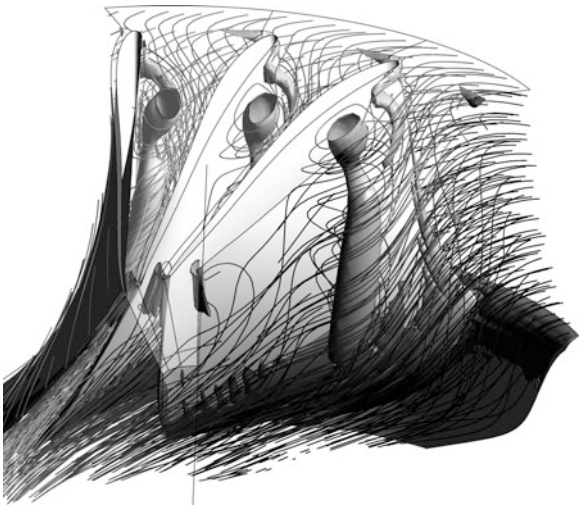

Fig. 7 Streamlines and interchannel vortex at the turbine runner at deep part load and high head

tested with the computational fluid flow model of the FT 80 machine, whose high reliability for dynamic simulations was presented in the previous section.

The active flow control was simulated for the FT 80 turbine, at part load and low head, $H/H_{opt} = 0.696$ and $Q/Q_{opt} = 0.707$. First, the pitching amplitude was set to $\Delta\tilde{\gamma} = 0.50°$ and its frequency to $\Delta\tilde{f}/f_n = 1.5$, where f_n is the turbine rotation frequency. Afterwards, the pitching frequency, $\Delta\tilde{f}$, was reduced and synchronized to the vortex rope rotating frequency, $\Delta\tilde{f}/f_n = 0.31$, and two different amplitudes were tested, $\Delta\tilde{\gamma} = 0.50°$ and $\Delta\tilde{\gamma} = 0.75°$.

The influence of the active flow control on the pressure pulsations in the turbine runner, with different pitching amplitudes and the pitching frequency synchronized to the vortex rope rotating frequency, $\Delta\tilde{f}/f_n = 0.31$, can be observed in Fig. 8. The pressure pulsation amplitude, normalized in relation to the head, $\Delta p / \rho\, g\, H$, is shown at three conformal planes: near to the crown, $v = 0.025$, at the distributor centre line, $v = 0.500$, and near to the band, $v = 0.975$. The pressure pulsation amplitude is plotted along the developed blade length, u, at these conformal planes, beginning at the trailing edge at the pressure side (TE-PS), $u = 0.0$, passing by the blade leading edge (LE), $u = 0.5$, and finishing at the trailing edge at the suction side (TE-SS), $u = 1.0$. At each plot, there are curves for the numerical simulations with stationary guide vanes, $\Delta\tilde{\gamma} = 0$, and pitching guide vane amplitudes of $\Delta\tilde{\gamma} = 0.50°$ and $\Delta\tilde{\gamma} = 0.75°$.

As it can be seen in Fig. 8, the numerical simulations demonstrate that the guide vanes pitching movement, in the same frequency as the draft tube vortex, rather intensifies the pressure pulsations in the runner, producing exactly the opposite effect as desired. It also suggest, based on the curves for $\Delta\tilde{\gamma} = 0.50°$ and $\Delta\tilde{\gamma} = 0.75°$, that the increase in the pitching amplitude at this frequency also intensifies the severity of the pressure pulsations.

On the other hand, Fig. 9 exemplifies the effect of varying the guide vanes pitching frequency, while the pitching amplitude remains constant. In this plot, the pressure pulsation is normalized in relation to the values obtained with stationary guide vanes. In the numerical experiments, the frequency assumed the values $\Delta\tilde{f}/f_n = 0$, $\Delta\tilde{f}/f_n = 0.31$ and $\Delta\tilde{f}/f_n = 1.5$, and the amplitude was $\Delta\tilde{\gamma} = 0.50°$. The curves presented in Fig. 9 correspond to two measuring points at a circular section of the draft tube cone, at the tail water side (DT-TW) and at a quarter circle offset (DT-270°).

Supposing that the dynamic characteristic of the excited system is similar to a second-order damped dynamic system, the pressure pulsation curves as functions of the pitching frequency were extrapolated up to $\Delta\tilde{f}/f_n = 3.0$. If in the future, with help of further numerical simulations, this assumption shows up to be correct, the increase in the guide vanes pitching frequency could possibly reduce the pressure oscillation amplitude, resulting in the desired effect in order to extent the machine operating range. Nevertheless, this dynamic behaviour as a function of the pitching frequency is by now just a hypothesis and has to be confirmed by future numerical experiments, with several combinations of the control parameters, $\Delta\tilde{\gamma}$ and $\Delta\tilde{f}$, and at different operating points. Supposing that this assumption is

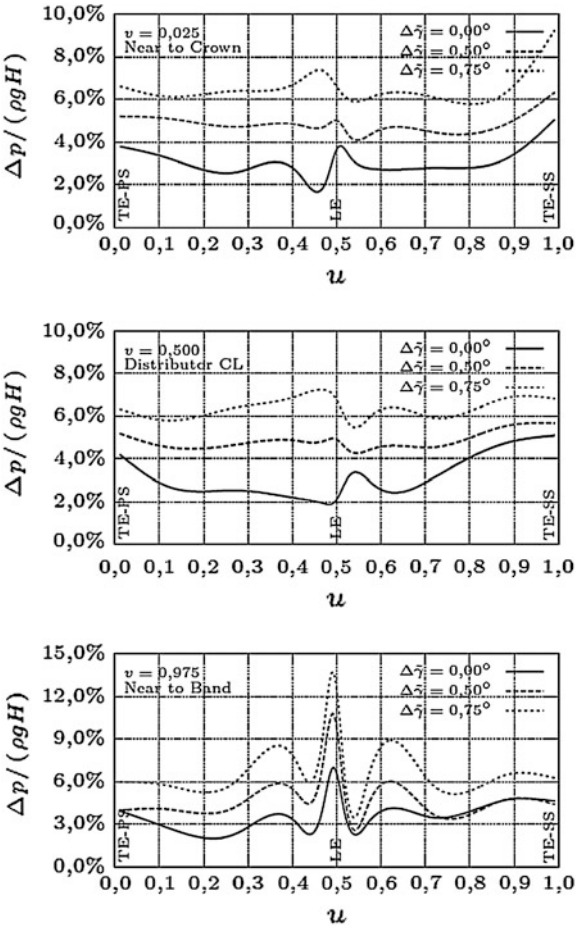

Fig. 8 Pressure pulsation amplitude along the blade developed length, u, at different conformal planes, $v = 0.025$, $v = 0.500$ and $v = 0.975$, as a function of the guide vanes pitching amplitude, $\Delta\tilde{\gamma} = 0.50°$ and $\Delta\tilde{\gamma} = 0.75°$, at constant pitching frequency, $\Delta\tilde{f}/f_n = 0.31$

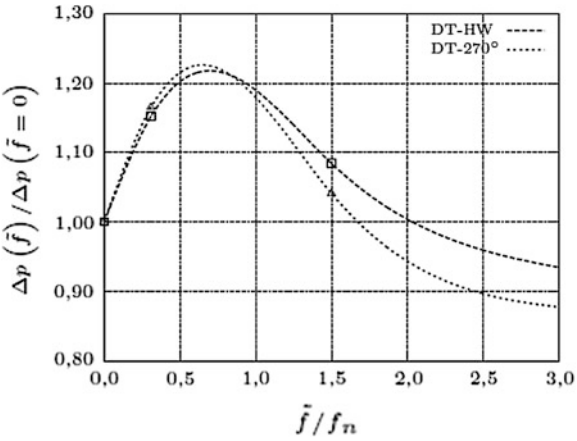

Fig. 9 Pressure pulsation amplitude at draft tube measuring points, DT-TW and DT-270°, as a function of the guide vanes pitching frequency, $\Delta\tilde{f}/f_n = 0.31$, at constant pitching amplitude, $\Delta\tilde{\gamma} = 0.50°$

Table 3 Example of theoretical gains applied to an existing power plant

Machine	FT 90
Number of machines	$z = 4$
Rated power per machine	$P_r = 150$ MW
Original lower power limit	$P_{\min} = 0.70$ Pr
Extended lower power limit	$P_{\min} = 0.45$ Pr
Increased availability	+7.5 %
Increased annual energy output	+4.8 %

correct, it shall also be verified that the guide vanes pitching frequency is practicable, from the point of view of the mechanical design.

4.2 Energy Output

Here, it is assumed that the introduction of the active flow control, through pitching guide vanes with optimal control parameters, will be able to reduce the pressure pulsations up to a point that moderate part load conditions can be added to the turbine operation range.

As planned before, this extension of the machine operating flexibility increases the possibility to offer auxiliary services to the electrical grid and the annual energy output.

Taking as example an existing hydraulic power plant with four 150-MW Francis machines, with slightly higher specific speed as simulated, $n_q \approx 90$ min^{-1}, where the operation at part load would be desirable, but avoided because of strong pressure oscillations, the increase in the annual energy output, with the application of the active flow control, could reach 4.9 %, through an increased availability of 7.5 %. The machine data for this real example and the operational gains can be found in Table 3.

5 Conclusion

The first numerical simulations with pitching guide vanes, in the particular case of the FT 80 turbine, pointed out that the possibility of reducing the pressure pulsations in the machine, at part load, requires further numerical simulation and experiments. The reduction in the pressure oscillation amplitude would allow operating the turbine in severe load conditions, without compromising its mechanical structure and extending its operating range. The additional operational flexibility, which would possibly be achieved with the proposed technique, would increase the offer for regulation services and would expand the annual energy output, in some hydraulic power plants, around 5 up to 10 %. Other renewable energy sources, such as wind, solar, wave and tidal energy, could also profit from

the extended capability of water turbines to regulate the electrical grid. Further investigations in the development of the active flow control, with pitching guide vanes, shall be the simulation of additional operating points, of machines with different specific speeds and of various sets of control parameters.

References

1. Magnoli, M.V., & Schilling, R. (2008). Vortex shedding in Francis runners trailing edges. Proceedings, 24th IAHR Symposium, Foz do Iguaçu, Brazil.
2. Wunderer, R., & Schilling, R. (2010). Numerical simulation of active flow control in hydro turbines. Proceedings, 12th ISROMAC, Honolulu, Hawaii.
3. Strelets, M. (2001). Detached eddy simulation of massively separated flows. Paper, 39th Aerospace Sciences Meeting and Exhibit, Paper 2001-0879.
4. Travin, A., Shur, M., Strelets, M., Spalart, P.R. (2000). Physical and numerical upgrades in the detached eddy-simulation of complex turbulent flows. 412 EUROMECH Colloquium, Munich, Germany.
5. Nicolet, C., Zobeiri, A., Maruzewski, P. Avellan, F. (2010) On the upper part load vortex rope in Francis turbine: Experimental investigation. Proceedings, 25th IAHR Symposium, Timisoara, Romania.
6. Schilling, R. & Magnoli, M. (2011) Möglichkeiten und Grenzen der numerischen Simulation bei der Weiterentwicklung von Wasserkraftmaschinen. Praktikerkonferenz Wasserkraft, Graz, Austria.
7. Wunderer, R. (2010). Numerische Simulation der aktiven Strömungsbeeinflussung in Turbomaschinen. PhD Thesis, TU Munich, Institute of Fluid Mechanics.

Author Biographies

M.Sc. Eng. Marcelo V. Magnoli completed his Mechanical Engineering study in 2001 at the University of São Paulo (USP) and obtained his Master Degree in 2005 on Mechanical Engineering at USP. He started his professional career as project engineer at the turbine manufacturer Voith in São Paulo in 2002, and actuated as proposal engineer and technical coordinator for proposals in Latin America from 2004 until 2007. Since 2007 he has been a doctoral candidate and research assistant at the Institute of Fluid Mechanics at the TU Munich. In 2011 he returned to Voith Hydro Holding GmbH & Co. KG in Heidenheim as hydraulic development Engineer.

Prof. Dr.-Ing. habil. Dr. h.c. Rudolf Schilling studied Mechanical Engineering at the University of Karlsruhe (THKA). He obtained his Doctor Degree in 1976 and habilitated in 1979 at the Institute of Fluid Mechanics and Fluid Machinery at THKA. He started his professional career as a design engineer at the pump manufacturer KSB in Frankenthal, then actuated as an engineer in R&D at the water turbine manufacturer Voith in Heidenheim and during 5 years he has been the head of R&D. Since October 1988 he has been working as full Professor for Fluid Mechanics and Hydraulic Machinery at the TU Munich.

3D RANS Modeling of a Cross Flow Water Turbine

Christian Pellone, Thierry Maitre and Ervin Amet

Abstract This paper presents several aspects of the URANS numerical modeling of a three-straight-bladed cross flow turbine. In a first part, a 2D analysis is presented as a reference configuration. The near wall grid is refined until the solution stabilizes. Calculations are performed for three tip speed ratios to cover the three classical regions: primary effects, transition, and secondary effects. Three-dimensional modeling uses 3D grids obtained by translating the 2D one in the span direction. A simplified version considers only the 3 straight blades though the complete version takes all the geometric parts into account: blades, arms, shaft, and hub. The mean and instantaneous power coefficients, obtained with the 2D and 3D grids, are compared to those given by the hydrodynamic LEGI tunnel on a small-scale model. Experimental uncertainties are also carefully quantified for these quantities. It is shown that the 3D modeling improves significantly the power predictions. The main loss regions are the blade tips and the spoke-arm attachments where horseshoe vortices take place. The power distribution along the span is strongly affected by these two zones. The analysis of the vorticity field highlights large 3D vortex structures shed by the blades and convicted inside the turbine.

Keywords Darrieus turbine · Numerical modeling · 3D complex geometry · Experimental validations

C. Pellone · T. Maitre (✉) · E. Amet
LEGI, BP 53, 38041 Grenobel Cedex 9, France
e-mail: Thierry.Maitre@legi.grenoble-inp.fr

C. Pellone
e-mail: Christian.Pellone@legi.grenoble-inp.fr

E. Amet
e-mail: Ervin.Amet@elena-energie.com

P. Gourbesville et al. (eds.), *Advances in Hydroinformatics*,
Springer Hydrogeology, DOI: 10.1007/978-981-4451-42-0_33,

1 Introduction

A water current turbine based on a lift-driven Darrieus turbine has been patented by the LEGI laboratory and is currently under investigation in a hydrodynamic tunnel [1]. Although yawing mechanisms can be used to control the blade pitch, the LEGI "Achard" turbine is a fixed pitch Vertical Axis Water Turbine (VAWT) for simplicity and robustness reasons. The blades can be straight or delta shaped. The models tested in the LEGI tunnel are built in aluminum.

In spite of its geometrical simplicity, the VAWT involves a highly stalling unsteady flow field. These flow features originate in large variations of the angle of attack on the blades during their revolution and high turbine solidity leading to strong unsteady effects. As a consequence, the dynamic stall phenomenon takes place at nominal operating point and affects the power delivered as well as the blade loading. The numerical modeling of the flow in a VAWT is obviously a challenge for the CFD.

The most affordable method is the Reynolds-averaged Navier–Stokes (RANS) model. In this approach, only the mean flow is solved, the influence of turbulence being introduced using the unknown Reynolds stress tensor. The most popular models are the one-equation Spalart–Allmaras (historically developed for aerodynamic applications) and the two equations k-ε and k-ω. The k-ω model of Menter [2] is well adapted for flows with strong adverse pressure gradient and flow reversal as those involved by VAWT. The SST formulation is a variant of the standard k-Ω model, combining the original Wilcox k-Ω model [3] for use near walls and the standard k-ε model away from walls using a blending function.

Much more elaborated CFD methods solve the turbulent flow itself. The Large Eddie Simulation (LES), initially proposed in 1963 by Joseph Smagorinsky [4] to simulate atmospheric air currents, consists in solving large eddies (larger than the grid spacing) and modeling sub-grid scales. Hybrids DES methods have been developed for industrial flows (high Reynolds) combining a RANS method for boundary layer regions and a LES method in outer regions.

Several 2D vertical axis (wind or marine) turbine modelings have been performed using RANS, LES, or DES. Lain and Osorio [5], Dai and Lam [6] and Nabavi [7] calculated the turbine instantaneous power using commercial codes (Fluent or CFX). Depending on the turbine geometry and the tip speed ratio, the gap between the calculated and measured average power is found in the range [0–20 %]. Amet et al. [8] modeled the Laneville wind turbine [9] using the compressible TURBFLOW solver. Instantaneous calculated lift and drag blade coefficients have been compared to experimental ones for $\lambda = 2$. Even if the hysteresis loop shapes are qualitatively obtained for lift and drag, significant discrepancies are found to come from the experiment apparatus itself rather than from the numerical model. Iida et al. [10] compared a LES model with a momentum model in the case of a three-straight-bladed NACA0018 Darrieus wind turbine. At nominal tip speed ratio $\lambda = 3$ and higher, the instantaneous power coefficients obtained with the two models are very close. At lower tip speed ratios,

LES seems to better capture the strong dynamic stall, giving a higher power than the momentum model. Nevertheless, no experimental data are provided. Simão Ferreira et al. [11] compared two URANS models (Spalart–Allmaras and k-ε) with the LES and DES models on a single-bladed NACA0015 Darrieus wind turbine. Calculated vorticity fields are compared with PIV measurements. The best vorticity field is given to buy the DES model. Concerning the tangential and normal blade forces calculation, it is found that the RANS models lead to results very close to those obtained with the DES.

Three-dimensional vertical axis wind turbine modelings have also been recently performed. Owell et al. [12] did a comprehensive study of a three-bladed turbine of high solidity (equal to 1 as for water application) and low aspect ratio (equal to 4). Parameters such as Reynolds number, tip speed ratio, and blade surface roughness were explored experimentally, and their corresponding effect on the mean torque and power coefficient were analyzed. The turbine was also calculated in 2D and 3D using the fluent solver with a relatively coarse mesh containing 1.3×10^6 cells. Mesh independence and suitable y^+ values less than 10 is assumed but not shown. The 3D mean power coefficients are found slightly higher than the experimental ones, taking into account measurement uncertainties estimated to 20 %. With 2D modelings, the mean power coefficients are strongly increased by a factor 1.5–2.3 (at nominal tip speed ratio) when the Reynolds number is increased. This is attributed to the absence of the tip vortices in 2D. Untaroriu et al. [13] investigated, with the CFX solver, the self starting capability of the Durham three-bladed wind turbine [14]. The 2D and 3D grids containing, respectively, 1.36×10^5 and 7.9×10^6 cells lead to a similar acceleration and final angular velocity. The last is close to the experimental value. On the contrary, the first is strongly over-estimated by a factor 10. It is attributed to the poor wall treatment of the used k-ε model at wall, although small y^+ value are used (equal to 1.7 in 2D and 6.3 in 3D). Castelli et al. [15] analyzed, using the Fluent solver, the effect of an inclination angle on the power delivered by a one-bladed wind turbine. Even if the considered geometry was tested in Bovisa's low turbulence facility (Milan), no comparison with experimental data is shown. The number of cells of the 3D grid is not given neither the y^+ wall value, but it is noticed that each simulation requires about 20 days. In these commented 3D works, only the three rotating blades are modeled. The power losses due to the turbine spokes, the hub, and eventually the ball bearings friction are evaluated experimentally.

LES and DES methods give more realistic wakes than those obtained with RANS methods but are highly time consuming and do not guaranty better power coefficient predictions. It appears that RANS methods remain attractive to solve the complex flow developed by a VAWT. Nevertheless, their validity has to be strengthened. As a matter of fact, 2D and 3D RANS modelings mentioned above do not give extensive details about the grid convergence in terms of total number of cells as well as y^+ maximum acceptable values. Moreover, the instantaneous power is rarely compared to experimental data. Navabi did it but he does not correct the experimental power with the rotating inertia, resulting in a strong phase shift. Another observed lack is the quantification of experimental errors, sometimes

obtained with rough estimations rather than with a detailed methodology. As a consequence, presented results seem sometimes contradictory or at least unusual. For example, it can be observed in [12] that the instantaneous power converges since the first turbine revolution though it is usually mentioned that 3 to 5 revolutions are necessary (up to 14 in [5]). Another surprising result is the factor 10 obtained in [13] between the calculated (2D and 3D) turbine acceleration and the measured one, knowing that thin 2D and 3D grids are used.

Taking into account the aforementioned comments, the main objective of the present work is as follows: firstly, to study the grid dependence, in particular the effect of the y^+ wall value on the power delivered; secondly, to compare the 2D and 3D calculated power coefficients with experimental values for which uncertainties is quantified and finally, to discuss the main loss regions and their respective impact on the global flow field as well as on the turbine efficiency.

2 Experimental Setup

The turbine rotates with the angular velocity ω and placed in a tunnel where the upstream velocity U_∞ is uniform. The azimuthal angle $\theta = \omega t$ defines the angular position of a blade. The tip speed ratio is given by $\lambda = \omega R/U_\infty$, where R is the radius of the turbine. The resulting forces that the fluid exerts on the turbine provide a torque T along the rotation axis and one can define a power coefficient as follows:

$$CP = T\omega/\left(\rho HRU_\infty^3\right) \tag{1}$$

where ρ stands for the density, $D = 2R$ for the turbine diameter, and H for the turbine height. In the following, $< x >$ designates the average value of x variable on a revolution. The solidity of the turbine is defined as $\sigma = NC/R$, where N is the number of blades (here 3) and C the blade chord.

The experimental hydrodynamic tunnel available at LEGI consists in a vertically closed circuit where water is pumped. The test section **1**, showed in Fig. 1, has a rectangular form (length x width x height = 1000 × 700 × 250 mm). In the test section, the velocity ranges from 1 to 2.8 m/s. The torque is measured via a frameless permanent magnet servomotor kit **15** mounted above the measurement platform **10**. It includes an electrical synchronous generator **14** used to drive the turbine at the desired rotational speed: A proportional-integral regulation is used to impose a constant rotation speed by controlling the electric current and consequently the instantaneous torque applied on the turbine. The PI parameters are chosen to avoid high pick torques that could damage the structure of the turbine, particularly at the hub blade attachments. Consequently, the rotational speed fluctuates slightly around the imposed value. This point will be discussed hereafter. The angular position and the rotational speed are given by the resolver **13**. The rotating shaft **3** is prolonged below the hub using a polymer material **4** to

realize the symmetry plane at the turbine center. The shaft is guided by a pair of ball bearings **5**, between the superior wall **9** and the platform **10** and by another ball bearing **6**, between the generator and the resolver housings. A lip-type sealing system **12**, between the turbine rotating shaft and the superior wall, prevents water leakage. The generator torque $T_{generator}$ does not give directly the hydrodynamic torque T_{exp} acting on the turbine because this last equilibrates three resistant torques accordingly to the following equation:

$$T_{exp} = T_{generator} + T_{friction} + T_{inertia}, \tag{2}$$

where $T_{friction}$ is the frictional torque introduced by the lip-type sealing and by the ball bearings, and $T_{inertia}$ is the inertial torque of the rotating system due to the variation of ω. Because the numerical modeling gives T_{exp}, the generator, frictional and inertial torques have to be measured. $T_{generator}$ is given by the current I delivered by the synchronous generator, $T_{friction}$ is obtained by rotating the shaft without the turbine, and $T_{inertia}$ is calculated with J $d\omega/dt$, where J is the inertia moment of the full rotating system. Uncertainties attached to these three contributions have been quantified but are not detailed in this paper.

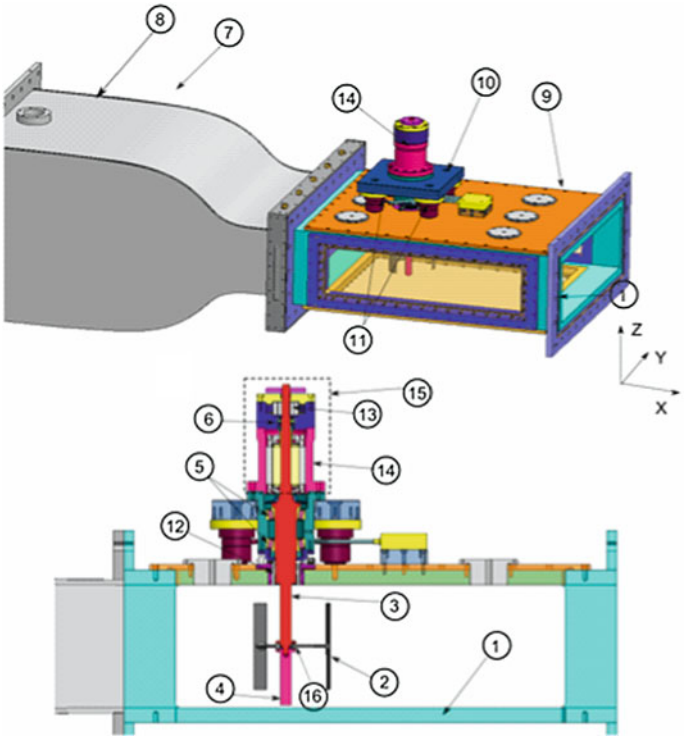

Fig. 1 Experimental setup

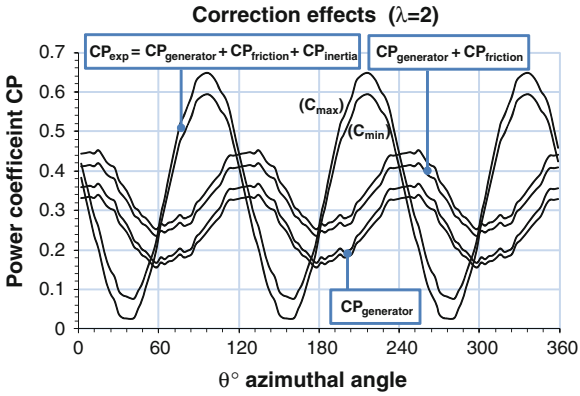

Fig. 2 Power correction for $\lambda = 2$

Figure 2 highlights the calculation of the experimental value of the power coefficient CP_{exp} for $\lambda = 2$. For each correction step, two curves (C_{min}) and (C_{max}) are used to delimitate the minimum and maximum CP_{exp} values coming from the precisions detailed above. The gap CP_{max}–CP_{min} is in the range of 0.02 at $\theta = 60°$ ($CP = 0.22$) and 0.06 at $\theta = 30°$ ($CP = 0.1$). The $< CP >_{exp}$ average value over one revolution is about 0.34 with a $\pm$ 6.6 % precision. The power coefficient increase due to friction effect is done without any phase shift. On the contrary, the inertia effect leads to a phase shift but does not change the $0.34 < CP >$ average value. As λ increases from 1 to 3, the average power precision varies from $\pm$5.6 % to $\pm$10.3 %.

3 Calculation Domain: Grid Settings and Modeling Parameters

The 2D calculation domain corresponds to the symmetry plane of the test section (Fig. 1). The diameter D and height of the turbine H are equals to 175 mm. The d = 22 mm diameter shaft is modeled. The blade's foil shape is a modified NACA0018 section that has been warped from the mid-chord such that the camber line fits the circular blade path. The chord of the modified cambered section is 32 mm length, corresponding to a 1.1 solidity. The trailing edge has a round shape, with a radius of 0.5 % of the chord. The turbine rotation axis is located at a 350 mm distance of the inlet section and at equal distance (350 mm) of the two lateral walls (vertical walls). The turbine height is 175 mm so that a distance of 37.5 mm separates the tip of the blades from the superior wall and the inferior *Altuglass* window of the test section. U_∞ is taken equal to 2.3 m/s. The corresponding chord Reynolds number Re_C, based on the R velocity at $\lambda = 2$, is equal to 1.510^5. No slip condition is imposed on solid boundaries. A uniform pressure is considered at the outlet. The 2 % turbulence intensity measured at inlet has been imposed in the calculation. The flow solver is Fluent V13.

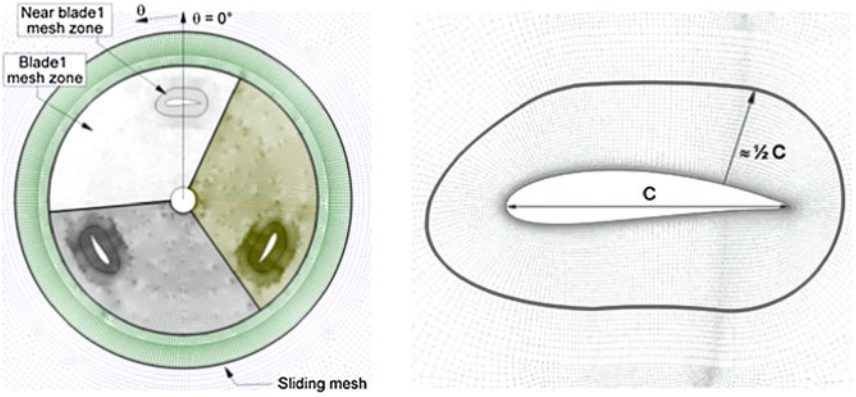

Fig. 3 Overall grid (*left*) and near blade grid (*right*)

Figure 3 presents the reference mesh of the flow domain. The near blade region, highlighted by a bold solid line on the right, is meshed with a quadrilateral structured O grid which spans roughly to C/2 normally to the foil. The figure shows the reference grid corresponding to a 5 μm thickness for the first row at wall. The Fig. 3 left shows the overall mesh containing about 100,000 cells. Notice the sliding mesh boundary. At the shaft's wall, the y^+ value, checked a posteriori during the calculations, is of the order on unity. At lateral walls, y^+ is about 40.

An y^+ sensitivity study is done in 2D. The near blade grid is modified resulting in 7 meshes corresponding to seven values of averaged y^+ ave values. The resulting parameters characterizing the 7 grids (case 1 to case 7) are summarized in Table 1. The grid points on the foil surface are not modified, except for case 1 obtained by halving in the 2 directions all the cells of the reference grid. The obtained case 1 grid contains about 400,000 cells, thought the 2 to 7 ones contain about 10^5 cells. Notice that the y^+ values are obtained with a steady calculation of one fixed blade at zero incidence and an upstream velocity equal to $U_{\infty \text{Steady}} = 2\ U_\infty = 5.6$ m/s.

Two 3D grids based on the 2D reference grid are built. They are obtained by sweeping the 2D grid along the blade span. The first, called the blades grid, represents only the 3 blades and the shaft (Fig. 4) and contains 3.7×10^6 cells. The second, called the full grid, take also into account the 3 arms and the cylindrical hub (Fig. 5) and contains 5.2×10^6 cells. Notice that 40 cells are used from the symmetric plane to the superior wall in the 2 cases. An unstructured grid is required at the blade-arm junction for the complete model. Taking 80, instead of 40, cells do not change anymore the results.

Concerning the rotor modeling, a second-order time implicit scheme is used. The time step Δt is set equal to 2.707×10^{-4} s, corresponding to a rotation angle $\Delta\theta$ of 1°. For the space discretization, a second-order upwind scheme is used. For stability reasons, the first revolution is carried out using a first-order scheme in both time and space. For 2D and 3D modelings, 5 revolutions are sufficient to

Table 1 y^+ values characterizing the 7 near blade meshes

Case	1	2	3	4	5	6	7
y^+ave	0.36	0.71	2	5.16	14.93	29.75	75.32
y^+max	0.79	1.57	4.89	11.08	26.79	48.30	105.70

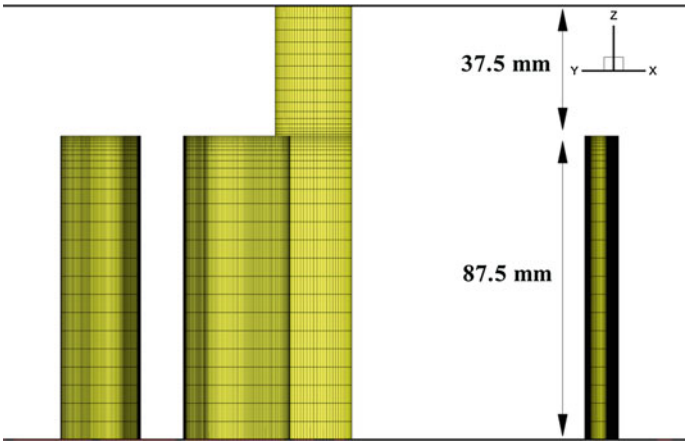

Fig. 4 Blades grid (3.7 10^6 cells)

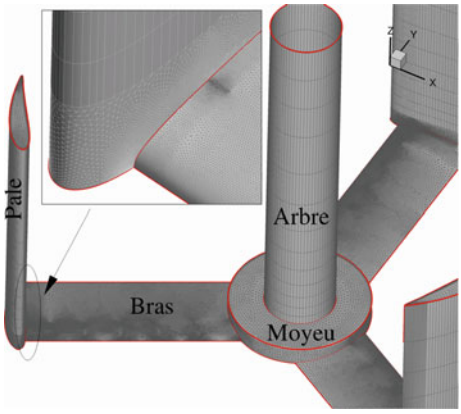

Fig. 5 Full grid (5.2 $\times$ 10^6 cells)

reach a periodic behavior. The solution sensitivity versus the time step, the number of dual time stepping per time step and the number of turbine revolutions have been carefully studied but are not presented in this paper.

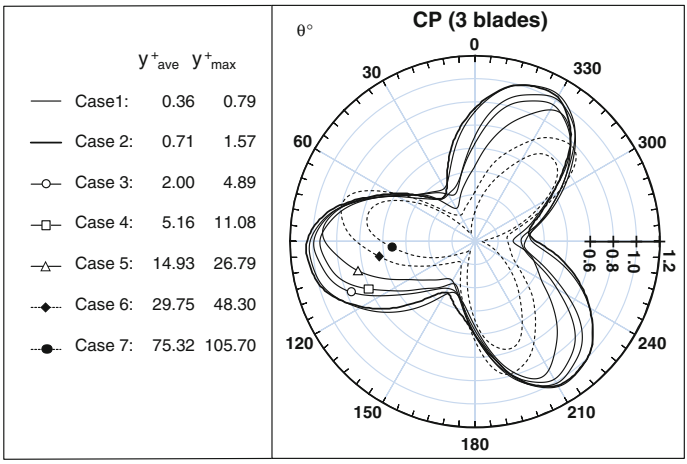

Fig. 6 y^+ sensitivity on CP

4 Results

Figure 6 presents the instantaneous power coefficient rosette for the three blades. The three-lobe shape comes from the main power contribution of the upstream blade passage. Cases 1 and 2 give close results corresponding to average power coefficients of, respectively, 0.578 and 0.575. From cases 3 to 7, average power coefficients decrease quickly from 0.501 to 0.061. As y^+ increases, the power drop starts at lower θ leading progressively to negative power contributions at 30°, 150°, 270°. Figure 7 shows the lift (left) and drag (right) blade coefficient distribution for the upstream hold disc of rotation. It is observed that the blade's drag strongly increases with y^+ . This is due to an over-evaluated stall (compared to cases 1 and 2), taking place on the inner blade side, increasing the pressure drag. On the contrary, no y^+ sensitivity is seen on the lift. With the used y^+ evaluation, one concludes that the power is stabilized for an average y^+ lower than 0.71.

The Table 2 gathers the calculated and experimental configurations. Notice that for the full turbine grid including the 3 arms, only the nominal tip speed ratio $\lambda = 2$ is considered.

In 2D and 3D, it has been checked that 5 revolutions are necessary to reach a periodic solution. It can be mentioned that the simulation including the arms is not completely converged.

Figure 8 shows the average power coefficient versus the tip speed ratio. Two-dimensional simulation strongly over-estimates the power at nominal $\lambda = 2$ ($< CP > = 0.57$) and higher. At lower λ, a significant drop in power is observed. At $\lambda = 1$, the calculated power is even smaller than the experimental one. The 3D calculation without arms leads to a power loss increasing quickly with λ. The gap with the experimental value at $\lambda = 2$ is halved ($< CP > = 0.46$). At $\lambda = 1$ and 3,

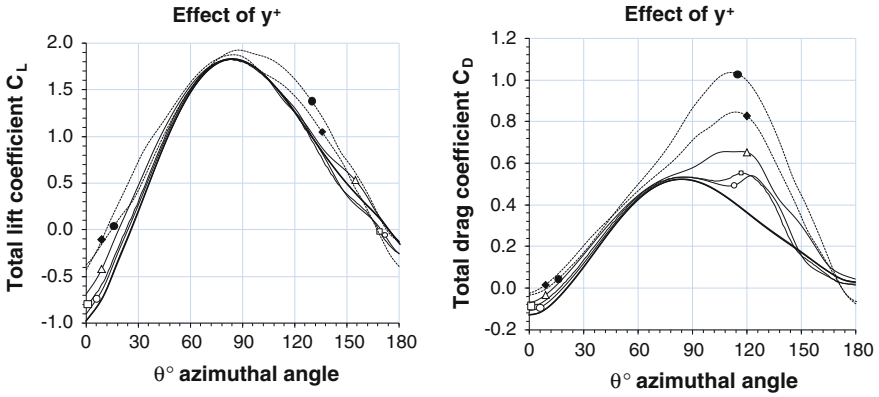

Fig. 7 y^+ sensitivity on blade lift (*left*) and drag (*right*)

Table 2 Calculated and experimental configurations

Configurations	2D	3D without arms	3D with arms (full grid)	Experimental
Considered λ	1; 1.5; 2; 2.5; 3	1; 2; 3	2	1; 1.5; 2; 2.5; 3
Number of cells	10^5	3.7 10^6	5.2 10^6	
Number of revolutions	11	5	3	

the power appears under-evaluated. At $\lambda = 2$, the full grid leads to a power practically equal to the experimental value ($< CP > = 0.34$).

Figure 9a, b and c present the instantaneous power coefficients versus θ for $\lambda = 1$, 2 and 3, respectively. For $\lambda = 2$, the numerical curves have a shape similar

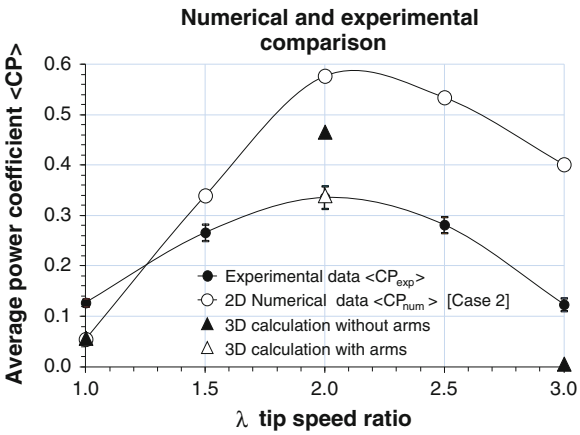

Fig. 8 Average power coefficient versus λ

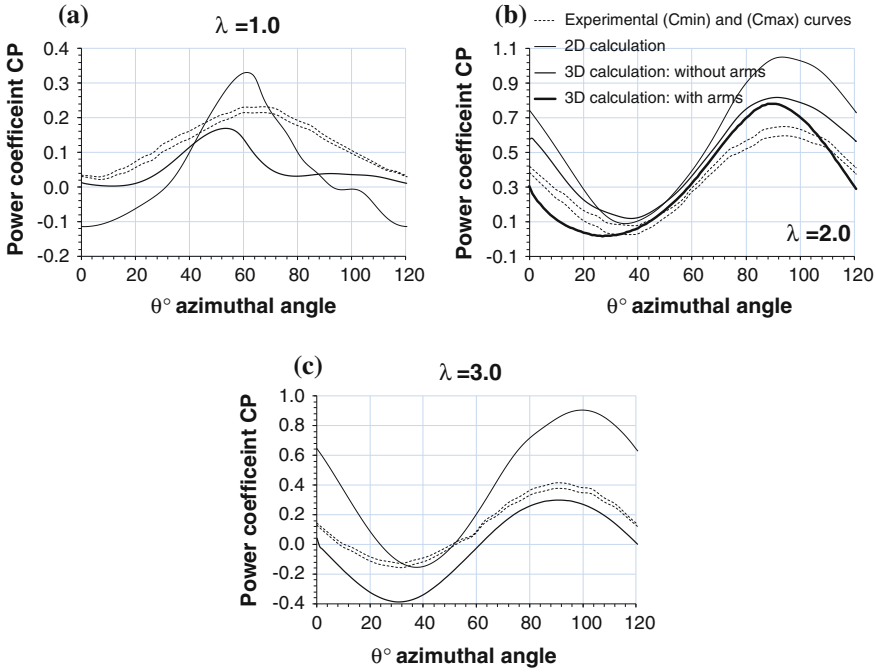

Fig. 9 **a** Instantaneous power at $\lambda = 1$. **b** Instantaneous power at $\lambda = 2$. **c** Instantaneous power at $\lambda = 3$

to the experimental one. The blades and full grids reduce the power pick given by the 2D calculation at 90°. Above 90°, the full grid introduces a high-power loss which is not observed on the experimental curve. The under-evaluated power observed between 0° and 30° comes from the loss of the following blade. For $\lambda = 3$, the blades grid reduces much more the power than in the case $\lambda = 2$. The CP shape is similar to the experimental one but under-evaluated on the θ cycle. For $\lambda = 1$, a different behavior is observed: The 2D and 3D curve shapes are different to the experimental one. The 2D power pick at 60° is over-evaluated as well as the following power decrease at higher θ. An unrealistic negative power is obtained at 120°. The blade grid leads to a better prediction until the pick at 55°. Then, as in 2D, the power loss is over-estimated but the resulting power at $\theta = 120°$ is correct. It can be concluded that, for $\lambda = 1$, the dynamic stall phenomenon is poorly captured by both the 2D and 3D simulations. For $\lambda = 2$, 3D grids improve the prediction, in particular the full grid, even if the power pick remains over-evaluated. For $\lambda = 3$, the 3D grid leads to a moderately under-evaluated power.

Figure 10 shows the power distribution along the blade span obtained with the blades and full grids for $\lambda = 2$. Two azimuthal blade positions $\theta = 60°$ and 100° are plotted. The power loss at tip and blade-arm junction is clearly seen. For $\theta = 60°$, the losses introduced by these blade boundaries do not contaminate the blade. Consequently, the 2D and 3D powers are very close (Cf Fig. 9b). On the

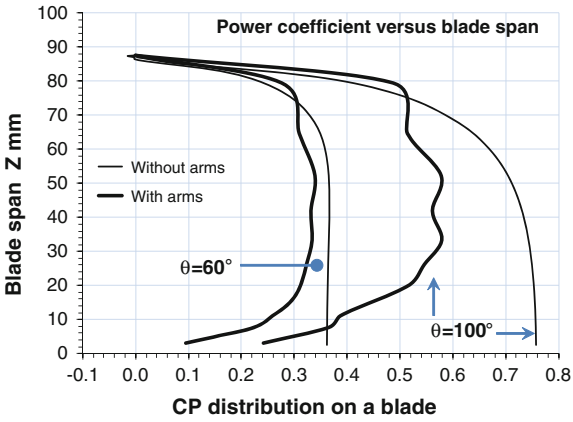

Fig. 10 Power distribution along the blade span

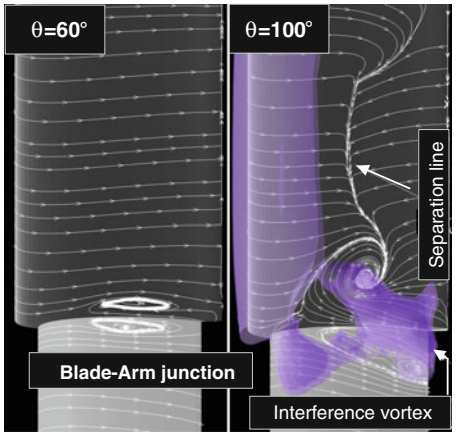

Fig. 11 Horseshoe vortex at arm junction

contrary, for $\theta = 100°$, the blade-arm loss addresses the whole blade. Figure 11 shows that the loss at blade-arm junction comes from a big horseshoe vortex which develops quickly between 60° and 100°. This vortex comes from a shear stress on two perpendicular walls and is also called "interference vortex".

Figure 12a and b present a vorticity map for the whole flow obtained with the blade grid for $\lambda = 2$ and $\theta = 90°$ and 180°, respectively. Notice that the view point is opposite in the 2 cases. There-dimensional iso-values of Z vorticity, as well as 2D iso-values on the symmetry plane, are plotted. The red color corresponds to a counterclockwise rotation. The tip vortex seems very intense and concentrated. Red eddies correspond to the main vortex structures shed by the blade at about $\theta = 180°$ as shown on the Fig.12b. It is observed, on Fig.12a, that the blade interacts with the main eddy shed by the preceding blade. The viscous wake is clearly seen on the symmetry plane. It is observed that the blade does not operate in the viscous wake of the preceding blade.

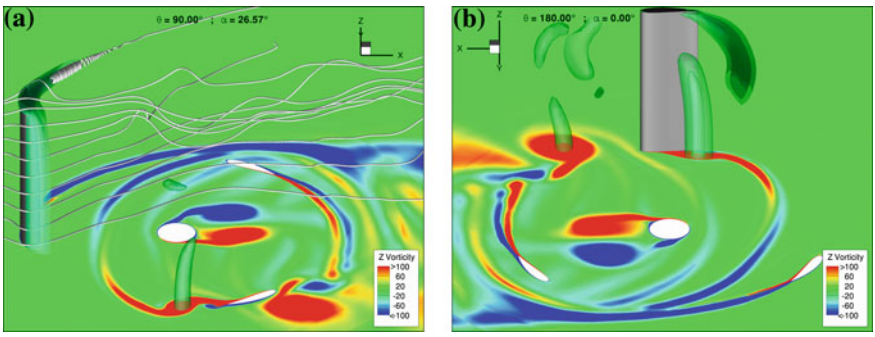

Fig. 12 **a** Z vorticity for l = 2 and $\theta = 90$. **b** Z vorticity for l = 2 and $\theta =$ &80

5 Conclusion

The 2D and 3D RANS calculations of a vertical axis water turbine have been performed with the k-Ω SST model of the Fluent solver. An y^+ sensitivity, performed in 2D for $\lambda = 2$, shows that the calculated power decreases very quickly with y^+. This comes from an over-evaluation of the main eddy developing in the inner part of the blade. This eddy leads to an unrealistic pressure drag. In the considered case, the maximum acceptable y^+ blade-averaged value is 0.71.

The instantaneous and average power coefficients have been carefully measured with their associated uncertainties. In particular, the phase shift introduced by the rotating parts inertia has been taken into account. As λ increases from 1 to 3, the average power precision varies from ± 5.6 % to ± 10.3 %. Concerning the turbine simulations, the 2D model strongly over-estimates the average power at nominal λ and higher. At low λ, a high-power drop leads to a value lower than the experimental one. The 3D simulations globally improve the power predictions. At nominal $\lambda = 2$, the simplified blades grid halves the gap with the experimental power and the full grid leads practically to this value. For $\lambda = 1$ and 3, the 3D simulations under-estimate the power. The better instantaneous power predictions are obtained in 3D at nominal and higher λ. It is important to notice that even if the average power obtained with the full grid at $\lambda = 2$ is equal to the experimental one, the instantaneous values differ significantly. The power pick at $\theta = 90°$ is over-estimated and is compensated by a strong power drop at greater θ. This drop comes from a large horseshoe vortex developing at the blade-arm junction. At the pick power position, this vortex influences the flow all over the blade span. For $\lambda = 1$, the dynamic stall phenomenon is poorly captured by both the 2D and 3D simulations.

References

1. Mentxaka, A., Aumelas, V., Maitre, T. & Pellone, C. (2010). Numerical and Experimental Analysis of a Darrieus Type Cross Flow Water Turbine in Bare and Shrouded Configurations. 25th IAHR Symposium on Hydraulic Machinery and Systems, 20–24 September, Romania.
2. Menter, F.R. (1994). Two-equation eddy-viscosity turbulence models for engineering applications. *AIAA Journal, 32*(8), 1598–1605.
3. Wilcox, D. C. (2008). Formulation of the k- ΩTurbulence Model revisited. *AIAA Journal, 46*(11), 2823–2838.
4. Smagorinsky, J. (1963). General circulation experiments with the primitive equations. *Monthly Weather Review, 91*(3), 99–164.
5. Lain, S., Osorio, C., (2010). Simulation and evaluation of a straight-bladed Darrieus-type cross flow marine turbine. Journal of Scientific & Industrial Research. Vol 69, December 2010, pp 906–912.
6. Dai, Y.M., Lam, W., (2009). Numerical study of straight-bladed Darrieus-type tidal turbine. ICE International Conference on Engineering-Energy, Vol 162, Issue 2, pp 67–76.
7. Nabavi, Y., (2008). Numerical study of the duct shape effect on the performance of a ducted vertical axis tidal Turbine. PHD Thesis. University of British Columbia, Vancouver, Canada.
8. Amet, E., Maître, T., Pellone, C., Achard, J.L., (2009). 2D numerical simulations of blade-vortex interaction in a darrieus Turbine. Journal of Fluids Engineering. Vol 131/111103, pp 1-15.
9. Laneville, A., & Vittecoq, P. (1986). Dynamic Stall: The case of the vertical axis wind Turbine. *Journal of Solar Energy Engineering, 108*, 140–145.
10. Iida, A., Kato, K., Mizuno, A., (2007). Numerical Simulation of Unsteady Flow and Aerodynamic Performance of Vertical Axis Wind Turbines with LES. 16th Australasian Fluid Mechanics Conference, Crown Plaza, Gold Coast, Australia, 2-7 December.
11. Ferreira, S., Bijl, C.J., Van Bussel, L.G., & Van Kuik, G. (2007). Simulating dynamic stall in a 2D VAWT: modeling strategy, verification and validation with particle image velocimetry. *Data Journal of Physics: Conference Series, 75*(2007), 012–023.
12. Howell, R., Qin, N., Edwards, J., & Naveed, D. (2010). Wind tunnel and numerical study of a small vertical axis wind turbine. *Renewable Energy, 35*, 412–422.
13. Untaroiu, A., Wood, H.G., Allaire, P.E., Ribando, R.J., (2011). Investigation of self-starting capability of vertical axis wind turbines using a computational fluid dynamics approach. Journal of Solar Energy Engineering, Vol. 133,/041010-1 041010-8.
14. Hill, N., Dominy, R., Ingram, G., & Dominy, J. (2008). Darrieus turbines: The physics of self starting. *Proceedings of Institute Mechanical Engineering Part A, 223*, 21–29.
15. Castelli, M.R., Benini, E., (2012). Effect of Blade Inclination Angle of a Darrieus Wind Turbine. Journal of turbomachinery, Vol. 134/031016-1.

FPM Simulations of a High-Speed Water Jet Validation with CFD and Experimental Results

Christian Vessaz, Ebrahim Jahanbakhsh and François Avellan

Abstract The present chapter reports the development of finite particle method (FPM) in the framework of a high-speed water jet simulation. The FPM kernel is used to improve the consistency of standard SPH for non-uniform particle distribution. The time integration is performed with a modified Verlet scheme. At the end of each time step, a particle shifting method is applied to mitigate the particle clustering issue by restoring a uniform particle spacing. The influence of particle spacing and maximum CFL number are investigated in the case of a high-speed water jet impinging on a flat plate. The influence of the impinging angle is analyzed for three different angles: 90°, 60°, and 30°. The time history of the pressure coefficient is recorded on the flat plate to compare the FPM simulations with available measurements and grid-based CFD simulations. The validation of the results is based on the comparison of the averaged pressure coefficient profile as well as the comparison of the free-surface location for the three different impinging angles.

Keywords Smoothed particle hydrodynamics · Finite particle method · Impinging jet · Particle shifting

Nomenclature

c	Color function [–]
C	Absolute velocity [m s^{-1}]
$\overrightarrow{C}$	Absolute velocity vector [m s^{-1}]

C. Vessaz (✉) · E. Jahanbakhsh · F. Avellan
EPFL—LMH, Avenue de Cour 33bis 1007 Lausanne, Switzerland
e-mail: christian.vessaz@epfl.ch

E. Jahanbakhsh
e-mail: ebrahim.jahanbakhsh@epfl.ch

F. Avellan
e-mail: francois.avellan@epfl.ch

P. Gourbesville et al. (eds.), *Advances in Hydroinformatics*,
Springer Hydrogeology, DOI: 10.1007/978-981-4451-42-0_34,

f	Arbitrary function [–]
h	Smoothing length [m]
m	Mass [kg]
$\overrightarrow{n}$	Normal vector [–]
N	Number of particle [–]
p	Static pressure [Pa]
$\overrightarrow{R}$	Shifting vector [m]
t	Time [s]
V	Volume [m^3]
W	Kernel [m^{-3}]
$\tilde{W}$	Renormalized kernel [m^{-3}]
X, Y, Z	Cartesian coordinate [m]
ρ	Density [kg m^{-3}]
α, β	Cartesian coord
$(i), (j)$	Particle
max	Maximum value
ref	Reference value

1 Introduction

The smoothed particle hydrodynamics (SPH) method is well adapted to simulate free-surface flows. Indeed, the Lagrangian approach of the SPH enables to simulate complex free-surface flows such as in the case of an impinging jet on a flat plate. This test case has been often used in 2D to validate SPH simulations with the analytical solution of Taylor (e.g. [1–4]). The verification of the simulations is important to validate the SPH solver before extending the fluid analysis to more complex flows. For instance, the simulations of a Pelton turbine [5, 6] require an accurate solver to compute the instantaneous torque in the buckets.

The standard SPH method described by Monaghan [7] suffers from a lack of accuracy compared to the grid-based numerical simulations. However, recent studies summarized by Liu and Liu [8] have proposed new developments, which improve the accuracy of the particle-based methods. In the present study, the FPM kernel from Fang et al. [9] is used to improve the consistency of the standard SPH. The numerical oscillations are reduced by the mass equation correction proposed by Fatehi and Manzari [10]. Finally, the temporal integration scheme of Molteni and Colagrossi [11] is implemented to increase the overall accuracy and stability of the simulations.

During the SPH simulations, the contraction of the streamlines as well as the tensile instability described by Monaghan [12] results in the clustering of particles. This particles clustering increases the spatial discretization error, which decreases the overall accuracy of the simulation. In the present study, a particle shifting

method is applied at the end of each time step to restore a more uniform particles distribution. The shifting strategy of Vessaz et al. [13] is used for the simulations of the impinging jet. This shifting method combines the benefits of the methods of Xu et al. [14] for internal flows and Jahanbakhsh et al. [1] for free-surface flows.

The FPM simulations of the 3D impinging jet on a flat plate are carried out with the code SPHEROS developed by Jahanbakhsh et al. [15]. The accuracy of these simulations is validated with the numerical simulations and experimental results from Kvicinsky et al. [16]; the numerical simulations being based on the grid-based volume of fluid method implemented in the commercial software ANSYS-CFX®.

2 Governing Equation

The standard SPH formulation of a function (1) and its derivatives (2) is based on a kernel approximation and a decomposition of the continuous matter into N particles.

$$f^{(i)} = \sum_{j}^{N} f^{(j)} W^{(ij)} V^{(j)} \tag{1}$$

$$f_{\alpha}^{(i)} = -\sum_{j}^{N} f^{(j)} W_{\alpha}^{(ij)} V^{(j)} \tag{2}$$

Each particle i (or j) has a mass m, a density ρ, and a volume V. The position of the particle is defined by the vector $\vec{X}$ whose components of the Cartesian coordinate system are X_α with $\alpha = [X, Y, Z]$. The approximated function f and the kernel W are expressed as (4) and (5) to simplify the notation. In the present work, the quintic Wendland kernel (6) used by Fatehi and Manzari [10] is chosen. This kernel is used with a constant smoothing length $h = 2.6X_{\text{ref}}$ where X_{ref} is the reference particle spacing.

$$V^{(i)} = \frac{m^{(i)}}{\rho^{(i)}} \quad \text{and} \quad X_{\alpha}^{(ij)} = X_{\alpha}^{(i)} - X_{\alpha}^{(j)} \tag{3}$$

$$f^{(i)} = f\left(\vec{X}^{(i)}\right) \quad \text{and} \quad f_{\alpha}^{(i)} = \frac{\partial f^{(i)}}{\partial X_{\alpha}} \tag{4}$$

$$W^{(ij)} = W\left(\vec{X}^{(ij)}, h\right) \quad \text{and} \quad W_{\alpha}^{(ij)} = \frac{\partial W^{(ij)}}{\partial X_{\alpha}} \tag{5}$$

$$\begin{aligned} W^{(ij)} &= \frac{21}{2\pi h^3} L\left(\frac{|X^{(ij)}|}{h}\right)\left(1 - \frac{|X^{(ij)}|}{h}\right)^4 \left(4\frac{|X^{(ij)}|}{h} + 1\right) \quad \text{with} \quad L(x) \\ &= \begin{cases} 1 & 0 \le x < 1 \\ 0 & x \ge 1 \end{cases} \end{aligned} \tag{6}$$

The derivatives of this standard SPH formulation are not consistent for a non-uniform particle distribution. Therefore, the FPM approach of Fang et al. [9] based on the Taylor series expansions (7) and (8) is applied and the FPM kernel $\tilde{W}$ is computed as (9).

$$\sum_j^N f^{(j)} W^{(ij)} V^{(j)} = f^{(i)} \sum_j^N W^{(ij)} V^{(j)} + f_\alpha^{(i)} \sum_j^N X_\alpha^{(ji)} W^{(ij)} V^{(j)} \tag{7}$$

$$\sum_j^N f^{(j)} W_\beta^{(ij)} V^{(j)} = f^{(i)} \sum_j^N W_\beta^{(ij)} V^{(j)} + f_\alpha^{(i)} \sum_j^N X_\alpha^{(ij)} W_\beta^{(ij)} V^{(j)} \tag{8}$$

$$\begin{bmatrix} \tilde{W}^{(ij)} \\ \tilde{W}_\beta^{(ij)} \end{bmatrix} = \begin{bmatrix} \sum_j^N W^{(ij)} V^{(j)} & \sum_j^N X_\alpha^{(ji)} W^{(ij)} V^{(j)} \\ \sum_j^N W_\beta^{(ij)} V^{(j)} & \sum_j^N X_\alpha^{(ji)} W_\beta^{(ij)} V^{(j)} \end{bmatrix}^{-1} \begin{bmatrix} \tilde{W}^{(ij)} \\ \tilde{W}_\beta^{(ij)} \end{bmatrix} \tag{9}$$

The water is assumed as weakly compressible and inviscid. The flow motion is governed by the Euler Eqs. (10) and (11) where p is the static pressure, $\vec{C}$ the velocity vector, and D/Dt the material derivative. The positions of the particles are derived from (12) while the pressure is derived from the equation of state (13) the density being known. In this equation, ρ_{ref} is the reference density and C_{ref} is the reference sound speed, which is set to $10 \cdot C_{\max}$ where $C_{\max}$ is the jet velocity.

$$\frac{D\rho^{(i)}}{Dt} = \rho^{(i)} \sum_j^N C_\beta^{(ij)} \tilde{W}_\beta^{(ij)} V^{(j)} \tag{10}$$

$$\rho^{(i)} \frac{DC_\alpha^{(i)}}{Dt} = \sum_j^N \left(p^{(i)} \tilde{W}_\alpha^{(ij)} + p^{(j)} \left(\frac{3}{4} \tilde{W}_\alpha^{(ij)} - \frac{1}{4} \tilde{W}_\alpha^{(ji)} \right) \right) V^{(j)} \tag{11}$$

$$\frac{DX_\alpha^{(i)}}{Dt} = C_\alpha^{(i)} \tag{12}$$

$$p^{(i)} = \frac{\rho_{\text{ref}} C_{\text{ref}}^2}{7} \left(\left(\frac{\rho^{(i)}}{\rho_{\text{ref}}} \right)^7 - 1 \right) \tag{13}$$

The time integration of the governing equations is solved with a modified Verlet scheme introduced by Molteni and Colagrossi [11]. The notations of the mass Eq. (10) and momentum Eq. (11) are simplified as

$$\frac{D\rho^{(i)}}{Dt} = E^{(i)} \text{ and } \frac{DC_\alpha^{(i)}}{Dt} = F_\alpha^{(i)} \tag{14}$$

The modified Verlet scheme (15) evaluates the variable at the midtime $n+1/2$, which corresponds to the time step $\Delta t/2 = (t^{n+1} - t^n)/2$. Then, the velocities are computed at the next time step $n+1$ and used to update the positions of the particles. Finally, the density is evaluated according to the new velocities and positions.

$$\begin{cases} C_\alpha^{n+1/2} = C_\alpha^n + \frac{\Delta t}{2} F_\alpha^n \\ X_\alpha^{n+1/2} = X_\alpha^n + \frac{\Delta t}{2} C_\alpha^n \\ \rho^{n+1/2} = \rho^n + \frac{\Delta t}{2} E^n \end{cases} \Rightarrow \begin{cases} C_\alpha^{n+1} = C_\alpha^n + \Delta t F_\alpha^{n+1/2} \\ \Downarrow \\ X_\alpha^{n+1} = X_\alpha^{n+1/2} + \frac{\Delta t}{2} C_\alpha^{n+1} \\ \Downarrow \\ \rho^{n+1} = \rho^{n+1/2} + \frac{\Delta t}{2} E^{n+1} \end{cases} \tag{15}$$

During the simulation, the time step Δt is adapted to fulfill the Courant–Friedrichs–Lewy (CFL) criteria defined as

$$C_{\text{ref}} \frac{\Delta t}{X_{\text{ref}}} \leq \max(\text{CFL}) \tag{16}$$

For reducing the numerical oscillations and stabilizing the simulation, the diffusive terms M_1, M_2, and A are introduced in mass (17) and momentum (18) equations.

$$\frac{D\rho^{(i)}}{Dt} = E^{(i)} \rightarrow \frac{D\rho^{(i)}}{Dt} = E^{(i)} + M_1^{(i)} + M_2^{(i)} \tag{17}$$

$$\frac{DC_\alpha^{(i)}}{Dt} = F_\alpha^{(i)} \rightarrow \frac{DC_\alpha^{(i)}}{Dt} = F_\alpha^{(i)} + A_\alpha^{(i)} \tag{18}$$

The damping of the spurious oscillation in the pressure field proposed by Fatehi and Manzari [10] is applied to (17). The terms (19) and (20) represent two different formulations for the approximation of the Laplacian of the pressure. The difference between M_1 and M_2 is used as a numerical filter to damp the pressure oscillations.

$$M_1^{(i)} = -\rho^{(i)} \Delta t \sum_j^N \left(p_\alpha^{(i)} - p_\alpha^{(j)} \right) \tilde{W}_\alpha^{(ij)} V^{(j)} \quad \text{with} \quad p_\alpha^{(i)} = \sum_j^N \left(p^{(j)} - p^{(i)} \right) \tilde{W}_\alpha^{(ij)} V^{(j)} \tag{19}$$

$$M_2^{(i)} = 2\rho^{(i)} \Delta t \sum_j^N \frac{\tilde{W}_\alpha^{(ij)} X_\alpha^{(ij)}}{\left| \vec{X}^{(ij)} \right|^2 + 10^{-4} h^2} \left(p^{(i)} - p^{(j)} \right) V^{(j)} \tag{20}$$

The artificial viscosity proposed by Molteni and Colagrossi [11] is applied to (18) but its formulation is modified according to Morris et al. [17].

$$A_\alpha^{(i)} = 0.01 Sh C_{\text{ref}} \sum_j^N \frac{2}{1+\frac{V^{(j)}}{V^{(i)}}} \left(\frac{X_\beta^{(ij)} C_\alpha^{(ij)} \tilde{W}_\beta^{(ij)} V^{(j)}}{\left|\vec{X}^{(ij)}\right|^2 + 10^{-4} h^2} \right) \text{ with } S = \begin{cases} 0 & C_\beta^{(ij)} X_\beta^{(ij)} \geq 0 \\ 1 & C_\beta^{(ij)} X_\beta^{(ij)} < 0 \end{cases} \tag{21}$$

At the end of every time step, the particles are shifted according to (22), which reduces the particle clustering by keeping the mean distance between two particles close to X_{ref}. In the present study, the shifting method is taken from Vessaz et al. [13]. This shifting method combines the benefits of the methods of Xu et al. [14] for internal flows and Jahanbakhsh et al. [1] for free-surface flows.

$$\delta\vec{X}^{(i)} = 0.0125 C_{\max} \Delta t \vec{R}^{(i)} \tag{22}$$

The shifting vector introduced by Xu et al. [14] is defined in (23) where $r^{(ji)} = \left|\vec{X}^{(ji)}\right|$ is the distance and $\vec{n}^{(ji)} = \vec{X}^{(ji)}/r^{(ji)}$ is the unit vector between the particle i and its neighbor j.

$$\vec{R}^{(i)} = \sum_j^N \left(\frac{\bar{r}^{(i)}}{r^{(ji)}} \right)^2 \vec{n}^{(ji)} \quad \text{with} \quad \bar{r}^{(i)} = \frac{1}{N} \sum_j^N r^{(ji)} \tag{23}$$

The shifting vector proposed by Jahanbakhsh et al. [1] is defined in (24). This approach prevents that the particles are artificially spread over the void domain in the case of a free-surface flow.

$$\vec{R}^{(i)} = \sum_j^N \left(\frac{X_{\text{ref}}}{r^{(ji)}} \right)^2 H\left(X_{\text{ref}} - r^{(ji)} \right) \vec{n}^{(ji)} \text{ with } H(x) = \begin{cases} 1 & x \geq 0 \\ 0 & x < 0 \end{cases} \tag{24}$$

The Vessaz et al. [13] shifting method selects for each particle which method is applied. The Fig. 1 presents an example of this blending between the Xu et al. [14] method (particle in blue) and the Jahanbakhsh et al. [1] one (particle in red). This selection is based on two criterions: the distance to the free surface (25) and the change of volume (26). The change of volume is used because it is directly linked to the pressure gradient by the state equation.

$$\vec{R}^{(i)} = \begin{cases} \vec{R}_{jah}^{(i)} & \forall c^{(j)}, \exists c^{(j)} \leq 0.75 \\ \vec{R}_{xu}^{(i)} & \forall c^{(j)}, c^{(j)} > 0.75 \end{cases} \text{ with } c^{(i)} = \sum_j^N W^{(ij)} V^{(j)} \tag{25}$$

$$\vec{R}^{(i)} = \begin{cases} \vec{R}_{jah}^{(i)} & \left| \frac{V^{(i)n+1}}{V^{(i)n}} - 1 \right| > 0.0001 \\ \vec{R}_{xu}^{(i)} & \left| \frac{V^{(i)n+1}}{V^{(i)n}} - 1 \right| \leq 0.0001 \end{cases} \tag{26}$$

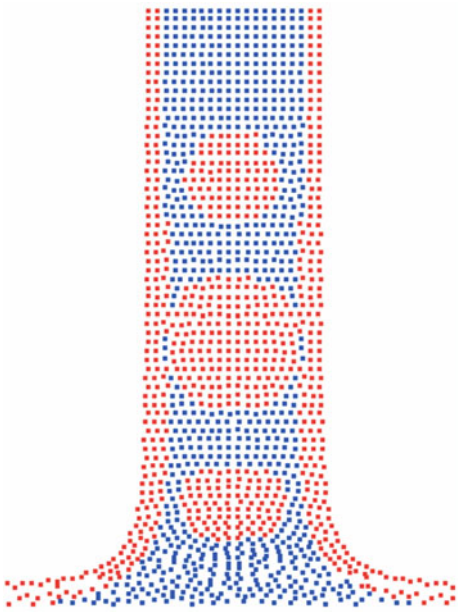

Fig. 1 Blending example for the Vessaz et al. [13] shifting method

3 Results

In the present case study, the FPM simulations of a 3D water jet are compared to the CFD and experimental results from Kvicinsky et al. [16]. The CFD results were generated by a grid-based volume of fluid method with the commercial software ANSYS-CFX®. Pictures of the impinging jet at the outlet of a Pelton injector are given in Figs. 2 and 3.

An outline of the case study is represented in Fig. 4. The center of the plate corresponds to the center of the Cartesian coordinate system and the plate is parallel to the *XY* plane. The plate is considered as a free-slip boundary. This boundary is represented by three layers of dummy particles located under the plate. The spacing in the boundary particles is equal to X_{ref}, the reference particle spacing in the fluid. The inlet of the jet has a diameter $D = 0.03$ m and is located at $Z_{\text{ref}} = 0.1$ m above

Fig. 2 Water jet impinging on the plate at 90° [16]

Fig. 3 Water jet impinging on the plate at 30° [16]

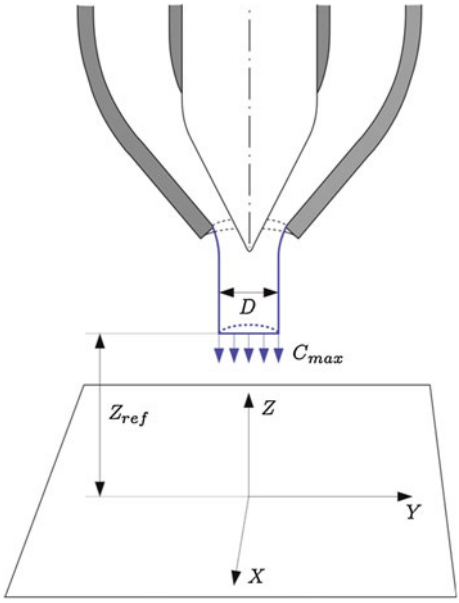

Fig. 4 Outline of the impinging jet test case

the flat plate. The inlet velocity is imposed to $C_X = C_Y = 0$ m s^{-1} and $C_Z = -C_{\max} = -19.81$ m s^{-1}. The gravity $g = -9.81$ m s^{-2} is applied along the Z axis.

The computational domain is split into four subdomains according to the XZ and YZ planes. The simulations are run on 4 cores of an Intel Xeon CPU X5570 at 2.93 GHz with 16 cores and 32 GB of memory. At $t = 0$ s, the fluid particles start to be injected at the inlet of the computational domain. The end of the simulation corresponds to the simulated time $t = 0.03$ s.

The influences of spatial and time discretization are investigated for different values of particle spacing and maximum CFL criterion given in Table 1. This table provides the elapsed computational hours and the total number of particles at the end of the simulations, which is equal to the fluid particles plus the dummy particles of the wall.

The evolution of the pressure coefficient on the flat plate is compared to the CFD and experimental results from Kvicinsky et al. [16]. The influence of the

Table 1 Computing time and number of particles

D/X_{ref}	Max (CFL)	Computing hours	Number of particles
10		0.71	38,106
20	0.3	5.97	181,028
40		78.42	956,409
	0.1	16.26	181,254
20	0.3	5.97	181,028
	0.5	5.43	167,069

particle spacing is analyzed for different X_{ref}, which correspond to 10, 20, and 40 particles uniformly distributed in the jet cross section. The time history of the pressure coefficient

$$C_p = \frac{p - p_{\text{ref}}}{\frac{1}{2}\rho_{\text{ref}} C_{\text{max}}^2} \tag{27}$$

at the center of the plate is given in Fig. 5 for the different spatial resolutions. To analyze the accuracy of the converged simulations, the pressure signals are averaged in time for the values of $t \cdot C_{\text{max}}/Z_{\text{ref}} \geq 3$. This averaged pressure coefficient is plotted in Fig. 5 along the X axis of the plate. The first observation is that the pressure peak is well reproduced for all the discretizations. The second observation is that small oscillations appear for $|X/D| < 0.25$ when the spatial discretization is the coarsest.

The influence of the time steps size is analyzed for a maximum CFL of 0.1, 0.3, and 0.5. The time-averaged evolution of C_p along the X axis of the plate is represented in Fig. 6. This figure highlights the instability of the simulation with a maximum CFL of 0.5. The simulations with a maximum CFL of 0.1 and 0.3 present similar C_p profiles.

Consequently, the particle spacing, which corresponds to $D/X_{\text{ref}} = 20$ and the maximum CFL of 0.3, is selected for the following simulations. These chosen parameters provide a reasonable accuracy for a computational time below six

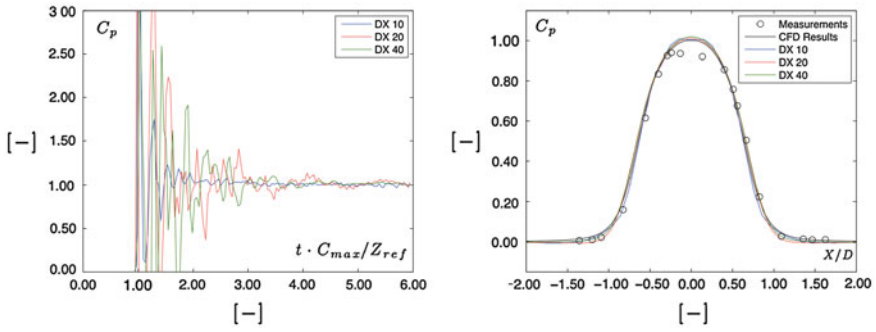

Fig. 5 Influence of particle spacing on the time history of C_p at the center of the plate (*left*) and averaged C_p along the X axis (*right*)

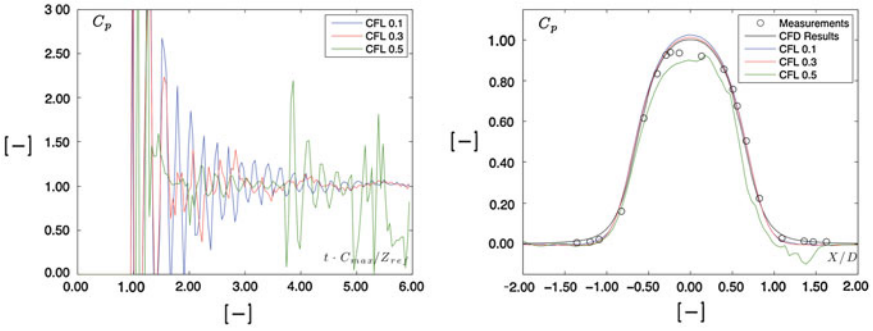

Fig. 6 Influence of maximum CFL on the time history of C_p at the center of the plate (*left*) and averaged C_p along the X axis (*right*)

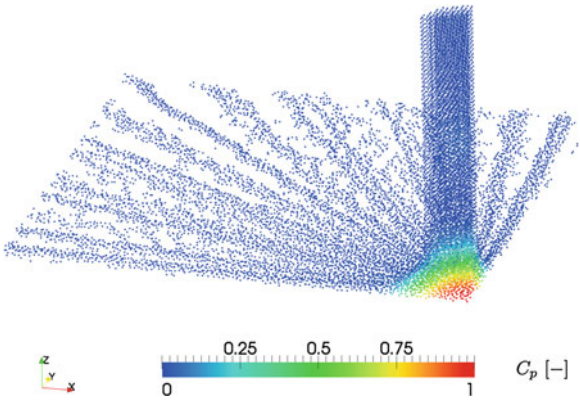

Fig. 7 Pressure coefficient at the end of the simulation

hours. The Fig. 7 represents the repartition of the pressure coefficient inside the flow at the end of the simulation. The qualitative prediction of the flow is in good agreement with the theory. The location of the free surface in the XZ plane is compared to the CFD and measurements of Kvicinsky et al. [16] in Fig. 8. The FPM results are able to reproduce accurately the free surface of the flow.

The influence of the impinging angle is investigated for the 60° and 30° cases. In both cases, the plate is rotated along the Y axis according to the prescribed angle. Similarly to the perpendicular case, the averaged C_p profile is recorded along the X axis. The Fig. 9 shows the comparison between these profiles and the CFD and measurements from Kvicinsky et al. [16]. According to these results, the FPM simulations are able to reproduce accurately the pressure profile. However, the 60° case shows that the spatial decomposition has to be equal to $D/X_{\text{ref}} = 20$, or finer, to fit properly the measurements.

The Fig. 10 shows the free-surface location in the plane XZ compared to the CFD and measurements from Kvicinsky et al. [16]. The 30° case fits properly the

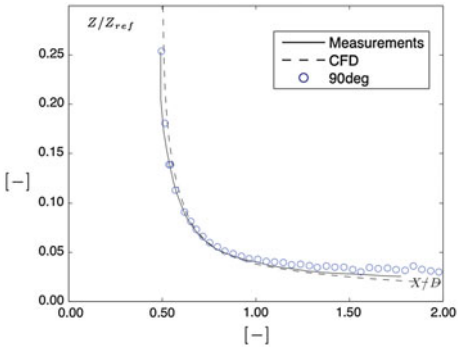

Fig. 8 Free-surface location in the plane *XZ* for an impinging angle of 90°

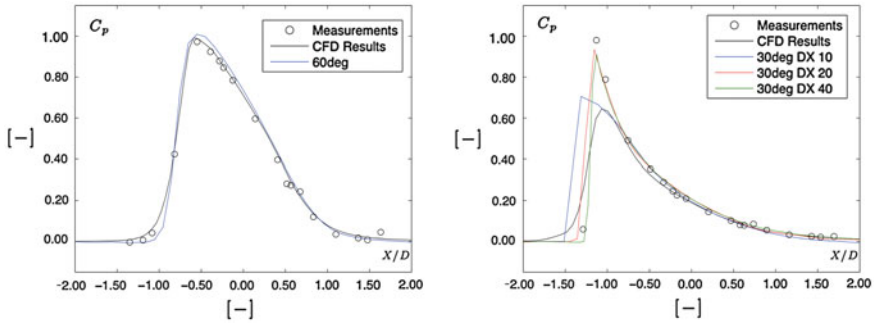

Fig. 9 Averaged C_p along the *X* axis for an impinging angle of 60° (*left*) and 30° (*right*)

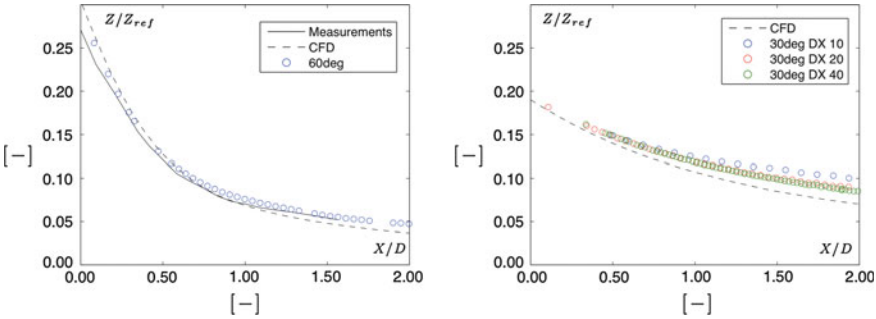

Fig. 10 Free-surface location in the plane *XZ* for an impinging angle of 60° (*left*) and 30° (*right*)

measurements, but the 60° case presents a higher water thickness on the plate compared to the CFD. This difference is reduced when the spatial discretization is increased. Unfortunately, it was not possible to make the measurements at this impinging angle, to validate the water thickness of the simulation.

4 Conclusion

The present analysis of a high-speed water jet impinging on a flat plate has shown the influence of different impinging angles. The spatial and time discretizations have been validated for the perpendicular case. The validation of the results is based on the pressure profile and on the free-surface location. The FPM simulations are in good agreements with the available CFD and measurements for the three different impinging angles. However, the simulations at a high impinging angle have shown that the spatial discretization has to be sufficient to fit properly the CFD and measurements.

Acknowledgements The authors would like to thank particularly the Ark, the foundation for innovation of Valais Canton, which is financially supporting within the Project HydroVS the research leading to the results presented in this chapter and ALSTOM Hydro for their financial support and technical assistance to the development of the SPHEROS software.

References

1. Jahanbakhsh, E., Pacot, O., & Avellan, F. (2011). Improving accuracy of viscous fluid simulation using finite particle method. *6th International SPHERIC Workshop*, (pp. 133–138).
2. Antuono, M., Colagrossi, A., Marrone, S., & Molteni, D. (2010). Free-surface flows solved by means of SPH schemes with numerical diffusive terms. *Computer Physics Communications, 181*, 532–549.
3. Marongiu, J.-C., Leboeuf, F., Caro, J., & Parkinson, E. (2009). Low Mach number numerical schemes for the SPH-ALE method. Application in free surface flows in Pelton turbines, *4th International SPHERIC Workshop*, (pp. 323–330).
4. Taylor, G. (1966). Oblique impact of a jet on a plane surface, (1110). *Philosophical Transactions of the Royal Society of London A: Mathematical and Physical Sciences, 260*(1110), 96–100.
5. Marongiu, J.-C., Leboeuf, F., Caro, J., & Parkinson, E. (2010). Free surface flows simulations in Pelton turbines using an hybrid SPH-ALE method. *Journal of Hydraulic Research, 48*, 40–49.
6. Marongiu, J.-C., Parkinson, E., Lais, S., Leboeuf, F., & Leduc, J. (2010). Application of SPH-ALE method to Pelton hydraulic turbines. *5th International SPHERIC Workshop*, (pp. 253–258).
7. Monaghan, J. J. (2005). Smoothed particle hydrodynamics. *Reports on Progress in Physics, 68*, 1703–1759.
8. Liu, M. B., & Liu, G. R. (2010). Smoothed particle hydrodynamics (SPH): An overview and recent developments. *Archives of Computational Methods in Engineering, 17*, 25–76.
9. Fang, J., Parriaux, A., Rentschler, M., & Ancey, C. (2009). Improved SPH methods for simulating free surface flows of viscous fluids. *Applied Numerical Mathematics, 59*, 251–271.
10. Fatehi, R., & Manzari, M. T. (2011). *A consistent and fast weakly compressible smoothed particle hydrodynamics with a new wall boundary condition*. Fluids: International Journal of Numerical Methods in Fluids.
11. Molteni, D., & Colagrossi, A. (2009). A simple procedure to improve the pressure evaluation in hydrodynamic context using the SPH. *Computer Physics Communications, 180*, 861–872.

12. Monaghan, J. J. (2000). SPH without a tensile instability. *Journal of Computational Physics, 159*, 290–311.
13. Vessaz, C., Jahanbakhsh, E., & Avellan, F. (2012). FPM simulations of a 3D impinging jet on a flat plate comparison with CFD and experimental results. *7th International SPHERIC Workshop*, (pp. 214–220).
14. Xu, R., Stansby, P., & Laurence, L. (2009). Accuracy and stability in incompressible SPH (ISPH) based on the projection method and a new approach. *Journal of Computational Physics, 228*, 6703–6725.
15. Jahanbakhsh, E., Pacot, O., & Avellan, F. (2012). Implementation of a parallel SPH-FPM solver for fluid flows. *Zetta, 1*, 16–20.
16. Kvicinsky, S., Longatte, F., Kueny, J.-L., & Avellan, F. (1999). Free surface flows: Experimental validation of volume of fluid method in the plane wall case. *3rd ASME/JSME Conference*.
17. Morris, J. J. P., Fox, P. J., & Zhu, Y. J. (1997). Modelling low Reynolds number incompressible flows using SPH. *Journal of Computational Physics, 136*, 214–226.

A Vortex Modeling with 3D CFD

Grégory Guyot, Hela Maaloul and Antoine Archer

Abstract Until now, the fine representations of the complex hydraulic phenomena such as Vortex rely on physical modeling for industrial purposes. EDF has been testing the 3D CFD code "Flow 3D©" for free surface flow simulation since five years. The main difficulty of using finite elements programs is the relevance and the stability of their numerical results. EDF decided to test in the field of vortex how reliable Flow 3D is. Flow 3D is a commercial CFD code using VOF method with a rectangular mesh. In this study, it is assumed that flow is liquid water with an interface simulated by VOF method. This study is based on a schematic hydraulic experimental model realized in the EDF-R&D laboratory. The chosen case is a simple configuration of a vertical downward drain hole. The basin is one meter length and around a half meter width. The water level is fixed, and the flow rate is adjustable. The main advantage of this experiment is that the geometry is easy to simulate with 3D CFD software. In this configuration, it is ensured that a vortex phenomenon exists and that it is stable during experimentations. An aerated vortex with no air flow rate has been chosen for the validation case. The aerated vortex length reaches the basin bottom. The first goal of the 3D CFD simulation is to check whether Flow 3D© is able to represent a vortex when it physically exists. The second objective is to find the simplest set of CFD parameters that represents the vortex as it appears in the physical experimentation.

Keywords Vortex · Water intake · Complex hydraulic phenomenon · Numerical simulation · CFD · VOF method

G. Guyot (✉) · H. Maaloul
EDF-CIH, Savoie Technolac, Le Bourget du Lac 73373, France
e-mail: gregory.guyot@edf.fr

H. Maaloul
e-mail: hela.maaloul@edf.fr

A. Archer
EDF-R&D, 6 quai Watier, Chatou 78401, France
e-mail: antoine.archer@edf.fr

P. Gourbesville et al. (eds.), *Advances in Hydroinformatics*,
Springer Hydrogeology, DOI: 10.1007/978-981-4451-42-0_35,

1 Introduction

This study was prompted by practical problems encountered in many situations of hydraulic engineering such as industry, irrigation, and water power generation. Water is often pumped from free surface basins or tanks by intakes. For some cases, air-entraining free surface vortices can appear. This phenomenon can cause operational troubles or damages for turbine, pumps, or hydraulic networks, such as loss of performance, noise and vibration, [1–3]. Nowadays, the most efficient way to avoid vortices is to ensure that the minimum water head is greater than the critical submergence head and to check that no vortex appears using physical models at reduced geometric scale.

Several studies have investigated the critical submergence [4, 5], and standards have been published [6, 7]. For non-conventional designs, these criteria can be considered inadequate and the use of a physical model is then necessary.

However, for some projects, a physical model study with several intake geometries may not be possible because of time and financial constraints.

Until now, the fine representation of the complex hydraulic phenomena such as Vortex relies on physical modeling for industrial purposes. But progress in the computational fluid dynamics (CFD) field leads to use this new tool for the vortex phenomenon [8, 9].

EDF has been testing the three-dimensional CFD code "Flow 3D©" since five years. This software is a commercial CFD code, based on a finite element method and using VOF method with a rectangular mesh. The main difficulty of using finite elements programs is the relevance and the stability of their numerical results. EDF decided to test in the field of vortex how reliable "Flow 3D©" is.

The aim of the study is to test the code and to find the easiest way to have compliant qualitative representation of vortex phenomenon.

In order to ensure that the CFD software is able to represent vortices when they physically exist, an oversimplified geometry and a schematic hydraulic configuration of intake are selected to be tested on a dedicated physical model. At a first attempt, a "steady" vortex without air flow is selected on the physical model and the same configuration is simulated with the CFD code. Influence of different sets of parameters is studied.

In this chapter, an attempt is made to propose a simplify method to detect with CFD the risk of vortices formation.

2 Experimental Setup

2.1 Geometrical Configuration

In this section, we describe the experimental setup in which the "steady" vortex is created. The prototype structure is a rectangular tank with 1 m length and 0.46 m width. The vertical downward intake pipe is centered at 0.23 m from the end wall

and from the two side walls. The internal diameter of the outlet pipe is 0.05 m, and the fillet radius is 2.5 mm.

Before the main tank, three trashracks in-between four grids are set to control the velocity field and to insure homogeneous flow conditions. The prototype is a closed circuit.

The prototype is made with Plexiglas to allow easy observations. The experimental setup is shown in Fig. 1.

A second geometry is also tested: an obstacle is put though the inlet flow so as to initiate a rotational flow. This obstacle is a brick, higher than the water level, which stop the flow from one side, as shown in Fig. 3 (Fig. 2).

2.2 Hydraulic Conditions

The flow rate is controlled and set at the fixed value of 3.9 m^3h^{-1} (that is 0.001083 m^3/s). The water depth in the basin is 0.10 m. Those parameters were selected to obtain a steady vortex without air flow in the tank and with an aerated core length equal to the water level, that is 0.1 m.

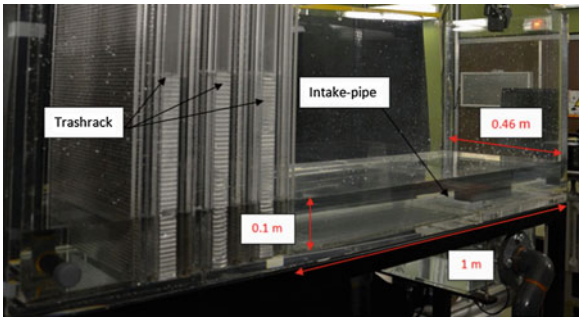

Fig. 1 View of the experimental setup

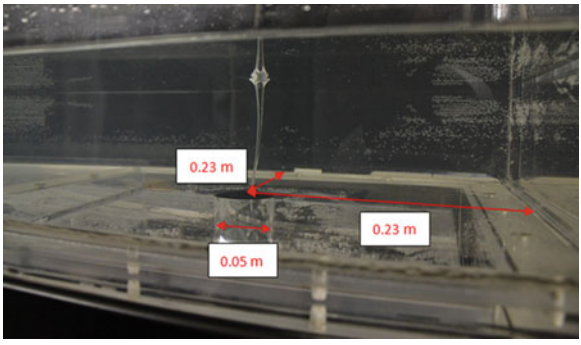

Fig. 2 View of intake pipe location

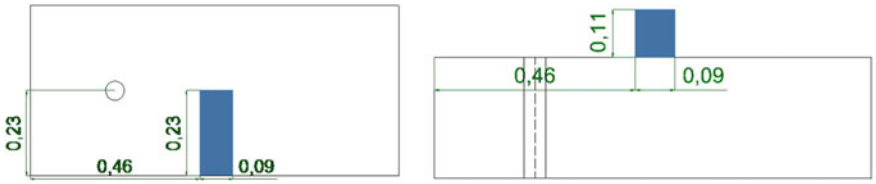

Fig. 3 Second configuration plan view and elevation

2.3 Measurements and Experimental Results

Vortex formation and aerated core length is first visually observed. Velocity fields measurements are then performed using particle image velocimetry (PIV). Tap water is used in the experiment, and no particular seeding is needed. Time delay between two successive images is adjusted according to the measurement location.

Plan velocity map (gibing two components of the flow velocity) are measured:

- At the tank inlet, 0.1 m downstream the grids: in different horizontal planes and different vertical plane parallel to the main flow direction;
- Around the vortex, in different horizontal planes, collecting the images from the bottom, in order not to deform light rays by the curved vortex free surface.

Vertical measurement planes are also caught, but they may be less relevant because of the vortex movement around its mean position.

Figure 4 gives the axial horizontal inlet velocity at mid-height of the flow (named as $Z = 0.05$ m).

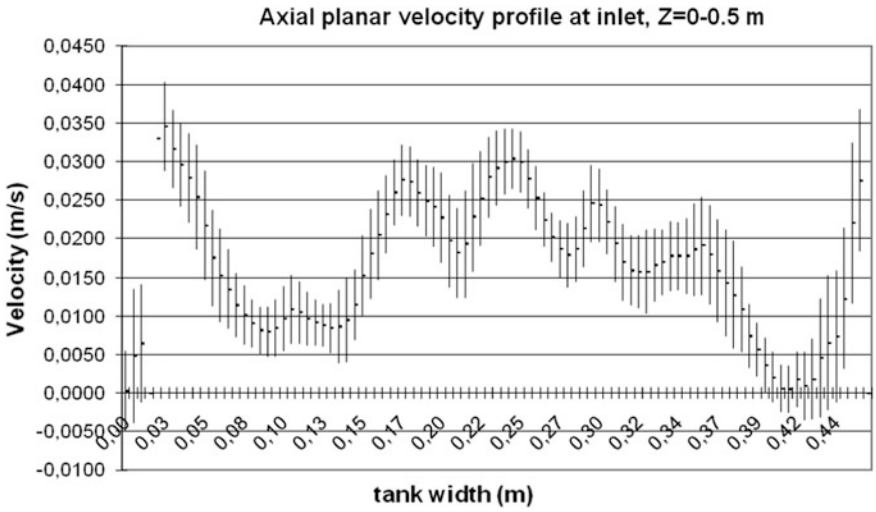

Fig. 4 Velocity profile at tank inlet

Though rectifying devices, the flow is not homogenous and large fluctuations occur. The low velocities are may be too low to give a stationary inflow.

Figure 5 gives the orthoradial velocity around the vortex core, at $Z = -0.05$ m level.

More measurements are needed to better characterize the flow around the aerated vortex.

Velocity measurement around a vortex is therefore not so easy: images must be collected from bottom to avoid diffraction by the free surface and the slow motion does not allow easy velocity averaging. Dedicated image treatment is then needed to get averaged velocity value.

3 "Flow 3D" VOF Numerical Simulation

3.1 The Numerical Model Geometry

We decide that the geometry used in the numerical model must be as real as possible. Nevertheless, the calculation time must be the most optimized one with reliable results.

So that after different tests, we select the configuration that is shown in the Figs. 6 and 7.

The geometry of the tank is totally respected. The trashracks are modelized by three lines of broken walls. The geometry is perfectly symmetric.

The hydraulic network is represented by single pipe.

The flow rate is provided by a rotative pump model. This model uses the performance curves given by the pump manufacturers to transform pressure drop created by the pump into a flow rate that pass though the device. In the numeric model, the pump is simulated by a phantom component meaning that there is no

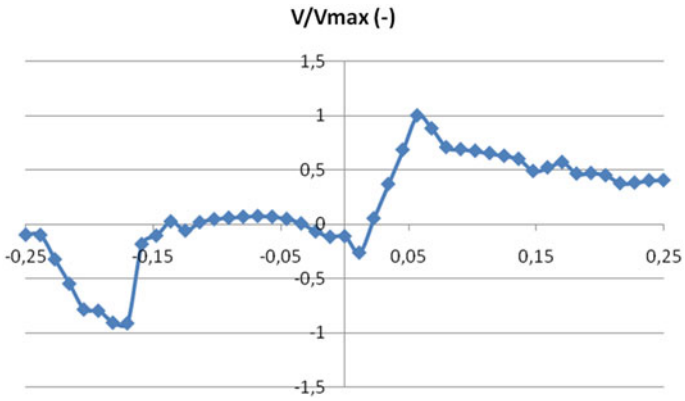

Fig. 5 Non-dimensional orthoradial velocity around the vortex core at $z = -0.05$ m

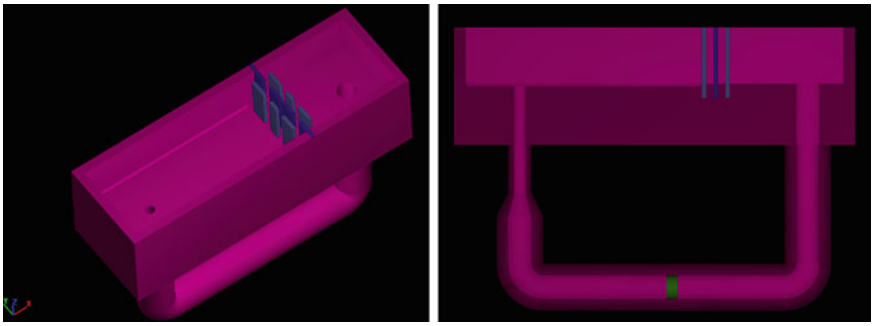

Fig. 6 View of the numerical setup for first configuration

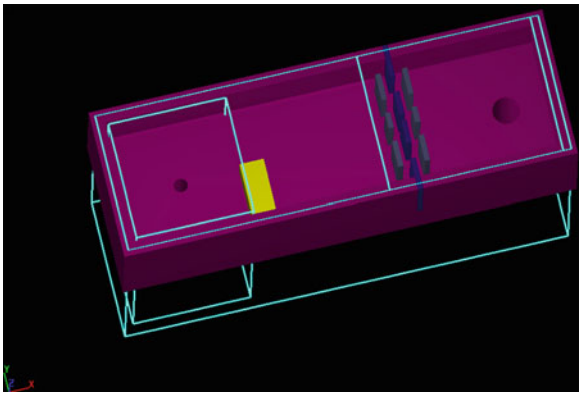

Fig. 7 View of the numerical setup for second configuration

obstacle or blockage effect in the modelized area, but the pump effect is well simulated.

Both geometric configurations mentioned (without and with the obstacle) are simulated by numerical approach.

The mesh is made of 2,000,000 square cells. The cell size is 0.01 m (Fig. 8).

3.2 CFD Model and Vortex Markers

Flow 3D is a commercial CFD code using VOF method with a rectangular mesh. In this study, it is assumed that flow is liquid water with an interface simulated by VOF method. The flow is assumed as transient during all the calculation. The turbulence model used in the following simulations is a very large eddy simulation (VLES) model. No roughness is considered but the fluid velocity is equal to zero at the walls.

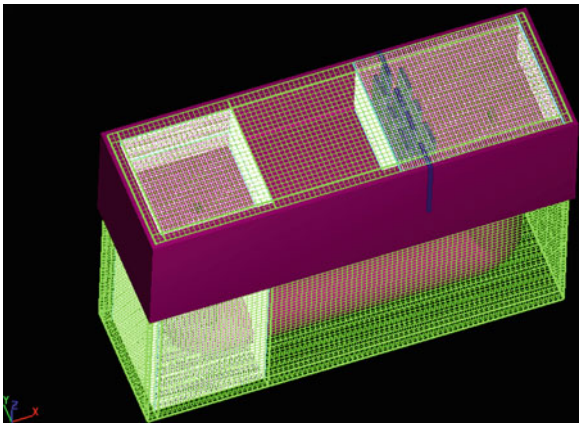

Fig. 8 View of the mesh

It is important to remind that one objective of this study is to determined the lightest set of parameter that allows the vortex appearance. Other sets of parameters have been tested to provide sensitive studies during the study such as RNG or LES model, different type of mesh, but the results of those simulations are not developed in this chapter. In order to write a clear article, only the chosen parameters are presented in this chapter.

At this step of our calculations, vortices are identified in the post processing by observation of the free surface deformation and by using the z-vorticity and the vorticity magnitude. Other makers could be used to determined the vortices strength, like helicity or Q criterion [10–12].

3.3 Result of Numerical Approach

3.3.1 First Configuration

The result given by the code is a steady vortex over the intake pipe as it appears in the physical model. The figures below show the vorticity taken on two planes for $z = -0.09$ m and $z = -0.04$ m (Fig. 9).

So, the code is able to represent a vortex when it exists in physical model even if the geometry is perfectly symmetric. The vortex core is slowly moving during the simulation as it is observed on in physical model.

This qualitative result is compliant but the vortex shape is not really similar to the shape observed on physical model as represented in the following figure. The Fig. 4 gives the axial horizontal inlet velocity at mid-height of the flow. In the physical model, the flow is not homogenous and a large fluctuation occurs, whereas in the numerical model, the velocity field is symmetric at the beginning of the tank as shown in the Fig. 10. This difference could be one of the raisons that explain the vortex shape difference between the numerical model (see Fig. 12) and the physical model (see Fig. 2) (Fig. 11).

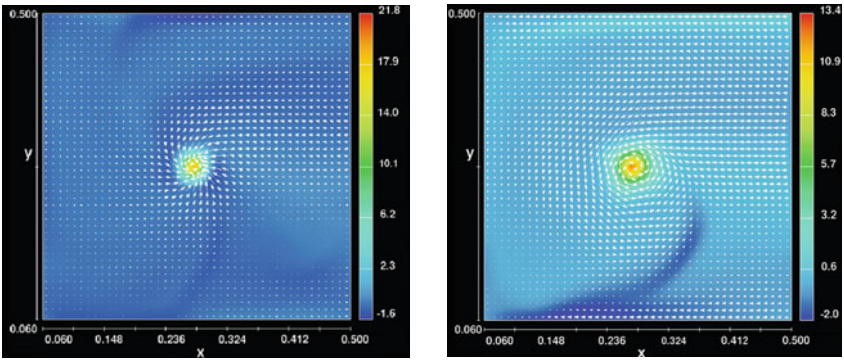

Fig. 9 **a** Vorticity at $z = -0.09$ m. **b** Vorticity at $z = -0.04$ m

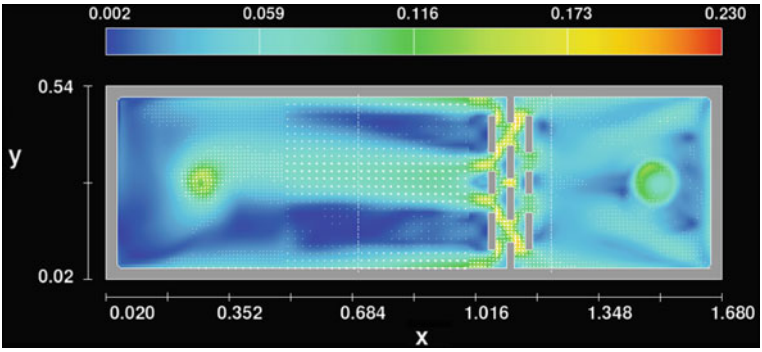

Fig. 10 Velocity field at $z = -0.09$ m

Fig. 11 3D view of the first configuration

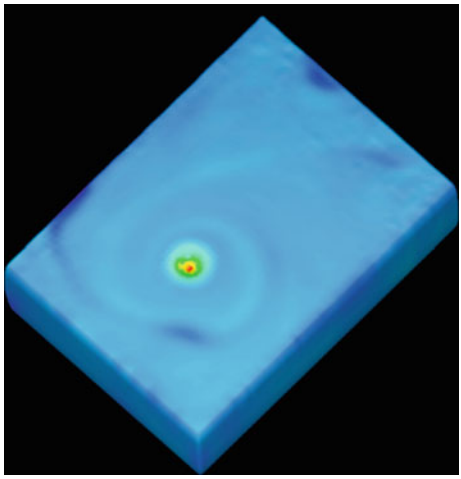

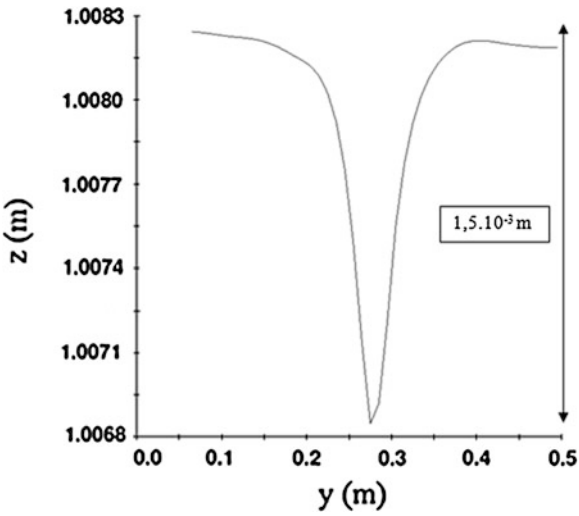

Fig. 12 Vortex shape for the first configuration

Vortex length is much shorter in CFD than in the experiment. The mesh size is probably of great influence too.

3.3.2 Second Configuration with Left Side Brick

The result given by the code is also a steady vortex over the intake pipe. This vortex is stronger than the one in the first configuration as it was seen in physical model. The figures below show the vorticity taken on two planes for $z = -0.09$ m and $z = -0.04$ m and give the vortex length (Figs. 13, 14, 15, 16, 17, 18).

3.3.3 Second Configuration with Right Side Brick

Like the previous simulation, the result given by the code is a steady vortex over the intake pipe as it appears in the physical model. This vortex is also stronger than the one in the first configuration 1. When the brick is shifted on the right side, the rotative direction of the vortex is inverted. But the vorticity remains the same as the second configuration with the obstacle on the left bank. The figures below show the vorticity taken on two planes for $z = -0.09$ m and $z = -0.04$ m.

The result given by the comparison between the two geometries if the second configuration is that the numerical vortices have a similar behavior as the physical one.

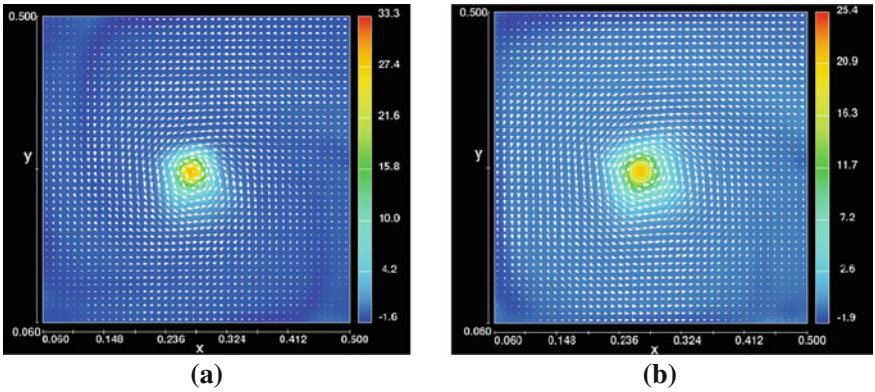

Fig. 13 **a** Vorticity at $z = -0.09$ m. **b** Vorticity at $z = -0.04$ m

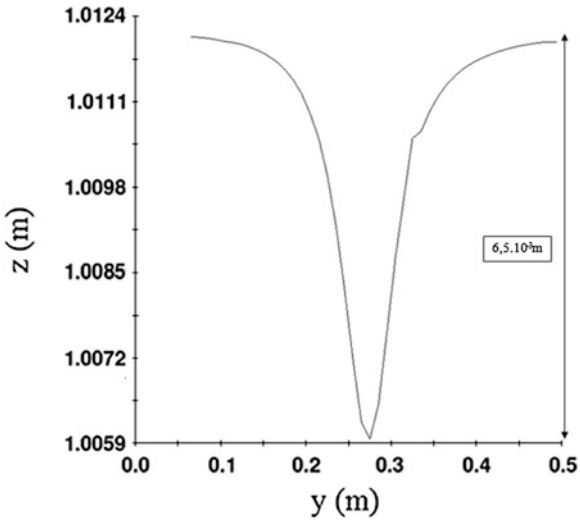

Fig. 14 Vortex shape for the second configuration

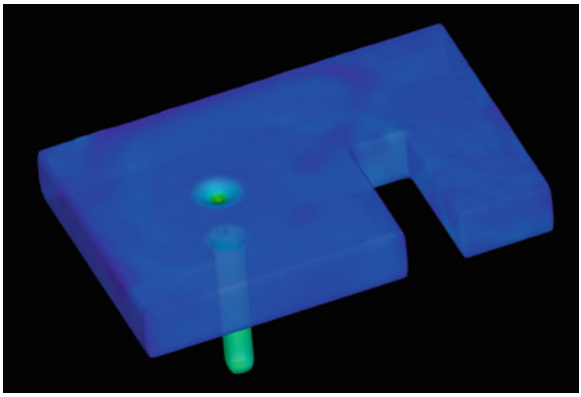

Fig. 15 3D view of the second configuration

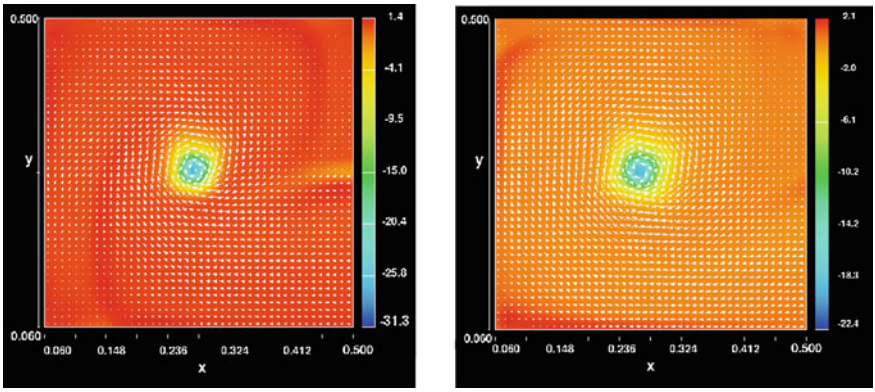

Fig. 16 **a** Vorticity at $z = -0.09$ m. **b** Vorticity at $z = -0.04$ m

Fig. 17 Vortex shape

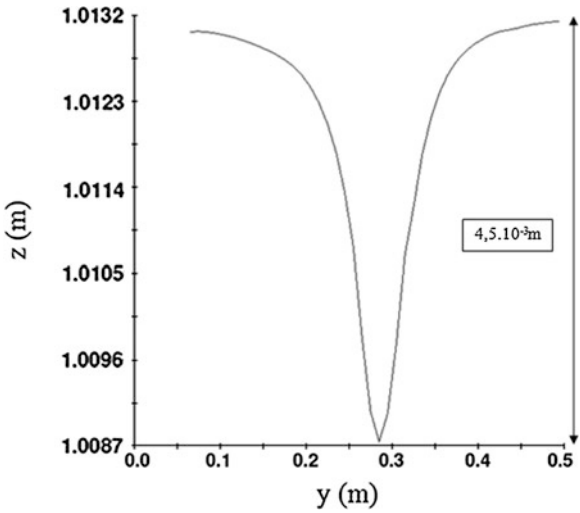

Fig. 18 3D view of the second configuration

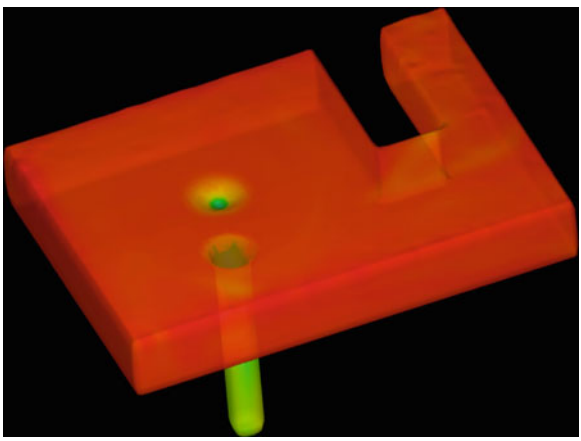

4 Conclusions

This study shows that a CFD code using a VOF method for interface tracking is able to represent a vortex when it appears in a physical model for a simple and perfectly symmetric geometry. The results given by the numerical approach are compliant for qualitative aspect, but they are not representative for the length of the vortex.

Then, the CFD tool can be envisaged for preliminary design. However, more complete validation work is needed: parametric numerical studies, including test of other vortex markers, and more complete experimental measurements are to be pursued.

Effort is still needed to model this complex albeit often met hydraulic phenomenon and to cease the use of physical models and their similarity laws.

References

1. De Siervi, F., Viguier, H.C., Greitzer, E.M., & Stan, C.S. (1982). Mechanisms of inlet-vortex formation. *Journal of Fluid Mechanic, 124*, 173–207.
2. Levi, E. (1991). Vortices in hydraulics. *Journal of Hydraulics Engineering, 117*(4), 399–413.
3. Hunt, J.C.R., Wray, A.A., Moin, P. (1998). Eddies,stream, and convergence zones in turbulent flows. Centre for Turbulence Research Report CTR-S88, 193.
4. Jain, A.K., Ranga Raju, K.G., & Garde, R.J. (1978). Vortex formation at vertical pipe intakes. *Journal of the Hydraulics Division, ASCE, 104*(10), 1429–1445.
5. Padmanabhan, M., & Hecker, G.E. (1984). Scale effects in pump sump models. *Journal of Hydraulic Engineering, 110*(11), 1540–1556.
6. AFNOR (2009). Fascicule de documentation de l'AFNOR n° FD CEN/TR 13930. Pompes rotodynamiques: conception des ouvrages d'aspiration: recommandations d'installation des pompes.
7. ANSI (1998). Pump intake design. American National Standard Institute ANSI/HI 9.8-1998.
8. Tokyay, T.E., Constantinescu, S.G. (2005). Large eddy simulation and reynolds averaged Navier-Stokes simulations of flow in a realistic pump intake: A validation study. *Impacts of global climate change* (pp. 1–12). doi:10.1061/40792(173)423
9. Minisci, E., Telib, H., Cicatelli, G. (2005). Hydraulic design validation of the suction intake of a vertical centrifugal pump station, by use of computational fluid dynamic (CFD) analysis. *Proceeding of the ASME Fluids Engineering Division Summer Meeting and Exhibition*, Houston, USA, June 19–23 2005.
10. Chong, M.S., Perry, A.E., & Cantwell, B.J. (1990). A general classification of three-dimensional flow fields. *Journal Physics of Fluids, A2*(5), 408–420.
11. Levy, Y., Degani, D., & Seginer, A. (1990). Graphical visualization of vertical flows by means of helicity. *AIAA Journal, 28*(8), 1347–1352.
12. Jeong, J., & Hussain, F. (1995). On the identification of a vortex. *Journal Fluid Mechanic, 285*, 69–94.

Bubble-Stirred Melts in Vitrification

Delphine Gautheron, Armand Bonnetier, Emilien Sauvage, Jean-François Hollebecque, Patrice Brun, Roland Riva and Yves Du Terrail

Abstract A numerical simulation was performed in Fluent® to optimize bubble stirring in a melting pot. The study focused mainly on optimization of the gas injection positions and sparging rates. Coalescence of bubble trains was studied in detail through a numerical analysis implementing the VOF method as well as an innovative method developed in the laboratory. This numerical study is also based on hydraulic similarity tests with a mock-up and oil bath. This article describes the numerical model of this complex phenomenon and quantifies the overall improvement in oil bath flow within the oil volume concerned.

Keywords Modeling · Simulation · Coalescence · Fluent® · Volume of fluid model

D. Gautheron (✉) · A. Bonnetier · E. Sauvage · J.-F. Hollebecque · P. Brun
CEA, DEN, DTCD, SCDV, LDPV: Marcoule, 30207 Bagnols-sur-Cèze, France
e-mail: delphine.gautheron@cea.fr

A. Bonnetier
e-mail: armand.bonnetier@cea.fr

E. Sauvage
e-mail: emilien.sauvage@cea.fr

J.-F. Hollebecque
e-mail: jean-françois.hollebecque@cea.fr

P. Brun
e-mail: patrice.brun@cea.fr

R. Riva
CEA, DEN, DM2S, STMF, 38054 Grenoble, France
e-mail: roland.riva@cea.fr

Y. D. Terrail
SIMaP, EPM ENSEEG, BP 75, 38402 Saint Martin d'Hères Cedex, France
e-mail: yves.duterrail@simap.grenoble-inp.fr

P. Gourbesville et al. (eds.), *Advances in Hydroinformatics*,
Springer Hydrogeology, DOI: 10.1007/978-981-4451-42-0_36,

1 Introduction

Multipoint bubble stirring is one of the options investigated for liquid homogenization. Depending on the height of the oil bath, we can observe the coalescence of bubble trains. Our objective is to manage coalescence to optimize the stirring of the oil bath. Hydraulic similarity studies are conducted to facilitate data acquisition for use with numerical models.

Two methods for simulating bubble stirring are examined here and compared with experimental measurements. One is a numerical method with VOF interface tracking, and the other a semi-empirical method simulating fluid entrainment by bubbling without explicitly following the liquid–gas interface. The bubbling typology and experimental method are first described, and then the numerical models, followed by the results obtained for a single bubble train. Coalescence is then discussed with the experimental and simulation results.

2 Description of Bubbling Models

2.1 Type of Bubble Flow

Bubble flow concerns the motion of a gas in a liquid. Buoyancy causes the gas bubbles to rise to the surface. This study concerns discrete bubble flow. The bubble path is determined by the net result of the forces exerted on the bubble: inertia, buoyancy, viscous drag, surface tension, and gas motion through the orifice. Hydraulic similarity tests are performed in an oil bath. Two dimensionless numbers are used to define the type of bubbles: the Reynolds number, Re, and the Eötvös number, Eö (also known as the Bond number, Bd). The bubble-rising velocity V_g determined experimentally or by correlation is about 0.5 m·s^{-1}, and their modal diameter d_e is 5 cm. Hence,

$$\mathrm{Re} = \frac{\rho_L V_g d_e}{\mu_L} = 2.9\text{–}12.5, \tag{1}$$

$$\mathrm{E\ddot{o}} = \frac{\rho_L g d_e^2}{\sigma} = 1,133, \tag{2}$$

with a liquid density $\rho_L = 970$ kg·m^{-3}, a liquid dynamic viscosity $\mu_L = 1.94$ to 8.28 Pa·s, the surface tension between gas and liquid $\sigma = 0.021$ N·m^{-1}, and the force of gravity $g = 9.81$ m·s^{-2}.

The bubble flow in our study lies outside the ranges routinely investigated (Fig. 1). The bubbles are of ellipsoidal-cap shape. Given the bath height of 0.45 m, the bubbles do not have time to reach their terminal velocity.

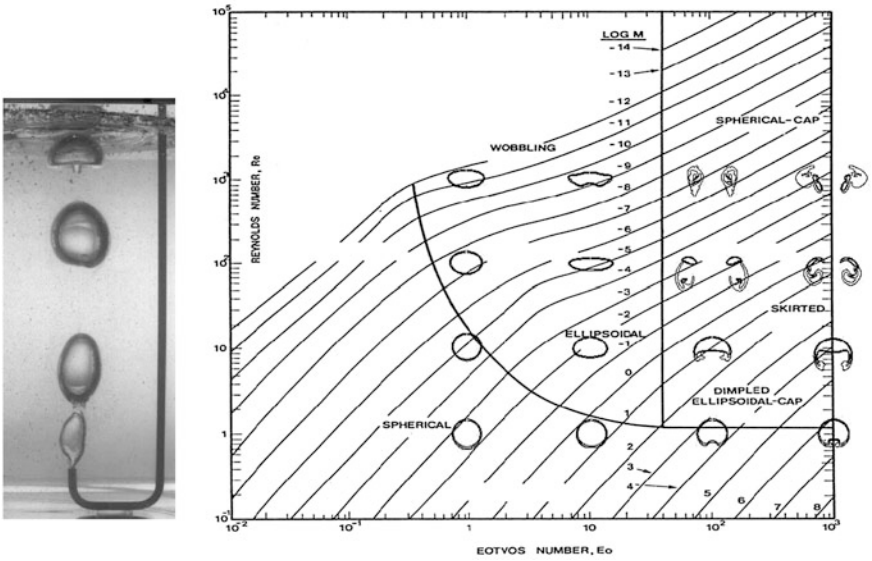

Fig. 1 Photo of bubble flow (*left*) and a diagram (Clift, Grace and Weber, 1978) showing simulated bubble shapes [10] (*right*)

2.2 Experimental Method

To validate the bubble flow model, hydraulic similarity tests were performed in an oil bath in a Plexiglas mock-up. Transparent oil was used to allow viewing of the bubble flow in the bath and to permit particle image velocimetry (PIV) measurements. The oil viscosity ranged from 1995 cSt to 8540 cSt with a density of 970 kg m^{-3}. Air was injected at flow rates ranging from 500 to 1,225 L h^{-1}.

2.3 Description of Volume of Fluid Modeling

In computational fluid dynamics (CFD), bubble flow can be modeled by the volume of fluid (VOF) method [1–3]. This numerical technique is used to track and localize the free surface (or liquid–liquid interface). It belongs to the class of Eulerian methods which are characterized by a mesh that is stationary or moves in a predictable manner to reflect the changing shape of the interface. The VOF model can represent two or more immiscible fluids by solving a single equation of momentum and following the volume fraction of each fluid in the range. The surface tension at the interface is also taken into account. The interface between the fluids is tracked by solving the continuity equation for the volume fraction of one of the fluids. For fluid q, the equation is

$$\frac{1}{\rho_q}\left[\frac{\partial}{\partial t}\left(\alpha_q \rho_q\right) + \nabla.\left(\alpha_q \rho_q \bar{\vec{v}}_q\right) = 0\right], \tag{3}$$

where ρ_q is the fluid density, α_q the fluid volume fraction in the cell, and $\vec{v}_q$ the fluid velocity. A single-momentum equation is solved throughout the range and the resulting velocity field is distributed between the fluids. The momentum Eq. (4) depends on the volume fractions of all the fluids with their density ρ and viscosity μ.

$$\frac{\partial}{\partial t}(\rho\vec{v}) + \nabla.(\rho\vec{v}\vec{v}) = -\nabla p + \nabla.\left[\mu\left(\nabla\vec{v} + \nabla\vec{v}^T\right)\right] + \rho\vec{g}, \tag{4}$$

where v is the velocity, p the pressure, and g the force of gravity.

The interface between the fluids is tracked by a piecewise linear approach. The first step is to calculate the position of the linear interface relative to the center of each partially filled element. The next step is to calculate the quantity of fluid advection through each face using the linear calculation representing the interface and information on the velocity distribution normal and tangential to the face. The third step is to calculate the volume fraction in each element using the equilibrium flow calculated during the preceding step.

One of the drawbacks of this method is its cost in terms of memory usage and computation time. A model representing bubble trains was therefore used to simulate only the fluid flow.

2.4 Semi-Empirical Bubble Train Flow Model

Work by Snabre [4, 5] resulted in a simplified numerical model reproducing as realistically as possible the stirring action induced by bubble flow in oil bath without tracking the gas–liquid interfaces. The method represents the bubble train by a column of fluid with a vertical volume force expressed by a semi-empirical law. The correlations used in the model are based on mock-up experiments covering a wide range of parameters. This method is capable of representing bubble flow with much shorter computing time. The model provides the mean velocity of a bubble train and takes into account the bubble flow rate and the fluid viscosity.

The bubble diameter (D_e) is defined by means of the Jamialahmadi correlation [6, 7]:

$$D_e = d_0\left(\frac{5}{\mathrm{Bd}_0^{1.08}} + \frac{9.261\,\mathrm{Fr}^{0.36}}{\mathrm{Ga}^{0.39}} + 2.147\,\mathrm{Fr}^{0.51}\right)^{\frac{1}{3}} \tag{5}$$

The dimensionless numbers used are the Froude number, Fr (the ratio of inertia to buoyancy), the Bond number, Bd (the ratio of buoyancy to surface tension), and the Galileo number, Ga (the ratio of the product of inertia and buoyancy to the square of the viscosity):

$$\mathrm{Fr} = \frac{V_g^2}{g d_0}, \mathrm{Bd} = \frac{\rho_L g d_0^2}{\sigma}, \mathrm{Ga} = \frac{\rho_L^2 g d_0^3}{\mu_L^2}, \tag{6}$$

where ρ_L is the liquid density, μ_L the liquid dynamic viscosity, d_0 the diameter of the injector orifice, σ the surface tension between the gas and liquid, V_g the gas flow velocity at the outlet of the injector, and g the force of gravity. The drag coefficient, C_d [8, 9]; the bubble velocity, V_B [4]; and the column void fraction, ε_G, are given by the following relations:

$$C_d = 1 + \frac{16v}{V_B D_e}, V_B^2 = \frac{4}{3}\frac{D_e g(1+\varepsilon_G)}{C_d}, \varepsilon_G = \frac{2}{3}\frac{QD_e}{V_B \mathrm{V_{ol}}} \tag{7}$$

where $\mathrm{V_{ol}}$ is the bubble volume, Q the gas flow rate, and v the kinematic viscosity.

At this point, we have determined the size of the bubbles released from the sparging tube and the void fraction in the column. The final step is to find the expression for the total force exerted by the bubbles on the fluid. It is simply equal to the product of F_t the bubble drag by N the mean number of bubbles present in the column: $F_{\mathrm{tot}} = F_t N$. Disregarding the bubble acceleration and deceleration phases, the drag force is equal to the Archimedes force: $F_{\mathrm{tot}} = \rho g \mathrm{V_{ol}}\, N$. The number of bubbles in the column is related to the void fraction: $N = \varepsilon_G(\pi d^2/4)H_Z/\mathrm{V_{ol}}$, where H_Z is the height of the column. The expression for the void fraction can be reduced to $f = \rho g \varepsilon_G$, which is the contribution of Archimedes' buoyancy to all the bubbles in the column. The result is not only very simple, but the hypothesis of disregarding the acceleration and deceleration phases is strong.

The path of the bubble train is defined by calculating the path of a single bubble with its velocity field in the bath. The bubble is modeled by a particle subjected to a force equivalent to Archimedes' buoyancy. The initial position of this particle is where the bubbles are formed. The positions are defined on the basis of observations during the hydraulic similarity tests. The Lagrangian tracking equation of a particle is

$$\frac{\mathrm{d}\vec{u}_p}{\mathrm{d}t} = F_D(\vec{u} - \vec{u}_p) + \frac{\vec{g}(\rho_p - \rho)}{\rho_p} + \vec{F}_{\mathrm{sup}} \tag{8}$$

where $\vec{u}$ is the fluid velocity, $\vec{u}_p$ the particle velocity, ρ the fluid density, ρ_p the particle density, $F_D(\vec{u} - \vec{u}_p)$ the drag force per unit of particle mass, and $\vec{F}_{\mathrm{sup}}$ an additional acceleration term. Once the path has been calculated, a user-defined function is used to determine the force and void fraction for the cells situated around the path.

3 Bubble Flow Simulation Results for a Single Bubble Train

3.1 Modeling by the Volume of Fluid Method

A single bubble train was modeled with the OpenFOAM® CFD software package (Fig. 2). To reduce the computing time, the simulation was performed in quarter-symmetry 3D; the computing time was 2 days for 1 s of simulation. The flow was assumed to be isothermal. The two-phase transient calculation was performed according to the VOF model. The free surface was taken into account by an interface, then by an imposed surface, without constraint. The inside diameter of the injection tube at the center of the tank was 4 mm; the tip of the injection tube was 50 mm above the bottom of the tank. The liquid was oil with a viscosity of 8,940 cSt and a density of 970 $kg{\cdot}m^{-3}$. The gas injected was air and the surface tension between the gas and liquid was 0.021 $N{\cdot}m^{-1}$.

Coalescence can be observed in a test with a single bubble train. It occurs when the lower bubble is entrained in the wake of the upper bubble and merges with it, increasing the size of the final bubble. This phenomenon diminishes as the liquid viscosity increases or the air injection rate decreases. The same phenomenon was observed experimentally (Fig. 3). Qualitatively, the shape of the modeled and experimental bubbles was the same, and coalescence within the bubble train occurred in both cases.

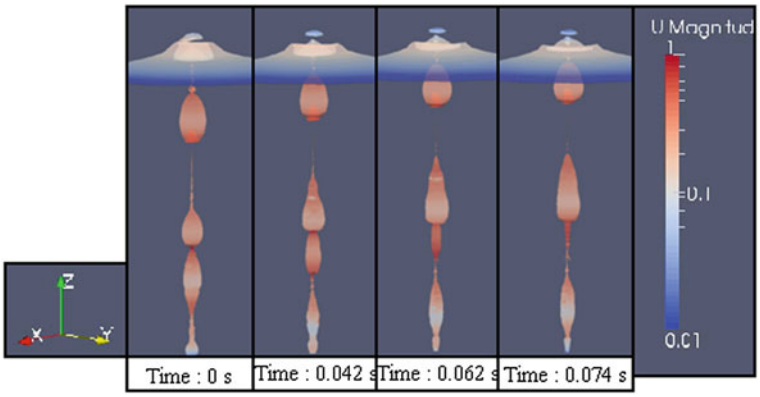

Fig. 2 VOF model of isolated bubble flow in an oil bath (viscosity 3,960 cSt, flow rate 980 $L{\cdot}h^{-1}$)

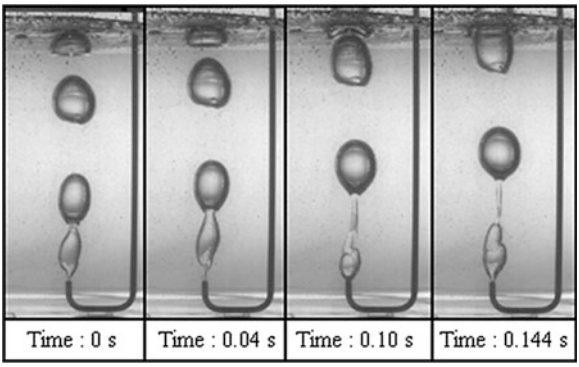

Fig. 3 Bubble train flow in an oil bath with a viscosity of 8,540 cSt and a flow rate of 1,225 $L \cdot h^{-1}$

3.2 Semi-Empirical Model

A single bubble train was modeled in a cylindrical tank containing oil (viscosity 1995 cSt and density 970 $kg \cdot m^{-3}$) with an injector at the center providing an air flow rate of 1,225 $L \cdot h^{-1}$ (Fig. 4). The bubble flow parameters included a bubble flow zone diameter $Dz = 0.038$ m and an imposed volume force $fz = 1{,}571\ N \cdot m^{-3}$. The computing time was about 15 min. The mean velocity field obtained with the model is similar to the experimental result.

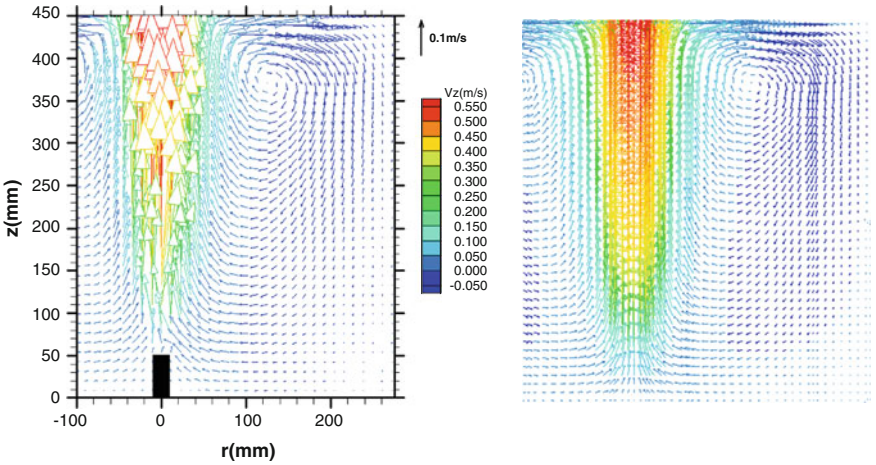

Fig. 4 Velocity field for a viscosity of 1,995 cSt and an air flow rate of 1,225 $L \cdot h^{-1}$. Experimental measurement by PIV (*left*) and semi-empirical model (*right*)

4 Coalescence Between Adjacent Bubble Trains

When two bubble trains are sufficiently close, mutual deviation of the bubble columns is observed. Coalescence then occurs between bubbles, forming a single bubble train. The bubbles rise and become distorted; the suction created by the wake of the first bubble allows the second bubble to catch up to it. The VOF model represents each bubble, and coalescence is naturally observed. Conversely, the semi-empirical model reproduces fluid flow for a bubble train and does not take coalescence into account in the case of several nearby bubble trains, as each path is calculated for the entire bath and two separate paths cannot combine to form a single trajectory.

In this section, we will modify the semi-empirical model to take this phenomenon into account. The idea is to calculate a single new path above the height at which the bubbles coalesce.

4.1 Experimental Observations

A tank with two bubblers was used to observe the coalescence between two bubble trains (Fig. 5). Various parameters were examined to determine their influence on the height of coalescence, including the injector spacing, air flow rates, and fluid viscosity.

The coalescence of two neighboring bubble trains strongly affects the fluid flow. Under the test conditions, it begins when the injectors are 140 mm apart. The height of coalescence increases slightly at lower viscosity and when the air flow rate is increased, but with little effect above 615 $L{\cdot}h^{-1}$. Except near the free

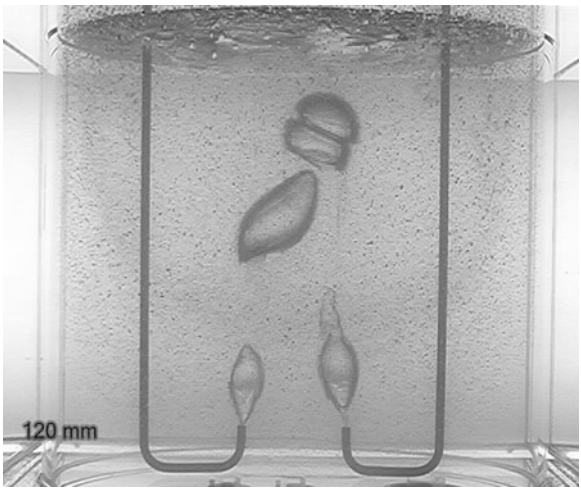

Fig. 5 Coalescence of two bubble trains in oil (viscosity 8,540 cSt, bubble flow rate 1,225 $L{\cdot}h^{-1}$, injector spacing 120 mm)

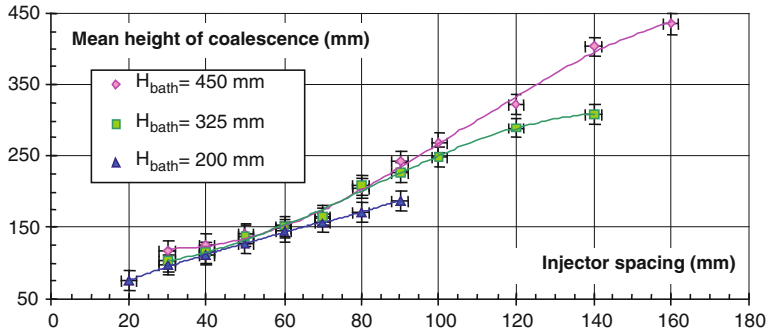

Fig. 6 Average height of coalescence for a viscosity of 8,540 cSt and an air flow rate of 1,225 $L{\cdot}h^{-1}$

surface, the height of the bath has no influence on coalescence when it occurs. Knowing the height of coalescence (Fig. 6) allowed us to use the semi-empirical method to compute the overall fluid flow properties.

4.2 Coalescence Modeled by the Volume of Fluid Method

Two bubble trains modeled with OpenFOAM® using the VOF method effectively coalesce in a manner similar to the phenomenon observed during testing in oil (Fig. 7). This method can be used to calculate the heights of coalescence for different viscosities, gas flow rates, and injector spacing without the need for testing in an oil bath.

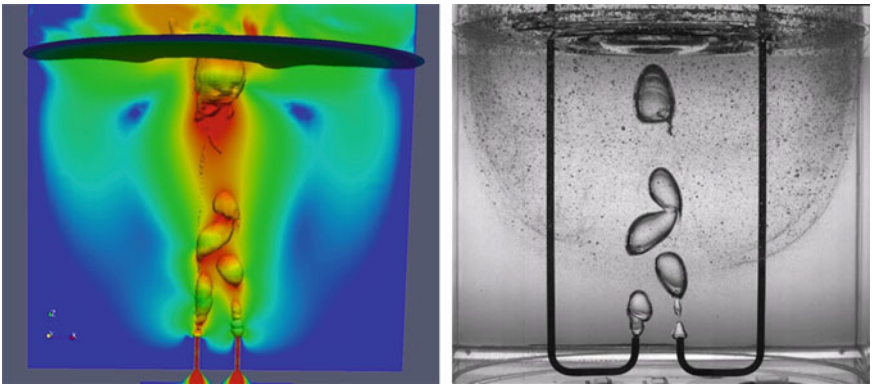

Fig. 7 *Left* VOF model (viscosity 2,000 cSt, air flow rate 1,225 $L{\cdot}h^{-1}$, and 60 mm injector spacing). *Right* experimental result with the same parameter values

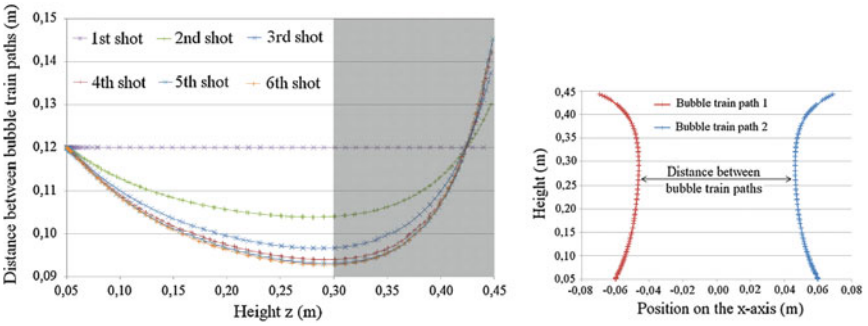

Fig. 8 Distance between bubble train paths for successive simulations designed to obtain convergence (*left*) and divergence for the sixth simulation (*right*)

4.3 Taking Coalescence into Account in the Semi-Empirical Method

The semi-empirical method was used with two neighboring bubble trains. To ensure the most realistic conditions, it was necessary to take account of the reciprocal influence of bubble trains. This was done by successively taking the results obtained by calculation and applying them as the initial conditions. The Navier–Stokes equations were solved between each Lagrangian shot to obtain the bubble train path. Convergence was generally observed from the sixth iteration.

The effect of path convergence may be noted for heights between 0.05 and 0.3 m. The effect of the surface on the path spacing is relatively large near the top of the bath ($z > 0.3$ m: shaded zone in Fig. 8). The surface velocities are free in the plane but restricted on the z-axis. The bubble trains are thus forced to diverge.

Two steps are necessary for complete calculation of coalescence with the semi-empirical method. First, we perform the previous calculation to obtain the flows of both bubble trains before coalescence. Then, beginning at the height of coalescence (determined by hydraulic similarity tests), we compute a single path for the new bubble train. Figure 9 shows the calculated fluid flow velocities at the first iteration on the left (no reciprocal influence between the two bubble trains). In the center plot, the paths converge at the bottom, but diverge as they approach the surface. In the third plot, the lower portions of the paths are the same, while above the height of coalescence, the calculation reflects the presence of a single bubble train.

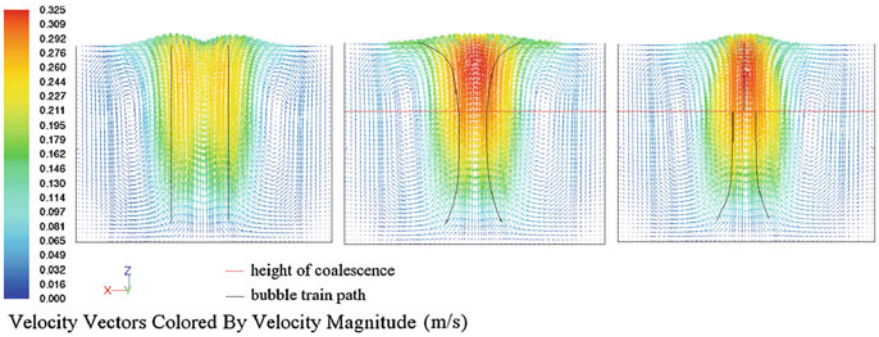

Fig. 9 Midplane path velocity vectors for the first shot (*left*), the sixth shot (*center*), and with a single path calculated above the height of coalescence (*right*)

5 Conclusion

Bubble flow in a high-viscosity liquid can be satisfactorily modeled by the VOF method. Coalescence between two adjacent bubble trains also occurs naturally. The coalescence of several bubble trains can be represented by a semi-empirical method capable of describing the overall fluid flow while considerably reducing the computation time, although the height of bubble coalescence must be known in order to implement coalescence in the semi-empirical model.

References

1. Geoffroy, O., Rouch, H., Sauvage, E. & Bonnetier, A. (2012). Mixing process by gas bubbling simulation.*7th* Open FOAM workshop, Darmstadtiun, Darmstadt, Germany.
2. ANSYS FLUENT 12.0/12.1 Documentation.
3. Akhtar, A., Pareek, V., & Tadé, M. (2007). CFD simulations for continuous flow of bubbles through gas-liquid columns: Application of VOF method. *Chemical Product and Process Modeling, 2*(1), 1–19.
4. Snabre, P., & Magnifotcham, F. (1998). Formation and rise of a bubble stream in a viscous liquid. *The European Physical Journal, 4(3),* 369–377.
5. Snabre, P. & Magnifotcham (1998). Recirculation flow induced by a bubble stream rising in a viscous liquid. The European Physical *Journal, 4(3)*, 379–386.
6. Jamialahmadi, M., Zehtaban, M., Muller-Streinhagen, H., Sarrafi, A. & Smith, J. (2001). Study of bubble formation under constant flow conditions. *Chemical Engineering Research and Design, 79(5)*, 523–532.
7. Kulkarni, A. A., & Joshi, J. B. (2005). Bubble formation and bubble rise velocity in gas-liquid systems: A review. *Industrial and Engineering Chemistry Research, 44*(16), 5873–5931.
8. Miyahara, T., Takahashi, T. (1985). Drag coefficient of single bubble rising through a quiescent liquid. Int Chemical Engineering, *25(1).*
9. Loth, E. (2008). Quasi-steady shape and drag of deformable bubbles and drops. *International Journal of Multiphase Flow, 34(6)*, 523–546.
10. Bonometti, T. (2005). *Développement d'une méthode de simulation d'écoulement à bulles et à gouttes*. PhD thesis, I.N.P. Toulouse.

3D Oil Spill Model: Application to the "Happy Bride" Accident

Cédric Goeury, Jean-Michel Hervouet, Olivier Bertrand, Régis Walther and Vincent Gouriou

Abstract The application of the European Water Framework Directive and the monitoring obligation on water quality for human consumption and industrial activities create a need for water quality assessment and monitoring systems. The MIGR'Hycar research project (see: http://www.migrhycar.com), partly funded by the French National Agency for Research (ANR), was initiated to provide decisional tools and fulfil operational needs for risks connected to oil spill drifts in continental waters (river, lakes, estuaries). Within the framework of the Migr'Hycar project, a three-dimensional (3D) numerical oil spill model has been developed. A Lagrangian model describes the transport of an oil spill near the free surface. The oil slick is represented by a large set of small particles. The model enables us to simulate the main transport process that acts on the spilled oil: advection (wind, current), diffusion (turbulence) and the shoreline oiling model. In order to validate the 3D 0uary 2006, the tanker "Sigmagas" suffering technical damage collided with another tanker "Happy Bride". 60 t of heavy fuel has been spilled in Loire estuary because of tanker collision. The oil slick drift in the estuary and the affected area location have been followed with aerial and land

C. Goeury (✉)
Saint–Venant Laboratory for Hydraulics, Joint Research Unit between EDF R&D CETMEF and Ecole des Ponts, Chatou, France
e-mail: cedric.goeury@edf.fr

J.-M. Hervouet
EDF R&D, Laboratoire National d'Hydraulique et Environnement (LNHE), Chatou, France
e-mail: j-m.hervouet@edf.fr

O. Bertrand · R. Walther
ARTELIA, Echirolles, France
e-mail: olivier.bertrand@arteliagroup.com

R. Walther
e-mail: regis.walther@arteliagroup.com

V. Gouriou
CEDRE, Brest, France
e-mail: vincent.gouriou@cedre.fr

P. Gourbesville et al. (eds.), *Advances in Hydroinformatics*,
Springer Hydrogeology, DOI: 10.1007/978-981-4451-42-0_37,

observations. These observations allow us to assess the quality of the numerical predictions. Promising results are found and presented in this paper.

Keywords Lagrangian model · Oil spill modelling · Stochastic diffusion · Shoreline oiling model · Loire estuary

1 Introduction

Although in almost half of all instances of contamination, the exact cause is never determined, oil spills can be due to human error, accidental or voluntary discharge of cargo residues, domestic or industrial tank overflow, leakage from fuel stations, traffic accidents or fire, and among other causes.

When faced with hydrocarbon contamination of inland waterways, authorities and other organizations can seldom rely on dedicated decision-making tools to intervene in an effective way.

Whereas considerable management and monitoring resources are rapidly deployed for off- or inshore oil incidents, the more frequent occurrence of continental water pollution is dealt with relatively modest means. A limited grasp of the nature and magnitude of such events often renders both industry and government powerless in controlling their impact.

The Migr'Hycar research project (www.migrhycar.com) was initiated to provide decisional tools and fulfil operational needs, for risks connected to oil spill drifts in continental waters (rivers, lakes, estuaries). These tools are meant to be used in the decision-making process after oil spill pollution and/or as reference tools to study scenarios of potential impacts of pollution on a given site. The Migr'Hycar consortium has been organized to closely match project objectives and comprises modelling technology developers (EDF, Saint–Venant Laboratory for Hydraulics, ARTELIA, VEOLIA), researchers with long-standing experience of hydrocarbon physicochemical behaviour (Agribusiness laboratory LCA, CEDRE), engineering consultants liaising closely with local and regional authorities (ARTELIA), two water intake operators directly concerned with project-related issues and well experienced in applying protective warning systems (EDF, VEOLIA) and a major player in the oil industry (TOTAL). The consortium has therefore the expertise required to develop a surface water risk monitoring and prevention system against oil spillage contamination.

The proposed application of the deterministic model developed for this project is the modelling of the collision that took place between two butane carriers in the Loire estuary on 14 January 2006. On this date, the Happy Bride's heavy fuel oil tank was struck by the Sigmagas and subsequently spilt its 60 m^3 reservoir of IFO 380. This event is presented below alongside a discussion of the results obtained and the areas for improvement to be considered. This will be preceded by a discussion of the bases of the hydraulics and transport models of the Loire estuary.

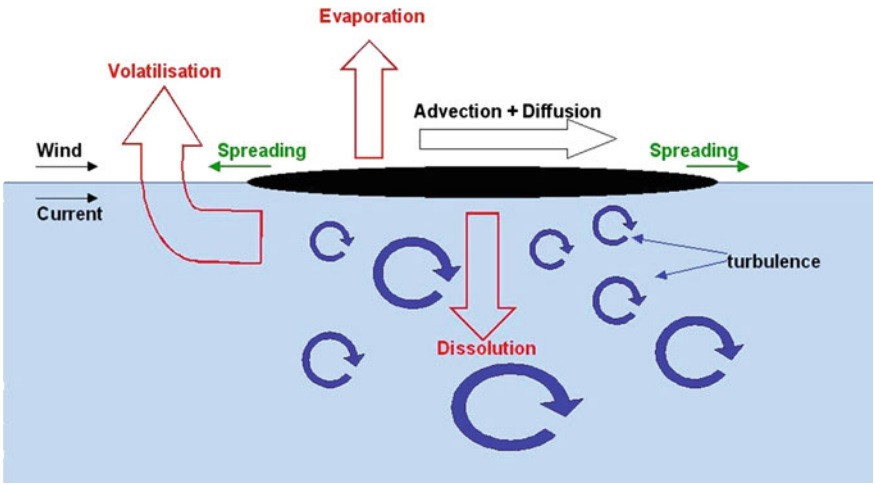

Fig. 1 Fate and transport oil surface slick processes

2 Presentation of the 3D Oil Spill Model

Within the framework of the Migr'Hycar project, a three-dimensional (3D) oil spill model has been developed by combining Lagrangian and Eulerian methods. This model enables us to simulate the main processes that act on the spilled oil: advection, diffusion, evaporation, dissolution, spreading and volatilization (Fig. 1). Though generally considered as a minor process, dissolution is important from the point of view of toxicity. The Lagrangian model describes the transport of an oil spill near the free surface.

To model the dissolved oil in water, an Eulerian advection–diffusion model is used. The fraction of dissolved oil is represented by a passive Eulerian scalar. This model is able to follow dissolved hydrocarbons in the water column (PAH: polycyclic aromatic hydrocarbons). The Eulerian model is coupled with the Lagrangian model.

In this work, only oil slick transport processes are described.

2.1 3D Hydrodynamic Model

Hydrodynamics is provided to the oil spill model using the TELEMAC-3D hydrodynamics model. TELEMAC-3D was developed by the National Hydraulics and Environment Laboratory, a department of Electricité de France's Research and Development Division.

This open source freeware program (www.opentelemac.org) solves the following governing equations:

$$\frac{\partial U_i}{\partial x_i} = 0, \tag{1}$$

$$\frac{\partial U_i}{\partial t} + \frac{\partial U_j U_i}{\partial x_j} = F_i - \frac{1}{\rho}\frac{\partial p}{\partial x_i} - \frac{1}{\rho}\frac{\partial \tau_{ij}}{\partial x_j}, \tag{2}$$

where $x_i = (x, y, z)$ denotes the spatial coordinates, t the time, $U_i = (U, V, W)$ the local time-averaged components of the flow velocity, F_i the component of external forces (gravity, Coriolis force,…), p the mean pressure, ρ the fluid density and τ_{ij} the component of the stress tensor calculated with the Boussinesq approximation and related to the gradient of the velocity and the turbulent eddy viscosity υ_t.

TELEMAC-3D solves the previous equation system using the finite element method on superimposed triangular meshes, the resulting elements being prisms. TELEMAC-3D can take into account the bed friction, the influence of the Coriolis force and meteorological factors, the turbulence, sub- and super-critical flows, river and marine flows, the influence of temperature or salinity gradient on density and dry areas in the computational domain, and among other processes [1].

2.2 Lagrangian Model

Eddies generated by turbulence affect the motion of petroleum particles in water and randomize their trajectory. Consequently, a stochastic approach is adopted to take this phenomenon into account. The advection–diffusion Eq. (3) is well adapted to modelling transport and dispersion of continuous contaminants, but since the present model uses a discrete particle description of contaminant transport and dispersion, a transformation must be applied to obtain a Lagrangian description.

$$\frac{\partial C}{\partial t} + \nabla \cdot (C\mathbf{U}) = \nabla \cdot \left(\frac{\nu_t}{\sigma_c}\nabla C\right), \tag{3}$$

where C is the pollutant concentration, σ_c the neutral turbulent Schmidt number and υ_t the turbulent viscosity. The turbulent Schmidt number can be set to $\sigma_c = 0.72$ [2].

The first transformation step consists of interpreting the concentration $C(\mathbf{X}, t)$ as a probability $P(\mathbf{X}, t)$ of finding a particle at a location $\mathbf{X}$ at a time t. Then, the non-conservative formulation of Eq. (3) leads to the Fokker–Planck equation:

$$\frac{\partial P}{\partial t} = -\left[\mathbf{U} - \nabla\left(\frac{\nu_t}{\sigma_c}\right)\right]\nabla P + \nabla \cdot \left(\frac{\nu_t}{\sigma_c}\nabla P\right), \tag{4}$$

A stochastic solution to Eq. (4) is obtained by specifying the hydrocarbon particle position $\mathbf{X}(t)$ according to the following Langevin equation [3]:

$$\mathbf{X}(t+\delta t) = \mathbf{X}(t) + \left[\mathbf{U} - \nabla\left(\frac{\nu_t}{\sigma_c}\right)\right] \cdot \delta t + \sqrt{\frac{2\nu_t}{\sigma_c} \cdot \delta t}\xi(t), \tag{5}$$

where δt is the time step and $\xi(t)$ a vector with independent, standardized random components. In the above relationship, ν_t and $\mathbf{U}$ are computed by TELEMAC-3D using a k–ε turbulence closure model. The velocity vector $\mathbf{U}$ takes the wind effect into account through the two-dimensional condition at the surface:

$$\nu \frac{\partial \mathbf{U}_h}{\partial n} = \frac{\rho_{\text{air}}}{\rho} a_{\text{wind}} \mathbf{W} \|\mathbf{W}\|, \tag{6}$$

with $\rho_{\text{air}} = 1.29$ kg/m^3, $\mathbf{U}_h$ the horizontal velocity at the surface and $\mathbf{W}$ the wind velocity 10 m above the water. The coefficient a_{wind} (dimensionless) is given by Flather [4].

2.3 Shoreline Oiling Model

2.3.1 Oil Beaching on Shoreline

When an oil slick reaches a shoreline, it may deposit if

- The slick thickness is greater than the water level under the oil slick.
- The size of the bottom roughness is greater than the water level.
- The deposited oil volume does not exceed the maximum surface loading and maximum sub-surface loading which is given by Cheng et al. [5]:

$$M^* = \rho_o \left(\text{Surf}_{\text{shore}} \cdot T_m + C_v D_p L_s\right), \tag{7}$$

where M^* is the maximum oil mass deposited on the shore, $\text{Surf}_{\text{shore}}$ the shore surface, ρ_o the oil density, T_m the maximum oil thickness, C_v the sediment oil content, L_s the width of the shore, and D_p the depth of oil penetration on the shore.

The oil-holding capacity of a shore depends on both oil and beach characteristics. The parameters C_v, D_p and T_m are derived from real oil spill observations, and their values are summarized in Table 1 [6]:

2.3.2 Oil Refloating in the Water Current

The deposited spilled oil may be reentrained into the sea current if

- The water level under the oil slick is greater than the slick thickness.
- The water level is greater than the size of the bottom roughness.

Table 1 Oil-holding capacity [6]

Shoreline type	Maximum surface oil thickness (T_m) (mm) by oil viscosity			Oil loading capacity (C_v) (m^3oil/m^2 sediment)			Depth of oil penetration (D_p) (mm)
	Light viscosity	Medium viscosity	High viscosity	Light viscosity	Medium viscosity	High viscosity	
Sandy beach	4	17	25	0.004	0.017	0.025	50
Gravel	2	9	15	0.0021	0.0091	0.0151	180
Rocky shore	1	5	10	0.001	0.005	0.01	0

- Random phenomena, such as gusts of wind, waves induced by boats, act on the spilled oil. This condition is taken into account using the probabilistic approach suggested by Danchuk [7].

The oil removal rate k_f is used to determine the probability of a particle of oil refloating $P_{\text{refloat.}}$

$$P_{\text{refloat}} = 1 - e^{-k_f t} \tag{8}$$

where k_f is the oil removal rate (day^{-1}) which depends on shore characteristics (sand: $k_f = 0.25$; gravel: $k_f = 0.15$; rock: $k_f = 0.85$).

Refloating for a particle is determined by choosing a random number $R_{(0,1)}$. The particle refloats if $R_{(0,1)} < P_{\text{refloat}}$.

3 The 3D Loire Estuary Hydraulic Model

Given its physical configuration and demographics, the Loire estuary is subject to considerable constraints and constitutes an area in which different human activities overlap. For the most part, the various industrial and commercial centres are concentrated around the major urban areas. The activity of the Nantes Saint-Nazaire port (now know as the Grand Port Maritime), in particular, has allowed several industries to settle in the industrial port area of Montoir-Donges.

At the same time, the organization and distribution of the drinking water production network reflect the specificities of the physical environment and as such consist of relatively few production units in relation to the population served. Water is supplied predominantly from surface sources.

Together, all of these elements make the estuary a sensitive environment where hydrocarbon pollution could have a serious impact both on the water and, by extension, on its use for agriculture, drinking water supply and industrial use at the EDF power plant at Cordemais.

The GIP Loire estuaire (GIPLE) (http://www.loire-estuaire.org) commissioned ARTELIA with a study to develop and operate a 3D hydrosedimentary model of the Loire estuary in the context of its "Programme to restore the Loire estuary

downstream of Nantes". This hydrodynamics model was reused in the context of the Migr'Hycar project. It correctly reproduces the tide propagation in the estuary and upstream as far as Nantes. A brief description of the model is given below.

3.1 Presentation of the Model

This model covers an area that extends from Ancenis upstream to the Grande Baie downstream, including the Bourgneuf Bay to the south and the headland of Le Croisic to the north, totalling around 90 km of river and 40 km of coastal waters out to sea. The horizontal finite element mesh consists of approximately 7,052 nodes and 12,855 triangles of size in the range 50–2500 m. The mesh is refined in the main channel of the Loire estuary. Ten horizontal meshes are stacked to generate the 3D mesh (Fig. 2).

The daily flow rate measured at Montjean was imposed at the upstream limit of the model (Ancenis). During floods, it includes the flow rates from the Sèvre and

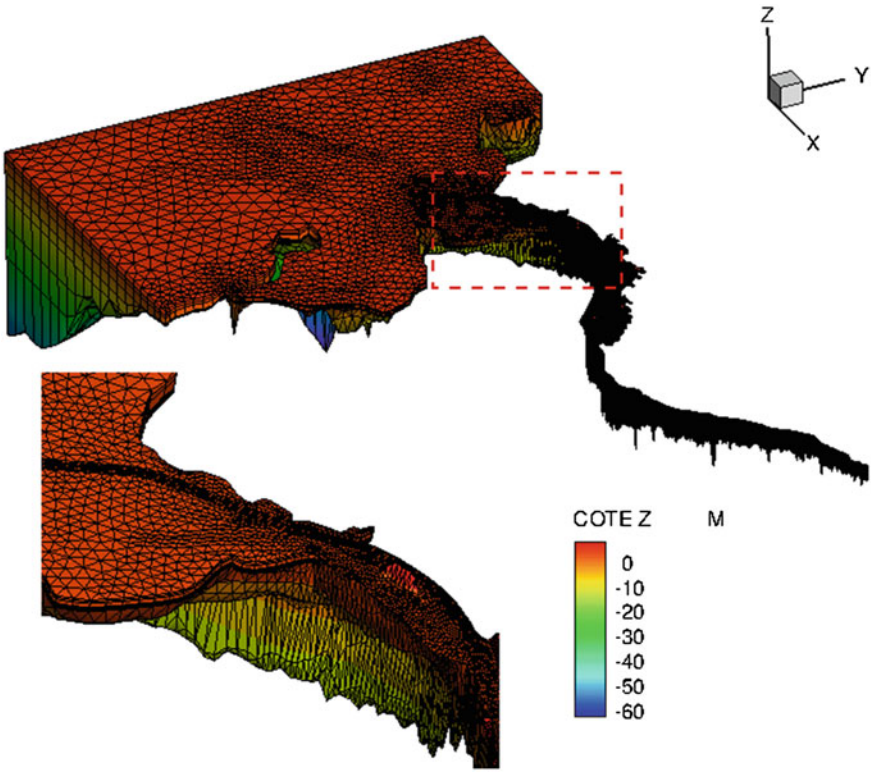

Fig. 2 Three-dimensional mesh of the Loire estuary

the Erdre rivers. The astronomical tide is imposed at the maritime limit of the model, with the average level calculated using tidal measurements from Saint-Nazaire for the period simulated.

3.2 Calibration

For the calibration of the model, the value of wind intensity at sea (as extracted from point CROISIC1 in the Prévimer database) is applied equally across the maritime part of the model and is then interpolated from the downstream limit of the Saint-Nazaire port access channel to downstream of Donges, where its value is considered negligible. The aim of taking wind into account in the model is not simulating tidal surges in the estuary, as this would require a more elaborate hydrometeorological model. In any case, surge is taken into account by the temporal evolution of the average level in the boundary conditions. The aim of including wind factors in the 3D model is to generate the 3D water circulation in the external estuary that is likely to lead to significant changes in the residual circulation of the astronomic tide. Such effects are in contrast negligible in the internal estuary, where the effects of turbid and haline stratification together with those of the tide and the flow rate of the Loire dominate. Later, to study the oil spill event, a spatially interpolated wind from the climate forecast system reanalysis (CFSR) model has been used [CFSR (ftp://nomads.ncdc.noaa.gov/CFSR)].

The main aim of the hydrodynamic calibration was to adjust the friction coefficients per zone in order to correctly represent tidal propagation within the estuary. The friction laws chosen are the Nikuradse law downstream of Sainte-Luce-sur-Loire and the Strickler law upstream of this point. The Nikuradse formulation depends on the grain size of sediment and on the velocity profile over the bottom, whereas the Strickler formulation only deals with the vertically averaged velocity. The Strickler formulation is preferable to include in friction other head losses, such as vegetation on the banks, groynes, weirs, bridge piers.

Taking liquid mud into account in the calibration stage required the use of a lower friction coefficient (in relation to the standard friction coefficient for a sandy river bed) in the area in which liquid mud is assumed to be present. This coefficient varies with the flow rate. The results obtained for tidal propagation in the estuary are presented in Fig. 3 for a flooding period.

Salinity and hydrodynamics were controlled using measurements from fixed stations for the low- and medium-flow periods in mid-October 2000 and for the flood in January 2004.

The period of October 2000, in which flow rate varied between 300 and 1,100 m^3/s, is very interesting as far as salinity measurements are concerned. Indeed, the measurement points at surface and bottom level clearly demonstrate:

- During spring tide: a period of significant mixing associated with a large amplitude in salinity in the downstream sections of the estuary.

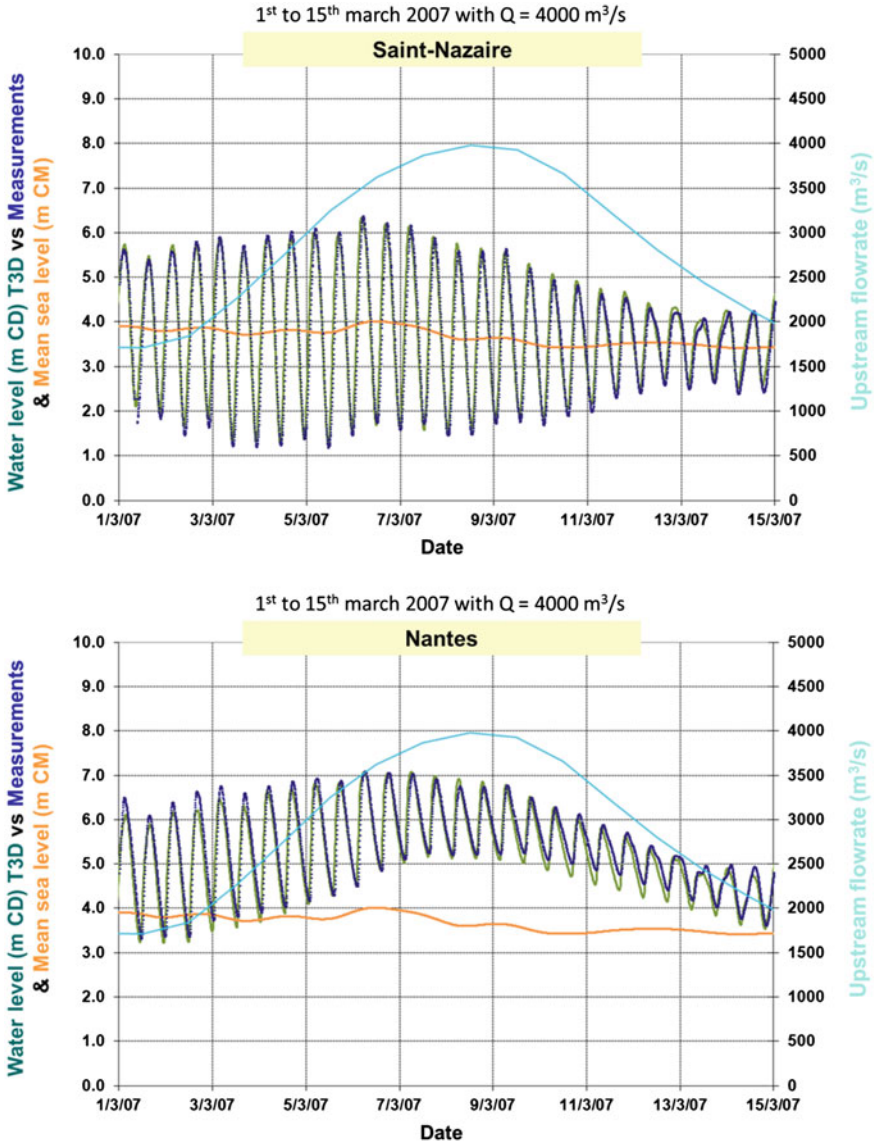

Fig. 3 Comparison of the water level between model and measurements at Saint-Nazaire (*top*) and Nantes (*bottom*) for a flooding period

- During neap tide: very different measurements at surface and bottom level, with a particularly large saline penetration upstream due to density effects when flow rates are low.

The flood period of January 2004 shows strong haline stratification in the navigation channel, particularly at Montoir during neap tide (Fig. 4). During spring tide, this stratification is present but less noticeable. Salinity, even during periods in which flow rates exceeded 4,000 m^3/s, penetrates along the bottom of the navigation channel due to its density. The short periods of vertical mixing are due to gusts of wind in excess of 10 m/s. The model reproduces the mixing caused by wind relatively well.

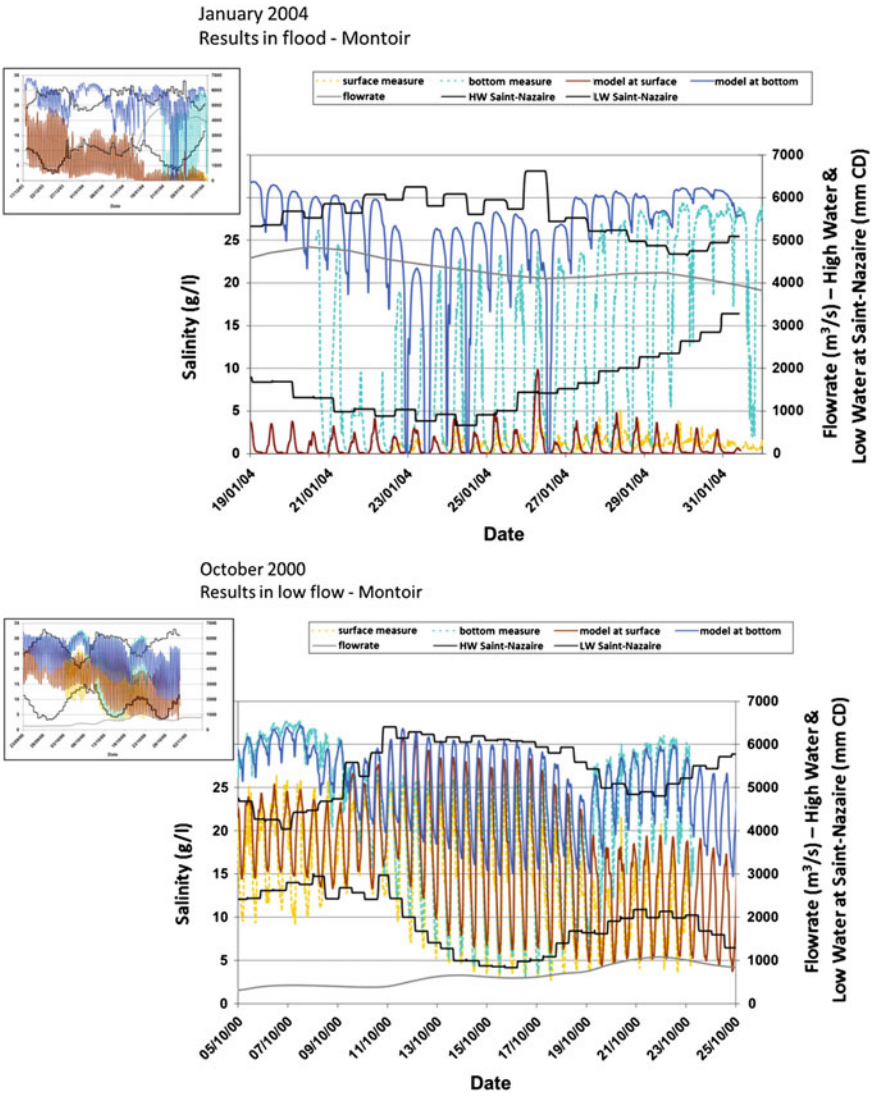

Fig. 4 Salinity varying with time at Montoir during flood (*top*) and low flow (*bottom*)

We can therefore conclude that the model reproduces the high levels of salinity stratification measured during the flood, as well as the saline penetration due to density as measured during neap tide.

4 Application to the Happy Bride and Sigmagas Collision

4.1 Description of the Accident

The Donges refinery produces liquid butane gas, part of which is transported by sea. Consequently, LPG tankers regularly transit through the Loire estuary. On 4 January 2006, the LPG tanker "Sigmagas" left the refinery after having loaded its cargo of butane, while the LPG tanker "Happy Bride" entered the channel on its way to the refinery. A few minutes before they crossed each other, the Sigmagas experienced a rudder problem which caused the vessel to veer to port on a collision course with the Happy Bride. At 8.20 pm, the Sigmagas hit the middle port side of the Happy Bride, rupturing a bunker oil tank. All the fuel oil contained in this tank (60 m^3 of IFO 380) subsequently spilled into the estuary. On 5 January, an aircraft operated by the French customs authorities reported a 17 km-long, 300 m-wide oil slick (with an estimated quantity of 13 m^3) running from Saint-Nazaire bridge in a west/south-westerly direction. The oil slick drift in the estuary and the affected area were followed with aerial and land observations. These observations allow the quality of the numerical predictions to be assessed.

4.2 Numerical Results

The mathematical model of oil slick drift developed in the Migr'Hycar project and the 3D hydrodynamic model of the estuary were used to simulate the drift of the polluting slick caused by the collision between the two liquid butane carriers.

1. *Situation on Thursday 5 January 2006* (Fig. 5)

At the time of the collision, the current was directed downstream towards the Loire estuary outlet (high tide at 7.50 pm) and the slick was therefore carried towards the estuary outlet. This phenomenon was no doubt amplified by the saline stratification of the water. In the first few hours following the spill, the oil slick remained located in the northern part of the estuary, as shown on the maps produced by the accident crisis management teams [8]. This result was mirrored by the simulations, especially under the effect of a south-westerly wind.

Fig. 5 Summary of observations and simulations on the 05 January 2006

2. *Situation on Saturday 7 January 2006* (Fig. 6)

Observations taken on land indicate the presence of small lumps of solidified oil in La Baule Bay and residues at the mouth of the estuary. The results obtained by the model match these observations.

Residual deposits are observed in the upstream and downstream vicinity of Donges refinery and on the right bank of the estuary. These deposits are probably due to lumps of oil previously deposited on the shore being picked up again as a

Fig. 6 Summary of observations and simulations on the 07 January 06

result of tidal-level variations. These pollution points are not detected by the model. The results show that improvements can be made by refining data on the adherence of the oil slick to the estuary banks. However, this parameter is very delicate because it depends not just on the location (distinguishing between different types of bank) but also on the date on which the simulated spill took place (different vegetation depending on the season).

The results obtained from this oil slick modelling procedure are encouraging and demonstrate the forecasting feasibility of the model with a view to preventing pollution of installations that might be affected in continental waters. In this same

area dominated by tidal currents and the Loire river flow, oil slick drift is affected to a large extent by wind conditions. By making better allowance for wind, and by processing more detailed data in time and in space, it should be possible to represent oil slick drift more accurately. The results can also be improved by a more detailed analysis of the adherence of the oil slick to the estuary banks.

5 Conclusions

While major oil spill catastrophes, occurring mainly in an oceanic or coastal environment, result in the rapid deployment of large-scale crisis monitoring and management tools, accidents of lesser importance, despite occurring much more frequently, are more often than not managed with only limited facilities, especially with regard to pollutant spills affecting continental waters. Given the limited knowledge of the nature and importance of such events, local authorities charged with taking the necessary health or economic protection measures are generally powerless when confronted with the environmental consequences. Accidents involving the oil pollution of continental waters are increasing at an alarming rate, with an average of one spill every 40 h over the 2008–2010 periods [9].

Application of the Water Framework Directive and the obligation to monitor the quality of water used for human consumption and for recreational or industrial activities have led to a massive rise in demand for water quality assessment and monitoring systems.

The Migr'Hycar project was set up in this context and has been used to develop a modelling tool to simulate the migration of oil slicks in continental and estuary waters. Linked to a database for hydrocarbon physical–chemical characterization, this tool is destined for operational use.

The Loire estuary test site, following the Happy Bride accident, was chosen in order to evaluate the relevance of the tools developed. This application illustrates the hydrodynamic complexity of the environment in these stratified areas where sea water mixes with freshwater from the river. A further difficulty is the need to properly reproduce the transport of oil pollution which is governed by currents and weather conditions. Given the complex dynamics of estuaries, 3D modelling seemed to be the only valid means of adequately predicting hydrocarbon drift and of assessing the impacts of dissolved compounds contained in the water from the surface to the bed.

The results obtained are encouraging and demonstrate the feasibility of pollution prevention for installations that could be affected by this type of pollution.

Acknowledgments The Migr'Hycar project (ARTELIA, CEDRE, EDF, LCA, LHSV, TOTAL, VEOLIA) is a collaborative project forming part of the PRECODD 2008 programme financed by the French National Agency for Research (ANR). GIP Loire estuary funded the development of the hydrodynamic model of the Loire.

References

1. Hervouet, J. -M. (2007). *Hydrodynamics of free surface flows*. Wiley.
2. Violeau, D. (2009). Explicit algebraic Reynolds stresses and scalar fluxes for density-stratified shear flows. *Physic of Fluids, 21*, 035103.
3. Gardiner, C. W. (2004). Handbook of stochastic methods for physics, chemistry and the natural sciences. *Springer Series in Synergetics*. Berlin: Springer.
4. Flather, R. A. (1976). Results from surge prediction model of the North-West European continental shelf for April, November, and December 1973. *Institute of Oceanography (UK), 24*.
5. Cheng, N.-S., Law, A.-K., & Findikakis, A. (2000). Oil transport in the surf zone. *Journal of Hydraulic Engineering, 126*, 803–809.
6. Schmidt Etkin, D., French McCay, D., & Michel, J. (2007). Review of the State-of-the-Art on the modelling interaction between spilled oil and shorelines for the development of algorithms for oil spill risk analysis modelling. *Technical Report*. US Department of Interior.
7. Danchuk, S., & Wilson, C. (2010). Effects of shoreline sensitivity on oil spill trajectory modelling of the lower Mississippi river. *Environment Sciences Pollution Research, 17*, 331–340.
8. CEDRE (2006). Cartographie de l'accident "Happy Bride". *Technical Report*.
9. Bonnemains, J., Bossard, C., Crepeau, E., & Fenn, E. (2011). *Atlas des marées noires dans les eaux intérieures du 1er janvier 2008 au 31 décembre 2010*. Association Des robins Des Bois.

Modelling Combined Wave–Current Flows Using a RANS CFD Solver with Emphasis on the Effect of the Turbulent Closure Model

Maria João Teles, Michel Benoit and António A. Pires-Silva

Abstract The nearshore hydrodynamics and coastal circulation result from the contribution of a variety of phenomena which have complex physical interactions at different scales. Among these interactions, we focus here on the interaction between waves and current. In the present work, the evaluation and analysis of wave–current interactions is made through numerical simulations based on Reynolds averaged Navier–Stokes (RANS) equations, applied to the modelling of the complete flow motion, namely waves and current simultaneously (i.e., without decoupling the two phenomena). The advanced CFD code *Code_Saturne* [1] is used for this purpose. The code is adapted for the study of waves and current interactions, using the arbitrary Lagrangian–Eulerian (ALE) method for dealing with free surface tracking, and considering turbulence effects in free surface flows. Several turbulence closure models are considered and compared, including two-equation models, namely k–ε and k–ω models, largely used in this kind of studies for their simplicity, and also a second-order Reynolds stress transport model R_{ij}–ε. In particular, we show that imposing additional boundary conditions at the free surface was crucial to model the interaction effects. Numerical results are compared with experimental data from [2] for the following four types of flow conditions: (1) only current, (2) only waves, (3) waves following current and (4) waves opposing current. A detailed study of the changes in the vertical profiles of mean horizontal velocities and shear stresses when waves and current interact is

M. J. Teles (✉) · A. A. Pires-Silva
Instituto Superior Técnico, TU Lisbon, Av. Rovisco Pais 1049-001 Lisbon, Portugal
e-mail: mjteles@gmail.com

A. A. Pires-Silva
e-mail: aps@civil.ist.utl.pt

M. Benoit
Saint–Venant Laboratory for Hydraulics, Université Paris-Est (joint research unit between EDF R&D, CETMEF and Ecole des Ponts ParisTech), 6 quai Watier, BP 49 78401 Chatou, France
e-mail: michel.benoit@saint-venant-lab.fr

P. Gourbesville et al. (eds.), *Advances in Hydroinformatics*, Springer Hydrogeology, DOI: 10.1007/978-981-4451-42-0_38,

presented, with a discussion about the effects of the turbulence closure model used in the simulations.

Keywords Wave–current interaction · Turbulence model · *Code_Saturne* · Eddy viscosity · Reynolds shear stress

1 Introduction

The interaction between waves and current in free surface flows is of a great importance for the hydrodynamics of coastal waters. It has been a subject of several experimental and numerical studies. The most important issues in such wave–current combined environments (in comparison with the cases where either only waves or only current is present) are the changes in the horizontal and vertical mean velocities and in the Reynolds shear stresses.

The design of coastal protections and harbour sheltering structures, the evaluation of sediment transport and coastal erosion, the assessment of wave power available at a certain spot or the impact of a farm of wave energy converters are examples of possible applications that will benefit from an enhanced knowledge and modelling of the effects of this two-way wave–current interaction.

The present work aims at studying the changes that occur when waves are superimposed on a turbulent current, with particular attention to the modifications of the vertical profiles of (1) the mean horizontal velocity, (2) shear stresses and (3) turbulent (eddy) viscosity. For this purpose, a RANS CFD model capable of resolving all this combined effects will be employed, namely *Code_Saturne* [1]. Some sensitivity tests will also be made regarding the turbulence closure model that exhibit the best performance to model this kind of flows.

2 Laboratory Data

A series of laboratory experiments were carried out by Umeyama [2] in a wave–current flume. This flume was 25 m long, 0.7 m wide. The bottom of the flume was flat, and it was filled with a water depth of 0.20 m. The flume was equipped with a flow circulation circuit able to deliver a constant discharge, which was about $Q = 59$ l/s for all the tests considered below (when a current is present).

Regular (monochromatic) waves were generated through a piston-type wave maker located at an end of the flume, and dissipated with a wave absorber at the other end of the flume. A series of four pairs of wave parameters (height and period) were successively considered (see Table 1).

Tests were run under the four following conditions: (1) current without waves (or “only current”), (2) waves without current (or “only waves”), (3) waves

Table 1 Wave heights and wave periods for the four different test cases from [2]

Tests	T1	T2	T3	T4
Wave height (m)	0.0202	0.0250	0.0260	0.0280
Wave period (s)	0.9	1.0	1.2	1.4

following current, and (4) waves opposing current. For each test, vertical profiles of mean velocities and shear stresses were measured at a distance of 10.5 m from the wave generator, by a laser Doppler anemometer.

3 *Code_Saturne* Model

3.1 Introduction

Code_Saturne [1] is a CFD code for laminar and turbulent flows in two- and three-dimensional domains, developed at the R&D division of Electricité de France (EDF). It solves the Reynolds averaged Navier–Stokes (RANS) equations by using a finite volume method. The equations are written in a conservative form and then integrated over the control volumes of each cell of the 3D mesh:

$$\frac{\partial \rho}{\partial t} + \nabla.(\rho \underline{u}) = \Gamma \tag{1}$$

$$\rho \frac{\partial \underline{u}}{\partial t} + \nabla.(\rho \underline{u} \otimes \underline{u}) = -\nabla(P) + \nabla.\left(\underline{\underline{\tau}} - \rho \underline{\underline{R}}\right) + \underline{S_u} \tag{2}$$

where ρ is the fluid density, $\underline{u}$ the fluid velocity vector, Γ a mass source term, P the pressure, $\underline{\underline{\tau}}$ the viscous stress tensor, $\underline{\underline{R}}$ the Reynolds stress tensor and $\underline{S_u}$ a momentum source term.

In order to close the system (1)–(2), a model has to be introduced for the turbulent correlations of the Reynolds stress tensor $\underline{\underline{R}}$. *Code_Saturne* has implemented a large range of first- and second-order turbulence models (see Ref. [1] for details). In the present work, it was decided to proceed to the analysis of the wave–current interactions with the two-equation models k–ε [3] and k–ω [4] and a Reynolds stress model (RSM), the so-called R_{ij}–ε SSG model [5].

The first two models were chosen due to their relative simplicity and because they are often used in this kind of studies of wave–current interaction. The second-order turbulence closure model choice was made since the R_{ij}–ε model accounts for the directional effects of the Reynolds stress fields (anisotropy) and does not rely on the eddy viscosity hypothesis. It solves six transport equations for the six components of the Reynolds stress tensor and one equation for the turbulent dissipation rate ε, without making any a priori assumption on the eddy viscosity distribution v_t (which can nevertheless be estimated a posteriori from the results of that model).

Regarding the modelling of a time-varying free surface, *Code_Saturne* has incorporated in its code the arbitrary Lagrangian–Eulerian (ALE) method. With this module, the Navier–Stokes equations gain a new term, which is the velocity of the mesh. For each time step, the mesh is updated accordingly. In this way, it is possible to represent of the free surface variations due to waves.

3.2 Model Set-Up

Regarding the model set-up, some conditions have to be ensured. For the mesh generation, in the direction of wave propagation, a number of about 10 cells per wave length had to be guaranteed in order to reach a good representation of the surface waves. On the other hand, right next to the moving wall corresponding to the wave maker, the mesh velocity had to be compatible with the fluid velocity in order to avoid mesh crossover and provoke the divergence of the simulation.

As *High Reynolds* number models were used, the mesh near the bottom could not be too refined. At the same time, a sufficiently fine resolution was required in the same region in order to analyse some important effects, such as the roughness influence on the vertical profile of the measured quantities. On Fig. 1 the computational domain representative of experiments from [2] is shown.

Waves propagate in the positive x direction. In order to generate waves, *Code_Saturne* was forced with a horizontal motion of the mesh on the left lateral boundary. To minimize undesirable super-harmonic free waves, a second-order wave board displacement of the piston-type wave maker was applied on the flume. The following expression [6] for the wave board motion $X_0(t)$ (3) was introduced:

$$X_0(t) = \frac{H}{2m_1}\sin(\sigma t) + \frac{H^2}{32h}\left(\frac{3\cosh(kh)}{\sinh^3(kh)} - \frac{2}{m_1}\right)\sin(2\sigma t) \tag{3}$$

$$m_1 = \frac{4\sin h(kh)}{\sin h(2kh) + 2kh}\left[\sin h(kh) + \frac{(1-\cos h(kh))}{kh}\right] \tag{4}$$

where k represents here the wave number (not to be confused with the turbulent kinetic energy, also denoted k), h the water depth, H the wave height, σ the relative angular wave frequency and t the time. The signal given by Eq. (3) had to be

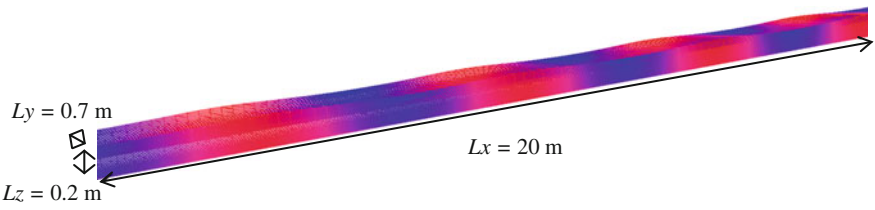

Fig. 1 Computational domain representative of experiments from [2]

progressively imposed at the lateral boundary, to avoid a sudden horizontal movement of the mesh and thus mesh crossover.

The reflections of waves at the right end of the channel were dealt with an artificial beach imposed at the downstream boundary, based on a viscous damping term that increased linearly from the bottom to the free surface.

Regarding the boundary conditions, special attention was devoted to the free surface. An additional condition had to be imposed for the turbulent dissipation ε [7] in order to get accurate results near the free surface.

$$\varepsilon = \frac{k^{3/2}}{\alpha h} \tag{5}$$

where is k the turbulent kinetic energy at the water surface and $\alpha = 0.18$ an empirical constant. With the imposition of this condition, the turbulent dissipation ε increases and the eddy viscosity decreases towards the free surface. These variations were observed during the experiments made by [3].

4 Discussion of Results

4.1 Effects of the Turbulence Closure Model on the Mean Horizontal Velocity

As mentioned in Sect. 2, the experiments from [2] were performed with different wave heights and periods. These conditions for the four test cases were simulated with *Code_Saturne* [8]. In the following, comparisons between numerical results and data of the vertical profile of the mean horizontal velocity for the test T1 (see Table 1) are shown for "only current" and "only waves" (Fig. 2), "waves following current" and "waves opposing current" (Fig. 3). A sensitivity analysis was made regarding the turbulence closure model that best describes this test case. It must be highlighted that this sensitivity test is made without any parameterization besides the default conditions and settings defined in *Code_Saturne*, with the exception of the boundary condition (Eq. 5) that was imposed for each test.

As it can be observed on these figures, the three turbulence closure models can represent quite well the vertical profile of mean horizontal velocity for the case "only current". Nevertheless, for the "only waves" case, the R_{ij}–ε model is the one that best fits the experimental data over the water column.

When waves are superimposed on a turbulent current, the profile of mean horizontal velocity is changed (Fig. 3). While the mean horizontal velocities near the free surface are reduced for the "waves following current" case, these velocities are increased when waves are opposing the current. This was observed by [2] and *Code_Saturne* was able to well reproduce this change in the current profile with the R_{ij}–ε model, especially when waves are following the current. When waves are opposing the current, even if the velocities are a bit

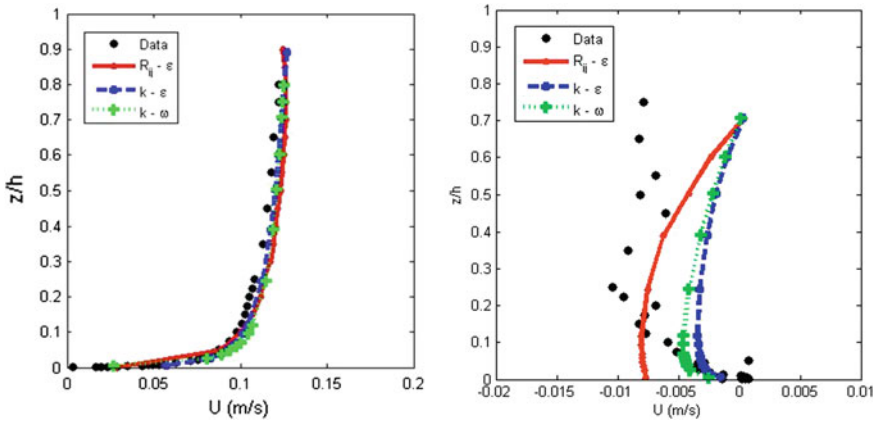

Fig. 2 Mean horizontal velocity vertical profile for "only current" (*on the left*) and "only waves" (*on the right*). Comparison with data from [2]

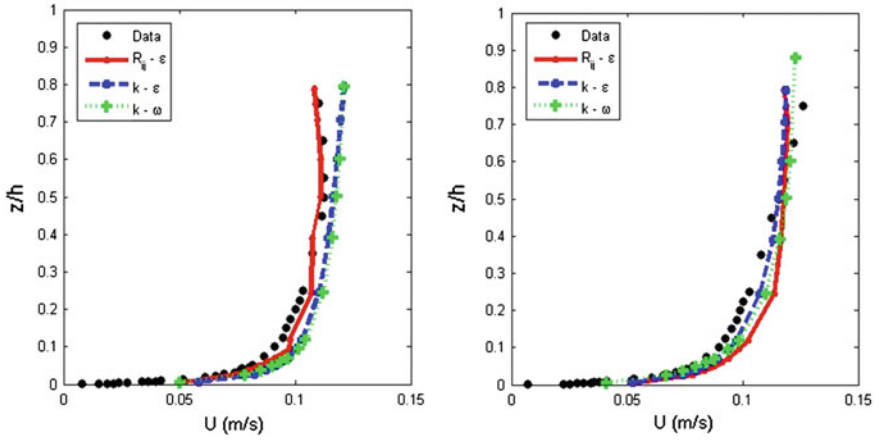

Fig. 3 Mean horizontal velocity vertical profile for "waves following current" (*on the left*) and "waves opposing current" (*on the right*). Comparison with data from [2]

underestimated near the free surface and a bit overestimated in the middle of the water column, a good overall agreement is observed.

4.2 Effects of the Turbulence Closure Model on the Reynolds Shear Stress

We also conducted a sensitivity analysis regarding the changes in the vertical profile of the Reynolds shear stress $R_{xz} = -\overline{u'w'}$ when waves and current interact

with the aim to determine which turbulence closure model was the most appropriate to describe theses changes. In the following, we show the comparison between *Code_Saturne* results and experimental data for "only current" on Fig. 4, "only waves" on Fig. 5 and "waves following current" and "waves opposing current" on Fig. 6.

As it can be seen from Fig. 4, all the three closure turbulence models are capable to correctly reproduce the shear stress profile obtained through experimental data when there is only a current in the channel. For what concerns the "only waves" test case, the shear stress profile is almost zero, as it can be observed on experimental data. In this case, *Code_Saturne* model overestimates the shear stress values over the whole water column when the k–ε and k–ω are applied (Fig. 5 on the left). On the right side of Fig. 5, it can be seen that a good agreement is found between the results from R_{ij}–ε model and data.

When waves are superimposed on the current, the dimensionless Reynolds shear stress profile is in general well simulated throughout the water depth with the three turbulence closure models.

From the tests made with *Code_Saturne,* it can thus be confirmed that the model is capable to reproduce quite well the wave–current interaction effects.

4.3 Analysis of the Vertical Profile of the Eddy Viscosity

Some experiments were made by [9] in a flume with only a current, and measures of the vertical profile of the eddy viscosity were obtained. Comparing this data

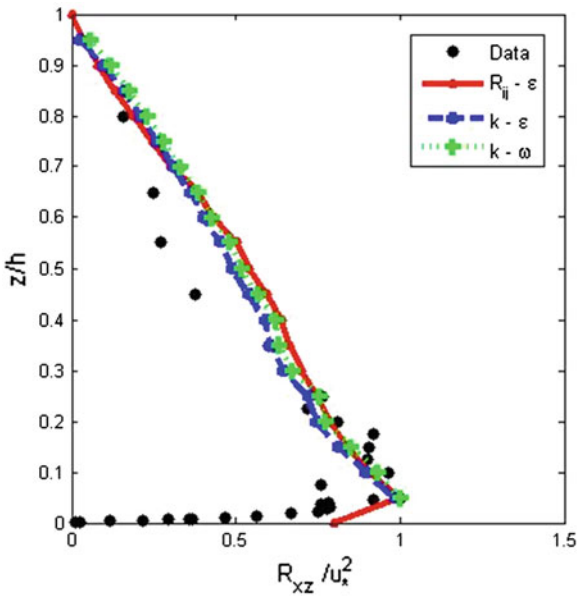

Fig. 4 Vertical profile of the dimensionless Reynolds shear stress $\frac{R_{xz}}{u_*^2} = \frac{-\overline{u'w'}}{u_*^2}$ for "only current" (i.e., no waves). Comparison with data from [2]

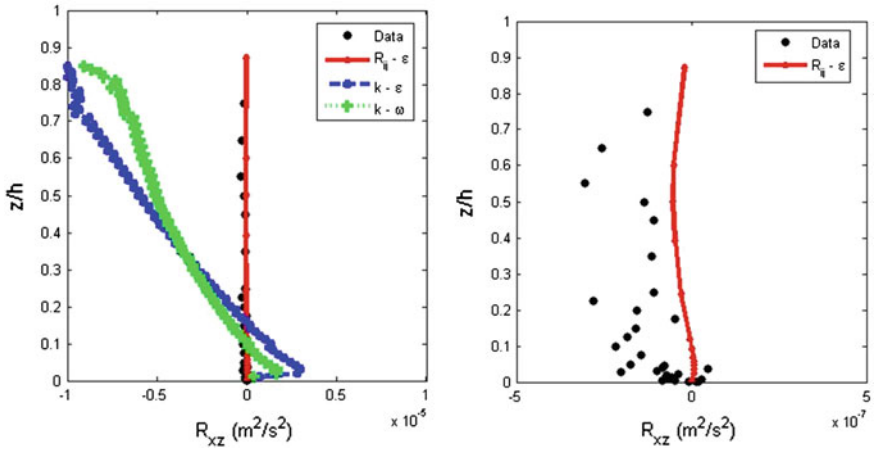

Fig. 5 Vertical profile of the Reynolds shear stress $R_{xz} = -\overline{u'w'}$ for "only waves" (i.e., no current) with the three turbulence closure models (*on the left*) and with only R_{ij}–ε model (*on the right*)

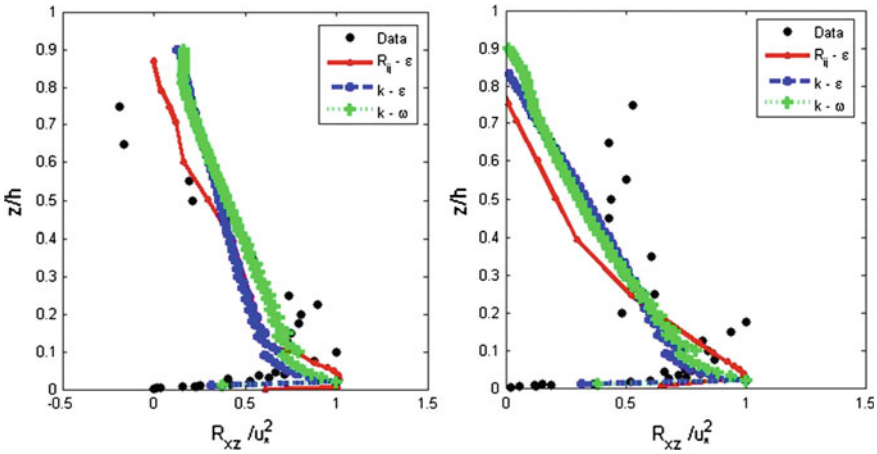

Fig. 6 Vertical profile of the dimensionless Reynolds shear stress $\frac{R_{xz}}{u_*^2} = \frac{-\overline{u'w'}}{u_*^2}$ for "waves following current" (*on the left*) and "waves opposing current" (*on the right*). Comparison with data from [2]

with *Code_Saturne* results obtained with the application of the three turbulence closure models, it can be seen that the same order of dimensionless values was achieved from all the models even if the k–ε and k–ω slightly overestimate it (Fig. 7). It should be noticed that the behaviour obtained in the turbulent viscosity profile (with a parabolic shape over depth) is achieved due to the boundary condition imposed for the turbulent dissipation rate the free surface [see Eq. (5)].

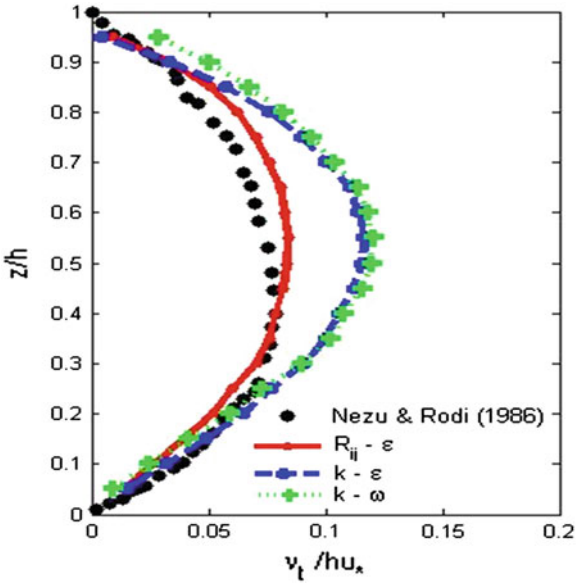

Fig. 7 Vertical profile of the non-dimensional eddy viscosity $v_t/(hu_*)$ for "only current". Comparison with data from [9]

On Fig. 8, the turbulent viscosity profiles for "waves following current" (on the left side) and "waves opposing current" (on the right side) are also shown.

In order to get a simple parameterization of the eddy viscosity development over the water column in this study, where waves and current interact, a dimensionless relation between the turbulent viscosity (v_t), acceleration due to gravity (g), mass transport velocity (U), water depth (h), wave period (T), wave length (L) and wave height (H) was sought. After considering several possible

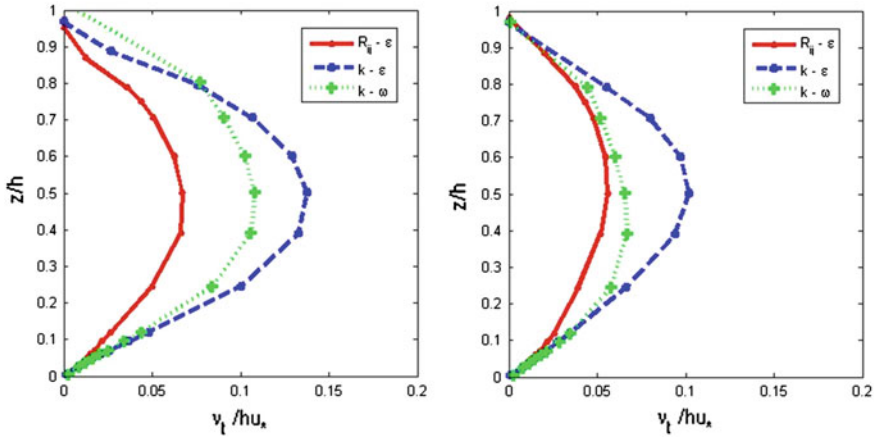

Fig. 8 Vertical profile of the non-dimensional eddy viscosity for "waves following the current" (*on the left*) and "waves opposing the current" (*on the right*)

dependences, it was found that the non-dimensional eddy viscosity $v_t/(gUT^2)$ at each relative elevation from the bottom (z/h) seems to decrease approximately linearly with the Ursell number (HL^2/h^3), as illustrated in Fig. 9, where the various variables correspond to the results of the simulations made with *Code_Saturne* with the application of the Reynolds stress transport model R_{ij}–ε.

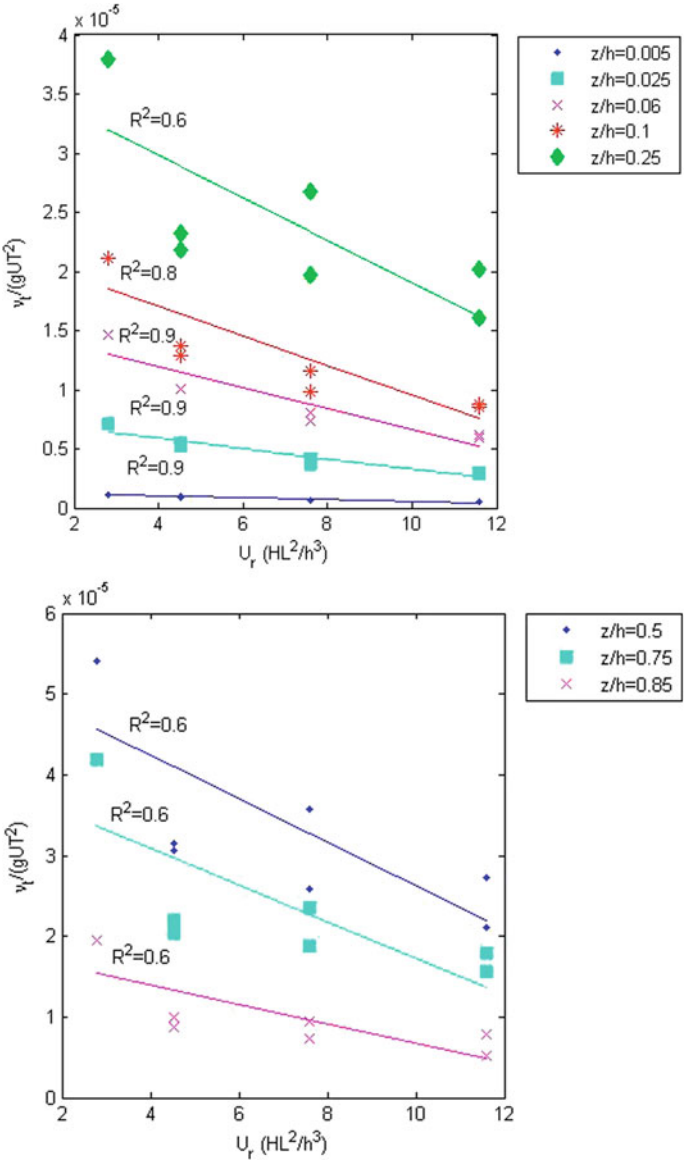

Fig. 9 Variations of the non-dimensional eddy viscosity $v_t/(gUT^2)$ for each z/h level as a function of the Ursell number HL^2/h^3

This tentative parameterization of the eddy viscosity needs, however, to be validated against a more extensive set of data. If confirmed, it could be used for instance in more simplified simulation models that rely on the eddy viscosity assumption for the turbulence closure scheme.

4.4 Analysis of the Vertical Profile of the Dimensionless Kinetic Turbulent Energy and Turbulent Dissipation

The dimensionless turbulent kinetic energy and the dimensionless dissipation rate are shown below with the three turbulence closure models for the cases "only current" (Fig. 10), "waves following current" (Fig. 11) and "waves opposing current" (Fig. 12). Semi-empirical formulas [10] were also included for the "only current" case and used to estimate the dimensionless turbulent kinetic energy (6) and dissipation rate (7).

$$\frac{k}{u_*^2} = 4.78\, e^{(-2z/h)} \tag{6}$$

$$\frac{\varepsilon h}{u_*^3} = 9.8 \left(\frac{z}{h}\right)^{-1/2} e^{(-3z/h)} \tag{7}$$

For the "only current" case, it can be observed that the profiles of the non-dimensional turbulent intensities are quite similar to each other. The comparison of the numerical simulations with the semi-empirical curves shows, in general, the same order of magnitude.

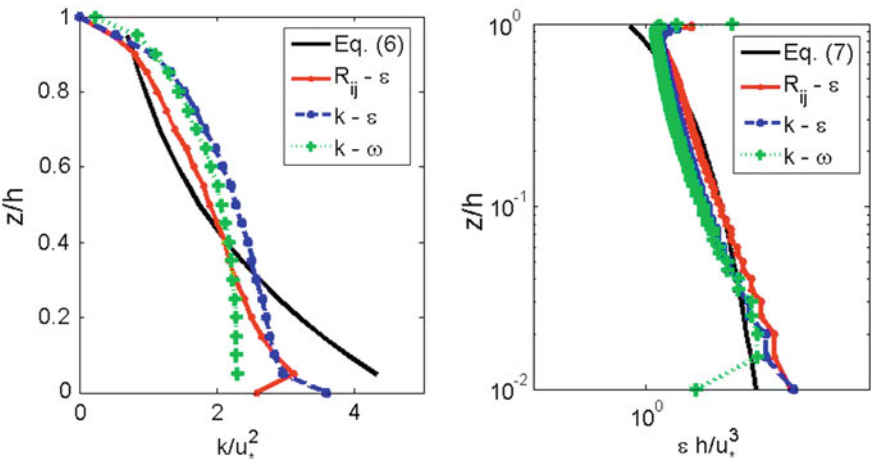

Fig. 10 Vertical profiles of the dimensionless kinetic turbulent energy and turbulent dissipation for "only current" (i.e., no waves)

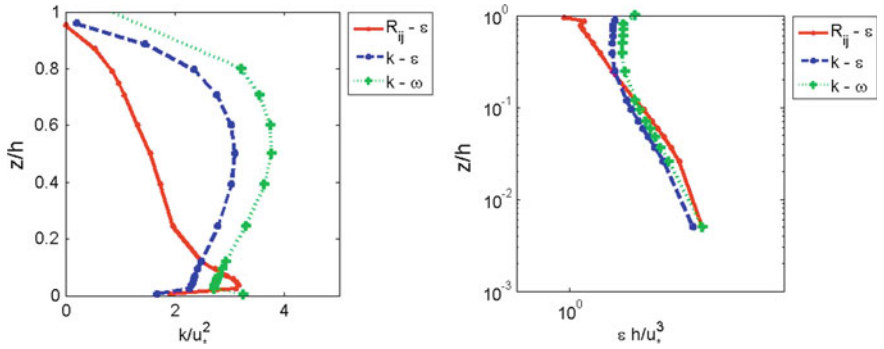

Fig. 11 Vertical profiles of the dimensionless kinetic turbulent energy (*on the left*) and turbulent dissipation (*on the right*) for "waves following the current"

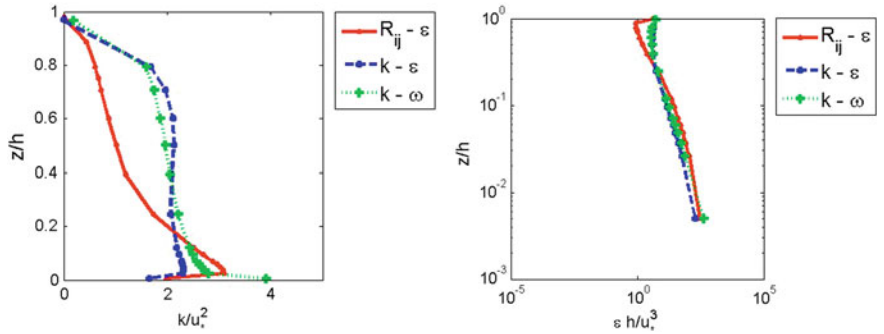

Fig. 12 Vertical profiles of the dimensionless kinetic turbulent energy (*on the left*) and turbulent dissipation (*on the right*) for "waves opposing the current"

Moreover, it was decided to also get the dimensionless turbulent energy and turbulent dissipation for "waves following the current" and "waves opposing the current" cases even if no empirical formulas were used.

5 Conclusions

Code_Saturne model was tested in free surface flows in a combined wave–current environment. Data from [2] was used to verify the performances and capabilities of the model. Different tests were available: "only current", "only waves", "waves following current" and "waves opposing current". A sensitivity test was also made, regarding the turbulence closure model that could best represent this kind of combined flows. Three turbulence closure models were used, namely two two-equation models, k–ε and k–ω and a RMS, R_{ij}–ε.

The vertical profile of the mean horizontal velocity is changed when waves are superimposed on a current. *Code_Saturne* was able to well reproduce the reduction of mean velocities near the free surface when waves are following the current and the increase of velocity when waves are opposing the current. Not only is the mean horizontal velocity profile changed, but also the Reynolds shear stress profile. When waves and current interact the bed shear stress decreases when comparing with the only current case. Once again, *Code_Saturne* gave quite good reproduction of this trend throughout the depth.

Regarding the sensitivity tests for the different turbulence closure model, the second-order RMS, R_{ij}–ε, has showed, in this case, to have the best performance to model this kind of flows. This second-order turbulence model is more general (and thus in principle more accurate and powerful) than the two-equation models. Indeed, it accounts for the directional effects of the Reynolds stress fields (anisotropy) and does not include the eddy viscosity modelling hypothesis in contrary to the two-equation models.

Finally, the expression (5) for the turbulent dissipation at the free surface, as proposed by Celik and Rodi [7], has shown to be essential to correctly reproduce the vertical profiles of Reynolds stress and eddy viscosity.

Acknowledgments Maria João Teles would like to acknowledge the support of a Ph.D. grant (SFRH/BD/61269/2009) from FCT (Fundação para a Ciência e Tecnologia), Portugal.

References

1. Archambeau, F., Méchitoua, N., & Sakiz, M. (2004). Code_Saturne: A finite volume method for the computation of turbulent incompressible flows—industrial applications. *International Journal of Finite Volumes, 1*(1), 1–62.
2. Umeyama, M. (2005). Reynolds stresses and velocity distributions in a wave–current coexisting environment. *Journal of Waterway, Port, Coastal and Ocean Engineering, 131*(5), 203–212.
3. Guimet, V., & Laurence, D. (2002). A linearised turbulent production in the $k - \varepsilon$ model for engineering applications. In W. Rodi & N. Fueyo (Eds.), *5th Engineering Turbulence modelling and Measurements*. Elsevier.
4. Menter, F. R. (1993). *Zonal two equation k–ω turbulence models for aerodynamic flows*. AIAA Paper 93-2906.
5. Speziale, C. G., Sarkar, S., & Gatski, T. B. (1991). Modeling the pressure-strain correlation of turbulence: An invariant dynamical systems approach. *Journal of Fluid Mechanics, 227*, 245–272.
6. Dean, R. G., & Dalrymple, R. A. (1991). *Water wave mechanics for engineers and scientists*. Singapore: World Scientific Press.
7. Celik, I., & Rodi, W. (1984). Simulation of free surface effects in turbulent channel flows. *Physicochemical Hydrodynamics, 5*, 217–227.
8. Teles, M. J., Pires-Silva, A. A., Benoit, M. (2013). Numerical modelling of waves and current interactions at a local scale. *Ocean Modelling, 68,* 72–87.
9. Nezu, I., & Rodi, W. (1986). Open channel flow measurements with a laser Doppler anemometer. *Journal of Hydraulic Engineering, 112*(5), 335–355.
10. Nezu, I., & Nakagawa, H. (1993). *Turbulence in open-channel flows*. Rotterdam: AA Balkema.

3D Numerical Modeling of a Side-Channel Spillway

Simulation numérique 3D d'un évacuateurde crues à seuil latéral

Géraldine Milési and Stéphane Causse

Abstract Within the framework of the rehabilitation of Electricité de Tahiti (GDF Suez) dams, Coyne et Bellier carried out a diagnosis and an overall study of the Tahinu dam. Tahinu is a 37-m-high earthfill hydroelectric dam, located in the island of Tahiti, French Polynesia. The review of the hydrological study and the application of French standards lead to increase the peak design flood from 500 to 644 m^3/s (+30 %). First, a 1D numerical modeling of the side-channel spillway (crest length 60 m) was performed to assess its discharge capacity. The conclusion was an insufficient capacity of the spillway that might induce an overtopping of the crest dam and of the sidewalls of the spillway channel. Then, to confirm these results and to take into account the specific configuration of the spillway (non-uniform distribution of the approach velocity and depth below crest, irregular geometry of the side-channel cross section, submerged weir, curved channel spillway), a 3D numerical modeling was carried out with Flow 3D®. Simulations showed more accurate results than 1D model (general pattern of the flow, upstream reservoir level). Consequently, heightenings of the dam crest and the sidewalls of the spillway channel were designed and optimized to secure sufficient freeboards for safety.

Keywords CFD · Dam · Flow 3D® · Hydraulics · Numerical simulation · Rehabilitation · Submergence · Weir

G. Milési (✉) · S. Causse
Tractebel Engineering, Le Delage: 5 rue du 19 mars 1962 92622 Gennevilliers, France
e-mail: geraldine.milesi@gdfsuez.com

S. Causse
e-mail: stephane.causse@gdfsuez.com

P. Gourbesville et al. (eds.), *Advances in Hydroinformatics*,
Springer Hydrogeology, DOI: 10.1007/978-981-4451-42-0_39,

1 Introduction

As part of the rehabilitation of Electricité de Tahiti (GDF Suez) dams, Coyne et Bellier—Tractebel Engineering carried out a diagnosis and an overall study of the Tahinu dam, mainly composed of hydrological, dam stability, and spillway capacity studies.

The review of the hydrological study and the application of French standards led to increase the peak design flood from 500 to 644 m^3/s. With an increase of nearly 30 % of the peak design flood, it was necessary to reevaluate the flow capacity of the side-channel spillway and to determine the reservoir level for different flow rates.

First of all, a 1D numerical modeling of the side-channel spillway was performed to check its discharge capacity. The key result of these calculations was an insufficient capacity of the spillway that might induce an overtopping of the crest dam and of the sidewalls of the spillway channel.

In order to confirm these results and to take into account the specific configuration of the spillway (non-uniform distribution of the approach velocity and depth below crest, irregular geometry of the side-channel cross section, submerged weir, curved channel spillway), a 3D numerical modeling was carried out with Flow 3D®. It is within this context that this chapter presents numerical modeling conducted and its results.

A rehabilitation plan has been established according to the results of the studies.

2 The Tahinu Dam

Tahinu is a 37-m-high earthfill hydroelectric dam, located in the island of Tahiti, French Polynesia. Completed in 1994, this dam is the highest of Tahiti. Its natural catchment of 10 sq km fills a reservoir, which has an area of 10 ha and a volume of 0.9 hm^3.

Currently, floods are discharged through a side-channel spillway located on the right bank of the dam. A Creager weir of 60 m long controls the inflow. The approach height of the weir is 0.5 m. The theoretical design head is 2 m for a capacity coefficient of 2.06 in free-fall conditions. A collector canal of 6.5 m depth collects the flow from the reservoir and delivers it to the chute spillway (slope of about 34 %). The chute spillway ends with a flip bucket.

3 1D Numerical Modeling

Calculations are based on analytical formulas describing flows in side-channel spillways [1]. This numerical modeling was developed in-house to take into account the important slope of the chute spillway, the different slope of the right and left sides in the channel spillway, and the submergence of the weir.

To determine the water levels in chute spillway, the Bernoulli's formula is used (1). The variables are as follows: ground level N_i; water depth h_i; channel slope α_i; head losses between two sections ΔH_{ij}. The head losses are calculated with the Manning–Strickler formula (2). The head losses vary with the flow rate Q, the Strickler number K, the wetted section S, the hydraulic radius R_h, and the distance between the two sections ΔL.

$$N_1 + h_1\cos(\alpha_1) + \frac{V_1^2}{2g} = N_2 + h_2\cos(\alpha_2) + \frac{V_2^2}{2g} + \Delta H_{12} \tag{1}$$

$$\Delta H_{12} = \frac{Q^2}{K^2 S^2 R_h^{4/3}} \Delta L_{12} \tag{2}$$

In the collector canal, the following formula (3) from the Ref. [1], based on the law of conservation of the linear momentum, has been used to calculate the water level. The difference of water level between two sections Δy_{ij} depends on the flow rate Q_i and the velocity V_i.

$$\Delta y_{12} = \frac{Q_1}{g}\frac{(V_1 + V_2)}{(Q_1 + Q_2)}\left[(V_2 - V_1) + \frac{V_2(Q_2 - Q_1)}{Q_1}\right] \tag{3}$$

Once water levels in the spillway are determined, the reservoir level, equivalent to the head H above the crest of the weir, is calculated with the formula (4) where the weir length has been discretized in x parts. Here, the discharge coefficient C_Q is variable and it can be reduced with submergence of the weir; charts provided in the Ref. [2] were used to determine the value of the discharge coefficient.

$$Q = \sum_{i=1}^{i=L_{\text{weir}}/x} Q_i = \left[\sum_{i=1}^{i=L_{\text{weir}}/x} C_{qi} L_i\right] H^{3/2} \tag{4}$$

1D numerical modeling allows us to calculate water levels, velocities, Froude number, etc. It is particularly adapted to perform quick calculations on simple geometries.

4 3D Numerical Modeling

4.1 Software

To set up the 3D model and to perform the calculations, two software programs were mainly used.

The first one, *Rhinoceros*® developed by the company *McNeel & Associates,* has been used to model the dam geometry. *Rhinoceros*® uses level points and break lines to generate a 3D geometry of the dam, thanks to its triangulation algorithm.

The software is also useful to create complex 3D objects like the weir or the spillway chute and for the post-processing;

The second software is *Flow 3D*® from the company *Flow Science*. This software has been used to set up the model (pre-processing), to perform the calculation (solver), and to analyze the results (post-processing). It is complete software that allows the user to perform hydraulic calculations for both types of flows: free surface flow and pressure flow. It is based on the resolution of Reynolds-averaged Navier–Stokes equations (RANS) using a finite volume method. In addition, Flow 3D uses a true volume of fluid algorithm for the determination of the water free surface.

4.2 Dam Geometry Model

The numerical model is composed of the earthfill dam and its reservoir, the weir, and the chute spillway. Concrete structures are displayed in green on Fig. 1.

4.3 Mesh Generation

Mesh generation is one of the most important steps to set up a numerical model. Indeed, the mesh directly affects the accuracy of results and computation time. The construction of the mesh must respect some rules to ensure the convergence and the stability of the calculation.

The mesh used in Flow 3D® is a structured rectangular mesh. The mesh is fixed; it means that its position remains unchanged during the calculation unlike other approaches where the mesh can evolve over time.

In order to mesh the computational domain, a multi-block approach was used. A total of 20 blocks were necessary. Three mesh sizes were used to refine areas with high-speed gradients. Figure 2 provides an overview of the generated mesh.

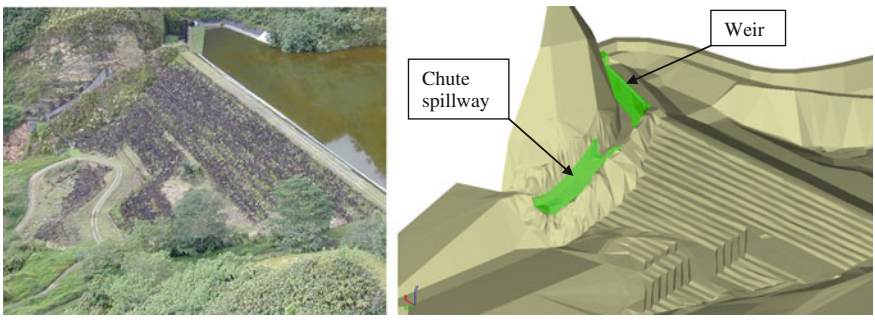

Fig. 1 Site photo and 3D geometrical model—dam, topography, concrete structures

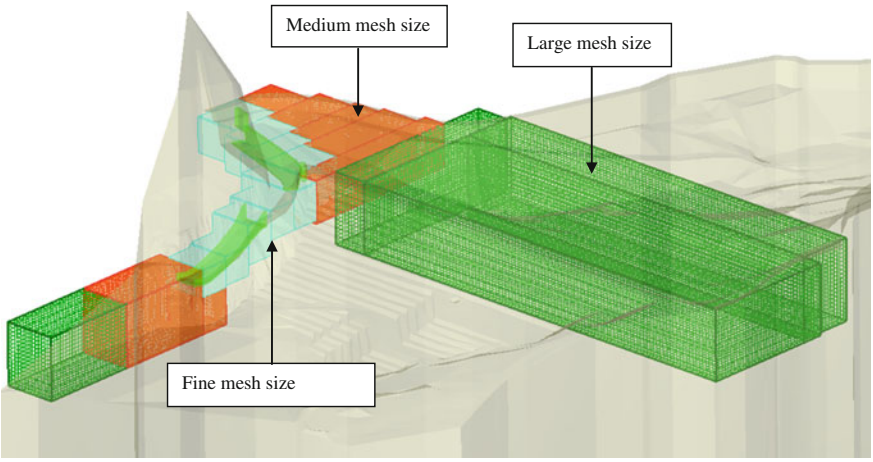

Fig. 2 Mesh generation—different mesh blocks

One of the rules to follow when building a mesh is compliance with a 2:1 ratio of the size of the mesh for two adjacent cells. Therefore, the large-size mesh is twice larger than the medium-size mesh which itself is twice larger than the fine mesh size.

Two models with different meshes have been developed to optimize the time of calculation and the accuracy of the results. The first one has a "coarse" mesh of approximately 500,000 cells (with mesh sizes of 2, 1, and 0.5 m), and the second one has a finer mesh of 3.6 million cells (with mesh size of 1, 0.5, and 0.25 m). This finer mesh has been used to simulate the design flow rate and the coarse mesh to simulate other flow rates (see Table 1). Note that the ratio between the size of a cell and the water depth above the weir for the peak design flood is 12.5 % with the coarse mesh and it is equal to 6.25 % with the fine mesh which is quite satisfactory according to the literature.

Table 1 Inlet boundary conditions

Simulation	Mesh type	Flow rate Q (m^3/s)	Return period T (year)	Reservoir level (1D) $Z_{reservoir}$ (m)	Upstream headwater (1D) H (m)
Case 1	Coarse mesh	751	PMF[a]	402.10	5.13
Case 2	Fine mesh	644	T = 10 000	401.00	4.03
Case 3	Coarse mesh	409	T = 500	399.19	2.22
Case 4	Coarse mesh	269	T = 100	398.67	1.70
Case 5	Coarse mesh	173	T = 10	398.27	1.30

[a] Probable maximum flood

To reach good mesh quality, the space between two blocks shall be smaller than 5 %. For the model with the coarse mesh, the space between the blocks is 0.37 %, whereas it is equal to 0.006 % for the finer mesh which is enough to neglect interpolation errors between blocks.

4.4 Boundary Conditions

The main boundary conditions are imposed at the entering of the computation domain and at the downstream limit. Here, a volume flow rate entering in the reservoir dam was defined and an outflow condition was used to evacuate the water from the domain.

The volume flow rate boundary condition needs two parameters: the volume flow rate and the water level. To determine a coherent water level corresponding to the flow rate, a first 1D calculation was performed. The table below lists the different simulations and the parameters associated with boundary conditions. For information, the upstream headwater depth H which is the difference between the reservoir level and the weir level is indicated in Table 1.

4.5 Physical and Numerical Parameters

The characteristics of the fluid are those of the water at 20 °C.

The head losses due to the friction between the fluid and the surface materials are taken into account by the mean roughness of the rock and the concrete estimated, respectively, to 0.5 and 85 mm.

Among the several turbulence models available, the RNG k–epsilon model was chosen.

5 Results

5.1 Stage–Discharge Curve

Several simulations were performed for different flow rates using the 1D and the 3D models.

To check that the flow has reached a steady state in the 3D simulation, the flow rate was measured in the spillway (at the upstream and at the downstream). When the measured flow rate was stable (after approximately 200 s), the water level in the reservoir was also considered stable. Results are presented in Table 2.

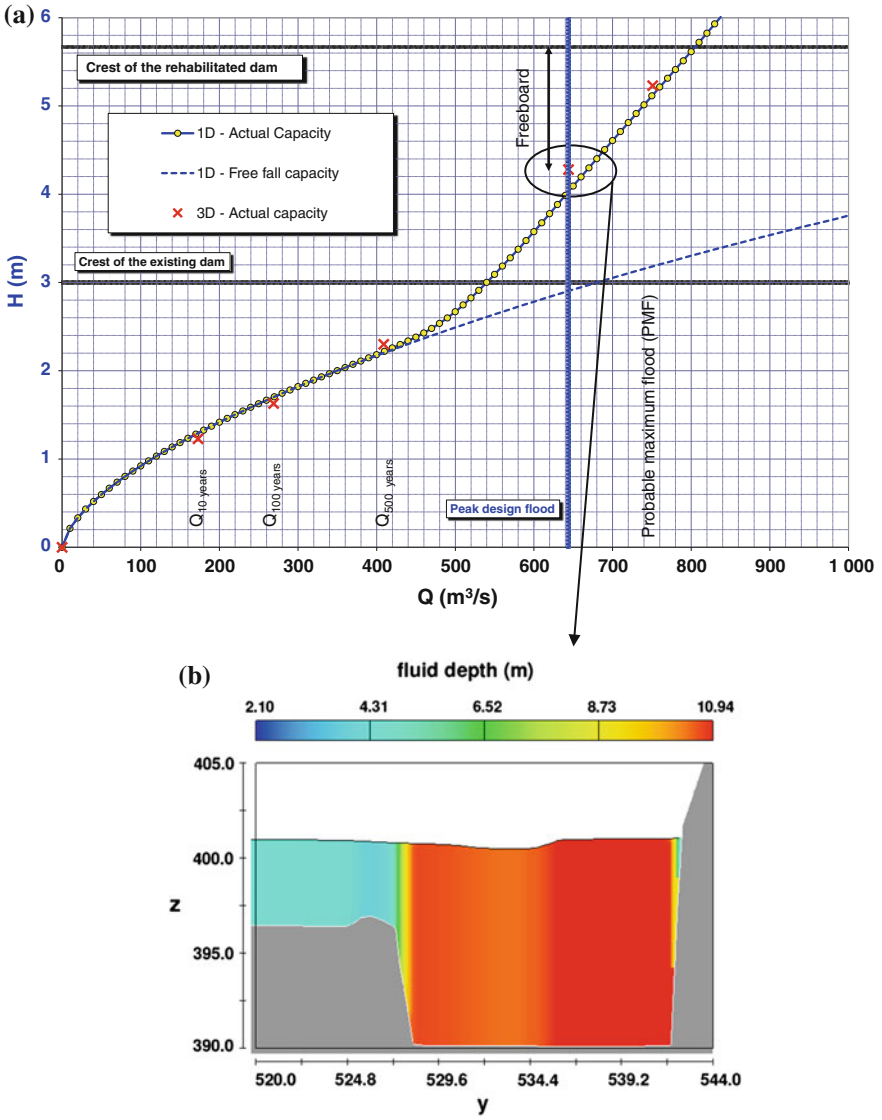

Fig. 3 Stage—discharge curve (**a**). Cross section of the weir for the design flood (**b**)

The results in 1D and 3D are very similar (difference <6.2 %). The 3D calculation allows us to validate the results issued from the 1D calculation, results that are certainly less accurate but most of the time sufficient to have a first appreciation.

Figure 3 illustrates the behavior of the spillway. It is interesting to observe the impact of the weir flooding on the reservoir level. For flow rates superior to

approximately 400 m^3/s, the weir is submerged by the tailwater depth, the discharge capacity is progressively decreasing compared to a non-submerged weir, and then, the reservoir level is increasing. For the peak design flood, the weir is completely submerged and the capacity coefficient is then reduced from 2.06 to 1.21. Results show that an overtopping of the dam crest of nearly 1 m is induced (no overtopping occurs for a non-submerged weir). As a consequence, it appears necessary to heighten the dam crest by 2.5 m to prevent overtopping and to comply with recommended freeboard, for these reference flood situations.

Table 2 Reservoir levels and upstream headwater depth—1D and 3D results

Simulation	Flow rate Q (m^3/s)	Reservoir level (1D) $Z_{reservoir\ 1D}$ (m)	H_{1D} (m)	Reservoir level (3D) $Z_{reservoir\ 3D}$ (m)	H_{3D} (m)	Difference $\Delta_{3D/1D}$ (%)
Case 1	751	402.10	5.13	402.20	5.23	1.95
Case 2	644	401.00	4.03	401.25	4.28	6.20
Case 3	409	399.19	2.22	399.27	2.30	3.60
Case 4	269	398.67	1.70	398.60	1.63	4.12
Case 5	173	398.27	1.30	398.20	1.23	5.38

5.2 Flow Features of Interest

A numerical simulation was performed using the finer mesh (case 2) to study the flow features of interest for the peak design flood ($Q = 644\ m^3/s$). The precision of the results was a priority for this case, that is why the finer mesh was chosen.

Although the results of the flow simulation in the collector channel in 1D and 3D are really close, the 3D modeling provides much more additional details on the behavior of the flow.

Firstly, the 3D model shows how irregular the free surface is (see Figs. 4, 5). Unlike the 1D model, the free surface determined now takes into account several factors such as the curvature of the channel, the raising of the free surface due to the narrow width of the collector canal, and the velocity distribution of the approach area of the weir. Thanks to these observations, it is possible to precisely define the water level in the spillway at the left and right sidewalls (see pictures 5c, d). As a consequence, these results outline the necessity to heighten the sidewalls to prevent overtopping and provide detailed data to optimize this heightening along both sidewalls (Figs. 4, 5 show the heightened sidewalls configuration).

Secondly, the 3D modeling of the spillway allows us to determine the pressure at each grid location. This is especially useful for calculating the forces exerted by the water (static, dynamic forces) on the sidewalls. Regarding rehabilitation, this served to determine the necessary reinforcement.

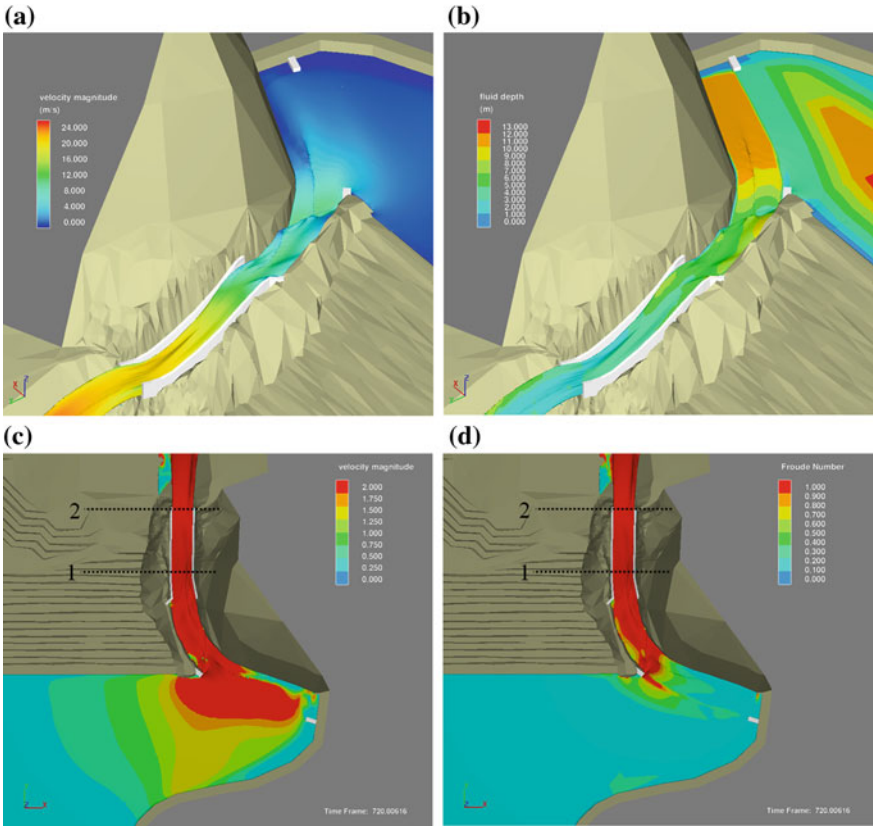

Fig. 4 3D views of the spillway—velocity magnitude (**a**, **c**); Water depth (**b**). Froude number (**d**)

Finally, 3D modeling provides multiple results as velocity, water depth, or the Froude number. The observation of the Froude number shows that the flow regime becomes supercritical at the end of the collector canal which is usual according to design rules for this type of spillways.

5.3 Overtopping

To confirm and assess the risk of overtopping, a numerical simulation of the existing dam was completed for the peak design flood ($Q = 644$ m^3/s), that is, without raising of crest dam and sidewalls spillway.

As shown in Fig. 6, a significant flow over the dam crest would occur for the peak design flood. The flow rate is estimated at about 140 m^3/s. In addition to

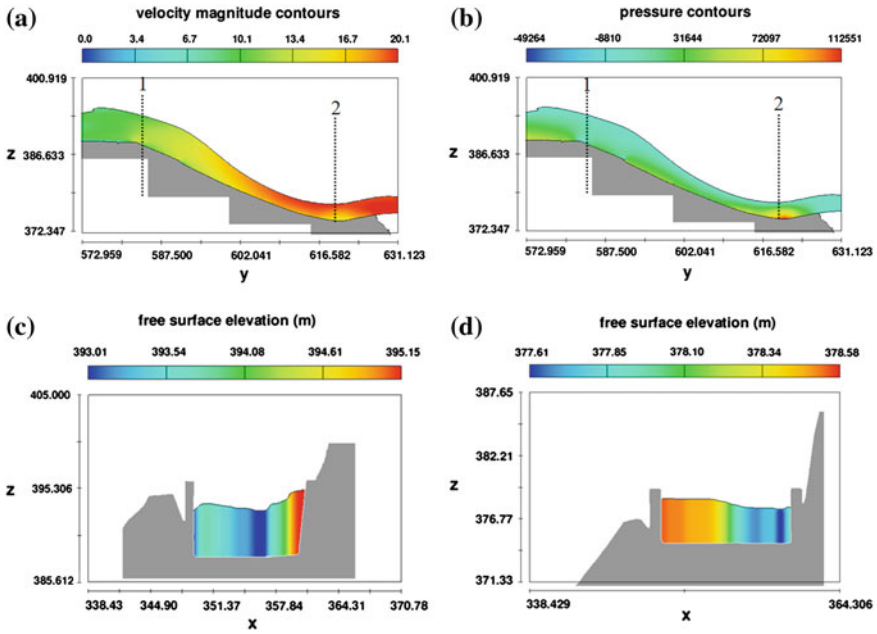

Fig. 5 2D views of the spillway—longitudinal profiles (**a**, **b**) and cross sections (**c**, **d**). **a** Longitudinal profile—velocity magnitude (m/s). **b** Longitudinal profile—relative pressure (Pa). **c** Cross section 1—free surface elevation. **d** Cross section 2—free surface elevation

providing detailed quantitative information (flow rate, speed, water depth), the 3D numerical simulation tool reveals also to be an effective communication tool, by providing a visual overview of the consequences of an overtopping.

6 Conclusions

The 1D calculations can be suited to usual spillway geometry where theoretical analysis is applicable. In our case, the 1D calculation was sufficient to have a first estimation of the reservoir level and then of the heightening of the dam crest. However, for particularly complex spillway geometry, the 3D model is much more appropriate and can provide quantity of valuable information. This type of simulation allows an accurate assessment of water levels, velocities, and pressures at any point in the flow. This is very useful in the context of reassessment studies and consequent rehabilitation works. It is possible to accurately estimate the forces acting on the sidewalls to optimize the design reinforcement. The heightening of the sidewalls can also be determined more precisely because the simulation provides different water levels on both sides. Finally, 3D computer modeling can

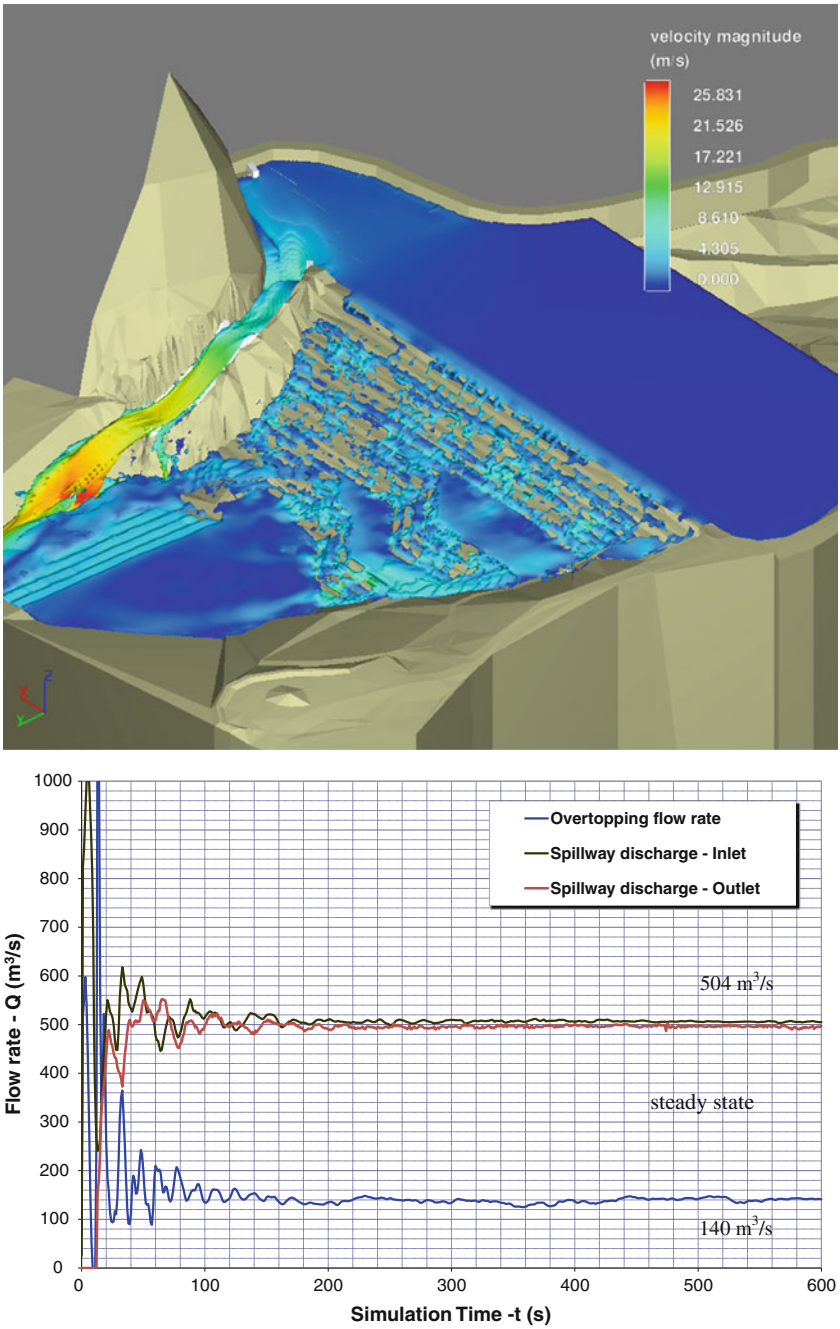

Fig. 6 Overtopping for the peak design flood ($Q = 644$ m^3/s)

effectively replace physical models for projects where the cost of physical models and the duration of the study are not compatible with the project objectives.

Acknowledgments The authors wish to thank Electricité de Tahiti (GDF Suez) for their permission to publish this chapter. Our thanks go also to Stefano Mascetti and Raul Pirovano (XC Engineering S.R.L.) for the Flow 3D® training, for their help and advice.

References

1. Khatsuria, R. M. (2005). *Hydraulics of spillways and energy dissipators*. New York: Marcel Dekker.
2. USBR. (1987). *Design of small dams* (3rd ed.). Washington: US Government printing office.

Numerical Modelling of Two-Dimensional Flow Patterns in Shallow Rectangular Basins

Matthieu Secher, Jean-Michel Hervouet, Pablo Tassi, Eric Valette and Catherine Villaret

Abstract The present work focuses on the two-dimensional (2D) depth-averaged turbulent flow in shallow rectangular basins. An accurate description of the hydrodynamics is required for further understanding the complex sediment transport processes. This work has practical engineering implication in relation to the rate of sediment deposited in reservoirs. The capability of the open-source TELEMAC modelling system to predict symmetric and non-symmetric recirculation flow patterns is analyzed by comparison with experimental results performed by Kantoush [4] for different geometry parameters and flow conditions. Numerical results are in good qualitative and quantitative agreement with experiments (regarding the number of recirculation cells and intensity of flow velocity) in symmetric and asymmetric situations. Furthermore, the influence of the mesh size, turbulence closure, and friction coefficients is also analyzed. Numerical results show good agreement in predicting 2D symmetric and non-symmetric flow patterns in laboratory conditions.

M. Secher · E. Valette
EDF—Centre d'Ingénierie Hydraulique, Savoie Technolac,
73370 Le Bourget-du-Lac, France
e-mail: matthieu.secher@edf.fr

E. Valette
e-mail: eric.valette@edf.fr

M. Secher · J.-M. Hervouet · P. Tassi (✉) · C. Villaret
EDF—R&D Laboratoire National d'Hydraulique et Environnement,
6 quai Watier, 78401 Chatou, France
e-mail: pablo.tassi@edf.fr

J.-M. Hervouet
e-mail: j-m.hervouet@edf.fr

C. Villaret
e-mail: catherine.villaret@edf.fr

J.-M. Hervouet · P. Tassi · C. Villaret
Laboratoire d'Hydraulique Saint-Venant, 6 quai Watier, 78401 Chatou, France

P. Gourbesville et al. (eds.), *Advances in Hydroinformatics*,
Springer Hydrogeology, DOI: 10.1007/978-981-4451-42-0_40,

Keywords Shallow flows · Rectangular basins · Symmetric and non-symmetric flow patterns · Flow instabilities

1 Context

For design and maintenance purposes, the knowledge of the flow in shallow water basins is relevant to highlight undesirable features such as stagnation areas, dead zones, separation and reattachment points and short-circuiting paths. In artificial dam reservoirs, large-scale flow patterns may have a strong influence on the rate of sediment deposited. If the sediment accumulated on the bottom reaches a certain threshold value, the water-storage capacity of the dam can be seriously compromised, with negative impact on the originally projected energy production. Moreover, the accumulation of sediments can contribute to the abrasion of the turbines and other components, with loss on their efficiency or even reduction in their life span.

Investigations on shallow, rectangular basins with sudden expansion at entrance and abrupt contraction at outlet have been recently reported in the literature [1–4]. Flow patterns in symmetric, finite-length basins have been studied numerically and experimentally. The main results have shown that, despite their simple configuration, symmetric flows in symmetric channels could become unstable under certain geometric and hydraulic characteristics. For these conditions, different types of flow patterns can emerge, namely channel-like flow, symmetric flow patterns characterized by two or four large eddies and asymmetric flow patterns [1].

Kantoush [4] conducted a number of experiments to study the effect of geometry on flow and sedimentation in symmetric shallow basins. Dewals et al. [3] performed numerical and theoretical analysis in a series of rectangular basins and compared their results with experimental data. By using a finite volume scheme with closure relationships for bottom friction and turbulent stresses, they showed that two-dimensional (2D) simulations performed with perfectly symmetric input data produce symmetric results and symmetric and non-symmetric flow patterns can be reproduced by a perturbation on the inflow conditions.

Dufresne et al. [2] extended the experimental database by considering a wider range of flow and geometric conditions. The impact of different flow and geometric parameters on the prediction of reattachment lengths was explored and a "shape parameter" was proposed to classify symmetric and asymmetric flows. For a large number of rectangular shallow reservoirs with different lateral expansion ratio and length, Camnasio et al. [1] conducted experimental studies to determine average velocity fields and streamlines. Their results were in agreement with previous work and confirmed the prediction of flow patterns based on the geometrical characteristics. Recently, Peng et al. [5] used the lattice Boltzmann model for shallow water equation and compared their results with the finite volume solver and laboratory experiences of Dewals et al. [3]. They also analyzed a determined range of values of Froude numbers and bed friction coefficients, concluding that

larger values of Froude number and bed friction yield flows with a weaker asymmetry and longer reattachment length.

The aim of this work is the numerical simulation of shallow rectangular basins with sudden expansion and contraction. The capabilities of the TELEMAC modelling system to reproduce symmetric and asymmetric flows are evaluated by comparing two-dimensional finite element simulations with experiences by Kantoush [4] for a wide range of geometrical configurations. The sensitivity of the model is also discussed, with emphasis on the closure turbulence model and geometrical parameters.

The outline of this article is as follows. The mathematical and numerical models are presented in Sect. 2. In Sect. 3, the experimental setup of Kantoush [4] used to compare the numerical simulations is briefly presented and the observed flow patterns are introduced. Numerical results and comparisons with experimental results are given in Sect. 4. In Sect. 5, the results of this work are summarized and the conclusions are presented.

2 Mathematical and Numerical Model

2.1 Governing Equations and Closure Relationships

Many engineering problems involving water motion can be treated as shallow turbulent flows, where the shallowness condition $h/l \ll 1$, valid whenever the depth h of the water layer is small compared to the wavelike extent l of the fluid motion, is achieved. In this work, numerical computations are based on the solution of the depth-averaged shallow water equations, expressed as function of the depth-averaged components of the flow velocity $u(\mathbf{x}, t)$ and $v(\mathbf{x}, t)$ with respect to Cartesian directions $\mathbf{x} = (x, y)$, the water depth $h(\mathbf{x}, t)$, the ground elevation measured from a reference altitude $b(\mathbf{x})$, the bed resistance terms τ_{bx} and τ_{by} in the x and y directions, respectively, the turbulent eddy viscosity ν_t, the constant density ρ, the gravitational acceleration g, and the time t [6].

In this work, computations were performed in a symmetric, rectangular domain $\Omega = L \times B$; where L and B are the basin length and width, respectively, b is the inlet (outlet) channel width of length a, see Fig. 1.

Computations are conducted using two different models for the turbulent flows, namely (1) a constant viscosity model, and (2) a two-length-scale turbulence model. The constant viscosity model is based on the assumption that the eddy viscosity ν_t is constant throughout the domain. The two-length-scale turbulence model is a depth-averaged version of the standard k-ε model introduced by Launder and Spalding [6].

A relationship for the bed resistance term is specified according to the classical quadratic, nonlinear dependency on the depth-averaged velocity, as follows:

$$\tau_b = \left(\tau_{bx},\ \tau_{by}\right) = \rho\ C_f\ (u,\ v)|U|,$$

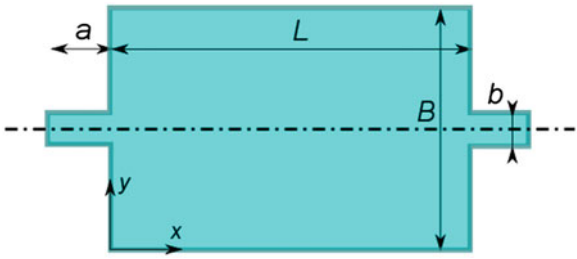

Fig. 1 General basin scheme (flow direction is from *left* to *right*)

where $|U| = (u^2 + v^2)^{1/2}$ is the Euclidean norm of the horizontal velocity vector, and C_f is the non-dimensional friction coefficient determined as function of the equivalent Nikuradse roughness k_s.

2.2 Initial and Boundary Conditions

At $t = 0$, the water surface elevation is constant, that is, $H = h(\mathbf{x}, 0) + b(\mathbf{x}) = H_0$; and the longitudinal and transversal velocity components are zero everywhere, that is, $u(\mathbf{x}, 0) = 0$ and $v(\mathbf{x}, 0) = 0$.

At the channel expansion inlet, a discharge is specified; at channel contraction outlet, the water depth is constant. A detail of the suitable boundary conditions is presented later in Sect. 4.

2.3 Dimensionless Parameters

The Vaschy-Buckingham theorem shows that 6 dimensionless parameters involving time, mass, and length can be obtained from 9 independent variables, namely the Reynolds number $R = 4|U|h/\upsilon$, with υ the water kinematic viscosity; the Froude number $F = |U|/(gh)^{1/2}$; the dimensionless friction number k_s/h; the lateral expansion ratio B/b; the dimensionless length L/B; and the dimensionless water depth H/B.

2.4 Numerical Solution

The computational framework for the solution of the shallow water equations is the TELEMAC modelling system.[1] This is an open-source, sequential and parallel

[1] www.opentelemac.org

free-surface solver based on the finite volume and finite element methods. Details of the numerical formulations for the models are given in Hervouet (2007) and not repeated here. The open-source TELEMAC modelling system was developed initially at the Laboratoire National d'Hydraulique et Environnement, a department of the research branch of Electricité de France. It is now a joint effort of several research teams in Europe (Telemac-Mascaret Consortium) and collaborations worldwide. For this work, numerical simulations were performed with the hydrodynamics module TELEMAC-2D of the TELEMAC modelling system.

Linear finite elements were chosen for the discretization of the water depth and quasi-bubble elements for the discretization of the velocity components [7]. The method used for solving the linear system is the conjugate gradient method with diagonal preconditioner.

3 Brief Description of the Experimental Setup and Flow Patterns

The numerical simulations presented in this work are compared with experimental results carried out by S. A. Kantoush at the laboratory of hydraulics constructions (LCH) of the Ecole Polytechnique Fédérale de Lausanne (EPFL) [2, 6]. Their tests were performed on an experimental facility consisting of a rectangular, PVC shallow basin with maximum length $L = 6$ m and width $B = 4$ m. Further details of the experimental setup, measurement techniques, and equipment can be consulted in [3, 4] and references therein.

Following [1], flow patterns can be classified according to the combined effects of the dimensionless length *L/B* and the lateral expansion ratio *B/b*. Channel-like flows (CH-L) occur on small expansion ratios and are independent of the length *L*. They are characterized by an unidirectional, symmetric flow, with a dominant central jet and the presence of two small eddies on both sides of the inlet expansion. This pattern was also analyzed by Abbot and Kline (1962). They found that for infinite length channels, the flow remains symmetric while the expansion ratio $B/b < 2.67$.

Symmetric flows without stagnation point (S0) occur in short basins (see Fig. 2b). A stagnation or reattachment point is defined as the point where a local

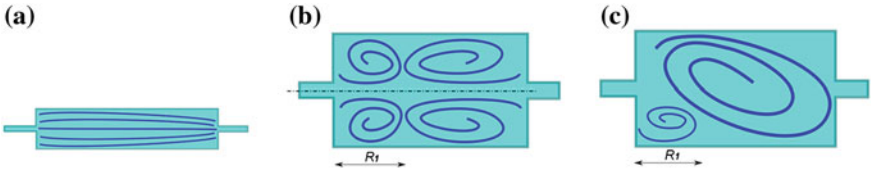

Fig. 2 Flow patterns classification. **a** CH-L/channel like, **b** S1/symmetric with one reattachment point R_1, and **c** A1/asymmetric with one reattachment point R_1. The flow is from *left* to *right*

fluid velocity is equal to zero [2]. The S0 flow pattern is characterized by two eddies placed symmetrically with respect to the channel centerline. Camnasio et al. [1] showed that this flow pattern develops if $L/B < 1$. Symmetric flows with one stagnation point (S1) are also generated for small L/B. For this case, a symmetric flow with four recirculation zones of unequal length develops. The eddies are symmetrically placed along the centerline of the channel and consist of two small eddies immediately upstream of the expansion and two larger eddies occupying approximately 2/3 of the basin length L.

When increasing L/B, asymmetric flow patterns have been observed (see Fig. 2c). The development of this kind of pattern may be explained by the Coanda effect [8], resulting from a perturbation of the flow field that pushes the main flow toward one side of the channel while increasing the velocity magnitude near the wall and decreasing the pressure near that wall. Depending on the length of the basin, one reattachment point can appear after a distance R_1. For this case, the flow pattern is denoted as A_1. A fluctuating, unstable zone between the symmetric and asymmetric flow patterns has been observed by Dufresne et al. [2] and Camnasio et al. [1]. For this case, flow patterns have shown to be highly sensitive to external perturbations.

To quantify the limit between symmetric unstable zone asymmetric flow patterns, Dufresne et al. [2] proposed a non-dimensional shape parameter T, based on the geometrical characteristics of the channel: $T = L(B-b)^{-0.6}b^{-0.4}$, see also [1]. Other patterns, such as asymmetric flows with two (A2) or three (A3) reattachment points have been analyzed by [1, 2, 4] and are not treated here. A sketch of flow patterns analyzed in this work is showed in Fig. 2.

4 Numerical Results and Discussion

In this section, numerical simulations are presented for shallow, rectangular basins with maximum length $L = 6$ m and maximum width $B = 4$ m. For all cases (except where indicated), the inlet and outlet channels were $b = 0.25$ m wide and $a = 1$ m long, see Fig. 1. At the inflow boundary, the discharge was set to $q = 0.007$ m^3/s and at outflow boundary the water depth was fixed to $h = 0.2$ m, corresponding to subcritical flows with Froude number $F = 0.10$ and to a Reynolds number $R = 112{,}000$, based on the bulk velocity and water depth at the inlet of the expansion.

Numerical simulations were conducted up to steady state using non-structured triangular meshes with Δx the representative element size. Sensitivity analysis of the time resolution has shown little impact on the results to approach to steady solutions for time steps Δt on the range [0.01; 1 s]. All computations were run on 8 CPU cores of Xeon E5620 processors with 2.4 Ghz clock speed and 8 Gb of RAM. For cases CH-L, S1, and A1, the computational time required to reach the steady state was approximately 100, 1,200, and 6,000 s, respectively.

4.1 Case CH-L

This test case corresponds to a basin with length $L = 6$ m, width $B = 0.5$ m, and geometrical ratios $B/b = 2$ and $L/B = 12$. The influence of the mesh size on the results was verified for $\Delta x = 0.1$ and 0.05 m and $\Delta t = 1$ s. For both cases, comparison with experimental data shows good agreement with observed flow field, see Fig. 3. Moreover, for $\Delta x = 0.05$ m, the model was able to capture the two small eddies on both sides of the inlet jet. By adopting $\Delta x = 0.05$ m, comparison of simulations performed with the constant viscosity model with $\nu_t = 10^{-4}$ m^2 s^{-1} and depth-averaged k-ε model showed little variations on the results. Finally, the influence of the bed roughness height was analyzed for $k_s = 10^{-2}$ and 10^{-4} m. In both cases, the simulated flow field remains very close to the experimental observations of Kantoush [4].

4.2 Case S1

This test case corresponds to a basin with length $L = 5$ m, width $B = 4$ m, and geometrical ratios $B/b = 16$ and $L/B = 1.25$. Preliminary computations performed with $\Delta x = 0.05$ m, $\Delta t = 1$ s, $k_s = 10^{-3}$ m and the constant viscosity with $\nu_t > 10^{-5}$ m^2 s^{-1} and k-ε turbulence models, showed that the main symmetric jet traversing the domain from the expansion at the inlet to the contraction at the outlet is well represented, but the observed four eddies structure does not develops [1, 4].

For similar numerical and physical parameters and constant turbulence model with $\nu_t = 10^{-5}$ m^2 s^{-1}, the model is able to represent the four circulation zones placed symmetrically with respect to the main jet, see Fig. 4. Furthermore, at approximately $x = 2.50$ m, the small deviation of the main jet due to the transfer of

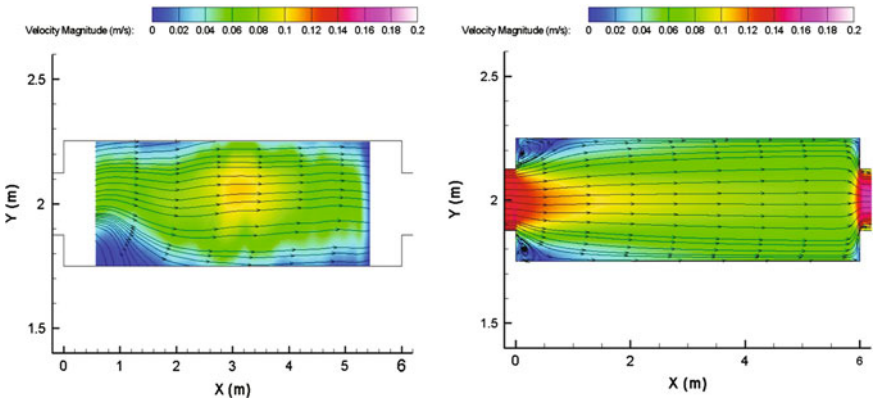

Fig. 3 Experiments (*left*) and numerical simulation (*right*) of velocity field and magnitude for the case CH-L ($L = 6$ m, $B = 0.5$ m and constant viscosity model)

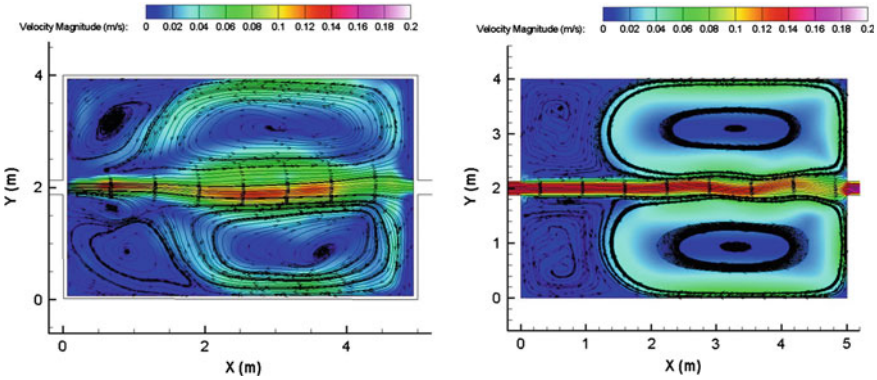

Fig. 4 Experiments (*left*) and numerical simulations (*right*) of velocity field and magnitude for the case S1 ($L = 5$ m and $B = 4$ m)

momentum toward the wall at right is well represented. A comparison between measured and simulated velocity profiles in two cross-sections of the basin, namely $x = 0.05$ m and $x = 2.50$ m, for a range of constant turbulent eddy-viscosity models with $v_t = [4.5 \times 10^{-6}; 1.5 \times 10^{-5}\ \mathrm{m^2\ s^{-1}}]$ and for the depth-averaged k-ε model are shown in Fig. 5. The solution computed with a constant turbulence model with $v_t = 10^{-5}\ \mathrm{m^2\ s^{-1}}$ compares very favorably with experimental data, despite an underestimation of about 5 % of the maximum observed velocity at $x = 0.05$ m.

4.3 Case A1

This test case corresponds to a basin with length $L = 6$ m, width $B = 4$ m, and geometrical ratios $B/b = 16$ and $L/B = 1.5$. Preliminary computations performed

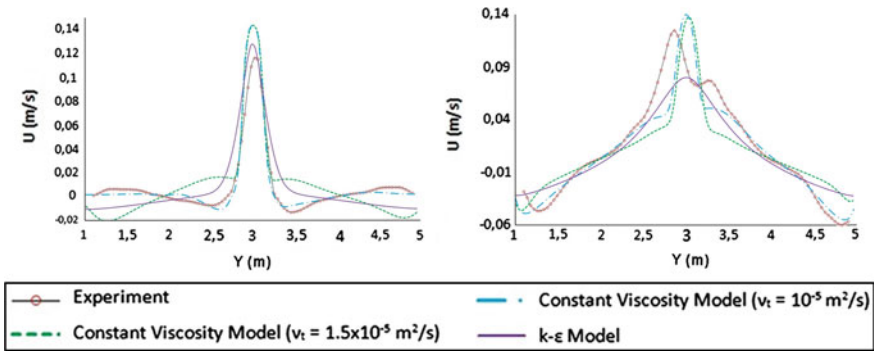

Fig. 5 Measured and simulated velocity profiles in two cross-sections of the basin at $x = 0.5$ m (*left*) and $x = 2.50$ m (*right*), for different values of v_t

with $\Delta x = 0.01$ m, $\Delta t = 1$ s; $k_s = 10^{-3}$ m and the constant viscosity with $v_t > 10^{-5}$ m^2 s^{-1} and k-ε turbulence models showed that simulations with a symmetric input data produce an erroneous, symmetric solution which does not correspond to physical reality [1, 4]. A simulation with constant turbulence model with $v_t = 10^{-5}$ m^2 s^{-1} was able to predict the observed A1-type flow, with two large recirculation zones of unequal length as showed in Fig. 6. The asymmetric pattern can be explained by the Coanda effect, where a change in the momentum of the flow at the basin entrance yields to a reduction in the pressure which modifies the hydrodynamics field by projecting the jet toward the wall [8].

The numerical results showed remarkably good agreement with simulations by Dewals et al. [3]. It is worth noting that, in contrast to results of Dewals et al., the simulations performed here were able to reproduce the asymmetric pattern observed by Kantoush [4], despite the symmetry and stability of the inflow discharge. To reproduce the asymmetric patterns, Dewals et al. specified a linear perturbation at the basin inlet [3]. As for the Lattice Boltzmann simulations of Peng et al. [5], simulations with the depth-averaged k-ε model have showed poor results when comparing with experimental observations. Furthermore, model results have showed to be highly sensitive to the finite element mesh topology. These topics will be subject of further investigations.

4.4 Transition Zone S1/A1

Between symmetric (S1) and asymmetric (A1) flow patterns, an instability transition area characterized by flows highly sensitive to external perturbations was observed by [1, 2]. Preliminary results showed that basins with geometrical configurations in the limit symmetric-asymmetric S1/A1 were difficult to reproduce. To investigate the capabilities of the TELEMAC-2D to reproduce flow

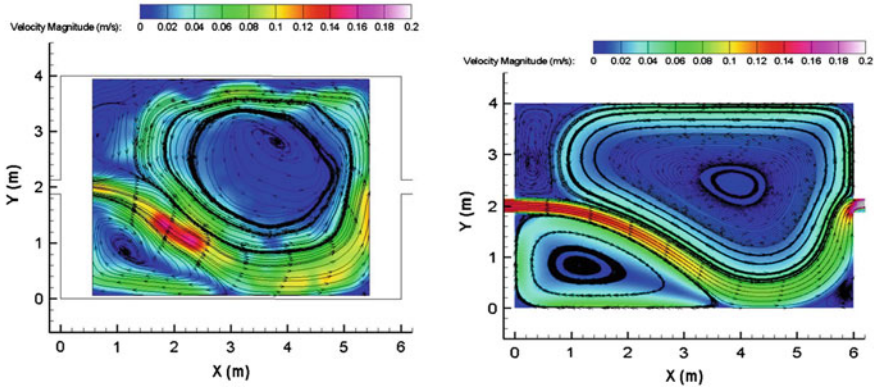

Fig. 6 Experiments (*left*) and numerical simulation (*right*) of velocity field and magnitude for the case A1 ($L = 6$ m and $B = 4$ m)

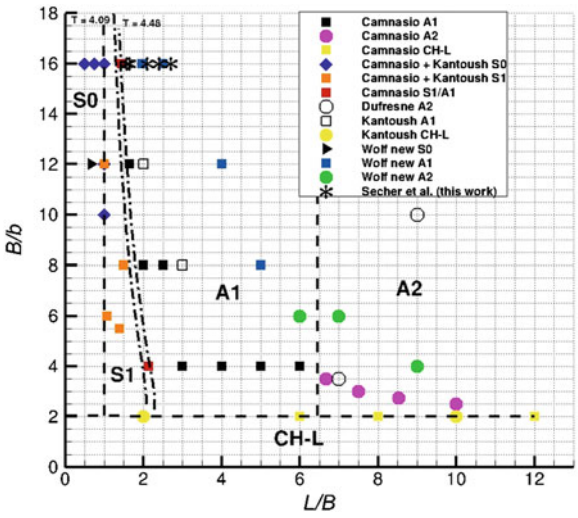

Fig. 7 Diagram of flow patterns classification (adapted from [1], see also Sect. 3). The numerical computations performed in Sect. 4.4 are indicated with the symbol "*", see Table 1 for geometrical characteristics. *Dash-dot lines* represent the threshold values that delimit the symmetric unstable area asymmetric flow patterns calculated with the non-dimensional parameter T [1, 2]

patterns in the transition zone, the number of geometrical configurations tested by [1–4] has been expanded with five new additional configurations, corresponding to lengths $L = 6.3$, 6.6, 8.4, 9.6, and 10.8 m with constant width $B = 4$ m and $b = 0.25$ m, see Fig. 7. For $\Delta x = 0.01$ m, $\Delta t = 1$ s, and $k_s = 10^{-3}$ m, numerical simulations showed that the model is less predictive if the geometry is close to the transition zone.

Computations performed near the asymmetric zone with the constant viscosity model with $\nu_t = 10^{-5}$ m^2 s^{-1} developed asymmetric flows for a symmetric discharge input. Table 1 synthesizes the computed flow patterns for the zone S1/A1, reproduced with both constant eddy-viscosity and k-ε turbulence models. In Fig. 7, dash lines indicate the (fuzzy) limit between each flow pattern. Dash-dot lines represent the threshold value predicted with the non-dimensional parameter T of Dufresne et al. [2]. The critical values corresponding to the zone symmetric instability area asymmetric flow patterns are $T = 4.09$ and $T = 4.48$ [1]. Numerical computations presented in this section are consistent with the observations of Camnasio et al. [1] and with the forecasting capability of the non-dimensional parameter T of Dufresne et al. [2].

Table 1 Simulated flow patterns for the new geometrical characteristics

Turbulence model	$L = 6.3$ m	$L = 6.6$ m	$L = 8.4$ m	$L = 9.6$ m	$L = 10.8$ m
Constant viscosity	A1	A1	A1	A1	A1
k-ε	S1	S1	A1	A1	A1

5 Conclusions

In this paper, the capabilities of the 2D hydrodynamics model (TELEMAC-2D) to simulate large, recirculating flows in shallow turbulent basins are demonstrated by comparison with experiments of Kantoush [4]. Numerical simulations also show that flow patterns depend on the geometrical characteristics of the basin, in agreement with previous observations by Camnasio et al. [1] and Dusfresne et al. [2].

For CH-L-type basins, the unidirectional, symmetric flow with two small eddies near the inlet is well reproduced for both the constant viscosity and depth-averaged two-length-scale k-ε turbulence models. For S1-type basins, the symmetric jet with four large-scale eddies is well represented with the constant viscosity model. For this case, the depth-averaged k-ε model was not able to reproduce the observed eddies. For A1-type basins, the two large, asymmetric recirculation zones observed in A1-type basins are well predicted by the numerical simulations. The formation of this asymmetric pattern can be explained by the Coanda effect. Furthermore, the simulations are able to reproduce the asymmetric pattern even for a fully symmetric discharge at the inlet, in contrast to simulations of Dewals et al. [3]. As in the previous case, the k-ε turbulence model represented poorly the experiments, as was also observed by Peng et al. [5].

In the transition zone S1/A1, numerical simulations show that model results are highly sensitive to the choice of turbulence model and the model is therefore less predictive. Furthermore, computations performed nearby the asymmetric zone with the constant viscosity model developed the experimentally observed asymmetric flows. In general, numerical results compare qualitatively well with experimental data, whereas the k-ε model results develop symmetric pattern, possibly due to numerical diffusion of the first-order numerical scheme. Except for the CH-L-type, the 2D model shows strong dependency on the turbulence model. Further investigations on this topic are underway, on the basis of 3D numerical simulations. Further work will also include coupling with sediment transport model (Sisyphe) in order to reproduce large-scale sedimentary patterns in shallow basins at laboratory and field scale.

Acknowledgments The authors would like to thank S. A. Kantoush (German University in Cairo) for their experimental data and advice. Helpful comments from B. Dewals (Université de Liège, Belgium) are gratefully acknowledged.

References

1. Camnasio, E., Orsi, E., & Schleiss, A. J. (2011). Experimental study of velocity fields in rectangular shallow reservoirs. *Journal of Hydraulic Research, 49*(3), 352–358.
2. Dufresne, M., Dewals, B. J., Erpicum, S., Archambeau, P., & Pirotton, M. (2010). Classification of flow patterns in rectangular shallow reservoirs. *Journal of Hydraulic Research, 48*(2), 197–204.

3. Dewals, B. J., Kantoush, S. A., Erpicum, S., Pirotton, M., & Schleiss, A. J. (2008). Experimental and numerical analysis of flow instabilities in rectangular shallow flow basins. *Environmental Fluid Mechanics, 8*, 31–54.
4. Kantoush, S. (2008). Experimental study on the influence of the geometry of shallow reservoirs on flow patterns and sedimentation by suspended sediments. Ph.D Thesis. Ecole Polytechnique Fédérale de Lausanne, Switzerland.
5. Peng, Y., Zhou, J. G., & Burrows, R. (2011). Modeling free-surface flow in rectangular shallow basins by using Lattice Boltzmann method. *ASCE Journal of Hydraulics Engineering, 137*, 12.
6. Hervouet, J.-M. (2007). *Hydrodynamics of free surface flows: Modelling with the finite element method*. England: Wiley.
7. Mewis, P. & Holtz, K.-P. (1993). A quasi-bubble approach for the shallow water equations: Advances in hydro-science and engineering. *Proceedings of the 1st international conference on hydroscience and engineering in Washington*, (volume 1, pp. 768–774). Washington D.C. USA.
8. Chiang, T. P., Sheu, T. W. H., & Wang, S. K. (2000). Side wall effects on the structure of laminar flows over a plane-symmetric sudden expansion. *Computers and Fluids, 29*, 467–492.

A 3-Dimensional Numerical Simulation of Flow Over a Broad-Crested Side Weir

Mohammad R. Namaee, Mohammad Rostami, S. Jalaledini and Mahdi Habibi

Abstract One of the applications of side weirs is predicting the accurate flow measurement in irrigation and floodwater spreading systems. However, the hydraulic behavior of this type of weir is complex and difficult to predict accurately. In this study, the flow over a broad-crested side weir is numerically investigated based on experimental data under subcritical condition. The numerical model considers flow over side weir using Reynolds's average Navier–Stokes (RANS) equations. The renormalization-group (RNG) k-ε model was used to account for turbulence modeling and the volume of fluid (VOF) scheme was also used in the model to find free surface of flow. The simulation results were validated by experimental data. The simulation results provided detailed analysis of flow pattern, pressure distributions in longitudinal and transverse sections over the side weir. This study shows that existing numerical models using RANS are useful in design of side weirs.

Keywords Side weir · 3D Simulation · Subcritical

1 Introduction

Management of floodwater spreading system essentially depends on accurate flow measurement. Side weirs are essentially weirs installed along the sides of the main channel to divert or spill excess water. In floodwater spreading systems, Side weirs are widely used to divert flows from main channels into lateral channel [1, 2].

M. R. Namaee (✉)
Hydraulic Structures from Khaje Nasir Toosi University of Technology,
Tehran—Karaj Special Road Km 10—St. Ashry martyr, 113613445 Tehran, Iran
e-mail: mnemaie@yahoo.com.Iran

M. Rostami · S. Jalaledini · M. Habibi
Hydraulic Engineering, Soil Conservation and Watershed Management Research Institute,
Tehran, Iran

P. Gourbesville et al. (eds.), *Advances in Hydroinformatics*,
Springer Hydrogeology, DOI: 10.1007/978-981-4451-42-0_41,

Estimation of flow characteristics over the side weirs is an important issue and an ongoing problem in the area of water measurement and especially in floodwater spreading systems. Side weirs are one of the most important and sensitive part of flood water spreading systems. So inappropriate and malfunction of them will have a fatal effect on the whole system [3]. Hence, it is necessary to study the hydraulic behavior of the side weir carefully. Traditionally, the studies of the performance of the side weirs are carried on only with physical models. But the necessary time for the construction and realization of the tests is, sometimes, the limiting factor of the search for optimization of the projects and the observation of all structure operation conditions. Add to that, the difficulties for modification of the structures geometric details that may raise the budget and time spent on the study. With the recent development of the computational resources, the numerical models can help studying the hydraulic behavior of the side weirs. The versatility of the numerical models, even if the model is not to be used in the final determination of the best geometry, differently of the physical models, turn the numerical models into valuable tools that can easily be used in the adjustment of various design details and in geometry modifications [4, 5].

The present work presents a numerical study of the flow over a side weir. A numerical model, based on free-surface computational fluid dynamics (CFD) model, is used in the development. The objective of the study is to determine the characteristics of the flow over the side weir, aiming to get the interaction between the physical model and the numerical model, though the comparison of the data obtained. In addition, the behavior of the flow inside the main channel is described, focusing the free-surface profile, the values of Froude number and velocities. Finally, the simulation results were validated by experimental data. These studies show that there is reasonably good agreement between the physical and numerical models for the pressure distributions, flow pattern, and lateral discharge using the CFD modeling techniques.

The commercially available CFD model Flow-3D software that was developed by the flow science was applied. This is rather satisfactory software for the solution of equations that represents the free-surface turbulent flow [6].

2 Physical Model

The experiments were carried out at the laboratory of Soil Conservation and Watershed Management Research Institute (SCWMRI) of Tehran, Iran. The experimental setup was consisted of a main channel and a lateral channel (Fig. 1). The main channel was 30 m long and the channel had a trapezoidal cross section. The main channel was 0.6 m deep with a 0.001 bed slope. The channel was constructed from earthen material. A combination of small coarse gravel and sand was mixed to provide the roughness coefficient of about 0.02 which is a experienced manning roughness coefficient in earth channels [7]. In order to get the required manning roughness coefficient, d_{50} of bed material was first estimated by

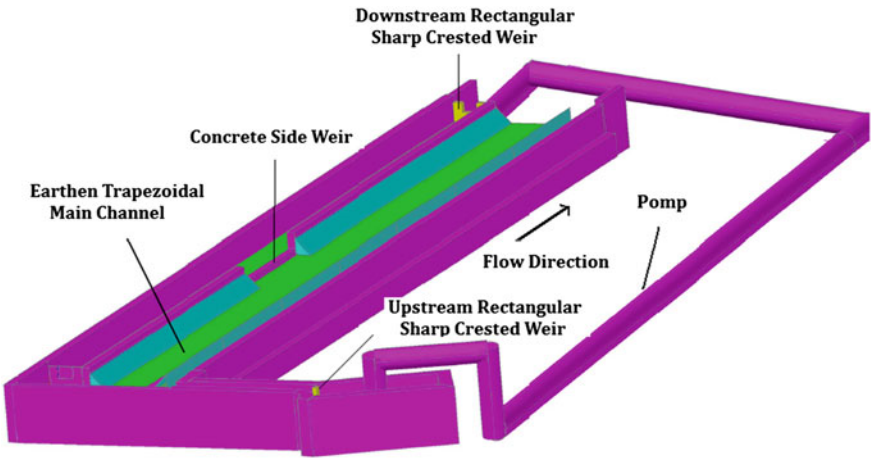

Fig. 1 Laboratory setup

Strickler formula which is the most popular for estimating manning's coefficient in natural streams [8]. Afterward, the bed material was mixed together so that the required d_{50} of the bed material which has been obtained by strickler formula has been nearly obtained. Figure 2 shows the main channel section with two different widths of 1 and 1.65 m, respectively. The lateral channel was 1.5 m wide and 0.8 m deep and was situated parallel to the main channel. A rectangular weir was placed at the end of the lateral channel in order to measure the discharge of the side weir. A point gauge with ±0.1-mm sensitivity was placed at 0.5 m from the weir. A concrete side weir with the length of 4 m and the width of 23 cm was constructed at the distance of 12.88 m from upstream inlet. The inlet discharges were measured via a rectangular sharp-crested weir. A calibrated standard rectangular was installed at the beginning of the main channel which is used to adjust inlet flow to an accuracy of ±0.1 L/s. Water was supplied to the main channel from a large 2-m-deep feeding basin. Water depth measurements were conducted using point gauges installed at the side weir region and the center line of the main channel. A special type of movable car which can move in both x and y directions on a rail were used to measure depth of flow. Eight piezometers were installed on the center line of the side weir to measure pressure values. A sluice gate was fitted at the end of the main channel in order to control the depth of flow as the downstream boundary condition. At the beginning of the experiments, after closing the sluice gate, flow with low discharges would be directed into the main channel until the bed materials were well saturated. Afterward, the discharges were increased little by little to prevent significant bed deformation. Also in order to dissipate the energy of the inlet flow, three cemented-stepped spillway were made at the beginning of the main channel. As discharges were increased slowly, movement of the bed material, especially at high discharges, was almost neglectable. Experiments were conducted at subcritical-flow and stable-flow conditions.

Fig. 2 The main channel with two different base widths

2.1 Experimental Measurements

Data collected includes the measurements of hydrostatic pressure at different locations both in the longitudinal and transverse direction of flow on the crest of the side weir and in the main channel. They were measured at 25 cm from the upstream and downstream edge of the weir by means of pizometers installed at the bottom of the side weir. In Fig. 3, locations of the measured hydrostatic pressures are shown with alphabetic letters.

3 Numerical Modeling

The commercially available CFD package FLOW-3D uses a finite-volume approach to solve the RANS equations by implementing of the fractional area/volume obstacle representation (FAVOR) method to define an obstacle [6]. The general governing RANS and continuity equations for an incompressible flow, including the FAVOR variables, are given by

$$\frac{\partial x}{\partial x_i}(u_i A_i) = 0, \tag{1}$$

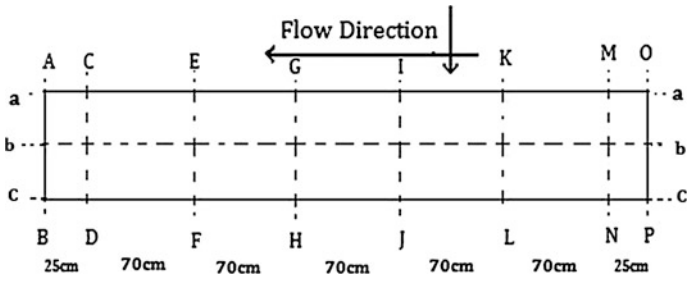

Fig. 3 Locations of measured hydrostatic pressures on the weir crest

$$\frac{\partial u_i}{\partial t} + \frac{1}{V_F}\left(u_j A_j \frac{\partial u_i}{\partial x_j} = \frac{1}{\rho}\frac{\partial P}{\partial x} + G_i + f_i\right), \tag{2}$$

where u_i represents the velocities in the x_i directions which are x, y, and z directions; t is time; A_i is the fractional area open to flow in the subscript directions; V_F is the volume fraction of fluid in each cell; ρ is fluid density; p is hydrostatic pressure; G_i is gravitational acceleration in the subscript directions; and f_i represents the Reynolds stresses for which a turbulence closure model is required [6, 9]. To numerically solve the free-surface profile over the side weir, it is important that the free surface is accurately tracked. In FLOW-3D, the free surface is defined in terms of the volume of fluid (VOF) function, F, which represents the volume of fraction occupied by the fluid [6]. A two-equation renormalized group theory model (RNG model) as outlined by Yakhot and Orszag [10] was used for turbulence closure. The RNG model is known for an accurate description of low-intensity turbulence flows and flows having strong shear regions [11]. For each cell, values of the state variables were solved at discrete times using a staggered grid technique. The staggered grid places all dependent variables at the center of each cell except for the velocities and the fractional areas [6]. Velocities and fractional areas are located in the center of the cell faces normal to their associated direction. Pressures and velocities are coupled by using successive over relaxation (SOR) method which is a semi-implicit method. This semi-implicit formulation of the finite difference equations allows for an efficient solution of low-speed and incompressible flow problems [9, 11, 12].

3.1 Model Geometry and Computational Grid

The geometry of the model was reproduced using AUTOCAD. The domain was discretized using two uniform mesh blocks. The number of grids and the dimensions of the numerical model in (x, y, z) is shown in Table 1. Figures 4 and 5 show the geometry and the position of the mesh blocks used in the numerical model.

3.2 Boundary Conditions

The upstream boundary condition in x direction was defined as "specified stagnation pressure." Outflow boundary was set at the downstream of x direction.

Table 1 The dimensions of the numerical model and number of the grids used in the numerical model

	$X(m)$	$Y(m)$	$Z(m)$	N_{cellx}	N_{celly}	N_{cellz}	N_{Total}
Block1	30	2.4	0.34	600	80	50	2,400,000
Block2	30	1.25	0.34	400	100	30	1,200,000
Total number of cells	–	–	–	–	–	–	3,600,000

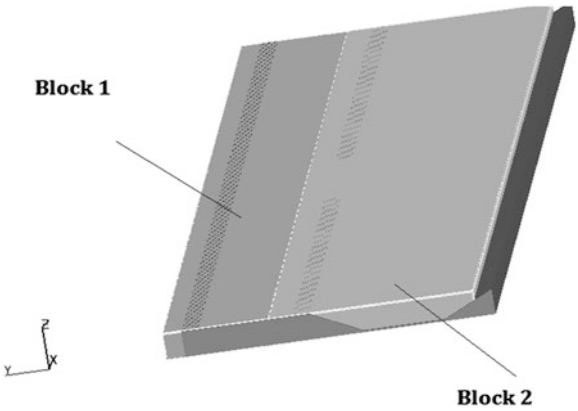

Fig. 4 The position of the mesh blocks used in the numerical model

Boundary condition for the z direction was labeled as "symmetry" which implies that identical flows occur on the other side of the boundary and hence there is no drag. The "wall function" was applied in the y direction and the negative z direction. The acceleration of gravity was applied in the negative z direction. The wall roughness was set using the roughness height computed from the manning formula. The evolution in time was used as a relaxation to the final steady state. The steady state was checked through monitoring the flow kinetic energy. Physical model configurations were simulated during 64 s. It should be mentioned that the simulation was done for the inlet discharge of 110 lit/sec.

3.3 Simulation Results

Figure 5 shows the variation of the Froude number in the main channel. As it can be seen in Fig. 6, the flow at the upstream and the downstream of the side weir is subcritical. In subcritical flow, the flow upstream, downstream, and along the length of the side weir remain subcritical at all points [3]. The key feature to note is that the water level in the main channel increases along the weir in the downstream direction. Therefore, the head acting on the weir is greater at the downstream end than at the upstream end. As a result, the discharge intensity of the spill flow is not constant but increases in the downstream direction [2, 3]. Figure 7 shows the water surface profile obtained at subcritical-flow condition. Figure 8 shows the longitudinal dynamic viscosity of water at longitudinal axis b–b on the side weir crest. Figure 9 also shows the simulation process of flow at different times of simulation.

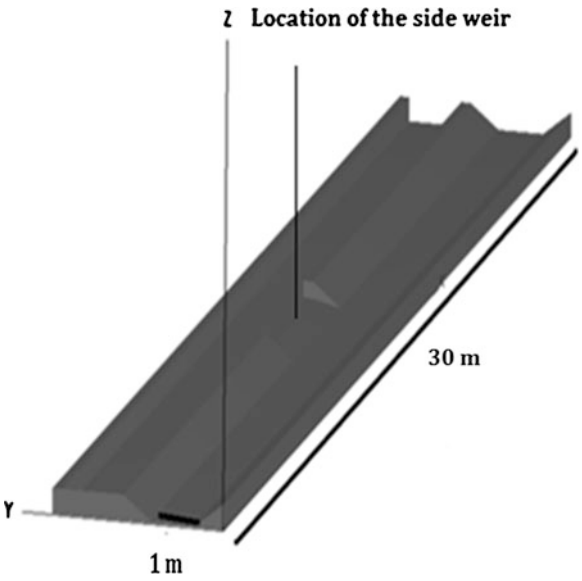

Fig. 5 The geometry of the numerical model

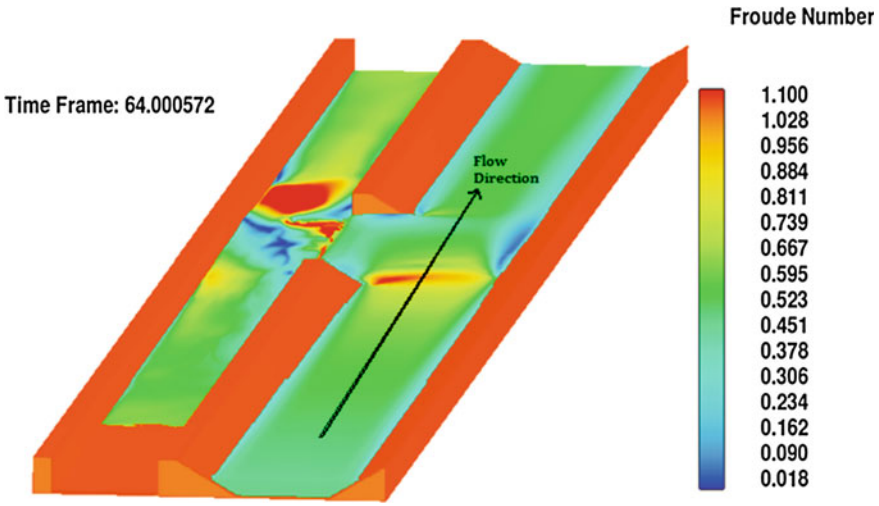

Fig. 6 The contour of Froude number in the main channel

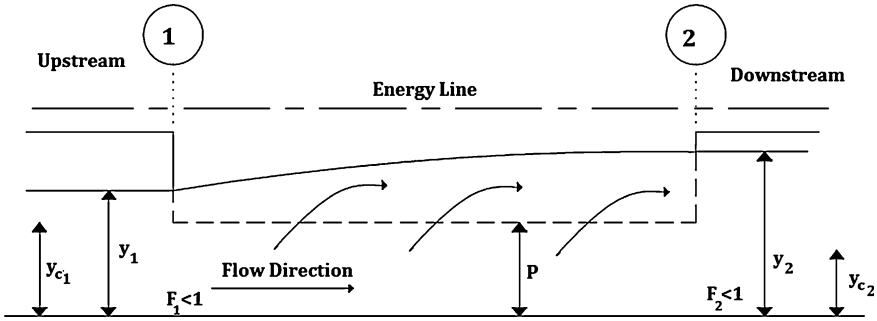

Fig. 7 Longitudinal flow profile at a side weir under subcritical condition [3]

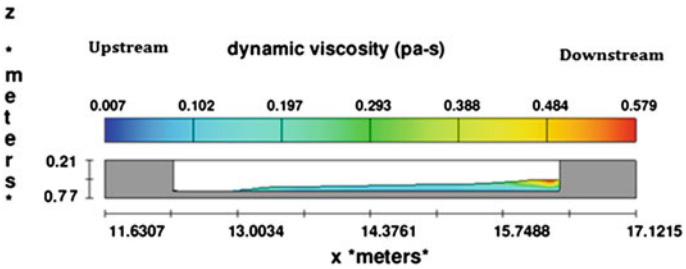

Fig. 8 The longitudinal dynamic viscosity of water at axis b–b of the side weir crest

3.4 Comparison Between the Numerical and Experimental Data

For validating the results obtained with the numerical simulation, they were compared with experimental data obtained from the physical model. The longitudinal and transverse pressure distributions over the side weir were measured at specified points. Figures 10, 11, 12, 13, 14, 15 show the result of comparison between the simulated longitudinal pressure distributions over the side weir with the experimental data, at axis a–a, b–b, and c–c, respectively. As it is clear in these figures, the highest difference between the experimental and the simulated results of pressure distribution is at the upper section of the side weir. Because in the numerical model, it was assumed that the bottom and the lateral walls of the main channel are fixed and firm, but in the experimental setup, they move especially at high discharges. So at the upper section of the side weir where the flow diverts into the side weir, as the result of the collision of the flow with the bed material, erosion will occur which affects the flow pattern. This is the reason for the difference between the simulated and the experimental data at this section.

In Figs. 16, 17, 18, 19, the simulated results of the transverse pressure distributions over the side weir are compared with the experimental data at sections A–B and O–P, respectively. As it is clear in the above figures, longitudinal and

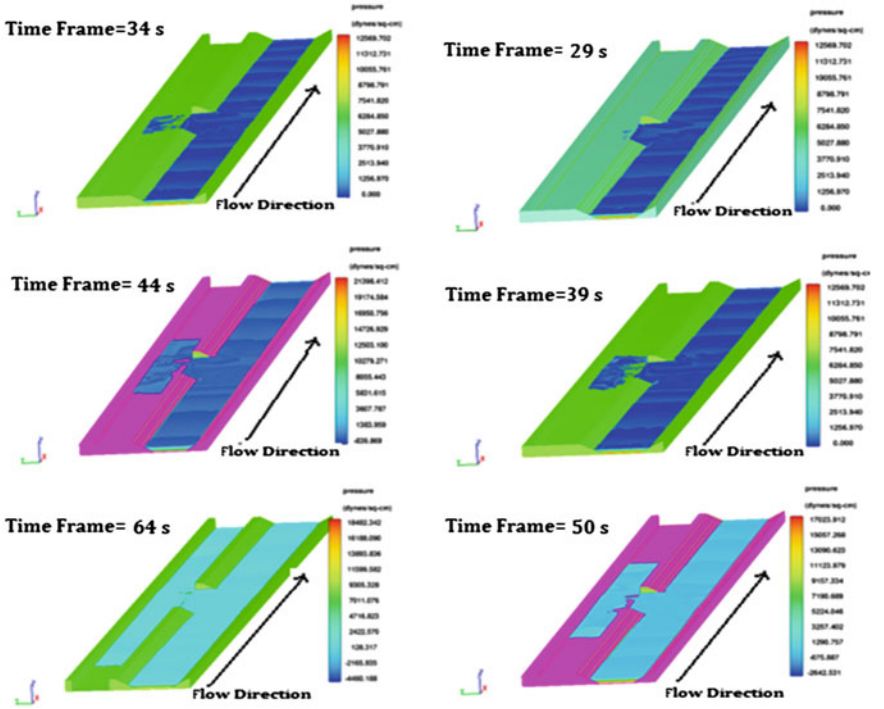

Fig. 9 The simulation process of flow at different times of simulation

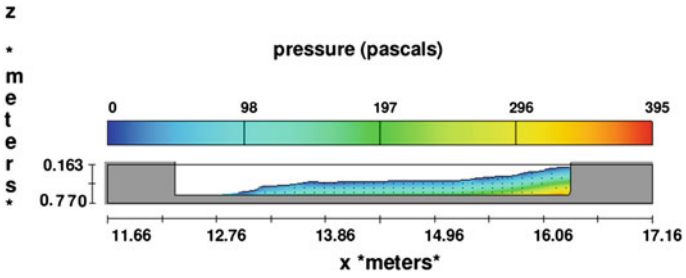

Fig. 10 Longitudinal contour of pressure distribution profile over the side weir at axis a–a

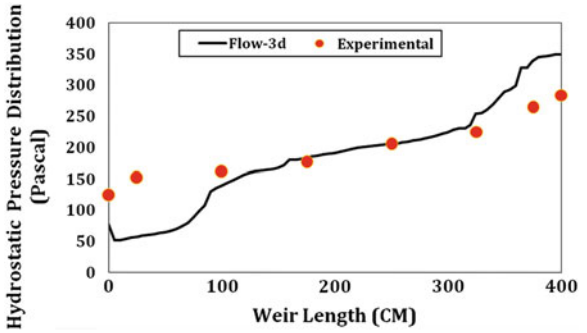

Fig. 11 Longitudinal pressure distribution profile over the side weir at a–a axis

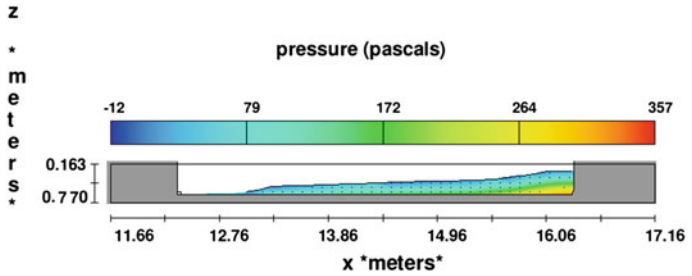

Fig. 12 Longitudinal contour of pressure distribution profile over the side weir at axis b–b

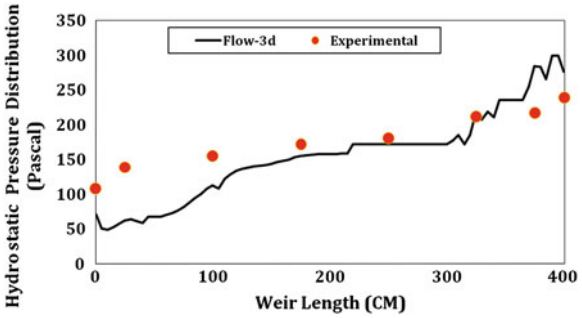

Fig. 13 Longitudinal pressure distribution profile over the side weir at axis b–b

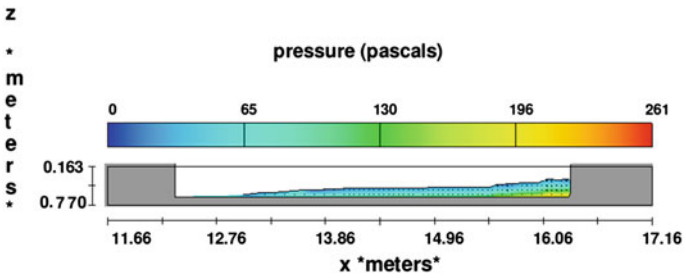

Fig. 14 Longitudinal contour of pressure distribution profile over the side weir at axis c–c

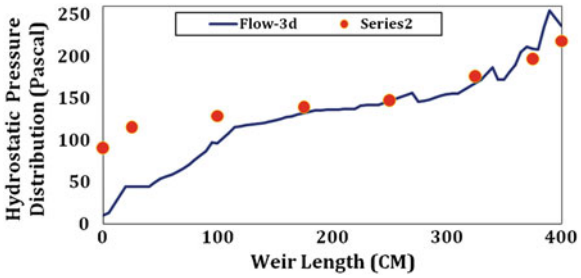

Fig. 15 Longitudinal pressure distribution profile over the side weir at axis c–c

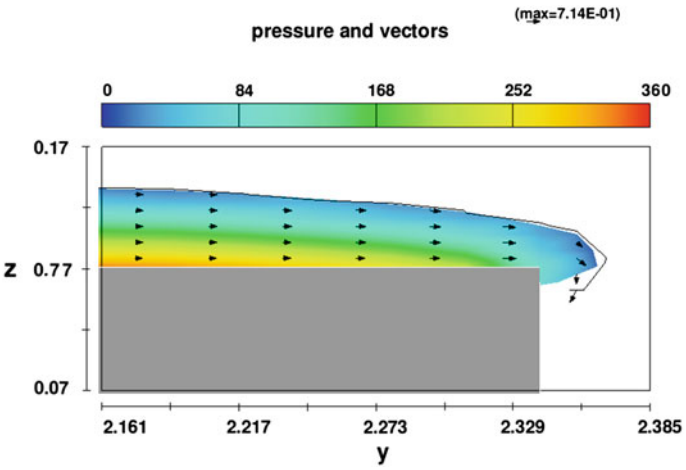

Fig. 16 Transverse pressure distribution contour over the side weir at section A–B

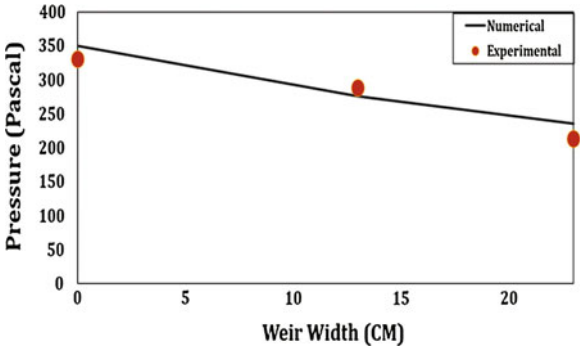

Fig. 17 Transverse pressure distribution profile over the side weir at section A–B

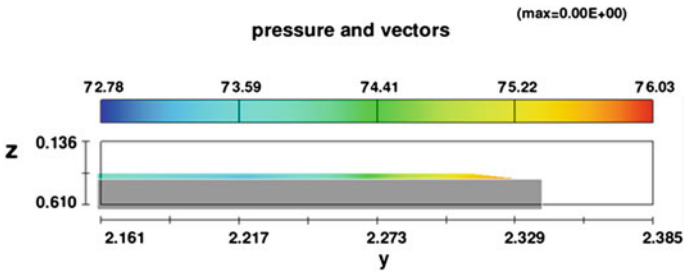

Fig. 18 Transverse pressure distribution contour over the side weir at section O–P

Fig. 19 Transverse pressure distribution profile over the side weir at section O–P

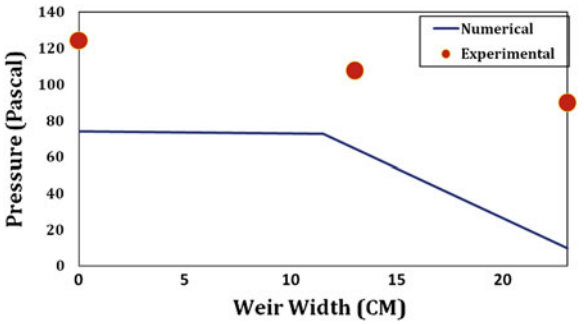

transverse pressure distributions in the downstream end of the side weir are almost in good agreement with the experimental data. But at the upstream section of the side weir, because of the rigid assumption of the lateral wall as mentioned above, numerical result differs with the experimental one.

4 Conclusion

In this chapter, the flow over a broad-crested side weir is numerically investigated based on experimental data. The simulation results provided detailed analysis of flow pattern and pressure distributions in longitudinal and transverse sections over the side weir at specified locations. The result of numerical model was in a good agreement with the experimental except at upper section of the side weir where the flow diverts into the side weir. In this location, because of the collision between the flow and the earthen material, a part of the lateral wall would be eroded in the experiments, but in the numerical model, this part is assumed to be rigid. This study shows that existing numerical models using RANS are useful in design of side weirs.

References

1. Bos, M.G. (1989). Discharge measurement structure. Pub. Water Resources Pubns.
2. Tan, H., Wang, L., & Gilbreth, K. (2001). Design of Side Weirs in Subcritical Flow. *Urban Drainage Modeling*, 438−449. Doi: 10.1061/40583(275)42
3. Bromwich, B.C., Rickard, C.E., Gasowski, Y., & May, P.W.R. (2003). Hydraulic design of side weirs. Pub. Thomas Telford Publishing.
4. Yeoh, G.H. & Tu, J. (2010). Computational techniques for multi-phase flows. Elsevier Ltd., U.S.A, pp. 407–500.
5. Szymkiewicz, R. (2010). *Numerical modeling in open channel hydraulic* (pp. 263–300). Poland: Springer.
6. Flow Science, Inc. (2000). Flow-3D user's manual.
7. Chow, V. T. (1959). *Open channel hydraulics*. New York: McGraw-Hill.
8. Subramanya, K. (1986). Flow in open channels. Tata McGraw-Hill Education.
9. Kim, Dae-Geun. (2007). Numerical analysis of free flow past a sluice gate. *Journal of Civil Engineering KSCE, 11*(2), 127–132.
10. Yakhot, V., & Orszag, S. A. (1986). Renormalization-group analysis of turbulence. *Journal of Applied and Computational Mathematics, 57*(141), 1722–1724.
11. Daraghi, B. (2010). Flow Characteristics of bottom outlets with moving gates. *Journal of Hydraulic Research, 48*(4), 476–482.
12. Sarfaraz, M., & Attari, J. (2011). On numerical simulation of uniform flow region over a steeply sloping stepped spillway. 6th National Congress on Civil Engineering, Semnan University, Semnan, Iran, April 26–27, 2011.

Rans Simulations of Flow Over Dunes with Low Lee and Sharp Lee Angles

Artemis Motamedi, Hossein Afzalimehr, Gerald Zenz, Majid Galoie and Artemis Motamedi

Abstract On the basis of laboratory experiments, this chapter presents the effect of different dune dimensions on flow separation. The present research assesses the quality of Reynolds-averaged Navier–Stokes turbulence model for predicting the flow over two-dimensional dunes. Three different dunes were developed with two lee-slope angles of 8° ($\Delta = 4\&6$ cm) and 38° ($\Delta = 4\&8$ cm). The length of the simulated separation zone was compared with experimental data. It is found that the numerical model provides a good overall consistency with the ADV measurements. Also the separation zone has a strong relation with the lee angle. At lee angles less than 10°, the shape of the crest or dune height has no effective impact on flow separation.

Keywords Dune · Lee angle · 3-D numerical modeling · Separation zone · Reattachment point

A. Motamedi (✉) · H. Afzalimehr
Department of Water Engineering, Isfahan University of Technology, Isfahan 84156, Iran
e-mail: artemis.mot@gmail.com

H. Afzalimehr
e-mail: hafzali@cc.iut.ac.ir

G. Zenz · M. Galoie
Institute of Hydraulic Engineering and Water Resources Management, TUGraz, Austria
e-mail: gerald.zenz@tugraz.at

M. Galoie
e-mail: m.galoie@student.tugraz.at

A. Motamedi
Department of Water Engineering, Iran and Institute of Hydraulic Engineering and Water Resources Management, Isfahan University of Technology, Isfahan 84156 TUGraz, Austria

P. Gourbesville et al. (eds.), *Advances in Hydroinformatics*,
Springer Hydrogeology, DOI: 10.1007/978-981-4451-42-0_42,

1 Introduction

Topography of river beds are formed by alternating highs and lows generating the macroscale bedforms such as bars, dunes, antidunes, riffles, and pools [6, 9]. These bedforms cause changes in the mean velocity, turbulence profiles, and sediment transport dynamics of the flow [2, 7, 8, 12, 15].

River dunes are rhythmic patterns that develop on the river bed due to the interaction between the turbulent flow and the moving bottom. They have heights in the order of 10–30 % of the water depth and lengths in the order of 10 times their heights; they migrate in downstream direction and are of asymmetrical shape with mild stoss-side slopes and steep leesides (Fig. 1), often reaching the angle of repose (about 30–35°) and sometimes may possess far lower leeside angles, perhaps of only 2–10° [4, 5, 11].

In this chapter, by using the physical model of fixed dunes, characteristics of a flow over a dune sequence were examined. Therefore, high-resolution RANS simulations were performed and were compared to experimental data obtained in the hydraulic laboratory of the Institute of Hydraulic Engineering and Water Resources Management of Graz University of Technology, Austria.

Although the fixed bedform is not a correct representation of the natural dunes, the study over fixed dunes will improve the understanding of turbulence over dunes. Moreover, the use of fixed bedforms allows a high spatial resolution of analysis and sampling very close to the boundary which is not possible with mobile bedforms.

2 Methods

2.1 Physical Modeling

The physical modeling experiments were done in the flume of 12 m long, 0.75 m wide, and 0.9 m deep (Fig. 2). Two honeycomb cages are placed in front of the outlet pipe to ensure the smooth, vortex-free, uniform flow of water through the

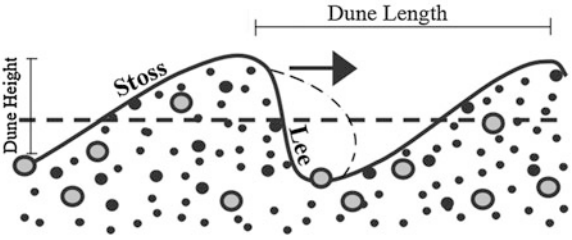

Fig. 1 The geometric variables characterizing the dune shapes and the separation zone behind of the crest

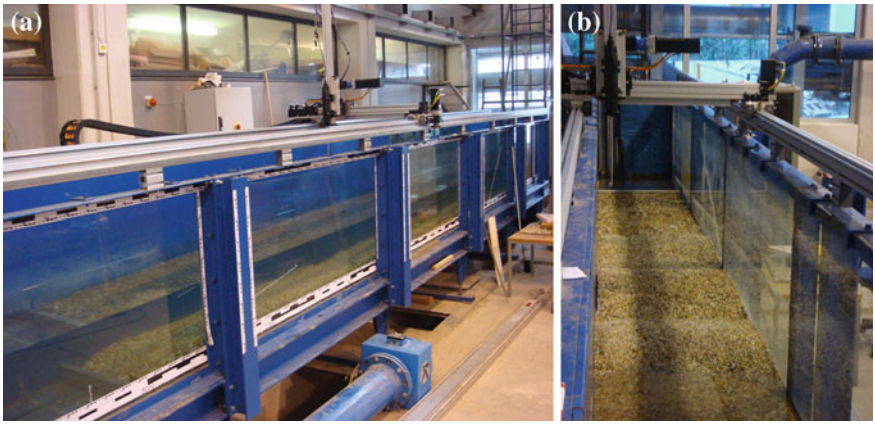

Fig. 2 Setup of experimental; **a** Side view, **b** Top view

experimental channel. An electromagnetic discharge meter with a digital display is fitted with the outlet pipe to facilitate the continuous monitoring of the discharge.

The dunes had mean wavelength $\lambda = 100$ cm and mean height varied for different dunes ($\Delta = 4$–8 cm) which are consistent with values of real dunes dimensions in field [14]. The angles of the stoss side was approximately 6° and leeside slope of the dunes were 8° and 38° (see Table 1). Each dune spanned almost the width of the flume.

Primary and secondary flow velocity components were measured over cross sections throughout the flow using Vectrino ADVs. Measurements were made at 13 profiles along the flume with 50 points per profile.

ADV is a high-precision instrument that measures all three components of velocity with fluctuations. The velocity data were collected for 2 min at the sampling rate of 200 Hz with the lowest point in each profile being 3 mm above the flume bed surface and below the side-looking probe. Factory calibration of the ADV is specified to be $\pm$ 1.0 % [13]. The sampling frequency was fixed at 200 Hz and the signal-to-noise ratio (SNR), which shows the sufficiency of seeding material, exceeded more than 15 (the manufacturer's recommended value). A correlation coefficient, output with each ADV sample, is a quality parameter that indicates the degree to which all particles within the sampling volume are moving

Table 1 Summary of hydraulic conditions and dune dimensions used in this study

Flow depths at trough (cm)	32, 20
Flow Discharges (Lit/s)	30, 15
Dune Heights (cm)	4, 6, 8
Dune Wave Length (cm)	100
Leeside angles (in degree)	8, 38
Stoss-side angle (in degree)	6
Maximum Velocity (m/s)	20
Maximum Reynolds number	60000
Maximum Froude number	0.15

in precisely the same manner. Low values may result from high turbulence, the presence of large individual particles or bubbles, a low SNR, or interference from boundaries. WinADV was used to filter out samples with correlation coefficients $\leq$ 85 % and signal-to-noise ratio $\leq$ 15 db.

2.2 Numerical Modeling

Experimental researches should be complemented with numerical simulations, not only for the further details of the flow mechanisms over fixed dunes but also to serve as predictive tools to perform parametric studies and better understanding of moving bed mechanism.

Yoon and Patel [15] presented calculations of the flow over dunes based on the solution of the Reynolds-averaged Navier–Stokes (RANS) equations and reported a good agreement between computed and measured time-averaged velocities. It should be mentioned that most numerical simulations are based on solutions of two-dimensional (2D) RANS equations. These simulations provide mean flow quantities, such as velocity profiles, Reynolds shear stress, and bed resistance, but do not give any information about the coherent unsteady flow structures (Lyn 2002). Coherent structures can be predicted either by direct numerical simulation (DNS) or Large Eddy Simulation (LES).

Simulating of dune separation zone has been done using the program called "Sediment Simulation In Intakes with Multiblock option", or "SSIIM". It was developed by Olsen [10] and based on the three-dimensional situation. This numerical scheme is based on a solution of the RANS equations, in which all effects of the turbulent motion must be captured by a turbulence model. The Navier–Stokes equations for non-compressible and constant density flow can be expressed as

$$\frac{\partial U_i}{\partial t} + U_j \frac{\partial U_i}{\partial x_i} = 1/\rho \frac{\partial}{\partial x_j}\left(-P\delta_{ij} - \rho\overline{U_i U_j}\right) \tag{1}$$

The left term on the left side in this Eq. (1) is the transient term. The next term is the convective term. The first term on the right-hand side is the pressure term and the most right term is the Reynolds stress term.

In this chapter, the model calculations were tested against field observations and produced reasonable replications of measured time-averaged velocity, separation zone, and in particular velocity profiles.

The domain was discretized by two different grids in order to examine grid sensitivity. The coarse grid consisted of 801 $\times$ 76 $\times$ 20 ($\sim$ 1.2 million) points whereas the fine grid employed 801 $\times$ 76 $\times$ 40 grid points, which sums to approximately 2.4 million grid points. The grid spacing of the fine and coarse grid in terms of wall units is $\Delta x \approx 1$ cm in the streamwise direction, $\Delta y \approx 1$ cm in spanwise direction. The spacing near the bed for finer grids is $\Delta z \approx 1$ mm and for coarser grids is $\Delta z \approx 1$ cm and is stretched above the bed toward the free surface.

Structured grids for the numerical modeling are shown in Fig. (3). The grid size for each dune is 100 cells in the streamwise direction, 75 cells in lateral direction, 20 and 40 cells in vertical direction. The cell size is in XY plane is approximately 1*1 (cm^2).

3 Results

In this part, ADV results are studied and compared with a calibrated model in predicting the separation zone. To achieve a better graphical scheme and clear comparison of the experimental and 3-D numerical results, a new graphical software was also developed. Figure (4) shows the measured velocity profiles over low- and sharp-angle dunes ($\Delta = 4$ cm), collected by ADV for a flow rate of 30 lit/s and water depth of 32 cm.

3.1 Grid Comparison

In Fig. (4), measured velocity profiles of (A) position (shown in Fig. 3) have been drown and compared with two different grid size simulations.

The agreement between measurements and simulations by fine grid indicates the separation zone which appears in dunes with sharp lee angles. [Negative velocities in (Figure 4b) could prove the flow separation]. Moreover, the results approve that the finer grid is better than coarser grid to predict the velocities and separation zones.

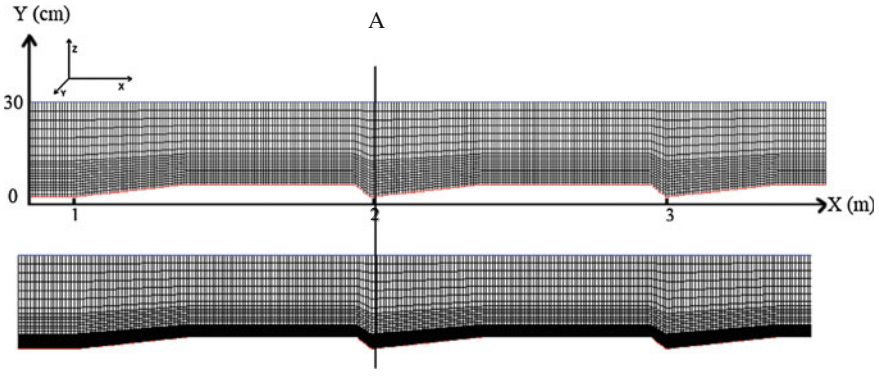

Fig. 3 Two different grids grid for the numerical modeling of sharp dune

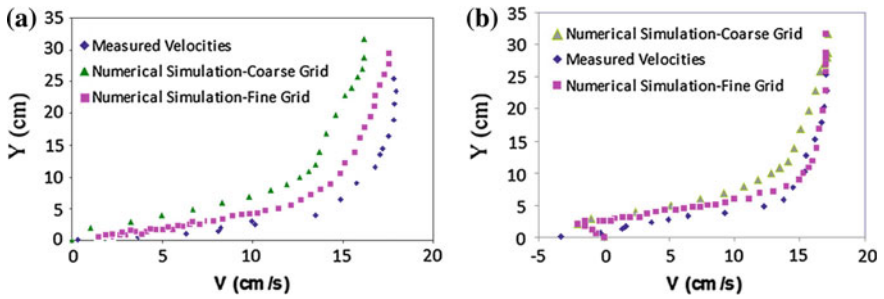

Fig. 4 Comparison of simulated streamwise velocities with the measured data in the interaction of 2 dunes. **a** presents the velocity profiles of low lee angle of dunes ($\alpha = 8°$), and **b** is for sharp lee angle ($\alpha = 38°$).The black dots represent the measured velocity by (ADV), while the other dots represent the simulated results from the fine and coarse grid

3.2 Simulated Separation Zone

Figure (5) shows simulated velocity profiles over sharp- and low-lee-angle dunes. The negative velocities show the separation region which is created downstream of the crest and the lengths are not same in different dunes. The results reveal a larger separation zone for sharper-angle dunes while a separated flow region is smaller in a same angle with lower height (Fig. 5c, d). Flow condition is same for all shown dunes, (flow rate of 30 lit/s and water depth of 32 cm).

Comparison of measured and simulated separation lengths in dune types (c, d) and (a, b) reveals that when the lee of a dune is around 8°, flow conditions cannot cause an effective impact on the flow separation. The results are the same as of several field studies which have shown that many dunes may possess far lower leeside angles, 2–10° [1, 4, 11] and may impart considerably different characteristics to the flow field. Best et al. [1] also indicated the absence of a zone of time-averaged permanent reverse flow on the low leeside both in physical and numerical models.

The length of flow separation, L, was measured and simulated from the crest, where the flow separates, to the flow reattachment point. Table 2 shows the length of the separation zone for different dunes in various discharges and water depths. The numerical model could present the separation lengths as $L = (1.7–2.3)\Delta$. The result of increasing the velocity by decreasing the water depth in Table 2 is to cause the larger separation zone downstream of the crest.

Also the results reveal a larger separation length for higher flow discharge at the same water depth. Also, for the same flow discharge and lower water depth, the separation is much bigger so that by reducing the water depth (around 0.6), the ratio of L/Δ becomes 1.2–2.2.

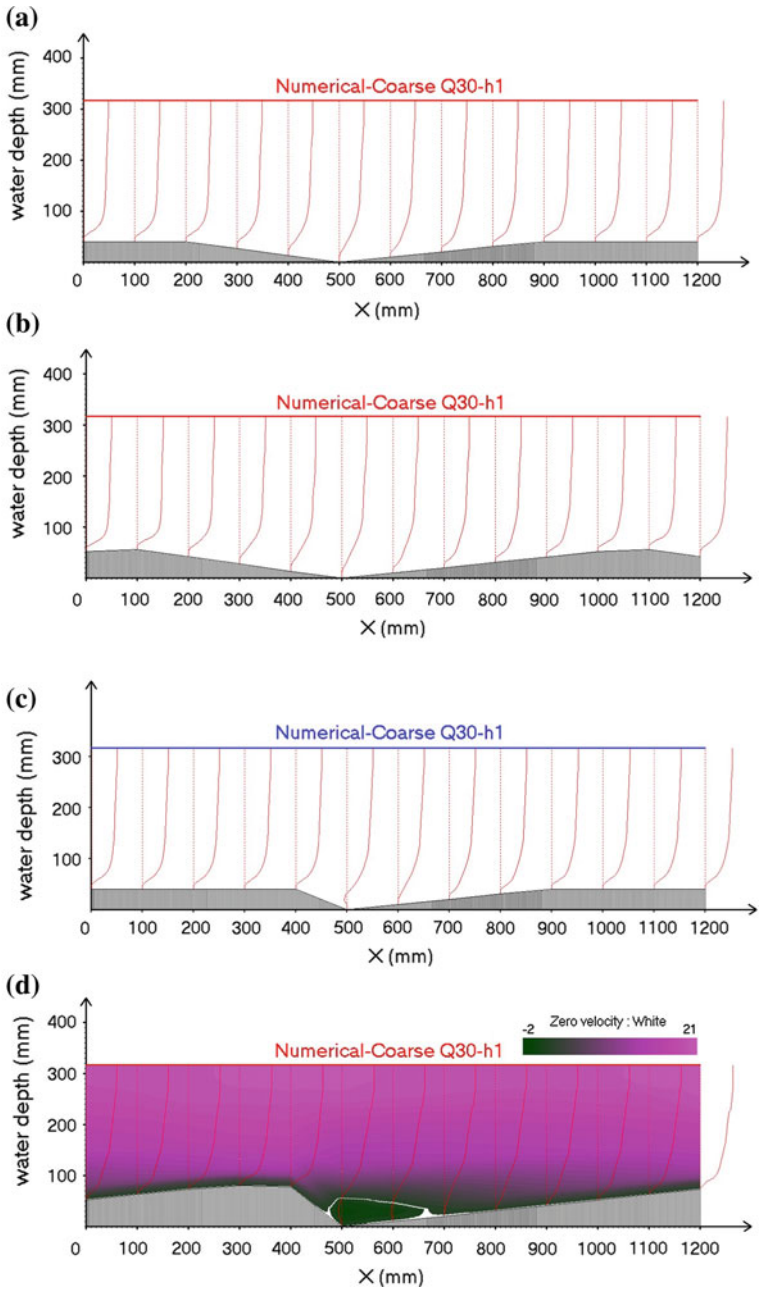

Fig. 5 Simulated velocity profiles over; **a** Low-lee-angle dunes (Δ= 4 cm, $\alpha = 8°$), **b** Low-lee-angle dunes with sharp crest (Δ= 6 cm, $\alpha = 8°$), **c** Sharp-lee-angle dunes (Δ= 4 cm, $\alpha = 38°$) and **d** Sharp-lee-angle dunes with sharp crest (Δ= 8 cm, $\alpha = 38°$). Contour map of time-averaged downstream velocity over simulated dunes type **d** and the separation region is presented as a sample

Table 2 The measured and simulated separation zone in different flow structure

Dune Types	Q (lit/sec)	Water depth (cm)	Max Velocity (cm/s)	Measured Separation Zone (L) (cm)	Simulated Separation Zone (L') (cm)	L/Δ
Sharp-angle dunes						
d	30	31.7	18	17.5	18.8	2.2
d	30	19.5	40	21.8	22.9	2.7
d	60	31.7	38	17.2, 18.2	18.8	2.2
d	60	19.5	82	26.1	22.3	3.3
c	30	31.7	19	5.5, 5.4	8.8	1.4
c	30	19.5	36	10, 12.1	9.7	3
c	60	31.7	36	7.8, 6.6	8.8	1.9
c	60	19.5	69	15.5, 14.9	9.6	3.8
Low-angle dunes						
a	30	31.7	19	0	0	0
a	30	19.5	33	0	0	0
a	60	31.7	38	0	0	0
b	30	31.7	20	0	0	0
b	30	19.5	40	0	0	0
b	60	31.7	41	0	0	0
b	60	19.5	61	0	0	0

4 Conclusion

The following conclusions are drawn from this study:

1. This study reveals that flow over low-angle physical and numerical models shows no separated permanent flow on the leeside of dunes (the same as the results of Best in [1]), since sharp-angle dunes over the bed have a considerable effect on the flow structure and they cause the flow to or not to separate in different flow regimes.
2. For flow separation, the angle on the leeside of the dune is the most important, and dune height and material are more important than flow velocity.
3. The numerical model provides a good overall consistency with the ADV measurements for both low- and sharp-angle dunes.
4. The result of a finer grid is more close to ADV measurement data.
5. There is a linear relation between the length of separation length and dune height.
6. For the same two dunes under the same velocity but different flow depths, larger separation occurs under lower flow depths.
7. A decrease in dune height causes a reduction in length of separation.

Acknowledgments The first author is grateful to Prof. Gerald Zenz for his kind support of this research in the Institute of Hydraulic Engineering and Water Resource Management, Graz university of Technology, Austria.

References

1. Best, J.L., Kostaschuk, R. & Hardy, R.J. 2004. The fluid dynamics of low-angle river dunes: results from integrated field monitoring, laboratory experimentation and numerical modelling. *In Proceedings Marine Sand-wave and River Dune Dynamics II*. Hulscher, S., Garlan, T. & Idier, D. The Netherlands.: University of Twente. 17–23.
2. Kironoto, B. A., & Graf, W. H. (1995). Turbulence characteristics in rough non-uniform open channel flow. *Proceedings of the Institution of Civil Engineers-Water Maritime and Energy, 112*, 336–348.
3. Kraus, N. Lohrman, A and Canrera, R. 1994. New acoustic meter for measuring 3D Laboratory Flows. Journal of hydraulic engineering 1,20 (3). 406-412.
4. Kostaschuk, R., & Villard, P. (1996). Flow and sediment transport over large subaqueous dunes: Fraser River, Canada. *Sedimentology, 43*, 849–863.
5. Kostaschuk, R. and J. Best (2004). The response of sand dunes to variations in tidal flow and sediment transport: Fraser Estuary, Canada. In: S. J. M. H. Hulscher, T. Garlan, and D. Idier (Eds.), Procedings of the 2 nd international workshop on Marine Sandwave and River Dune Dynamics, 1-2 April, 2004, pp. 849–863, University of Twente and SHOM, Enschede, the Netherlands.
6. Leopold, L. B., & Wolman, M. G. (1957). River Channel Patterns: Braided, Meandering and Straight, USGS Professional Paper 282-B: 39–103.
7. MacVicar, B. J., Roy, A. G. (2007). Hydrodynamics of a forced riffle-pool in a gravelbed river: 1. Mean velocity and turbulence intensity, Water Resources Research, 43, W12401
8. MacVicar, B.J., Rennie, C.D. (2009). Lateral distribution of turbulence and secondary currents in non-uniform open channel flow. 33rd IAHR Congress: Water Engineering for a Sustainable Environment, Vancouver, Canada, 1908–1915
9. Montgomery, D. R., & Buffington, J. M. (1997). Channel-reach morphology in mountain drainage basins. *Geological Society of America Bulletin, 109*, 596–611.
10. Olsen, N.R.B. (2011). A three-dimensional numerical model for simulate of sediment movements in water intakes with multiblock option. Users‘s Manual, by Nils Reidar B. Olsen, Department of Hydraulic and Environmental Engineering, The Norwegian University of Science and Technology
11. Roden, J. E. (1998). The Sedimentology and Dynamics of Mega-Dunes, Jamuna River, Bangladesh. PhD thesis, Department of Earth Sciences and School of Geography, University of Leeds, 310 pp.
12. Song, T., & Chiew, Y. M. (2001). Turbulence measurement in nonuniform open-channel flow using acoustic Doppler velocimeter (ADV). *Journal of Hydraulic Engineering, ASCE, 127*(3), 219–232.
13. Snyder WH, Castro IP (1999) Acoustic Doppler velocimeter evaluation in stratified towing tank. *Journal of Hydraulic Engineering 125*:595–603
14. Wilbers, A. W. E., & Ten Brinke, W. B. M. (2003). The response of subaqueous dunes to floods in sand and gravel bed reaches of the Dutch Rhine. *Sedimentology, 50*, 1013–1034. doi:10.1046/j.1365-3091.2003.00585.x.
15. Yang, S-Q., Chow, A.T. 2008. Turbulence Structures in non-uniform flows. *Advances in Water resources*, 31, 1344–1351
16. Yoon, J.Y and Patel, V.C. 1996. Numerical Model of turbulent Flow over Sand Dune. *Journal of Hydraulic Engineering 122*(1), 10–18.

Particle Image Velocimetry (PIV) Measurement and Numerical Modeling of Flow Over Gravel Dune

Artemis Motamedi, Hossein Afzalimehr, Gabriele Harb and Majid Galoie

Abstract This research presents recent advances on morphodynamic modeling of dunes. Boundary layer separation over gravel fixed dune has been investigated by using particle image velocimetry (PIV) technique. In order to complement and verify the measurements, both ADV and PIV techniques were used. The experiments were focused on the flow pattern based on different dune discharge. The final aim of this research is to improve the knowledge about separation zone. Therefore, the numerical model successfully simulates flow over dune. In order to assess the accuracy of experimental results, a numerical model (SSIIM) was used. The results of this numerical model show that ADV has a weakness point in measuring data 3 cm near to bed, whereas PIV results are more closed to the numerical model.

Keywords Dune · Lee angle · PIV · Numerical modeling · Separation zone

1 Introduction

In rivers, complex interactions among the turbulent flow, the sediment transport, and the bed morphology give rise to various types of river bed configurations. Depending on the flow regime type, the river bed can be either planed or covered

A. Motamedi (✉) · H. Afzalimehr
Department of Water Engineering, Isfahan University of Technology, Isfahan 84156, Iran
e-mail: artemis.mot@gmail.com

H. Afzalimehr
e-mail: hafzali@cc.iut.ac.ir

G. Harb · M. Galoie
Institute of Hydraulic Engineering and Water Resources Management, Tugraz, Austria
e-mail: gabriele.harb@tugraz.at

M. Galoie
e-mail: m.galoie@student.tugraz.at

P. Gourbesville et al. (eds.), *Advances in Hydroinformatics*,
Springer Hydrogeology, DOI: 10.1007/978-981-4451-42-0_43,

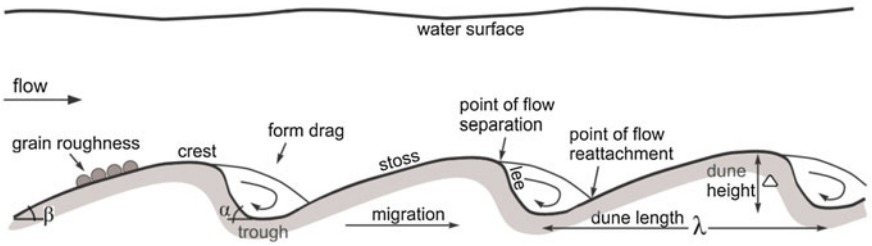

Fig. 1 Sketch of a train of dunes and flow separation

by ripples, dunes, or anti-dunes. In sandy or gravel-bed rivers, with subcritical turbulent flow, typically river dunes will be formed (e.g., [3, 4, 8, 15, 17, 20]). The stoss-side of dunes is gentle while avalanching at the leeside results in a dune with a brinkpoint and a slope at the angle of repose which is about −30° for sand in rivers. Although these dunes are common in many environments, several field studies have shown that many dunes may possess far lower leeside angles, perhaps for only 2–10° [11, 12 15] that may cause considerably different characteristics to the flow field. Because of the importance of dunes within both contemporary and ancient sedimentary environments, many studies have been devoted to the study of dune morphology and shape [10, 16, 20].

Over well-developed dunes, usually a flow separation zone is formed with a recirculating eddy in the dune lee (Fig. 1). In the shown figure, the flow over dune is illustrated. In the sudden expansion of the flow behind a dune, the static pressure increases in the direction of the flow. For a large enough pressure increase, the flow velocity near the boundary may become zero or even become reversed. Thus, eventually, if the leeside of a dune becomes so steep that the boundary layer encounters a sufficiently large advise pressure gradient, it separates from the boundary under the formation of eddies or vortices (see, e.g., [6], [9]).

Therefore, the aim of this research is to compare the physical modeling of flow over low and sharp-angle dunes, with numerical modeling (SSIIM) in order to answer these main questions.

Do the low-angle dunes necessarily cause the flow to separate?

What is the influence of the dune dimension on flow separation?

Is there any appropriate numerical model to simulate the flow over dunes?

To address these questions, in this research for the gravel fixed dunes, the stoss angle was considered around 6° and lee angle is 38° for sharp angle and 8° for low angle and the velocity was measured by PIV and ADV techniques. The dune dimensions also have taken from field measurements. It is chosen close to the unsteady field data of [20] which suggested heights of 10–30 % of the flow depth and lengths of 1–8 times the flow depth. In this research, the height was considered around 12 % and the length is three times of the flow depth.

2 Methods

2.1 Physical Modeling

The experiments were carried out in a specially designed re-circulating flume 12 m long, 0.75 m wide and 0.9 m deep [13] and it carried out in the Institute of Hydraulic Engineering and Water Resources Management of Graz University of Technology, Austria. One of the walls of the flume is made of perspex windows, providing a clear view of the flow. One centrifugal pump providing the flow around (30 lit/s) is located outside the flume. An electromagnetic discharge meter with a digital display is fitted with the outlet pipe to facilitate the continuous monitoring of the discharge. To ensure the same operating conditions in different experiments the water depth and the discharge are kept constant for all experiments. To perform the experiments, a total of two-dimensional model dunes were developed and placed with equal distances on the bottom surface ($\Delta = 4$ cm, $\lambda = 100$ cm, $\beta = 6°$ and $\alpha = 38°$ and 8°), in which the parameters were shown in Fig. 1 and the schematic view was presented in Fig. 2. Each dune spanned almost the width of the flume.

The velocity profiles were measured using both ADV and PIV. A side looking acoustic Doppler velocimeter (ADV) was used for velocity measurements. All together 13 different measuring locations at the trough and crest points of the dunes starting from crest to crest have been selected. The velocity data were collected for 120 seconds at the sampling rate of 200 Hz with the lowest point in each profile being 2mm above the flume bed surface and with the highest point (about 32 cm) at the trough.

Particle image velocimetry (PIV) has become popular recently. PIV is now a reliable method to measure quantitative parameters in complex flows [1, 19] and can be applied to the study of near-wall flows [7]. A real improvement of this

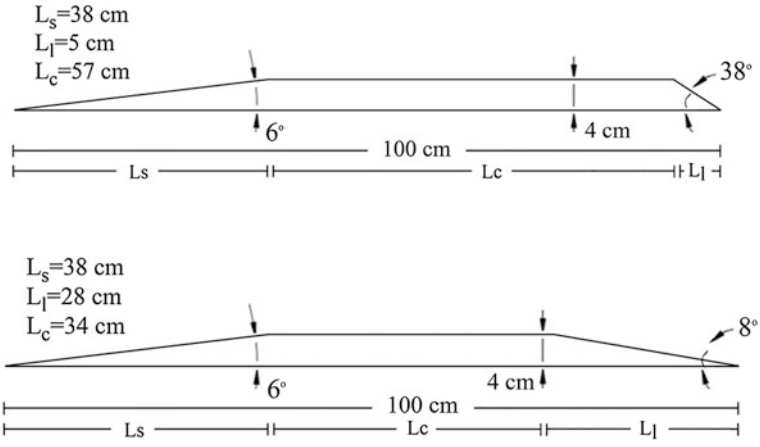

Fig. 2 Profile of the sharp and low-angle dune used for physical and numerical modeling

technique was the use of two cameras and to make a stereoscopic reconstruction in order to obtain the three components of the velocity field in a plane (i.e., 2D3C) [18, 21].

In the present research, the laser light sheet was oriented in the center plane of the flume. The single-pulsed Nd:YAG laser emits laser pulses with a maximum energy of 23 mJ per pulse/head at a frequency of 250 Hz with a temporal width of 4,000 ns and a wavelength of 527 nm. The thickness of the light sheet was 0.3 mm. The camera used (Photron FASTCAM SA-1) has an internal memory of 16 GB with 1.024 × 1.024 px sensor. The maximum frame rate at full resolution is 5.4 kHz. In the present research, the high-speed camera was coupled with the laser, so the same sampling rate was used. This internal memory limit results in a maximum of over 10,000 frames for a single measurement with duration over approximately 40s.

The current meter also was deployed at 13 positions over individual dunes, and a velocity profile was measured at each position.

In this flume, the discharge was equal to 30 lit/s, and in order to control flow velocity, a vertical gate at the end of the flume was used and the water depth (a vertical distance between the water surface and the bed at the lowest point of dune) was fixed at 32 cm.

In fully developed turbulent flow the Reynolds number was found to be $\mathrm{Re} = \frac{u_m h}{v} = 0.6 * 10^5$ and the Froude number, $Fr = \frac{u_m}{\sqrt{gh}} = 0.11$ where $u_m = 20cm/s$ is the maximum velocity observed at the height z =8 cm above the crest.

2.2 Numerical Modeling

To simulate dune separation zone, the program called "sediment simulation in intakes with multiblock option," or "SSIIM" was used. It was developed by Olsen [14] and based on the three-dimensional situation. This numerical scheme is based on a steady-state solution using a RNG k-ε turbulence model.

Structured grid for the numerical modeling is shown in Fig. 3.The grid size is 800 cells in the stream-wise direction, 75 cells in lateral direction, and 40 cells in vertical direction. The total number of cells equals $2.4 * 10^6$ and the cell size in *XY* plane is approximately 1 × 1 (cm^2).

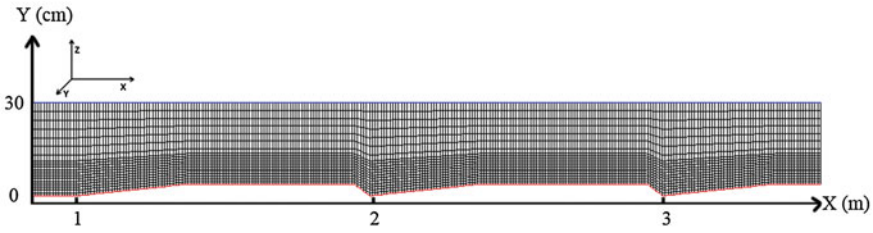

Fig. 3 Structured grid for the numerical modeling of sharp dune

3 Results

The mean downstream measured velocities over the experimental dunes by using PIV (Fig. 4) show that the flow separation is occurred in the flow over sharp-angle dunes. In Fig. 5, also measured velocity profiles in D, E, and G sections have been drown.

The profiles indicate the separation zone which appears in section D and follows to section H. Also, as it can be seen in Fig. 6, the developed numerical model with SSIIM confirms that flow separation exist in the dune leeside. The simulated separation zone is presented in Fig. 6.

Best and Kostaschuk [5] used measurements over low-angle dunes to show that flow separation occurs over dunes with maximum lower leeside slopes of 14°. In the present study, in order to check the ability of the calibrated model in predicting the separation zone, the numerical model with the same flow structures was applied.

The results indicate that a region of permanent flow separation does not form in the lee of these low-angle dunes (Fig. 7). Results from the ADV measurements also show the similar results to numerical model (Fig. 8).

The present research assesses the quality of Reynolds-averaged Navier–Stokes turbulence model for predicting the flow over two-dimensional dunes. Even though it is not possible to state at which exact leeside slope, the flow will separate [4], but the numerical model provides a good overall consistency with the ADV and PIV measurements. It seems that if the lee slope exceeds 8°, flow separation needs to be considered.

Generally, both physical and numerical models agree well with maximum downstream velocities of 0.20 ms^{-1} and show the flow separation in ($\alpha = 38°$) and no separation in ($\alpha = 8°$).

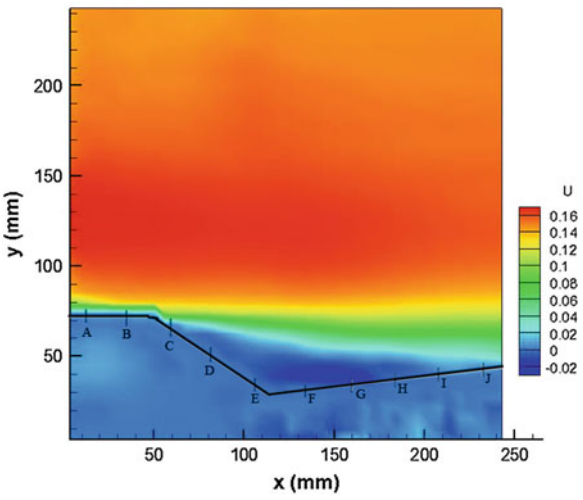

Fig. 4 Plot of measured downstream velocity (using PIV) in the physical model ($\alpha = 38°$). Flow is *left* to *right*

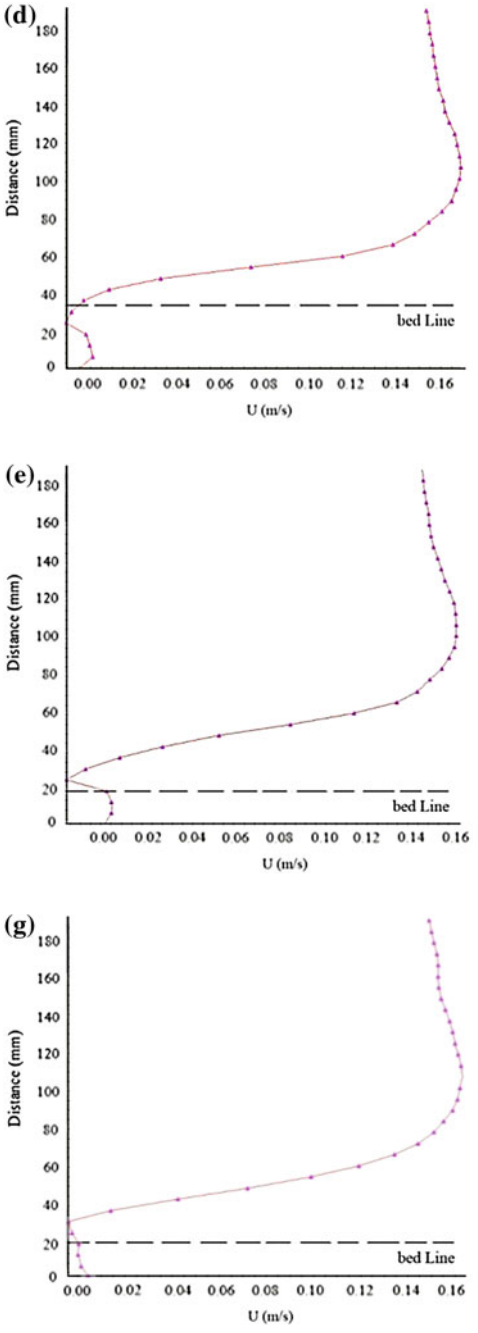

Fig. 5 Measured velocity profile by using PIV—section *D*, *E*, and *G* as an example

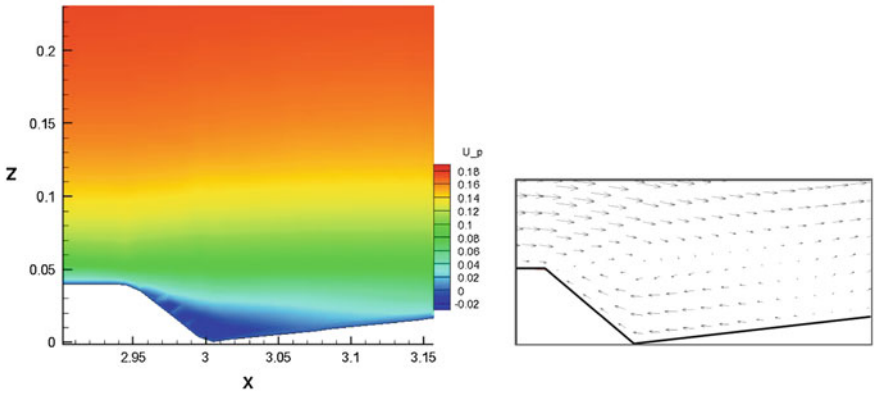

Fig. 6 Plot of downstream velocity in the simulated model ($\alpha = 38°$). Flow is *left* to *right*

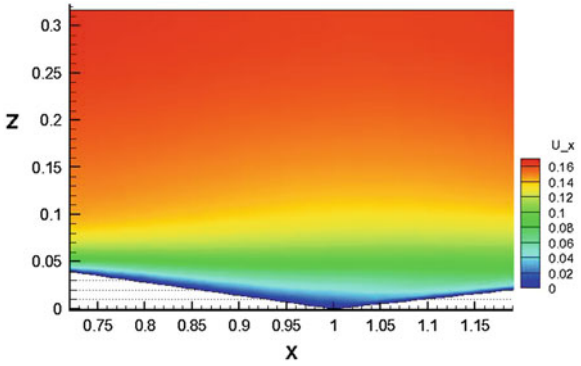

Fig. 7 Plot of downstream velocity in the simulated low-angle dune ($\alpha = 8°$). Flow is *left* to *right*

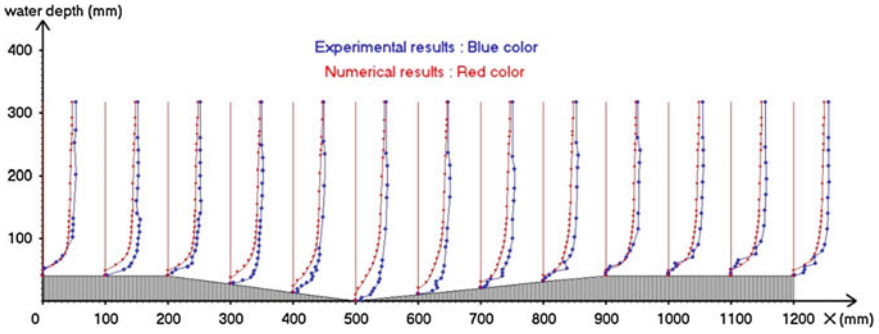

Fig. 8 Comparison of simulated and measured velocity profiles (ADV) over low-angle dune ($\alpha = 8°$)

4 Conclusion

The results confirm that no zone of permanent flow separation exists in the dune leeside and numerical model provides a good overall consistency with the ADV and PIV measurements for both low- and sharp-angle dunes. It may also possible to find the critical leeside slope of the separation zone by developing the SSIIM model on dunes.

Acknowledgments First, the author is grateful to Prof. Gerald Zenz for his kind support of this research in the Institute of Hydraulic Engineering and Water Resource Management, Graz university of Technology, Austria.

References

1. Adrian, R. J. (1991). Particle imaging techniques for experimental fluid mechanics. *Annual Review of Fluid Mechanics, 23*, 261–304.
2. Adrian, R. J. (1997). Dynamic ranges of velocity and spatial resolution of particle image velocimetry. *Measurement Science and Technology, 8*(12), 1393–1398.
3. Allen, J. R. L. (1968). The nature and origin of bed form hierarchies. *Sedimentology, 10*, 161–182.
4. Best, J. (2005). The fluid dynamics of river dunes: A review and some future research directions. *Journal of Geophysical Research*, *110* (F04S01), doi:10.1029/2004JF000218.
5. Best, J., & Kostaschuk, R. A. (2002). An experimental study of turbulent flow over a low-angle dune. *Journal of Geophysical Research, 107*, 3135–3153.
6. Buckles, J., Hanratty, T. J., & Adrian, R. J. (1984). Turbulent flow over large amplitude wavy surfaces. *Journal of Fluid Mechanics, 140*, 27–44.
7. Carlier, J., & Stanislas, M. (2005). Experimental study of eddy structures in a turbulent boundary layer using particle image velocimetry. *Journal of Fluid Mechanics, 535*, 143–188.
8. Carling, P. A., Golz, E., Orr, H. G., & Radecki-Pawlik, A. (2000). The morphodynamics of fluvial sand dunes in the river Rhine, near Mainz Germany. I. *Sedimentology and Morphology, 47*, 227–252. doi:10.1046/j.1365-3091.2000.00290.x.
9. Chang, P. K. (1970). *Separation of flow*. Oxford: Pergamon Press.
10. Gabel, S.L. (1993) Geometry and kinematics of dunes during steady and unsteady fows in the Calamus River, Nebraska, USA. Sedimentology, 40, 237–269.
11. Kostaschuk, R., & Villard, P. (1996). Flow and sediment transport over large subaqueous dunes: Fraser river, Canada. *Sedimentology, 43*, 849–863.
12. Kostaschuk, R. & J. Best (2004). The response of sand dunes to variations in tidal flow and sediment transport: Fraser Estuary, Canada. In: S. J. M. H. Hulscher, T. Garlan, & D. Idier (Eds.), *Proceedings of the 2nd International Workshop on Marine Sandwave and River Dune Dynamics*, (pp. 849–863). The Netherlands: University of Twente and SHOM, Enschede 1–2 April.
13. Motamedi,A. Afzalimehr, H. and Zenz, G. (2011) "Separation Zone and Morphodynamic Evaluation of Course Dunes using a process based 3D numerical model", European Journal of Scientific Research, ISSN 1450-216x vol.62 No.3, pp. 380–388
14. Olsen, N.R.B. (2011). A three-dimensional numerical model for simulate of sediment movements in water intakes with multiblock option. Users's Manual, by Nils Reidar B. Olsen, Department of Hydraulic and Environmental Engineering, The Norwegian University of Science and Technology.

15. Roden, J. E. (1998). The sedimentology and dynamics of Mega-Dunes, Jamuna River, Bangladesh PhD thesis, Department of Earth Sciences and School of Geography, University of Leeds, p. 310.
16. Sanderson H.C., and Lockett, F.P.J., (1983) "Flume Experiments On Bedforms and Structures at the Dune-Plane Bed Transition," Spec. Publs, Int. Assoc. Sedimentologists, vol. 6, pp. 49–58.
17. Simons, D. B., & Richardson, E. V. (1963). Forms of bed roughness in alluvial channels. *Transactions American Society of Civil Engineers, 128*(1), 284–323.
18. Soloff, S., Adrian, R., & Liu, Z. C. (1997). Distortion compensation for generalized stereoscopic particle image velocimetry. *Measurement Science Technology, 8*, 1441–1454.
19. Westerweel, J. (1997). Fundamentals of digital particle image velocimetry. *Measurement Science Technology, 8*(12), 1379–1392.
20. Wilbers, A. W. E., & Ten Brinke, W. B. M. (2003). The response of subaqueous dunes to floods in sand and gravel bed reaches of the Dutch Rhine. *Sedimentology, 50*, 1013–1034. doi:10.1046/j.1365-3091.2003.00585.x.
21. Willert, C. (1997). Stereoscopic digital particle image velocimetry for applications in wind tunnel flows. *Measurement Science Technology, 8*, 1465–1479.

Hydroinformatics Vision 2011

Klaus Peter Holz, Jean Cunge, Rainer Lehfeldt and Dragan Savic

1 Introduction: Working Group Organisation and Reporting

What is currently called "Hydroinformatics" (HI) has been developed within International Association for Hydro-Environment Engineering and Research (IAHR) and International Water Association (IWA), more precisely driven by a HI joint committee of both organisations. The committee is currently being in the process of enlargement to the third organisation: IAHS. The joint HI committee set up a working group on *HI Vision*; and the target of the working group was to produce two documents within limited time (end of April, beginning of May 2011):

(a) A full report to the joint IAHR/IWA/IAHS HI committee leading team. It is understood that the vocation of the report is to be made available at the same time to anybody interested in the field.

K. P. Holz (✉)
Brandenburg University of Technology, Cottbus, Germany
e-mail: kpeter.holz@hydroinf.com

J. Cunge
Société Hydrotechnique de France, Grenoble, France
e-mail: jacunge@orange.fr

R. Lehfeldt
Federal Waterways Engineering and Research Institute (BAW) Hamburg, Hamburg, Germany
e-mail: lehfeldt@hamburg.baw

D. Savic
Exeter University, Devon, UK
e-mail: D.Savic@exeter.ac.uk

P. Gourbesville et al. (eds.), *Advances in Hydroinformatics*,
Springer Hydrogeology, DOI: 10.1007/978-981-4451-42-0_44,

(b) A draft of shorter Synoptic report resuming the full report. Present document is a draft of this paper to be presented through the leading team of the committee to the governing bodies of the three organisations (e.g. IAHR Council) and also published.

It must be understood that there was no preposterous ambition within working group and the authors of the report to produce a kind of an "*HIvision manifest*" for the future. The ambition is to describe current situation as stemmed from years of experience, to enumerate a number of future (say next 10 years) developments and possibilities as are foreseen by the authors today, to produce a point of departure for further discussions and exchanges of views and, at the same time, to propose a number of practical actions, to be implemented now, and of aims which result from this vision of the future.

N.B.: the readers of the present Synoptic Report interested in arguments leading to its statements and in developments leading to its conclusions are encouraged to take knowledge of the full Report and its Appendices.[1]

From the point of view of the set up of tasks within working group, there is a "core working group" of four persons who were taking care of writing, editing and organising the work. Then, there are three "circles" of people interested in HI and in the results of the working group activities:

- The 1st circle of volunteers to read consecutive versions of the report and to respond to the "Core" within very short delay of the order of 10–15 days with criticism, modifications, comments and complements. This 1st circle counts some 15 persons.
- The 2nd circle of volunteers. They agreed to the same as the 1st circle, but with the delays much longer (of the order 4–6 weeks) and with less stringent engagement. This means that their comments and criticism may not be integrated in time in all consecutive versions. This 2nd circle counts some 20 persons.
- The 3rd circle of persons, who, the Core group of working group feels, should be informed about the progress. Although immediate reactions of these persons were not expected, their comments and opinions were of course welcome and taken into account.

Thus, the 1st circle members are really co-authors or, at least, permanent reviewers of the working group production: their intervention guarantees the quality of the results; the 2nd circle members are "more passive" reviewers of this production at intermediate stages.

[1] Appendices of the full Report are: Appendix 1: Authors and Reviewers of the Report; Appendix 2: Some Research Fields for HydroInformatics; Appendix 3: @qua network; Appendix 4: List of contacts to be set up with international working groups and conferences.

To make the common work more efficient and easier to all concerned, there has been opened a *discussion forum on Internet*. The address of the Web site is http://groups.google.com/group/hydroinformatics-vision.

This **HI Vision Forum** was open automatically to the members of 1st circle and 2nd circle until the end of the working group task. Others who are interested to participate in forum discussions were most welcome.

The above described organisation results from the wish of the "Core" to make sure that the views presented in the report reflect, or at least are accepted, by sufficient number of the HI Community members in order to avoid major errors or omissions.

2 Hydroinformatics: Where Do We Stand?

HI has a tradition and remarkable merits in the development of computational simulation software for physical processes of the water-environment world. Nevertheless, it is felt that for a long time, now there has been a *limitation* in innovation areas as compared to developments and evolution of what is called "water sector". HI, which within the IAHR stemmed from the activities of numerical simulation and hydrodynamic modelling, is still, within this environment, *generally* understood in such limited way. Steps are now needed to reshape HI to the needs of today and, even more important, of the future.

Indeed, already now and more in the future, there is the need for creative solutions to the challenges coming about with the move of society towards open information, to globalisation of business and markets and to networking in the Internet. The potential and options of modern information and communication technologies (ICT) will be implemented everywhere within the water domain. Question is: Will these future developments occur without being based on, influenced, helped by the experience of the IAHR/IWA HI currently existing community or does this community steps aside and constraints its interest to modelling technologies in hydrodynamics? In other terms, there is an alternative:

- Either this community concentrates on academic research in hydraulics and hydrology using to that end all ICT developments available and leaving water sector industry and stakeholders to "use the results of the research".
- Or this community will participate proactively, offer and use its past experience, in developing a new approach to water sector activities of research, implementation, applications, communication, information management, in common with all stakeholders (engineering, management, political, citizens), through innovative interwoven way of collaboration?

For the second possibility of the alternative (second bullet point above), the framework of the existing (since 1992) IAHR/IWA HI committee is obviously too

limited. That is why first of all enlargement of the committee to the International Association for Scientific Hydrology (IAHS) was decided couple of years ago, but up to now has not been implemented effectively. More significantly the committee choosing to follow the second possibility of the alternative decided to create a working group with the purpose to try to define a *Vision* for this domain. With obvious background, thinking that the future must not be constrained by IAHR/IWA/IAHS limits, but must extend bridges towards all domains of interest concerning water where HI concepts exist or will appear.

3 HydroInformatics Vision Aspects as Perceived by the Working Group

What is a "vision"? Various aspects of HI vision as conceived by the authors of the report are:

- *General aspects* HI is a domain of science and technology covering the management of information on the field of water and related subjects. This does not provide clear-cut frontiers and allows for overlapping with other domains. It does not define any specific (except for the word "water") clarification or limitations. Both drinking water pressurised pipe networks and socio-economic consequences down to legislation concerning water use may serve here as a typical examples of this domain. *Vision* What this domain will become within next, say, 10 years?
- *Specific aspects* HI ambitions to coordinate sciences and technologies related to water and water sector thus assuming horizontal role in interweaving the findings, initiatives and policies. *Vision* The interweaving, coordinating and synergetic use of findings and technology will become *conscious* and *organised* activity. In other words, postindustrial ICT revolution and increasing importance for humanity of water will at any rate tend *automatically* to link all strings together. This unavoidable evolution can be guided, accelerated and aided to reduce as much error as possible first through the *wide* recognition of that situation by *concerned stakeholders* and then thanks to their *conscious* attitudes and activities. This can be considered as the vision for ambitious community. The vision leading to ally and unite concepts in ways most useful for human purposes. It involves the problems of ethics, sustainability, future of the planet earth, etc., although the report has no ambition to develop them all.
- *Organisational aspects* Related to HI ambitions but, this time, to coordinate and interweave organisations, governments and individuals such as IAHR/IWA/IAHS committee on HI, governmental agencies. Those are many visions, not just one! *Vision* Staying within our (current HI community) frontiers of possibilities and competences, the ambition could be limited to build bridges over the

gaps, to act upon educational aspects, to encourage research in certain directions, to convince the stakeholders from and outside of engineering domains to work together using means of information management *and* of exchange that we can supply.

4 Changes that Condition HydroInformatics Vision-Background

The background against which one must consider the place of HI changed dramatically during last decade. Essential characteristic of the change in water/environmental areas is the reciprocal interactive evolution of societal and technical domains.

Water/environment issues, within these present days of climate change and growing global population, have become a major challenge for human economies and their social organisations. They necessitate more and more complex approaches at a more and more trans-national level. The essential aim of such management is to avoid, if possible or at least minimise, the risks of crises in water supply and waste water treatment for populations, in water scarcity for irrigation, in management of consequences of floods and so forth. The traditional vision of a "water domain" founded on a separation of problems and cycles (small/large) on one hand and "professions" (drinking water, sewage and evacuation, hydrology, fluvial, maritime, groundwater) on the other hand seems to fade away, leaving the room for unification/integration of all of this into a coherent unity.

Society over recent decades has become much more aware of the threatened sustainability of "the second economy", which we commonly call the "natural environment". Most built infrastructures are considered as interferences in the environment, and their impacts must be correspondingly minimised and, if possible, made controllable. This trend is supported in more recent times by the long-ongoing discussion on climate change. The water world, especially, has become much more sensitive to and aware of these issues. A new awareness of the notion of "environmental footprints" introduced itself in the society.

Awareness and sensitivity in a society which is becoming more open, transparent and communicative, has been multiplied by modern developments of the ICT. The Internet is accessible nearly everywhere at any time providing Web services for communication, information and sharing on documents, pictures, music and videos. Because of ease of access to and variety of information and views, the citizens in a postmodern condition of society (commonly associated with what the European Union Lisbon agenda likes to call an 'information society') have become more curious and active, and even proactive about upcoming changes and the consequences of these for their futures, and even for their lives. Politically oriented developments within societies that are, ostensibly at least, directed towards more educated and more engaged citizens, have led to more

individuals and public interest groups who want to understand what is happening within their environments: what is being planned on the local or global political level and why this should be good and beneficial to them. Groups want to be heard and to participate in decision making processes: they want to be involved in matters about which they care and communicate. It is essential, however, that they clearly understand if and which are the *objective constraints* related to physical laws or political/economic reasons and that whatever is done or wished *is the subject* to these constraints. The technical means for communication and information necessary to these ends are at hand. ICTs have dramatically changed whole economies and societies, and system components are becoming smaller and increasingly network-orientated and mobile, and the flexibility of software is opening new dimensions. "Information-sharing" and "cooperation" between citizens and stakeholders, consultants, authorities and lawmakers have become a central and feasible issue of the day.

Professional engineering and business are unthinkable today without the evolution of the Internet and mobile devices meanwhile representing the dominant infrastructure of ICT. Networking-embedded systems and networking services are offering new perspectives in nearly all fields from engineering to households; they are pushing developments in all areas, representing an enormous business market which will also reflect mentally on societal developments.

In view of these societal and technological changes, all of what is called "water sector" activities (including all activities and aspects of use, management, legislation and directives, protection and political decisions concerning water) is being completely transformed and modified. These transformations are founded on three pillars:

1. Dealing with water problems on different scales of structures and the integration in face of foreseen scarcity, generalised pollution, climate change and the growth of mega-cities.
2. Change in the composition of decision making bodies: instead of engineers only, a whole new entity composed of stakeholders including the general population, elected bodies, NGOs, the media, etc., is now evolving.
3. Penetration of all activities, structures, behaviour and reflexes of the whole water industry and indeed of all concerned groups and individuals by ICT, Internet and mobile communication networks.

It is in this context that the *definition of HI* as collection (including data surveys, etc.), creation (including modelling), interpretation (including integration of various domains inputs), communication (including projection of the results and impacts towards large public) and management (including aid in participation of decision makers) of information concerning water sector activities should be used. This is new, and to underscore this evolution, the working group proposes to use from now onwards the term HI (with capital I) rather than traditional one of HI. Indeed, HI, for becoming an accepted player in these fields, has to change mentality and views; it has to implement techniques and methods from ICT and information science to collaborate intensively with other disciplines, not only on

the technical level. Only in this way can relevant aspects of socio-economics, law and regulations, culture and traditions as well as workflow, psychology, information policies and media be integrated into 'system' approaches. Such systems will change the working situation of engineers, their education objectives, create job opportunities and influence societies; they will support decision making in collaboration with the public showing benefit and risk to involved citizens and stakeholders and help generating consensus.

HI takes and will take advantage of the general progresses of ICT (hard and soft), as all human activities do. Clearly, the increase of CPU power (massive parallel computing, cloud computing, etc.) extends the possibilities of our numerical models, and of 3-D displays; clearly, Web 2.x opens the access to our information to millions of new users; and the new products in the fields of micro-sensors, alternative power supply, wireless telecoms, revolutionise the whole domain of real-time monitoring and, consequently, real-time management. But the evolution in HI is finally driven, not by these techno-progresses but by the growing awareness that, even if modelling is historically the centre of HI, it should be connected interwoven with all the various aspects-businesses of the water-environment domain.

Viewed like that HI is the template to business process approach of all projects as well as implementation of management systems within water sector.[2]

5 HydroInformatics and its Main Areas of Interest and Activities Against the Background

5.1 Informatics and Information in the Water Sector

"HI" comprehends all information technologies, methods, models, processes and systems applied in the "water-sector" and water-issues-related neighbouring fields. Information is understood in an abstract sense; it may be about physics, environment, economy, social issues, organisation, law, regulations and more. Models and processes concern physics, business, workflow, communication, management and more again. Thus, HI applies, generates, models, manages, transforms, condenses and archives information concerning the "water sector".

Traditionally, HI has been focused on the numerical simulation of physical processes in so-called "models". This limitation is too narrow. The term model has to be widened up to any kind of *information to be modelled* in the water sector.

[2] A *business process* or *business method* is a collection of related, structured activities or tasks that produce a specific service or product (serve a particular goal) for a particular customer or customers. Business processes can be modelled through a large number of methods and techniques.

As information combines data, methods, syntax and semantic, any simulation model is just a piece of information in the same manner as an engineering report, a digital elevation model (DEM), a water level monitoring application and an operational plan of a treatment plant or a workflow map.

Activities in the water sector are oriented towards building, managing and operating water-related infrastructure and utilities as well as towards observation/understanding/management of hydro environment for providing water, for improving its quality, for managing its quantity and for protecting against damages in view of sustainability and climate change. The activities are embedded in the objectives of a sustainable socio-economic development of society and communication processes between citizens, stakeholders, companies and politicians.

We are at a time when the influence of modelling is growing rapidly. Models of complex physical and human behaviour are coming into routine use. Ordinary, everyday devices contain inbuilt processors running embedded models. We barely notice the insidious spread of models into our lives. HI community should be leading the way by embracing and promoting many and varied uses of models in water and environmental management and engineering.

Besides techniques and methods directed towards the description and functioning of systems, models remain the core technological elements of HI, but have to be understood, however, in a wider than traditional sense. Traditionally, they described the physics of flow and transport and its interaction with other aspects such as the growth and decay of species, habitats and populations, and then in terms of quality and quantity. These models interact with further models about socio-economic and societal developments of regions, generating a nonlinearly interacting system of models of whatever is supposed to constitute "the real world".

Projects, infrastructure and the business of organisational units have to be managed and coordinated. Strategies for workflow and for running processes of technical, business, financial and communication systems have to be designed for in-house and public and political environments. The transformation and interfacing of information from various fields has to be modelled by descriptions and methods which support their implementation in digital form. To create tools and methods, allowing all water sector stakeholders to conceive and interweave (if not normalise) integrated and coherent Information Systems is no doubt the future.

Models of physics and organisational processes might be seen just as generators of information providing raw data from diverse application fields. In "HI", this information has to be cultivated according to the pragmatics for which it has been produced. It has to be processed and adapted to the needs and objectives of the water sector. Important aspects are of course the diverse nature of interacting simulation models of physics, environments, societies, economies and organisations.

Models, however, are not the only aspects: information, be it raw from observation or from simulation, has to be transformed in such a way as to be communicated in a transparent manner to professionals, politicians and citizens for decision making and consensual understanding. Moreover, "models" are not necessarily in the form of software; they may also be intellectual concepts which,

if they concern the water sector and if they ask for informatics to be forwarded, must be put into action or disseminated within the HI domain.

HI domain, activity or movement embraces the full range of what is commonly called *business models*[3] from public open-source developments through to private commercial developments, without bias towards any particular business model.

Some explicit examples of the subjects that HI is related to and with which close interactivity, already existing, will develop tremendously:

1. Major role played by GIS as system structuring all information, as pivotal point of integrated Information System. Note that GIS as specific tool fades away, becomes a part of other bases like ORACLE Spatial.
2. Real-time problems: sensors, SCADA, Real-Time databases and related telecom systems;
3. Tools of operational management (work management systems), of the maintenance and of asset Management.

Whenever water-related problems, or, more widely, the environmental questions are concerned, there is *continuity* in the background of all of the activities that follow. Typically, in most situations, there is an initial "problem" stemming from engineering needs, from political or investment projects, etc. Then, one tries to find "solutions" that are nothing else but elements leading to or aiding the decisions. This logical chain from "generating fact" to the solution decision goes across a number of "businesses" or "stakeholders" and must be repeatable at any time. So, it is obviously highly desirable to maintain strong consistency in concepts, data and information along this chain. Such is not necessarily the case, but precisely this is a major point for HI because it is its "natural role" to ensure such consistency, mainly by conservation of *uniqueness* of data and information. When one considers the chain beginning with projects conceived by, say, administration or politicians and continuing through design, impact studies, decision to implement, construction and operation, there is a need for guidelines ensuring the consistency. HI can supply means and ways to elaborate such guidelines for various types of activities related to water sector.

5.2 Research and Science

The sustainable development of the water sector comes down, in implementation and praxis, to engineering tasks, and thus, "HI" must be seen as an engineering

[3] A *business model* describes the rationale of how an organisation creates, delivers, and captures *value*—economic, social or other forms of value. The process of business model design is part of business strategy.

In theory and practice, the term business model is used for a broad range of informal and formal descriptions to represent core aspects of a business, including purpose, offerings, strategies, infrastructure, organisational structures, trading practices, and operational processes and policies. Hence, it gives a complete picture of an organisation from high-level perspective.

discipline. In this sense, "HI" has its own research objectives which aim at the foundation and promotion of the water sector in all its aspects.

In short, research in HI domain might be summarised, albeit very unconventionally, under the term: "information and its model building". This may be understood in the sense of structuring information about physical and organisational processes. New techniques have to be developed, new methods designed, the range of validity and performance investigated and models be interfaced by a standardisation of procedures and data. Innovative concepts about geometrical representation and information-defined objects using by modern ICT must be investigated, with virtual communication and collaboration processes considered with *emphasis on nonengineering clients*, such as partners, as well as processes for education and promoting understanding in decision making. Integrated processes reflected in HI tools, which are sufficiently interconnected, may open new request and necessities for further applied research, basically in the bottle necks of existing technologies (such as new features in graphical tools, much faster computational engines, wireless nets and mobility).

5.3 Education and Life Long Learning

HI aims at the education of staff to do these kinds of jobs; such persons might even be seen as "information managers and advisors". Their profile is not one that is supposed to "manage" people or organisations: they are supposed to manage information within the complex areas of the water sector and to that end they must be knowledgeable in specific domains of this area. They must be knowledgeable enough to understand the constraints, difficulties, limitations and possibilities of these domains in order to be able to coordinate the information coming from each such domain and to organise the feedbacks and interactions that will be beneficial to the further development of both.

These persons must have a sufficient knowledge about water and environmental processes to run and validate the corresponding models; they must understand the processes that are mapped in the related models; they must be able to condense and interface information; they must be able to organise workflow and information processes; they must be able to manage documentation and presentation; they must be able to make information transparent so as to advice decision makers and communicate with the public. *Social skills* in collaborating with people of different professional and cultural backgrounds are needed. To optimise this whole, they must be able to make information and findings flow in interactive ways from one domain to another so that the knowledge, the progress, the innovations and the applications in a domain can be improved thanks to information coming from other domains.

This profile demands knowledge about the physics of water in hydraulics, hydrology and the environment, about mathematics and computational methods, about information modelling and communication as well as about the supportive

means of ICT. Complementary to these are methods of geometrical modelling, presentation, documentation and a spectrum of selected topics from computer and social science, economy and psychology, the latter supporting the skills necessary for a multicultural interdisciplinary collaboration in an international, sometimes virtual and environment. Those concerned should have a minimum of culture in civil engineering because of its central role in project implementation, but also in water/environmental legislation as well as in geography and cartography. The education should be "hands on" with models of all kind. The process of taking responsibilities should be inculcated through training by internships in companies. The outcome of such curricula should be an engineer who can support consensual views and actions of decision makers and users, on the one hand, and executive professionals and engineers, on the other hand, with respect to science, engineering and social environments. The engineer should be able to maintain this qualification lifelong by corresponding learning periods.

This leads to an intensive demand for HI educated engineers, managers and, above all, leaders in public services and in the private sector in a rapidly changing society.

5.4 Universities, Research and Professions

Universities are changing in modern times with the transition towards an "information society", under the "Bologna Declaration" and as mass education institutions. They are reacting to their new role by introducing new profiles and grades of professionalism. In Europe, the "Bachelor" is seen as a first profession qualification degree, while the "Master" has become the second degree that may or may not be sought by the future professionals, whether praxis or research-oriented. The "Dr Thesis" is a grade awarded at the end of a system of corresponding courses and a research project that in many cases is trivial or formal; in most cases, it has nothing common with requirements of new contribution to the field as it used to be until the middle of second part of 20th century. This requires universities to react correspondingly in terms of numbers and qualifications, and this requires a clear profile and definition of "HI education". At present, the profile is pretty vague and differs from place to place. Therefore, due to the international character of HI and in order to guarantee as much as possible the sanity of the profession, some standards concerning the educational profile are needed. The universities in the short term (some 10–15 years) should "standardise" their ideas about what is an objective and professional "HI" profile. Without this, the profession cannot interact or provide feedback to the university and the university cannot satisfy the needs of the profession. Today's most common idea on both sides is that "HI = modelling and/or GIS and/or programming, etc." and that is clearly not sufficient.

Standards cannot be imposed formally: they have to be developed by Academia in collaboration with the Profession and its Praxis. If there is a known curriculum framework and if the Water Sector professions recognise in practice the minimum

content of this curriculum, such as is necessary to be called a "HI diploma", then the profile of "HydroInformatician" will need to be clearly defined and founded. Note that, following Bologna agreement, the fundamental change of concept concerning doctor's degree opens the way to better specification of HI curricula in the sense that it gives 3 years more for specialised studies that replace original research required in time for Dr. degree.

Currently, the link between the research and practice is weak, and the time necessary to transfer the R&D results towards practice is shockingly long if one compares it with ICT domain. To improve the situation, there is a need to open existing HI community to (or even more: to create larger HI community inclusive of) engineering consultants that do the bulk of water-related engineering as well as to the water systems management companies and institutions (specifically urban water utilities).

5.5 And the IAHR/IWA Committee

It should be remembered that the present document is elaborated by a working group of the joint IAHR/IWA committee, and both IAHR and IWA have an obvious role in the future of HI. This role should be experienced through a number of activities:

- The research within the aquatic domain in areas such as modelling, measuring, surveying and computational hydraulics is traditional within the IAHR/IWA membership. However, the task to promote the links between this research and the requirements, quests and problems coming from Water Sector through HI should be better understood and carried out within all concerned groups.
- University Education: IAHR, by its very composition of a majority of university researchers and teachers, should proactively participate in the "Universities and Profession" activities described above.
- Within the Water Sector, many HI activities have been implemented and created (e.g. within IWA, but this is only an example). It should be the IAHR's role to try to bridge the relational gaps between these groups and institutions by offering them what the IAHR in this domain has been developed during the last decades.

The above points can be considered as the tasks for the HI committee.

6 HydroInformatics: Quo Vadis? What To Do?

There are two aspects of the future that are concerned in our present initiative. One is objective: whatever we wish, whatever we do, what is going to happen within next, say, 10–15 years; another one is subjective: what we wish, what we can do, what we shall try to do during this period.

1. What is going to happen? It seems clear today that the whole water sector is going to be completely penetrated by ICT and Internet-like technologies. All this may lead in a more or less distant future to the unification and possibly the standardisation of management of information within areas of water industry. The things will converge towards the concept of "smart water networking" including of course projects and implementation of works in coastal areas and river basins, for food and agriculture, for industrial use, energy production and biogas, for drinking and waste processing. Nevertheless, it is very likely that the driving force towards this will be urban water management and utilities. This is so because the population needs today are greatest in this area, because most of human population is going to be regrouped in the megacities, because this area is today very far behind the sophistication of ICT tools used in other water domains (e.g. numerical modelling) and, hence, the gradient of implemented innovative applications will be the steepest. Quite obviously all other domains will join in the run and the driving forces will come from the ICT industry, not from the hydraulic research, because the former produces industrially applicable, often off-the-shelf systems and devices that may modify the whole systemic approach while the latter can only produced embeddable tools like 4th generation modelling software. Because of the importance of the water, these developments will very quickly penetrate the domain of decision making, i.e., politics, financing of investments, social sciences, information and communication with citizens etc. On the other side of the spectrum, they will most likely completely modify current (traditional) way of working of consulting and also the relationship between the applications/industry (including consulting and contractors) and university research on the field of hydraulics, hydrology and water management:

   - It is *very* likely that today's market of the modelling software will decline and possibly fade away. It may well be replaced by "Modelling Software and Expertise as a Service". All recent developments of "Software as a Service", "Infrastructure as a Service", "Development as a Service" that so far have been limited to the area of computer and informatics applications will no doubt overflow into the water domain within next couple of years. Already most of applications we use on our laptops are stored somewhere in the cyberspace. And "cloud computing" will help it.
   - This will lead to a pressure from "modelling software and expertise" business on the water-oriented research to go beyond today's limitations in mathematical theory computational hydraulics and computational fluid dynamics. Same will happen to physics, e.g. sedimentation theories. This will also lead to a pressure on the university education and curricula. Indeed, such enormous, revolutionary changes will ask for different *technicalleadership* within the structures of water sector industry, i.e., for different generation of engineers. Given minimal 5 years cycle of engineering education, given the delay necessary to the education institutions to adapt themselves (at least another

5 or 10 years), there will be enormous push, coming from the needs of industry, towards LLL and postgraduate specialisation in specific courses and institutions.

- Networking-embedded systems and networking services are offering new perspectives in nearly all fields of technological infrastructure from engineering to households; they are pushing developments in all areas, representing an enormous business market. This also holds for the field of HI. Integrated intelligent electronic nets of all components and services must be designed and operated for generation, management, distribution and billing of fresh and waste water in cities, on the level of water-basins, for the management of floods and droughts beyond the regional level. But also the interlinking of water systems with other areas such as power generation, cooling and intermediate storage of energy under ever changing conditions has to be considered. Only through the use of such technologies, the challenges put by global warming and climate change could possibly be faced in the future.
  As an example of what would happen whatever we do consider the one of currently predominant business models: the sale or granting of in-perpetuity (generally 20 or 25 year) licenses to use software packages. We definitely see the demand for pay-by-use software, and technology advances now support this business model in a reasonable way. But we are already on the way towards Software as a Service becoming a regular business model for HI. There are already few companies doing just this, the information confirmed by the comments from 1st and 2nd circles of persons participating in elaboration of present reports. It is clear that current "model" based on selling packages is changing and will not last in the future. What we do not know is what will replace it—there are a number of possibilities!

2. What we wish or can do? We, i.e., what we used to call up to now and typically within IAHR/IWA territory, the HI Community? Assuming that what will happen at any rate within the near future was correctly described above, there are two possibilities: either we stay where we are and look on this new world from the top of our ivory towers; or we try to accompany the movement, to accelerate it as much as possible, to make some parts of it more coherent, take the leadership of our immediate neighbourhood towards integrating these changes. Incidentally, it means of course to stretch our networks beyond IAHR trying, however, to keep intellectual leadership in order not to lose the experience and tradition gained during last 30 years of existence of our "IAHR HI Community".

In this context, assuming that we chose the second way and that we can consider ourselves as leaders (among others) in the area, what should we do? *One may identify three skills that are necessary for leading strategically for long-term growth: understanding the operational environment, making clear decisions and involving others in the strategic process."*[4]

[4] Taken from a paper in Forbes Magazine but seems correct!

- Actually the most of the preceding paragraphs are devoted to "understanding the operational environment". The very attempt to describe (in a lengthy way) what we understand by "HI", as well as the present situation in industry and education, is precisely that.
- "Making clear decisions". In our case, it is first to state clearly the ambitions we have, and next the decisions of actions that we should take.

  Ambitions, even though we limit their extension to our domain of possible influence (that is rather limited…), are considerable. Namely *we wish to promote and maintain the name of HI*. We wish to make it accepted as a domain, the essence of which is to coordinate the results and the contents of a number of various fields of knowledge (including some "soft science" fields); to facilitate interactive transfers of concepts and ways of thinking from one field to another; to help in the elaboration of decisions (projects, actions, and policies) based on synergetic considerations of the results of various fields; to pave feedback paths from social requirements, through HI ways, tools and means, towards various fields while transferring concepts from one field to another in order to enrich them and to progress. Conceived as such HI is enriching itself through the progress of other domains and directing them towards applications. HI is itself a generator of innovations by the very fact of being a transversal approach that uses the progress of various disciplines. Our ambition is to push this concept through and participate in its development.

  There would seem to be a role for the HI Community not only to adapt to improved ICT but also to propose, test and communicate changing business and delivery models. This can be done through exchanges of opinions, criticism, etc. Such exchanges imply some kind of permanent correspondence platform or forum. New business models will be imposed by the market following ICT progress but the HI Community can help to discard what is not so good.

  The actions we can take:

  – To develop a wide (as wide as possible, *within and outside* of IAHR/IWA/IAHS) network of people and institutions interested and willing to participate in discussions, exchanges of view, of information.
  – To influence the education (LLL, graduate, undergraduate), both the institutions and curricula in order to help the advent of new engineering leadership.
  – To accompany, as individuals and members of institutions, of projects, of associations the "objective" developments and events as described above, trying to make those that are within our area as coherent and bold as possible.
  – To use as a springboard to this the IAHR/IWA/IAHS HI committee, International Journal of HI, HI bi-annual conferences.
- "Involving others in the strategic process". This of course is the essence of leadership activity (as distinct from management). It actually is the way of implementing the actions enumerated above. Our working group activity is the first step. The further steps would follow stemming from our report. We should take more of a coordination role by more actively making links with other organisations involved in the development of HI. For example, there is

considerable overlap between the activities of the integrated environmental modelling community and HI. Because of this situation, the HI working group will initiate, before the formal end of its activities, launching contacts with a number of organisations. The full report will be sent to them, and they will be asked to participate in setting up together some kind of the mailing-exchange list of addresses to contact. But then again it will be for the "HI community", with the IAHR/IWA/IAHS committee as the basis, to organise and act.